ISSN 0915-6348

NATIONAL INSTITUTE FOR FUSION SCIENCE

JSPS-CAS Core University Program Seminar Proceedings of Japan-China Joint Seminar on Atomic and Molecular Processes in Plasma Oct. 26 - 31, 2009, Xi'an, China

Eds. F. Koike and C. Dong

(Received - Feb. 12, 2010)

NIFS-PROC-81

Feb. 24, 2010

RESEARCH REPORT
NIFS-PROC Series

TOKI, JAPAN

JSPS-CAS Core University Program Seminar

Proceedings of Japan-China Joint Seminar on Atomic and Molecular Processes in Plasma

October 26 - 31, 2009, Xi'an, China

Edited by

Fumihiro Koike and Chenzhong Dong

Abstract

As one of the activities of JSPS-CAS Core University Program, Japan-China Joint Seminar on Atomic and Molecular Processes in Plasma was held on October 26 - 31, 2009 in Xi'an, China. The total number of the officially registered participants was 54, in which 18 from Japan, 35 from China, and 1 from USA. And this seminar is an extension of the last two seminars that were held on March 6 – 11, 2004 in Lanzhou, China, and on October 6 -12, 2007 in Dunhuang, China.

In the nuclear fusion plasma, there are quite a variety of atomic processes such as ionization, excitation, radiative recombination, non-radiative recombination (di-electronic recombination, collisional electron transfer), cascade radiation, and cascade Auger decay over the wide range of plasma temperature. The knowledge of those processes is indispensable for the evaluation and improvement of the plasma properties. Because of the diversity of the subject, it is desirable to investigate them by international collaboration groups. The present seminar may contribute to realize the above stated aim; especially it has given an opportunity for the collaborative workers to illustrate their achievements. This seminar summarizes the collaborative researches for the last decade and propose the issues for the future prospect.

Key words:
atomic processes, plasma spectroscopy, excitation, ionization, recombination, charge transfer, X-ray, polarization spectroscopy, atomic database, tokamak, divertor, LHD, molecular processes, atomic structures, radiative recombination, di-electronic recombination

Preface

As one of the activities of the Core University Program (CUP) entitled “atomic and molecular processes in plasma”, a seminar “China-Japan Joint Seminar on Atomic and Molecular Processes in Plasma” was held on October 26 to 31, 2007 at Xi’an Jiaoda Nan Yang Hotel, Xi’an, China. This is the seminar that was organized under the CUP agreement between Chinese Academy of Science (CAS) and Japan Society for the Promotion of Science (JSPS), which was initiated in 2000 and will last 10 years. And, further, this seminar is an extension of the last two seminars that were held on March 6 – 11, 2004 in Lanzhou, China, and on October 6 -12, 2007 in Dunhuang, China. Since the first seminar in 2004, the researchers from both Japan and China carried out a number of significant studies in atomic and molecular processes in relation to the fusion plasma. The proposal of the present joint seminar has placed its intention not only on the presentations of the collaborative studies, but also on offering an opportunity for the wide range of researchers from both countries to be acquainted with each other, who would have made an extensive exchange of information about the recent progress of the research activities, and also would have made an extensive discussion about the plan of the future collaborations.

In the present seminar, the total number of 38 oral talks was presented by experts from Japan, China and USA, and, furthermore, quite a few contributions were presented by posters. The total number of the officially registered participants was 54, in which 18 from Japan, 35 from China, and 1 from USA. In the opening remarks, firstly, Professor Jiaming Li of Shanhai Jiao Tong University presented a warm address. Professor Takako Kato, who is an emeritus professor of National Institute for Fusion Science, gave a cordial greeting to the seminar.

The seminar was in always a friendly and active atmosphere. As of the intermission of the seminar, participants visited The Museum of Terra Cotta Warriors and Horses and they further enjoyed several kinds of ethnic activities in the suburbs of Xi’an City. During the seminar, the participants exchanged their new research results, discussed about the outlook for new research fields. They tried to promote further developments in mutual collaborations between the countries and the experts. It has given an atmosphere that a subsequent meeting should be desirable to be planned in the near future.

The present issue of the proceedings has collected 34 papers from the delegates of the seminar. It covers the spectroscopic properties of atoms and ions in the plasma, the collisions of electrons or ions with atoms or ions in the plasma, the analysis and diagnostics of the confinement fusion plasma, the atomic data compilations and the database constructions, the

molecular processes in the confinement fusion plasma, and, further, topics from wide area of atomic physics related to plasma. The present issue also includes the scientific program of the seminar, the group photo as well as the list of participants.

On behalf of the organizing committee, we would like to express our sincerest thanks to all the participants who made active contributions not only in the formal presentations but also in the fruitful discussions. We would like to acknowledge everybody who devoted very hard work for preparing the seminar. Finally, we would like to acknowledge the administrative as well as the financial supports from Northwest Normal University, and the National Institute for Fusion Science.

Chenzhong Dong
Local Chairperson,
Northwest Normal University, Lanzhou, China
Fumihiro Koike
Organizing Committee,
Kitasato University, Sagamihara, Japan

Contents

The 3rd China–Japan Joint Seminar on Atomic and Molecular Processes in Plasma

Behavior of carbon impurity ions during radiation collapse and non- radiation collapse

T. Kato, I. Murakami, D. Kato, H. Funaba, K. Sato, C. Suzuki and N. Yamamoto[1]

National Institute for Fusion Science, Toki, Gifu, 509-5292, Japan,
[1.] Institute for Laser Engineering, Osaka University, Suita, Osaka 565, Japan

Abstract
We measured time-dependent EUV spectra to make a quantitative study of impurity spectral lines (C III, C IV and C V) during radiative collapse and non- radiation collapse in the Large Helical Device (LHD) at the National Institute for Fusion Science. We estimate the time dependent electron temperatures from the intensity ratios of spectral lines from C V using a collisional radiative model of carbon ions. We find that the intensity ratios of C V are affected by recombination at the end of plasma in the case of radiation collapse. In the case of non- radiation collapse, the temperature derived from CV spectra increases after the NBI heating terminates. This indicates the radiating ions are closer to the center of the plasma.

1. Introduction:

Plasma impurities are important from the viewpoint of energy balance and particle transport in plasma simulation or modeling of many kinds of plasmas, including fusion plasmas, astrophysical plasmas and industrial plasmas. Impurities play a key role for plasma evolution. We would like to know the absolute values of ion and electron densities, electron temperature, radiation power, etc. Spectroscopic measurements give a useful, quantitative way to study both plasma and impurity behavior. For that reason spectroscopy is a central technique for plasma diagnostics. In this paper, we present EUV spectra from fusion plasma experiments in the Large Helical Device (LHD), and study the behavior of impurities in representative cases showing radiation collapse and non- radiation collapse.

Radiation collapse in a fusion machine is related to the problems of the density limit and the threshold temperature [1]. "Radiation collapse" occurs when the plasma temperature decays rapidly together with strong emission of radiation. It is related to the power balance between input power and emitted radiation power. Radiation collapse is thought to be caused by an increase of electron density and a decrease of electron temperature, leading to a significant increase in radiation loss. This phenomenon is not understood quantitatively at present. The effect of the plasma electric field on radiation collapse was discussed recently [2]. In order to investigate how and why fusion plasmas collapse, we can measure time dependent impurity emission spectra and study the intensity ratios of carbon ions. In previous studies [3,4], we have measured the intensity ratios of carbon ions as plasma diagnostics to estimate the plasma temperature or density. In this paper we show some quantitative features of radiation collapse by comparing temporal behaviour of the intensity ratios of carbon ions with other measurements of plasma parameters.

Ionization and excitation processes are dominant in plasmas while the heating is on. These processes have often been studied. However the recombination processes have not been studied as well in experiments. In this paper we are interested in recombination processes when the plasma decays. We compare the behavior of

carbon ions during radiation collapse with non-radiation collapse. In the case of radiation collapse, the temperature derived from intensity ratios decreases towards the end of plasma. However in the case of non-radiation collapse the derived temperature is found to increase after the heating is terminated. This suggests the radiating ions are closer to the plasma center.

2. Experimental:

In some cases the plasmas maintain a high temperature until plasma heating stops because the plasma heating proceeds evenly, while on many other occasions the plasma undergoes a very abrupt radiation collapse. "Radiation collapse" is used for the phenomenon when a plasma decays very rapidly together with a large cooling rate from radiation [1]. A typical example of each is given in Fig.1. The main component of the plasma is hydrogen and hydrogen gas is puffed into this plasma continuously.

For a radiation collapse case (#55644), the total neutral beam injection (NBI) heating time was 2.3s and a peak stored energy of ~700 kJ was attained after approximately 1 s. The maximum electron density was over 10×10^{19} m^{-3} and saturated for measurement. The radiated power attained a maximum over 8 MW just prior to 1.2 s. This behaviour can be seen in Fig.1(a) from which it is obvious that there is an abrupt increase in radiated power that coincides with the decay of the stored energy.

For the stable sustained heating (#55642) (neutral beam heating) presented in Fig1(b) the stored energy increased to a value of ~1300 kJ. Thereafter the stored energy decayed steadily over a further 0.3 s. The NBI for plasma heating continued until ~3.3 s and high temperature plasma ended at 3.7 s. The electron density was seen to rise steadily at first and decrease gradually after a further 2.5 s and decayed abruptly in less than 0.1 s after the input energy became negligible at 3.7 s. The radiated power measured by a bolometer essentially followed the electron density curve but was seen to peak abruptly during the cooling phase between 3.5 and 3.7 s after the initiation of the discharge when a maximum value of 3.0 MW was emitted at 3.7 s.

Spectra were recorded on a Schwob-Fraenkel 2.0 m SOXMOS Spectrograph containing two CCDs fibreoptically coupled to microchannel plate/phosphor assemblies which gave an average resolving power of ~600 with a 600 mm^{-1} grating and ~ 300 with 130 mm^{-1} throughout the wavelength range of interest. It was possible to record spectra from both the centre of the discharge and also close to the edge or 24 cm from the centre. Generally the line of sight of the measurement is fixed through the center of the plasma. It includes the region from the lower temperature edge to the high temperature core. We can tilt the direction of the spectrometer and can measure off center. The spectra in this experiment were measured every 20 ms and 400 ms. The effect of the plasma rotation (~10 km/s) on the wavelength measurement is smaller than the accuacy of the measurement. The Stark and Zeeman effects are also negligible. The time dependent spatial distribution of the electron temperature and density was measured by Thomson scattering [5] and the radiation power measured by imaging bolometers [1] in our experiments.

3. Intensity ratios of CV ions by collisional radiative model

Theoretical calculations for the line intensities are performed with the use of our collisional-radiative model for He-like ions[6]. We used the excitation rate

coefficients evaluated by Suno and Kato[7] for the transitions relating to the levels with n = 2 where n is a principal quantum number. We analyzed the two sets of the intensity ratios of C V; I(248.6A, 1s2p ^{3}P– 1s3d ^{3}D) / I(227.2A, 1s2s ^{3}S– 1s3p ^{3}P) and I_i(40.73A, 1s2 ^{1}S- 1s2p ^{3}P) / I_r (40.27A 1s2 ^{1}S– 1s2p ^{1}P).

The line intensities are written as follows,

$I_{ij} = A_{ij} n_i$,

where n_i is a population density of an excited state i, and A_{ij} is a transition probability from the i-th state to the j-th state. The population density n_i of He-like ions is written

$n_i = a_i n(1s^2) + b_i n(1s)$.

Here $a_i n(1s^2)$ is an ionizing component which is proportional to the population of the $1s^2$ ground state of He-like ions and $b_i n(1s)$ is a recombining component which is proportional to the population of the 1s ground state of the upper ion (H-like ion). In the case of ionizing plasma, strong lines are emitted from low levels whereas in the case of recombining plasma strong lines are emitted from higher levels [8].

The intensity C V 227A is stronger than C V 248.6A in ionizing plasma because excitation from lower states is stronger to the level 1s3p than 1s3d. On the contrary the line CV 248.6A is stronger than C V 227A in recombining plasma because recombination rate to 1s3d levels is larger than to 1s3p levels. Thus this line ratio is a useful signature of the atomic kinetics. The theoretical intensity ratios for a CV line pair I(248)/I(227) are shown in Fig.2 (a) for ionizing, equilibrium and recombining plasmas as a function of electron temperature with electron density $n_e = 10^{13}$ cm^{-3}. The intensity ratios increase when the recombination process increases. The theoretical intensity ratios for the line pair I_i(40.73)/I_r(40.27) are plotted in Fig.2 (b) as a function of electron temperature with $n_e = 10^{13}$ cm^{-3}. In ionizing plasma, the singlet resonance line I_r(40.3A) is stronger than the intercombination line in the triplet system I_i(40.7A), whereas the intercombination line are stronger than the resonance line in recombining plasmas. The behaviour of the intensity ratios I(40.73)/I(40.27) are similar to those of I(248)/I(227).

3. Measurement

3.1 Spectra in 200 – 346 Å range:

We measured EUV spectra from LHD plasma with a grazing incident spectrometer SOXMOS [3] using a 133 mm^{-1} grating. Two different wavelength regions, 200 – 346A and 953 – 1232A were measured together every 20 ms as shown in Fig.3. These spectral ranges are chosen to include the emission lines from carbon ions. The line intensity ratios give useful information for plasma diagnostics. In this paper we use the line intensity ratios to investigate the plasma state. The main observed line pairs used to obtain the intensity ratios are as follows; C V 227.18A(1s2s ^{3}S – 1s3p ^{3}P) and 248.6A(2s2p ^{3}P – 1s3d ^{3}D), C IV 312.4A(2s – 3p) and 289.22A (2p – 4d), C III 977.02A (2s2 ^{1}S – 2s2p ^{1}P) and 1175.5A (2s2p ^{3}P – 2p^2 ^{3}P), H I 1024A(1s – 2p) and 1215.7A(1s – 3p). Time-history comparisons suggest that the increase of total radiation emission at the beginning is mainly from C IV lines and later from C V lines [4].

3.1.1. Radiation collapse case

We studied time dependent line intensity ratios for a plasma with radiation collapse measured at NIFS-LHD (shot number #55644). The plasma was heated by Neutral Beam Injection (NBI) and a hydrogen gas puff was started at 0.5 s from the beginning of the plasma and continued until 1.1 s. The time history of the intensity

ratios I(1175A)/I(977A) of CIII and I(248)/I(227) of CV is shown in Fig.4. Intensity ratios are almost constant during the heating until 0.94 s when the electron density begins to increase due to the gas injection. The intensity ratios increase from 0.94 s until 1.08 s. The electron temperature begins to decrease at 1.0 s and plasma decays before 1.2 s [4]. The lines from CV ions disappear after 1.18 s although lines from CIII are observed for a long time because the NBI heating continues and supports a low temperature plasma even after the radiation collapse. The low counting rates of CV lines after 1.2 s in Fig.4 (a) are probably noise due to low temperature.

The values of the observed line intensity ratios I(248)/I(227) are around 0.7 during the heating. These small values indicate that the emission is produced by excitation in an ionizing plasma, and the electron temperature is estimated to be about 400 eV. After 0.94 s the intensity ratio increases rapidly and this indicates a contribution from recombination. We also estimated the temperature from another line pair (the intercombination line to the resonance line pair of C V) for other experiments with Xe puffing and the derived temperature was about 200 eV as discussed in the next section. The radial position for 400 eV of our shot is $\rho = 0.95$ from the temperature distribution measured by Thomson scattering where ρ is the scaled radius ($\rho = 1$ is the last closed magnetic surface). The spatial distribution of the radiation power measured by bolometer has a peak at $\rho = 0.94$. Therefore we conclude the electron temperature of C V region is the same as the peak region of the radiation power measured by the bolometer. In Fig. 5 we plot the observed intensity ratios against the temperature derived from the bolometric measurement. This figure shows that the intensity ratios are larger at lower temperature. The intensity I(248A) increases more rapidly than I(227A) at lower temperature. This indicates that the recombination effect on the population density of the upper level 1s3d ^{3}P of the line 248A is stronger than that of of 1s3p ^{3}P of the line 227A. In order to explain the increase of the ratios quantitatively it is necessary that the ion ratio C VI/ C V be about 30 which means the amount of H-like C is 30 times of He-like C. We made a time dependent theoretical calculation for carbon ions. It is found that the total radiation loss is mainly produced by excitation although the line CV 248A is affected by recombination and the ion abundances are changing due to the recombination process.

3.1.2. Comparison with non-radiation collapse.

We also measured the spectra for a shot (#55642) in which the plasma decays without radiation collapse after the NBI heating terminates. The temperature and stored energy decay gradually over 0.4 s as shown in Fig.1(b) after 3.28 s. We derived the time history of the observed intensity ratios I(248)/I(227) of carbon lines. It is found that the behaviors of the intensity ratios are quite different from the case of radiation collapse as shown in Fig.6. The intensity ratios of CV decrease rapidly although they increased in the case of radiation collapse as shown in Fig. 4. This means that the temperature where CV ions exist is increasing from our calculation shown in Fig.2. The values of the observed intensity ratios in the later period are small compared to the theoretical calculations. This might be an atomic data problem. After the heating turns off, the plasma becomes smaller and the electron density increases according to the density measurement by Thomson scattering. Therefore it appears that CV ions move towards the center in the decay phase. However this phenomenon needs more careful analysis.

The intensity ratio I(248A)/I(227A) increases after radiation collapse and the derived temperature from the intensity ratios decreases. This means that the position of CV ions is always at the edge. On the other hand the intensity ratio decreases for

non- radiation collapse after NBI is terminated. The derived temperature increases after NBI is terminated. The observed intensity ratios are too small compared to the theoretical values in the later period.

3.2 Spectra in 30 - 42 Å range

In order to confirm the results obtained in the previous section on the intensity ratios of CV in recombining plasmas for radiation collapse and for non-radiation collapse, we analyzed the resonance line 40.27A ($1s^2\ ^1S$ – $1s2p\ ^1P$) and inter-combination lines 40.73A ($1s^2\ ^1S$ – $1s2p\ ^3P$) measured from LHD with a 600 mm^{-1} grating. The spectra were measured every 400 ms. The measured spectra for radiation collapse (#61450, Xenon gas puff) is shown in Fig. 7 and the time dependent intensity ratios are shown in Fig.8. The plasma begins to collapse at 0.8 s for this shot. As is seen in Fig.8, the intensity ratio I(40.73A)/ I(40.27A) increases for a time; the temperature derived from the intensity ratios decreases from 230 eV to 120 eV in time assuming an ionizing plasma. This derived temperature is a lower limit value.

In the case of non-radiation collapse (#61411, Neon gas puff), NBI stops at 2.3 s. The observed intensity ratio decreases after NBI stops as shown in Fig. 9. The derived temperatures assuming ionizing plasma increases from 150 eV (2.3 s) to 200 eV (2.6 s) and finally decrease to 90 eV (3 s) when plasma disappears. It indicates the position of C^{4+} ions move inwards after NBI off. This behavior is the same as discussed in Sec. 3.1.2. The electron density distribution measured by Thomson scattering also shows the density near the center increases at the end of the plasma.

It is found that the intensity ratios I(40.73A)/I(40.27A) for n = 1 – 2 transitions show the similar results as the line ratios I(248A)/I(227A) for n = 2 - 3 transitions as discussed in Sec. 3.1. The derived temperature decreases for radiation collapse and the derived temperature increases for the case of non-radiation collapse after NBI stops. When we observe the radial distribution of the electron density for non-radiation collapse, the electron density near the center increases by more than a factor two at the end of plasma although the electron temperature decreases.

5. Summary and discussions

We measured time-dependent spectra from carbon ions for the shots with radiation collapse and non-radiation collapse. The main part of the radiation loss is probably CIV and CV line emission from the time history of line intensities. The plasma decays in 0.1s for the case of radiation collapse. For a shot of radiation collapse (#55644), the intensity ratios CV I(248A)/I(227A) and CIII I(1175A) / I(977A) increase at the end of plasma. They show the electron temperature decreases after radiation collapse. They also show an increase of the recombination component after 0.94 s. In order to explain the increase of the observed intensity ratios, it is necessary to include the recombination component from H-like ions which is about 30 times of He-like ions. We could explain the increase of CV lines by recombination processes from CVI to CV. However most of the radiation is produced by excitation, not by recombination.

We compared the time history of the intensity ratios for experiments with radiation collapse and non-radiation collapse. The plasma decays in 0.4s in the case of non-radiation collapse after NBI terminated. The intensity ratios of CV I(248A)/I(227A) for non-radiation collapse (#55642) decrease and indicate an ionizing plasma, quite different from those for radiation collapse. The derived electron temperature where C^{4+} exists increases after NBI is turned off. This might indicate the C^{4+} ions move

towards the center after NBI turns off or might an effect of recombination at the same position. We will study the recombination effect on the spectra for non- radiation collapse.

In order to confirm the results obtained from the intensity ratio I(248A)/I(227A) , we analysed the two CV lines, the resonance line (40.27A) and the intercombination line (40.73), for the shot of radiation collapse (#61450) and for non- radiation collapse (#61411). These intensity ratios I_i(40.73A)/ I_r(40.27A) show similar behavior to those of I(248A)/I(227A); the derived temperature decreases for radiation collapse, although it increases for non-radiation collapse.

We would like to clarify why the derived temperature increases after the heating is terminated. Do the carbon ions C^{4+} move towards the centre of the plasma or is this just the recombination effect?

We found the different behaviour of the intensity for shorter wavelength lines 40.27A, 40.73A) and longer wavelength lines (248A, 227A). The intensities of 248A and 227A increase at the end of plasmas for both radiation collapse and non-radiation collapse. However the intensities of the resonance line and the intercombination line decrease for non- radiation collapse case after NBI terminated.

We will study this difference further. We plan to extend our time-dependent model for carbon ions. We will also study radiation collapse caused by radiation from other elements such as neon, iron and xenon.

The observed intensity ratios I(248A)/I(227A) for non radiation collapse are too small (below 0.5) compared to the theoretical values. This might be atomic data problems for n = 3 transitions. We could not find complete data sets for n = 3 transitions in ref. [7]. We need accurate data for n =3 transitions of He-like C^{4+} ions.

Acknowledgement:
This work was partly supported by the research collaboration program in NIFS.

References:

[1] B.J. Peterson et al 2006 Plasma Fusion Research, **1**, 45
[2] K. Ida et al, 2005 Nuc. Fusion **45**, 391
[3] T. Kato et al, 2002 Current Developments in atomic, molecular and chemical physics with applications, Kluwer Academic/Plenum Publishers, New York, 265 - 272
[4] T. Kato et al, 2007 Transactions of fusion science and technology, 126, 51
[5] K. Narihara, I. Yamada, H. Hayashi and K. Yamauchi, 2001 Rev. Sci. Instrum. , 72, 1122
[6] T. Fujimoo and T. Kato, Phys. Rev. A 30, 379 (1984)
[7] H. Suno and T. Kato, Atomic Data & Nuclear Data Tables, 92, 407 – 455 (2006)
[8] T. Fujimoto, j. Phys. Soc. Japan, Vol.47, 265, 273, (1979), Vol. 49, 1561, 1569 (1980)

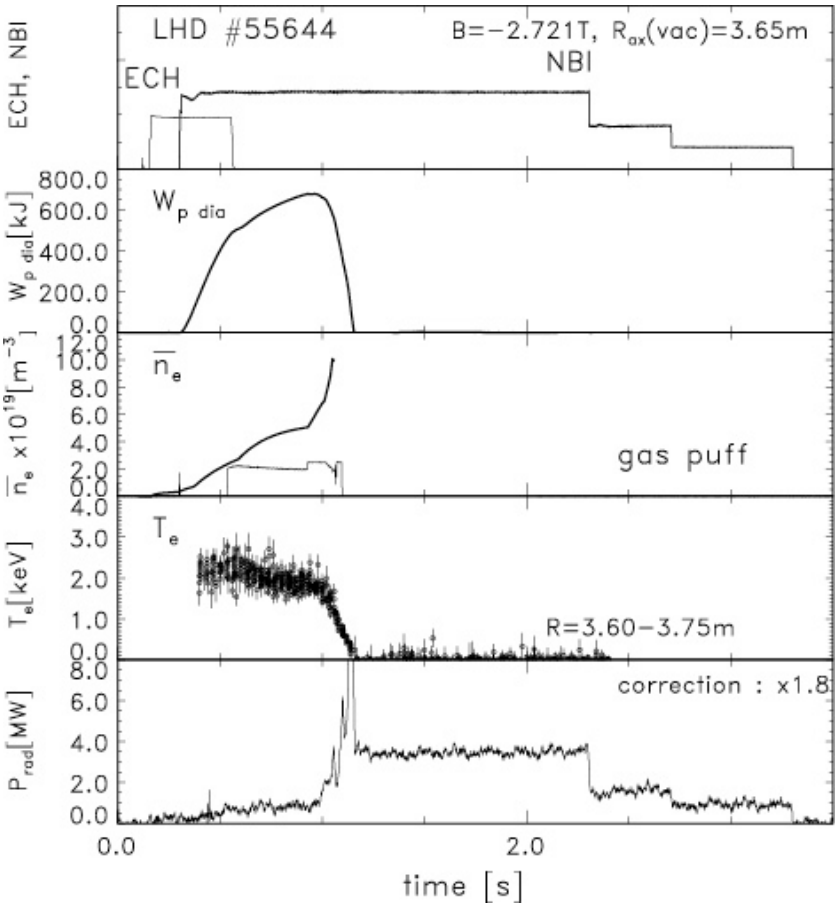

Fig.1(a) Experimental summary for a shot (#55644) with radiation collapse (top) ECH (Electron cyclotron heating) and NBI (Neutral Beam Heating) timing, (second) stored energy, (third) line averaged electron density and gas-puffing timing, (forth) electron temperature for R = 3.60 – 3.75m, (bottom) radiative power by bolometric measurement

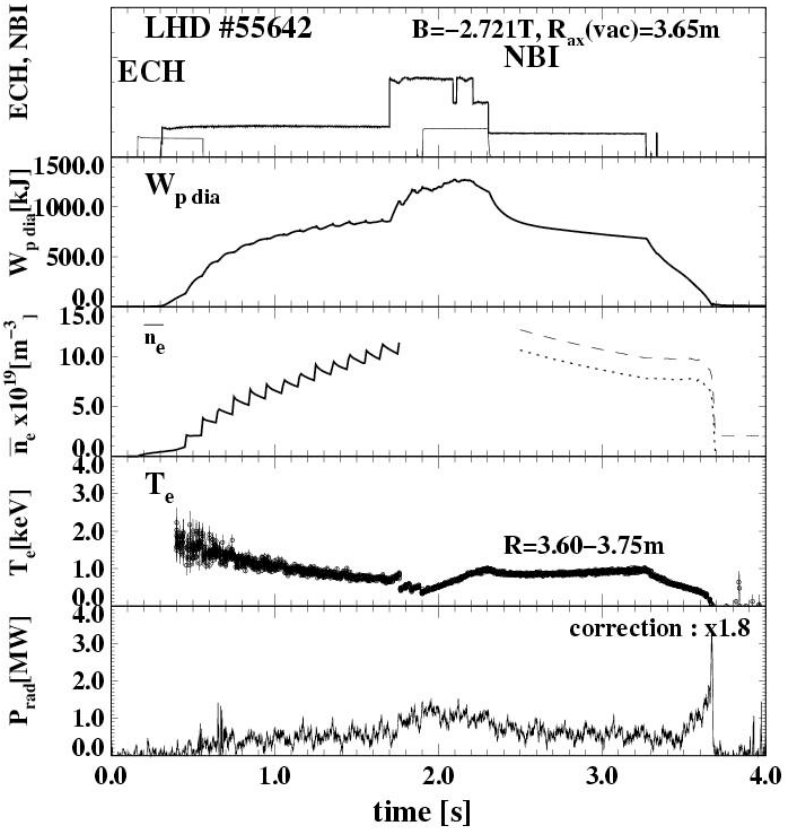

Fig.1(b) Experimental summary for a shot (#55642) without radiation collapse (#61411), (top) ECH (Electron cyclotron heating) and NBI (Neutral Beam Heating) timing, (second) stored energy, (third) line averaged electron density, (forth) electron temperature for R = 3.60 – 3.75m, (bottom) radiative power by bolometric measurement

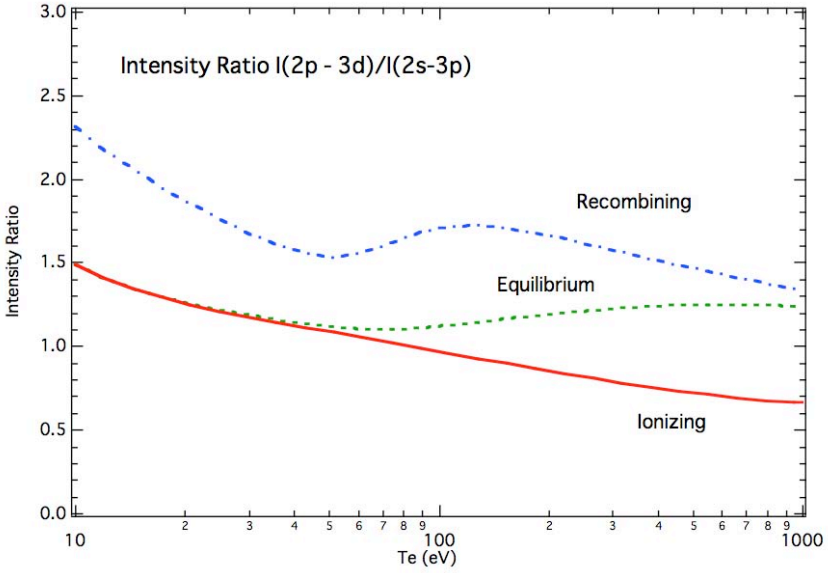

Fig.2(a) Theoretical intensity ratios for CV I(248.6A, 1s2p ^{3}P– 1s3d ^{3}D) / I(227.2A, 1s2s ^{3}S– 1s3p ^{3}P) with $n_e = 10^{13}$ cm^{-3}.

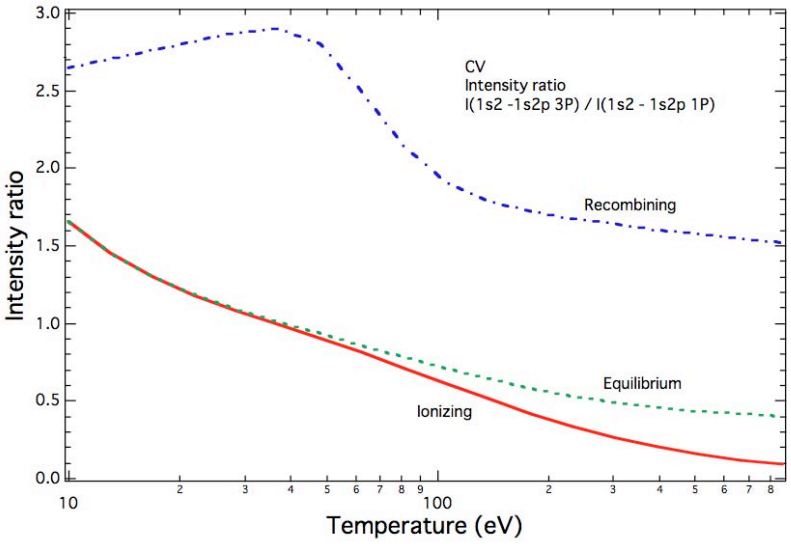

Fig.2(b) Theoretical intensity ratios for CV I_i(40.73A, 1s^2 ^{1}S- 1s2p ^{3}P) / I_r (40.27A 1s^2 ^{1}S– 1s2p ^{1}P) with $n_e = 10^{13}$ cm^{-3}.

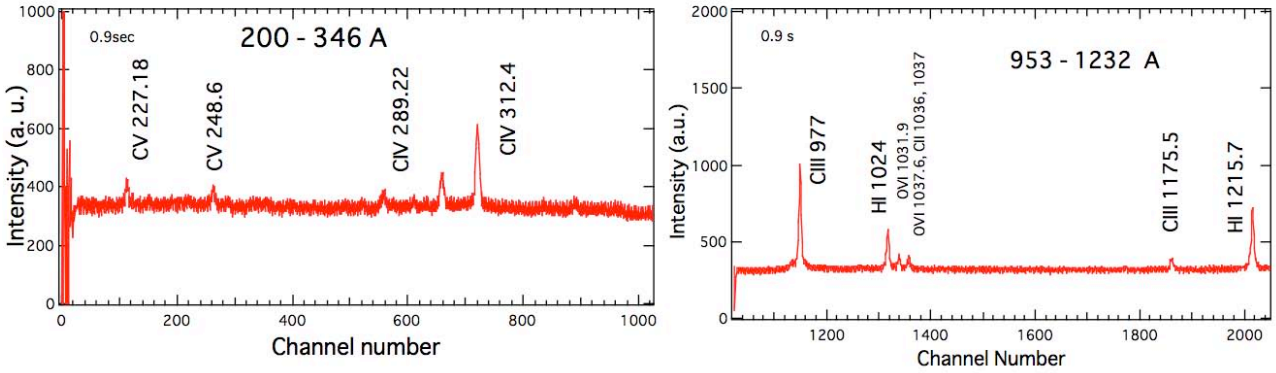

Fig.3 Observed spectra of carbon ions during the NBI heating (t = 0.9 s) before radiation collapse (#55644).

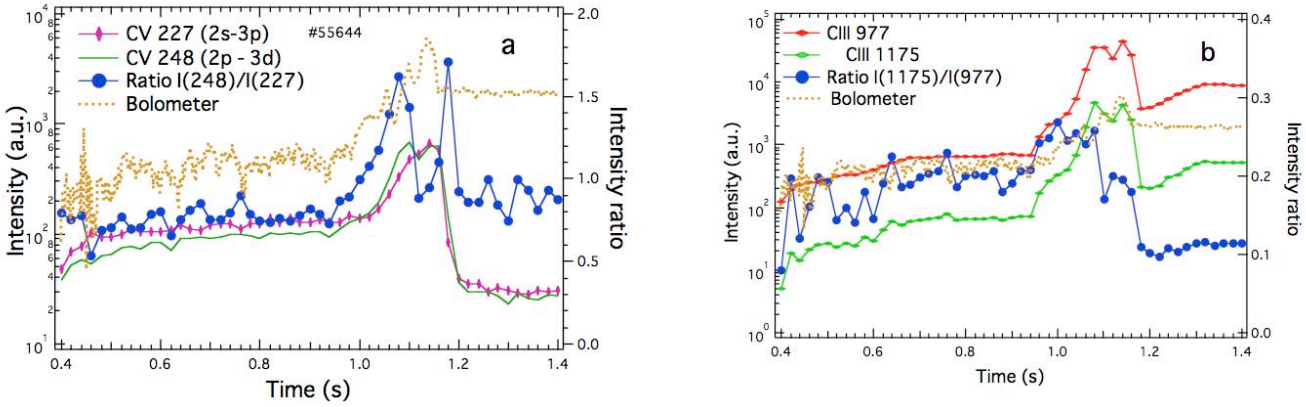

Fig.4 The time history of the observed intensity ratios (filled circle) of (a) C V lines I(248) /I(227) and (b) C III lines I(1175)/I(977). The time evolution of two lines is also plotted. Radiation power measured by the bolometer is shown by a dotted line.

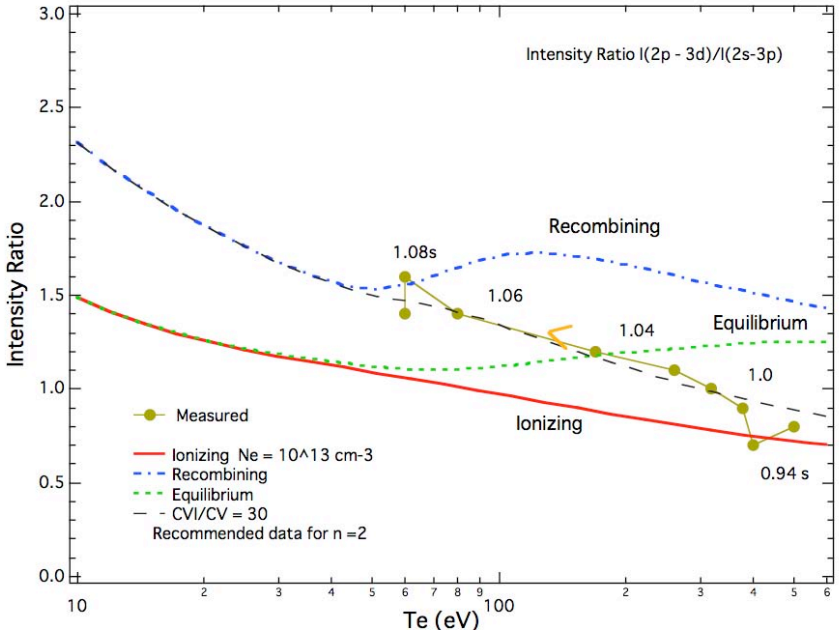

Fig.5 The observed intensity ratios of CV I(248A) /I(227A) as a function of electron temperature (eV) are shown by filled circles with the measured time. Theoretical intensity ratios are also plotted. The solid line indicates the case for ionizing plasma, the dot-dashed line for recombining plasma, the dotted line for equilibrium plasma conditions. The dashed line for the case the ion density ratio n(CVI)/n(CV) = 30.

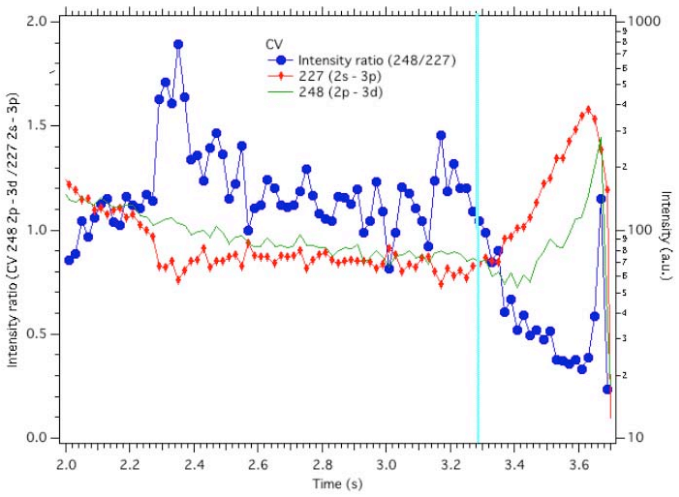

Fig.6 The time history of the observed intensity ratios for I(248A) /I(227A) in the case of non- radiation collapse (#55642). The time evolution of two lines is also plotted.

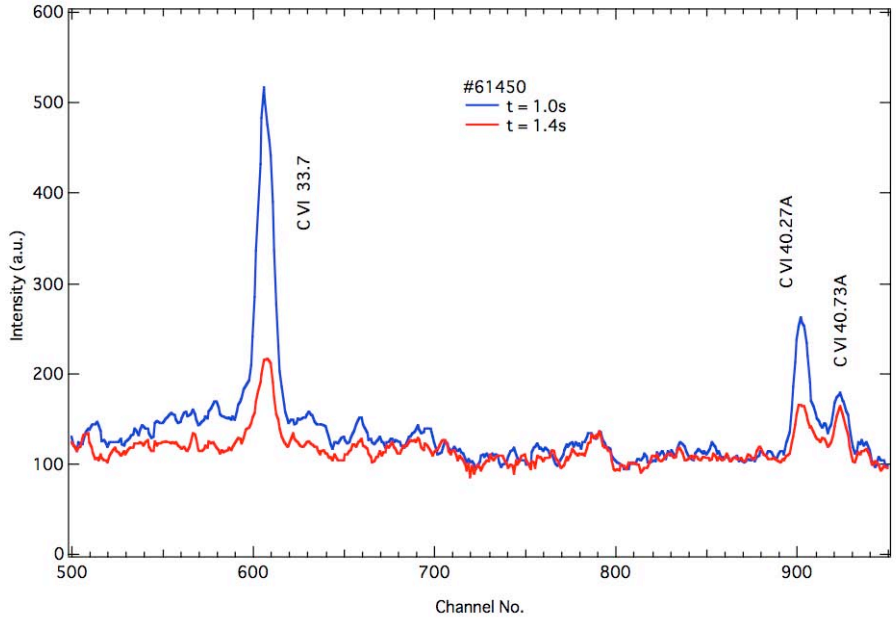

Fig.7 Measured spectra of He-like C ions for radiation collapse (#61450) at t =1.0 s and t = 1.4 s.

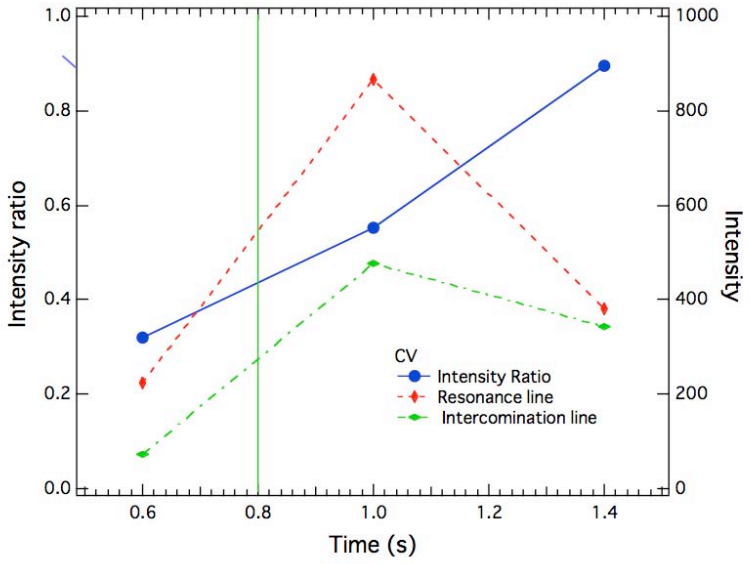

Fig.8 Observed intensity ratios of I(40.73A, $1s^2\ ^1S - 1s2p\ ^3P$)/I(40.27A, $1s^2\ ^1S - 1s2p\ ^1P$) for radiation collapse (#61450). The time evolution of two lines is also plotted. The plasma begins to collapse at 0.8 s.

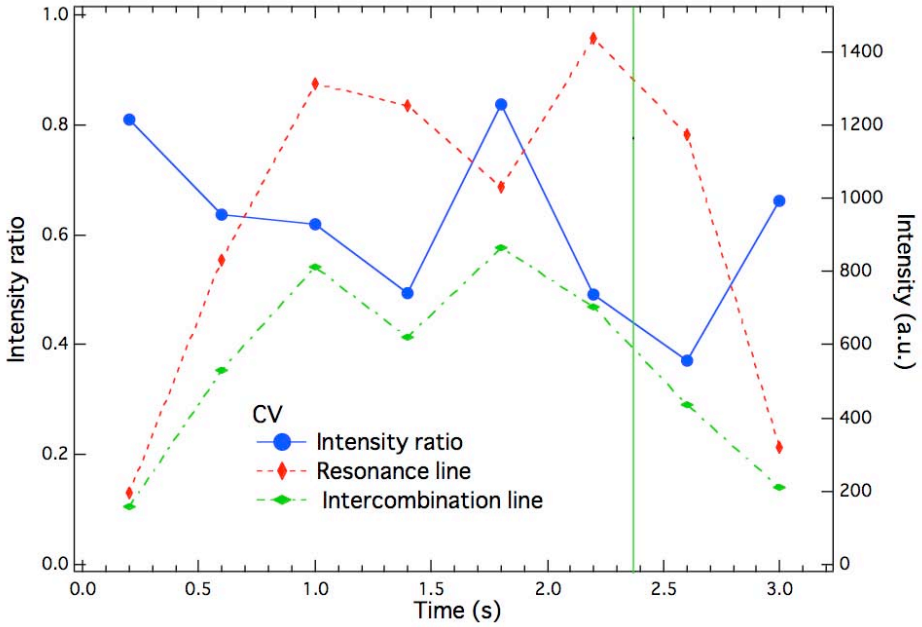

Fig.9 Observed intensity ratios of I(40.73A, $1s^2\ ^1S - 1s2p\ ^3P$)/I(40.27A, $1s^2\ ^1S - 1s2p\ ^1P$) for non- radiation collapse (#61411). The time evolution of two lines is also plotted. NBI stops at ~2.3 s and plasma decays from 2.3s.

A scenario to provide atomic data for fusion research in the stage of precision physics

Jia-Ming Li[†*,1], Xiang Gao[*,2], Cheng Cheng[*], Xiao-Le Zhang[*] and Bo Qing[†]

[†] Department of Physics and Key Laboratory of Atomic and Molecular Nanosciences of Chinese Education Ministry, Tsinghua University, Beijing, 100084 China

[*] Department of Physics, Shanghai Jiao Tong University, Shanghai, 200240 China

Abstract

In order to provide abundant atomic data for fusion research in the stage of precision physics, we propose a scenario which is a combination of indispensable theoretical computations and bench-mark experimental measurements. Such abundant atomic data are compiled mainly by theoretical computations. Accuracies of such abundant data (i.e., atomic energy levels and corresponding cross sections) are ascertained only by a finite number of bench-mark experimental measurements based on analytical continuation of scattering matrices.

I Introduction

Fusion energy research is vitally important for future energies. For fusion plasmas, to simulate numerically temporal-spatial motions of plasmas and to perform diagnostic analysis about plasma's conditions require knowledge about atomic energy levels and related collision processes, especially in the stage of precision physics. Necessary atomic data are not only enormous but also accurate enough for their requirements. Therefore to compile such atomic data can not be finished completely by experimental measurements. Here we propose a scenario to provide such atomic data; a combination of indispensable theoretical computations and bench-mark experimental measurements. More specifically, we adopt theoretical calculation methods which can calculate atomic energy levels and the adjacent continuum states(i.e., scattering matrices or scattering phase shifts) with enough accuracy in a unified manner such as R-matrix type methods[1-6]. Based on analytic continuation of the scattering matrices, there exist intimate relations between atomic energy levels and the related electron-ion collision processes[10,12]. Adopting R-matrix type methods, atomic energy levels(both ground and excited states) can be calculated with enough accuracy which can be determined by comparisons with precise spectroscopic measurements[5]. Through analytical continuation properties, the precision spectroscopic measurements of atomic energy levels can then be served as stringent tests of the related electron-ion collision data. By traditional experimental measurements of electron-ion collision processes[7-9], collision data can only be measured with limited accuracies which can not be compared with the spectroscopic precision. Based on the proposed scenario, necessary abundant atomic data (not only atomic energy levels but also related collision processes) can be provided mainly by theoretical computations which should be checked by only a finite number of bench-mark experimental measurements in order to guarantee required accuracies. Such data sets should meet needs for fusion researches in the stage of precision physics. Note that we adopt relativistic theoretical computation methods[2], therefore the present proposed scenario is more suitable for high Z atomic systems, which are important for inertial confinement fusion researches.

[1] E-mail: lijm@sjtu.edu.cn
[2] E-mail: seangx1231@sjtu.edu.cn

II A proposed scenario

Our proposed scenario is a combination of indispensable theoretical computations and bench-mark experimental measurements. First we briefly summarize theoretical methods by which bound states and the adjacent continuum states can be calculated in a unified manner such as R-matrix type methods[1-6]. More specifically, short-range electron-ion scattering matrices S_{ij} (apart from Coulomb phase shifts) can be calculated with definite accuracy which shall be examined by bench-mark spectroscopic measurements. In the eigenchannel representation[3-6,11-14], the short-range scattering matrix with a specific total angular momentum and parity J^{π} will be diagonized, namely,

$$S_{ij}^{J^{\pi}} = \sum_{\alpha}^{N} U_{i\alpha} \exp\left(i\, 2\pi\mu_{\alpha}\right) U_{j\alpha} \qquad (1).$$

Therefore, the eigenchannel physical parameters (N eigen quantum defects μ_{α} and $N \times N$ transformation matrix $U_{i\alpha}$) and the corresponding eigenchannel wavefunctions $\Psi_{\alpha}^{J^{\pi}}$ (with normalization per unit energy) are calculated over an energy range of interests (including bound states and continuous states)[3-6]. For the orthogonal transformation matrix $U_{i\alpha}$, it can be expressed in N(N-1)/2 independent Euler angles θ_{lm} [11]. Note that $\left\{U_{i\alpha}; \mu_{\alpha}\right\}$ vary smoothly with the energy because of the analytical property of the short-range scattering matrix. Using the eigenchannel wavefunctions Ψ_{α}, we can calculate the dipole and various transition matrix elements, which also vary smoothly with energy. As an example, we display our calculation result of μ_{α} and θ_{lm} for C^{+}[6] in Fig.1.

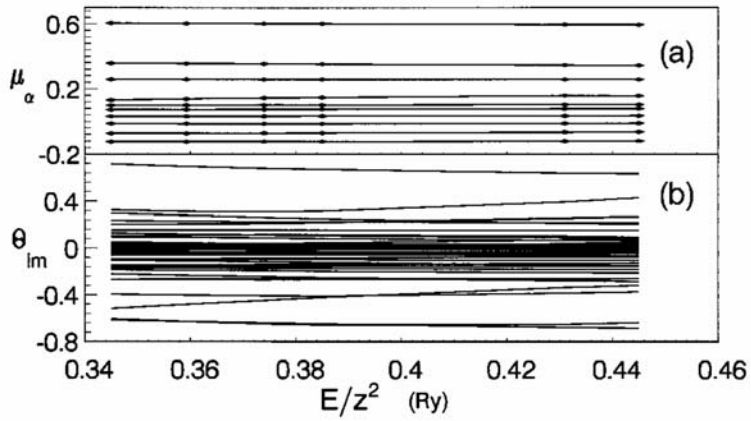

Fig.1 Eigen-quantum-defects μ_{α}, Euler angles θ_{lm} for $U_{i\alpha}$ matrix in ^2D_e symmetry of C^{+}

The physical wavefunctions are the linear combination of eigenchannel wavefunctions[3-6,11-13],

$$\Psi(E) = \sum_{\alpha} A_{\alpha} \Psi_{\alpha}(E) \qquad (2)$$

The mixing coefficients A_{α} are determined by various asymptotic boundary conditions at infinity; depending on various physical phenomena in discrete energy, autoionization energy and continuous energy regions[3-6, 11-13].

In electron-ion collision processes(i.e., in continuous energy region), according to asymptotic in-coming boundary conditions[12] the transition matrix T for the specific J^{π} from an initial state $\alpha_o \tilde{J}_o$ to a final state $\alpha_f \tilde{J}_f$ can be expressed as,

$$T_{ij}^{J^{\pi}}(\alpha_0 \tilde{J}_o, \alpha_f \tilde{J}_f) = e^{i\sigma_i} \cdot [\sum_{\alpha} U_{i\alpha} \exp(i\, 2\pi\mu_\alpha)\, U_{j\alpha}] \cdot e^{i\sigma_j} - \delta_{ij} \qquad (3),$$

where σ_i is the Coulomb phase shifts and the α_o , α_f represent the additional quantum numbers necessary to define the target states completely. Base on T matrix, we can calculate scattering amplitudes, cross sections and other scattering quantities(such as spin polarizations etc.). For example, the angular-integrated cross section from an initial target state $\alpha_o \tilde{J}_o$ to a final target state $\alpha_f \tilde{J}_f$ is[2],

$$\sigma_{(\alpha_o \tilde{J}_o)\to(\alpha_f \tilde{J}_f)} = \frac{\pi}{2k_i^2} \sum_{J\pi} \frac{(2J+1)}{(2\tilde{J}_o+1)} \sum_{j_i, j_j} \left| T_{j_i, j_j}^{J\pi}(\alpha_o \tilde{J}_o, \alpha_f \tilde{J}_f) \right|^2 \qquad (4).$$

As an example, we show our calculation results of total cross sections and excitation cross sections for e+Na collisions[15] in Fig.2 and Fig.3.

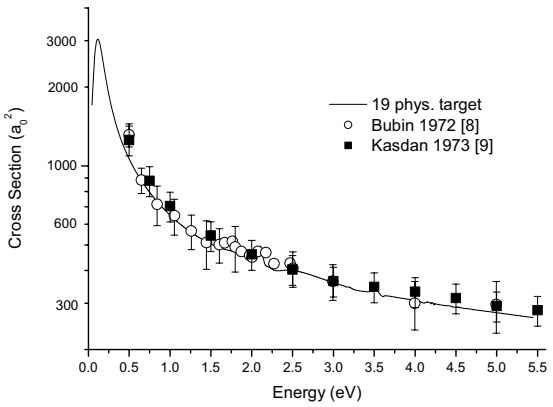

Fig. 2 Total cross section for scattering of electrons by sodium.

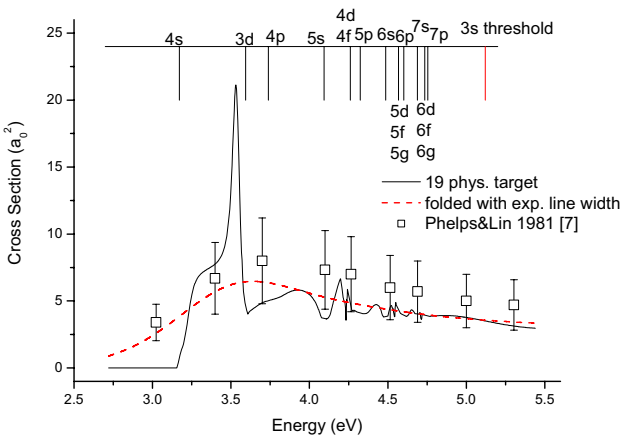

Fig. 3 The 3s-4s Excitation Cross Sections.

Our calculated cross sections are in agreement with the experimental measurements[7-9] within the experimental error bars. The uncertainty of the experimental measurements is about ≥ 10%. Because the R-matrix method treat the bound states and adjacent continua on equal footing, the precision of the calculated bound state energies can then be used as a precise criterion for evaluating the accuracy of the continuum states phase shift calculations[15]. For $^1S^e$ partial wave of e+Na system, there exist only one bound state, the affinity of which can be measured accurately by laser spectroscopy experiments[16]. Our calculated electron affinity of $Na^-[2p^6 3s^2]$ $^1S^e$ is 0.541 eV, which is in good agreement with the experimental values 0.548 eV[16] within about 1%. We can then anticipate the calculation precision of other partial waves should be at the same level. Such precision about 1% is already much more accurate than state-of-the-art scattering experiments about ≥10%. For electron-ion collision processes, there exists infinite Rydberg states which can be used to evaluate the accuracy of the short-range scattering matrices in continuous energy region. More specifically, if all channels are closed, all energy levels of bound state can be obtained by solving the following equations in Multichannel Quantum Defect Theory[3-6, 11-13]:

$$\det\left[U_{i\alpha} \sin \pi(\nu_i + \mu_\alpha)\right] = 0 \qquad (5\text{-}1),$$

$$E = I_i - \frac{(q+1)^2}{2\nu_i^2}, \ \ for\ all\ i \qquad (5\text{-}2),$$

where I_i is the i[th] ionization threshold, q is the ionization degree. As an example, we give a graphical illustration of the solution of Eq.5 in the $J^\pi = 1^-$ partial wave for e+Ar^+ collisions[11]. All energy levels are the crossing points in Fig.4.

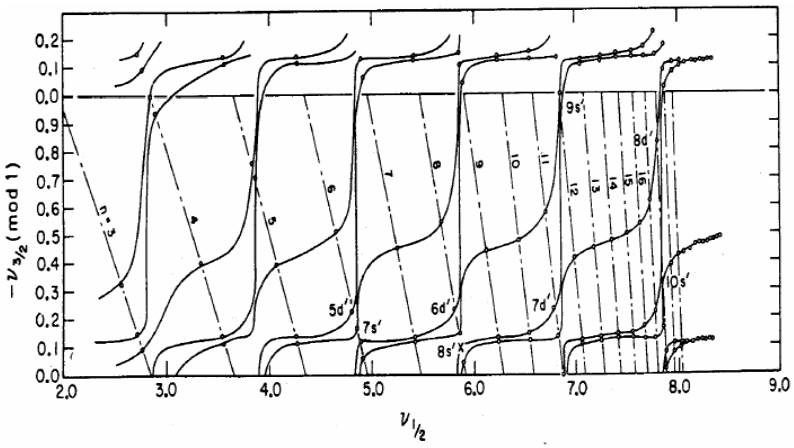

Fig. 4 Quantum defect $-\nu_{3/2}$ (mod 1) vs $\nu_{1/2}$ plot of Ar. Crossing points are level positions. The full curves indicate the curve F = 0, i.e. Eq.(5-1). The relation $-\nu_{3/2}$ between $\nu_{1/2}$, i.e. Eq.(5-2), shown by dot-dashed lines. Note that there are only two thresholds $^2P_{3/2,1/2}$ corresponding to $\nu_{3/2}$ and $\nu_{1/2}$.

Based on the experimental energy levels E_n measured by precision spectroscopy, the experimental $(\nu_{1/2}^{\exp}, \nu_{3/2}^{\exp})_n$ can be readily calculated by Eq.(5-2) and compared with the theoretical calculated values in such graphical representations. Note that with more than two thresholds, comparisons between precisely measured energy levels and theoretical calculated values can be performed without graphical representations, which are more convenient just for illustration purposes. Through analytical continuation properties, the accuracy of short-range scattering matrices can be ascertained. Therefore, by Eq.3 and Eq.4, various cross sections can be calculated with accuracy compatible with spectroscopic precision. As another example, let us consider electron-impact excitation processes between electron and Ne-like ion which are important processes for X-ray lasers with electron-impact excitation mechanism[17]. X-ray lasers should be very important diagnostic tools for inertial confinement fusion plasmas. In electron-impact excitation processes, $e + \mathrm{A}^{+q}_{\mathrm{Ne-like}}(2p^6) \rightarrow e' + \mathrm{A}^{+q}_{\mathrm{Ne-like}}(2p^5 3p)$, there involve various partial waves. Let us focus on the $^2D_{3/2,5/2}$ partial waves. We adopt a relativistic R-matrix method[2] to calculate the short-range scattering matrix for $^2D_{3/2,5/2}$ partial waves[18]. Table I displays our calculated results in the energy range below the zero incident energy as a simple illustrative example. In such discrete energy region, there are infinite number of Rydberg states for Na-like atomic systems whose energy level positions can be used as stringent tests of the accuracy of our calculated short-range scattering matrices (i.e., short-range phase shifts $\pi\mu$ and the short-range scattering matrices $e^{2i\pi\mu}$) for e+Ne-like collisions. With the experimental energy level positions measured by precision spectroscopy which is one of most accurate experimental measurements in physical science, the experimental quantum defects $\mu_{\exp}$ can be

calculated according to Eq.(5-2).

Table 1. The quantum defects μ (in unit of 10^{-6}) of ^{2}D Rydberg series of Na and Si^{3+}.

	Na				Si^{3+}			
μ in 10^{-6}	n=3	n=4	n=5	n=6	n=3	n=4	n=5	n=6
$\mu^{\exp}{}_{n3/2}$	10221.7±0.6	12218.0±1.4	13146.2±2.8	13644.3±4.9	64223.5±6.5	76958.0±12.0	82073.8±23.7	84660.1±41.3
$\mu_{n3/2}{}^{\mathrm{MC+B+QED}}$	10210.49	12158.43	13012.71	13400.43	65220.34	78121.37	83162.35	85528.30
$\mu^{\exp}{}_{n5/2}$	10227.8±0.6	12228.1±1.4	13157.5±2.8	13657.0±4.9	64232.1±6.5	76960.0±12.0	82070.4±23.7	84660.1±41.3
$\mu_{n5/2}{}^{\mathrm{MC+B+QED}}$	10216.69	12168.35	13024.31	13412.94	65230.01	78126.00	83161.37	85523.56
$\Delta\mu_n{}^{\exp}$	6.1±1.2	10.1±2.9	11.3±5.7	12.7±9.8	8.6±13.0	2.1±24.1	-3.4±47.4	Unresolved
$\Delta\mu_n{}^{\mathrm{MC+B+QED}}$	6.20	9.92	11.60	12.51	9.67	4.63	-0.98	-4.74
$\Delta\mu_n{}^{\mathrm{SC}}$	6.44	10.34	12.14	13.12	4.70	-3.09	-9.80	-13.99
$\Delta\mu_n{}^{\mathrm{CORR}}$	-0.35	-0.59	-0.74	-0.85	-16.42	-19.72	-20.63	-20.60
$\Delta\mu_n{}^{\mathrm{B+QED}}$	0.11	0.17	0.20	0.23	21.40	27.44	29.45	29.85

$\Delta\mu_n^{\exp}$**:** experimental data representing fine structure splittings, i.e., $\Delta\mu_n^{\exp} = \mu_{n5/2}^{\exp} - \mu_{n3/2}^{\exp}$;

positive and negative corresponding to anomalous and normal spltittings respectively

$\Delta\mu_n^{MC+B+QED}$ **:** with the two main mechanisms as well as two minor mechanisms

$\Delta\mu_n^{SC}$**:** calculated results only with the two main mechanisms (spin-orbit interactions and relativistic corrections of exchange interactions).

$\Delta\mu_n^{CORR}$**:** contributions owing to electron correlations representing one of two minor mechanisms

$\Delta\mu_n^{B+QED}$**:** contributions owing to transverse interactions(especially electromagnetic retardation effects) representing one of two minor mechanisms

Our calculated results $\mu^{MC+B+QED}$ are in good agreement with spectroscopic data $\mu^{\exp}$ within 2% which will provide confidence of the accuracy of our calculated short-range scattering matrices. It is interesting to note that both experimental data $\Delta\mu^{\exp}$ and our calculated results $\Delta\mu_n^{MC+B+QED}$ show anomalous fine structure splittings for ^2D Rydberg states of Na atoms (i.e., $E_{n^2D_{5/2}} = I - \frac{1}{(n-\mu_{n5/2})^2} < E_{n^2D_{3/2}} = I - \frac{1}{(n-\mu_{n3/2})^2}$ and $\Delta\mu > 0$). Such anomalous fine structure splittings result from 4 mechanisms[18]: two major mechanisms and two minor mechanisms. In the 7th row of Table I, $\Delta\mu_n^{SC}$ represents the two major mechanisms; (1) spin-orbit interactions giving arise to normal fine structures and scaling as $\propto Z^4$, and (2) relativistic corrections of electron exchange interactions giving arise to anomalous fine structures and scaling as $\propto -Z$. Therefore such two major mechanisms almost cancel each other for Na-like Si ions (Si^{3+}). Based on the two major mechanisms only, $\Delta\mu_n^{SC}$ of the 7th row in Table I changes sign from n=3 to n=4 for Si^{3+} because the relativistic corrections of electron exchange interactions become smaller as n increases. However such crossing point is different from the experimental data $\Delta\mu^{\exp}$ of the 5th row in Table I

which change from n=4 to n=5. Therefore the two minor mechanisms should be taken into accounts; (3) electron correlation effects giving arise to normal fine structures shown in the 8th row of Table I($\Delta\mu_n^{CORR}$<0), and (4) Breit interactions representing electromagnetic retardation effects and Quantum Electrodynamics corrections giving arise to anomalous fine structures shown in the 9th row of Table I($\Delta\mu_n^{B+QED}$>0). Considering the 4 mechanisms together, the calculated $\Delta\mu_n^{MC+B+QED}$ of the 6th row are in good agreement with the experimental data $\Delta\mu^{\exp}$ of the 5th row for both Na and Si^{3+}. In order to check the calculated short-range scattering matrices in the energy range of excitation thresholds for e + Ne-like ion collisions, it requires some bench-mark experimental measurements of photo-absorption spectra of Na-like ions near inner 2p threshold which may be carried out in synchrotron radiation facilities. Note that based on Multichannel Quantum Defect Theory all the energy levels of infinite bound states as well as autoionization resonance states can be obtained without missing any one[3-6, 11-13] as long as the compact eigenchannel parameters $\{U_{i\alpha};\ \mu_\alpha\}$ have been calculated by R-matrix type theoretical methods[3-6]. As an example, we display photo-absorption cross sections near the $1s2l$ thresholds (i.e., oscillator strength densities) from the inner-shell 1s into autoionization resonance states for Li atoms shown in Fig.5[6], which are in good agreement with experimental measurements performed in synchrotron radiation facility[19].

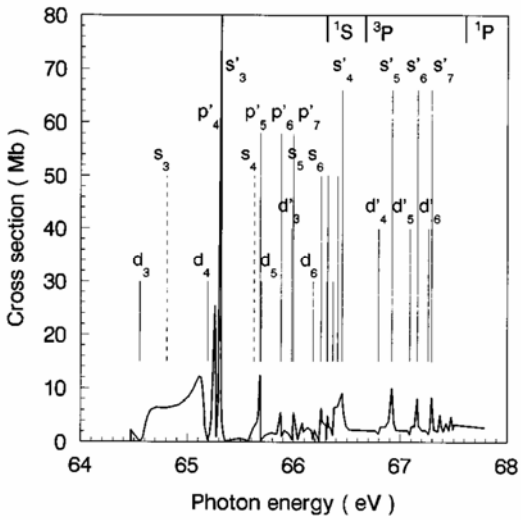

Fig. 5 Inner-shell photoionization cross section near ($1s2l$) thresholds for lithium.

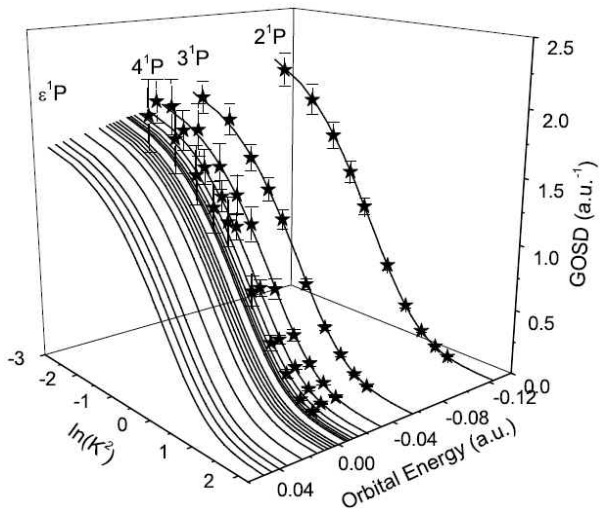

Fig. 6 Generalized Oscillator Strength Densities of the ^{1}P channel of helium. $e^- + He(1^1S) \rightarrow e^- + He^*(n^1P);\quad n = 2,3,4,.....$

Let us return to electron-ion collision processes of which cross sections are needed in fusion energy research in rather wide energy range from low-energy, through intermediate-energy, to high-energy regions. Applications of Eq.3 and Eq.4 in partial wave expansions are only appropriate for low-energy region. For intermediate-energy and high-energy regions, the transition matrices T should be calculated as a whole. At high electron energies as Born approximation is valid, various cross sections can be readily calculated, i.e., $T \cong T^{Born}$. In our proposed scenario, all excited states and their corresponding wavefunctions can be calculated by R-matrix type methods(Note that the bound states and adjacent continua can be treated on equal footing based on Multichannel Quantum Defect Theory). As an example, all high-energy electron-impact excitation cross sections of $He(1s^2 1^1S \rightarrow 1snp\ n^1P;\ n = 2,3,....,\infty)$ are displayed as generalized oscillator strength densities(GOSD) shown in Fig.6[20] where momentum transfers $\ln(K^2)$ represent scattering angles and orbital energies ε_{n^1P} correspond to excitation energies

$E_{ex} = \varepsilon_{n^1P} - \varepsilon_{1^1S}$ (i.e., energy transfers in electron collision processes). Note that all high-energy electron-impact cross sections $(1^1S \to n^1P)$ form a smooth surface of generalized oscillator strength densities which are in good agreement with the recent available bench-mark experimental data[21]. At intermediate energy region as Born approximation can not be applied, the transition matrix T can be calculated by the following two methods; (1) starting from Born approximations[15,20], i.e., $T = T^{Born} + \Delta T$, where ΔT can be calculated by partial wave expansions involving only a finite number of penetrating partial waves(i.e., low angular momentums). (2) transition matrix T can be calculated by solving Lippmann-Schwinger equation directly without partial wave expansions[22]. Various other collision processes such as ion + atom collisions can be treated similarly.

More discussions will be presented in Section III.

III Discussion

In our proposed scenario which is a combination of indispensable theoretical computations and bench-mark experimental measurements, we have elucidated indispensable roles of theoretical computations in order to provide enormous atomic data with adequate accuracy. The R-matrix type methods[1-6] should be adopted, because bound states and adjacent continuum states can be treated in a unified manner. More specifically, we can calculate the eigenchannel physical parameters $\{U_{i\alpha}; \mu_\alpha\}$ and the corresponding eigenchannel wavefunctions $\Psi_\alpha^{J^\pi}$ (with normalization per unit energy) which are smooth functions of energy in the range of interests (including bound states and continuum states)[3-6] as shown in Fig.1. Based on these parameters $\{U_{i\alpha}; \mu_\alpha\}$, all energy levels(including infinite number of Rydberg states and autoionization resonance states) can be calculated accurately in the framework of Mutichannel Quantum Defect Theory[3-6, 11-13] without missing any one as shown in Fig.4. Note that, in some atomic systems such as the rare-earth elements, there will be some isolated resonance states(e.g., arising from $4f^n$ valence configurations) embedded in the eigenchannels, which will perturb the smoothly varying eigenchannel physical parameters $\{U_{i\alpha}; \mu_\alpha\}$ locally. Such local effects of the isolated resonance state can be treated analytically by using some extra physical parameters representing the position of the isolated resonance state and the interactions between the isolated resonance state and the eigenchannels[23]. Furthermore, through analytical continuation properties of short-range scattering matrices, the precision spectroscopic measurements of atomic energy levels can then be served as stringent tests of the accuracy of the short-range scattering matrices, i.e., related electron-ion collision data. By traditional experimental measurements of electron-ion collision processes, collision data can only be measured with limited accuracies($\geqslant$10%) which can not compared with the spectroscopic accuracy. Furthermore, with the calculated eigenchannel wavefunctions Ψ_α, various transition matrix elements can be calculated and corresponding cross sections can be obtained, for examples, as shown in Fig.5 and Fig.6. Accuracies of cross sections can be ascertained by a finite number of bench-mark experimental measurements only. Therefore, based on our proposed scenario, mainly by theoretical computations one can provide necessary abundant atomic data (not only atomic energy levels but also related collision processes) with adequate accuracies, which should be guaranteed by a finite number of bench-mark experimental measurements only based on analytical continuation of scattering matrices. Finally, we would like to conclude by the following comments, we adopt full relativistic theoretical computation methods as shown in Table I, it is more suitable for high-Z atomic systems, which are important for inertial

confinement fusion researches. Based on the present proposed scenario, necessary abundant atomic data can be provided with enough accuracies for relevant research fields in the stage of precision physics, not only in fusion researches but also in astrophysics researches and space sciences.

Acknowledgments

This work is supported by Ministry of Science and Technology and Ministry of Education of China, the Key grant Project of Chinese Ministry of Education (NO.306020), the National Natural Science Foundation of China(Grant No.10734040), the National High-Tech ICF Committee in China and the Yin-He Super-computer Center, Institute of Applied Physics and Mathematics, Beijing, China, and National Basic Research Program of China (Grant No.2006CB921408).

Reference

[1] P.G. Burke. and W. D. Robb., Adv. At. Mol. Phys., **11**, 143(1975); K. A. Berrington, W. B. Eissner, and P. H. Norrington, Comput.Phys.Commun. **92**, 290 (1995).

[2] J. J. Chang, J. Phys. B. **10**, 3335 (1975); P. H. Norrington, I. P. Grant, J. Phys. B. **20,** 4869 (1987); S. Ait-Tahar, I. P. Grant, P. H. Norrington, Phys. Rev. A. **54**, 3984 (1996).

[3] U. Fano and C. M. Lee (J. M. Li), Phys. Rev. Lett. **31**, 1573 (1973); C. M. Lee(J. M. Li), Phys. Rev. A. **10**, 584 (1974); C.M. Lee(J.M. Li), Phy. Rev. A, **10**,1598(1974).

[4] M. Aymar, C. H. Greene, E. Luc-Koenig, Rev. Mod. Phys. **68**, 1015 (1996).

[5] W. Huang, Y. Zou, X. M. Tong, J. M. Li, Phys. Rev. A. **52**, 2770 (1995); Y. Zou, X. M. Tong, J. M. Li, Acta. Phys. Sin. **44**, 50 (1995) (in Chinese).

[6] Jia-Ming Li, Lan Vo Ky, Yi-Zhi Qu, Jun Yan and Pei-Hong Zhang, Phys. Rev. A. **55**, 3239 (1997).

[7] J. O. Phelps, and C. C. Lin, Phys. Rev. A. **24**, 1299 (1981); C. C. Lin, and J. B. Boffard, Adv. At., Mol. Phys., **51**, 385 (2005).

[8] D. L. Moores and D. W. Norcross, J. Phys. B. **5**, 1482 (1972).

[9] A. Kasdan, T. M. Miller, and B. Bederson, Phys. Rev. A. **8**, 1562 (1973).

[10] M. J. Seaton, Rep. Prog. Phys. **46**, 167 (1983).

[11] C. M. Lee(J. M. Li), K. T. Lu, Phys. Rev. A. **8**, 1241 (1973).

[12] J. M. Li, Acta. Phys. Sin. **29**, 419 (1980) (in Chinese).

[13] C.M.Lee(J.M. Li), W.R.Johnson, Phys. Rev. A22, 979 (1980).

[14] C.M. Lee(J.M. Li), Phy. Rev. A, **11**,1692(1975).

[15] X. Gao, X. Y. Han, Lan Voky, Nicole Feautrier and J. M. Li, submitted to Phys. Rev. A.

[16] T. A. Patterson, H. Hotop, A. Kasdan, D. W. Norcross, and W. C. Lineberger, Phys. Rev. Lett. **32**, 189 (1974).

[17] J. Nilsen, J. Quant. Spectros. Radiat. Trans., **47**, 171(1992).

[18] X. Gao, C. Cheng and J. M. Li, submitted to Chin. Phys. Lett.

[19] L. Journel, D. Cubaynes, J. M. Bizau, S. AL Moussalami, B. Rouvellou, F. Wuilleumier, L. Vo Ky, P. Faucher, and A. Hibbert, Phys. Rev. Lett. **76**, 30 (1996) ; L.M. Kiernan, M.K. Lee, B.F. Sonntag, P. Zimmermann, J.T. Costello, E.T. Kennedy, A. Gray, and Lan Vo Ky, J. Phys. B **29**, L181 (1996).

[20] X. Y. Han, and J. M. Li, Phys. Rev. A. **74**, 062711 (2006).

[21] X. J. Liu, L. F. Zhu, Z. S. Yuan, W. B. Li, H. D. Cheng, J. M. Sun, and K. Z. Xu, J. Electron Spectrosc. Relat. Phenom. **135**,15 (2004); K. Z. Xu, R. F. Feng, S. L. Wu, Q. Ji, X. J. Zhang, Z. P. Zhong, and Y. Zheng, Phys. Rev. A **53**, 3081 (1996).

[22] A. S. Kadyrov, I. Bray, A. T. Stelbovics and B. Saha, J. Phys. B. **38,** 509 (2005).

[23] U. Fano, Phys. Rev. **124**, 1866 (1961).

Charge transfer and association processes of protons colliding with potassium

C. H. Liu[1, 2], Y. Z. Qu[1 *], J. G. Wang[2], Y. Li[3], and R. J. Buenker[3]

[1] *College of Material Sciences and Optoelectronic Technology, Graduate University of the Chinese Academy of Sciences, P.O. Box 4588, Beijing 100049,China*
[2] *Institute of Applied Physics and Computational Mathematics, Beijing 100088, China*
[3] *Fachbereich C-Mathematik und Naturwissenschaften, Bergische Universität Wuppertal, D-42097 Wuppertal, Germany*

Abstract

The nonradiative charge transfer process for $H^+ + K(4s)$ collision is investigated by using the quantum-mechanical molecular orbital close-coupling method for collision energies from 1eV to 10 keV. The radiative decay and radiative charge transfer cross sections are calculated using the optical potential approach and the fully quantal method, respectively, for the energy range of 10^{-5} - 10 eV. The radiative association cross sections are obtained by subtracting the radiative charge transfer part from total radiative decay cross sections. The nonradiative charge transfer is the dominant mechanism at energies above 2 eV, and the radiative charge transfer become primary in the low energy region of $E < 1.5\text{eV}$.

Key Words: atomic collision, radiative, charge transfer, association

1. INTRODUCTION

The charge transfer in collisions of protons with alkali-metal atoms affects the ionization balance in the atmospheres of planets, dwarf stars, and the interstellar medium [1]. Because of the near-resonant condition, these charge exchange processes are known to possess large cross sections in a wide energy range and are also important in laboratory plasma environments [2]. At low temperature, such as in ultracold experiments, collision energies are much smaller than 1 eV, nonradiative charge transfer can be important if strong avoid crossings beyond the small inter-nuclear distance occur in the potential curves of the initial and final diabatic states. In the absence of suitable crossings, the radiative charge transfer will often be more efficient by the emitting a photon. We have studied the radiative and nonradiative charge transfer, as well as the radiative association processes of protons colliding with sodium [3-5]. Here we extend our investigations to the collision of protons with the heavier alkali-metal atom, potassium, to provide accurate data which can be useful in various applications. In the collisions of H^+ with the ground 4s state of K, the charge exchange reaction may occur by nonradiative charge transfer $H^+ + K(4s) \rightarrow H + K^+$, or by radiative charge transfer $H^+ + K(4s) \rightarrow H(1s) + K^+ + h\nu$, or by radiative association $H^+ + K(4s) \rightarrow KH^+ + h\nu$.

In the keV energy region, the nonradiative charge transfer process has been

* yzqu@gucas.ac.cn

extensively investigated both experimentally and theoretically [6-12], but for the low-energy region ($E < 100$ eV) no experimental or theoretical work has been performed to the best of our knowledge. In this work, we study the nonradiative charge transfer process in a wide energy range of 0.001-10 keV by a quantum-mechanical molecular-orbital close-coupling (QMOCC) method.

For energies below several eV, the radiative processes may become dominant over nonradiative charge transfer. We will study the radiative decay and radiative charge transfer processes using the optical potential and the fully-quantal methods, respectively. The radiative association cross sections are obtained by taking differences between radiative decay and radiative charge transfer results. The molecular data needed are calculated by the multireference single- and double-excitation configuration interaction (MRD-CI) method.

2. THEORETICAL METHODS

2.1. Nonradiative charge transfer

The QMOCC method to describe nonradiative charge transfer in ion-atom collisions has been formulated in detail in the literature [13, 14], and it is only briefly outlined in the present work. In the diabatic representation, the radial scattering amplitude describing the relative motion of the nuclei can be obtained by solving a coupled set of second-order differential equations written as

$$\left[\frac{d^2}{dR^2} - \frac{J(J+1)-\Lambda^2}{R^2} + 2\mu E\right] g_\gamma^J - 2\mu \sum_{\gamma'} U_{\gamma,\gamma'}(R) g_{\gamma'}^J = 0, \qquad (1)$$

where μ is the reduced mass of the ion-atom pair, E is the relative collision energy in the center-of-mass frame, R is the coordinate of the relative nuclear motion, J is the total angular momentum quantum number, Λ is the projection of the total electronic angular momentum along the internuclear axis, and $U(R)$ is the diabatic potential matrix in which the off-diagonal elements are responsible for driving charge transfer in the diabatic representation [14, 15].

The Eq. (1) may be solved with the log-derivative method of Johnson [16]. The K matrix can be extracted from the scattering amplitude, and thus the scattering matrix S is given by $S_J = [I + iK_J]^{-1}[I - iK_J]$, with I the identity matrix. Finally the charge-transfer cross sections from channel α to channel β are expressed in terms of the scattering matrix elements $\sigma_{\alpha\to\beta} = \pi / k_\alpha^2 \sum_J (2J+1) |(S_J)_{\alpha\beta}|^2$, where k_α denotes the initial momentum.

2.2 Radiative charge transfer and radiative association

The radiative charge transfer cross section in the fully quantum-mechanical approach [17-19] can be given by

$$\sigma = \int_{\omega_{\min}}^{\omega_{\max}} \frac{d\sigma}{d\omega} d\omega \qquad (2)$$

with $\frac{d\sigma}{d\omega}=\frac{8}{3}\left(\frac{\pi}{k_A}\right)^2\frac{\omega^3}{c^3}\sum_J\left[JM^2_{J,J-1}(k_A,k_X)+(J+1)\ M^2_{J,J+1}(k_A,k_X)\right]$, where ω is the angular frequency of the emitted photon and c is the speed of light. The subscripts A and X denote the upper and the lower states, respectively, and $M_{J,J'}(k_A,k_X)=\int_0^\infty dR f_J^A(k_AR)D(R)f_{J'}^X(k_XR)$, where $D(R)$ is the transition dipole moment connecting the two electronic states, k_A and k_X are the entrance and exit momenta, respectively. The partial wave $f_J^i(k_iR)$ ($i=A,X$) is the regular solution of the homogeneous radial equation

$$\left\{\frac{d^2}{dR^2}-\frac{J(J+1)}{R^2}-2\mu\left[V_i(R)-V_i(\infty)\right]+k_i^2\right\}f_J^i(k_iR)=0, \tag{3}$$

On the other hand, the optical potential method [17, 18, 20] can be adopted to obtain the total cross sections for radiative decay, including both the radiative charge transfer and radiative association processes. The radiative decay cross section is

$$\sigma(E)=\pi/k_A^2\sum_J^\infty(2J+1)[1-\exp(-4\eta_J)], \tag{4}$$

and the phase shift η_J is given in the distorted-wave approximation as $\eta_J=\pi/2\int_0^\infty dR\left|f_J^A(k_AR)\right|^2A(R)$, where $A(R)$ is the transition probability for the radiative transition given by

$$A(R)=\frac{4}{3}D^2(R)\frac{\left|V_A(R)-V_X(R)\right|^3}{c^3}. \tag{5}$$

In order to extend the radiative decay calculation to higher energy, replacing the summation in Eq. (4) and applying the JWKB approximation, one obtains the expression for the semiclassical cross section

$$\sigma(E)=2\pi\sqrt{\frac{2\mu}{E}}\int pdp\int_{R_A^{\rm ctp}}^\infty dR\frac{A(R)}{\sqrt{1-V_A(R)/E-p^2/R^2}}, \tag{6}$$

where p is the impact parameter and $R_A^{\rm ctp}$ is the classical turning point in the incoming channel [17, 21]. For relatively large energies ($E\gg V_A$), the double integral is nearly energy independent, and therefore $\sigma(E)$ varies as $1/E^{1/2}$ [18 -20].

By subtracting the radiative charge transfer part from the total radiative decay cross sections, one obtains the radiative association cross sections.

3 RESULTS AND DISCUSSIONS

3.1. Nonradiative charge transfer

In the present study, the ab initio CI calculation is carried out for potential curves

of six Σ^+ electronic states in A_1 symmetry and two Π states in B_1 symmetry of the KH^+ molecule using the MRD-CI package [22, 23]. In the calculation of hydrogen, the cc-pVQZ correlation-consistent, polarization valence, quadruple-zeta basis set [24] is used. In addition to the above basis set, (2s3p) diffuse functions are added. Then the final contracted basis set for the hydrogen atom is (8s, 6p, 2d, 1f)/[6s, 6p, 2d, 1f]. For the potassium atom, an effective core potential (ECP) [25] is employed to describe the ten core electrons. A threshold of 10^{-10} Hartree is used to select the configuration wave functions [25] of which the electronic wave functions are composed. The errors in our calculated energies for the considered electronic states are no more than 0.07 eV in the asymptotic region.

The adiabatic potentials are displayed in Fig. 1, in which $1\,^2\Sigma^+$, $2\,^2\Sigma^+$, $3\,^2\Sigma^+$, $4\,^2\Sigma^+$, $5\,^2\Sigma^+$, $6\,^2\Sigma^+$, $1\,^2\Pi$ and $2\,^2\Pi$ correspond to $K^+ + H(1s)$, $K(4s) + H^+$, $K^+ + H(2p\sigma^+)$, $K^+ + H(2p\sigma^-)$, $K(4p\sigma) + H^+$, $K(5s) + H^+$, $K^+ + H(2p\pi)$ and $K(4p\pi) + H^+$ states in the asymptotic region, respectively. The $2\,^2\Sigma^+$ state represents the initial channel for our considered processes.

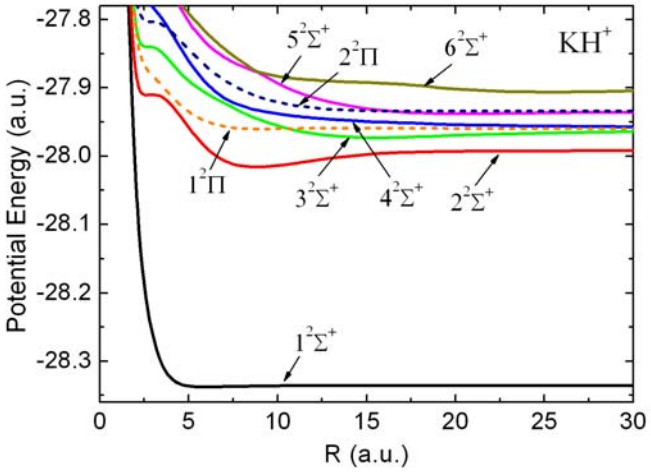

FIG. 1. Adiabatic potential curves for KH^+. The solid and dashed lines refer to the Σ^+ and Π channels, respectively.

We also calculated the radial and rotational couplings. The positions of the peaks in radial couplings are consistent with the avoided crossings of the adiabatic potentials. The main gateway to the charge exchange will be $2\,^2\Sigma^+ - 3\,^2\Sigma^+$ and $2\,^2\Sigma^+ - 1\,^2\Pi$ couplings because of the very close encounters in the associated potential curves. Furthermore, at the higher energies in a semi-classical impact-parameter approach, it is possible to include electron translation factors (ETFs) [26], which leads to matrix elements having the correct boundary conditions and independent of the choice of origin. But in this paper, the ETFs are not included in our description of the collision. Since the influence of ETFs is expected to be important when the incident energy $E > 1$keV/amu [27, 28], the validity of our method is restricted to the low-impact energy region (typically $E < 5$keV/amu [3]).

Using the potentials and couplings described above, we calculated the nonradiative charge transfer cross sections by the QMOCC method for $H^+ + K(4s)$ collision in the energy range of 0.001-10 keV., as shown in Fig. 2. In the keV energy

region, a number of experimental measurements [7-9] and theoretical calculations [6, 7, 10-12] have been performed. Our QMOCC results are in good agreement with these results in the overlapping energy region of 0.1-5 keV. There is no experimental work in the low-energy region for $E < 100$ eV, and only one theoretical results obtained by semiclassical MOCC methods [6]. Our results are larger than theirs at energies less than 100 eV. This is similar to what was obtained in previous calculations on H^++Na($3s$) [3, 6]. Their semiclassical treatment for the scattering calculation and the effective one-electron approximation for the KH^+ molecular structure calculation may be responsible for this discrepancy. At energies larger than about 5 keV/amu, our QMOCC cross sections increase with the increasing of the collision energy, but the other theoretical and experimental results decrease gradually. This is because we have not included ETFs, which may be important in this relatively high-energy region.

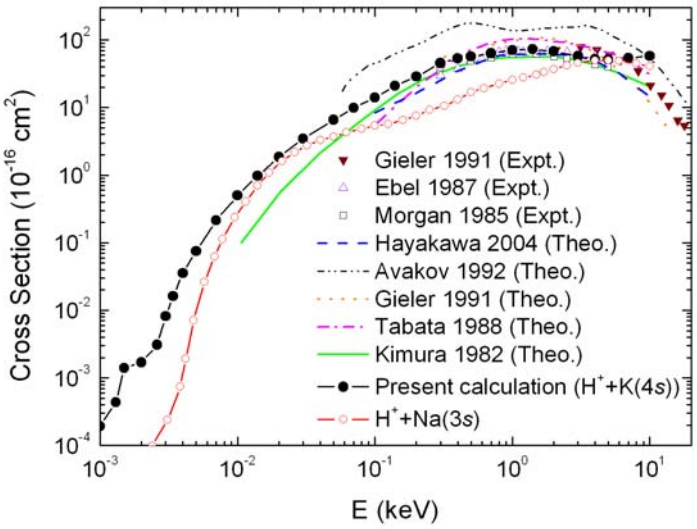

FIG. 2. The total nonradiative charge transfer cross sections for H^++K($4s$) collisions, and comparison with the results for H^++Na($3s$) collisions.

The state-selected cross sections show that the partial cross sections to the $3\,^2\Sigma^+$ channel dominante at energies below 2.5 eV, and the $1\,^2\Pi$ state will become the most important charge transfer final state in the intermediate-energy region.

In the higher-energy region ($E > 100$eV), the charge transfer processes are mainly induced by the couplings at small internuclear separations, where the potential curves $2\,^2\Sigma^+$, $3\,^2\Sigma^+$ and $1\,^2\Pi$ come very close to each other. As the the energy decreases, the efficient internuclear separation range moves to a larger region and the energy gap between the $2\,^2\Sigma^+$ and $3\,^2\Sigma^+$ states increases. The most efficient mechanism for populating the excited states will be via the rotational coupling between the $2\,^2\Sigma^+$ and $1\,^2\Pi$ states at $R \approx 4$a.u.. As the collision energies go below 2.5 eV, the classical turning point for each partial wave will move to larger R where the energy gap between the $2\,^2\Sigma^+$ and $1\,^2\Pi$ curves is larger (see Fig. 1), thus making rotational coupling relatively inefficient. The avoided crossing between the $2\,^2\Sigma^+$ and $3\,^2\Sigma^+$ states, around 15 a.u. becomes dominant.

3.2. Radiative decay, radiative charge transfer and radiative association process

In this work, for radiative processes, the upper A and the lower X states in Eqs. (2)-(6) corresponde to the $2\,^2\Sigma^+$ and $1\,^2\Sigma^+$ states respectively. For the dipole matrix element between $1\,^2\Sigma^+$ and $2\,^2\Sigma^+$, our results are in good agreement with those in Refs. [29, 30], especially at relatively large internuclear separation, where it provides the main contribution for low-energy processes.

Using Eq. (5), we calculated the transition probability $A(R)$. It is similar in shape to that of Watanabe *et al.* [29]. But the unit of $A(R)$ in Ref. [29], shown as $10^{-8}s^{-1,}$ is apparently an error, so that our $A(R)$ cannot be compared to theirs directly.

Using the optical potential method, we have calculated the radiative decay cross sections for energies from 10^{-5} to 10 eV, as shown in Fig. 3. The cross sections decrease as the collision energy increases. Rich resonance structures appear in the energy range of 10^{-5} - 0.3 eV. These resonances are attributed to the presence of quasi-bound or virtual rotational-vibrational levels in the entrance channel, and may give rise to an enhancement of the rate coefficients [18, 20]. In order to extend the treatment to higher energy, we also performed a semiclassical calculation using Eq. (6) at the higher-energy region of 1-100 eV. In the overlapping 1-10 eV energy range, the optical-potential cross sections are in agreement with the semiclassical results.

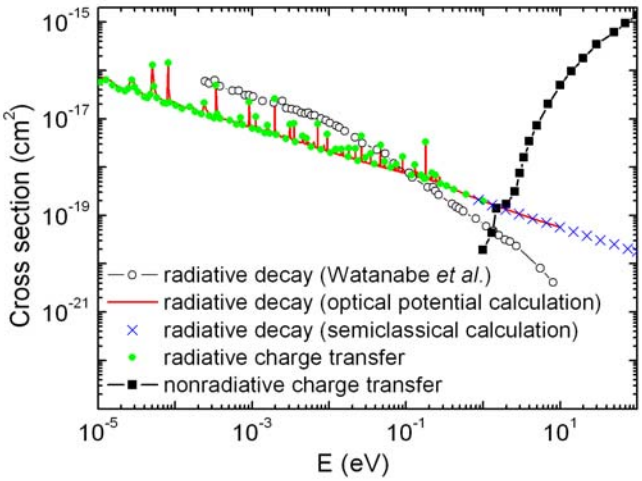

FIG. 3. Radiative decay and radiative charge transfer cross sections for H^++K($4s$)

In Fig. 3, our radiative decay cross sections are compared with the results of Watanabe et al. [29]. Perhaps because of the fewer calculated energy points, they did not find the rich resonance structures. In addition, for collision energy $E<10^{-2}\text{eV}$, their calculated cross sections are about four times larger than ours except at the positions of resonances. Our cross sections have an energy dependence of $1/E^{1/2}$, which is consistent with the Langevin cross-section formula for a polarization potential. But the cross sections of Ref. [29] have the $1/E$ dependence at energies above 10^{-2} eV. As in our previous work [4], we reexamined the optical potential calculations using the code of Ref. [31], the same as that used by Watanabe *et al.* [29].

We arrive at the same conclusion as in our previous paper, i.e., the probable imprecision in the calculation of Ref. [29] results in an incorrect energy dependence of the cross sections, and the discrepancy in the magnitude of the cross sections probably comes from the difference in transition probability $A(R)$.

The radiative charge transfer cross sections calculated by the fully quantum-mechanical approach are also shown in Fig. 3 by the green filled circles. Since the lower $1\,^2\Sigma^+$ state of the present system only has a very shallow well (~0.056 eV) at short range, the radiative charge transfer is responsible for most of the radiative decay process [4, 20]. For comparison, the nonradiative charge transfer results are displayed in the same figure. Below 1.5 eV, the radiative charge transfer process is the dominant charge transfer mechanism. As the collision energy increases, the nonradiative charge transfer cross sections show a sharp increase and become dominant over the radiative results at energies above 2 eV.

The radiative association cross sections, which are obtained by subtracting the radiative charge transfer part from the radiative decay cross sections, are displayed in Fig. 4, and compared with the radiative decay results, as well as the corresponding results for the H^++Na($3s$) collisions[4, 5]. The radiative association cross sections are about one order of magnitude smaller than the radiative decay results at energies from 0.01 to 0.3 meV. As the collision energies increase, the difference between the radiative decay and charge transfer cross sections decreases (see Fig. 3). The radiative association cross sections decrease more rapidly than the radiative decay results. This is because the interaction time for emitting the radiation is reduced [32] as the collision energies increase.

The radiative decay cross sections for H^++K($4s$) collisions are about two times larger than those of H^++Na($3s$), but the radiative association results of H^++K($4s$) differ very little from those of H^++Na($3s$) at energies less than 0.3 meV, even becoming smaller than those of H^++Na($3s$) collisions at larger energies. This is caused primarily by the differences in transition probability $A(R)$. For the H^++K($4s$) collision, the larger $A(R)$ at $R > 5$ a.u. results in greater radiative decay cross sections. But the radiative association depends on not only the dipole matrix element, but also the shape of the potential well in the final state. Because the well of the lower $1\,^2\Sigma^+$ state for KH^+ (0.056 eV) is shallower than that of NaH^+ (0.125 eV) [4], the radiative association cross sections for H^++K($4s$) do not appear to be larger than those of H^++Na($3s$).

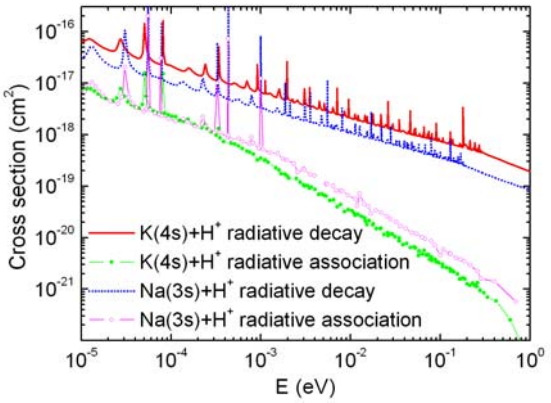

FIG. 4. Comparison of the radiative decay and association cross sections for both H^++K(4*s*) and H^++Na(3*s*) collisions [4, 5].

4. CONCLUSION

We have calculated the total and state-selective nonradiative charge transfer cross sections for protons colliding with K(4s) atoms in a wide energy range of 0.001-10 keV using the QMOCC method. The radiative decay process is investigated using the optical-potential and semiclassical methods for collision energy ranges of 10-5-10 eV and 0.01-100 eV, respectively. The radiative charge transfer cross sections are calculated by the fully-quantum method. We obtain the radiative association results by subtracting the radiative charge transfer part from the radiative decay cross sections. The calculations utilize *ab initio* molecular data obtained from the MRD-CI approach. The nonradiative charge transfer is the dominant mechanism at energies above 2 eV, and the radiative charge transfer becomes the primary mechanism for energies below 1.5 eV. Our radiative decay results generally disagree with the calculations of Watanabe et al. [29]. The discrepancy in the magnitude of the radiative decay cross sections appears to be caused by differences of transition probability, and the distinction in the energy dependence of the cross sections are probably due to the inadequate precision in the calculation of Watanabe et al. [29].

ACKNOWLEDGMENTS

This work was supported in part by NSF of China under Grants No. 10774186, No. 10876043, and No. 10676014, and the National Key Laboratory of Computational Physics Foundation under Grant No.9140C6904030808.

REFERENCES

[1] R. E. Johnson, Icarus 143, 429 (2000).
[2] R. K. Janev, in Atomic and molecular processes in fusion edge plasma, (Plenum press), 1995.
[3] C. H. Liu, Y. Z. Qu, L. Liu, J. G. Wang, Y. Li, H.-P. Liebermann, P. Funke, and R. J. Buenker, Phys. Rev. A **78**, 024703 (2008).
[4] C. H. Liu, Y. Z. Qu, Y. Zhou, J. G. Wang, Y. Li, and R. J. Buenker, Phys. Rev. A **79**, 042706 (2009).
[5] C. H. Liu, Y. Z. Qu, J. G. Wang, Y. Li, and R. J. Buenker, Phys. Lett. A **373**， 3761

(2009).
[6] M. Kimura, R. E. Olson and J. Pascale, Phys. Rev. A **26**, 3113 (1982).
[7] M. Gieler, P. Ziegelwanger, F. Aumayr, H. Winter, and W. Fritsch, J. Phys. B **24**, 647 (1991).
[8] F. Ebel and E. Salzborn, J. Phys. B **20**, 4531 (1987).
[9] T. J. Morgan, R. E. Olson, A. S. Schlachter, and J. W. Gallagher, J. Phys. Chem. Ref. Data **14**, 971 (1985).
[10] S. Hayakawa, K. Kadomura, M. Kimura, C. M. Dutta, Phys. Rev. A **70**, 022708 (2004).
[11] G. V. Avakov, L. D. Blokhintsev, A. S. Kadyrov and A. M. Mukhamedzhanov, J. Phys. B **25**, 213 (1992).
[12] T. Tabata, R. Ito, Y. Nakai, T. Shirai et al. Nucl. Instrum. Methods Phys. Res. B **31**, 375 (1988).
[13] B. H. Bransden and M. R. C. McDowell, in Charge exchange and the theory of ion-atom collisions, (Clarendon press, Oxford) 1992.
[14] B. Zygelman, D. L. Cooper, M. J. Ford, A. Dalgarno, J. Gerratt, and M. Raimondi, Phys. Rev. A 46, 3846 (1992).
[15] T. G. Heil, S. E. Butler, and A. Dalgarno, Phys. Rev. A, 23, 1100 (1981).
[16] B. R. Johnson, J. Comput. Phys. 13, 445 (1973).
[17] B. Zygelman, and A. Dalgarno, Phys. Rev. A **38**, 1877 (1988).
[18] P. C. Stancil, and B. Zygelman, Astrophys. J. **472**, 102 (1996).
[19] L. B. Zhao, P. C. Stancil, J. P. Gu, H.-P. Liebermann, Y. Li, P. Funke, R. J. Buenker, B. Zygelman, M. Kimura, and A. Dalgarno, Astrophys. J. **615**, 1063 (2004).
[20] L.B. Zhao, J.G. Wang, P.C. Stancil, J.P. Gu, H.-P. Liebermann, R.J. Buenker, and M. Kimura, J. Phys. B 39, 5151 (2006).
[21] D. R. Bates, Mon. Not. R. Astron. Soc. 111, 303 (1951).
[22] R. J. Buenker and R. A. Phillips, J. Mol. Struct.: THEOCHEM 123, 291 (1985).
[23] R. J. Buenker, J. Chem. Phys. 103, 5613 (1995).
[24] T. H. Dunning, Jr., J. Chem. Phys. 90, 1007 (1989).
[25] M. M. Hurley, L. F. Pacios, P. A. Christiansen, R. B. Ross, and W. C. Ermler, J. Chem. Phys. 84, 6840 (1986).
[26] M. Kimura, and N. F. Lane, Adv. At., Mol., Opt. Phys. 26, 79 (1990).
[27] J. G. Wang, P. C. Stancil, A. R. Turner, and D. L. Cooper, Phys. Rev. A 67, 012710 (2003).
[28] L. F. Errea, C. Harel, H. Jouin, L. Méndez, B. Pons, and A. Riera, J. Phys. B 27, 3603 (1994).
[29] A. Watanabe, C. M. Dutta, P. Nordlander, M. Kimura, and A. Dalgarno, Phys. Rev. A **66**, 044701 (2002).
[30] S. Magnier, Chem. Phys. **326**, 375 (2006).
[31] A. C. Allison, Comput. Phys. Commum. 3, 173 (1972).
[32] F. A. Gianturco, and P. Gori Giorgi, Astrophys. J. 479, 560 (1997).

Electron correlation effects of heavy atomic ions in EUVL plasmas

Fumihiro Koike

Physics Laboratory, School of Medicine, Kitasato University 1-15-1 Kitasato,Sagamihara 228-8555 Japan

E-mail: koikef@kitasato-u.ac.jp

Abstract. The effect of correlations between $4p$, $4d$, and $4f$ has been studied extensively. The characteristic spectral structures of $4p-4d$ and $4d-4f$ optical transitions, due to the unique structures of $N=4$ open sub-shells in heavy atomic ions, have been studied theoretically. To gain an insight of this effect, a series of careful MCDF calculations for $4d^q$ ($q=0$ to 10) atomic ions with atomic numbers $Z=48$ to 56 has been carried out. The difference of orbital energy differences between $4p$ and $4d$ orbitals and $4d$ and $4f$ orbitals coincidently falls within the range of a few % for almost all the atomic ions investigated.. The $4p^6 4d 4f$ and $4p^5 4d^3$ configurations may mix strongly, and the optical $4p-4d$ and $4d-4f$ transitions may take place coherently, providing us with quite a peculiar EUV emission spectrum. The effect of spectral narrowing and shift is expected to be quite common to the atomic specieds with the atomic numbers in the range $Z=48$ to 56.

1. Introduction

The extreme ultra-violet light (EUVL) emissions of 4d open-shell atomic ions are of interest in relation to the semiconductor technologies and also to the study of highly charged heavy atomic ions in plasmas. Extensive efforts have been made in recent years for understanding the emission spectra from the plasmas[1, 2, 3, 4, 5, 6]. Those spectral structures are of interest also from the view point of academic atomic spectroscopy, whereas they are obtained mainly on the purpose of EUV light source development.

During the last years, a series of sophisticated charge transfer experiments have been carried out for xenon ions[7, 8] and for tin ions[8, 9] by Tanuma and his co-workers. In these experiments, a beam of charge selected atomic xenon or tin ions has been introduced into the gas chamber and the EUV emissions from the excited atomic ions that were created by collisional electron capture from neutral gas atoms have been observed. Because the gas pressure has been kept as low as to maintain a single collision condition, their individual spectral data are of the ions with a unique charge state. This gives a great advantage for comparison of the data with theory.

To give a theoretical counterpart of these experimental data, we performed a set of accurate calculations of electronic states and optical processes based on a Multi-Configuration Dirac-Fock (MCDF) approximation. In these computations, the General purpose Relativistic Atomic Structure Program 92 (GRASP92)[10] and the Relativistic Atomic Transition and Ionization Properties (RATIP)[11] computer codes are used. An advantage of these programs is that we can treat the two electron non-local exchange integrals as they are[6]. In this context, we

can properly evaluate the electron correlations through configuration interactions including the excited orbitals in CSF's in a sophisticated way.

To gain, especially, an insight of the role of the intra N-shell optical transitions, which are relevant for the 13.5 nm EUV emissions from $4d$-open shell Sn ions, we calculated the $4p-4d$ and $4d-4f$ transitions for ions with atomic numbers Z ranging 48 to 56. We have pointed out the important role of the configuration interactions between the $4p$ sub-vallence hole configurations and $4f$ intra-shell excited configurations. It has been pointed out that the modifications of the optical emission spectral structures due to those type of configuration interactions are common to those ionic species.

We describe the procedure and the result of the present theoretical caiculations in the next section. In section 3, we discuss the physical aspect of the electron correlations in the relevant system. And, finally, in section 4, we give a short summary of the present study.

2. The Calculation of $4p-4d$ and $4d-4f$ Transition Arrays of $Z=46-56$ Ions

One of the best candidates for 13.5 nm region EUV light source are considered to be of the intra N shell ($n=4$ shell) transitions of tin (Sn) multiplly charged atomic ions. It is normally indispensable to take into account the electron correlations if we are to evaluate the the transition energies within the accuracy of a few electron volts, because the correlation energy of the atomic valence electrons falls in this range. To gain an insight of the effects that are pointed out by

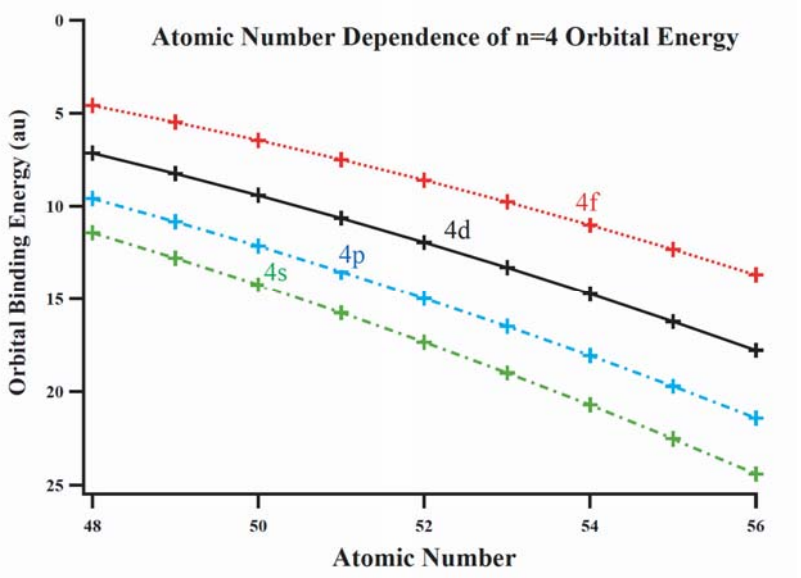

Figure 1. Atomic number Z dependence of the energies of $N=4$ atomic orbitals. The calculated range of the atomic number is $Z=48$ to $Z=56$. Dotted curve: $4f$ orbital, Solid curve: $4d$ orbital, Dot-dashed curve in upper entry: $4p$ orbital, and Dot-dashed curve in lower entry: $4s$ orbital.

O'Sullivan and Faukner[12], we have carried out careful MCDF calculations for $4d^q$ ($q=0$ to 10) atomic ions with atomic number $Z=48$ to 56. Although, they argued only the Sn atomic ions, those effects should be present also in other atomic species. As an example, we show ,in Fig.2, the single electron atomic orbital energies for Sr-like atomic ions of $Z=48$ to 56. To obtain the single electron atomic orbitals and their energies, we have made their MCDF optimizations including the basis wavefunctions up to $6p$, $5d$, and $5f$. In this figure, we can

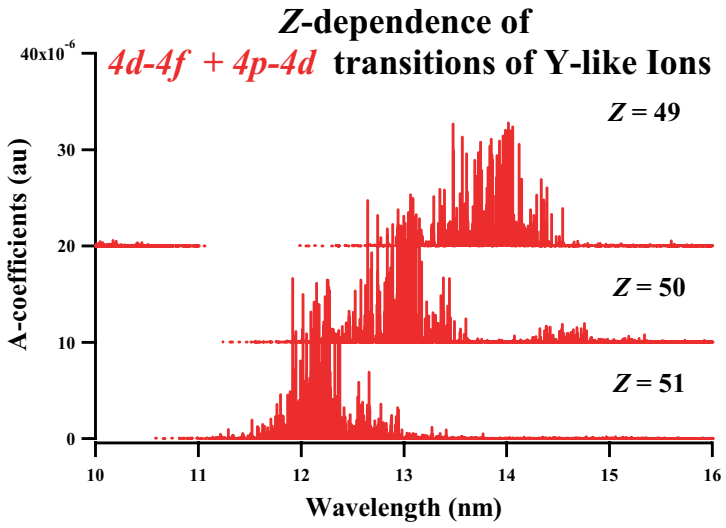

Figure 2. Atomic number Z dependence of Einstein's A-factors for $4d-4f+4p-4d$ transitions of Y-like ions. The interference effects of $4d-4f$ and $4p-4d$ transitions are taken into account by configuration interaction calculations.

find that the differences of orbital energies between $4p$ and $4d$ orbitals, and $4d$ and $4f$ orbitals coincide within the range of a few %. The $4p^6 4d 4f$ and $4p^5 4d^3$ configurations may mix strongly, and the optical $4p-4d$ and $4f-4d$ transitions may take place coherently, providing us with quite a peculiar EUV emission spectrum. The result of the orbital energy calculation stands for the argumentation made by O'Sullivan and FauknerOSullivan1994. Also, we find, from this figure, that we may expect that the so called the effect of spectral narrowing and shift is quite common to the atomic specieds with the atomic numbers in the range $Z = 48$ to 56. As an example of the effect of spectral narrowing and shift, we illustrate, in Fig.3 the calculated Einstein's A-factor distributions of Y-like ions of atomic species with $Z = 49, 50,$ and51. In this figure, we can also observe the change of the spectral shape in the atomic number Z. Due to the interference between the $4p^6 4d^4 - 4p^6 4d^3 4f$ and $4p^6 4d^4 - 4p^5 4d^5$ transitions, we can observe a strong enhancement of the EUV emissions in 13.5 nm region of $Z = 50$, which provides us with the narrowing and shift in appearance of the emission spectra. Due to the term splitting both in the ground and the excited states, the spread of the A factor distribution would have been a couple of ten eV without the interference between the $4p-4d$ and $4d-4f$ transitions. Although the figures are not illustrated in the present paper, we have observed quite a similar interference effect in transitions for wide range of atomic numbers, say, for the range $Z = 48$ to 56, and also for wide range of occupation numbers of N shells.

3. Discussion

The precise and acculate theoretical data of the atomic structures and dynamics that includes the information about the relativistic effect and the electron-electron correlation effects provide us with a good base for precision analysis of highly charged atomic ions in a plasma.. Owing to the general nature of many electron atoms or atomic ions, the inclusion of the effect of configuration interactions among virtually excited states is indispensable to obtain physically realistic atomic state wavefunctions. Especially, it is important to take into account the modification of the

atomic state wavefunctions due to the interactions among various many-electron configurations, which can be evaluated by only an SCF iterations in MCDF calculations. We can point out also that the spectral shift and narrowing should be the effects which are quite common to the $4d$ open shell atomic ion species with moderate atomic numbers. From the view point of atomic multi-configuration Dirac-Fock calculations, which can provide us with plausible shapes for the single electron orbitals by the procedure of non-linear numerical orbital SCF optimization, these effects are due to the coincident agreement of the orbital energy differences among the $N = 4$ sub-shells. This coincident agreement itself is the outcome of electron correlations, and a multi-configuration SCF can account for such correlations in the single electron orbital wavefunctions.

Acknowledgments
This work is partly supported by the Leading Project for advanced semiconductor technology of MEXT. This work was partly supported by the JSPS-CAS Core-University Program in the field of Plasma and Nuclear Fusion.

References
[1] Gillaspy J D 2006 *EUV Sources for Lithography Edited by V. Bakshi, SPIE Press Bellingham, Washinton, USA* 47
[2] Tolstikhina Yu et al 2006 *EUV Sources for Lithography Edited by V. Bakshi, SPIE Press Bellingham, Washinton, USA* 113
[3] G. O'Sullivan G et al 2006 *EUV Sources for Lithography Edited by V. Bakshi, SPIE Press Bellingham, Washinton, USA* 149
[4] Saloman E B 2004 *J. Phys. Chem. Ref. Data* **33** 921
[5] Sasaki A et al 2006 *Proc. of SPIE* **6151** 61513W.
[6] Koike F, Fritzsche S 2007 *J. Phys. Conf. Ser.*bf 58 157.
[7] Tanuma H et al 2005 *Nucl. Instr. Meth.* **B235** 331
[8] Tanuma H et al 2007 *J. Phys. Conf. Ser.* **58** 231
[9] Ohashi H et al 2007 *J. Phys. Conf. Ser.* **58** 235
[10] Parpia F A, Fischer C F and Grant I P 1996 *Commpt. Phys. Commun.* **94** 249
[11] Fritzsche S 2001 *J. Elec. Spec. Rel. Phenom.* **114-116** 1155
[12] O'Sullivan G, Faukner R 1994 *Opt. Eng.* **33**, 3978.

Modified Classical Over Barrier Model for MCI in collisions with multiple electron target at energies below 1 keV/u

ISHII Kunikazu, and OKUNO Kazuhiko[1]

Department of Physics, Nara Women's University Kitauoyanishi, Nara, 630-8506 Japan

1) Department of Physics, Tokyo Metropolitan University, Minami-Ohsawa, 192-0397, Japan

e-mail: ishii@cc.nara-wu.ac.jp

Abstract

There are a number of experimental and theoretical studies about charge transfer collisions at energies above 1 keV/u. It is well known that charge transfer cross sections above 1 keV/u have almost no energy dependence. On the other hand, it is reported that the charge transfer cross sections depend on the collision energy below 1 keV/u.

In order to clarify an energy dependence of charge transfer cross sections in low energy region, we have quantitatively calculated by using modified classical over barrier model for Kr^{q+} with multi-electron targets such as Ne, N_2, O_2 and CO. Essential of this model is taking the induced dipole potential into consideration. As a result, this calculation can reproduce a systematic energy dependence of experimental results. This suggests that the bending trajectory of the projectile due to an induced dipole potential should be considered to describe pictures of collisions at low energy regime below 1 keV/u.

Keywords: Charge transfer, Highly charged ion, Classical over barrier model, Polarization potential

1.Introduction

The model for plasma diagnostics or analysis is based on various parameters in the collisions of highly charged ions such as charge transfer cross sections for wide collision energy range. Charge transfer cross sections of highly charged ions in collisions with atoms and molecules are fundamental data in atomic physics and are the base of simulation codes for plasma diagnosis in thermonuclear plasma or plasma physics. Recently, a number of experimental and theoretical data of charge transfer cross sections for various multiply charged ions in collisions with various targets are studied and summarized data tables are available in the literature and on the database in the web[1][2][3].

It is well known that charge transfer cross sections of highly charged ion at collision energies around keV/u energies do not depend on the collision energy and projectile ions capture electron(s) from the target very state-selectively[4]. These characteristics have

been successfully reproduced by the classical over barrier (COB) model[5][6] and have extended this model to multiple electron capture processes[7].

Contrary to a number of experimental data obtained above 1 keV/u, studies involving charge transfer cross sections below 1 keV/u are scarcely available until now due to experimental difficulties. We employed an octopole ion beam guide and measured charge transfer cross sections for various collision systems. Most of charge transfer cross sections below 1 keV/u were found to vary drastically as a function of the collision energy. For two electron target of He, we have developed the modified COB taking the Langevin type orbiting model and actual energy levels of the collision partners into consideration and have successfully reproduce these energy dependence[8]. For multiple electron targets such as Ne, Ar, N_2, O_2 and CO, it was found systematic energy dependences of which cross sections exhibit minimum dips at around 1 eV/u and begin to increase again with decrease of the collision energy[9]. We explained this energy dependence only qualitatively at that time. In this paper, we have quantitatively calculated charge transfer cross sections of multiply charged ions for multiple electron target using the modified COB.

2. Calculation

In this section, we describe our calculation model developed on the basis of the extended classical-over-barrier model formulated in [5][6][7]. Essential of this model is taking the induced dipole potential into consideration. That is the bending trajectory of the projectile instead of conventional straight trajectory.

In a conventional COB model, a charge transfer cross section of r-electrons by an A^{q+} ion from a target B with n_e electrons is calculated by

$$\sigma_{q,q-r} = \sum_j \sum_{t=1}^{t_{max}} P_t^{(j)} A_t, \tag{1}$$

where $A_t = \pi(b_{t,in}^2 - b_{t+1,in}^2)$ the ring-shaped geometrical cross section, $P_t^{(j)}$ the transfer probability associated with the t-th target electron in a string (j), and t_{max} the smaller number of q and n_e. For highly charged ions with many electron target such as present collision systems, it is well known that projectile ion captures electron(s) into higher energy levels than the ground states of the projectile so that the transfer probability $P_t^{(j)}$ can be considered as almost unity. Here we assume the probabilities are simply unity and then the cross sections are simply given by the geometrical cross sections

$$\sigma_{q,q-t} = \pi(b_t^2 - b_{t+1}^2) \tag{2}$$

The impact parameter $b_{t,in}$ is determined from the critical nuclear distance $r_{t,in}$ in the "way-in", at which distance the perturbed binding energy of t-th electron equals to a maximum potential barrier V_m formed by the collision partners,

$$-I_t - \frac{q}{r_{t,in}} = V_{m,in} = -\frac{1}{r_{t,in}}(\sqrt{q} + \sqrt{t})^2, \tag{3}$$

and we obtain,

$$r_{t,in} = \frac{1}{I_t}(2\sqrt{qt} + t). \tag{4}$$

From the definition given above, $r_{t,in}$ corresponds to the classical turning point.

In low velocity collisions, the interaction potential $V(r)$ may be approximated by the induced dipole potential[10],

$$V(r) = -\frac{\alpha q^2}{2r^4}, \tag{5}$$

with α the polarizability of the target. The relationship between the classical turning point r_c and the corresponding impact parameter b_c is obtained as,

$$b_c = r_c\sqrt{1 - \frac{V(r_c)}{E_o}} = r_c\sqrt{1 + \left(\frac{r_{orb}}{r_c}\right)^4}, \tag{6}$$

where $r_{orb} = (\alpha q^2/2E_o)^{1/4}$ is the classical orbiting radius, inside this radius the incident particle begins to orbit towards the target center.

It should be pointed out that r_{orb} is velocity dependent and becomes large at low incident energies, while the values of $r_{t,in}$ are velocity independent. Here, if $r_{t,in} < r_{orb}$, then the geometrical cross section for the capture of t-th electron should be replaced by the Langevin cross section, $\pi b_{orb}^2 = \pi\sqrt{2\alpha q^2/E_o}$, because the incident ion "orbiting" towards the target nucleus inevitably passes the point of $r_{t,in}$ during orbiting. In this model we assume an transition probability in the orbiting radius is constant and we use this as a fitting parameter.

It is well known a transfer ionization process which is emitting electron after charge transfer since projectile sometimes captures electrons into doubly excited states. To compare this model to experimental cross sections which include transfer ionization process, we include the probability for transfer ionization process in this model. Finally charge transfer cross sections can be described by

$$\sigma_{q,r} = \Sigma_r \pi(b_t^2 - b_{t+1}^2)P_t^{TI}, \tag{7}$$

where P_t^{TI} is the probability of transfer ionization. Here, we also assume P_t^{TI} as a fitting parameter.

3. Results and Disscusion

We have calculated the modified COB for single and multiple charge transfer cross

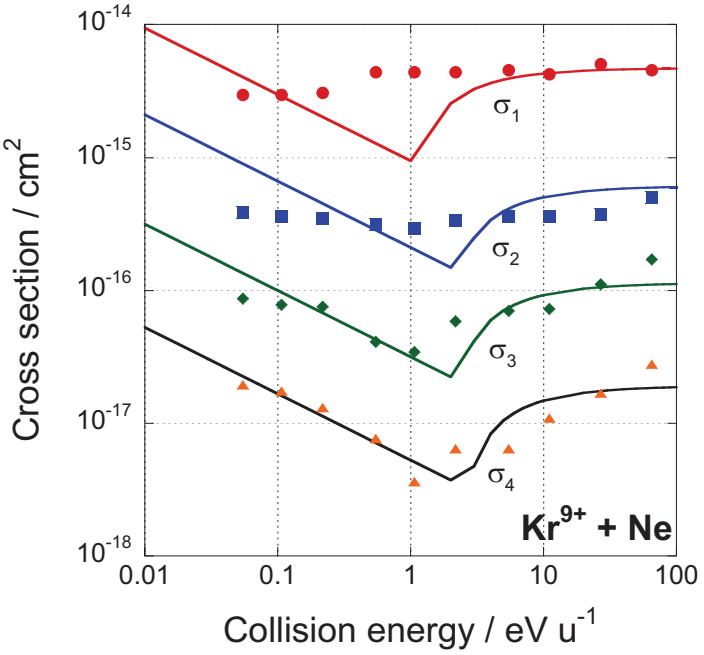

Figure 1: Calculated result of modified COB model for Kr^{9+} + Ne together with experimental results. Solid lines are calculated cross sections for single and multiple electron capture and solid symbols are experimental results as reported in reference[9].

sections of multiply charged Kr ions with multiple electron target as reported in the reference[9]. Here we introduce the results for Kr^{9+} + Ne. Figure 1 shows calculated results of modified COB model for Kr^{9+} + Ne together with experimental results. Solid lines are calculated results and symbols are experimental results. The experimental charge transfer cross sections of Kr^{9+} in collisions of Ne depend on the collision energy. Similar dependence, of which cross sections have a dip as a function of collision energy, have been observed in the collision systems of Kr^{q+} + Ne, CO, N_2 and O_2[9].

As is shown in Figure 1, the calculated cross sections for Kr^{9+} + Ne are in good agreement with experimental results even for multiple electron capture processes. Especially, systematic energy dependence of which cross sections have a dip at around 1 eV/u as a function of collision energy, could be reproduced well. For other multiple electron target

such as CO, N_2 and O_2, our calculation may be good agreement with experimental results since the differences between present Ne and other targets on the present model are only ionization potentials and polarizability of the targets.

In this calculation, we actually use two parameters, which are probabilities for transfer ionization processes and transition probabilities in the orbiting radius, as a kind of fitting parameter. The values of probabilities for transfer ionization process used in present calculations are 90% of double electron capture(DC) and 80% triple electron capture(TC), respectively. Those for double electron capture are 10 % of DC, 15 % of TC and 80 % of quadruple one(QC) , those for triple one are 5 % of TC and 15 % of QC, and those quadruple one are 5 % of QC, respectively. For probabilities in orbiting radius, we use 90 %, 20 %, 3 %, and 0.5 % for single, double, triple, and quadruple capture, respectively.

Present results suggest that most of projectile after multiple electron capture seems to occur transfer ionization and polarization potential play a dominant role in the low energy region below 100 eV/u. To determine experimentally the probabilities which use as fitting parameters in this model, it is necessary to perform coincident measurements between projectile and target recoil ions at low energy regime.

4. Conclusion

We have modified the COB models to represent systematic energy dependence of charge transfer cross sections at energies below 1 keV/u. Essential of modification is taking an induced dipole potential into consideration. That is, we consider the bending trajectory of the projectile instead of conventional straight trajectory approximation. As a result, present results of calculations are in reasonably agreement with experimental results and our simple model can reproduce systematic energy dependences of which charge transfer cross sections have minimum dips at a few eV/u as a function of collision energy. It is concluded that an induced dipole potential play an important role especially in multiple-charge transfer processes.

References

[1] H. Tawara, T. Kato and Y. Nakai, At. Data Nucl. Datatables **32**, 235 (1985).

[2] R. K. Janev, R. A. Phaneuf and H. Hunter, At. Data Nucl. Datatables **40**, 249 (1988).

[3] https://dbshino.nifs.ac.jp/index.html.

[4] M. Barat and P. Roncin, J. Phys. B: At. Mol. Opt. Phys. **25** 2205-224 (1992).

[5] H. Ryufuku, K. Sasaki and T. Watanabe, Phys. Rev. A **21** 745 (1980).

[6] A. Bárány et al., Nucl. Instrum. Meth. Phys. Res. B **9** 397 (1985).

[7] A. Niehaus, J. Phys. B: At. Mol. Opt. Phys. **29** 2925 (1986).
[8] K. Ishii, A. Itoh and K. Okuno, Phys. Rev. A **70** 042716 (2004).
[9] K. Ishii, K. Okuno and N. Kobayashi, Phys. Scr. **T80** 176 (1999).
[10] G. Gioumousis, D. P. Stevenson, J. Chem. Phys.**29** 294 (1958).

Ion Beams with Insulator Capillaries

Takao M. KOJIMA[1], Tokihiro IKEDA[1], Yasuyuki KANAI [1], Vladimir ESAULOV [2], and Yasunori YAMAZAKI [1,3]

1) RIKEN Atomic Physics Laboratory, 2-1 Hirosawa, Wako, Saitama 351-0198, Japan
2) Laboratoire des Collisions Atomiques et Moleculaires, Universite Paris Sud, Orsay 91405, France
3) Institute of Physics, University of Tokyo, Meguro-ku, Tokyo 153-8902, Japan

e-mail: kojima@riken.jp

Abstract

As an extension of our studies of the ion beam guiding with insulator capillaries, an experimental investigation with Teflon capillaries (tubes) has been started very recently. With a brief review of the history of capillary studies and our recent activities, the preliminary results of the beam guide experiment with bent Teflon tubes are presented. Using 8 keV Ar^{8+} beams, beam transmission through bent Teflon tubes of 1 mm inner diameter and about 50 mm long has been observed for radii of curvature r = 270 and 150 mm. In the case of r=150 with about 1.5 nA injection, oscillation of transmitted current has been clearly observed. This oscillation seems to reflect the charge-discharge process of the inner wall of the tube, since the beam guiding phenomena of insulator capillaries are considered due to charge up of the inner wall surface.

Keywords: beam guide, charge up, glass capillary, higly charged ion, insulator surface, ion-surface interaction, teflon tube

1.Introduction

In these years, the ion beam guiding effect of insulator capillaries/tubes has been a matter of interest in the fields of atomic and molecular physics, surface science, material science, etc. The guiding phenomena include processes of interactions between charged particles and insulator surfaces which have not yet been understood totally.

The first observation of ion beam guiding with insulator capillaries was reported by Stolterfoht *et al.* [1]. They irradiated a micro capillary array made on a thin Polyethylene terephthalate (PET) foil with 3 keV Ne^{7+} beams (see Fig. 1a), and measured the ions transmitted through the capillaries as a function of the tilted angle of the foil. The transmitted ions were detected even at 20° while the transmission intensity was two order of magnitude smaller than that at 0°. They attributed the effect to charge up of the inner wall surface of the capillary holes. Namely, the first some impacts of ions

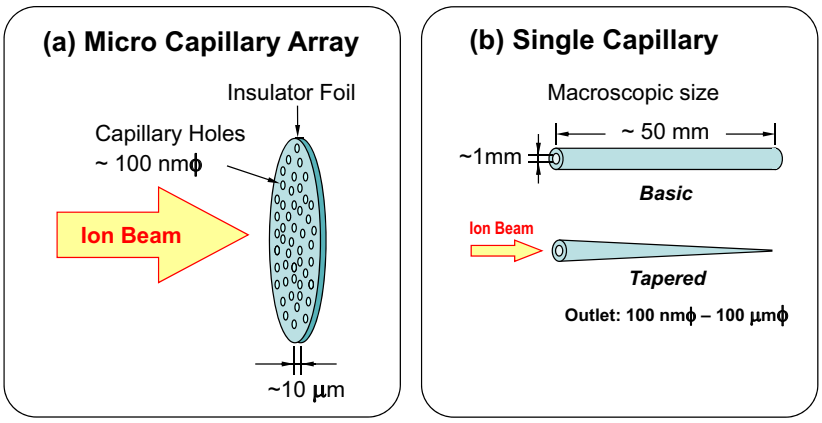

Figure 1: Two types of capillary beam guide. (a) Micro capillary array made on a thin foil of insulator material, e.g. PET, Al_2O_3, etc. (b) Single (tapered) glass capillary/tube.

make a self-organized charge distribution on the surface, and the potential of the charge deflects and guides the following ions to the outlet. After the first observation, the guiding phenomena with capillary arrays of insulator materials, such as PET, ceramics, etc., have been intensively studied experimentally [2-12] as well as theoretically [13-15].

Ion beam guiding effect has also been observed with single tapered glass capillaries (see Fig. 1b). The first experiment of beam guiding with a single tapered glass capillary was performed with 2 MeV He^+ beams by Nebiki *et al.* [16]. They observed not only guiding but also focusing effect. The transmission efficiency, *i.e.* the ratio of the transmitted intensity to the injected intensity, was much larger than the ratio of outlet area to inlet area. In this case, for MeV light ions, the focusing and guiding effect is considered due to mainly scattering of ions at the inner wall surface with small incident angles. This is a different mechanism from the charge-up potential deflection mentioned above.

On the other hand, we observed the focusing and guiding effect of single tapered glass capillaries for keV highly charged ions, and we attributed the effect mainly to the charge up of the inner wall surface similarly to the case of micro capillary arrays [17,18]. Since then, we have been investigating the guiding and focusing properties of single tapered glass capillaries and their applications for both of keV and MeV ions and also for some exotic particles. We found that MeV muons (μ^+, μ^-) can be focused with single tapered glass tubes [19]. We observed the guiding of 10 keV positrons (e^+) with a single straight glass tube [20]. We developed a technique to introduce MeV ion microbeam into liquid by using a tapered glass capillary with a thin glass exit window [21].

Very recently, as an extension of these works, we have started an experimental investigation with Teflon capillaries (tubes). Teflon is a flexible material so that the tube can

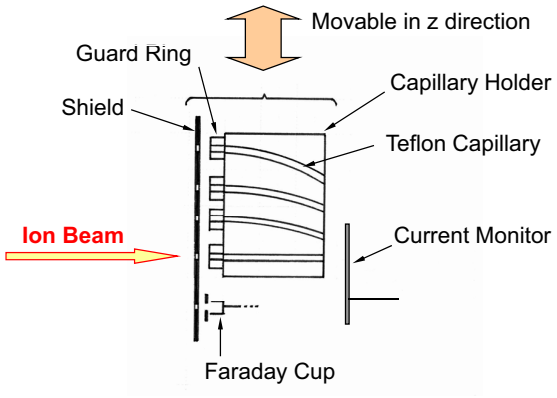

Figure 2: A schematic view of the experimental setup. Four Teflon tubes are set at the holder. Three of them are bent with radii of curvature r = 100, 150 and 270 mm, respectively, and the other is a straight tube. Injected current is estimated from the current measured with the Faraday cup. The transmitted intensity is measured with the current monitor.

be bent with a radius of curvature. For keV highly charged ions, the guiding effect due to the inner wall charge up could be expected even for a bent tube. This might be a first step of realization of flexible tube beam guide and/or very small simple beam bender. In this paper, we present the first, preliminary results of the experiment.

2. Experiment with bent Teflon tubes

The experiment was performed at the low velocity highly charged ion experimental facility in RIKEN. The experimental setup is schematically shown in the Figure 2. The outer and inner diameters and length of the Teflon tubes were 2 mm, 1 mm, and ∼50 mm, respectively. Four tubes were set at the holder. One was straight, and the others were bent with radii of curvature r = 270, 150 and 100 mm, respectively. The length of the holder in beam direction was 45 mm. (Note that the total length of the tube becomes longer as the radius of curvature becomes smaller.) The shield and the holder were combined and movable in vertical direction, therefore we could select the tube for ion beam injection. Injected beam current was estimated from the current measured with the Faraday cup. The transmitted intensity was measured with the current monitor.

The primary beam was 8 keV Ar^{8+} produced at an electron cyclotron resonance (ECR) ion source. The size and the angular dispersion of the beam were about 1.8 mm as the full width at half maximum (FWHM) and about 2.2° as FWHM, respectively. Primary beam current was monitored as a current on the shield and holder, which was considered to be proportional to the injected current.

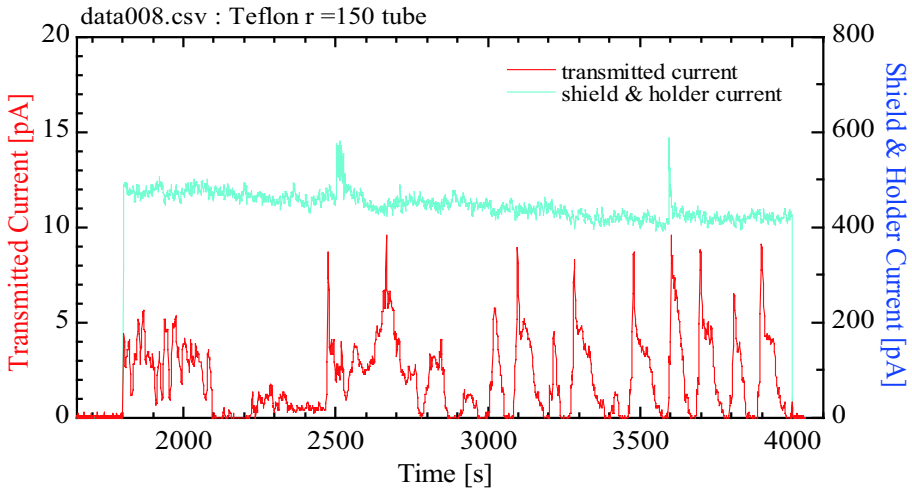

Figure 3: Transmitted current through r=150 tube with about 300 pA 8 keV Ar^{8+} injection. Primary beam is turned on at 1800 s. Shield and holder current is also given as a reference which is supposed to be proportional to both the primary beam intensity and the injected current.

3. Results

For each radius of curvature, we measured the transmitted current with injection of $\simeq$75, $\simeq$300 and $\simeq$1500 pA. In the case of 75 pA injection, no transmitted current was detected for all bent tubes. For 300 and 1500 pA injection, transmitted current was observed for r=270 and 150 tubes. Figures 3 and 4 show the time dependence of the current transmitted through the r=150 tube with 300 and 1500 pA injection, respectively. With 300 pA injection (Fig. 3), the transmitted current is very unstable. With 1500 pA

Table 1: Summary of observed transmission property of the tubes with radii of curvature r=270, 150 and 100 mm for 8 keV Ar^{8+}. Note that these are very preliminary results.

r (mm)	Transmission efficiency		Remark
270	Max$\sim$0.1	(300 pA injection)	
	Max$\sim$0.17	(1.5 nA injection)	
150	Max$\sim$0.03	(300 pA injection)	Clear oscillation was observed
	Max$\sim$0.02	(1.5 nA injection)	for 1.5 nA injection.
100	$\sim$0	(300 pA injection)	Transmitted current sometimes
	$\sim 10^{-3}$	(1.5 nA injection)	became negative.

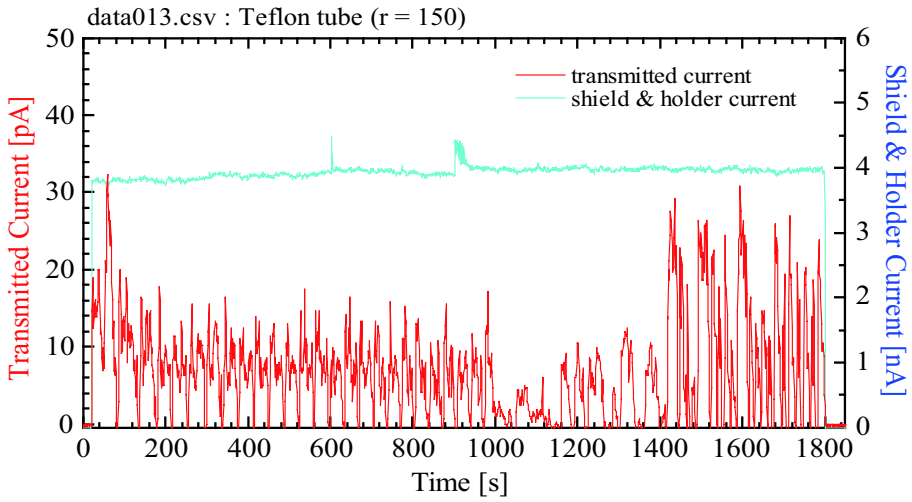

Figure 4: Transmitted current through r=150 tube with about 1.5 nA 8 keV Ar^{8+} injection. Primary beam is turned on at 20 s. Shield and holder current is also given as a reference which is supposed to be proportional to both the primary beam intensity and the injected current.

injection (Fig. 4), the transmission is not a stable direct current either, but somewhat 'stably' oscillated during the period of 200-800 seconds. It might correspond to the cyclic processes of charge up → discharge → charge up → discharge → ... on the inner wall surface. These preliminary results are summarized in Table 1.

Acknowledgement

This work is partly supported by a Grant of Special Projects for Basic Science of RIKEN "Development and Applications of Exotic Quantum Beams".

References

[1] N. Stolterfoht *et al.*, Phys. Rev. Lett. **88**, 133201 (2002).
[2] N. Stolterfoht *et al.*, Nucl. Instrum. Methods B **225**, 169 (2004).
[3] R. Hellhammer *et al.*, Nucl. Instrum. Methods B **232**, 235 (2005).
[4] Gy. Vikor *et al.*, Nucl. Instrum. Methods B **233**, 218 (2005).
[5] M. Fursatz *et al.*, J. Phys.: Conf. Series **58**, 319 (2007).
[6] R. Hellhammer *et al.*, Nucl. Instrum. Methods B **258**, 159 (2007).
[7] Y. Kanai *et al.*, Nucl. Instrum. Methods B **258**, 155 (2007).
[8] R. T. Rajendra Kumar *et al.*, Nanotechnology **16**, 1697 (2005).
[9] M. B. Sahana *et al.*, Phys. Rev. A **73**, 040901 (2006).
[10] H. F. Krause *et al.*, Phys. Rev. A **75**, 042901 (2007).

[11] P. Skog *et al.*, Nucl. Instrum. Methods B **258**, 145 (2007).
[12] A. R. Milosavljevi *et al.*, Phys. Rev. A **75** 030901 (2007).
[13] K. Schiessl *et al.*, Nucl. Instrum. Methods B **232**, 228 (2005).
[14] K. Schiessl *et al.*, Phys. Rev. A **72**, 062902 (2005).
[15] K. Schiessl *et al.*, Nucl. Instrum. Methods B **258**, 150 (2007).
[16] T. Nebiki *et al.*, J. Vac. Sci. Technol. A **21** 1671 (2003).
[17] T. Ikeda *et al.*, Appl. Phys. Lett. **89** 163502 (2006).
[18] T. Ikeda *et al.*, J. Phys.: Conf. Series **58**, 68 (2007).
[19] T. M. Kojima *et al.*, J. Phys. Soc. Jpn. **76**, 093501 (2007).
[20] N. Oshima *et al.*, Materials Science Forum **607** 263 (2009).
[21] Y. Iwai *et al.*, Appl. Phys. Lett. **92** 023509 (2008).

Influence of Debye plasma on the magnetic sublevel excitations of $1s^2\ {}^1S_0$ - $1s2p\ {}^{3,1}P_1$ and the polarization of the corresponding emission lines of Fe^{24+} ions

JIANG Jun[1], DONG Chenzhong[1,2] and LI Bowen[1]

1) College of Physics and Electronic Engineering, Northwest Normal University, Lanzhou 730070, China

2) Joint Laboratory of Atomic and Molecular Physics, NWNU & IMP CAS, Lanzhou 730070, China

e-mail: dongcz@nwnu.edu.cn

Abstract

Electron impact excitations from the ground state to the individual magnetic sublevels of $1s2p\ {}^1P_1$ and ${}^3P_1$ states for highly charged ions of He-like Fe^{24+} imbedded in a weakly coupling plasma are studied by using a fully relativistic distorted-wave method. The Debye-Hückel potential is applied to investigate the influence of plasma screening. It is found that, for the ${}^1S_0$ - ${}^1P_1$ resonance line, the excitation cross sections decrease at all incident energy with the increasing of the screening, but the linear polarization of the emission lines following the excitation are less sensitive and almost invariant for a given impact energy. For the ${}^1S_0$ - ${}^3P_1$ line, however, the influence of plasma screening on the cross sections are relatively smaller than those for the ${}^1P_1$ excitations especially at the low impact energy, but the influence on the linear polarization of this line is significant.

Keywords: electron impact excitation, relativistic distorted wave, Debye plasma

1.Introduction

During the recent decades, considerable interest has been grown in the study of atomic processes in hot and dense plasma environments [1-10] and references therein). Since the line emissions due to excitation can provide detailed information of the physical processes in plasma environment, a number of studies have been done to investigate the influence of plasma on electron-ion impact excitation processes [7-10]. These studies have covered both weakly and strongly coupled plasmas. The electron-ion interaction in the case of weakly coupled plasmas is adequately described by the Debye-Hückel potential, while in the case of strongly coupled plasma the interaction is usually described by the ion-sphere model potential. It is widely accepted that the static Debye-Hückel model is valid for weakly coupled high-temperature and relatively low-density plasmas.

In fast-ignition research, the initial velocity distribution of fast electrons which generated by ultrahigh intensity lasers are highly anisotropic. To address the velocity dis-

tribution function (VDF) of the fast electron, x-ray-line polarization spectroscopy as a good tool for diagnosing in high-density plasmas has been proposed [11-13]. Because the anisotropy of the fast electron VDF can be derived by the observation of the polarization degree. Recently, several experiments have been done to investigate the anisotropic fast electron VDF by using x-ray polarization spectroscopy. Kieffer *et al.*[11,12] first measured the polarization of He-like resonance line $1s2p\ ^1P_1$ - $1s^2\ ^1S_0$ of Al in plasma produced by ultrahigh intensity lasers, and found an increase of polarization as the density increases and deduced electron VDF from pancakelike at low density to a beamlike in the overdense plasma. Yoneda *et al.*[14] measured the polarization of resonance lines of He-like and H-like F ions in the high-density plasma produced by ultrashort-pulse laser and a larger beamlike anisotropic VDF was found. Nishimura *et al.*[15] reported the x-ray polarization of Cl He-like resonance line in plasma produced by ultrahigh intensity lasers. Nevertheless, some of the x-ray polarization including the H-like He-like and Li-like ions were measured in EBIT [16-23]. In addition, the plasma polarization spectroscopy has also been applied to various plasmas diagnostic, such as solar flares [24,25], tokamk plasmas [26], Z-Pinch plasmas [27]. Theoretically, the degree of polarization depends on the extent of deviation from the statistical populations of excited magnetic sublevels. If cascade contribution can be ignored, the polarization reflects the excitation mechanism of each magnetic sublevel. Inal and Dubou [28] have calculated the polarization degrees of the He-like and Li-like iron ions with a non-relativistic theory; Itikawa *et al.* [29] have calculated the polarization degree of the He-like Li,O and Z$\rightarrow\infty$ ions; Reed and Chen [30] have investigated the relativistic effect on the polarization of several heavy He-like ions by using the fully relativistic program of Zhang [31]; and Kai *et al.* [32-34] have investigated the He-like Be, C, O, Cl, Fe, Kr, Xe and Cu ions by using Breit-Pauli R-matrix method. We calculated the polarization degree for quadrupole (M2) line ($(2p_{3/2}^{-1}3s_{1/2})_2$ - $2p^6\ ^1S_0$) of Ne-like Ba^{46+} ions [35], in which the resonant excitation process were considered, and some good agreement were obtained when compared with the experimental measurements by Takács *et al.*[36].

With such theoretical and experimental advancements in the polarization of X-ray lines emissions in plasma, it is of great interest to investigate the effect of an external environment like that of plasma screening on the magnetic sublevel excitations and the corresponding influence on linear polarization of line emissions following the excitation. In this paper, the electron impact magnetic sublevel excitation of $1s^2\ ^1S_0$ - $1s2p\ ^{1,3}P_1$ line of He-like Fe^{24+} ions and the polarization of emission lines following the excitation are studied in Debye plasmas. The paper is organized as follows. In Section II, we firstly provide a short description of the theoretical method and computational procedure. In

Section III, the electron impact excitation cross sections and the corresponding polarization are analyzed. Finally, in the Section IV, a few conclusions about the effects of plasma screening on the electron impact excitations and polarizations are summarized.

2. Theoretical methods

The polarization degree of the radiation emitted without detecting the scattered electron is then defined by

$$P = \frac{I_{\parallel} - I_{\perp}}{I_{\parallel} + I_{\perp}}, \tag{1}$$

where $I_{\parallel}$ and $I_{\perp}$ are the intensities of photons with electric vectors parallel and perpendicular to the electron beam direction, respectively. If assume that electron impact excitation is the dominant mechanism, the linear polarization degree for radiation from the $J = 1$ to the $J = 0$ line is [28]

$$P = \frac{\sigma_0 - \sigma_1}{\sigma_0 + \sigma_1}, \tag{2}$$

where the σ_2 and σ_1 are the electron impact excitation cross sections from the ground state to the $M_f = 0$ and $M_f = 1$ magnetic sublevels, respectively.

The direct electron impact excitation cross section for the magnetic sublevels is given in Ref [35,37] and reference therein. The total cross sections $\sigma_{if}(\varepsilon)$ is given by,

$$\sigma_{if}(\varepsilon) = \frac{\pi a_0^2}{k_i^2 g_i} \Omega_{if}(\varepsilon), \tag{3}$$

where a_0 is the Bohr radius, k_i is the relativistic wave number of the incident electron, g_i is the statistical weight of the initial level of the N-electron target ion and Ω_{if} is the impact strength from an initial state i to final state f.

In order to consider the plasma screening effects, a similar plasma conditions is assumed with done by Pindzola *et al.*[3], that is the densities of plasma is high enough to influence the continuum electron and electron-ion interaction, but not enough to affect the target electrons of the atomic ion, and for simplicity, we also choose the Debye screening model as in the classic paper of Whitten, Lane, and Weisheit [10]. In this case, the coulomb radial matrix element so-called Slater integrals is given by

$$D^k(ab, cd) = \int_0^{\infty} \int_0^{\infty} [P_a P_c + Q_a Q_c] \frac{r_<^k}{r_>^{k+1}} e^{-r/\lambda} [P_b P_d + Q_b Q_d] dr_1 dr_2, \tag{4}$$

where $r_<$ and $r_>$ are the lesser and greater of r_1 and r_2. The Debye-Hückel screening radius is given by

$$\lambda = \sqrt{\frac{k_B T_e}{4\pi e^2 n_e}} \tag{5}$$

where T_e and n_e are the plasma electron temperature and density, respectively, and k_B is the Boltzmann constant.

In our calculations, the wave functions of the target states are generated by the widely used atomic structure package Grasp92 [38]. The continuum wave functions are generated by the component COWF of Ratip package [39] by solving the coupled Dirac equation,

$$\left(\frac{d}{dr} + \frac{\kappa}{r}\right) P_\kappa(r) - \left(2c - \frac{\varepsilon}{c} + \frac{V(r)e^{-r/\lambda}}{cr}\right) Q_\kappa = -\frac{X^{(P)}(r)}{r}, \tag{6}$$

$$\left(\frac{d}{dr} - \frac{\kappa}{r}\right) Q_\kappa(r) + \left(-\frac{\varepsilon}{c} + \frac{V(r)e^{-r/\lambda}}{cr}\right) P_\kappa = \frac{X^{(Q)}(r)}{r}, \tag{7}$$

where, c is the speed of light, and ε is the kinetic energy of the continuum electron. Direct and exchange potentials, V and X are given by Grant *et al.*[40]. These equations are solved by the method of outward integration.

3. Results and discussion

As a check of the present numerical results, we first calculated the electron impact excitation cross sections of the magnetic sublevels of the $1s^2\ ^1S_0$ - $1s2p\ ^1P_1$ and $^3P_1$ excitations and the linear polarization degree of this two emission lines. And a comparison between the present calculations with the calculations of Hakel *et al.*[41] and experiments of Beiersdorfer *et al.*[17,41] (measured in Livermore EBIT in which the density is less than 10^{-12} cm^{-3}) was made. It can be seen from the table I that the present results are in good agreement with the calculations of Halkel and the experiments of Beiersdorfer. Furthermore, the present results are also in very good agreement with calculations of Inal and Dubau [28], who also used a distorted-wave computer code for calculating the excitation cross sections of the magnetic sublevels, as found in Fig. 1, 2 and 4 of their paper. Then, we calculated the electron-impact excitation cross section of the 1s-2p excitation of H-like Ne^{9+} for the incident electron energy ε_i = 1.25 keV, 1.50 keV and 2.00keV under the plasma screening, for the choice of $N_e = 1.1 \times 10^{24}$ and T_e = 500 eV, in this case the Debye length is 2.997 a_0, and the cross sections are $12.108{\times}10^{21} cm^2$, $11.074{\times}10^{21} cm^2$ and $9.844{\times}10^{21} cm^2$, respectively. It can be found that the preset results

Table 1: The direct electron impact excitation cross sections (cm^2) from the ground state $1s^2\ ^1S_0$ to the specific magnetic sublevels M_f of the level $1s2p\ ^1P_1$ and $^3P_1$ of He-like Fe^{24+} ions.

		6.8 keV			8.0 keV		
		Present	Theor.[41]	Exp.[17]	Present	Theor.[41]	Exp.[41]
$1s2p\ ^3P_1$	M=0	3.78×10^{-23}	3.617×10^{-23}		3.52×10^{-23}	3.379×10^{-23}	
	M=1	5.20×10^{-23}	5.112×10^{-24}		3.78×10^{-23}	3.784×10^{-23}	
	total	1.42×10^{-22}	1.384×10^{-22}		1.11×10^{-22}	1.095×10^{-23}	
	P	-0.188	-0.18	$-0.22^{+0.05}_{-0.02}$	-0.036	-0.057	+0.02±0.06
$1s2p\ ^1P_1$	M=0	2.50×10^{-22}	2.559×10^{-22}		2.81×10^{-22}	2.685×10^{-22}	
	M=1	6.33×10^{-23}	5.982×10^{-23}		6.96×10^{-23}	6.876×10^{-23}	
	total	3.77×10^{-22}	3.755×10^{-22}		4.20×10^{-22}	4.060×10^{-22}	
	P	+0.596	+0.59	$+0.56^{+0.17}_{-0.08}$	+0.602	+0.59	+0.50±0.10

agree with the DW calculations of Pindzola *et al.*[3] and the three state close-coupling results of Whitten *et al.*[10] excellently.

In Fig.1, we show the cross sections from the ground state $1s^2\ ^1S_0$ to the specific magnetic sublevels of the $1s2p\ ^1P_1$ and $^3P_1$ states of Fe^{24+} ions as a function of the incident electron energy (in threshold units, they are 6.67keV and 6.70keV for $^3P_0$ and $^1P_1$ respectively) in the presence of a plasma field. In this figure, the solid-line refers to the results without the plasma screening, the dash-line, dot-line, dash-dot-line and dash-dot-dot-line refer the results for the Debye length λ = 50, 10, 5, and 2 (a_0), respectively. As can be seen from figure 1(a), for the excitation from the ground state to the $1s2p\ ^1P_1$ states, which is a dipole allowed transition, the total cross sections increase to a maximum value at the incident energy of about 2 times excitation threshold, and then decrease smoothly with increasing incident energy. The total cross section decreases at all incident energies with the increasing of the plasma screening, namely with the decreasing of the debye length. For the excitation to the $^1P_1$ M = 0 sublevel (figure 1(b)), the cross sections have a similar variational trend with the total cross sections to the $^1P_1$ states, that is to say, with the increasing of incident energy, the cross sections increase to a maximum value at incident energy of about 1.5 times excitation threshold and then decrease smoothly. For the excitation to the $^1P_1$ M = 1 sublevels (figure 1(c)), however, the cross sections increase smoothly with the increasing incident energy and decreases at all incident energies as the debye length decreases. It can be seen from figures 1(d)-(f), for the excitation from the ground state to the $1s2p\ ^3P_1$ states and it magnetic sublevels, which is a spin-forbidden transition, the total cross sections and the cross sections to M = 1 sublevel decrease rapidly with increasing incident energy, nevertheless, the cross sections are less sensitive to the plasma screening especially in the case of low impact energy. For the excitation to the $^3P_1$ M=0 sublevel, the cross sections decrease smoothly with the

increasing of incident energy and the influence of plasma screening is more evident than the excitations to the $^3P_1$ state and $^3P_1$ M = 1 sublevel.

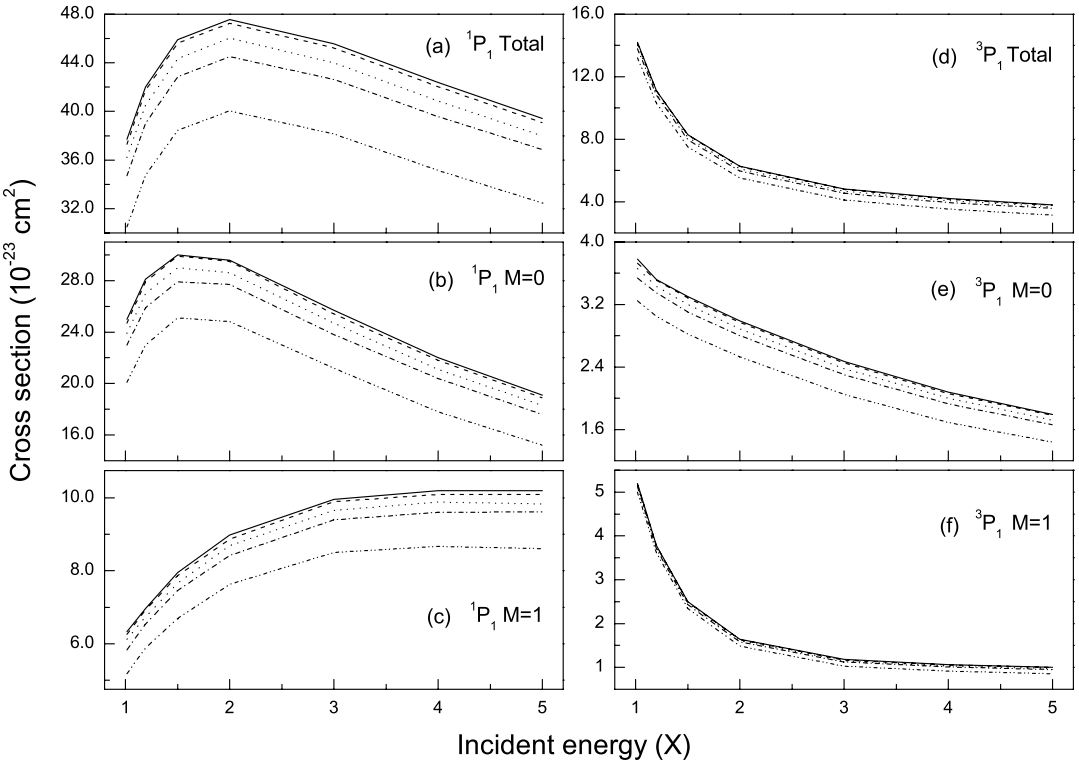

Figure 1: The electron impact excitation cross sections of Fe^{24+} from the ground state $1s^2$ $^1S_0$ to $1s2p$ $^1P_1$ as a function of the incident electron energy (in threshold units, 6.668keV and 6.702keV for $^3P_1$ and $^1P_1$, respectively). The solid-line is the present results without the plasma screening effects. The dash-line, dot-line, dash-dot-line and dash-dot-dot-line refer the results with the Debye-Hückel screening length λ = 50, 10, 5 and 2 (a_0) respectively.

Fig. 2 show the dependence of the cross sections on the debye length from ground state to the $1s2p$ $^1P_1$ and $^3P_1$ states and the individual magnetic sublevels for the incident energy of 1.5 times the excitation threshold. From this figure, it can be found that when the debye length larger than 10 a_0 the effects of the plasma screening on the cross sections are very small for these two excitations, when the $\lambda < 10$ a_0, with the debey length decreasing, the cross sections decrease sharply. It is, however, worth noting that the total cross sections and the cross sections of the M = 0 and M = 1 sublevels for the excitation

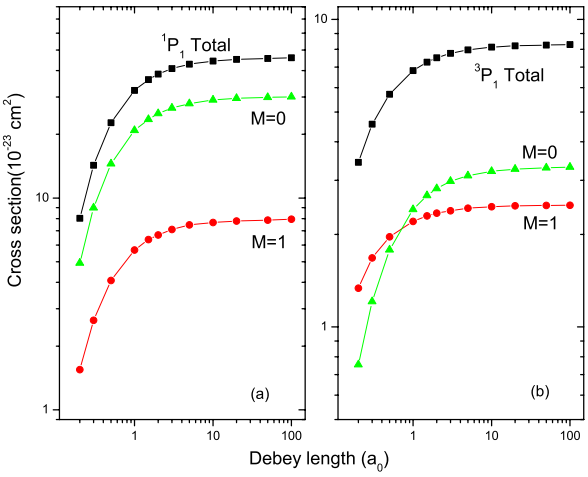

Figure 2: The electron impact excitation cross sections of Fe^{24+} from the ground state $1s^2$ J=0 to the specific magnetic sublevels M_f of the level $1s2p$ J=1 as a function of debye length. The incident electron energy is 1.5 time threshold

to the $^1P_1$ (Fig. 2(a)) states have a similar variational trend, but for the excitation to the $^3P_1$ states (Fig. 2(b)), the cross sections of M = 0 sublevel decrease much sharper than those for the M = 1 sublevel excitation.

Table II gives the linear polarizations of the $1s2p\ ^{1,3}P_1$ - $1s^2\ ^1S_0$ lines in the presence of plasma screening for several impact energies. From this table, it can be found that, with increasing of incident energy, the polarization of the $^1P_1$ resonance line for the unscreened case ($\lambda = \infty$) decrease from 0.60 to 0.358, and the effects of plasma screening on the polarization are quite small. However, with the increasing of incident energy, the polarization of the $^3P_1$ line for ($\lambda = \infty$) vary from the negative to positive. Nevertheless, the influence of plasma screening on the polarization this line are significant especially at the low impact energy, but for the high impact energy, the influence becomes small. As a example, Fig. 4, shows the Debye length dependence of the linear polarization of the $1s2p$ $^1P_1$ and $^3P_1$ to the $1s^2\ ^1S_0$ at the incident energy is 1.5 times the excitation threshold. We found that for the $^3P_1$ line the polarization degree decreases from 14% to -28% with the decreasing of the debye length. However, for the $^1P_1$ line, changes of the polarization degree are very small, and when $\lambda > 2a_0$, the polarization are almost invariant. The reason is that the variational trend of the cross sections excite to the M = 0 and M = 1 sublevels for $^3P_1$ and $^1P_1$ state are different (see in Fig.3).

Table 2: The polarization of the $1s2p\ ^{1,3}P_1$ - $1s^2\ ^1S_0$ emission lines, ε_i is the incident electron energy (X, threshold unit), λ's are the Debye length (a_0).

	$^1P_1$					$^3P_1$				
ε_i	λ=2	λ=5	λ=10	λ=50	λ=∞	λ=2	λ=5	λ=10	λ=50	λ=∞
6.8keV	0.590	0.595	0.592	0.596	0.596	-0.269	-0.224	-0.205	-0.191	-0.188
8.0keV	0.593	0.597	0.601	0.602	0.603	-0.090	-0.054	-0.046	-0.038	-0.036
1.5X	0.579	0.578	0.582	0.583	0.581	0.085	0.108	0.115	0.120	0.122
2X	0.529	0.533	0.534	0.538	0.534	0.205	0.218	0.222	0.225	0.226
3X	0.427	0.434	0.438	0.440	0.441	0.248	0.256	0.259	0.261	0.261
4X	0.345	0.359	0.362	0.367	0.368	0.230	0.240	0.243	0.245	0.246

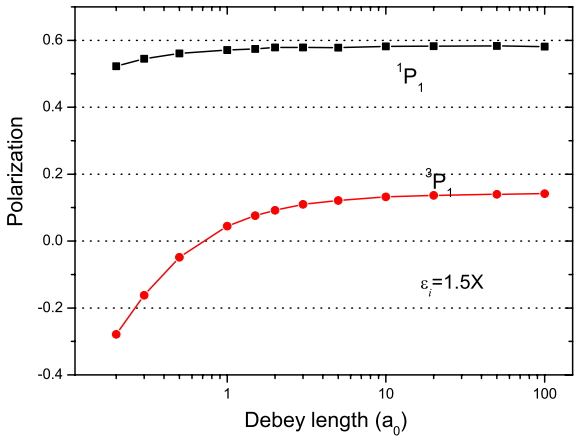

Figure 3: The polarization of Fe^{24+} from the level $1s2p$ J=1 to the ground state $1s^2$ J=0 as a function of debye length. The incident electron energy is 1.5 times threshold.

4. Conclusion

In this paper, electron impact excitations from the ground state to the individual magnetic sublevels of $1s2p\ ^1P_1$ and $^3P_1$ states for highly charged ions of He-like Fe^{24+} imbedded in a weakly coupling plasma are studied by using a fully relativistic distorted-wave method. The Debye-Hückel potential is applied to investigate the influence of plasma screening. It is found that, for the $^1P_1$ resonance line, with the increase of the plasma screening, the excitation cross sections decrease at all incident energy, but the influence on polarization of this line following the excitation are very small. However, for the $^3P_1$ line, the influence of the plasma screening on the cross sections are relatively small especially at the low impact energy, but the influence of polarization of this line is significant. The

reason is that the plasma screening effects on excitation cross sections of the magnetic sublevels for the $^1P_1$ and $^3P_1$ states are different.

Acknowledgement

This work is partly supported by National Natural Science Foundation of China (Grant Nos. 10774122, 10847007, 10876028), the Core-University Program between Japanese Society of Promotion of Science and Chinese Academy of Sciences, the Specialized Research Fund for the Doctoral Program of Higher Education of China (Grant No. 20070736001), the Foundation of Center of Theoretical Nuclear Physics of National Laboratory of Heavy Ion Accelerator of Lanzhou, and the Foundation of Northwest Normal University (Grant No. NWNU-KJCXGC-03-21).

References

[1] S. Chakraborty and Y. K. Ho, Phys. Rev. A **77**, 014502 (2008).
[2] S. Kar and Y. K. Ho, Phys. Rev. A **73**, 032502 (2006).
[3] M. S. Pindzola, S. D. Loch, *et al.* Phys. Rev. A **77**, 062707 (2008).
[4] Z. Q. Wu, G. X. Han, J. Yan, and J. Q. Pang, J. Phys. B **35**, 2305 (2002)
[5] L. Liu, J. G. Wang, and R. K. Janev, Phys. Rev. A **77**, 042712 (2008).
[6] L. Liu, J. G. Wang, and R. K. Janev, Phys. Rev. A **77**, 032709 (2008).
[7] C. G. Kim and Y. D. Jung, J. Phys. B **34**, 5007 (2001).
[8] J. S. Yoon, and Y. D. Jung, Phys. Plasmas **3**, 3291 (1996)
[9] Y. D. Jung, and I. D. Cho, Phys. Rev. A **52**, 5333 (1995)
[10] B. L. Whitten, N. F. Lane, and J. C. Weisheit, Phys. Rev. A **29**, 945 (1984)
[11] J. C. Kieffer, J. P. Matte, M. Chaker, *et al.* Phys. Rev. E **48**, 4648 (1993).
[12] J. C. Kieffer, J. P. Matte, H. Pépin, *et al.*, Phys. Rev. Lett. **68**, 480 (1992).
[13] Y. Inubushi, *et al.* Rev. Sci. Instrum. **75**, 3699 (2004).
[14] H. Yoneda, N. Hasegawa, S. Kawana, and K. Ueda Phys. Rev. E **56**, 988 (1997).
[15] H. Nishimura, Y. Inubushi, *et al.*, Plasma Phys. Control. Fusion **47** B823 (2005)
[16] J. R. Henderson, P. Beiersdorfer, *et al.*, Phys. Rev. Lett. **65**, 705 (1990).
[17] P. Beiersdorfer, D. A. Vogel, K. J. Reed, *et al.*, Phys. Rev. A **53**, 3974 (1996).
[18] P. Beiersdorfer, J. Crespo Lóez-Urrutia, *et al.*, Rev. Sci. Instrum. **68**, 1073 (1997).
[19]P. Beiersdorfer, G. Brown, S. Utter, *et al.*, Phys. Rev. A **60**, 4156 (1999).
[20]A. S. Shlyaptseva, R. C. Mancini, *et al.*, Rev. Sci. Instrum. **68**, 1095 (1997).
[21] D. L. Robbins, A. Ya. Faenov, *et al.*, Phys. Rev. A **70**, 022715 (2004).
[22] D. L. Robbins, P. Beiersdorfer, *et al.*, Phys. Rev. A **74**, 022713 (2006)
[23] N. Nakamura, D. Kato, N. Miura, *et al.*, Phys. Rev. A **63**, 024501 (2001).

[24] E. Haug, Sol. Phys. **61**, 129 (1979).
[25] E. Haug, Sol. Phys. **71**, 77 (1981).
[26] T. Fujimoto, H. Sahara, T. Kawachi, *et al.* Phys. Rev. E **54**, R2240 (1996).
[27] Dong E. Kim, Elena O. *et al.*, Journal of Plasma and Fusion Research **78**, 745 (2002).

[28] M. K. Inal, and J. Dubau, J. Phys. B **20**, 4221 (1987).
[29] Y. Itikawa, R. Srivastava, and K. Sakimoto, Phys. Rev. A **44**, 7195 (1991).
[30]K. J. Reed, and M. H. Chen, Phys. Rev. A **48**, 3644 (1993).
[31]H. L. Zhang, D. H. Sampson, and R. E. H. Clark, Phys. Rev. A **41**, 198 (1990).
[32]T. Kai, S. *et al.*,Nucl. Instrum. Methods Phys. Res. B **235**, 249 (2005)
[33]T. Kai, S. Nakazaki, T. Kawamura, *et al.*, Phys. Rev. A **75**, 012703 (2007)
[34]T. Kai, S. Nakazaki, T. Kawamura, *et al.*,Phys. Rev. A **75**, 062710 (2007)
[35] J. Jiang, C. Z. Dong, L. Y. Xie, J. G. Wang, Phys. Rev. A **78**, 022709 (2008)
[36]E. Takács, E.S. Meyer, J.D. Gillaspy, *et al.*,Phys. Rev. A **54**, 1342 (1996).
[37] J. Jiang, C. Z. Dong, L. Y. Xie, J. G. Wang, *et al.*, Chin. Phys. Lett. **24**, 691 (2007)
[38] F. A.Parpia, C. F. Fischer and I. P. Grant, Comput. Phys. Commun **94**, 249 (1996)
[39] S. Fritzsche *et al.*, Nucl. Instr. and Meth. in Phys. Res. B **205**, 93 (2003)
[40] I. P. Grant, *et al.*, Comput. Phys. Commun. **21**, 207 (1980).
[41]P. Hakel, R C. Mancini, C. Harris, *et al.*, Phys. Rev. A **76**, 012716 (2007)

Charge Exchange Spectroscopy of Multiply Charged Ions Astrophysical/Industrial Interest

TANUMA Hajime[1], OHASHI Hayato[1], SUDA Shintaro[1], FUJIOKA Shinsuke[2], NISHIMURA Hiroaki[2], and NISHIHARA Katsunobu[2]

[1] Department of Physics, Tokyo Metropolitan University, Hachioji, Tokyo 192-0397, Japan

[2] Institute of Laser Engineering, Osaka University, Suita, Osaka 565-0871, Japan

E-mail: tanuma@phys.metro-u.ac.jp

Abstract. Extreme ultra-violet emission spectra of multiply Xe charged ions were measured following electron capture into the excited states of slow ions passing through rare gas targets to provide the spectroscopic data about Xe ions. The comparison with the results of the theoretical calculation indicates the strong configuration interaction in the $n = 4$ sub-shells. Also the non-statistical intensity ratio in the fine-stracuture transitions has been reported.

Keywords: charge exchange, multiply charged ions, atomic spectroscopy, atomic transition, optical emission, extreme ultra-violet, tin ions, xenon ions

1. Introduction

Spectroscopic data on the multiply charged ions have been required for the application of the atomic physics, i.e. astrophysics, plasma diagnostics, and so on. However, the available atomic data on the heavy elements is quite scare for highly charges states of these ions.

Recently, much effort has been focused on the development of an extreme ultraviolet (EUV) light source for the next generation lithography, which is the one of the key technologies in the manufacturing of the semiconductor devices [1, 2]. One of the candidates of the high power EUV light source is the laser plasma of xenon and tin [3]. Therefore, intimate spectroscopic information on multiply charged xenon and tin ions is necessary to understand the physics of EUV plasmas of xenon and tin [4, 5].

On the other hand, the *Hinode*, launched on 22 September 2006, is a solar observational satellite equipped with three advanced telescopes. One of the telescopes is the EUV imaging spectrometer (EIS) has covered the wavelength ranges of 17–21 and 25–29 nm and observed the emissions from moderate charge states of iron ions to reveal the heating mechanism and dynamics of the active solar corona [6]. Although the

atomic data of iron ions is compiled better than other elements, many works are still performing to obtain the accurate spectroscopic data of multiply charged iron ions.

Also the soft X-ray emissions from comets, planets, and all sky have been observed by other satellites. The mechanism of the emissions regarded as the charge exchange reaction of the multiply charged ions in the solar wind [7]. However, the energy resolution of the X-ray spectrometers equipped in the satellites is not enough to discuss in details. Then the transition edge sensor (TES) X-ray micro-calorimeter, which has the high energy resolution of less than 5 eV for 6 keV X-ray, will be used in the next observational satellite [8]. Before the launching of it, the performance of the detector should be checked using the same emissions of the expected transitions in the laboratory. Also, to analyze the satellite data, the state selective emission cross sections in the charge exchange processes are necessary and must be measured.

We have measured the optical emission spectra following the electron capture of multiply charged ions in collisions with neutral gas targets to provide fundamental spectroscopic data, namely the transition wavelengths of multiply charged ions.

2. Experiment

The multiply charged ions were produced with a 14.25 GHz electron cyclotron resonance (ECR) ion source [9]. For tin ions, we inserted pellets of sintered tin oxides, SnO_2, in the plasma chamber and introduced O_2 as the support gas. In the case of iron ions, the vapor of penta-carbonyl iron, $Fe(CO)_5$, was introduced into it. And xenon and oxygen ions were produced with the introduction of source gases.

The produced ions in the plasma chamber were extracted with an electric potential up to 20 kV. The charge-selected ion beam by a dipole magnet was directed into a collision chamber, where the ion beam intersected an effusive beam of target gas from a multi-capillary plate. Optical radiation in the EUV region from the collision center was observed with a compact flat-field grazing-incident spectrometer (SSK-260, Shin Seiki Co.) equipped with a liquid-nitrogen cooled CCD camera (C4880, Hamamatsu).

A wavelength calibration was performed with observation of more than 20 emission lines of O VI and O VII in collisions of O^{6+} and O^{7+} with He and Xe gases. The uncertainty of the observed wavelength was estimated as 0.02 nm.

3. Results and discussion

The observed emission spectra in collisions of multiply charged Xe ions with He atom are shown in Figure 1. The charge state of Xe ions, q, was in the range 9–23. The EUV spectral measurement also has been performed with the incident of Xe^{7+} and Xe^{8+} ions, but no emission line was observed in the wavelength region of 6–22 nm. The similar measurements have carried out using Xe gas target, and the optical emission could be observed in the Xe^{8+} incident case.

The EUV emissions of multiply charges Xe ions are mainly corresponding to the

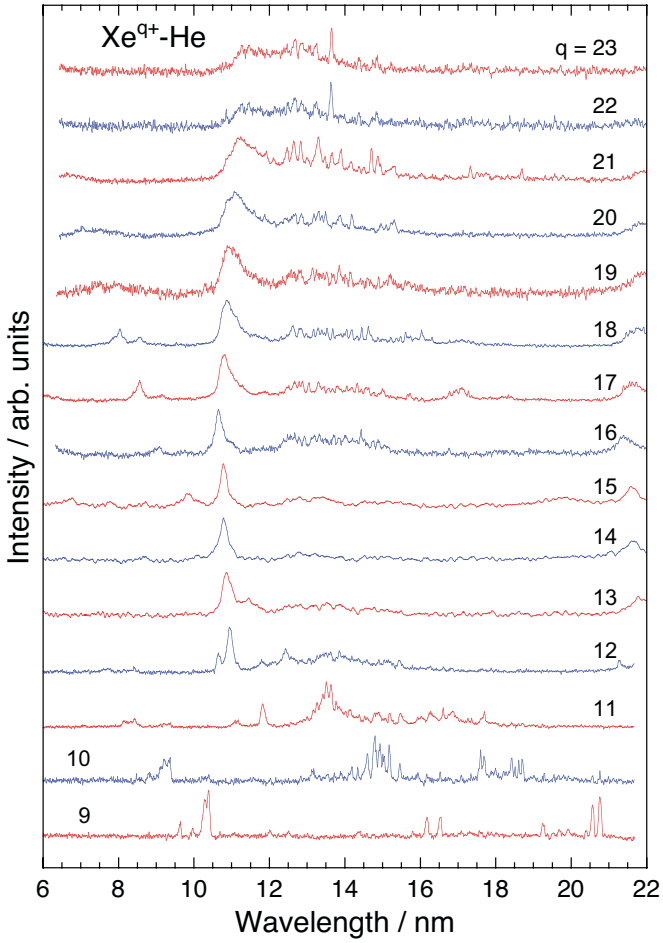

Figure 1. The EUV emission spectra of radiation resulting from the collisions of Xe^{q+} ($9 \leq q \leq 23$) ions with He atomic target at the collision energy of $20q$ keV in the laboratory frame.

optical transitions of 4d-4f, 4d-5p, 4d-5f, and 4p-4d, which stand for $4d^k$-$4d^{k-1}4f$, $4d^k$-$4d^{k-1}5p$, $4d^k$-$4d^{k-1}5f$, and $4p^64d^{k-1}$-$4p^54d^k$ transitions, respectively. Because the $4d^{k-1}n\ell$ configuration has a number of fine-structure levels, 4d-$n\ell$ transitions make a band-like emission, called an unresolved transition array (UTA).

Figure 2 shows charge-state dependence of the average wavelengths of some prominent lines in the observed spectra with both He and Xe targets. The results of the theoretical calculation for UTAs with the HULLAC code are also shown in this figure [10, 11]. The 4p-4d transitions, which have very similar wavelengths to those of the 4d-4f transitions according to the calculation, are omitted in this figure. Here we assume that the charge states of the emitting ions are $(q-1)+$ for the incident of Xe^{q+} ions, because the single electron capture and the transfer ionization can be regarded as the dominant processes in the collisions of multiply charged ions with He [12, 13]. From this experimental result, we can confirm that the 13.5 nm emission from the light source plasma for the EUV lithography is attributed to mainly Xe^{10+} ions and find that the

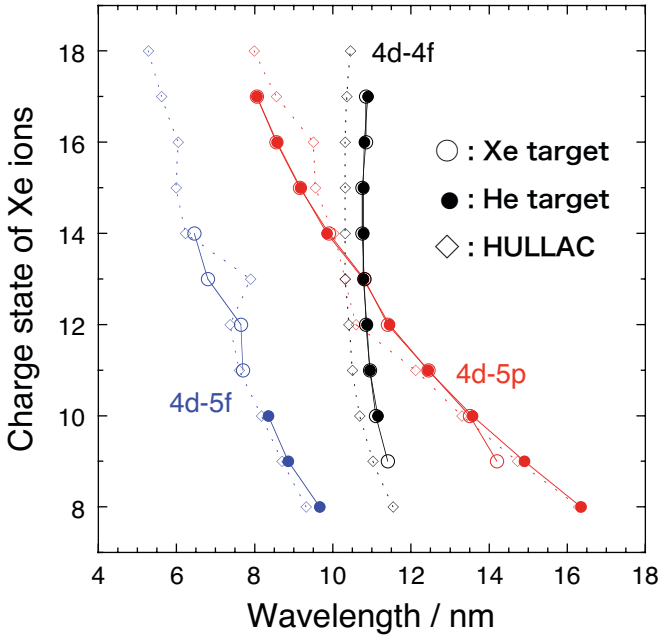

Figure 2. Charge state dependence of the transition wavelengths: open circles, peak positions of the prominent observed emissions in collisions of Xe^{q+} with He target; solid circle, those with Xe target; diamond, the average wavelengths of the 4d-4f, 4d-5p, and 4d-5f transitions calculated with the HULLAC code [10, 11].

small contribution of more highly charge states can be expected.

The good qualitative agreement in the comparison of observed and theoretical wavelengths of 4d-5p and 4d-5f transitions indicates that the prominent emission peaks can be attributed to the single electron capture or transfer ionization, which provides the charge states of $(q-1)+$ in collisions of Xe^{q+} ions. On the other hand, the 4d-4f transitions have approximately constant differences of about 0.5 nm. This discrepancy can be explained by considering the strong interactions between $4p^6 4d^{k-1} 4f$ and $4p^5 4d^{k+1}$ configurations [14, 15], which have been pointed out by O'Sullivan and Faukner [16]. The similar experiments for multiply charged Sn ions also show the discrepancy with the theoretical calculation only for the 4d-4f transitions [17, 18, 19, 20].

The emission spectra in collisions of Xe^{8+} with four rare gas targets is shown in Figure 3. The prominent peaks at 16.84 and 16.95 nm are identified as 5s $^2S_{1/2}$-7p $^2P^o_{3/2}$ and 5s $^2S_{1/2}$-7p $^2P^o_{1/2}$ transitions, respectively. The relative intensity of two lines, which is defined as $I(^2S_{1/2}\text{-}^2P^o_{3/2})/I(^2S_{1/2}\text{-}^2P^o_{3/2})$, should be 2.0 according to the statistical weight because the transition probabilities must be same for these transitions. However, the experimental values are about 0.7 for each target. This phenomenon also observed in the similar experiment for the 7s-7p transitions, which are in the visible light region. At present, we can not find the reason of the discrepancy from the statistical weight, but the strong spin-orbit interaction in the heavy xenon atom should be expected to influence this phenomenon.

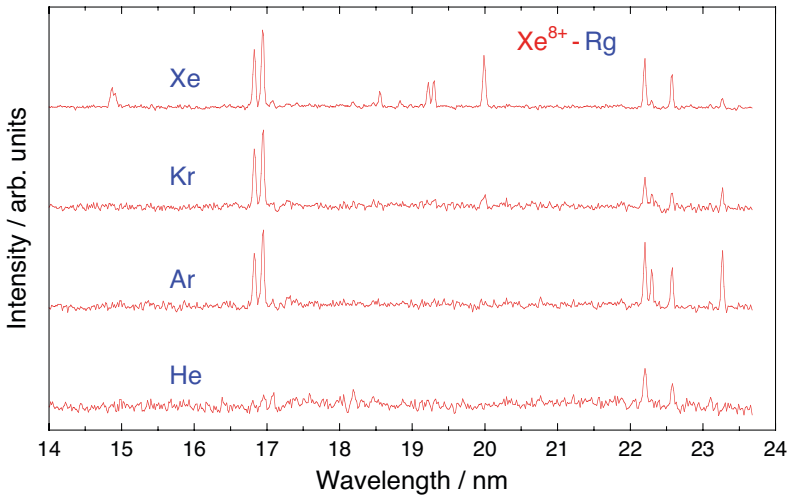

Figure 3. The EUV mission spectra observed in collisions of Xe^{8+} ions with four rare gas targets.

4. Conclusion

The charge exchange spectroscopy of multiply charged Xe ion in the EUV region have been carried out successfully to obtain the fundamental atomic data of transition wavelengths for each charge state. Not only multiply charged Xe ions, the spectroscopic measurement has been already performed with the injection of Sn^{q+} ($8 \leq q \leq 21$), and Fe^{q+} ($7 \leq q \leq 16$) at collision energy of $20q$ keV. The details of these experimental results should be reported elsewhere. On the other hand, the high-resolution spectrum measurement of ions composing of the solar wind is still in progress.

Acknowledgments

The authors are grateful for discussions with A. Sasaki and other member of the working group for the EUV modeling. This work was financially supported in part by the Ministry of Education, Culture, Sports, Science, and Technology, Japan (MEXT) as part of the "Leading Project for EUV lithography source development", and part of this work was performed in a collaborative program with the Institute of Laser Engineering, Osaka University.

References

[1] Bakshi V 2006 *EUV Source for Lithography* (Washington: SPIE press)
[2] Nishihara K *et al.* 2008 *Phys. Plasmas* **15** 056708
[3] Svendsen W and O'Sullivan G 1994 *Phys. Rev.* A **50** 3710
[4] D'Arcy R *et al.* 2009 *Phys. Rev.* A **79** 042509
[5] D'Arcy R *et al.* 2009 *J. Phys. B: At. Mol. Opt. Phys.* **42** 165207
[6] Watanabe T *al.* 2009 *Astrophys. J.* **692** 1294
[7] Fujimoro R *et al.* 2007 *Astron. Soc. Japan* **59** S133

[8] Irwin K D 1995 *PhD thesis, Stanford Univ.*
[9] Tanuma H, Matsumoto J, Nishide T, Shiromaru H and Kobayashi N 2001 *J. Chin. Chem. Soc.* **48** 389
[10] Sasaki A 2003 *J. Plasma Fusion Res.* **79** 315
[11] Sasaki A *to be published.*
[12] Andersson H, Astner G and Cederquist H 1988 *J. Phys. B: At. Mol. Phys.* **21** L187
[13] Selberg N, Biedermann C and Cederquist H 1996 *Phys. Rev.* A **54** 4127
[14] Koike F, Azuma Y, Hasegawa S, Nagata and Nishihara K 2005 *J. Electron. Spec. Relat. Phenom.* **144** 1227
[15] Koike F and Fritzsche S 2007 *Radiat. Phys. Chem.* **76** 404
[16] O'Sullivan G and Faukner R 1994 *Opt. Eng.* **33** 3978
[17] Tanuma H, Ohashi H, Fujioka S, Nishimura H, Sasaki A and Nishihara K 2007 *J. Phys.: Conf. Series* **58** 231
[18] Ohashi H, Tanuma H, Fujioka S, Nishimura H, Sasaki A and Nishihara K 2007 *J. Phys.: Conf. Series* **58** 235
[19] Kato T *et al.* 2008 *J. Phys. B: At. Mol. Opt. Phys.* **41** 035703
[20] Ohashi H, Suda S, Tanuma H, Fujioka S, Nishimura H, Sasaki A and Nishihara K *submitted to J. Phys. B*

Observation of magnetic dipole forbidden transitions in LHD and its application to burning plasma diagnostics

Shigeru MORITA, Motoshi GOTO, Ryuji KATAI[1)], Chunfeng DONG[2)], Hiroyuki SAKAUE, Hangyu ZHOU[2)]

National Institute for Fusion Science, Toki 509-5292, Gifu, Japan
[1)]Institute of Laser Engineering, Osaka University, Osaka 565-0871, Japan
[2)]Graduate University for Advanced Studies, Toki 509-5292, Gifu, Japan

Abstract

The magnetic dipole forbidden (M1) transition has been studied in Large Helical Device (LHD) and F-, Si- and Ti-like M1 transitions are successfully observed for highly ionized Ar, Kr, Mo and Xe ions. The wavelengths measured in visible range for the heavy elements, which are carefully determined with extremely small uncertainties of 0.02-0.05Å as a standard wavelength of usual electric dipole (E1) plasma emissions, are compared with theoretical predictions. The result shows a good agreement with recent Hatree-Fock calculation including semi-empirical adjustment. The M1 intensity for the F-like ions is examined by analyzing the intensity ratio of M1 to E1. Density dependence of the ratio is experimentally verified by comparing with collisional-radiative model calculation on level population. The M1/E1 line ratio for the F-like ions is applied to the α (He^{2+}) particle diagnostics in ITER, where the steady state operation of burning plasmas based on D-T nuclear fusion reaction is expected with α particle heating. Unfortunately, the present estimation suggests a negative result for the α particle measurement because the ratio is largely enhanced by the collisional excitation with bulk ions due to high ion temperature of ITER assumed to be 10keV and the resultant effect of the collisional excitation with α particles becomes less. Meanwhile, the M1 transition, in particular, Ti-like WLIII (W^{52+}) transition (3627Å) emitted in visible range, is very useful for diagnostics of the impurity behavior and the core plasma parameters in ITER.

Keywords: magnetic dipole transition, α particle, ITER
PACS number: 52.70.-m, 52.70.Kz, 52.25.Vy

E-mail address: morita@nifs.ac.jp
Present address (R.Katai): Hamamatsu Photonics K.K., Nishi-ku, Hamamatsu 431-1202, Shizuoka, Japan

1 Introduction

The solution of the time-dependent unperturbed Schrödinger equation is expressed by

$$i\hbar\frac{\partial\Psi_k}{\partial t}=H_0\Psi_k\,. \tag{1}$$

Using the time-independent eigenfunctions, ψ_k, and eigenvalues ,E_k, it can be replaced by

$$\Psi_k=\psi_k(\mathbf{r})\exp(-iE_kt/\hbar)\,, \tag{2}$$

where ψ_k is the sum over the complete set of eigenfunctions. Introducing the classical vector potential, the matrix element is defined as

$$\left\langle\psi_b\left|\exp(i\mathbf{k}\cdot\mathbf{r})\hat{\boldsymbol{\varepsilon}}\cdot\nabla\right|\psi_a\right\rangle, \tag{3}$$

where $\hat{\boldsymbol{\varepsilon}}$ is the unit vector for polarization of radiation and k the propagation vector of radiation. Values of *a* and *b* stand for the initial and final states of the transition. The exponential of exp(*i***k**·**r**) can be thus expanded as

$$\exp(i\mathbf{k}\cdot\mathbf{r})=1+(i\mathbf{k}\cdot\mathbf{r})+\frac{1}{2!}(i\mathbf{k}\cdot\mathbf{r})^2+\cdots. \tag{4}$$

If the quantity (*kr*) is small (k~10^{-3}Å and r<10Å in general atom), the exponential can be replaced by unity. This is known as the electric dipole (E1: $\Delta\ell=\pm1$) transition, which is usually observed in the plasma spectroscopy. If the higher terms in the series of eq.(4) is not negligible, on the other hand, the transition changes to the magnetic dipole (M1: $\Delta n=0$ and $\Delta\ell=0$) and electric quadrupole (E2: $\Delta\ell=0,\pm2$). In general, the magnetic interaction is smaller than the electric interaction in the fine structure constant. For large values in atomic number, Z, however, the forbidden transition becomes important.

The specific character of the magnetic dipole forbidden (M1) transition is seen in the wavelength, λ, and transition probability, A, as plotted in Figs.1 (a) and (b), respectively[1-5]. The wavelength of the M1 transition is much longer than that of the E1 transition. In particular, the wavelength becomes constant in visible range for the Ti-like M1 transition at Z>50 where the L-S coupling gradually changes into the j-j coupling. The transition probability, which is the most important parameter in the plasma spectroscopy, quickly changes with Z (see Fig.1 (b)). The value for the F-like M1 transition increases as $A\propto Z^{12}$, whereas the E1 transition increases with $A\propto Z^3$. Therefore, the M1 transition is important in heavier elements in the plasma diagnostics. The spectroscopy of such heavy elements in the visible range can bring a large advantage for the impurity diagnostics in D-T burning plasmas in the future fusion device such as ITER, where Mo or W is planned as the plasma facing component. The vacuum ultraviolet (VUV) and extreme ultraviolet (EUV) spectroscopy are quite difficult in the burning plasma because of the tritium handling, the instrumental position close to the device and the necessary use of many mirrors. Furthermore, the M1 transition sensitive to the ion impact excitation has a capability for diagnostics of high-energy particles like α (He^{2+}: 3.5MeV) particle, which is the fusion product of D-T reaction.

The M1 transition has been experimentally studied in Large Helical Device (LHD: R/<a>=3.6m/0.64m, B_t<3T, V_p=30m^3) with its identification for heavy elements. The study of the M1 transition is very important to establish a complete atomic structure model through the exact understanding of the higher term seen in the eq.(4). In this

paper, the experimental result on the M1 study is presented with the analysis on the ratio of M1 to E1 for the F-like ions. Feasibility on the burning plasma diagnostics is also discussed.

2 Visible spectra of M1 transition

Ar spectra in visible, VUV and EUV ranges are observed from Ar discharges in LHD[6,7]. A typical example of the visible M1 lines measured with a 50cm visible spectrometer is shown in Fig.2. Five M1 transitions of ArX ($2s^22p^5\ ^2P_{3/2}$-$^2P_{1/2}$: 5533Å), ArXI ($2s^22p^4\ ^3P_2$-$^3P_1$: 6917Å), ArXIII ($2s^22p^2\ ^3P_1$-$^3P_2$: 8340Å), ArXIV ($2s^22p\ ^2P_{1/2}$-$^2P_{3/2}$: 4412Å), and ArXV ($2s2p\ ^3P_1$-$^3P_2$: 5944Å) are seen in the spectrum. The ArXIV line blended with two ArII lines can be resolved if the spectrum is recorded by a high-resolution 2400g/mm grating. The wavelengths of the Ar M1 transition are carefully determined as reference lines of NeI (5944.834Å), ArII (4400.986Å and 4426.001Å), and BII (2×3451.287Å) and NeI (6929.467Å). Since the two M1 transitions of ArX and ArXV are completely isolated from other lines, those are useful for the plasma diagnostics. The F-like M1 transition of ArX at 5533Å is used for the intensity analysis with resonance transition existing in EUV range of ArX (ArX $2s^22p^5\ ^2P_{3/2}$-$2s2p^6\ ^2S_{1/2}$: 165.53Å).

The M1 transitions from highly ionized Kr and Mo and Xe ions are also observed in LHD[8]. The inert gases are introduced by gas puffing and the solid material is injected using impurity pellet injector[9-11]. Typical spectra from those elements in visible range are shown in Fig.3. The Si-like KrXXIII (Kr^{22+}: $3s^23p^2$ - $^3P_1$-$^3P_2$, 3841.07Å) is identified as reference lines of HI 3835.384Å and ArII 3850.581Å. In general, the finding of the M1 transition for such heavy elements is easy, because those spectral lines are clearly broadened, which is based on the high ion temperature, compared to other usual E1 spectral lines in low ionization stages. Another good method for finding the M1 transition is to use the polarization. The σ and π components of the M1 transition shows entirely the opposite direction to magnetic field line when it is compared with the E1 transition[12]. This method is, of course, limited to the visible spectroscopy.

The result of the wavelengths determined in the present study is summarized in Table 1. The LHD discharge is very stable even if a large amount of impurity is brought in the plasma. Signal intensity enough for the atomic physics study can be observed within 0.2-1.0s. Then, the error bars in the present experiment are quite small compared to other experimental results which are mainly obtained from EBIT and tokamak experiments. When the observed wavelength is compared with relatively old calculations[1-3], the agreement between the experiment and theory is quite poor. However, recent Hatree-Fock approach[24] including relativistic corrections done with semi-empirical adjustments based on several experimental results shows a good agreement with the present results, e.g., XeXXXIII. Although the Ti-like WLIII is tried to observe in LHD, it is unfortunately difficult because of the absence of enough electron temperature. In case of Ar M1 transition, which is not listed in the table, the theory shows an excellent agreement with the experimental result since the LS-coupling is simply applicable to the atomic configuration.

3 Intensity ratio of M1 to E1

Several theoretical calculations on the M1/E1 line intensity ratio have been done until now[26,27]. However, there exists no detailed experimental study on the intensity ratio[28]. In order to study the ratio experimentally, therefore, the simplest atomic configuration of F-like ions is selected. The energy level diagram of ArX is illustrated in Fig.4. The width of arrows, which denotes the atomic processes taken into account in the model, represents the magnitude of the population flow at typical plasma parameters. The population at level 3 proportionally increases with the electron density, since the population at level 1 follows the corona equilibrium. On the other hand, the population mechanism at level 2 is complicated because the transition probability is small ($1.06\times10^{2}s^{-1}$) and several processes are competitive.

Five processes are considered for the analysis of the level 2 population, i.e., electron- and proton-impact excitation and de-excitation, electron-impact ionization and E1 and M1 transitions. A set of quasi-steady-state rate equations for F-like ions is written by

$$n_1 = n_{g1}, \tag{5}$$

$$n_2[n_e(C^e_{21}+C^e_{23} + S_2) + n_pC^p_{21} + n_{fp}C^{fp}_{21}+ A_{21}] = n_1(n_eC^e_{12} + n_pC^p_{12} + n_{fp}C^{fp}_{12}) + n_3(A_{32} + n_eC^e_{32}) \tag{6}$$

and $$n_3[n_e(C^e_{31} + C^e_{32} + S_3) + A_{31} + A_{32}] = n_1n_eC^e_{13} + n_2n_eC^e_{23}, \tag{7}$$

where the subscripts of 1, 2, and 3 are denoted in Fig.4. The symbols for each atomic process are used in usual manner. The value of n_{g1} is normalized to unity.

A typical result from the calculation is shown in Fig.5. The level 2 is populated by the collisional excitation from level 1 and the radiative cascade from level 3, of which the transition rates are proportional to the electron density. In low-density range, therefore, the ratio of M1/E1 is constant because the level 2 is depopulated through the radiative transition of M1. Increasing the density, the collisional de-excitation at level 2 begins to predominate over the radiative process. Since the level 2 population is saturated in high-density range, the density dependence is appeared in the line intensity ratio of E1/M1.

The spectra of E1 and M1 are measured from neutral-beam-heated plasmas of LHD. The intensities are analyzed after absolute calibration of visible, VUV and EUV spectrometers[29], as plotted in Fig.6. Experimentally obtained density dependence of the line ratio tends to be in good agreement with the model calculation, although a clear discrepancy is observed in their absolute values. The line of ArXIII (164.82Å) is blended with the ArX (165.53Å) line and several FeVII lines exist in the same wavelength range as the ArX 165.53Å line, e.g., 164.955Å, 165.087Å, 165.630Å, 165.658Å, 165.724Å, 165.764Å, 165.919Å, 165.996Å and 166.010Å in addition to the CrXIX 165.45Å line. The presence of these lines could make the ArX ratio smaller, since the intensity of the ArX 165.53Å is relatively weak. The situation is also very similar to the case of FeXVIII. Since the FeX (94.012Å) line is strong after the iron pellet injection, the E1 line of FeXVIII (93.93Å) blended with the FeX line seems to have a big error.

The collisional excitation by fast protons, which originate in the NBI for plasma heating, is examined. The result is also shown in Fig.6 for the fast proton densities of 10^{17} to $10^{19}m^{-3}$. The number of fast-protons provided by NBI is $4.17\times10^{20}s^{-1}$ at input

power of 12MW with injection energy of 180keV. The density of the fast-proton is estimated to be $1.4\times10^{19}m^{-3}$ where the energy slowing down time of 1s and the LHD plasma volume of $30m^3$ are taken into account. The ratio of M1/E1 is largely affected by the presence of the fast proton in lower density range. The contribution of the fast proton excitation is reduced in higher density range, since the electron excitation becomes dominant. The study can be practically attempted for TiXIV and FeXVIII M1 lines, since the ArX has no chance to observe the influence of the fast proton excitation, as seen in Fig.6 (a). The ratio for TiXIV tends to be in a good agreement with the calculation. However, the lowest operational density limit in LHD is $0.2\times10^{19}m^{-3}$. The contribution of the fast proton excitation could not be experimentally verified so clearly at present.

4 Application to burning plasmas in ITER

International thermonuclear energy reactor, ITER, is being constructed for the purpose of D-T burning plasma production. The impurity diagnostics using visible spectroscopy is desired instead of the usually used EUV spectroscopy because of its difficulty in ITER. In order to solve this problem, the M1 transition has been studied in LHD. Several M1 transitions are successfully observed with enough intensity for measurements of F-, Si- and Ti-like ions in low-density plasmas ($\leq2x10^{19}m^{-3}$). The result strongly suggests that the M1 transition is sufficiently applicable to the ITER diagnostics. Here, we calculate the radial position of those ions in ITER as a function of central electron temperature, as shown in Fig.7. In the ITER the use of a heavy material having high melting point such as Mo and W is planned as a plasma facing component. The impurity diagnostics is possible in the plasma center of ITER when we use the Ti-like WLIII (W^{52+}). The ion temperature and rotation measurements are also possible. The use of F-like WLXV (W^{60+}) and Si-like WLX (W^{65+}) is probably difficult because high-electron temperature around 20keV is required for production of such ions. If several elements as seen in the Fig.7 can be used, the M1 transition is further useful because the diagnostics can be applicable to wider temperature range.

Alpha particle (He^4) generated in burning plasmas is a main heating source for the maintenance of the steady state operation in fusion reactor. At present the following nuclear fusion reaction is considered for the fusion reactor;

$$D + D \rightarrow He^4\ (3.52MeV) + n\ (14.06MeV). \quad (8)$$

The α particle confined in the fusion device deposits its energy to the bulk plasma by colliding with other particles. The information on the alpha particle becomes indispensable in such next-generation fusion device such as ITER. A variety of alpha particle diagnostic methods have been proposed and demonstrated up to this day, nevertheless, no conclusive method still exists at present. Here, a possibility for the alpha particle diagnostics using the intensity ratio of M1/E1 is examined. Emission intensity of the M1 transition can be enhanced by the presence of high-energy ions as mentioned above. Figure 8 shows excitation rate coefficients of the M1 transition ($2s^22p^5\ ^2P_{3/2}$-$^2P_{1/2}$) for F-like FeXVIII and KrXXVIII induced by collisions with proton (p), deuteron (d), triton (t) and alpha particle (α). The cross section necessary for the rate coefficient is calculated using the flexible atomic code (FAC) [3] and the extrapolation of the values is done for several ion cases[27]. The alpha particle has larger rate coefficient above 3keV compared to other particles.

The M1/E1 line intensity ratio is well explained with three levels population calculation and the effect of fast ions from NBI is also examined as described above. A similar calculation with the alpha particle is done for F-like ions. The atomic data used in the calculation is listed in the reference of 24. The energy distribution of the alpha particle is simply assumed to be a mono-energetic distribution in this calculation. Figure 9 shows the M1/E1 line ratios for ArV, TiXIV, FeXVIII, KrXXVIII, MoXXXIV and XeXLVI as a function of electron density. The result is calculated for three different cases of only electron impact excitation (solid line), electron + deuterium + triton impact excitation and electron + deuterium + triton + α particle impact excitation in order to examine the effect of ion impact excitation. The density of α particles is assumed to be 1% to the electron density with electron and ion temperatures of 10keV and electron density of $1x10^{20}m^{-3}$ at the plasma center. The contribution of the bulk ion to the ratio is dominant, because the ion temperature is high enough for the excitation of M1 transition. The additional presence of the α particles makes only a small increment in the ratio, i.e., less than a few %. Therefore, the result seems to be negative for the α particle diagnostics, at least, in the present atomic configuration of F-like ions.

When the atomic number increases, the wavelength of F-like M1 transition becomes shorter and the information on the energetic particle begins to disappear. Another candidate for the alpha particle measurement is to use the Ti-like M1 transition such as WLIII (W^{52+}). However, the reliable calculation for the Ti-like m1 transition is not possible at present, because the atomic structure is really complex and several atomic data are in the absence for the Ti-like ion of which the ground configuration has thirty four fine structure levels.

5 Summary

The M1 transition has been studied in LHD for several elements and the intensity was examined by analyzing the intensity ratio of M1 to E1. The wavelengths for heavy elements such as Kr, Mo and Xe are compared with theoretical predictions and show a good agreement with recent Hatree-Fock calculation including semi-empirical adjustment. Density dependence of the ratio is experimentally verified with collisional-radiative model calculation on level population. The M1/E1 line ratio for F-like ions is applied to the alpha particle measurement in ITER. Unfortunately, the estimation indicates a negative result for the α particle measurement because of the less amount of the α particle in the burning plasma. The combination with polarization and Zeeman spectroscopy on the M1 measurement possibly brings new information on the burning plasma diagnostics.

Acknowledgements

This work was partially carried out under the LHD project financial support (NIFS09ULPP527). This work was also partially supported by the JSPS-CAS Core-University program in the field of 'Plasma and Nuclear Fusion'.

References

1 Kaufman V, Suger J. 1986, J. Phys. Chem. Ref. Data, 15: 321
2 Huang K N, 1985, At. Data Nucl. Data. Tables, 32: 503
3 Feldman U, Indelicato P, Sugar J. 1991, J. Opt. Soc. Am. B, 8: 3
4 Biemont E, Träbert E, Zeippen C J. 2001, J. Phys. B, 34: 1941
5 Utter S B, Beiersdorfer P, Träbert E. 2003, Phys. Rev. A, 67: 012508
6 Katai R, Morita S, Goto M. 2006, J.Plasma Fusion Res. SERIES, 7: 9
7 Katai R, Morita S, Goto M. 2007, Plasma Fusion Research, 2: 014
8 Katai R, Morita S, Goto M. 2007, Plasma Fusion Research, 2: 006
9 Morita S, Y.Shirai, M.Goto, et al. 2002, Nucl.Fusion, 42: 876
10 Nozato H, Morita S, Goto M, et al. 2003, Sci. Instrum., 74: 2032
11 Katai R, Morita S, Goto M, et al. 2007, Jpn. J. Appl. Phys., 46: 3667
12 Iwamae A, Atake M, Sakaue A, et al. 2007, Phys. Plasmas, 14: 042504
13 Serpa F G, et al. 1997, Phys. Rev. A, 55: 1832
14 Chen H, Beiersdorfer P, Harris C L, Utter S B. 2002, Phys. Scr., 66: 133
15 Träbert E, Utter S B, Beiersdorfer P. 2000, Phys. Lett. A, 272: 86
16 Tupitsyn I I, et al. 2003, Phys. Rev. A, 68: 022511
17 Träbert E, Beiersdorfer P, Utter S, et al. 1998, Phys. Scr., 58: 599
18 Morgan C, et al. 1995, Phys. Rev. Lett., 74: 1716
19 Watanabe H, et al. 2001, Phys. Rev. A, 63: 042513
20 Crespo López-Urrutia J R, Beiersdorfer P, et al. 2002, Can. J. Phys. 80: 1687
21 Porto J V, Kink I, Gillaspy J D. 2000, Phys. Rev. A, 61: 054501
22 Utter S B, Beiersdorfer P, Träbert E. 2003, Phys. Rev. A, 67: 012508
23 Sugar J, Kaufman V, Rowan W L. 1991, J. Opt. Soc. Am. B, 8: 22
24 Biemont, E, Träbert E, Zeippen C J. 2001, J. Phys. B, 34: 1941
25 Kato D et al. 2001, J. Chinese Chem. Soc., 48: 525
26 Suckewer S, Hinnov E. 1979, Phys. Rev. A, 20: 578
27 Foster V J, Keenan F P, Reid R H G. 1994, Phys. Rev. A, 49: 3092
28 Katai R, Morita S, Goto M. 2007, J. Quant. Spec. Rad. Trans., 107:120
29 Chowdhuri M B, Morita S, Goto M, et al., 2007, Rev. Sci. Instrum., 78:023501
30 Gu M F, et al., 2005, Astrophys. J., 627: 1066.

Table 1 Wavelength determination of M1 transitions in the present study. Results are compared with former experimental works and theoretical predictions.

Spectra	Transition	Observed (Å)		Calculated (Å)
		This work	Others	Others
KrXXII (Kr^{21+})	$3s^23p^3$	3463.75±0.05	3464.7±0.6 [13]	3446±30 [1]
E_i=990eV	$^2D_{3/2}$-$^2D_{5/2}$		3466.6±0.2 [14]	3438±2 [23]
KrXXIII (Kr^{22+})	$3s^23p^2$	3841.07±0.03	3840.9±0.3 [1]	3832±40 [1]
935eV	$^3P_1$-$^3P_2$		3841.4±0.2 [15]	3845 [20]
			3841.146±0.002 [16]	3837.0±6.5 [16]
MoXXIX (Mo^{28+})	$3s^23p^2$	2842.10±0.05	2841.1±0.2 [1]	2834±40 [1]
1590eV	$^3P_1$-$^3P_2$		2840±2 [17]	2712.1511 [2]
XeXXXIII (Xe^{32+})	$3d^4$	4139.01±0.02	4139.4±2.0 [18]	4052 [20]
1920eV	$^5D_3$-$^5D_2$		4138.8±0.7 [19]	3952.5 [3]
			4139±2 [20]	4138.3 [24]
WLIII (W^{52+})	$3d^4$	not observed	3626±2 [21]	3627.2 [24]
4927eV	$^5D_3$-$^5D_2$		3626.7±0.5 [19]	3624.7 [19]
			3627.13±0.10 [22]	3625.68 [25]

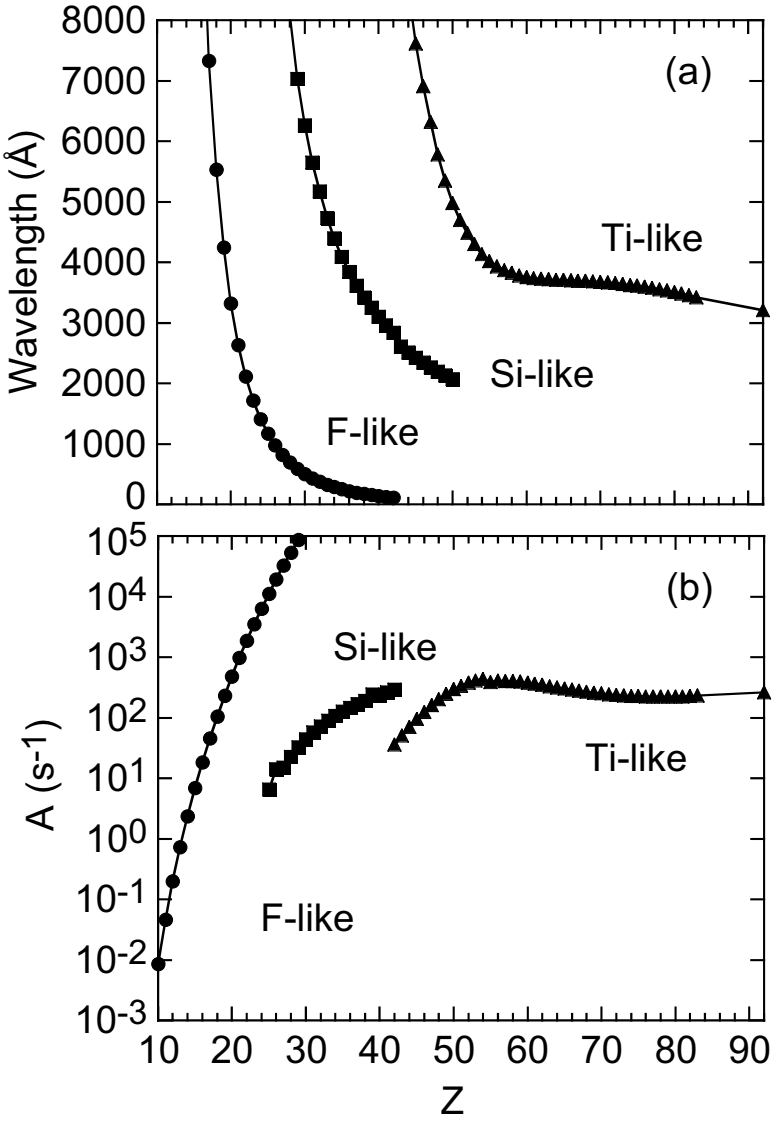

Fig.1 (a) Wavelength and transition probability of magnetic dipole forbidden (M1) transitions for F- (solid circles)[1], Si- (solid squares)[1,2] and Ti-like (solid triangles)[3-5] isoelectronic sequences as a function of atomic number, Z.

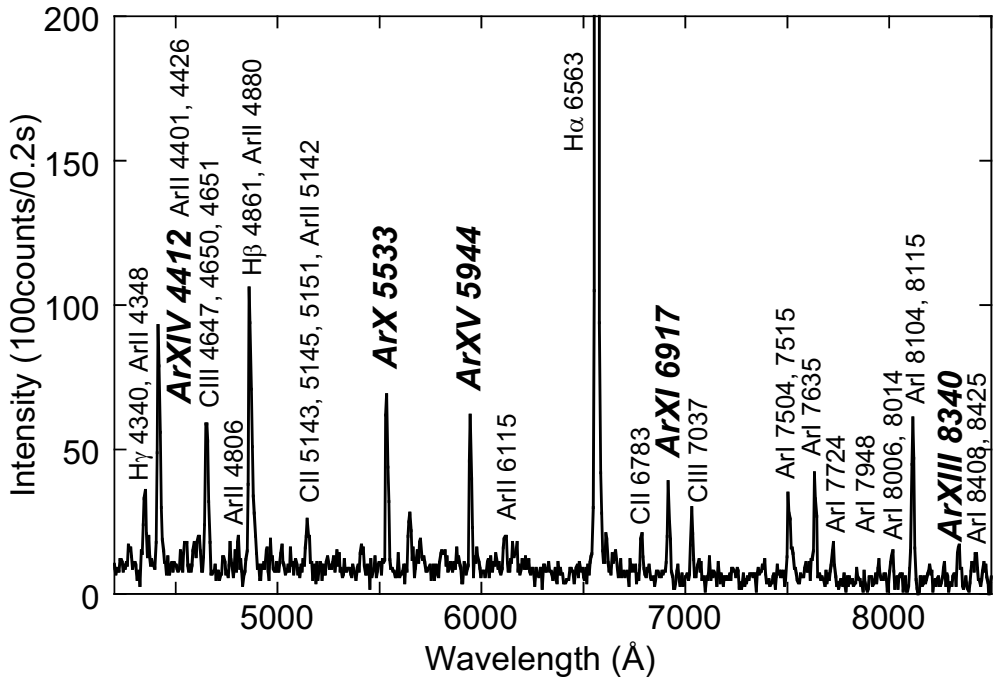

Fig.2 Ar spectrum in visible range from Ar discharges in LHD. Thick italic fonts denote M1 transitions from argon ions.

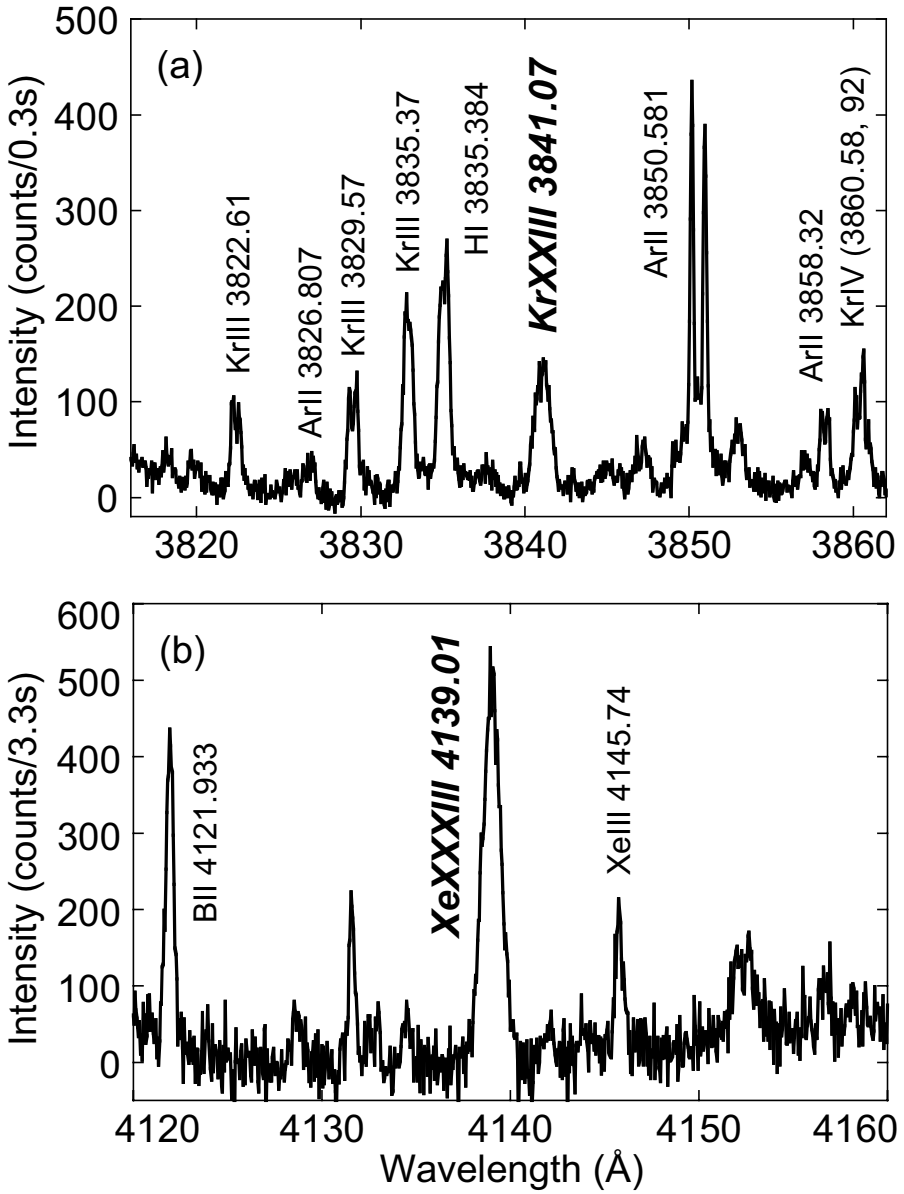

Fig.3 (a) Si-like KrXXIII (3841.07Å) and Ti-like XeXXXIII (4139.01Å) M1 transitions in visible range from LHD discharges with Kr and Xe gas puff, respectively.

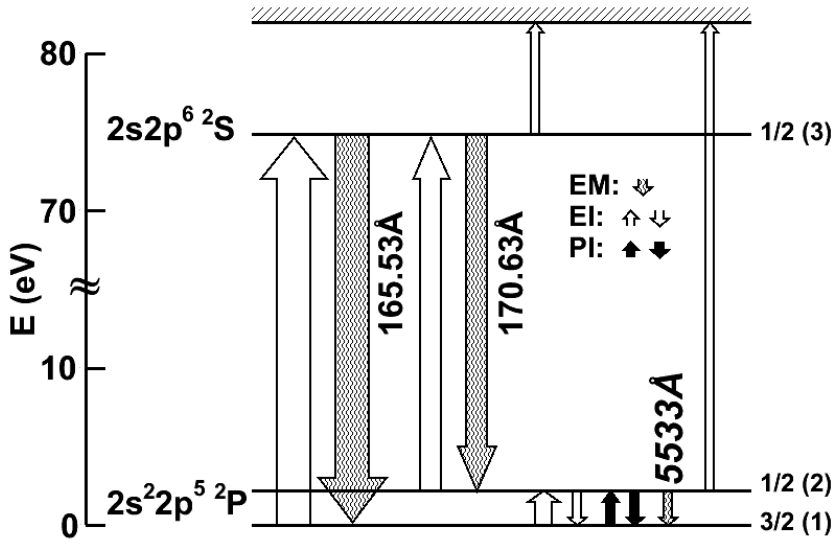

Fig.4 Partial energy diagram of F-like ArX M1 (5533Å) and E1 (165.53Å) transitions. EM, EI and PI indicate radiative decay, electron-impact excitation and de-excitation, proton-impact excitation and de-excitation, respectively. Width of each arrow means relative amplitude of transitions. Integers in right-hand brackets of 1, 2 and 3 denote energy levels used in quasi-steady state rate equation.

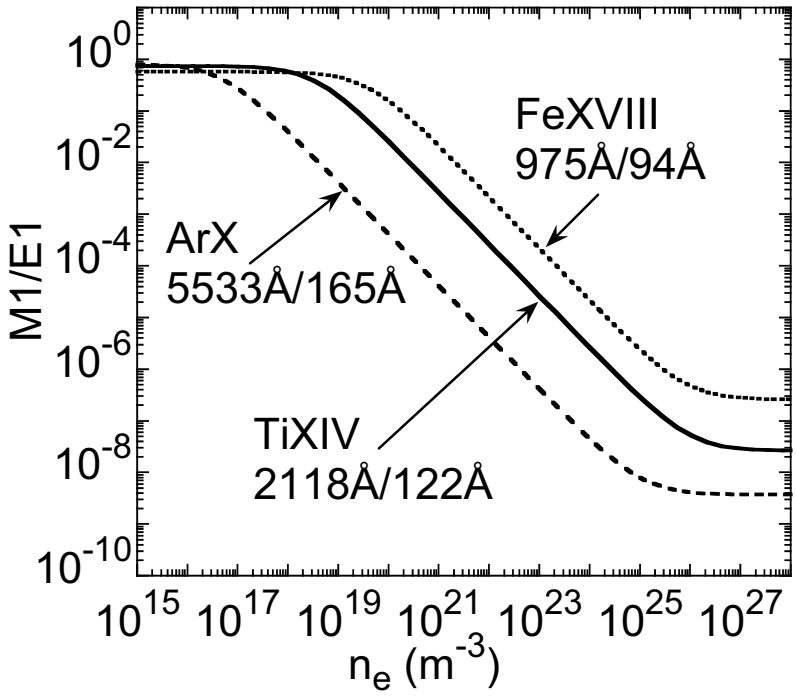

Fig.5 Calculated line ratios of M1 to E1 for F-like ArX (dashed line), TiXIV (solid line) and FeXVIII (dotted line) as a function of electron density.

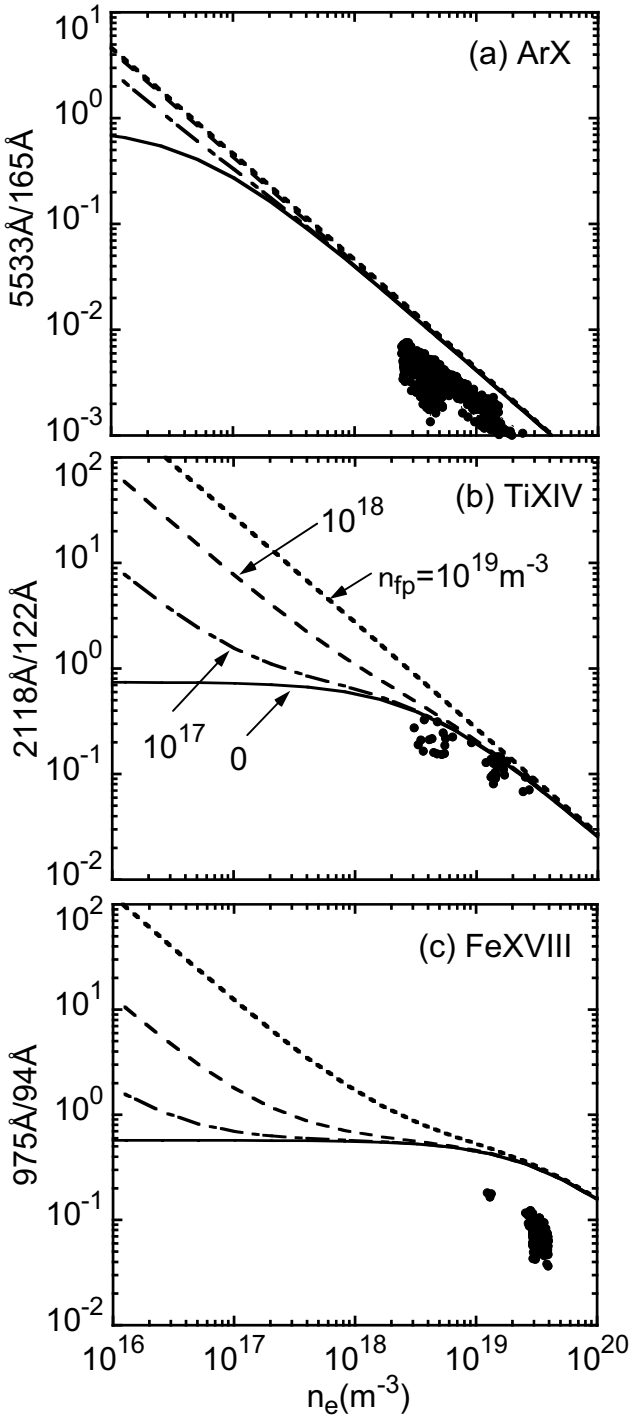

Fig.6 Line ratios of M1 to E1 for F-like (a) ArX, (b) TiXIV and (c) FeXVIII M1 transitions from calculation (solid line) and experiment (solid circles) as a function of electron density. Effect on fast protons with mean energy of 90keV is also calculated at three different fast proton densities of 10^{17} (dashed-dotted line), 10^{18} (dashed line) and $10^{19}m^{-3}$ (dotted line)

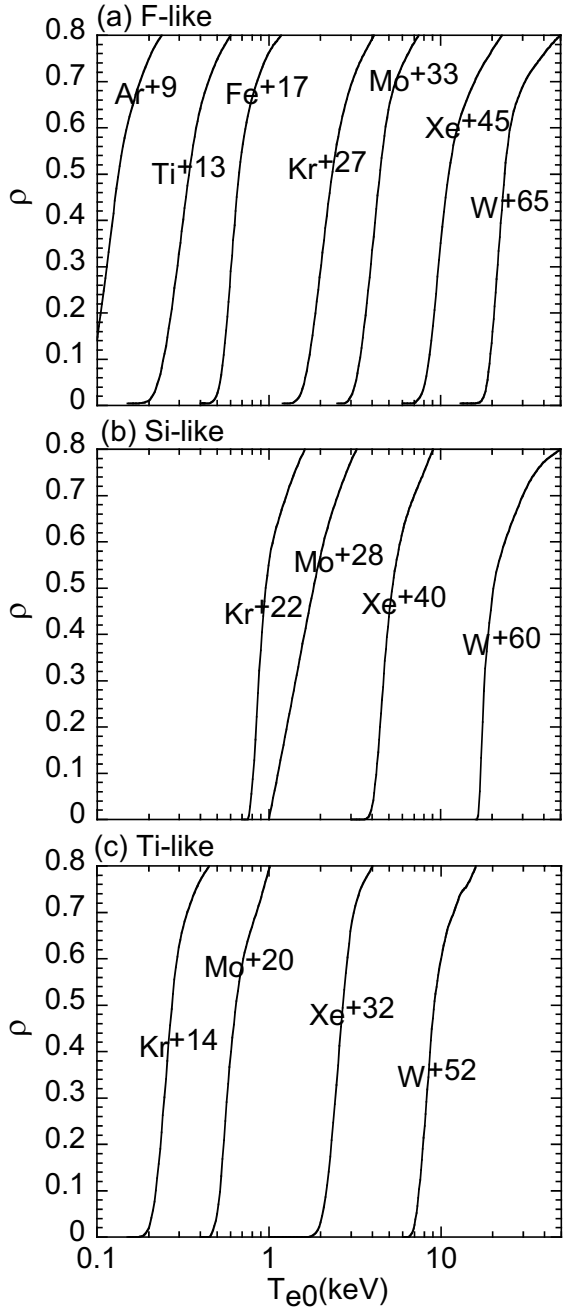

Fig.7 Radial location of (a) F-like (b) Si-like and (c) Ti-like ionization stages for heavy elements as a central electron temperature in ITER parameters. Value of ρ (≡r/a) denotes normalized plasma radius (r: plasma radius, a: plasma minor radius). In the calculation parameters of D=0.1m2/s and V=1m/s are assumed with radial profiles of $T_e=T_{e0}(1-\rho^3)$ and $n_e=n_{e0}(1-\rho^3)$, where $n_{e0}=10^{20}m^{-3}$.

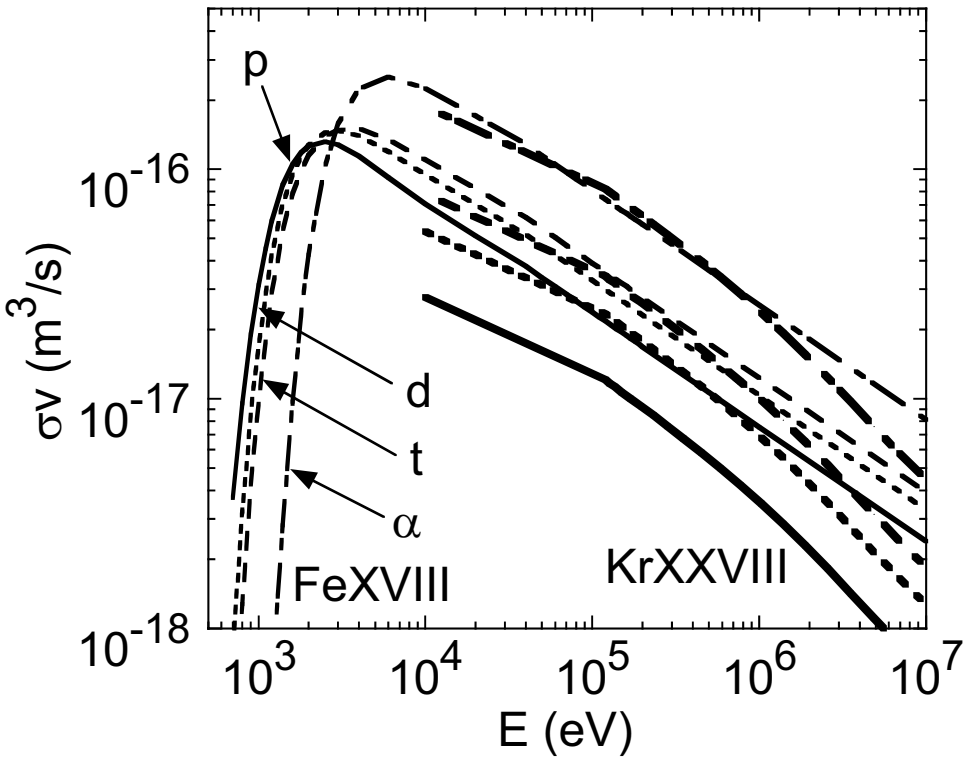

Fig.8 Rate coefficients σv of M1 ($2s^2 2p^5\ ^2P_{3/2}$-$^2P_{1/2}$) collisional excitation with protons (solid line), deuterons (dotted line), tritons (dashed line) and alpha particle (dash-dotted line) for FeXVIII and KrXXVIII [1, 3].

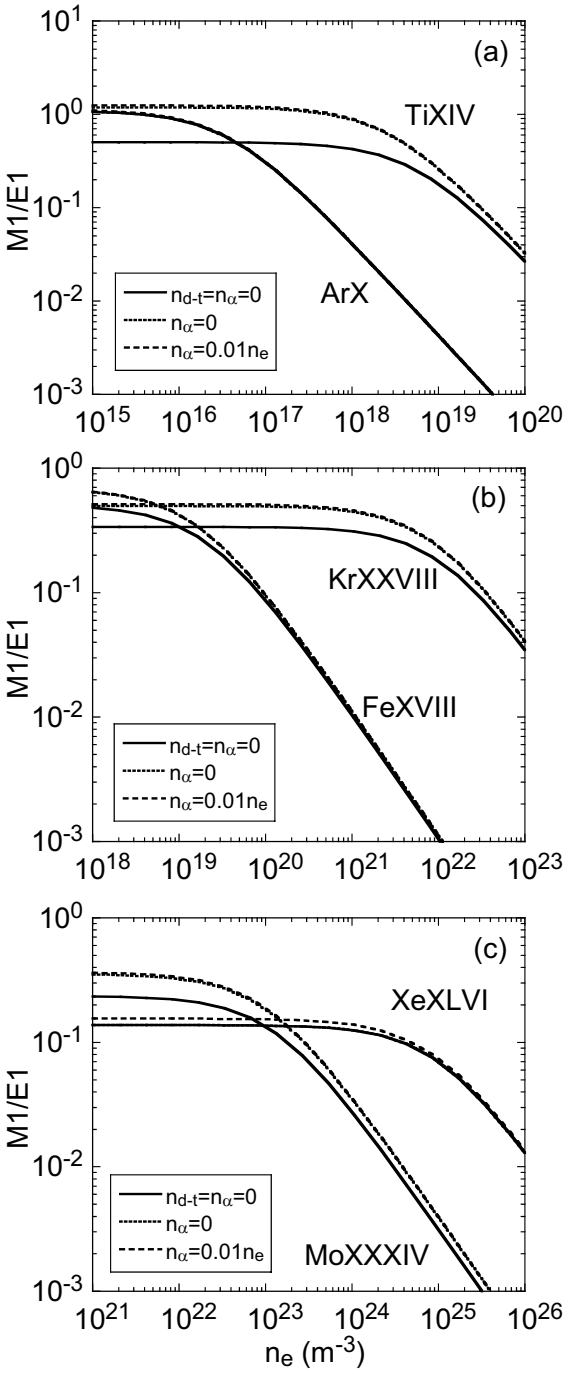

Fig.9 Ratio of M1 to E1 for F-like (a) ArX and TiXIV, (b) FeXVIII and KrXXVIII and (c) MoXXXIV and XeXLVI as a function of electron density. Result is calculated in three different cases (a) without D^+ (deuterium), T^+ (tritium) and He^{2+} (α particle) collisional excitation (solid line), (b) without He^{2+} collisional excitation (dotted line) and (c) with He^{2+} collisional excitation (dashed line). Density of α particles is assumed to be 1% to electron density.

Benchmark integral cross sections for electron impact excitation of the $n = 2$ states in helium

M. Hoshino[1], H. Kato[1], D. Suzuki[1], H. Tanaka[1], I. Bray[2], D.V. Fursa[2], S.J. Buckman[3], O. Ingólfsson[4] and M.J. Brunger[5]

[1] *Department of Physics, Sophia University, Chiyoda-ku, Tokyo 102-8554, Japan*
[2] *Centre for Antimatter-Matter Studies, Curtin University of Technology, GPO Box U1987, Perth,WA 6845, Australia*
[3] *Centre for Antimatter-Matter Studies, Australian National University, Canberra, ACT 0200, Australia*
[4] *Department of Chemistry, University of Iceland, Science Institute, Dunkaga 3, Reykjavík 107, Iceland*
[5] *Centre for Antimatter-Matter Studies, Flinders University, GPO Box 2100, Adelaide, SA 5001, Australia*

e-mail: masami-h@sophia.ac.jp

Abstract

In this paper, we present integral cross sections (ICS) for electron impact excitation of the $n = 2$ levels in helium in the impact energy range of 23.5 to 35 eV. The ICS of each final state, 2^3S, 2^1S, 2^3P and 2^1P, has been determined by integration of the angular differential cross sections (DCS) over all of 0° to 180°, where those DCS were obtained from both our previous experiments (M. Hoshino *et al., J. Phys. B* **42**, 2009, 145202) and through extrapolation using the convergent close coupling calculation. The present experimental ICS for the optically allowed 2^1P transition state are also compared with those obtained from the BEf-scaling (Y.-K. Kim, *Phys. Rev. A* **64**, 2001, 032713) method. Very good agreement between the experimental and BEf-scaled 2^1P ICSs is generally found in the measured impact energy region.

Keywords: Low energy electron impact, helium excitation, differential cross section, integral cross section.

1.Introduction

Inelastic cross sections for electron impact excitation of the $n = 2$ levels in helium are scientifically important from both fundamental and applied perspectives, particularly at energies in the range from the first ionization threshold to below about 35 eV. These cross sections dominate the discrete inelastic processes for both the optically allowed 2^1P transition state, as well as in near-threshold excitation for the optically forbidden 2^3P, 2^1S and 2^3S states. From the theoretical perspective, the helium system has also become a

standard case for evaluating the validity of collision theory, because a three-electron system in the Coulomb field is fundamental in understanding quantum mechanical collision dynamics. This is particularly true for an appreciation of the exchange interaction and also for typical electron-correlation phenomena. From an applied perspective, knowledge of these cross sections is essential in the design of fusion reactors. This follows as helium is produced as a by-product (usually called 'ash') in the fusion reactor, which can then contribute as one of the important plasma-temperature loss processes in the reactor. On the occasion of the development of the ITER project, it is therefore worthwhile providing a reliable database of helium cross sections so that these effects can be accounted for in its final design.

Recently, especially in the low incident energy regime, there have been many high quality measurements of differential cross sections (DCS) focusing on excitation of the $n = 2$ levels. These include data from Brunger *et al* [1], Trajmar *et al* [2], Cartwright *et al* [3] and Röder *et al* [4] who employed a conventional crossed-beam approach in conjunction with a hemispherical electrostatic monochrometor and analyzer. Allan and colleagues [5, 6] and Cubric *et al* [7] have built magnetic angle changer devices into their spectrometers. Lange *et al* [8] and Le Clair *et al* [9] have also measured the DCS utilizing a time-of-flight technique. Recently, we have reported benchmark DCS data for electron impact excitation of the $n = 2$ levels, including new experimental data and convergent close-coupling (CCC) calculations, at near-ionization threshold energies [10]. In this paper, we present the corresponding experimental integral cross sections (ICS) for the 2^3S (threshold energy, $E_{th} = 19.8$ eV), 2^1S (E_{th}= 20.6 eV), 2^3P ($E_{th} = 20.9$ eV), and 2^1P ($E_{th} = 21.2$ eV) states. These ICS were obtained from the DCSs [10] at near-ionization threshold energies below 35 eV. We also further test the validity of the BEf-scaling method suggested by Kim [11], by comparing its ICS with experimental ones for the dipole allowed transition to the 2^1P state in the low energy region.

2. Experimental procedures

To measure the inelastic differential cross sections for $n = 2$ electronic state excitation of He, a crossed beam apparatus has been employed. A detailed description on its use is provided elsewhere [12] and it will therefore only be briefly summarized here. Electrons from an electrostatic hemispherical monochromator intersect with an effusive helium beam at right angles, and the scattered electrons are energy analyzed in a second hemispherical analyzer. Note that high purity helium was used throughout our measurements. Both the monochromator and the analyzer are enclosed in differentially pumped casings, respectively, to reduce the effect of background gases and to minimize any stray electric fields as

well as to minimize any electron background. The incident electron energy is calibrated against the 19.36 eV resonance of He [13]. With respect to the incident electron beam, the scattered electron angular range covered is from 10° to 130°, with an angular resolution of ±1.5°. The cross section normalization method employs a measurement of the ratio of the inelastic to elastically scattered intensity of He under the same experimental conditions, and the use of the known elastic differential cross sections [14] for the particular kinematical conditions under study. Experimental errors are estimated at 15-20%, including components due to the uncertainty in our analyzer transmission response, an uncertainty due to errors associated with the elastic normalization cross sections and uncertainties due to any fluctuations in target density and/or incident electron beam current during the measurements. The experimental DCS have been measured at the energies of 23.5, 24, 25, 27.5, 30 and 35 eV for each final electronic state of the $n = 2$ levels.

3. Theory

The details of the CCC method for electron-helium scattering have also been given earlier by Fursa and Bray [15]. Briefly, an orthogonal Laguerre basis is first used to diagonalize the He^+ ion Hamiltonian to obtain negative- and positive-energy one-electron orbitals. These are then used to construct two electron configurations with one of the orbitals being the He^+ 1s orbital. This is known as the frozen-core approximation and leads to a reduction of 0.84 eV in the helium ionization energy (24.6 eV). By relaxing the frozen-core approximation we can improve the ionization energy, but at a price of generating many more states for subsequent scattering calculations. Instead, we reduce the incident energy by 0.84 eV and thereby ensure that the total energy in the CCC calculation is the same as in the experiment. As all of the helium discrete excited states are excellent frozen-core states, this approximation is adequate for our purposes.

The helium Hamiltonian is next diagonalized utilizing the constructed two-electron configurations of appropriate symmetry to obtain the helium states to be used in the scattering calculations. By construction, the number of helium states is (almost) twice the number of one-electron orbitals. These states are used to expand the total wavefunction which results in the close-coupling equations. The CCC formulation is in momentum space with the equations taking the form of coupled Lippmann-Schwinger equations. These are solved, after partial wave expansion, typically for the first 10-20 partial waves, with analytical techniques ensuring the treatment of all partial waves when necessary. The solution of the coupled equations leads to the scattering amplitudes that are used to generate data for comparison with experiment.

Convergence in the scattering amplitudes needs to be established against the free pa-

rameters of the Laguerre basis. These are the basis size N_l and the exponential fall-off parameter λ_l, for orbital angular momentum $l \leq l_{max}$. Given that presently we are interested in $n = 2$ excited states, setting $l_{max} = 4$ is sufficient. To make the study of convergence considerably simpler, we set $\lambda_l = \lambda_0$ and $N_l = N_0 - l$. This leaves us to check convergence with just the two parameters N_0 and λ_0. The rate of convergence for a particular experimental observable is energy dependent. In this work, we present the results over the energy range of 23.5 - 35 eV. Rather than finding the optimal combination of N_0 and λ_0, at each presented energy, we carried out calculations increasing N_0 from 15 to 20 and varying λ_0 from 1.5 to 2.0 to find a single set of parameters that yields sufficiently convergent results for all of the presented cross sections at all of the energies. By taking $N_0 = 20$ and $\lambda_0 = 2.0$ we believe that the presented results are converged to within 5% at most scattering angles, within the frozen-core model.

4. Results and Discussion

A. Differential cross sections

In figures 1 a)-d), we present the 30 eV DCS results from our previous experimental investigation [10] into electron impact excitation of the $n = 2$ levels in helium. The results from our corresponding CCC calculations and, where possible, data from previous experimental studies are also plotted in figure 1 [1, 3-7, 10, 16, 17]. This work is repeated here because in our publication [10] we inadvertently omitted the important study from Cubric *et al* [7]. Note that all the error bars plotted on our data in Fig. 1 represent a one standard deviation level estimate of the uncertainty on the present measurements. Clearly very good agreement was found in general between the DCSs of our CCC calculations and all the available experimental DCS data for each final state at 30 eV. In more detail, it is clear from figure 1 a) that for excitation of the 2^3S state, the shapes of their angular distributions suggest important destructive and constructive interference effects between the partial waves, whereas in figure 1 b), the 2^1S cross section exhibits a very deep minimum in the scattering angle range 40-60°. These minima are seen in both our measurements and CCC calculations, with the experimental depth being shallower than predicted by our theory. However, this difference is simply understood in terms of the finite angular resolution (±1.5° (FWHM)) of our spectrometer. For the 2^3P state (figure 1 c), we believe that exchange will be the predominant scattering process with their angular distributions, which increase monotonically in magnitude with the scattering angle, until around 130° where they then start to again decline in magnitude, being consistent with that population mechanism. Finally, in figure 1 d) for the 2^1P excitation, corresponding

to the dipole allowed transition, the angular distributions are forward peaked, with the degree of forward angle peaking in the cross sections increasing as the incident electron energy increases. In the cases of the other impact energies, our DCSs have shown similar behavior to those at 30 eV and all have agreed very well with the CCC calculation results [10]. On this basis we believe we have shown that the $n = 2$ level scattering systems in helium have been benchmarked.

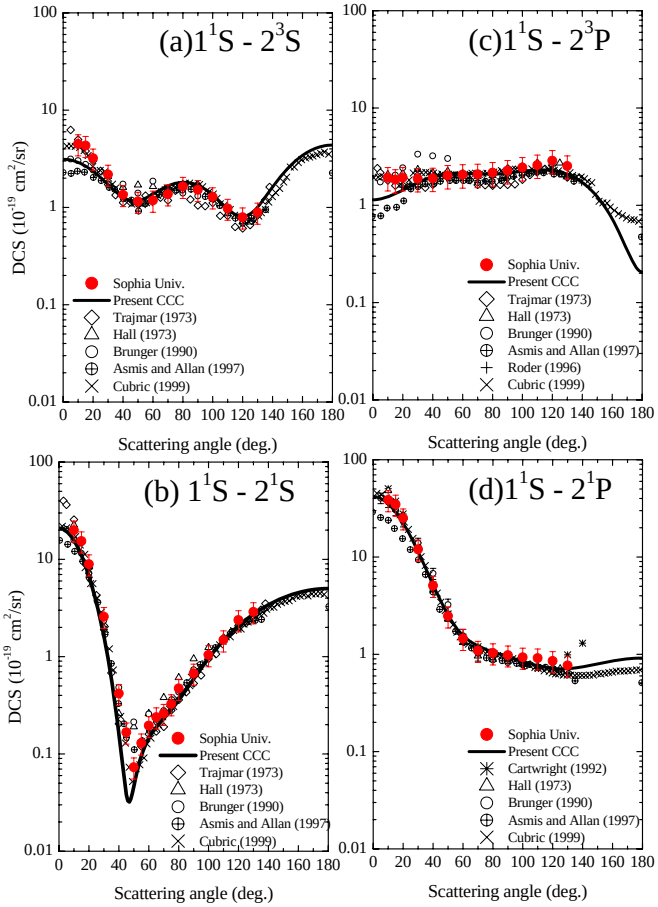

Figure 1: Differential cross sections for 30 eV electron impact excitation of the $n = 2$ levels in helium, a) 2^3S, b) 2^1S, c) 2^3P, and d) 2^1P states. The present data (•) and CCC calculations (solid curves) are compared against the previous data from Brunger *et al* (○), Asmis and Allan (⊕), Röder *et al* (+), Hall *et al* (△), Trajmar (◇), Cartwright *et al* (*) and Cubric *et al* (×).

B. Integral cross sections

Integral cross sections (ICS) for each final electronic state have now been obtained at the measured impact energies of 23.5, 24, 25, 27.5, 30, and 35 eV. In general, these ICS

are determined by integration of the DCS over the entire scattering angle range from 0° to 180°. In the present case, we have used our measured DCS and those obtained by an extrapolation based on the CCC calculation for the inaccessible angular ranges $\theta \leq 15°$ and $130° \leq \theta$. In Figs. 2 a)-d), the current ICSs for each final state together with the previous measurements [16-20] are shown as a function of impact energy. All of our ICSs for each final state are found to agree with the previous studies to within our experimental errors.

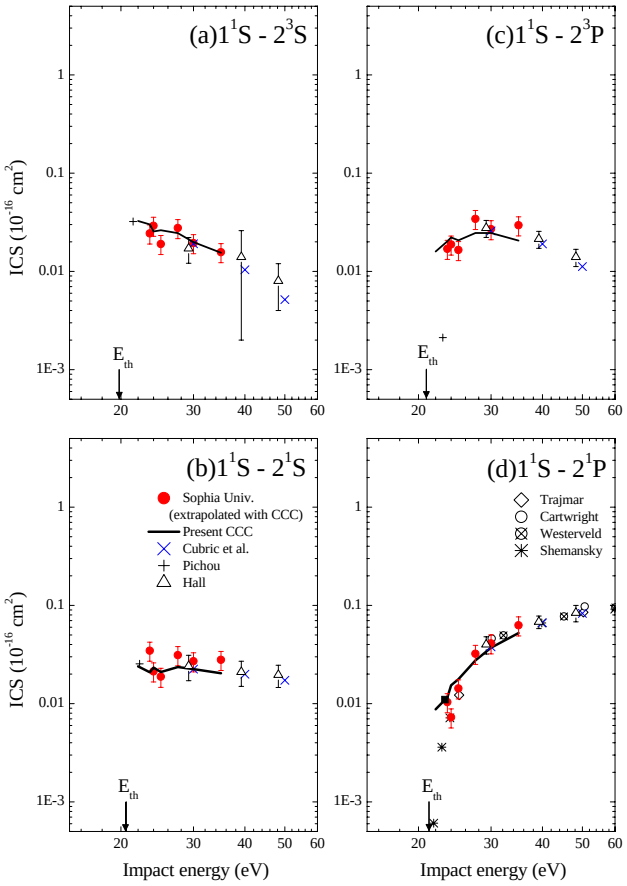

Figure 2: Integral cross sections for transitions to a) 2^3S, b) 2^1S, c) 2^3P, and d) 2^1P states as a function of impact energy. The term, E_{th}, corresponds to the threshold energies of each final state. The present data (●) and CCC calculation (solid lines) are compared against the previous data from Cubric *et al* (×), Pichou *et al* (+), Hall *et al* (△), Trajimar (◇), Cartwright *et al* (○), Westerveld *et al*(⊗), and Shemansky *et al* (*).

For the transition to the 2^3S and 2^1S states, the behaviors of these ICSs are very similar. Namely their magnitude increases drastically from their E_{th} until about 22 eV, thereafter it decreases slowly as the impact energy increases. For the 2^3P state, the ICS has a broad

maximum around 30 eV and then it decreases slowly in magnitude like the 2^3S and 2^1S states. On the other hand, for the optically allowed transition to the 2^1P state, the ICS increase smoothly from the E_{th} as the impact energy increases. Our 2^1P ICS, especially, is connected well with the data of Shemansky *et al* [20] for near excitation threshold energies. The data embodied in Fig. 2, also clearly presents a strong case for the $n = 2$ level ICSs to be considered to be benchmarked. This is certainly to be expected given what we found at the DCS level, as described above.

C. Scaling law for the dipole allowed 2^1P transition

In order to discuss the dipole allowed transition to the 2^1P state in more detail, we have compared our ICS in Fig. 2 d) with the ICSs obtained from a BEf-scaling law, which was originally suggested by Kim [11]. A full description of the BEf-scaling approach for calculating ICSs with atoms and molecules can be found in Ref. [11]. The BEf-scaling method can derive ICSs of the dipole allowed electron impact transitions using the plane wave Born (PWB) approximation. In this formulation the ICS for transition to state a, σ_{ICS}, is given as;

$$\sigma_a = \frac{E_0}{E_0 + B + E} \frac{f_{accr}}{f_{Born}} \sigma_{Born}.$$

Here σ_{Born} is the integral cross section calculated by the PWB approximation. The E_0, B, and E are the impact energy of incident electron, and the binding energy and excitation energy of the target, respectively. The term, $E_0/(E_0 + B + E)$, corrects the deficiency of the PWB approximation at low E_0 without losing its validity at higher E_0. The term of f_{accr}/f_{Born} plays the role of replacing the wavefunction used to calculate σ_{Born} with an accurate wave function, where f_{accr} and f_{Born} are the accurate dipole f-value and dipole f-value calculated from same wavefunction as used for σ_{Born}.

Figure 3 shows the comparison between the present ICS results, including relevant previous measurements, and the scaled σ_{2p}. Given the very good agreement between our ICSs, as well as all the other available 2^1P experimental ICSs [3, 7, 16, 17, 20], and the scaled ICS from the simple PWB approximation [21], it follows that the scaling law should be also very useful to estimate ICSs, for the dipole allowed transition of the He 2p transition, in the experimentally challenging near threshold energy region.

5. Conclusion

We have reported new experimental and CCC calculation results of integral cross sections for electron impact excitation of the 2^3S, 2^1S, 2^3P and 2^1P levels in helium, for electrons with incident energies in the range 23.5 - 35 eV. Agreement between the present

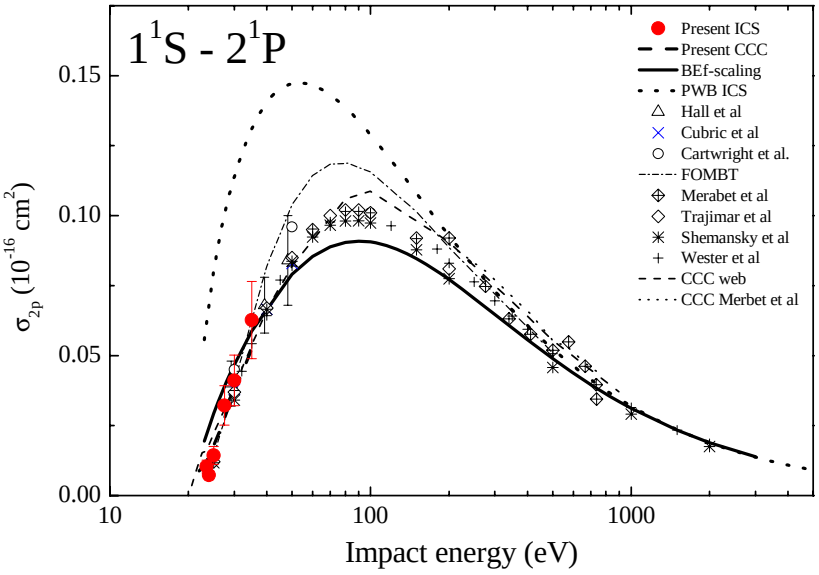

Figure 3: Integral cross sections of the optically allowed transition to the 2^1P state in a wider energy range. The present data (●) and present CCC calculation (broken line) are shown together with the previous works from Hall et al (△), Cubric et al. (×), Cartwright et al. (○ and − - −), and the others are found in ref [21]. The BEf-scaling results is given by the solid line in this plot.

results and available earlier measurements was generally good in this near threshold energy region. The present and past integral cross sections of the dipole allowed transition to the 2^1P state also have been compared with ICS obtained from the BEf-scaling law over a wider energy region. A very good agreement between the present and previous results and the scaled ICS, obtained from the simple plane wave Born approximation, was found over the energy range considered. While some small deviations do remain, the present ICS results further confirm that the $n = 2$ excitation in helium is a scattering system that can be considered to have been benchmarked.

Acknowledgement

This work was supported in part by the Australian Research Council through its Centres of Excellence Program. This work was also conducted under the support of the Japanese Ministry of Education, Sport, Culture and Technology. One of us (HK) also acknowledges the Japan Society for the Promotion of Science (JSPS) for his fellowship as a grant-in-aid for scientific research. We all thank the International Atomic Energy Agency (IAEA) for

its support of this work as a part of a data base project. We are also grateful for access to the Australian National Computing Infrastructure Facility and its Western Australia node iVEC.

References

[1] Brunger M J, McCarthy I E, Ratnavelu K, Teubner P J O, Weigold A M, Zhou Y and Allen L J 1990 J. Phys. B: At. Mol. Opt. Phys. **23** 1325.

[2] Trajmar S, Register D F, Cartwright D C and Csanak G 1992 J. Phys. B: At. Mol. Opt. Phys. **25** 4889.

[3] Cartwright D C, Csanak G, Trajmar S and Register D F 1992 Phys. Rev. A **45** 1602.

[4] Röder J, Ehrhardt H, Bray I and Fursa D V 1996 J. Phys. B: At. Mol. Opt. Phys. **29** L421.

[5] Asmis K R and Allan M 1997 J. Phys. B: At. Mol. Opt. Phys. **30** 1961.

[6] Allan M 2000 J. Phys. B: At. Mol. Opt. Phys. **33** L215.

[7] Cubric D, Mercer D J L, Channing J M, King G C and Read F H 1999 J. Phys. B: At. Mol. Opt. Phys. **32** L45.

[8] Lange M, Matsumoto J, Lower J, Buckman S J, Zatsarinny O, Bartschat K, Bray I and Fursa D V 2006 J. Phys. B: At. Mol. Opt. Phys. **39** 4179.

[9] Le Clair L R, Trajmar S, Khakoo M A and Nickel J C 1996 Rev. Sci. Instrum. **67** 1753.

[10] Hoshino M, Kato H, Tanaka H, Bray I, Fursa D V, Buckman S J, Ingolfsson O and Brunger M 2009 J. Phys. B: At. Mol. Opt. Phys. **42** 145202.

[11] Kim Y-Ki 2001 Phys. Rev. A **64** 032713.

[12] Tanaka H, Ishikawa T, Masai T, Sagara T, Boesten L, Takekawa M, Itikawa Y and Kimura M 1998 Phys. Rev. A **57** 1798.

[13] Brunt J N H, King G C and Read F H 1977 J. Phys. B: At. Mol. Phys. **10** 1289.

[14] Boesten L and Tanaka H 1992 Atom. Data Nucl. Data Tables **52** 25.

[15] Fursa D V and Bray I 1995 Phys. Rev. A **52** 1279.

[16] Hall R I, Joyez G, Mazeau J, Reinhardt J and Schermann C 1973 J. Phys. **34** 827.

[17] Trajmar S 1973 Phys. Rev. A **8** 191.

[18] Pichou F, Huetz A, Joyez G, Landau M, and Mazeau J, 1976 J. Phys. B: At. Mol. Phys. **9** 933.

[19] Westerveld W B, Heideman H G, and van Eck J, 1979 J. Phys. B: At. Mol. Phys. **12**, 115.

[20] Shemansky D E, Ajello J M, Hall D T and Franklin B 1985 Astrophys. J **296** 774.

[21] WWW homepage of the NIST Electron-Impact Cross Section Database.
(http://physics.nist.gov/PhysRefData/Ionization/Xsection.html)

Spectrum Simulation of Li-like Oxygen Plasma

Deng Banglin(邓邦林), Jiang Gang*（蒋刚）

Institue of Atomic and Molecular Physics of Sichuan University

Abstract Based on the collisional radiative model from the FAC (flexible atomic code), X-ray emission spectra for L-shell of Li-like oxygen plasma consisting of three kinds of oxygen ions (Li-like oxygen ion and another two neighboring ions) are simulated. Atomic processes in the model include dielectronic recombination (DR), radiative recombination (RR), collisional ionization (CI) and resonance excitation (RE) from the neighbouring ion charge states of the target ion (Li-like oxygen ion). To analyse the contribution of different atomic processes to the X-ray spectrum, the results show that DR, RR, CI and RE , other than direct collisional excitation, are very important processes. In addition, the spectrum reflects the relationship between X-ray wavelengths, relatively radiative intensity and the electronic temperature, which could be qualitatively used to plasmas diagnostics.

Keywords: Li-like oxygen, FAC, Spectrum simulation, Dielectronic recombination, Radiative recombination

1 Introduction

Oxygen is a very important element by reason of its existence in many astrophysical as well as laboratory spectra[1] and in the winds of early-type stars[2]. Lithium-like oxygen is one of the most important atomic species in UV or X-ray plasma diagnostics of astrophysical sources[3]. For understanding the plasmas energetics and determining of plasmas parameters，theoretical analyses and calculation of emission from these plasmas are necessary[4].

The interaction among the ions and atomic in the plasmas includes intricate processes of atomic physics and dynamics processes, which is the fundamental reason of X-ray radiation spectrum of plasma being produced[5]. In this letter, we use the collisional radiative model (CRM) in the flexible atomic code (FAC)[6] to calculate the population and rate coefficients of different atomic processes and to simulate X-ray spectrum emission from Li-like oxygen plasma. We analyze the influence of atomic processes to the X-ray spectra, and obtain the relations among X-ray wavelengths, relatively radiative intensity and the electronic temperature. It could be qualitatively used to plasmas diagnostics. Hence, we must establish a rate equations to calculate the rate of different atomic processes before simulate the X-ray spectra.

2 Theoretical method

In the CRM, three ions system of oxygen plasma is considered, i.e. target ion O^{5+} and the neighbouring ions (O^{6+} and O^{4+}). The equilibrium of the three ions dynamics processes can be presented sententiously as follows:

$$\begin{aligned} O^{6+}(CE) &\xrightarrow{DR,RR} O^{5+}(CE) \xrightarrow{DR,RR} O^{4+}(CE) \\ O^{6+}(CE) &\xleftarrow{CI,AI} O^{5+}(CE) \xleftarrow{CI,AI} O^{4+}(CE) \end{aligned} \tag{1}$$

* Corresponding author: Jiang Gang
Email: gjiang@scu.edu.cn

From the Eq.(1), one can see that several determined collisional and radiative processes are considered in the model, them is collisional ionization (CI), radiative recombination (RR), collisional excitation (CE), dielectronic recombination (DR) and autoionization (AI).

For simulating spectrum preferablely, some indirect processes in the multi-ion model and their subsequent radiative cascades should contain the neighbouring charge states of the target ion. Hereby, the rate equations involving statistical equilibrium take multi-ion atomic states into account. It can be written minutely as

$$\begin{aligned}
&\sum_i \Bigg\{ \sum_{j(<i)} CE_{pi}^{pj}\left(j \to i\right)\cdot n_{pj}\cdot n_e + \sum_{j(>i)} A_r\left(j \to i\right)\cdot n_{pj} \\
&-\left[\sum_{j(>i)} CE_{pi}^{pj}\left(j \to i\right)\cdot n_e + \sum_{j(<i)} A_r\left(j \to i\right)\right]\cdot n_{pj} \\
&+\sum_j \left[CI_{p-1,j}\cdot n_e + Aa_{p-1,j}\right]\cdot n_{p-1,j} - \sum\left[CI_{pj}\cdot n_e + Aa_{pj}\right]\cdot n_{pj} \\
&+(DR_{pj}+RR_{pj})\cdot n_e\cdot n_{p+1,j} - (DR_{p-1,j}+RR_{p-1,j})\cdot n_e\cdot n_{pj}\Bigg\} = 0
\end{aligned} \quad , \tag{2}$$

also can be written simply as :

$$\sum_{ij} C_{pi}^{qj} n_{qj} = 0 \ , \tag{3}$$

where n_{qj} is the population of level j in ion q , n_e is the electronic density. If $q \neq p$ or $i \neq j$, C_{pi}^{qj} is the total rate of the populating of state pi to qj , if $q=p$ and $i=j$, $C_{pi}^{qj} = -D_{pi}$, where D_{pi} is the total depletion rate of state pi, and D_{pi} can be presented as follows :

$$D_{pi} = \sum_{qj \neq pi} C_{pi}^{qj} \ . \tag{4}$$

Because Eq.(2) and Eq.(3) are one and the same just different form, it does not provide a unique solution. The usual way to solve the rate equations is introducing a normalization condition into Eq.(3). The normalization condition is

$$\sum_{qj} n_{qj} = 1 \ . \tag{5}$$

Towards the multi-ion model, a self-consisitent solution with such normalization condition simultaneously brings the ionization equilibrium and the level population for each ion. However, it needs to include all the important ionization and recombination channels of all charge states into Eq.(3). This is unpractical and unnecessary usually[7]. As a rule, the normalization condition can be applied for each ion instead of all ions of the atomic charge states,

$$\sum_j n_{qj} = n_q \tag{6}$$

where n_q is the fractional abundance of ion q obtained from a separate ionization balance calculation, or equivalently, one can set $C_{p0}^{qj} = 1$ for all p, $C_{p0}^{qj} = 0$ for $q \neq p$, and replace the right side on Eq.(3) with a vector

$$b = [n_0, 0, ..., n_q, 0...]^T \ . \tag{7}$$

It turn the Eq.(3) into inhomogeneous, therefore, the Eq.(3) have a unique solution. Then, we can botain the intensity of a line produced by radiative decay from state *pi* to *pj* .

$$I_{ij}^{p} = AN_H n_{pi} A_{pj}^{pi}, \tag{8}$$

where A is the elemental abundance relative to hydrogen, N_{H} is the hydrogen density, and A_{pj}^{pi} is the radiative decay rate coefficients (Einstein A-coefficient) from the state *pi* to *pj*.

We can not use a standard way which is easy and saving time to gain the solution of rate equations, because of that the number of double-excited staes producing DR and resonance excitation (RE) far exceeds those directly responsible for line emission.[8] So , the atomic model must be as simple as possible. A reduced atomic model in the FAC is introduced to instead of solving the forementioned rate equations. This model is constructed by putting a large number of atomic states in a group so-called superlevel. Concretely, eliminating a few tens of the lowest lying levels, states from the same complex and the same ion are gouped to form a superlevel containing only one real state. Then, the atomic density of superlevel can be worked out[9]. It is defined as

$$n_{pJ} = \sum_{j} n_{pj}, \tag{9}$$

where the summation is over the all states *j* to form the superlelvel *J*.

The coefficients C_{pI}^{pJ} are given as

$$C_{pI}^{pJ} = \sum_{ij} C_{pi}^{pj} n_{qj}, \tag{10}$$

where the summation over *i* and *j* includes all the states forming superlevels *I* and *J* , respectively. If the original rate equations are satisfied with these definitions, the similar equations contents the reduced atomic model and the solution of Eq.(3) also can be achieved iteratively. In this work, the iteration is terminated when the difference between the level populations in two consecutive steps is within 10^{-4}.

3 **Results and discussion**

To understand the relationship between spectrum and properties of plasmas, the discussion of the contributions of individual processes to the line formation is necessary. However, fist of all, we should compare the total recombination and ionization rate coefficients obtained in this work with previous publications.

Figure 1 shows the total DR rate coefficients of the present calculation together with the results of Krylstedt P, Pindzola M S and N R Badnell (1990) (hereafter KP90)[10] for O^{5+}. The present DR rate coefficients fit with those of KP90 in lower temperature ($T=10^{5.6}$-$10^{6.4}$K). However, in the higher temperature, the result is not so satisfying , the reason is that the theoretical formulae we used to calculate the DR rates are different from the formulae in the KP90[4][11]. But it still does not affect the analysis of us about the the relationship between spectrum and properties of plasmas[4]. Figure 2 shows the total RR rate coefficients of the present calculation together with the results of Barfield (1979) (B79)[12] , the present RR rate coefficients are consistent with the data of B79. Figure 3 shows the present CI rate coefficients and the previous data of Franco and Daltabuit(1978) (FD78)[13] .Those two curves are accordant approximately.

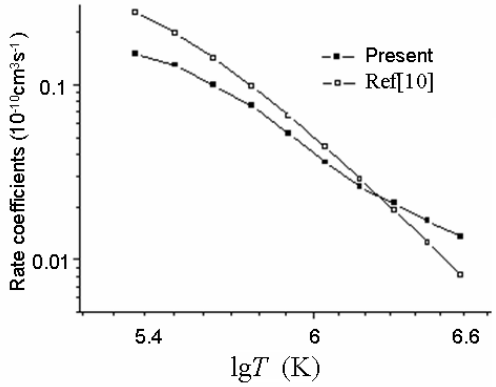

Fig. 1 The total DR rate coefficients of O^{5+}

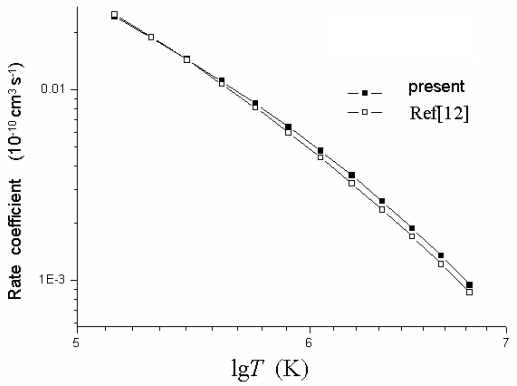

Fig. 2 The total RR rate coefficients of O^{5+}

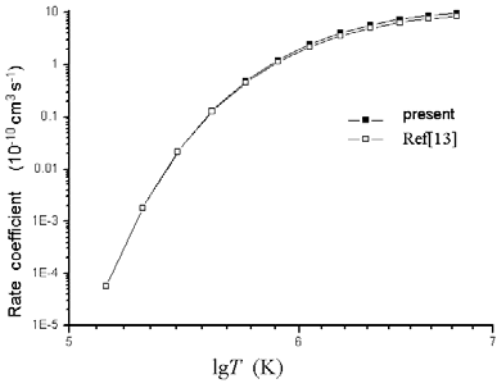

Fig. 3 The total CI rate coefficients of O^{5+}

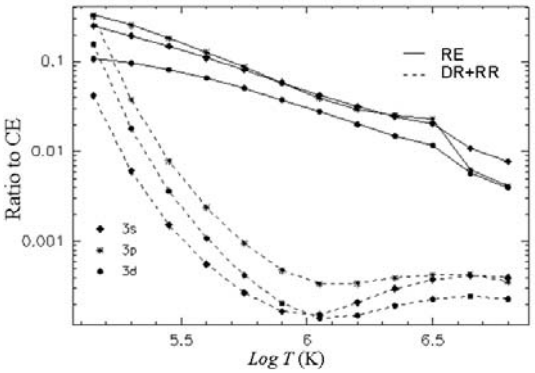

Fig. 4 Rate coefficients of indirect processes relative to direct CE for 3s, 3p, and 3d

In the selective scope of the plasma temperature, CE has the most important contribution for emission spectra of Li-like oxygen plasma, however, other dynamic processes are also crucial for forming spectrum[14]. In order to analyze the contribution of the indirect processes, a ratio of the collective effects of DR+RR, RE (for O^{5+}) to 3s, 3p, and 3d excited states relative to the direct CE is plotted in Fig.4. From the figure, we can see that the indirect processes are alse crucial for total rate coefficients and generally more important for 3s and 3p states than 3d states in lower temperature, and the contributions of RE and DR+RR reach 20%. Obviously, their contributions to the line emission cannot be ignored. Meanwhile, it can be shown that the rate coefficient of DR or RR decreases along with the increase of the temperature of electrons in plasma. It is mostly because that the energy of electron turns higher when it's temperature increases, then the electron with higher energy is more hardly to be captured, resulting in the decrease of the rate coefficient of DR or RR. On the contrary, the ratio of rate coefficient of DR, RR to that of the direct CE reduces as the rate coefficient of CE goes up. When the temperature goes up to $10^{6.1}$K, the minimum of DR+RR can be found. This phenomena indicates that the values of CE rates coefficients increase fast near this temperature.

Table 1. Line-formation rate coefficients of O^{5+}

I	log	Coefficients (10^{-10}cm^{3}s^{-1})							
		RT	CE	RE	CE+CS3	CE+CS	RE+CS	DR+RR+CS3	DR+RR+CS
0	5.15	2.37E+02	1.17E-04	3.47E+02	1.45E-02	2.37E+02	3.49E+02	8.30E-03	8.30E-03
0	6.80	1.87E+02	2.23E-05	2.21E+00	7.82E+00	1.87E+02	2.73E+00	3.20E-03	1.52E-02
1	5.15	4.31E+08	7.90E+01	7.91E-01	7.91E+01	7.91E+01	7.96E-01	4.90E-03	6.04E-03
1	6.80	4.32E+08	5.38E+01	1.39E-01	5.81E+01	5.89E+01	1.62E-01	1.43E-03	2.83E-03

2	5.15	4.38E+08	1.57E+02	1.58E+00	1.57E+02	1.57E+02	1.59E+00	9.68E-03	1.27E-02
2	6.80	4.38E+08	1.08E+02	2.76E-01	1.16E+02	1.18E+02	3.22E-01	2.86E-03	5.78E-03
3	5.15	2.22E+10	3.73E-02	9.36E-03	3.74E-02	3.75E-02	9.37E-03	7.68E-04	1.57E-03
3	6.80	2.21E+10	3.71E+00	3.30E-02	3.72E+00	4.35E+00	3.37E-02	9.63E-05	1.74E-03
4	5.15	2.94E+10	4.51E-03	1.58E-03	4.51E-03	4.81E-03	1.58E-03	8.44E-04	1.53E-03
4	6.80	2.95E+10	2.24E+00	1.05E-02	2.24E+00	2.62E+00	1.08E-02	4.62E-05	9.34E-04
5	5.15	2.93E+10	8.96E-03	3.17E-03	8.96E-03	9.55E-03	3.17E-03	1.69E-03	3.06E-03
5	6.80	2.94E+10	4.46E+00	2.11E-02	4.46E+00	5.23E+00	2.16E-02	9.22E-05	1.88E-03
6	5.15	9.05E+10	1.66E-02	1.81E-03	1.66E-02	1.69E-02	1.81E-03	8.94E-04	2.64E-03
6	6.80	9.00E+10	3.07E+00	1.37E-02	3.07E+00	3.45E+00	1.38E-02	1.78E-05	7.88E-04
7	5.15	9.04E+10	2.48E-02	2.70E-03	2.48E-02	2.53E-02	2.70E-03	1.34E-03	3.95E-03
7	6.80	8.99E+10	4.61E+00	2.04E-02	4.61E+00	5.18E+00	2.05E-02	2.67E-05	1.19E-03

In the calculation of rate coefficients of atomic processes, we take the cascade contributions into account. Table 1 lists partial data of the contributions of cascade in these processes. *LogT* is the base 10 logarithm of the temperature in Kelvin, RT is the total depletion rate of the state in units of s^{-1}, CE and RE are the rate coefficients without cascade respectively, CE+CS, RE+CS and DR+RR+CS are the rate coefficients with all cascade contributions included, CE+CS3 and DR+RR+CS3 are the rate coefficients including only the cascade contributions from n=3 states. All rate coefficients are in units of $10^{-10}cm^3s^{-1}$. From this table, one can see that the influence of cascade contributions is very obviously in the ground states, on the contrary, it is not so clear in the excited states, but can not be neglected. Namely, cascade is indispensable for the lower levels. The ions of the thin oxygen plasmas (the electron density N_e is $10^{10}\mathrm{cm}^{-3}$) what we focus on in this letter almost occupy in the lower levels. So, the cascade is important for simulate X-ray spectra of oxygen plasmas.

Owing to the foregoing calculation of rate coefficient of the several dynamics processes, we have obtained the basal data which spectrum simulation needs. On the condition of that the electron density N_e of oxygen plasmas is given as a constant ($10^{10}cm^{-3}$), and based on the Lorentz lineshape, we simulated the spectra emitted from Li-like oxygen plasma by FAC in Fig.5.

In the Figure 5, there are three columns spectra corresponding to three different models which are single-ion (O^{5+}, corresponding N_{ion}=1), double-ion (O^{5+} and O^{6+}, corresponding N_{ion}=2), and three-ion (O^{4+}, O^{5+} and O^{6+}, corresponding N_{ion}=3). The first column includes only CE and the subsequent radiative cascades from O^{5+}, the second column includes DR and RR from O^{6+} as well, and the third column also includes the RE and CI effects and innershell excitation lines from O^{4+}. Plots in the same row have the same temperature but involve different indirect processes, and T_e is the temperature of plasmas in units of *Kev*. Comparing the lines shape of the three columns spectra in Fig.5, it is easy to understand the contribution of different indirect processes to the emissive lines shape. Obviously，the more atomic processes we considered, the lines shape of spectra is more refined. Comparing the lines shape of the four rows, we can find the relationship between the temperature and lines shape of Li-like oxygen plasma, which is that the intensity of lines shape falls down as the temperature of plasma goes up.

4 Summary

In summary, the x-ray spectra from Li-like oxygen plasmas are simulated by FAC. Starting from the root causes of the formation of spectra, cascade and the indirect processes including DR, RR, CI and RE are very important other than the direct CE during the x-ray spectrum simulation for L-shell plasma of Li-like

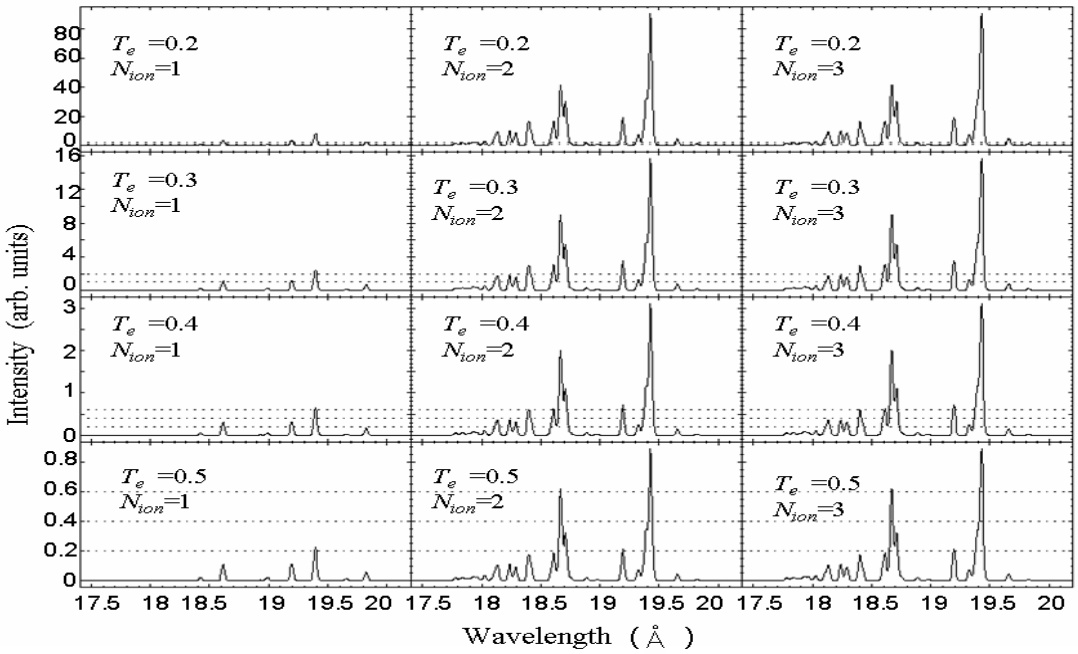

Fig. 5 Simulated spectra of oxygen ions.

oxygen. we analyze the relations between dynamics processes, temperature and the lines shape of spectra, and find that the intensity of spectra changes obviously with the transform of the temperature. The X-ray spectra we simulated could provide some theoretical basis for Li-like oxygen plasma diagnostics.

References

1 Nahar S N 1998 *Phy. S. Rev.* A ,**58:** 3766

2 Zsargó J，Fullerton A W，Lehner N，et al 2003 *Astron. Astrophys.,* **405:** 1043

3 Nahar S N and Pradhan A K 2003 *The Astrophysical Journal Supplement Series,* **149:** 239

4 Peng Feng，Jiang Gang and Zhu Zhenghe 2006 *Chin. Phys. Lett.,***23:** 3245

5 Peng Feng, Zhu Zhenghe, Huang Jie 2006 *Journal of Atomic and Molecular Physics,* **23:** 422

6 Gu M F 2003 *The Astrophysical Journal,* **582:** 1241

7 Huang Jie, Zhao Qian, Peng Feng, et al 2007 *Journal of Atomic and Molecular Physics* **,24:** 496

8 Lucy L B．2001 *Mon. Not. R.. Astron. Soc.,* **326**: 95

9 Fang quan yu and Yan Jun 2006 *The theory of atomic structure collisions and spectra(Beijing:National Defense Industry Press)* pp 427-435

10 Krylstedt P，Pindzola M S，and Badnell N R 1990 *Phys. Rev. A* ,**41**: 2506

11 Safronova U I and Mancini R 2009 *Atomic Data and Nuclear Data Tables,* **95:** 54

12 Barfield W D 1979 *The Astrophysical Journal* ,**229:** 856

13 Bliman S，Cornille M and Katsonis K 1994 *Phys. Rev. A* ,**50:** 3134

14 Lebert R，Bergmann K，Schriever G，et al．1999 *Microelectronic Engineering* ,**46:** 465

Effect of C_3H_6 on NO Conversion in a Nonthermal Plasma Reactor

Yi-Xi Cai[1], Le-Fu Zhang [1,2], Jun Wang[1], Xiao-Hua Li[1], Jing Wang[1]

(School of Automotive and Traffic Engineering, Jiangsu University, Zhenjiang,212013, China)
(Jiangsu economy and information technology commission ,Nanjing ,210008，China)

Abstract： In order to study the reaction mechanism of nonthermal plasma convert NO_x in NO/ N_2/ C_3H_6 and NO/N_2/O_2/C_3H_6 mixture gases, a tubular coaxial dielectric barrier discharge reactor was designed; the effects of the C_3H_6 initial concentration on NO oxidation and reduction were observed. The results showed that NO reduction is very low and energy consumption is very high in NO/ N_2 mixture gases, however, when C_3H_6 was added NO conversion rate significantly increased. In NO/N_2/O_2 mixture gases, NO oxidation and reduction reaction simultaneously occurred in the reactor and the oxidation of NO to NO_2 was the main reaction; when C_3H_6 was added to the mixture gas NO conversion rate significantly increased, meanwhile,the energy consumption largely reduced.

Keywords： Dielectric barrier discharge; Nonthermal plasma; NO conversion; C_3H_6

Nonthermal plasma is an emerging technology for industrial emissions removal, which could simultaneously remove multifarious contaminations and have no harmful byproducts [1, 2]. During the past 20 years, there were many studies for nonthermal plasma applied to vehicle engine emissions control. Researches of this technology to remove NO_x, particulate matter(PM), volatile organic compounds(VOCs), SO_2 have obtained some achievements [3-5]. However, reactions between nonthermal plasma and emissions are complicated and the reaction mechanism are not clearly studied. Some Researchers point out that the improvement of NO conversion efficiency and the reduction of energy consumption can be implemented by addition of hydrocarbon to the mixture gases, thereinto,C_3H_6 is the most effective one[6].

In this paper, an simulation experiment was carried out focusing on the effect of C_3H_6 on NO conversion efficiency. The mixture gases were treated by nonthermal plasma which was produced by a self-design tubular coaxial dielectric barrier discharge reactor.

1. Experiment system

The simulation experiment system should meet the following basic requirements for an overall consideration.

(1) To ensure the stability and repeatability of the system. The mixture gases should keep its initial state and will not react with each other before the reactor turn on.

(2) Both of dielectric barrier thickness and discharge gap distance of the NTP reactor should satisfy the chemical reaction's needs for mixture gases.

(3) The NTP reactor should be economical, practical and easy to install.

Based on the principles above, an experiment

[1] qc001@ujs.edu.cn
[2] zhanglefu2000@yahoo.com.cn

system was designed(Fig.1), which consisted of a gas mixture unit, a NTP reactor, a Q-V Lissajous monitor system for discharge power and some gas analyzers. The NTP reactor is a tubular coaxial dielectric barrier discharge reactor, which can work continuously for more than ten hours that was proved by a durability test.

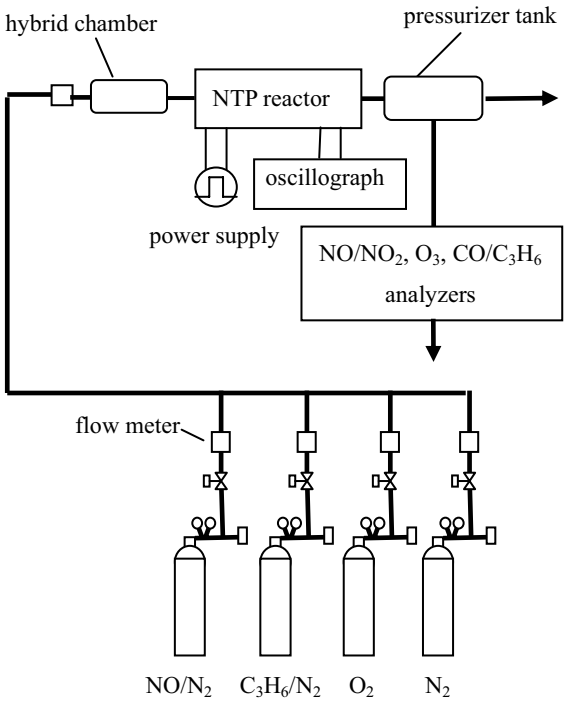

Fig.1 Sketch diagram of experiment system

The gas mixture unit include C_3H_6, NO, O_2 ,N_2 gas cylinders、mass flow meters and control valves which control the mass flow of each gas and the total gas flow, so the composition and retention time of mixture gases in NTP reactor could be controlled. The purity of each gas cylinder are shown in table1.

Tab.1 Parameters of gas cylinders

Gas cylinder	Purity	Capacity and material
C_3H_6 (N_2)	2%	40L, steel
NO (N_2)	2%	40L, stainless steel
N_2	≥99. 999%	40L, steel
O_2	≥99. 999%	40L, steel

2. Experimental results and discussions

2.1 Reaction mechanism

Electron-impact and chemical reactions occurred in the NTP reactor are very complicated [7]. Generally, there are two types of NO conversion reaction: NO oxidation and reduction reactions [8].

(1) oxidation reactions

$$N+NO \rightarrow N_2+O \quad (1)$$

(2) reduction reactions

$$O+C_3H_6 \rightarrow C_2H_5CHO \quad (2)$$

$$O+C_3H_6 \rightarrow C_2H_5+HCO \quad (3)$$

$$O+C_3H_6 \rightarrow CH_2CHO+CH_3 \quad (4)$$

$$CH_3+O_2 \rightarrow CH_3O_2 \quad (5)$$

$$C_2H_5+O_2+M \rightarrow C_2H_5O_2+M \quad (6)$$

$$NO+CH_3O_2 \rightarrow NO_2+CH_3O \quad (7)$$

$$NO+C_2H_5O_2 \rightarrow NO_2+C_2H_5O \quad (8)$$

$$HCO+O_2 \rightarrow CO+HO_2 \quad (9)$$

$$O+C_3H_6 \rightarrow CH_2CO+CH_3+H \quad (10)$$

$$H+O_2 \rightarrow HO_2 \quad (11)$$

$$CH_3+O_2 \rightarrow CH_3O_2 \quad (12)$$

$$HO_2+NO \rightarrow NO_2+OH \quad (13)$$

$$HO_2+NO \rightarrow HNO_2+O \quad (14)$$

$$CH_3O_2+NO \rightarrow NO_2+CH_3O \quad (15)$$

The total flow rate of mixture gases was fixed at 10L/min, NO concentration was adjusted to

400×10^{-6}. The specific energy density (SED[①]) input to the NTP reactor was controlled by changing the voltage of power supply (V_{p-p}) which was varied in the range of 13.6～22.1kV, the discharge frequency was fixed at 10kHz.

2.2 Effect of C_3H_6 on NO conversion in N_2/NO system

In the N_2/NO system, NO initial concentration was fixed at 400×10^{-6}, C_3H_6 initial concentration was respectively fixed to 200×10^{-6},400×10^{-6} and 600×10^{-6}, else gas was N_2.When the NTP reactor powered off, the concentration of each gas component was not found changed, so it concluded that C_3H_6 , NO and N_2 would not react with each other under normal condition. When the reactor powered on, conversion rate of NO as a function of SED value was shown in Fig.2 at the condition of C_3H_6 different initial concentration. The result indicated that conversion rate of NO greatly increased by adding 200×10^{-6} of C_3H_6 in N_2/NO mixture gases. The greater conversion rate of NO could be achieved at higher SED area. About 87.26% NO was converted to N_2 when SED value reached 600J/L. However, the NO removal efficiency did not improve while continuing increasing SED value. When C_3H_6 initial concentration was increased from 200×10^{-6} to 400×10^{-6}, conversion rate of NO obviously increased when SED value was lower than 200J/L, but higher initial concentration of C_3H_6 could hardly result in removing more amount of NO. when SED value was higher than 600J/L, there was no significant change in conversion rate of NO with the increase of C_3H_6 initial concentration.

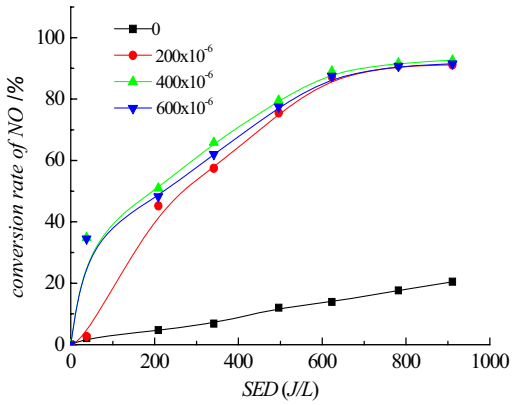

Fig.2 Conversion rate of NO as a function of *SED* in the NO/C_3H_6/N_2 mixture gas

Fig. 3 showed CO concentration as a function of SED value at different C_3H_6 initial concentration. CO concentration linearly increased with the increase of SED value. Higher SED value caused more decomposition of C_3H_6, so more CO was produced. Increasing C_3H_6 initial concentration resulted in greater collision probability between active particles and C_3H_6 molecules, so more CO was produced. NO_2 was not detected when the mixture gases passed through the NTP reactor.

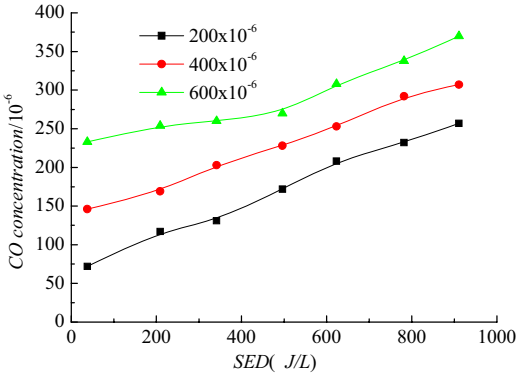

Fig.3 CO concentration as a function of *SED* in the NO/C_3H_6/N_2 mixture gas

2.3 Effect of C_3H_6 on NO conversion in NO/O_2/N_2 system

The mixture gases were composed of NO、O_2、N_2 and C_3H_6, in which O_2 initial concentration was 10%，NO initial concentration was 400J/L .When the mixture gases went through the NTP reactor, the

[①] SED =Power consumption / Gas flow rate.

NO and C_3H_6 concentration decreased and some new substances such as O_3、CO and NO_2 were produced.

Fig.4 showed C_3H_6 concentration as a function of SED value at different C_3H_6 initial concentration. It's clear that only small amount of C_3H_6 was dissociated when SED value was less than 250J/L, while when SED value reached 250J/L, C_3H_6 concentration began to sharply decrease with the increase of SED value，the higher SED value was, the more amount of high energy electron was produced, so the collision probability between high energy electron and O_2 molecules became greater, more radical O was produced through excitation and dissociation. C_3H_6 was decomposed to form CO and H_2O by O radicals and O_2 molecules, as well as other particles.

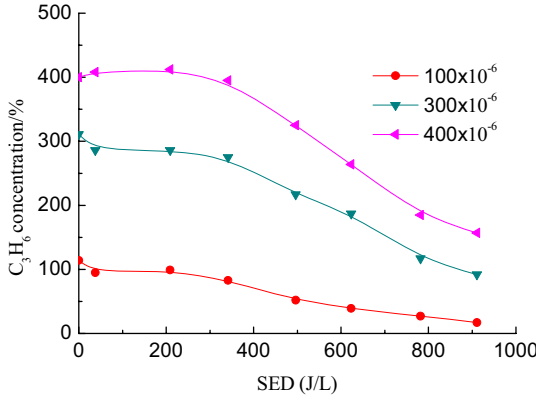

Fig.4 C_3H_6 concentration as a function of *SED* in the $N_2/O_2/NO/C_3H_6$mixture gas

Fig.5 showed NO conversion rate as a function of SED value when C_3H_6 initial concentration was respectively 0、100×10^{-6}、300×10^{-6}、400×10^{-6}. It can be seen that NO conversion rate first increased with the increase of SED value and it changed with the increase of SED value when SED value reached to 400J/L, NO conversion rate began to decrease when SED value reached 600J/L, especially without or with little C_3H_6 (100×10^{-6}) in the mixture gases. This was because exorbitant SED value caused N_2 molecular bond disconnection and the NO production, in addition, when SED value is exorbitant, the temperature in NTP reactor became higher, so NO chemical reaction was restrained. In the absence of C_3H_6, the greatest conversion rate of NO was 53% ,while it could reach 88% when 100×10^{-6} C_3H_6 added at 500J/L. It have been observed that adding C_3H_6（100×10^{-6}） to $NO/O_2/N_2$ mixture gases could greatly increase NO conversion rate, whereas continually increasing C_3H_6 can hardly improve NO conversion rate.

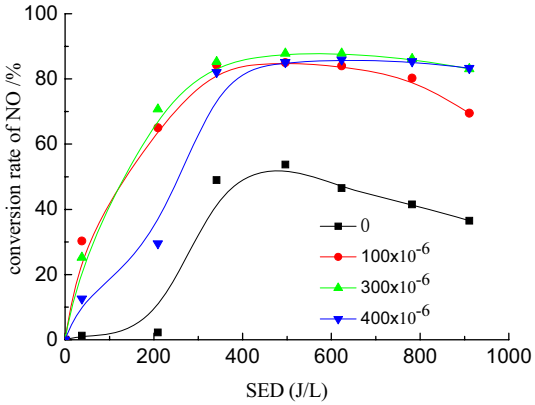

Fig.5 Conversion rate of NO as a function of *SED* in the $N_2/O_2/NO/C_3H_6$mixture gas

At different C_3H_6 initial concentration, NO_2 producing rate as a function SED was shown in Fig.6. When SED value was lower than 250J/L, the N_2 Molecular bond energy was too strong to be broken, while O_2 was dissociated to O radical, and some C_3H_6 was converted to strong oxidizing substance such as CH_3O_2、$C_2H_5O_2$ and HO_2, so oxidation reaction of NO was promoted. When SED value was in the range of 250J/L to 600J/L, N radicals were produced through the excitation and dissociation reaction, so NO reduction reaction became dominant reaction and NO_2 producing rate decreased. When SED value was higher than 600J/L, additional NO_2 was produced as the concentration of N, CH_3O_2, $C_2H_5O_2$ and HO_2 was increased, so NO_2 producing rate was increased.

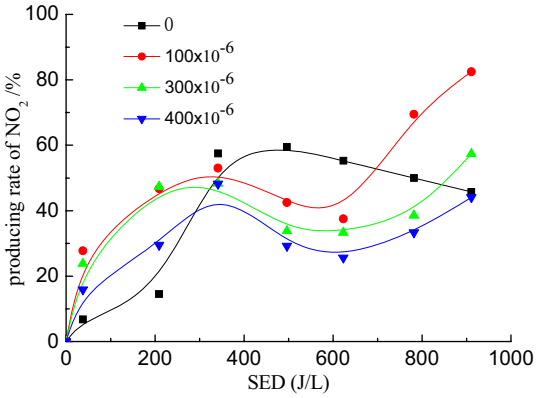

Fig.6 Producing rate of NO_2 as a function of *SED* in the $N_2/O_2/NO/C_3H_6$mixture gas

NO_2 producing rate slightly reduced when C_3H_6 initial concentration increased, which reason was that the reduction reaction of NO was promoted because of more C_3H_6 in feed. The O_3 concentration as a function of SED value was similar to NO_2, as shown in Fig. 7.

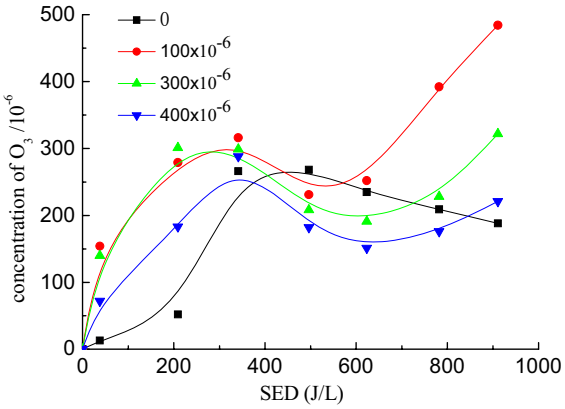

Fig.7 Concentration of O_3 as a function of *SED* in the $N_2/O_2/NO/C_3H_6$mixture gas

CO concentration as a function of SED value was shown in Fig.8. CO concentration hardly varied when SED value was less than 270J/L, While SED value was higher than 270J/L, CO concentration began to increase. The more C_3H_6 was added, the more CO was produced.

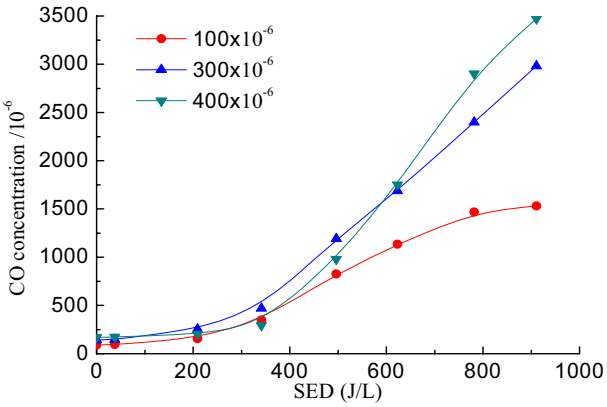

Fig.8 CO concentration as a function of *SED* in the $N_2/O_2/NO/C_3H_6$mixture gas

3. Conclusions

Dielectric barrier discharge could breakdown gas to produce nonthermal plasma under atmospheric pressure, high energy electrons and radical substances could directly dissociate and convert harmful gases. In this paper, the effects of C_3H_6 on NO conversion in $NO/N_2/C_3H_6$ and $NO/N_2/C_3H_6/O_2$ mixture gases were studied in the NTP reactor. Some conclusions could be drawn as follows:.

(1) NO conversion rate in NO/N_2 mixture gases was low, which was only 20% when SED value reached 900J/L, adding the right amount of C_3H_6 in mixture gases could enhance the NO reduction, which could reach 87%.

(2) In $NO/O_2/N_2$ mixture gases, a very small quantity of NO_x was removed and most of NO was converted to NO_2. When C_3H_6 added, 88% of NO was converted whereas the greatest conversion rate of NO was 53% without C_3H_6.

(3) It is observed that the addition of C_3H_6 could obviously increase NO conversion rate. However, it was difficult to convert NO to N_2, so the NTP technology assist catalytic system need to be applied to NO_x removal.

4.Acknowledgment

This work was financially supported by National Natural Science Foundation project

(50776041) and Natural Science Foundation of Jiangsu Province (BK2008225).

References

[1] Mei-Xiang, Pei, Zheng Huang, Wen-Feng Shang-Guan, et al. Chinese Journal of Environmental Engineering.2005, 5 (5): 56-60.

[2] Hyun-Ho Shin, Woong-Sup Yoon. SAE Paper 2000-01-2969.

[3] Hong-Bin Ma, Paul Chen, Ming-Lang Zhang, et al.. Plasma Chemistry and Processing. 2002, 22 (2): 239-254.

[4] S. Yao, C. Fushimi, K. Madokoro, et al**.** Plasma Chem Plasma Process, 2006, 26: 481-493.

[5] Yoshihiko Matsui, Masayuki Hashimoto, Aki Sakaguchi**.**SAE Paper 2001-01-3511.

[6] Anhony R Martin, James T Shawcross, J Christoper Whitehead. J. Phys. D: Appl. Phys, 2004, 37: 42-49.

[7] Yonghao Wang, Qing Yang, Ruifang, Rong, et al. Modern Vehicle Power, 2005, 1: 38-42. (in Chinese).

[8] Bae Hyeock Chun, Hyeong Sang Lee, Chang Soo Nam, et al. SAE Paper 2000-01-2897.

Plasma chemistry reactions in the $NO/O_2/N_2$ mixture gas

Yi-Xi Cai[1], Le-Fu Zhang [1,2], Jun Wang[1], Wei-Dong Zhao[1], Jing Wang[1]

(School of Automotive and Traffic Engineering, Jiangsu University, Zhenjiang,212013, China)
(Jiangsu economy and information technology commission ,Nanjing ,210008，China)

Abstract: To research the plasma chemical reaction mechanisms in the $NO/O_2/N_2$ mixture gas, a DBD-type (dielectric barrier discharge) NTP（non-thermal plasma）reactor was designed and an experimental system was established .This paper focused on the influence of the NO and O_2 initial concentrations on NO conversion rate and the variations of NO_x and O_3 concentrations with SED (specific energy density) when the $NO/O_2/N_2$ mixture gas passed the NTP reactor. It was confirmed that NO was simultaneously involved in oxidation and reduction reactions and the former was the main reaction and NO_2 concentration increased at the NTP reactor outlet. The NO conversion rate decreased with the increase of the NO and O_2 initial concentration, the O_3 concentration firstly increased and then decreased with the increase of SED value.

Key words: dielectric barrier discharge; non-thermal plasma; NO; conversion rate

1 Introduction

NO_x is one of the toxic emissions from vehicles, which is formed in the high-temperature and riched-oxygen combustion process; many countries have made restrict regulations to limit NO_x emission. In recent years，NTP and catalyst technology have been researched to reduce NO_x emission. NTP can effectively oxide NO to NO_2 [1-4], NO_2 has a stronger oxidation, which can continuously oxidize PM (particulate matter) to CO_2 in diesel emission environment .In addition, NO_2 can significantly widen the effective temperature range of SCR(selective catalyst reduction) system[5-7]. This paper mainly discusses the plasma chemical reactions in the $NO/O_2/N_2$ mixture gas.

2 Experimental systems

2.1 NTP reactor experimental system

The sketch map of the coaxial DBD-type NTP reactor was shown in figure 1.Its structure parameters were as follows: external diameter of stainless steel inner electrode was 100mm, inside diameter of dielectric quartz was 104mm, its thickness was 3mm, copper sheet was wrapped outside the quartz tightly which width was 50mm.

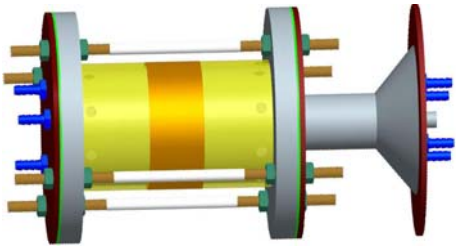

(a)

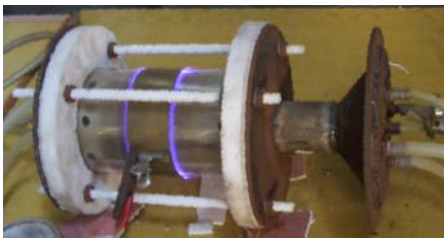

(b)

Fig. 1 sketch map of the NTP reactor

Figure2 showed the experimental

[1] qc001@ujs.edu.cn
[2] zhanglefu2000@yahoo.com.cn

system layout, industrial oxygen cylinder, nitrogen cylinder and nitric oxide cylinder (98% N_2 gas balance) were used to compose the $NO/O_2/N_2$ mixture gas, then the mixture gas flowed into the NTP reactor, the concentration of O_3 and NO_x were measured from the NTP reactor outlet by O_3 and NO_x analyzers.

Fig. 2 Sketch map of the experimental system

During the experiment, Q-V Lissajous figure was used to measure electrical parameters of the NTP reactor[8], when discharge frequency was adjusted to 10kHz and discharge voltage peak increased form 6kV to 11kV, the power range of the NTP reactor was 10W to 150W, its electric field strength was from 10kV/cm to 65kV/cm. Different electric field strength and power of the NTP reactor could influence on chemistry reactions between NO,O_2 and N_2, so different concentration of NO_x and O_3 can be obtained during the change of the discharge voltage of the NTP reactor.

2.2 Laboratory instruments

Laboratory instruments included: LZB glass rotameter, Interscan-4480 ozone analyzer (1-1999ppm), testo335 gas analyzer (NO: 0-3000ppm, NO2:0-500ppm), NTP reactor Power (0-25kV, 8-20 kHz adjustable), TDS3034B Tektronix oscilloscope, Tektronix P6139A high-pressure probe.

3 Result and discussion

3.1 The influence of O_2 initial concentration on the NO conversion rate

The NO_x and O_3 concentration as a function of SED at the different O_2 initial concentration was shown in figure 3. The unit of SED is Joule per liter (J/L), which was defined as the ratio of discharge power to volume flow of the $NO/O_2/N_2$ mixture gas. The experiment was performed under normal temperature; the volume flow of the mixture gas was 10L/min, and NO initial concentration was 400×10^{-6}.The fig.3 showed that: (1) with the increase of SED value, the NO concentration decreased, while the NO_2 concentration increased; (2)when the O_2 initial concentration was 5%, the NO_x total concentration decreased with the increase of SED; when the O_2 initial concentration was 10%, firstly ,the NO_x total concentration slightly decreased with the increase of SED, however, when SED value exceed to 300J/L, NO_x total concentration almost kept unchanged;(3)the O_3 concentration firstly increased and then decreased with the increase of SED, and reached its maximum when SED was approximately 450J/L; the higher the O_2 initial concentration was, the higher the O_3 concentration was.

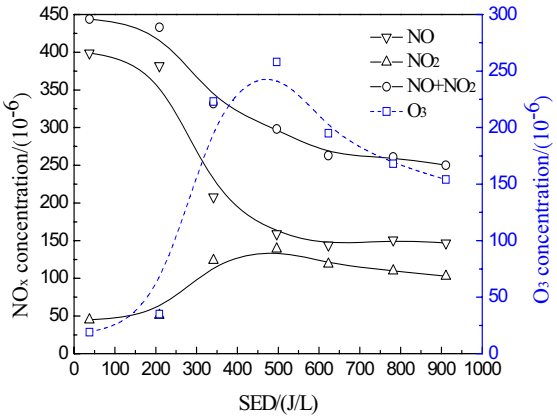

(a) 5%

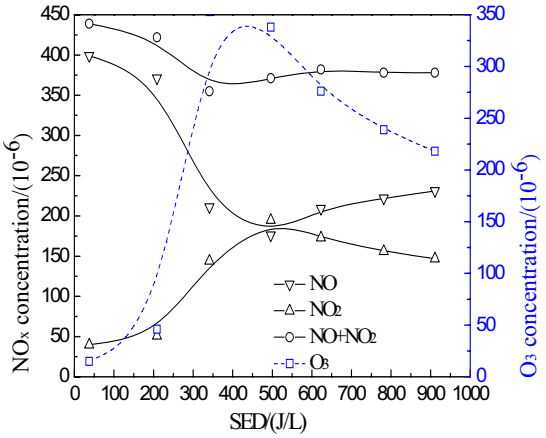

(b) 10%

Fig. 3 The NO_x and O_3 concentration as a function of SED at the different O_2 initial concentration

NO conversion rate decreased when the O_2 initial concentration increased in the mixture gas; when the O_2 initial concentration changed from 5% to 10%, NO conversion rate could reach to 50%-70%. The corresponding SED to the highest NO conversion rate was 450~550J/L.

3.2The influence of NO initial concentration on self-conversion rate

When the volume flow of the mixture gas was 10L/min and O_2 initial concentration was 10%, the NO_x and O_3 concentration as a function of SED at the different NO initial concentration was shown in figure 4. The fig.4 showed that : (1) when the NO initial concentration was 250×10^{-6} and SED was less than 450J/L, the NO concentration decreased and the NO_2 concentration increased with the increase of SED; when SED value was about 450J/L, the O_3 concentration reached its maximum, the NO concentration reached its minimum and the NO_2 concentration trended to stable, at the same time, the NO_x total concentration reached to its minimum; when SED was more than 450J/L, the O_3 concentration began to decrease, instead , the NO concentration increased, and the NO_2 concentration kept almost stable, so the NO_x total concentration increased with the increase of SED value.;(2) when the NO initial concentration was 500×10^{-6}, the variation of each gas concentration as a function of SED, as was shown in fig.4 (b), was similar to fig.3 (a) ;(3) the lower the initial NO concentration was, the higher the NO conversion rate was; the corresponding SED value to the highest NO conversion rate was 400~450J/L.

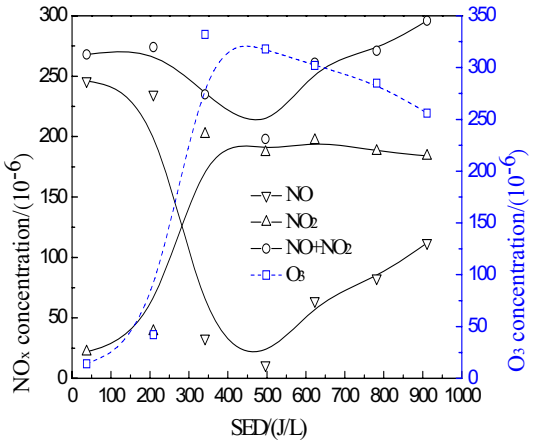

(a) 250×10^{-6}

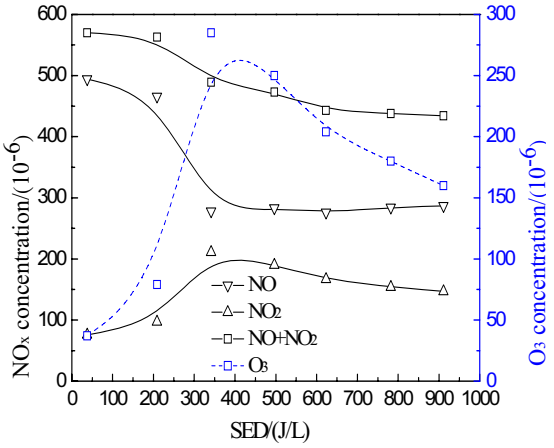

(b) 500×10^{-6}

Fig. 4 The concentration of NO_x and O_3 as a function of SED at the different NO initial concentration

4 Discussion on reaction mechanism

The main plasma reactions of the $NO/O_2/N_2$ mixture gas in discharge area of the NTP reactor were as follows [9,10]:

$$e + O_2 \rightarrow e + O(^3P) + O(^3P, ^1D) \quad (1)$$

$$e + N_2 \rightarrow e + N(^4S) + N(^4S, ^2D) \quad (2)$$

$$O(^3P) + NO + M \rightarrow NO_2 + M \quad (3)$$

$$O(^3P) + O_2 + M \rightarrow O_3 + M \quad (4)$$

$$O_3 + NO \rightarrow NO_2 + O_2 \quad (5)$$

$$N(^2D) + O_2 \rightarrow NO + O \quad (6)$$

$$N(^4S) + NO \rightarrow N_2 + O \quad (7)$$

High-energy electrons collided with O_2 and N_2 molecules via reaction (1) and (2), formed ground-state particles $O(^3P)$, $N(^4S)$ and excited-state particles $O(^1D)$, $N(^2D)$. Because decomposition energy of O_2 molecules was less than that of N_2 molecules, the probability of reaction (1) was higher than reaction (2) when SED was smaller, NO mainly converted to NO_2 through reactions (3) ~ (5), and the NO conversion rate increased with the increase of SED. Reaction (2) became a main reaction when SED became larger, as a result, more N (^4S) and N (^2D) particles were produced, which would produce additional NO through reaction (6), consequently, the NO conversion rate decreased .Besides, in larger SED area, with the decrease of O_2 initial concentration in $NO/O_2/N_2$ mixture gas, the probability of reaction (7) became large, more NO would be reduced，therefore, the NO conversion rate decreased with the increase of the O_2 initial concentration in larger SED area. When the NO initial concentration decreased in the $NO/O_2/N_2$ mixture gas, its conversion rate increased.

5 Conclusions

Through designing a DBD-type NTP reactor and establishing an experimental system, the effects of NO and O_2 initial concentrations on the NO conversion rate had been studied when the $NO/O_2/N_2$ mixture gas passed through the discharge area of the NTP reactor, and the relationship of NO_x and O_3 concentrations with SED had been researched too. From the discussions above, some conclusions could be drawn:

1) NO oxidation and reduction reactions simultaneously occurred in the NTP reactor, in which the oxidation of NO to NO_2 was the main reaction, most NO was converted into NO_2, NO_x total concentration was almost unchanged.
2) The NO conversion rate decreased with the increase of the O_2 and NO initial in the $NO/O_2/N_2$ mixture gas, NO conversion rate was higher when SED was in the range of 400~550J/L.
3) The O_3 concentration increased with the increase of the O_2 initial concentration in the $NO/O_2/N_2$ mixture gas, it firstly increased and then decreased with the increase of SED, when SED was approximately 450J/L, the O_3 concentration reached its maximum.

6 Acknowledgments

This work was financially supported by National Natural Science Foundation project (50776041) and Natural Science Foundation of Jiangsu Province (BK2008225).

References

1. Yamamoto K., Kawamura K., Yukimura K., Kambara S., Moritomi H., Yamashita T. *Vacuum*. 2004, *73*(3-4), 583.
2. Magureanu M, Mandache N. B., Eloy P., Gaigneaux E. M., Parvulescu V. I. *Appl. Catal. B: Environ*. 2005, *73*(3-4), 12-20.
3. Hammer T., Kappes T., Baldauf M. *Catalysis Today*.2004,*89*(1-2),5-14.
4. Mario Moscosa-Santillan, Axel Vincent, Esteban Santirso, Jacques Amouroux. *Journal of Cleaner Production.* 2008,*16*, 198-207.
5. Dan Ye, Deng-Shan Gao, Gang Yu, Xiang-Lin Shen, Fan Gu. *Journal of Hazardous Materials B*.2005, *127*, 149-155.
6. J Grundmann,S Muller, R.-J Zahn. *Plasma Chemistry and Plasma Processing*. 2005, *25*(5),

455-466.

7. J Grundmann, S Muller, R.-J Zahn, A Quade, H Steffen.*Topics in Catalysis*. 2007,(42–43), 303-305.
8. Wang Jun,Yi-Xi Cai, Feng-Zhi Zhuang, Jing Wang,. *Journal of Jiangsu University:Natural Science Edition*.2008,*29*(5),398-401. (in Chinese).
9. McLarnon C R, Penetrante B. M. *SAE Paper* No. 982433 (1998) .
10. Y. H Lee, J. W Chung, Y. R Choi, J. S Chung, M. H Cho, W Namkung .*Plasma Chemistry and Plasma Processing*, 2004,*24*(2),137-154.

Electron stereodynamics in charge-asymmetric Coulomb explosion of N_2 molecules with slow highly charged ions

ICHIMURA Atsushi[1] and OHYAMA-YAMAGUCHI Tomoko[2]

[1] *Institute of Space and Astronautical Science (JAXA), Sagamihara 229-8510, Japan*
e-mail: ichimura@isas.jaxa.jp

[2] *Tokyo Metropolitan College of Industrial Technology, Shinagawa 140-0011, Japan*
e-mail: yamaguti@s.metro-cit.ac.jp

Abstract.

A nontrivial electron stereodynamical effect recently found in Coulomb explosion of N_2 molecules with slow (20 – 200 eV/amu) Kr^{8+} ions is investigated. We analyze a population asymmetry observed in charge-asymmetric recoil ion pair distributions associated with the left and right projectile scatterings. The three-center Coulombic over-the-barrier model is developed so as to describe a whole collision process as formation of a triatomic quasi-molecule and its decay into three moving atomic ions. The asymmetry measured is well explained in the present model where two-step electron localization is crucial.

Keywords: highly charged ion, Coulomb explosion, charge asymmetry, three-center over-the-barrier model, two-step electron localization, electron stereodynamics

1. Introduction

Stimulated by a progress of momentum imaging technique, much effort has been devoted to the measurements of Coulomb explosion of a molecule in ion-impact collisions to reveal the dynamics including many electrons and nuclei [1, 2, 3, 4, 5]. Among them is a triple coincidence measurement in coplanar geometry by Kaneyasu and coworkers [1, 2] for collisions of slow (20 – 200 eV/amu) Kr^{8+} ions with N_2 molecules. We investigate a nontrivial electron stereodynamical effect found by them.

In their experiments [1, 2], a pair of recoil ions $(N^{Q+}, N^{Q'+})$ with charge states $1 \leq Q, Q' \leq 3$ was detected transversely (left and right) to the beam axis together with a Kr ion scattered forward. The most remarkable finding thereby was unequal strengths between two peaks appearing in two-dimensional time-of-flight (TOF) spectra for a charge-asymmetric ($Q \neq Q'$) recoil ion pair. A coincidence population $P_{<>}$ of a slower ion with lower charge state $Q_<$ and a faster ion with higher charge state $Q_>$ was found evidently larger than a population $P_{><}$ of slower $Q_>$ and higher $Q_<$. This asymmetry effect is expressed by a parameter defined as $A(Q_>, Q_<) = (P_{<>} - P_{><})/(P_{<>} + P_{><})$, ranging

in $-1 \leq A \leq 1$. The experimental result [1, 2] indicates that A is positive and increases conspicuously as the collision velocity v decreases.

The formation of a pair of faster and slower recoil ions was explained [2] in terms of transverse momentum transfer between a projectile Kr^{8+} ion and a target N_2 molecule. When the faster recoil ion is detected in the left (right) directions, the projectile should be scattered in the forward right (left) directions. The right (left) scattering of the projectile is interpreted to occur when it passes a right (left) side of the target; the scattering is dominated by a repulsive force in an event causing Coulomb explosion because it needs removal of several electrons from the target. Hence the asymmetry between the slower and faster ions means an asymmetry with respect to the shorter and longer distances from the projectile during a collision; the coincident population $P_{<>}$ ($P_{><}$) represents the ion pair formation with $Q_{\rm near} < Q_{\rm far}$ ($Q_{\rm near} < Q_{\rm far}$) for charge states at the *near* and *far* atomic N sites.

In this view, the experimental observation [1, 2] of $A > 0$ tells that the far site is more ionized than the near site. This finding could be counter-intuitive if one took a naive picture that electrons are likely to be removed by the projectile more from the near site than from the far site. The observation was qualitatively interpreted by Ehrich and coworkers [1] as due to electron polarization by the projectile. They carried out a time-dependent density-functional calculation for the evolution of electron density distribution. The result indicates that residual target electrons are largely polarized during a collision but get depolarized after that.

To get insights into this problem, we have made theoretical investigations [8, 9, 10] by modyfying a three-center Coulombic over-the-barrier model developed for collisions of a slow highly charged ion with a homo-nuclear diatomic molecule [6, 7]. In the first analysis [8], we took a conventional but questionable two-step picture, *i.e.*, 'electron removal followed by Coulomb explosion'. In this treatment, after electron removal is completed, residual electrons in the molecule are depolarized as the projectile recedes and get localized into two atomic sites on the way of fragmentation. Hence, although leading to a correct sign of the asymmetry A, the polarization effect gave too small a effect to account for large asymmetries measured. Through subsequent studies [9, 10], we have modified the model so as to describe an *inseparable* process of electron removal and Coulomb explosion; we treat a whole process as formation of a three-center quasi-molecule and its decay into three (one scattering and two dissociating) moving atomic ions.

In the present work, we carry out the calculation of the asymmetry A by fully extending the model to explain the the experimental observation [1, 2].

2. Three-center over-the-barrier model

We address collisions of a slow ($v \ll 1$ au) highly charged ion A^{q+} with a homonuclear diatomic molecule BC. Molecular bond-length is not fixed equilibrium but allowed to be elongated during a collision due to Coulomb explosion.

Many-electron dynamics is treated as formation and decay of a triatomic quasi-molecule,

$$A^{q+} + BC \quad \rightarrow \quad ABC^{q+} \quad \rightarrow \quad A^{(q-r)+} + B^{Q_B+} + C^{Q_C+}, \tag{1}$$

where $r = Q_B + Q_C$ is the number of removal electrons from the molecule. In a similar way to the two-center over-the-barrier model by Niehaus [11], the 'way in' of a collision is described by a sequence of quasi-molecule formations of respective electrons in numerical order of 'rank' t ($= 1, 2, \ldots$), while the 'way out' by their decays in the reverse order. One-electron dynamics is described with a three-center Coulomb potential $U(\boldsymbol{r})$ determined by ion core charges q_A, q_B, and q_C. According to a classical *over-the-barrier* criterion, the electron is delocalized and localized by two saddle points of the potential (see Figure 1).

The quasi-molecule of t-th electron is formed at a critical distance R_t determined by an equation $E(R) = U_{\rm high}(R)$ through the electron diabatic energy $E(R)$ and the height $U_{\rm high}(R)$ of the higher saddle point. Here the electron with rank t is assumed initially bound in the target with its t-th ionization potential.

The quasi-molecule decays into three atomic ions via two-step electron localization associated with the higher and lower saddle points. In relation to a connected domain of electron classical motion for $U_{\rm high} > E > U_{\rm low}$, the nuclear configuration space is divided into three domains labeled by $\mathcal{D}_{A-BC}$, $\mathcal{D}_{C-AB}$, and $\mathcal{D}_{B-CA}$ (*e.g.*, the left panel of Figure 1 corresponds to $\mathcal{D}_{C-AB}$). Hence, the electron localization probabilities are accordingly given by

$$\mathcal{D}_{A-BC}: \quad p_A = p_{\rm high}^{A}, \qquad p_B = p_{\rm high}^{BC} \times p_{\rm low}^{B}, \qquad p_C = p_{\rm high}^{BC} \times p_{\rm low}^{C}, \tag{2}$$

$$\mathcal{D}_{C-AB}: \quad p_A = p_{\rm high}^{AB} \times p_{\rm low}^{A}, \quad p_B = p_{\rm high}^{AB} \times p_{\rm low}^{B}, \qquad p_C = p_{\rm high}^{C}, \tag{3}$$

$$\mathcal{D}_{B-CA}: \quad p_A = p_{\rm high}^{CA} \times p_{\rm low}^{A}, \quad p_B = p_{\rm high}^{B}, \qquad p_C = p_{\rm high}^{CA} \times p_{\rm low}^{C}, \tag{4}$$

where branching probabilities $p_{\rm high}$ and $p_{\rm low}$ are numerically calculated from classical phase-space volumes at $E = U_{\rm high}$ and $E = U_{\rm low}$.

From these one-electron probabilities, we obtain the ion pair formation probabilities as

$$P(Q_B, Q_C) = \sum_{\rm string} \prod_{t=1}^{t_{\max}(b)} p_{j(t)}(q_A(t), q_B(t), q_C(t)), \tag{5}$$

where a suffix $j(t)$ labels a localization site A, B, or C according to a given 'string' [11], $\{j(t);\ t = 1, 2, \cdots, t_{\max}\}$, expressing the evolution of ion-core charges $(q_A(t), q_B(t), q_C(t))$

due to sequential electron localization in reverse order of t. The number, $t_{\max}(b)$, of active electrons forming a quasi-molecule is determined for an impact parameter b from the critical distances R_t. The evolution starts from $t = t_{\max}$, where we take $q_{\rm A} = q$ (projectile charge) and $(q_{\rm B}, q_{\rm C}) = (t_{\max}/2,\ t_{\max}/2)$ for even $t_{\max}$. For odd $t_{\max}$, we consider two sets of evolution from $((t_{\max}+1)/2,\ (t_{\max}-1)/2)$ and from $((t_{\max}-1)/2,\ (t_{\max}+1)/2)$, and take their average. A summation is taken over all possible 'strings' leading to a recoil-ion pair $(Q_{\rm B}, Q_{\rm C})$.

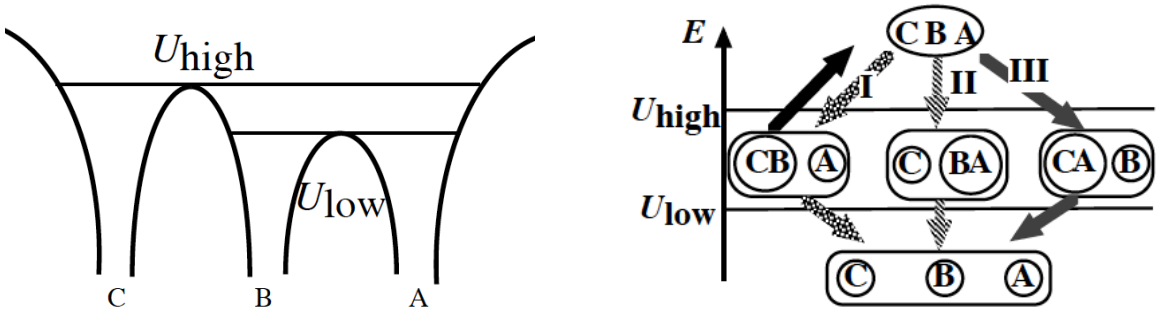

Figure 1: The three-center Coulombic over-the-barrier model. A single electron potential (left panel) have two saddle points $U_{\rm high}$ and $U_{\rm low}$. Thus the decay of a three-center quasi-molecule proceeds via two-step electron localization with three pathways (right panel).

3. Results and Discussion

We apply the present model to collisions of Kr^{8+}+N_2 in the velocity region of $v = 0.02$ – 0.1 au and consider all ten covalent electrons in N_2 molecule.

We assume linear trajectories of projectile incidence and of target dissociation. Time τ evolution of the scattering-dissociation trajectory is given by $\boldsymbol{R}(\tau) = \boldsymbol{b} + \boldsymbol{v}\tau$ and $\boldsymbol{d}(\tau) = d(\tau)\hat{\boldsymbol{d}}$, where $d(\tau)$ denotes half the bond length with its initial value taken as $d(-\infty) = 1.03$ au (equilibrium one in the isolated N_2 molecule); $\hat{\boldsymbol{d}}$ is the initial molecular alignment taken as $\hat{\boldsymbol{d}} \perp \boldsymbol{v}$. Since $\boldsymbol{b} \cdot \boldsymbol{v} = 0$, orientation of the impact parameter vector $\boldsymbol{b}$ is given by an azimuthal angle $\phi = \cos^{-1}(\hat{\boldsymbol{b}} \cdot \hat{\boldsymbol{d}})$. To calculate $d(\tau)$, we solve Newton equation with a potential given by a sum of empirical interatomic N–N potential and Coulomb repulsion between dissociating ions with charges of $q_{\rm B} = q_{\rm C} = t/2$ after passing the t-th critical distance. A result is shown in Figure 2, where the axis is taken $z = v\tau$ representing the projectile position along a trajectory of incidence. It is seen from the figure that the molecule dissociates more rapidly as the impact parameter b decreases, because the number $t_{\max}$ of active electrons increases to cause stronger Coulomb repulsion.

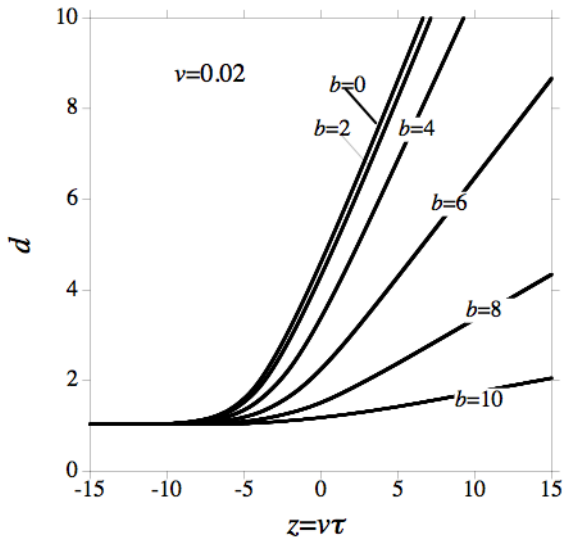

Figure 2: Time τ evolution of dissociation trajectories $d(\tau)$ at a collision velocity of $v = 0.02$ au for different impact parameters $0 \leq b \leq 10$ au. The axis is taken to be the projectile z coordinate along linear trajectories of incidence.

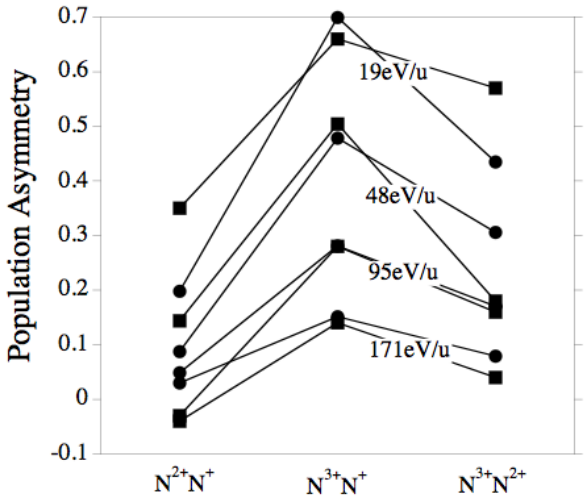

Figure 3: Population asymmetry parameters A for three charge-asymmetric fragmentation channels ($N^{2+}N^{+}$, $N^{3+}N^{+}$ and $N^{3+}N^{2+}$). The present results (circles) are compared with the experimental results [2] (squares).

Using the trajectories determined in this way, we calculate probabilities $P(Q_{\rm B}, Q_{\rm C})$ of ion pair formation using Equation (5) by assuming that the quasi-molecule of t-th electron decays at a critical nuclear configuration as $R = R_t$ and $d = d(z_t/v)$ with $z_t \equiv \sqrt{R_t^2(b) - b^2}$. We further obtain the population asymmetry parameter A as

$$A(Q_>, Q_<; v) = \frac{\sigma(Q_<, Q_>; v) - \sigma(Q_>, Q_<; v)}{\sigma(Q_<, Q_>; v) + \sigma(Q_>, Q_<; v)}, \tag{6}$$

$$\sigma(Q_{\rm B}, Q_{\rm C}; v) = 4 \int_0^\infty b{\rm d}b \int_0^{\pi/2} {\rm d}\phi P(Q_{\rm B}, Q_{\rm C}; b, \phi, v), \tag{7}$$

where a suffix B (C) denotes a near (far) atomic site. The result of calculation is shown in Figure 3 and compared with the measurement [2]. It is seen that the calculation well reproduces maginitudes of the asymmetry parameter observed as well as its dependences on collision velocities and on ion pair charge states.

Acknowledgement

This work is partly supported by MATSUO FOUNDATION and by the JSPS-CAS Core-University Program in the field of 'Plasma and Nuclear-Fusion'.

References

[1] Ehrich M, Werner U, Lutz H O, Kaneyasu T, Ishii K, Okuno K and Saalmann U 2002 *Phys. Rev* A **65** 030702(R)

[2] Kaneyasu T, Azuma T and Okuno K 2005 *J. Phys.: At. Mol. Opt. Phys.B: At. Mol. Opt. Phys.* **38** 1341

[3] Ishii K, Inoue Y, Ogawa H, Itoh A and Sakamoto N 2007 *J. Phys.: Conf. Series* **58** 275

[4] Mizuno T, Majima T, Tsuchida H, Nakai Y and Itoh A 2007 *J. Phys.: Conf. Series* **58** 173

[5] Jinag Y H *et al* 2009 *J. Phys. B: At. Mol. Opt. Phys.* **42** 13402

[6] Ichimura A and Ohyama-Yamaguchi T 1999 *Physica Scripta* T **80** 190

[7] Ichimura A and Ohyama-Yamaguchi T 2001 *Physica Scripta* T **92** 162

[8] Ohyama-Yamaguchi T and Ichimura A 2005 *Nucl. Instr. Methods* B **235** 382

[9] Ohyama-Yamaguchi T and Ichimura A 2007 *J. Phys.: Conf. Series* **58** 247

[10] Ohyama-Yamaguchi T and Ichimura A 2009 *J. Phys.: Conf. Series* **163** 012047

[11] Niehaus A 1986 *J. Phys. B: At. Mol. Phys.* **19** 2925

Recent progress in atomic and molecular processes in plasma

J. G. Wang [1], L. Liu [1], Y. Y. Qi [2], Y. Wu [1], S. B. Zhang [3] and R. K. Janev [4]

[1] The key laboratory of Computational Physics, Institute of applied Physics and Computational mathematics, P. O. Box 8009, Beijing 100088, China
[2] School of Electrical Engineering, Jiaxing University, Jiaxing 314001
[3] Hefei National Laboratory for Physical Sciences at Microscale and Department of Modern Physics, University of Science and Technology of China, Hefei 230026
[4] Macedonian Academy of Sciences and Arts, P. O. Box 428, 1000 Skopje, Macedonia

Abstract

In the recent works, atomic processes in Debye plasmas are investigated by a series of methods including the classical, semi-classical and quantum-mechanical ones. It's found that due to the plasma screening of the interactions both the binding energies and the number of bound states are reduced, while the radial extension of the wave functions become broader. Taking into account these plasma screening effects on the atomic structure and interactions, we have studied the photo processes, electron-impact processes and heavy particle collisions in a wide range of plasma screening conditions. Our work demonstrates that the screening effects are very important in Debye plasmas, which should be taken into account in the modeling and diagnostics of these plasmas.

INTRODUCTION

The effects of screened Coulomb interaction between charged particles in hot, dense plasmas on the atomic structure and collision properties have been subject to extensive studies in the last 30 – 40 years (see, e.g., [1,2] and references therein). These studies have been motivated mainly by the research in laser produced plasmas, EUV and X-ray laser development, inertial confinement fusion and astrophysics (stellar atmospheres and interiors). The densities (n) and temperatures (T) in these plasmas span the ranges $n \sim 10^{15}$ - 10^{18} cm^{-3}, $T \sim 0.5 - 5$ eV (stellar atmospheres), $n \sim 10^{19} - 10^{21}$ cm^{-3}, $T \sim 50 - 300$ eV (laser plasmas) and $n \sim 10^{22} - 10^{26}$ cm^{-3}, $T \sim 0.5 - 10$ keV (inertial confinement fusion plasmas). The Coulomb interaction screening in these plasmas is a collective effect of the correlated many-particle interactions, and in the lowest particle correlation order (pair-wise correlations) it reduces to the Debye-Hückel potential (for the interaction of an ion of charge Z with an electron) [1,2]

$$V(r) = -\frac{Ze^2}{r}\exp(-\frac{r}{D}) \ , \qquad (1)$$

where $D = (k_B T_e / 4\pi e^2 n_e)^{1/2}$ is the Debye screening length, T_e and n_e are the plasma electron temperature and density, respectively, and k_B is the Boltzmann constant. The representation of charged particle interaction in a plasma by the potential (1) is adequate only if the Coulomb coupling parameter $\Gamma = e^2/(ak_B T_e)$ and plasma non-ideality parameter $\gamma = e^2/(Dk_B T_e)$ satisfy the conditions $\Gamma \le 1$, $\gamma << 1$, where $a = [3/(4\pi n_e)]^{1/3}$ is the average inter-particle distance. There is, however, a wide class of laboratory and astrophysical plasmas in which these conditions are fulfilled (Debye plasmas). Expressions for the screened Coulomb interaction for strongly coupled and non-ideal plasmas can be found elsewhere (see, e.g., [1, 2]).

Recently, we studied systematically the atomic structure and dynamics of hydrogenic ions imbedded in a Debye plasma by a series of methods including the classical, semi-classical and quantum-mechanical ones [3-10]. In this report, we summarize our results on the atomic structure, photo-excitation and photo-ionization, electron-impact excitation and heavy particle collisions in a wide range of plasma screening conditions. These examples serve to illustrate the progress in this area.

Atomic units will be used in the remaining part of this article, unless explicitly indicated otherwise.

Atomic structure

In the non-relativistic approximation, the radial Schrödinger equation for a hydrogen-like ion with nuclear charge Z in a Debye plasma is given by

$$\left(-\frac{d^2}{2dr^2} + \frac{l(l+1)}{2r^2} + V(r)\right) P_{nl}(r;Z,D) = E_{nl}(Z,D) P_{nl}(r;Z,D) \quad (2)$$

where $P_{nl}(r;Z,D)$ and $E_{nl}(r;Z,D)$ are the radial electron wave function and electron energy with the principal and angular quantum numbers *n* and *l*, respectively, and the potential $V(r)$ is given by Eq.(1).

By making the scaling transformations

$$\rho = Zr, \delta = ZD, \varepsilon_{nl}(\delta) = E_{nl}(Z,D)/Z^2 , \quad (3)$$

Eq. (2) is reduced to the form

$$\left(-\frac{d^2}{2d\rho^2} + \frac{l(l+1)}{2\rho^2} - \frac{\exp(-\rho/\delta)}{\rho}\right) P_{nl}(\rho;\delta) = \varepsilon_{nl}(\delta) P_{nl}(\rho;\delta) \quad (4)$$

$P_{nl}(\rho;\delta)$ and $\varepsilon_{nl}(\delta)$ are the scaled electron wave function and electron energy, respectively. The scaled radial Schrödinger equation (4) for the discrete spectrum has been subject to solution in the past by a variety of approximate (perturbation, e.g., [11]), variational, e.g., [12], and references therein) and direct numerical integration methods (e.g., [13] and references therein). We solve Eq. (4) numerically, under the standard boundary conditions, by employing the fourth-order symplectic integration scheme described in Refs. [14, 15].

As it is well known (see, e.g., [16]), the potential (1) that decreases with increasing *r* faster than $-1/r^2$ supports only a finite number of bound states for any finite value of *D*. Moreover, the *l*-degeneracy of the energy levels, characteristic for the pure Coulomb potential, is

lifted in the screened Coulomb potential (1). The finite number of bound states for any finite value of D implies that with decreasing D the electron binding energy decreases and at a certain critical value D_{nl} it becomes zero. In figure 1 we show the scaled energies ε_{nl} of the 1s, 2l and 3l states as function of the screening parameter $\mu = 1/\delta$. With increasing μ the scaled energies rapidly approach the continuum edge.

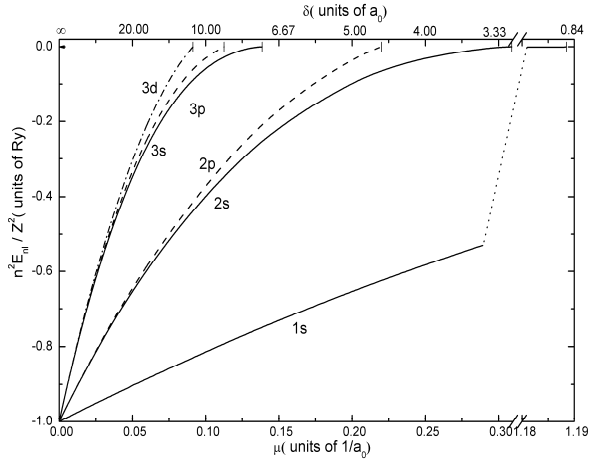

FIGURE 1. Scaled energies for the six lowest states of hydrogen-like ion as function of scaled screening parameter $\mu = 1/ZD$.

In figure 2 we show the scaled wave functions of the 1s states for a number of the screening lengths δ. As δ decreases, the spread of electronic wave functions becomes broader, its peak is shifted towards the larger radial distances, but the peak magnitude decreases. Moreover, when δ decreases to the critical scaled Debye lengths $\delta_{1s}^{c} = 0.839908a_0$ [4,5,13], the wave function will extend to infinity since the state is on the continuum edge.

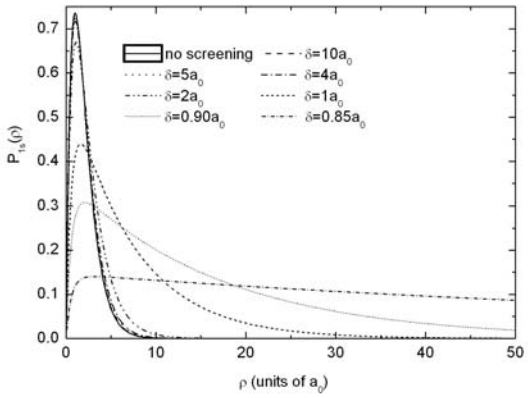

FIGURE 2. Wave functions of the 1s state for a number of scaled screening lengths δ.

In figure 3 we plot the energy-normalized continuum p-wave functions at a scaled energy $\varepsilon = 0.0005 a.u.$ for the unscreened case and the screened cases with a number of scaled Debye lengths. The wave functions obviously change with the screening interactions. The positions of peaks and nodes move to the longer distance as δ decreases, which results in change of the phase and amplitude of continuum wave functions in plasmas.

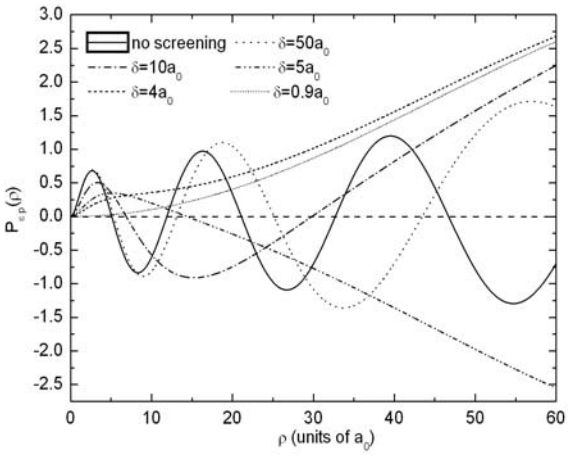

FIGURE 3. Wave functions of the εp continuum state at scaled electron energies $\varepsilon = 0.0005 a.u.$ for a number of scaled screening lengths δ

The change of atomic energy levels and wave functions will directly affect the couplings and, thereby, the dynamics of atomic processes in plasmas.

Photo-exicitation and photo-ionization

Studies of photo-excitation process have been performed earlier [17-19] for a limited number of Debye lengths and have concentrated on the calculation of oscillator strengths [18, 19] or radiative transition probabilities [17]. In our study [4] we cover the entire range of Debye screening lengths and analyze in detail the properties of transition frequencies and spectral line intensities and shifts. Particular attention has been paid to the $\Delta n = 0$ transitions whose line intensities increase (in contrast to the $\Delta n \neq 0$ transitions) with increasing the screening strength, $1/D$. The line intensities of Lyman and Balmer series were also studied in detail, including different line intensity ratios within a given series.

In figure 5 we plot the absorption oscillator strengths as a function of the scaled Debye length for the Lyman series ($n \leq 5$). For the unscreened case ($\mu = 1/\delta = 0$), our results are in excellent with the exact values. With increasing the interaction screening, the absorption oscillator strength gradually decreases until a critical Debye length, δ_{nl}^{c} , is reached where the upper level *np* merges with the continuum edge. Under local thermodynamic equilibrium conditions, the line intensity, normalized to the population of ground state hydrogen-like ions, can be calculated as elaborated in Ref. [4]. In figure 6, we plot the intensities, normalized to the population of 1s state, of spectral lines of the Lyman series of C^{5+} ions for the fixed Debye screening length $D = 10a_0$ and a plasma temperature of 1012 eV. (For this value of *D*, the 9*p* state of C^{5+} lies in the continuum.) The plasma screening effects are manifested in the decrease of line intensities and the red shift of their frequencies when the Debye screening length decreases. The frequency red shift is result of the decrease of energy difference with decreasing *D* (see figure 1), while the decrease of line intensity is due to the frequency decrease. The lines close to the termination of the series in the screened interaction case become significantly weaker with respect to the unscreened case, as illustrated by 7*p* – 1*s* and 8*p* – 1*s* lines.

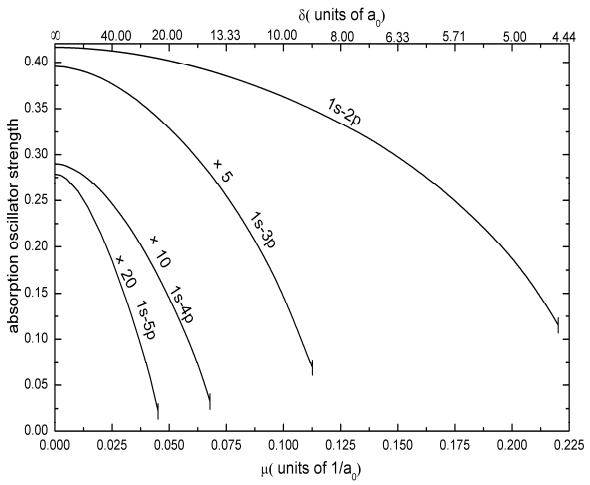

FIGURE 5. Dependence of absorption oscillator strengths on the screening parameter μ , [4].

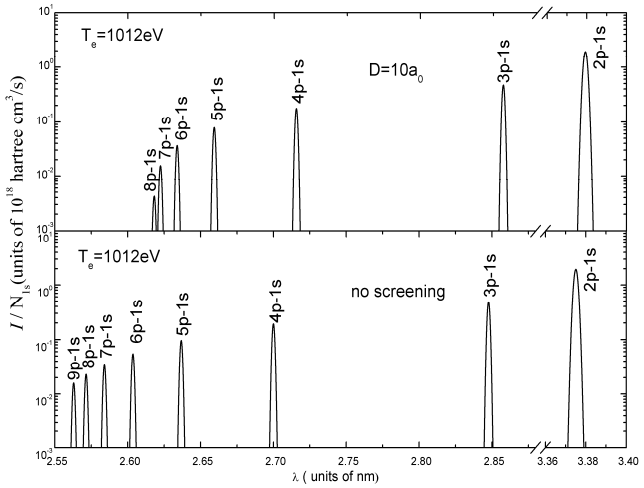

Figure 6. Line intensities of Lyman series lines for the C^{5+} ion for $D = 10a_0$ and T_e = 1012 *eV*. The bottom panel shows the lines in the case of no interaction screening [4].

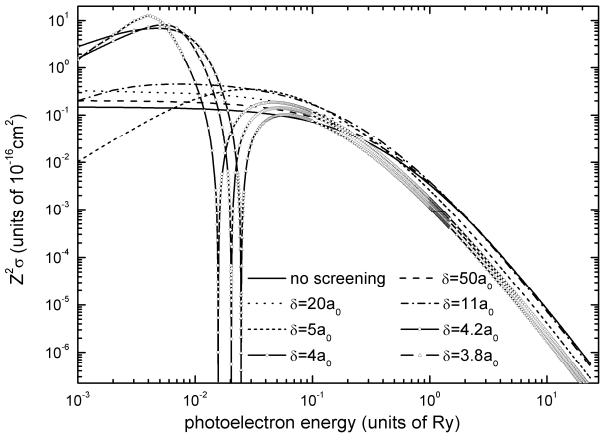

Figure 7. Photo-ionization cross sections for the $2s$ excited state of hydrogen-like ions as a function of the photoelectron energy for a number of the scaled screening length $\delta(a_0)$

A number of papers [18, 20-22] were published to study the photo-ionization process for the hydrogen atom or hydrogen-like ions in plasmas. Due to the importance of photo-ionization in plasma diagnostics and simulations, we did elaborate calculations for the scaled photo-ionization cross sections for the hydrogenic ions in a wide plasma screening parameter range. As an example, we plot in figure 7 the photo-ionization cross sections for the 2s state of hydrogen-like ions. For the unscreened and weakly-screened ($\delta > 10a_0$) cases, the cross sections vary smoothly with increasing of photoelectron energy. As δ decreases, the low-energy cross section (in contrast with the unscreened case) decreases with the decreasing of photoelectron energy, and when $\delta \le 4.2a_0$ a Cooper minimum appears, which alters dramatically the cross section behavior.

Electron impact excitation

Whitten and Weisheit [23, 24] have studied the plasma screening effects on the electron-impact excitation for hydrogen-like ions by both the Born approximation and close-coupling methods. Jung et al. [25-28] have published a series of papers in which the semi-classical impact parameter approximation was used. Their work focuses mainly on the low-energy, near threshold region. In our recent work [9], we have investigated the plasma screening effects on the high-energy electron-impact excitation of hydrogen-like ions using the first Born approximation. The screened interactions were described by the Debye-Hückel model, and the scaled wave functions were calculated numerically in a symplectic integration scheme.

As an example, the scaled differential cross sections (DCS) for $1s \rightarrow 2s$, $1s \rightarrow 2p$ and $2s \rightarrow 2p$ transitions are given in figure 8. The DCS for the unscreened case decreases

monotonously with the increase of scattering angle and the maximum value appears at the 0^o scattering angle. For the screened cases, the interaction screening reduces the DCS, especially at the 0^o scattering angle, since the DCS at small angle is determined by the large-impact-parameter scattering processes, and the long-range interactions are screened significantly by the Debye-Hückel potential. This also results in reduction of the magnitude of total excitation cross section at high energies.

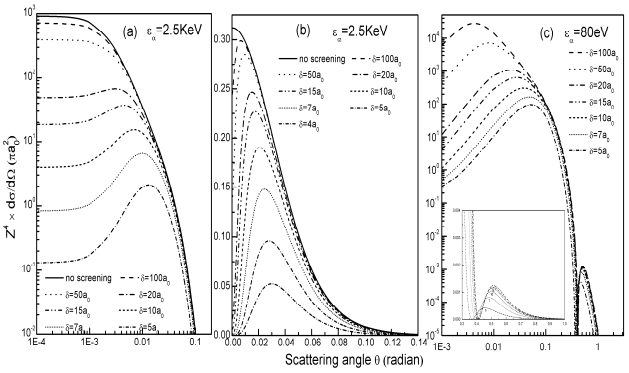

FIGURE 8. Differential cross sections for the unscreened and screened cases for various scaled Debye lengths. Panel (a): $1s \rightarrow 2p$, (b): $1s \rightarrow 2s$ at scaled electron energy $\varepsilon_\alpha = 2.5keV$ and (c): $2s \rightarrow 2p$ at $\varepsilon_\alpha = 80eV$. [9]

We also studied the low-energy electron impact excitation process in the screened Coulomb interations. The R-matrix method for electron-atom and photon-atom interactions has been utilized to calculate the electron-impact excitation of hydrogen in the low energy region, and we will not repeat its description here. The physical orbitals of hydrogen atom with the screened Coulomb potential (1) are calculated by piece-wise exact power series expansions of the radial function, while the pseudo-orbitals are optimized by the CIV3 computer code. The used R-matrix code is a modified version based on the Belfast atomic R-matrix packages in which the Coulomb interactions in the (N+1)-electron non-relativistic Hamiltonian are replaced by Yukawa-type screened Coulomb interactions (in atomic units):

$$H^{N+1} = \sum_{n=1}^{N+1}[-\frac{1}{2}\nabla_n^2 - \frac{Z}{r_n} * \exp(-\frac{r_n}{D}) + \sum_{m>n}^{N+1}\frac{1}{r_{mn}} * \exp(-r_{mn}/D)] \tag{5}$$

where $\mathbf{r}_n$ is the electron radius vector (with respect to the nucleus Z), $r_{mn} = |\mathbf{r}_m - \mathbf{r}_n|$ is the inter-electron distance and D is the screening length. The electron-electron interaction term is expanded as:

$$V_{ee} = \frac{\exp(-r_{mn} \cdot D^{-1})}{r_{mn}} = \begin{cases} \sum_{l=0}^{\infty} \frac{r_<^l}{r_>^{l+1}} P_l(\cos\theta) & D^{-1} = 0 \\ -D^{-1}\sum_{l=0}^{\infty}(2l+1) j_l(i \cdot D^{-1} r_<) & \\ h_l^{(1)}(i \cdot D^{-1} r_>) P_l(\cos\theta) & D^{-1} > 0 \end{cases} \tag{6}$$

where $r_> = \max(r_m, r_n)$, $r_< = \min(r_m, r_n)$, P_l, j_l and $h_l^{(1)}$ are the Legendre polynominals, the spherical Bessel functions and the spherical Hankel functions of the first kind with complex argument, respectively.

In figure 9, the 1s→2s (panels (a) and (b)) and 1s→2p (panel (c)) excitation collision strengths are shown in the n = 2 resonant energy region when the screening length D decreases from D =∞ to D = 8 a.u., and the binding energies of 2s and 2p states with changing D are shown in the inset in Fig 9a. The significant changes in the structure and values of the collisions strengths, especially for

the 1s→2s transition, are obviously related to the changes of the resonance parameters when D decreases, particularly in the regions of D where ^{1,3}P and ^{1}D Feshbach resonances change their character. These peaks are clearly observed in the 1s→2s collision strength for D=45 a.u. (at E=0.74794 Ryd) and for D=29a.u. (at E=0.745118 Ryd), in Fig.9a, where the $^{3}P^{o}$ (2) and $^{1}P^{o}$(1) resonances have already acquired a shape-type character. The resonant structure in figure 9b reflects the effects of $^{1}D^{e}$ resonance on the 1s→2s collision strength after passing the 2s threshold at D≈19a.u. After passing the 2p threshold at E = 0.739402Ryd (D =13a.u.), the $^{1}D^{e}$ resonance gives the main contribution to the 1s→2p collision strength as seen in figure9c. (For D > 14 a.u. this collision strength in the considered energy range is dominated by the $^{1}P^{o}$(2) shape resonance.)

The relatively small but sharp peaks (cusps) observed in the 1s→2s collision strength (see figure 9a and the inset of figure 9b) represent the effects of virtual states [26] associated with the $^{3}P^{o}$(2) (for D < 34 a.u.), $^{1}P^{o}$(1) (for D < 21 a.u.) and $^{1}S^{e}$(2) (for D < 27 a.u.) when these states approach the 2p and 2s thresholds, respectively. We should note that similar virtual state effects have also been observed in the electron-helium excitation cross sections in the n = 2 thresholds region, where the Coulomb degeneracy is also lifted.

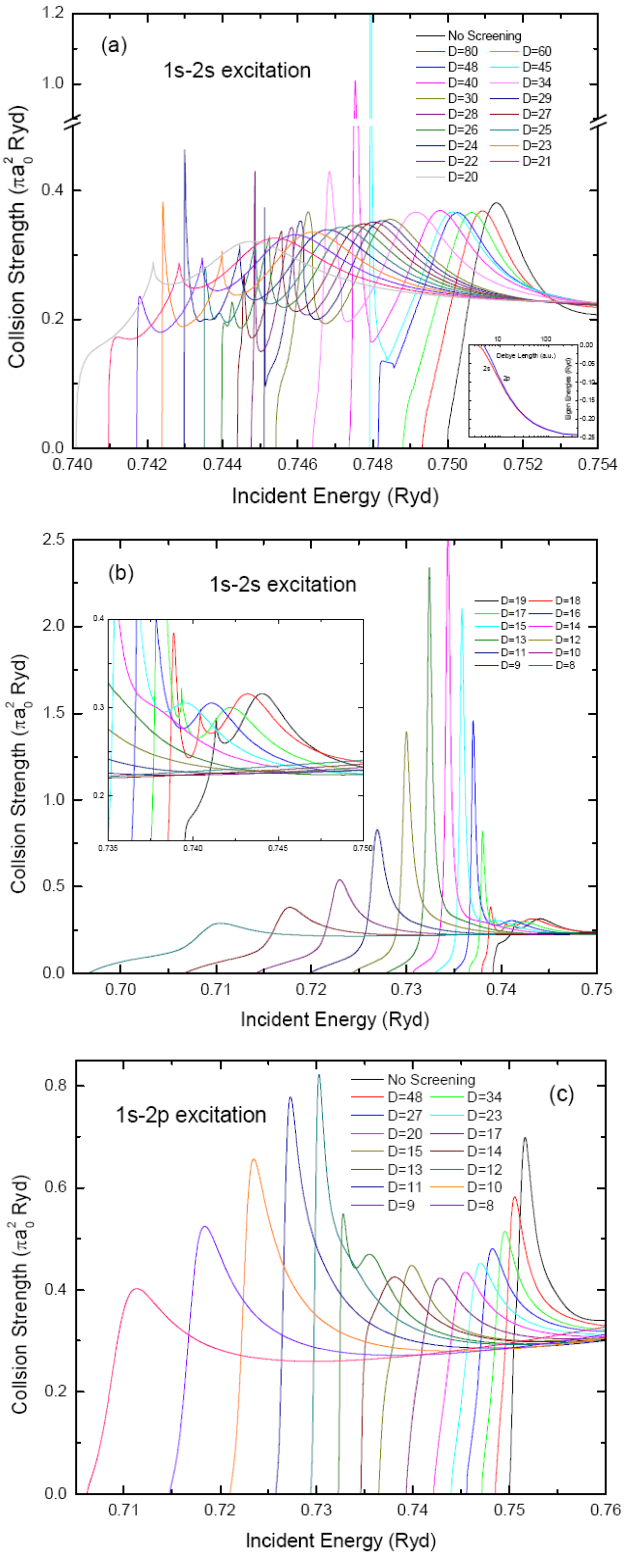

FIGURE 9. Dynamic evolution of 1s→2s (panels (a) and (b)) and 1s→2p (panel (c)) collision strengths when the screening length varies.

Heavy particle collisions

The studies in heavy-particle collisions in hot, dense plasmas are those for proton-impact

excitation of *n=2* fine structure levels of hydrogen-like ions within a close-coupling scheme employing both the static Debye-Hückel and the ion-sphere model potentials [29], electron capture in proton - hydrogenic ion collisions [30] and symmetric resonant charge exchange in hydrogen-like ion - parent nucleus collisions [31] by the classical Bohr-Lindhard model, and the classical trajectory Monte Carlo study of electron capture and ionization in hydrogen atom-fully stripped ion collisions [3]. In all above mentioned studies, the change of the electronic bound state wave functions and energies in the screened Coulomb potential was taken into account at most within the first-order perturbation theory.

In our recent work [5, 6] we have studied the excitation, ionization and electron capture processes in He^{2+}+H (1s) collisions in the Debye plasma by employing the two-center atomic orbital close-coupling (TC-AOCC) method [32] with plane wave electron translational factors (PW ETFs) in the energy range 5-300keV/u. The atomic orbitals have been determined variationally from the corresponding single-center Schrödinger equation with the potential (1). A large-scale AO basis was applied to ensure reliable results both in the unscreened and screened interaction cases.

The state-selective excitation cross sections is shown in figure 10 for the unscreened interactions (a) and for screened interactions with D = $12a_0$ (b), $6.0a_0$ (c) and $4.0a_0$ (d). The total cross sections are also shown. In the screened case with D = $12a_0$, only the states with $n \leq 3$ lie in the discrete part of the spectrum of H. The total excitation cross section in the screened case is only slightly reduced with respect to the unscreened case, but the changes in the *3l* excitation cross sections are significant. These changes can be attributed to the changes of corresponding couplings for D = $12a_0$. In the cases of screening with D = $6.0a_0$ (c) and D = $4.0a_0$ (d), only the states *2l* and *2s*, respectively, remain in the discrete spectrum of H. The observed changes in the magnitude and energy behavior of *2s* and *2p* excitation cross sections with respect to the unscreened case, or the D = $12a_0$ screened case, can again be attributed to the changes in the couplings.

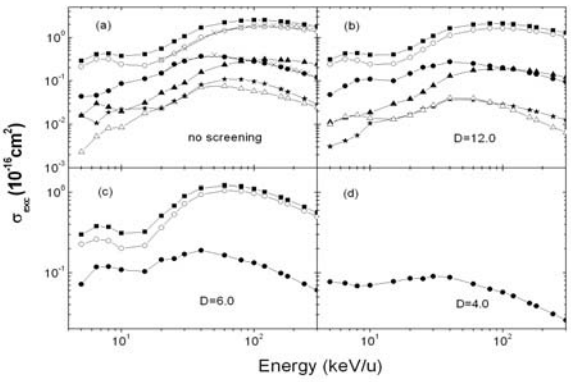

FIGURE 10. Energy behavior of *2l* and *3l* excitation cross sections and their sum for the unscreened case (a) and screened cases with D=$12a_0$ (b); D=$6.0a_0$ (c); D=$4.0a_0$ (d). The symbols are for: total cross section: filled squares; *2s*: filled circles; *2p*: open circles; *3s*: open triangles; *3p*: filled triangles; *3d*: filled stars. The lines connecting the calculated data are to guide the eye. The crosses on *2s* and *2p* excitation curves in panel (a) are the data of Ref.[33].

In figure 11 we show the *nl*-capture cross sections for the screened interactions with D = 6.0, 4.0, 2.0 and $1.5a_0$ (panels (a)-(d), respectively). For D = $6.0a_0$, the discrete spectrum of He^+ contains only the $n \leq 3$ states. Just as in the case of unscreened Coulomb potentials, the population of *2p* electron capture channel dominates up to ~125 keV/u, from where on the population of $He^+(1s)$ state becomes dominant. In the D = $4.0a_0$ screening case only the $n \leq 2$ and *3s* states remain in the discrete spectrum of He^+. In the D = $2.0a_0$ and D = $1.5a_0$ screening cases only the *1s*, *2s* and *1s* states are left in the He^+ spectrum, respectively. While the observed reduction of *2s* capture cross section with respect to its values in the D = $4.0a_0$ case is due to the lack of its population via the *2p* state (now absent in the He^+ spectrum), the relative small changes in the magnitude and energy behavior of the *1s* capture cross section indicates that the population of $He^+(1s)$ is dominated by the H $(1s)$-$H^+(1s)$ exchange coupling (and the momentum transfer at high energies).

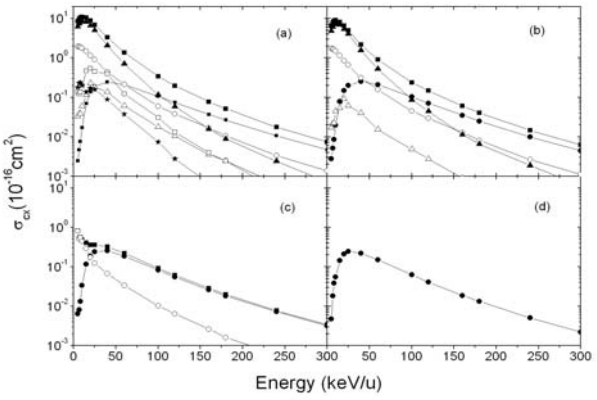

FIGURE 11. Energy dependence of state selective cross sections for electron capture to $He^+(nl)$ states, $n \leq 3$ for screened Coulomb potentials with D = 6.0, 4.0, 2.0 and $1.5a_0$ (panel (a)-(d), respectively) and their sum. The symbols are for: summed cross sections: filled squares; *1s*: filled circles; *2s*: open circles; *2p*: filled triangles; *3s*: open triangles; *3p*: open squares; *3d*: filled stars. The lines connecting the calculated points are to guide the eye.

The energy dependence of total ionization cross section is shown in figure 12 for the unscreened case and for interaction screening with D = 12, 6, 4, 2.5, $2a_0$. Total ionization cross section contains contributions from population of target-centered continuum states (ITC) and population of projectile-centered continuum states (IPC). The effects of reductions of both the binding energies and the electron-projectile interaction result in a varied dependence of ionization cross section on the screening length, as shown in figure 12. Our cross section for the zero-screening case practically coincides with the theoretical results of Ref.[33,34] in the overlapping energy range (above 20keV/u) and with the experimental data [35].

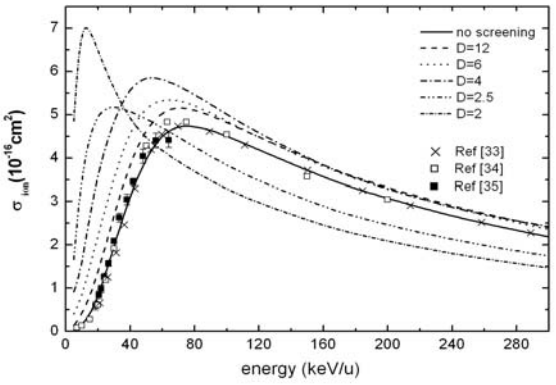

FIGURE 12. Total ionization cross section for the unscreened case (solid line) and for interaction

screening with D = 12, 6, 4, 2.5, $2a_0$ (other lines) as function of collision energy. The crosses and open squares are the results of TC-AOCC calculations of Ref.[33] and Ref.[34], respectively, and the filled squares are the experimental data of Ref.[35].

Conclusion

We have investigated systemically the atomic structure and dynamics of hydrogenic ions embedded in Debye plasmas. In general, the screening of Coulomb interactions affects the atomic structure in three fundamental ways: (i) reduction of the number of states in the discrete spectrum of the target and projectile system, thus limiting the number of reaction channels; (ii) change (decrease) of energies of bound states (as well as their differences) with decreasing the screening length, and (iii) broadening of electron radial distribution of the bound state and change of phase and amplitude of the continuum wave function. These effects result also in changes of atomic interaction properties, including the photon absorption, electron-impact and heavy particle collision processes. The obtained results should be important for the simulation and diagnostics of hot, dense plasmas.

Acknowledgments

One of us (R. K. J) would like to acknowledge the warm hospitality of the Institute of Applied Physics and Computational Mathematics during the period when this work was performed. This work was partly supported by the National Natural Science Foundation of China (Grants Nos. 10875017, 10734140 and 10604011) and the National Key Laboratory of Computational Physics Foundation (No. 9140C6904030808).

References

1. D. Salzman, *"Atomic Physics in Hot Plasmas"* (Oxford Univ. Press, Oxford, 1998).

2. M. S. Murillo and J. C. Weisheit, *Phys. Rep.* **302**, 1 (1998).

3. H. Zhang, J. G. Wang, B. He, Y. B. Qiu, and R. K. Janev, *Physics of Plasmas* **14**, 053505 (2007).

4. Y. Y. Qi, J. G. Wang, R. K. Janev, *Phys. Rev. A* **78**, 062511 (2008).

5. L. Liu, J. G. Wang, R. K. Janev, *Phys. Rev. A* **77**, 042712 (2008).

6. L. Liu, J. G. Wang, R. K. Janev, *Phys. Rev. A* **77**, 032709 (2008).

7. L. Liu and J. G. Wang, *J. Phys. B **41**, 155701* (2008).

8. S. L. Zeng, L. Liu, J. G. Wang, R. K. Janev, *J. Phys. B* **41**, 135202 (2008).

9. Y. Y. Qi, Y. Wu, J. G. Wang and Y. Z. Qu, *Phys. Plasmas* **16**, 023502 (2009).

10. Y. Y. Qi, Y. Wu, J. G. Wang, *Phys. Plasmas* (2009).

11. P. Chandhury and S. Bhattacharya, *Chem. Phys. Lett.* **296**, 51 (1998).

12. C. Stubbings, *Phys. Rev. A* **48**, 220 (1993).

13. F. J. Rogers, H. C. Graboske and D. J. Harwood, *Phys. Rev. A* **1**, 1577 (1970).

14. E. Forest and R.D. Ruth, Physica D **43**, 105 (1990); H. Yoshida, *Phys. Lett. A* **150**, 262 (1990).

15. X.S. Liu, X.Y. Liu, Z.Y. Zhou, P.Z. Ling and S.F. Pan, *Int. J. Quantum Chem.* **79**, 343 (2000).

16. L.D. Landau and E.M. Lifshitz, *"Quantum Mechanics: Non-Relativistic Theory"* (Pergamon, London, 1958).

17. K. M. Roussel and R. F. O'Connell, *Phys. Rev. A* **9**, 52 (1974).

18. J. C. Weisheit and B. W. Shore, *Astrophys. J.* **194**, 519 (1974).

19. F. E. Höhne and R. Zimmermann, *J. Phys. B: At. Mol. Phys.* **15**, 2551 (1982).

20. Y. D. Jung, *Phys. Fluids B* **5**, 3432 (1993); *ibid.* **5**,4456 (1995).

21. L. B. Zhao and Y. K. Ho, *Phys. Plasmas* **11**, 1695 (1994).

22. A. C. H. Yu and Y. K. Ho, *Phys. Plasmas* **12**, 043302 (1995).

23. B. L. Whitten, N. F. Lane and J. C. Weisheit, *Phys. Rev. A* **29**, 945 (1984); *ibid.* **30**, 650 (1984).

24. J. C. Weisheit, *Adv. At. Mol. Phys.* **25**, 101 (1988).

25. Y. –D. Jung, *Phys. Plasmas* **2**, 332 (1995); *ibid.* **2**, 1775 (1995).

26. Y. –D. Jung, *Phys. Plasmas* **4**, 21 (1997).

27. Mi-Young Song and Young-Dae Jung, *J. Phys. B: At. Mol. Opt. Phys.* **36**, 2119 (2003)

28. Y. –D. Jung and J. –S. Yoon, *J. Phys. B: At. Mol. Opt. Phys.* **29**, 3549 (1996).

29. K. Scheibner, J. C. Weisheit and N. F. Lane, *Phys. Rev. A* **35**, 1252 (1987).

30. C.-G. Kim and Y. –D. Jung, *Phys. Plasmas* **5**, 2806 (1998); *ibid.* **5**, 3493 (1998).

31. Y. –D. Jung, *Europhys. Lett.* **69**, 753 (2005).

32. W. Fritsch and C. D. Lin, *Phys. Rep.* **202**, 1 (1991).

33. J. Kuang and C. D. Lin, *J. Phys. B: At. Mol. Opt. Phys*. **30**, 101 (1997).

34. N. Toshima, Phys. Rev. A **50**, 3940 (1994).

35. M.B. Shah and H.B. Gilbody, *J.Phys.B: At. Mol. Phys*. **14**, 2361 (1981).

Recoil momentum of target ions in collisions of Ar^{6+}+CO_2 at energies below 300 eV/u

INOUE Yoko, ISHII Kunikazu[1], and OGAWA Hidemi[1]
Graduate school of Humanities and Sciences, Nara Women's University Nara 630-8506 Japan
1) Dept. of Physics, Nara Women's University Nara 630-8506 Japan
e-mail: bay.inoue@cc.nara-wu.ac.jp

Abstract

In order to study the collision dynamics and fragmentation process of molecule by highly charged ion impact for single electron capture (SC) processes at the low energies below 1 keV/u, we have experimentally obtained collision energy dependence of the recoil momentum and have compared it with those calculated by a theoretical model using a deflection function with polarization potential. We obtain fairly good agreement between the measured and calculated results. This suggests that the polarization potential plays a crucial role in the low-energy region.

Keywords: highly charged ion, molecular fragmentation, slow collision

1.Introduction

The charge transfer process of multiply charged ions (MCIs) is of great importance not only in atomic collision physics for fundamental interests but also in such fields as plasma physics, astrophysics and development of X-ray laser [1, 2]. Recently, the field of fragmentation processes of diatomic molecules in electron capture collisions of MCIs at energies above 1 keV/u has grown rapidly. For molecular fragmentation, it is understood that a diatomic molecular target undergoes Coulomb explosion after electron capture, and then, the two fragments fly in opposite directions with kinetic energies given by the dissociation energy [3]. Kaneyasu et al.[4] and Ohyama-Yamaguchi et al.[5] conducted studies on molecular fragmentation processes induced by MCI collisions at low energies below 1 keV/u. Kaneyasu et al. measured two fragment ions in a direction perpendicular to a projectile beam axis in coincidence with a projectile after double (DC) and triple electron capture (TC) collisions of Kr^{8+} with N_2. As a result, an interesting observation was reported that recoil momenta of non-dissociated molecular ions depend on collision energy, while those of dissosiated fragment ions do not depend on the collision energy. We have also measured those for single electron capture (SC) collisions of Ar^{6+} with N_2, and have made these energy dependence clear [6].

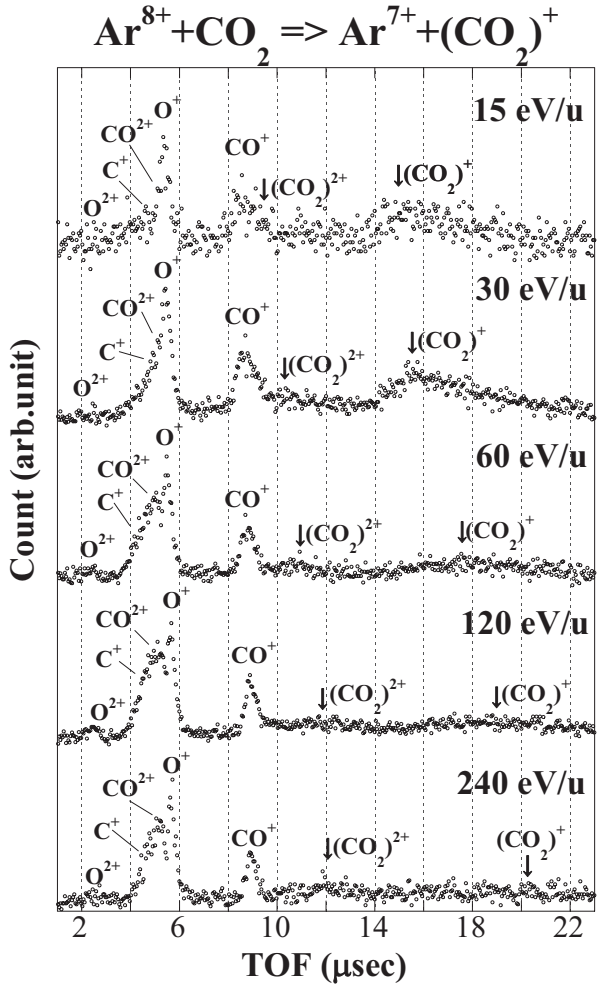

Figure 1: TOF spectra of non dissociative and dissociative ions in SC collisions of Ar^{8+}+ CO_2 at energies from 15 to 240 eV/u.

In this study, in order to investigate the collision energy dependence of recoil momentum, we measure recoil momenta of recoil ions for Ar^{8+}+ CO_2 collision system at energies from 15 to 240 eV/u. The energy dependence of the measured recoil momentum is compared with those obtained by theoretical calculations using the Coulomb potential and the polarization potential.

2. Experiment

The experimental method was performed using a mini-EBIS (Electron Beam Ion Source) atomic collision facility of Nara Women's University [7, 8]. First, MCI beams extracted from the mini-EBIS were made to collide with effusive CO_2 gas in the col-

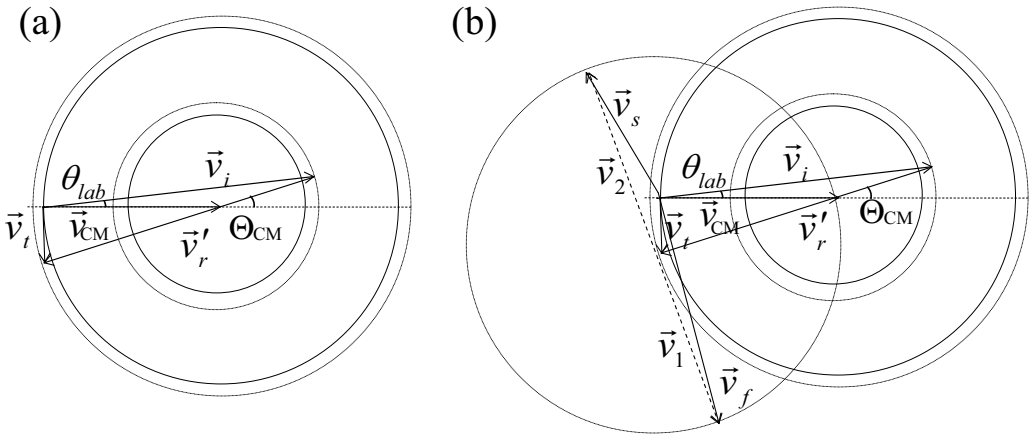

Figure 2: Correlation diagram (Newton Diagram) of velocity vectors in the laboratory frame and the C-M frame for (a) non-dissociative process and (b) dissociative process. The θ_{lab} and Θ_{CM} are scattering angles in the laboratory frame and the C-M frame, respectively.

lision region. Outgoing projectile ions from the collision region were analyzed using a parallel-plate electrostatic analyzer with a two-dimensional position sensitive detector. Two fragment ions or non-dissociated molecular ions were detected separately by two TOF analyzers installed at 90° and -90°, respectively, with respect to the projectile beam axis. It should be noted that no-extraction fields in the collision region made it possible to identify the recoil momentum of target ions after collisions at low energy. In this experiment, we measured the time difference between the projectile ions and the target ions. Finally, all signals were directly recorded as a single event by a PC, using digitizers.

3. Results and Discussion

The SC processes of Ar^{8+} + CO_2 are given as follows:

$$
\begin{aligned}
\mathrm{Ar}^{8+} + \mathrm{Ar} &\rightarrow \mathrm{Ar}^{7+*}(nl) + \mathrm{CO}_2^{+} + Q_1, && (1)\\
&\rightarrow \mathrm{Ar}^{7+*}(n'l') + \mathrm{CO}^{+} + \mathrm{O} + Q_2, && (2)\\
&\rightarrow \mathrm{Ar}^{7+*}(n''l'') + \mathrm{C}^{+} + \mathrm{O}_2 + Q_3, && (3)\\
&\rightarrow \mathrm{Ar}^{7+*}(n'''l''') + \mathrm{O}^{+} + \mathrm{CO} + Q_4, && (4)\\
&\rightarrow \mathrm{Ar}^{7+*}(n''''l'''') + \mathrm{CO}_2^{2+} + e^{-} + Q_5, && (5)\\
&\rightarrow \mathrm{Ar}^{7+*}(n'''''l''''') + \mathrm{CO}^{2+} + \mathrm{O} + e^{-} + Q_6, && (6)
\end{aligned}
$$

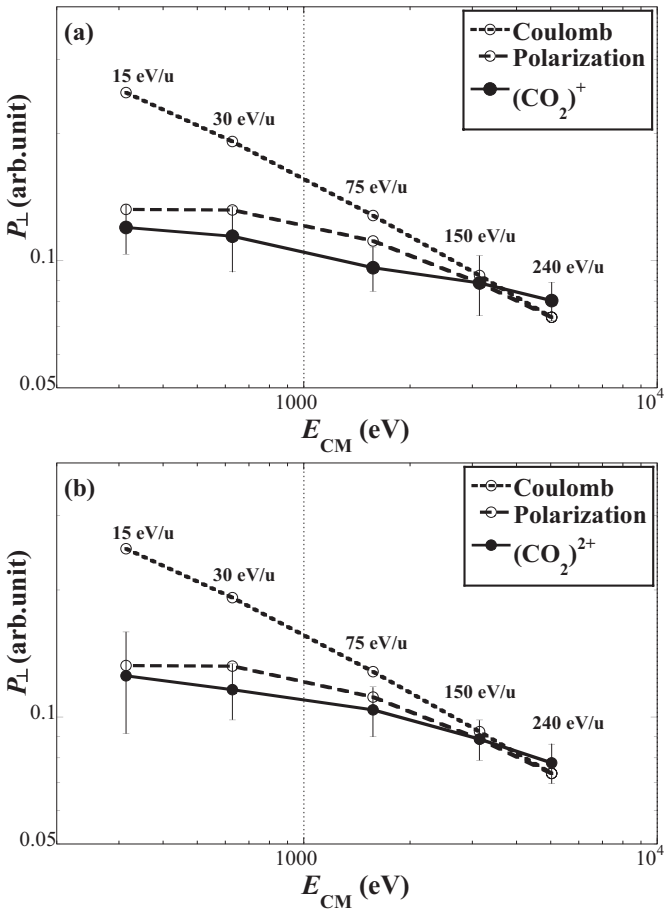

Figure 3: Collision energy dependence of recoil momenta of (a) CO_2^+ and (b) CO_2^{2+} in collisions of Ar^{8+} with CO_2 at collision energies from 15 to 240 eV/u. The filled circles show experimental recoil momenta of non-dissociated molecular ions. The dotted and dashed lines show the theoretical collision energy dependence of recoil momentum.

Reaction (1) indicates that Ar^{8+} ions capture an electron into the energy state of $Ar^{7+}(nl)$ from a CO_2 with reaction energy Q_1. The reactions (2), (3) and (4) represent molecular dissociative processes. Both reactions (5) and (6) represent the transfer ionization processes occurring via DC process with non-dissociative and dissociative processes of CO_2^{2+} ions, respectively.

Measured TOF spectra of SC processes in collisions of Ar^{8+} with CO_2 at energies from 15 to 240 eV/u are shown in Figure 1. The peak positions of fragment ions appear to be independent of the collision energy but those of non-dissociated CO_2^+ and CO_2^{2+} molecular ions appear to depend on the collision energy. The correlation diagram (Newton Diagram) of the velocity vectors of projectile ions and targets in the laboratory frame

and the center of mass (C-M) frame is shown in Figures 2(a) and 2(b). In the Newton Diagram, the vectors $\vec{v_i}$ and $\vec{v_t}$ are the velocities of projectile and target molecules, respectively, after inelastic collisions in the laboratory frame. The vectors $\vec{v}_{CM}$ and $\vec{v_r}'$ are the velocity for the center of mass and the relative velocity between projectile and target ions in the C-M frame, respectively. Experimentally, the vectors for CO_2^+ and CO_2^{2+} molecular ions correspond to $\vec{v_t}$ and the vector for the CO^+, CO^{2+}, O^+, O^{2+} and C^+ fragment ion corresponds to $\vec{v_f}$ or $\vec{v_s}$. Here, $\vec{v_f}$ and $\vec{v_s}$ are given by $\vec{v_f} = \vec{v_t} + \vec{v_1}$ and $\vec{v_s} = \vec{v_t} + \vec{v_2}$, respectively, where $\vec{v_1}$ and $\vec{v_2}$ are the dissociation velocity vectors due to Coulomb explosion. In the case of a homonuclear diatomic molecule, $\vec{v_1}$ is equal to -$\vec{v_2}$. In general, the velocity vectors of molecular ions, $\vec{v_t}$, depend on the collision energy, but those of fragment ions, $\vec{v_1}$ and $\vec{v_2}$, are independent of the collision energy. Furthermore, the dissociation velocity vectors $\vec{v_1}$ and $\vec{v_2}$ are considerably larger than the velocity vector $\vec{v_t}$ of the non-dissociated molecular ion, i.e., $\vec{v_f} \cong \vec{v_1}$ and $\vec{v_s} \cong \vec{v_2}$. Therefore, the energy dependence of the experimental TOF spectra can be qualitatively explained by using the velocity vectors in the Newton Diagram.

In order to clarify the collision energy dependence of recoil momenta, we compare experimental recoil momenta with theoretical ones. The experimental recoil momentum($P_\perp$) is estimated as $P_\perp = \mu v_r' \sin\Theta_{CM}$ (see Figures 2(a) and 2(b)), where μ, v_r', and Θ_{CM} are the reduced mass, relative velocity, and scattering angle, respectively, in the C-M frame. Assuming $\sin\Theta_{CM} \approx \Theta_{CM}$ and noting the energy conservation before and after the collision, E'_{CM}= $E_{CM} + Q$, and the energy dependence of the recoil momentum is expressed as $P_\perp \propto \sqrt{E'_{CM}}\ \Theta_{CM}$.

We calculate the energy dependence of recoil momentum by using the deflection function $d\varphi/dr$ in the classical trajectory equation with interaction potential $V(r)$, which is given as

$$\frac{d\varphi}{dr} = \pm\frac{b}{r^2}\sqrt{1 - \frac{b^2}{r^2} - \frac{V(r)}{E'_{CM}}}\ , \tag{7}$$

where φ, r, and b are the deflection angle, internuclear distance, and impact parameter, respectively [9]. The relation between b and r_0 is given by $b^2 = r_0^2(1 - V(r_0)/E'_{CM})$, where r_0 is the internuclear distance of the closest approach. In the case of $V(r)$ in powers of r, $V(r) = C/r^s$, we obtain $\Theta_{CM} \propto (b^s\ E'_{CM})^{-1}$.

It is well known that electron transfer occurs at some particular internuclear distance R. In this study, we have used the internuclear distance R as the r_0 calculated by the classical over-barrier model [10, 11] using the Atomic Spectra Database of the NIST [12].

According to this model, R is given by $R = (2\sqrt{qt} + q)/I_t$, where q is the charge state of the incident ion and I_t is the t-th ionization potential of the target.

In the present calculation, we have theoretically estimated the energy dependence of recoil momentum using two types of potentials– the Coulomb potential and the polarization potential. In the case of the Coulomb potential ($s = 1$), assuming $b \approx R$, $P_\perp$ is expressed as follows:

$$P_\perp \propto (\sqrt{E'_{CM}}\, R)^{-1}. \tag{8}$$

On the other hand, for the polarization potential ($s = 4$), $V(r) = -(\alpha q^2)/(2r^4)$, and $P_\perp$ is expressed as follows:

$$P_\perp \propto \left(\sqrt{E'_{CM}}\, R^4 \left[1 + \frac{\alpha q^2}{2R^4 E'_{CM}}\right]^2\right)^{-1}, \tag{9}$$

where α is the polarizability of CO_2.

Figures 3(a) and 3(b) show the experimental and theoretical energy dependences of recoil momenta of CO_2^+ and CO_2^{2+} molecular ions. The experimental dependence for non-dissociated molecular ions is good agreement with the theoretical dependence using the polarization potential rather than that using the Coulomb potential. This suggests that the polarization potential becomes to be important with decreasing the collision energy below 300 eV/u.

4. Conclusion

We have experimentally measured the recoil momentum of molecular ions for SC collisions and compared it with the theoretical one in order to elucidate the collision energy dependence of the recoil momentum. The experimental energy dependence of recoil momenta of CO_2^+ and CO_2^{2+} are in agreement with the theoretical dependence using polarization potential at energies below 300 eV/u. It is concluded that polarization potential plays a crucial role in the low-energy region. The coincidence measure of TOF spectra with energy gain spectra of the projectile after the collision is necessary to gain a better understanding of the energy dependence of recoil momentum.

Acknowledgement

This work was supported in part by a Grant-in-Aid for Scientific Research from the

Ministry of Education, Culture, Sports, Science and Technology of Japan.

References

[1] Tawara H, Kato T and Nakai Y 1985 *Atomic Data and Nucl. Data Tables* **32** 235
[2] Janev R K, Phaneuf R A and Hunter H 1988 *Atomic Data and Nucl. Data Tables* **40** 249
[3] Barat M and Roncin P 1992 *J. Phys. B: At. Mol. Phys.* **25** 2205
[4] Kaneyasu T, Azuma T and Okuno K 2005 *J. Phys. B: At. Mol. Phys.* **38** 1342
[5] Ohyama-yamaguchi T and Ichimura A 2006 *J. Phys. B: Conf. Ser.* **34** 245
[6] Inoue Y, Ishii K and Ogawa H 2009 *J. Phys. B: Conf. Ser.* **163** 012043
[7] Okuno K 1986 *J. Phys. Soc. Jpn.* **55** 1504
[8] Ishii K, Inoue Y, Ogawa H, Itoh A and Sakamoto N 2006 *J. Phys. B: Conf. Ser.* **34** 245
[9] Bransden B H and McDowell M R C 1992 P.21 Charge exchange and the theory of ion-atom collisions, Oxford, New York
[10] Ryufuku H, Sasaki K and Watanabe T 1980 *Phys. Rev. A* **21** 745
[11] Niehaus A 1986 *J. Phys. B: At. Mol. Phys.* **19** 2925
[12] Ralchenko Yu, Kramida A E and NIST ASD Team 2008 *NIST Atomic Spectra Database* (version 3.1.5) (*http://physics.nist.gov/asd3*)

Electron Temperature Measurement of Radiation-heated CH Foam on Shenguang II laser facility

Yang Zhao*, Jiamin Yang, Jiyan Zhang, Fengtao Jin

Research Center of Laser Fusion, China Academy of Engineering Physics,

Mianyang 621900,People's Republic of China

In this paper we describe a spectroscopic diagnostic method for measuring electron temperature of radiation-heated CH foam on Shenguang II laser facility. A tracer layer of aluminum was embedded in the middle of the CH foam and a point-projection method used in the opacity experiment was induced to measure the transmission spectrum of the embedded Al foil. The electron temperature was deduced by the comparison of the experimental absorption spectrum with the calculated one with a detailed level accounting opacity code and is about 80eV. The hydrodynamic simulation shows that it's reasonable to determine the CH foam temperature by measuring the embedded Al absorption spectrum. Thus, the electron temperature of radiation-heated CH foam was achieved.

I. INTRODUCTION

The X-ray radiation is a significant driver in inertial confinement fusion (ICF) and some astrophysical phenomena [1]. The redistribution of energy within a medium through the emission and absorption of photons is radiation transport. In low density foam, Supersonic propagation of radiatively driven fronts has been observed [2]. An intense radiation flux rapidly ionizes and heats the low-density material which has a small opacity to incident radiation. Radiation thus passes through the heated material and is absorbed at the boundary of the cold material, creating a front which propagates as an ionization wave. In order to analyze the physical process of supersonic radiation transport, it's of importance to determine the electron temperature of the low-Z foam heated by the radiation wave.

In the experiment, the radiation resource was generated by injecting laser beams into the hohlraum, and it was led into the radiation transport tube and drives a supersonic heat wave in the CH foam. A tracer layer of aluminum was embedded in the middle of the CH foam and a point-projection method used in the opacity experiment [3] was induced to measure the transmission spectrum of the embedded Al foil. The electron temperature was deduced by the comparison of the experimental absorption spectrum with the calculated one with a detailed level accounting opacity code [4]. The result of Multi-1D code [5] shows that the Al plasma and the adjacent CH foam plasma has the same electron temperature after thin Al layer was ionized by the radiation wave. Therefore, it's reasonable to determine the CH foam temperature by measuring the embedded Al absorption spectrum. Besides, the evolution of the time-resolved absorption spectra could also provide the information about the radiation

* Email: edwardszy@yahoo.com

flux transported to the embedded Al layer and the velocity of the radiation wave.

II. EXPERIMENTAL SET-UP

The experiment was performed on the Shenguang II high power laser facility. Schematic of the experimental set-up is shown in Fig. 1. A cylinder gold hohlraum with 2000μm in length and 800μm in diameter was used as an x-ray converter. Eight frequency-tripled beams (λ = 0.35μm) were injected into the hohlraum, with 45 degree incident angle, from two Φ380μm laser entrance holes (LEH) at both end of the hohlraum. Each laser beam has energy of 260 J in 1 ns, which was focused on the laser entrance holes (LEH). Two CH foam disks with thickness of 200μm and density of 39.6 mg/cc were symmetrically fixed inside the hohlraum to prevent the blown-off Au plasma and the reflected laser from irradiating the sample. A soft x-ray spectrometer was used to monitor the temporal process of radiation from LEH at an angle of 30^{o} relative to the hohlraum axis.

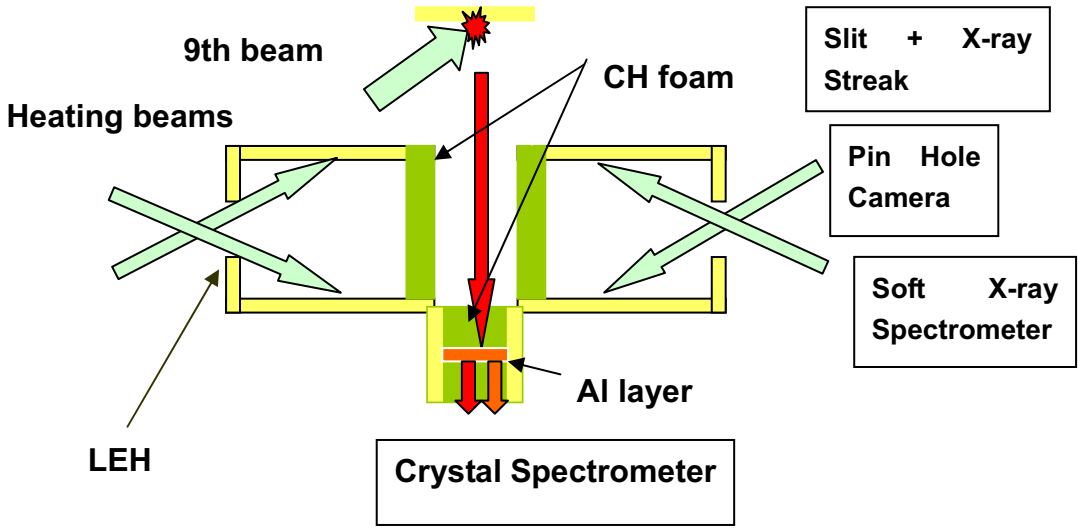

Fig. 1 Schematic of the experiment set-up

A gold tube that was 300μm long and 600μm in diameter was mounted on the side of the hohlraum, inside the tube resides the CH foam with density of 39.6 mg/cc and a tracer layer of aluminum was embedded in the middle of the CH foam. The X-ray backlighting source was obtained by focusing the 9th frequency-tripled laser beam (130 J, 130 ps) onto a gold disk. The 9th beam was synchronized and delayed by 1.0ns with respect to the trailing edges of the eight heating pulses. An x-ray streak camera and an x-ray pinhole camera were used to monitor the temporal behavior and the size of the backlighter, respectively. A PET (2d = 8.742Å) plane crystal spectrometer was used to measure the spectrum. In order to achieve large spectrum range and ensure high resolution, the spectrum was recorded by X-ray film. In order to achieve the transmission spectrum, the self-emission spectrum was measured by turning off the 9th laser beam.

III. EXPERIMENTAL RESULT

The temporal behavior and the spot size of the backlighter were measured with the

x-ray streak camera and the x-ray pinhole camera, respectively. The large size of the backlighter with 120μm (full width at half maximum) in diameter slightly lower the spectral resolution, but can satisfy the requirement for enough backlighting intensity. The time history of the synchronized 9th laser pulse with the eight heating pulses was shown in Fig. 2(a) and the time behavior of the X-ray backlight radiation and the cavity radiation was shown in Fig. 2(b). The pulse width of the x-ray backlighter is 237ps. It can provide short enough pulse for time- resolving measurement. The short backlighter can provide absorption measurement in a unitary plasma state and it is helpful to make comparison between experimental transmission spectrum and theoretical model at a certain temperature and density.

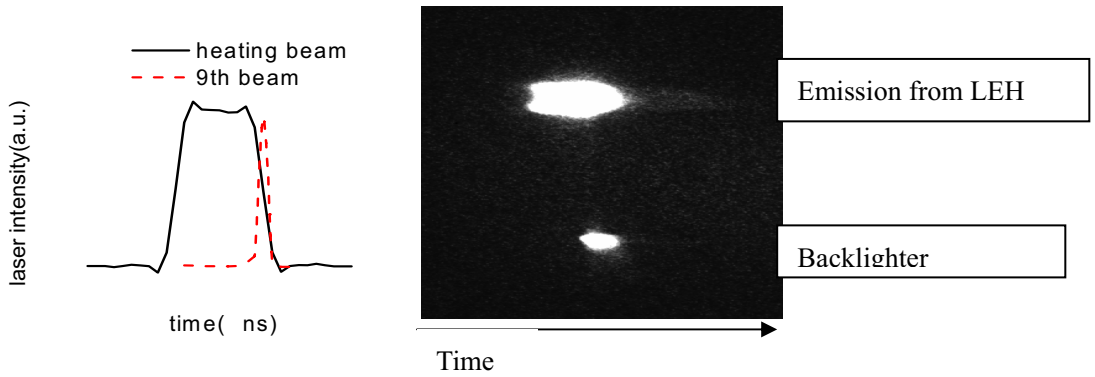

Fig. 2 (a) The time history of the synchronized 9th laser pulse with the eight heating pulses. (b)The time behavior of the synchronized X-ray backlight radiation and the cavity radiation

The time behavior of the radiation temperature measured by SXS from laser entrance hole was shown in Fig. 3. It shows that the absorption shot and the self-emission shot had the same temperature revolution. It demonstrated the repeatability of the temperature drive.

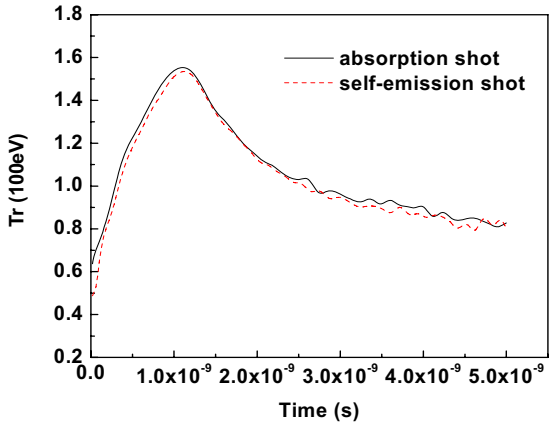

Fig. 3 The time behavior of the radiation temperature measured by SXS from the angle 30º relative to the hohlraum axis.

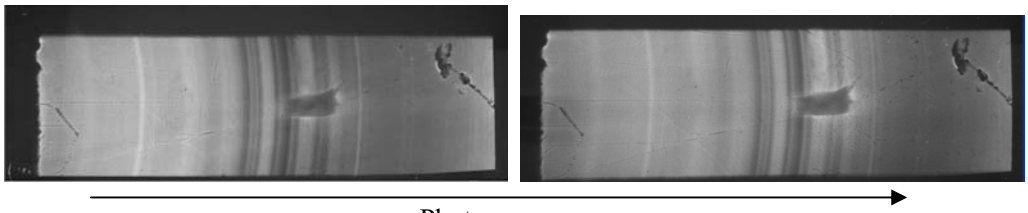

a) absorption shot：delay 1ns　　b) absorption shot：delay 0ns

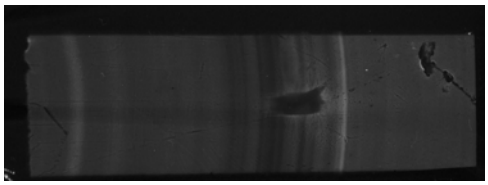

c)　self-emission shot

Fig. 4 The x-ray film record of Al absorption spectrum when the backlighter was delayed by 0ns and 1ns relative to the heating pulses and self-emission spectrum.

The spectral image recorded by the crystal spectrometer is presented in Fig. 4. The film was scanned along the dispersive direction with a photo densitometer to obtain the optical densities. Contributions to the film exposure are film fog, instrumental fluorescence, and useful dispersed spectrum. First, the digitized data was subtracted by the inherent film fog and then converted to the relative intensity using the response curve of the film. Second, the fluorescence on the borders of the film that were blocked from the source of light was removed. Reference lines were used to calibrate the spectral wavelength in the spectrum [6]. So the absorption spectra was described as

$$I_{record}(\upsilon) = I_S(\upsilon)e^{-\tau(\upsilon)} + I_{SE}(\upsilon)$$

where I_S is the backlighting source spectrum, I_{SE} is the self-emission spectrum. The frequency-dependent transmission through the Al sample could be obtained from

$$e^{-\tau(\upsilon)} = \frac{I_{record}(\upsilon) - I_{SE}(\upsilon)}{I_S(\upsilon)}$$

Since the CH plasma and Al plasma were respectively optically thin and optically thick to the backlighter, obvious K-shell absorption lines of Al was observed. Figure 5 shows the experimental transmission spectrum (solid line), which shows Kα absorption lines from He-like to B-like Al ions. The electron temperature was deduced by the comparison between the experimental results and the calculation results of a detailed level accounting opacity code [4]. The areal mass density, which is determined by the initial Al sample thickness, determines the calculated depth of the absorption valley. In order to make best fitted with the experimental spectrum, the areal mass density adopted in the calculation may have to be varied, due to the uncertainty of initial thickness. The DLA calculation gave the best fitted to the experimental result at 0 ns delay at a density of 0.28 g/cm^3 and a temperature of 75eV by using an areal density of 16 g/cm^2 . And at 1ns delay the calculated result could best fitted with the experimental result at

a density of 0.28 g/cm^3 and a temperature of 80eV by using an areal density of 18 g/cm^2.

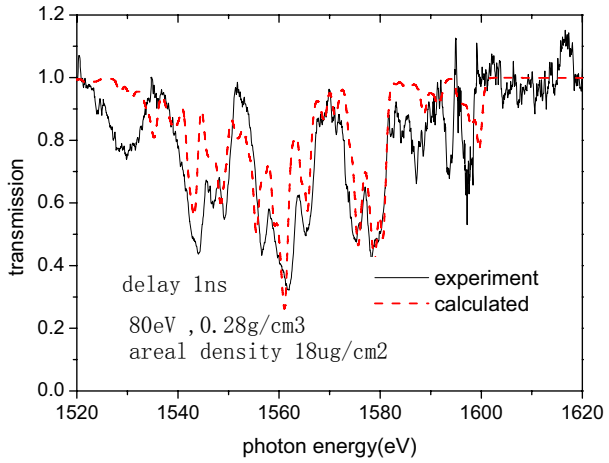

(a)

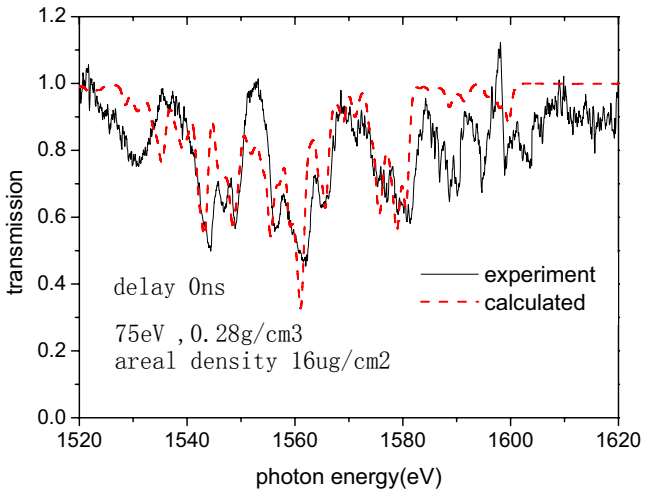

(b)

Fig. 5 Comparison of the measured transmission spectra with the calculated one with the DLA model.

The only discrepancy was appeared in the He-like lines. It is known that there existed a harder spectrum component besides the thermal X-rays. The gold material converted a few percent of the laser energy into radiation from M-band transitions, which had energy near 2 keV. The potion of M-Band radiation preheated the Al material through photo excitation. So the potion of He-like Al ions increased and the He-like absorption valley became deeper. Secondly, the temperature and the density of the Aluminum vary in the duration of the backlighter. Finally, in the DLA atomic code, Saha-Boltzmann statistics assuming Local thermodynamic Equilibrium (LTE) were adopted to calculate the relative populations in configurations of different charge states. But there existed NLTE effect in the experimental plasma.

IV. HYDRODYNAMIC SIMULATIONS

Hydrodynamic simulations were used to obtain the time evolution of density and

temperature of the embedded Al plasma and CH foam. The time behavior of the radiation temperature measured by SXS was adopted as the radiation source used in the Multi-1D code [5].

Figure 6(a) shows the expansion process of the CH foam and the embedded Al layer. Figure 6(b) shows the evolution of aluminum layer, it can be seen from the figure that between 0.7 ns and 2.0 ns, the thickness of the aluminum layer was invariable, and so was the density.

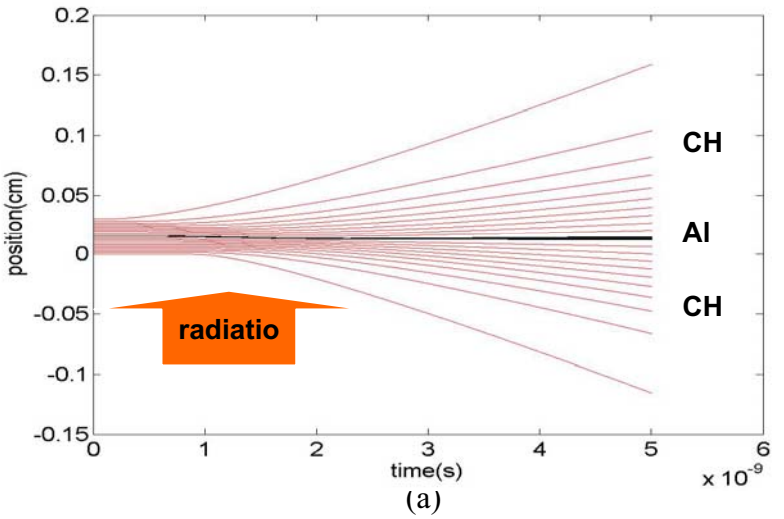

(a)

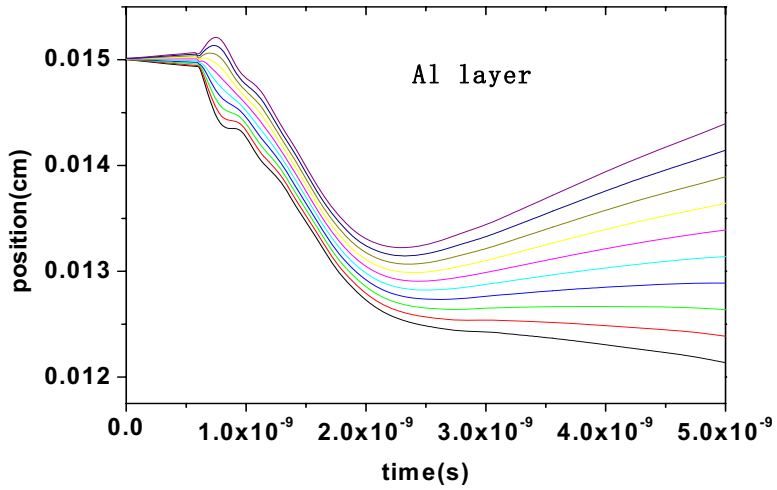

(b)

Fig 6 The expansion process of the CH foam and embedded Al layer

Figure 7(a) shows that the electron density in the center and edge of the Al layer quickly reach homogeneity after 0.7ns. Figure 7(b) shows that the time behavior of the electron temperature in the center and edge of the Al layer is always homogeneous. And it also shows that the temperature difference between Al layer and adjacent CH foam is obvious from 0.5ns to 1.0ns, and after 1ns, the difference between the two materials is less than 5eV. So the temperature of the Al layer represented the temperature of the adjacent CH layers. Thus, it's reasonable to determine the CH foam temperature through Al layer temperature.

The CH foam on both side of the Al has the same time evolution of temperature. It was illuminated by the truth that the heat capacity of the Al tracer layer was negligible, and the tracer layer has no influence to the intensity of the heat wave.

The temperature of different time delays discussed above is shown in this figure. The temperature achieved by the absorption spectrum is lower than the result of the hydrodynamic simulation results. It because the radiation source adopted here was measured from the LEH, not from the diagnostic hole, which had lower radiation temperature.

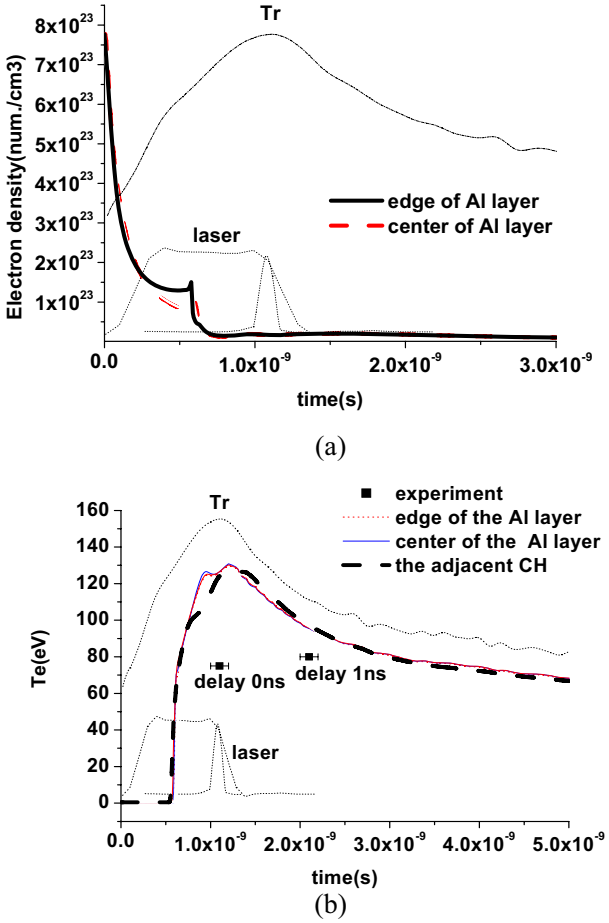

Fig. 7 The time behavior of the electron density (a) and temperature (b) of CH and embedded Al layer. The solid square is the temperature fitted with the measured absorption spectrum.

V. CONCLUSION

A spectroscopic diagnostic method for measuring electron temperature of radiation-heated CH foam was presented. The simulated results show that the Al plasma and the adjacent CH foam plasma have the same electron temperature after thin Al layer was ionized by the radiation wave. Therefore, it's reasonable to determine the CH foam temperature by measuring the embedded Al absorption spectrum.

Since the distributions of the transmission spectra are sensitive to the electron temperature which is correlated with the radiation temperature, a group of the time-resolved absorption spectra could provide the information about the radiation flux transported to the embedded Al layer. In the future a long backlighter generated by 1ns long pulse and a crystal spectrometer coupled with a streak camera will realize measuring a group of continues time-resolved absorption spectra in one shot. Furthermore, it is possible to determine the velocity of the radiation wave by changing the position of the embedded tracer layer and achieving the evolution of the temperature.

Reference

[1] J. P. Apruzese, et. al., Phys. Plasmas. 2002, 9: 2411.
[2] Shao-en Jiang, et. al., Science In China Series G, 2005, 35: 473.
[3] Yang Zhao, et. al., Rev. Sci. Instrum., 2009, 80: 043505.
[4] Jiao-long Zeng, Phys. Rev. E, 2000, 62: 7251.
[5] Ramis, R.,et. al., Comp. Phys. Comm., 1988, 49: 475.
[6]Yang Zhao, et. al., High Power Laser And Particle Beam.2008, 20: 419 (in Chinese).

EUV Spectroscopy of Highly Charged Fe Ions in EBIT and LHD

H. A. Sakaue[1], D. Kato[1], T. Kato[1] H. Kikuchi[2], S. Morita[1], I. Murakami[1], N. Nakamura[2], S. Ohtani[2], H. Tanuma[3], H. Tawara[1,4], E. Watanabe[2] T. Watanabe[5] and N. Yamamoto[6].

[1]NIFS, [2]ILS/UEC, [3]TMU, [4]MPIK, [5]NAOJ, [6]ILE/OU

Abstract

Extreme ultra-violet (EUV) spectra over 100 - 300 Å from highly charged iron ions have been observed from two different plasma sources (Tokyo EBIT, Compact EBIT and LHD). The observed line intensity ratio has been found to be in reasonable agreement with the present CR model. On the other hand, it is found that the observed electron density dependence of the line intensity ratios in the LHD plasmas are also reproduced well with the present CR model only when the contribution of the thermal proton impact excitation is fully included.

Keywords: atomic processes, plasmas, EUV spectroscopy, HCI's, EBIT

1.Introduction

EUV spectroscopy has been known and already established to be one of the best tools to diagnose and investigate important features, such as the electron density and temperature, of the astrophysical as well as laboratory (high temperature fusion and general) plasmas. Through detailed analyses of EUV spectra the temporal and spatial distributions of the electron density n_e and temperature T_e can be obtained. In the present work, we observe the EUV spectra produced under different plasma conditions in the two types of EBITs (Tokyo-EBIT[1] and Compact EBIT[2,3]) and the Large Helical Device (LHD) at National Institute for Fusion Science. In the LHD with hydrogen plasmas. Based upon the observed EUV spectra, the line intensity ratios for a pair of the lines (114.412 Å [$1s^22s2p^2\ ^2P_{3/2} \rightarrow 1s^22s^22p\ ^2P_{3/2}$]/117.144 Å [$1s^22s2p^2\ ^2P_{1/2} \rightarrow 1s^22s^22p\ ^2P_{1/2}$]) from Fe XXII ions are determined as a function of the electron density, n_e, generated under different plasma parameters. These results are analyzed and compared with the present collisional-radiative (CR) model recently developed by Yamamoto *et al*.[4]. We observe that the electron densities in the LHD increase as a function of time after an iron pellet injection, meanwhile the line intensity ratios are changed little. We interpret this phenomenon which results from the fact that the relative proton density over the electron density decreases during transient plasmas after an injected Fe pellet ablation/ionization.

2. Experiments

In the present EBIT experiment, we used the Tokyo-EBIT and Compact EBIT (CoBIT). We used low electron energy (200 eV – 2.4 keV) with its current of ~ 20 mA in the present work.

In Fig. 1 (a), we show the present experimental setup with a flat-field grazing-incidence EUV spectrometer attached to the Tokyo-EBIT and CoBIT. No particular calibrations for the sensitivity and reflection efficiencies of the spectrometer were carried out as they are not expected to change significantly in a narrow wavelength range of the present interest (114-117 Å).

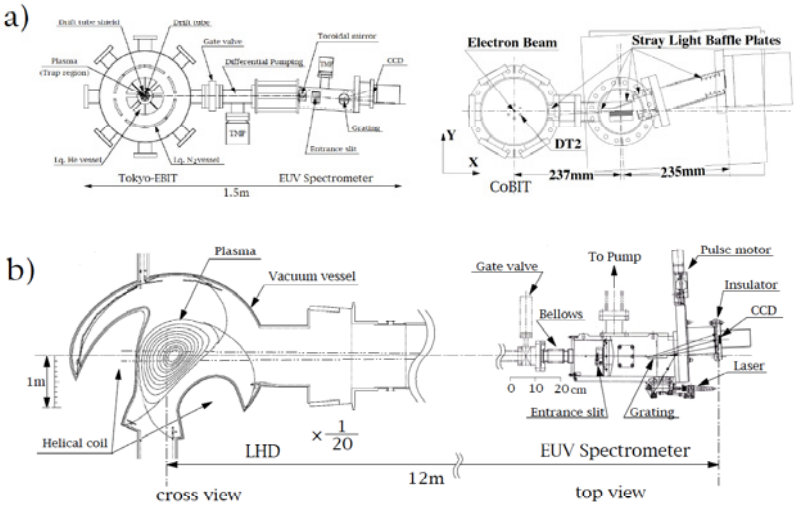

FIG. 1. Schematic drawings of EUV spectrometer setup used in the Tokyo-EBIT, CoBIT and the LHD.

The EUV spectra are observed over a wide wavelength range of 100 ~ 300 Å with the spectral resolution of ~ 0.6 Å. We show the observation setup with an LHD EUV spectrometer in Fig. 1 (b). The toroidal magnetic field up to 3 T for plasma confinement is generated with two sets of superconducting helical coils, making quasi-steady state plasma operations possible. The LHD plasmas are initiated and heated with a combination of the electron cyclotron resonance heating (ECH), ion cyclotron range-of-frequency (ICRF) heating and neutral beam injection (NBI) heating. The present EUV spectrometer with a flat-field grazing-incidence, similar to that used in the EBIT experiments, was installed on an outboard mid-plane diagnostic port perpendicular to the toroidal magnetic field through a bellow flange at a distance of 12 m from the plasma center. A typical resolution of the EUV spectrum from the LHD is 0.35 Å, which is slightly better than that used in the EBIT experiments.

We have analyzed a number of the EUV spectra observed from the LHD, which were taken in discharge numbers of #64912 and #64921 with a stainless-steel (SUS) and iron pellet injection, respectively, and #64242 without any pellet injection. It is noticed here that the iron atom and ions sputtered out of the vacuum wall are always present in LHD discharges as an intrinsic impurity since stainless steel plates are used on most parts of the vacuum vessel as plasma facing materials. The electron temperature T_e at the plasma core is measured with laser Thomson scattering and the electron density n_e is measured with a Far-Infra-Red (FIR) interferometer, respectively. The combined error bars of the absolute electron density are estimated to be ± 6 %.

3. Results and Discession

Figure 2 demonstrates a typical dependence of the observed EUV spectra on the

(mono-energetic) electron energy (E_e = 300 – 2300 eV) over the wavelength range of 100 – 300 Å from highly charged iron ions produced in the EBIT. In spectra shown in this figure, no corrections to the spectrometer response and efficiencies are applied. It is clear from these observed EUV spectra that the overall EUV spectra show significant variations which are dependent on the electron energy. When the electron energy E_e increases from 1.8 to 2.4 keV, the dominant iron ion charge q produced is varied from 20+ to 22+. The strong emission line of Fe XV (284.16 Å) were observed at 500 eV. As electron energy decreases from 500 to 300 eV, the dominant emission lines transfer from Fe XV to Fe IX (Fe^{14+} ~ Fe^{8+}) successively.

In spectrum of each electron energy, only emission lines from two or three kinds of charge states of iron HCI are observed.

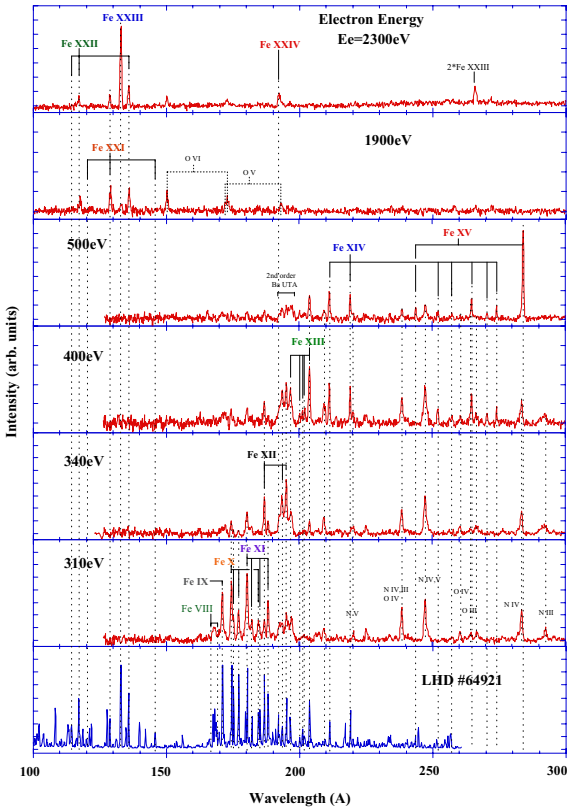

FIG. 2. Electron energy (300 – 2300 eV) dependence of EUV (100 – 300 Å) spectra from highly charged iron ions in the EBIT. A typical spectrum of LHD with iron pellet injection is shown in the bottom.

We could measure the EUV spectra with a narrow cha energy in this way. Most of the observed lines from the EBIT are due to transitions to the ground states, meanwhile the transition lines between the excited states are only weakly observed. For example, Fe XXII $2s2p^2\ ^2D_{3/2} \rightarrow 2s^22p\ ^2P_{1/2}$ (135.812 Å) and Fe XXI $2s2p^3\ ^3D_1 \rightarrow 2s^22p^2\ ^3P_0$ (128.755 Å) transitions were observed, but no Fe XXII $2s2p^2\ ^2D_{5/2} \rightarrow 2s^22p\ ^2P_{3/2}$ (156.019 Å) and Fe XXI $2s2p^3\ ^3D_3 \rightarrow 2s^22p^2\ ^3P_2$ (145.732 Å) transitions were observed. A typical EUV spectrum from impurity iron ions observed during a steady phase of the LHD discharge with iron pellet injection (shot #64921) is shown in Fig. 2. The plasma parameters at the plasma center were found to be T_e = 2.0 keV and n_e = 4.3 x 10^{13} cm^{-3}.

Figure 3 shows the observed line intensity ratios of n_e-sensitive line Fe XXII 114.412 Å [$1s^22s2p^2\ ^2P_{3/2} \rightarrow 1s^22s^22p\ ^2P_{3/2}$] to n_e-insensitive line Fe XXII 117.144 Å [$1s^22s2p^2\ ^2P_{1/2} \rightarrow 1s^22s^22p\ ^2P_{1/2}$] as a function of the electron density in the EBIT and LHD plasmas. The line intensity ratio ($I_{114.412\ Å}/I_{117.144\ Å}$) for the EBIT shown in Fig. 3 (solid triangle) is the average value taken at E_e = 2.0, 2.1 and 2.2 keV and plotted at the electron density of n_e ~ 1 x 10^{12} cm^{-3} estimated with the Hermann theory. Therefore, this should be taken as an upper limit to the present EBIT electron density, as plotted in Fig. 3, since no exact overlapping between the electron beam and ion clouds is known. The dotted line in Fig. 3 shows the calculated results for EBIT under 2.0 keV monoenergetic electron impact using the present CR model.

The line intensity ratio for the LHD are shown in Fig. 3 (solid circle: Shot number #64242, solid squares: Shot number #64912 and open circles: Shot number #64921). We have calculated line intensity ratios in the LHD plasmas based on two different models: One includes only the electron impact excitation without any contribution of proton collisions 'n_p/n_e = 0'. Another includes both the proton impact excitation as well as the electron impact excitation 'n_p/n_e = 1'.

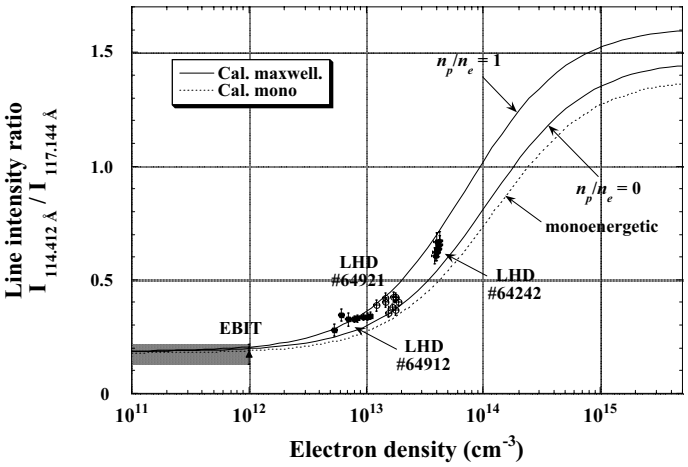

FIG. 3. Observed line intensity ratio $I_{114.412\,Å}/I_{117.144\,Å}$, from EBIT and LHD plasmas as a function of electron density, n_e.

The solid lines represent the calculated line intensity ratio for plasmas with a Maxwellian distribution using RmaX data. As clearly seen in Fig. 3, this line ratio starts to increase drastically at the electron density region of 10^{13} - 10^{14} cm^{-3} due to the enhanced population in the fine structure level in the ground state configuration under intense electron impact. Furthermore, it is also important to note that the population of the excited level in the fine-structure of the ground state can be significantly enhanced when the thermal proton impact collision is taken into account.

The observed line intensity ratio in low electron beam current (30 mA at ~ 2 keV) EBIT with the estimated geometrical electron density (< 10^{12} cm^{-3}) has been found to be in reasonable agreement with its lowest limit calculated in the present CR model. On the other hand, it is found that the observed features of the dependence of the line intensity ratios on the electron density (over 10^{13} – 10^{14} cm^{-3} at ~ 2 keV) in the LHD plasmas are also reproduced well with the present CR model only when the contribution of the thermal proton impact excitation is fully included.

Acknowledgements

This work was partly supported by the JSPS-CAS Core-University Program in the field of "Plasma and Nuclear Fusion" and performed under the Research Cooperation program in the National Institute of Natural Sciences (NINS).

Refference

[1] F. J. Currell *et al*., J. Phys. Soc. Jpn. 65, 3186 (1996)
[2] N.Nakamura *et al*., Rev. Sci. Instrum. 79, 063104 (2008)
[3] H.A.Sakaue *et al*., J. Phys.: Conf. Ser. 163, 012020 (2009)
[4] N. Yamamoto *et al*., ApJ, 689, 646 (2008)

Atomic and molecular database activities at NIFS

D. Kato*, I. Murakami, H.A. Sakaue, and T. Kato
National Institute for Fusion Science, 322-6 Oroshi-cho, Toki, Gifu 509-5292, Japan

Abstract
Recent activities on atomic and molecular data research and database development in NIFS are summarized. Comprehensive collision data set for Fe ions were compiled for electron-density diagnostics of laboratory and solar plasmas. Spectroscopic studies on atomic processes of highly charged impurity ions are performed by means of Electron-Beam-Ion-Trap (EBIT) and Large-Helical-Device (LHD). New database for photo-absorption cross sections is under development upon data demands in radiation transport studies for magnetic fusion devices. Importance of acquiring atomic collision data for tritium and knowledge on hydrogen isotopic effects in edge plasmas is pointed out.

Keywords: atomic and molecular database, cross section, plasma diagnostics

1. Introduction

Atomic and molecular databases for controlled nuclear fusion researches have been developing at each data center over the world upon increasing data demand for a variety of atomic and molecular processes in plasmas. To acquire knowledge about the data, international collaboration is certainly important. Under the auspice of the JSPS-CAS Core-University Program (CUP), we have been exchanging the data knowledge and conducting cooperation of data compilation and evaluation as well as atomic physics researches.

In this paper, we summarize activities of atomic and molecular data research and database development centered at NIFS which has been presented in the last (third) JSPS-CAS seminar on “Atomic and Molecular Processes in Plasma” in Xi’an, China.

* Corresponding author’s E-mail address: kato.daiji@nifs.ac.jp

2. NIFS atomic and molecular numerical databases

List of the databases developed in NIFS is shown in Table 1. The database development has been undertaken since 1970's for plasma spectroscopy and evaluation of plasma radiation loss by high-Z impurity ions. Cross sections and rate coefficients of gaseous atomic collisions inside Debye length (AMDIS, CHART, AMOL, CMOL) and sputtering (SPUTY) and reflection (BACKS) coefficients of solid targets are included in the databases.

Data retrieval service [1] through internet has been opened since 1997, which facilitate international collaboration with our database. NIFS has also been participating international data center network organized by IAEA. AMDIS database is linked to online database platform developed at IAEA, GENIE [2]. Access counts via the GENIE attain 25 % of total counts for AMDIS.

Data input (update) for some specific subject is performed by domestic working groups; the working groups have been organized since 2001. Besides the working group, we acquire many data input from collaborators including foreign researchers. On the occasion of summary, report of the data input is published in NIFS-DATA series [3] and disseminated internationally. Recently, a working group has collected electron and atomic collision data for heavy elements including Fe, Ni, Mo, W, Ne, Ar, Kr, and Xe published since 2000. The report is prepared for a coming issue of the NIFS-DATA series.

3. Data evaluation and collisional-radiative models for impurity ions

Fe ions are observed as an impurity in magnetic confinement plasmas with Large-Helical-Device (LHD) at NIFS, and abundant of heavy elements in solar atmosphere. Thus, the Fe data are known potentially important for fusion and solar plasma diagnostics. Fig. 1 shows Fe spectra in extreme-ultra-violet (EUV) region observed at LHD and orbiting solar observatory HINODE. Measurements of Fe M-shell lines identified in this wavelength region are known useful means of the solar plasma diagnostics in the transition region lying in between chromosphere and corona. Apparent discrepancy in intensity ratios of two Fe XIII lines seen at 202.0 Å and 203.8 Å is ascribed to different electron densities of LHD plasma and the solar atmosphere. The density dependence of the two lines is given by excitation in the

ground-term fine structure levels of $3s^2 3p^2\ {}^3P_J$ primarily due to collisions with ambient electrons and protons. To evaluate correct electron densities, collisional-radiative (CR) models are developed. Electron collision data were evaluated by means of distorted-wave and R-matrix methods, and comprehensive data set were thoroughly searched in literatures [4].

Electron-Beam-Ion-Trap (EBIT) is known as a versatile tool for study on electron-ion interaction. Atomic spectroscopy and measurements of electron collision cross sections for ions of virtually any charge state are feasible with the EBIT, provided the electron beam is controlled properly. Recently, a compact EBIT (CoBIT) has been constructed and operated to measure EUV spectra of Fe M-shell ions trapped inside the CoBIT [5].

Tungsten is a prime candidate for plasma-facing-component in ITER. However, accumulation of tungsten ions in the core plasma is a big concern, which may cause radiation collapse of the core plasmas. Tungsten injection into LHD plasmas was conducted with tracer-encapsulated solid pellet (TESPEL). Emission lines observed in the EUV region were tentatively indentified (4p-4d, 4d-4f, 4f-5d transitions), and little tungsten concentration in the core plasma (electron temperatures of about a few keV) has been inferred.

In LHD (and any laboratory plasma, in principle), plasma temperature and density can be obtained by independent measurements, *e.g.* laser Thomson scattering, FIR interferometry. Synthesized spectra with the CR model are, therefore, used to study ionization and recombination dynamics and transport of impurity ions in LHD plasmas. It is noted that the CR models for various impurity ions developed at NIFS have been introduced to Chinese visitors invited to collaborate on the CR models for applications to EAST plasmas.

We are developing a web based online server which implement the CR model for He-like ions of Z=6-26 elements [6]. The web server calculates line intensity ratios for given electron temperatures and densities upon user input through web programs (see Fig. 2). This web service has been introduced in Code Center Network (CCN) organized by Atomic and Molecular Data Unit in IAEA.

4. New database development

New database for photo-absorption cross sections is under development upon data demands in radiation transport studies for magnetic fusion devices. It has been pointed out that radiation cooling rates were significantly reduced due to opacity of radiation in peripheral plasmas. Impurity ions and neutrals in the peripheral region absorb (trap) photons emitted from core plasmas, and suppress the radiation cooling. Recommended data for nine species of atoms (H, He, Li, N, O, Ne, Na, Cl, and Ar), six species of di-atomic molecules (H_2, O_2, N_2, CO, NO, and HCl), seven species of tri-atomic molecules (O_3, CO_2, N_2O, NO_2, SO_2, H_2O, and H_2S), and some poly-atomic molecules including hydrocarbons have been evaluated by Prof. N. Sakamoto (passed away in 2008) in Nara Women's Univ. We are preparing publication of his data set with helps of Prof. M. Inokuti (passed away in early 2009) in Argonne National Lab. and Dr. H. Tsuchida in Nara Women's Univ. Preliminary web page for the database is shown in Fig. 3.

Contents of our databases are requested to meet increasing data demands in varieties of plasma (discharge) applications, *e.g.* industry, ecology, medicine, etc. To meet this demand, interdisciplinary coordination of the database development is necessary. At the initiative of Prof. H. Tanaka in Sophia Univ., we have undertaken collaboration with domestic society of electrical engineering using discharge. They have their own databases for electron collision cross sections by process gas targets deduced from measured electron transport coefficients with the aid of a two-term Boltzmann code. We opened a web based database for recommended data set of electron collision cross sections compiled by a working group of Institute of Electrical Engineering of Japan [7]. Fig. 4 shows a web page of the database. The database includes data for six species of atoms (He, Ne, Ar, Kr, Xe, and Rb) and eleven species of molecules (CO, N_2, NO, O_2, CO_2, CF_4, CH_4, GeH_4, SiH_4, C_2H_6, and Si_2H_6).

Tritium inventory and recycling in controlled fusion reactors are important issues in safety and economic aspects. Recently, a scientific research program has been initiated under auspices of MEXT, Japan. It is know that hydrogen isotopic effects are significant in some atomic

collisions (see Fig. 5) [8]. Nevertheless, this isotopic effect has not been well adopted in plasma modeling and simulation yet. Plasma behaviors under tritium-rich condition are little understood, since experiments with tritium are very difficult to conduct. Comprehensive data set for atomic collisions involving hydrogen isotopes is required to increase practicality in the plasma modeling and simulation. It is noted that a data compilation has been performed by Wang and Stancil [9] for hydrogen ion-molecule collisions.

Acknowledgments

Present work are supported by JSPS-CAS Core-University Program on "Atomic and Molecular Processes in Plasma" and Grand in Aid for Scientific Research for Priority Areas "Tritium for Fusion" of MEXT, Japan.

References

[1] https://dbshino.nifs.ac.jp/
[2] http://www-amdis.iaea.org/GENIE/
[3] PDF copies of full texts are available online at http://www.nifs.ac.jp/report/nifsdata.html
[4] I. Skobelev, I. Murakami and T. Kato, "Recommended Data on Proton-Ion Collision Rate Coefficients for Fe X - Fe XV Ions", NIFS-DATA-95 (2006); "Recommended Data on Proton-Ion Collision Rate Coefficients for Fe XVII - FE XXIII Ions", NIFS-DATA-99 (2007); "Recommended Data on Electron-ion Collision Strengths and Effective Collision Strengths for Fe X, Fe XI and Fe XIII Ions", NIFS-DATA-104 (2009).
[5] *e.g.* H.A. Sakaue *et al.*, J. Phys: Conf. Ser. 163 (2009) 012020.
[6] T. Fujimoto and T. Kato, ApJ 246 (1981) 994; Phys. Rev. A 30 (1984) 379.
[7] Technical Report #853, Sept. 2001, issued by Institute of Electrical Engineering of Japan.
[8] T. Kusakabe et al., Phys. Rev. A 70 (2004) 052710.
[9] J.-G. Wang and P.C. Stancil, Phys. Scr. T96 (2002) 72.

Table 1: List of NIFS atomic and molecular numerical databases. Records in the databases are counted on Aug. 28, 2009.

DB Name		Contents	Period	Records
AMDIS	EXC	Electron impact excitation of atoms	1961-2008	408,164
	ION	Electron impact ionization of atoms		
	DIO	Electron impact dissociation of simple molecules		
	REC	Electron recombination of atoms		
CHART		Charge exchange of ion-atom collision	1957-2007	5,305
AMOL		Electron collision with molecules	1956-2008	3,765
CMOL		Heavy particle collision with molecules		
SPUTY		Sputtering yield of solid	1931-2000	1,241
BACKS		Reflection coefficient of solid surface	1976-2002	396
(AM Bibliographic database)				
ORNL		Bibliography on atomic collisions collected at ORNL, USA	1959-2008	77,714

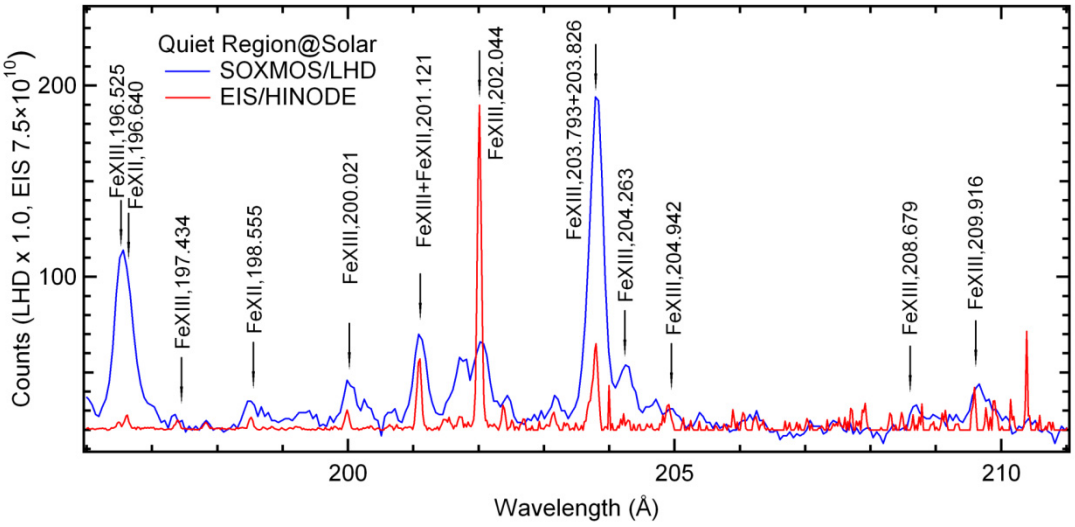

Figure 1: Fe spectra observed with SOXMOS at LHD (blue) and EIS instrument on board HINODE (red).

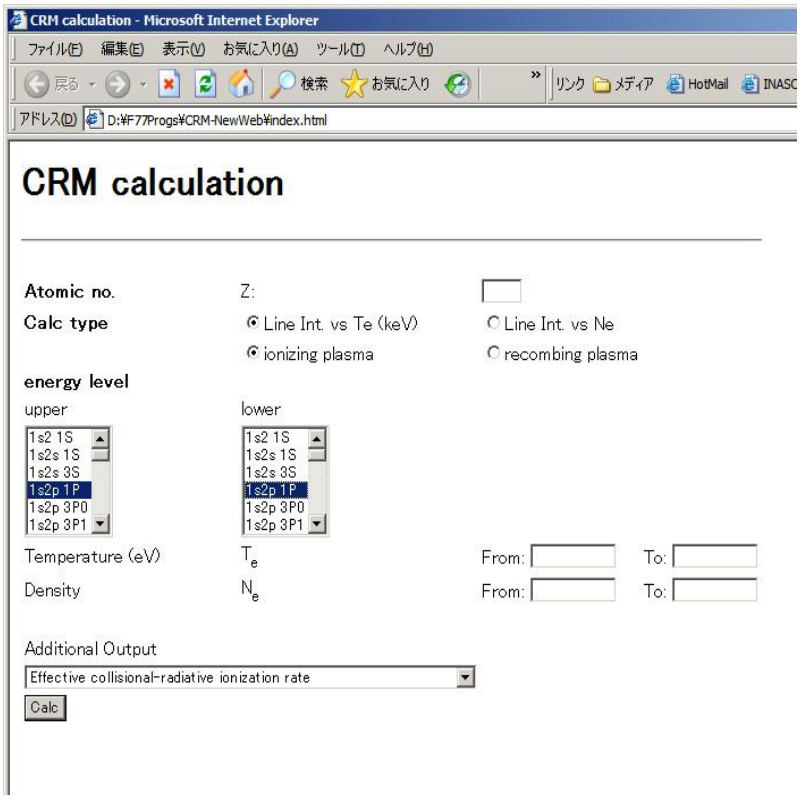

Figure 2: Web page of the CR model for He-like ions.

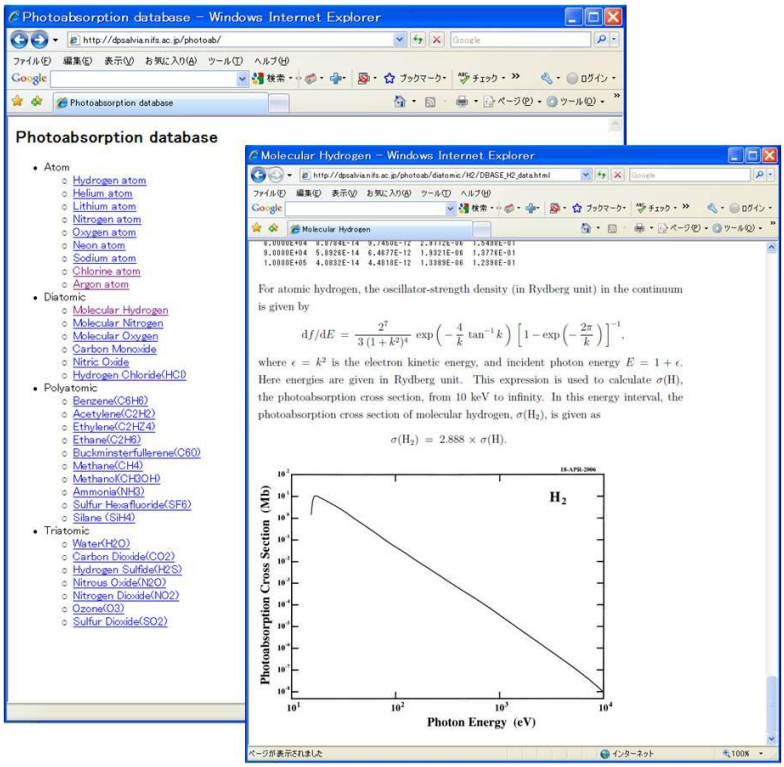

Figure 3: Web page of database for photo-absorption cross section.

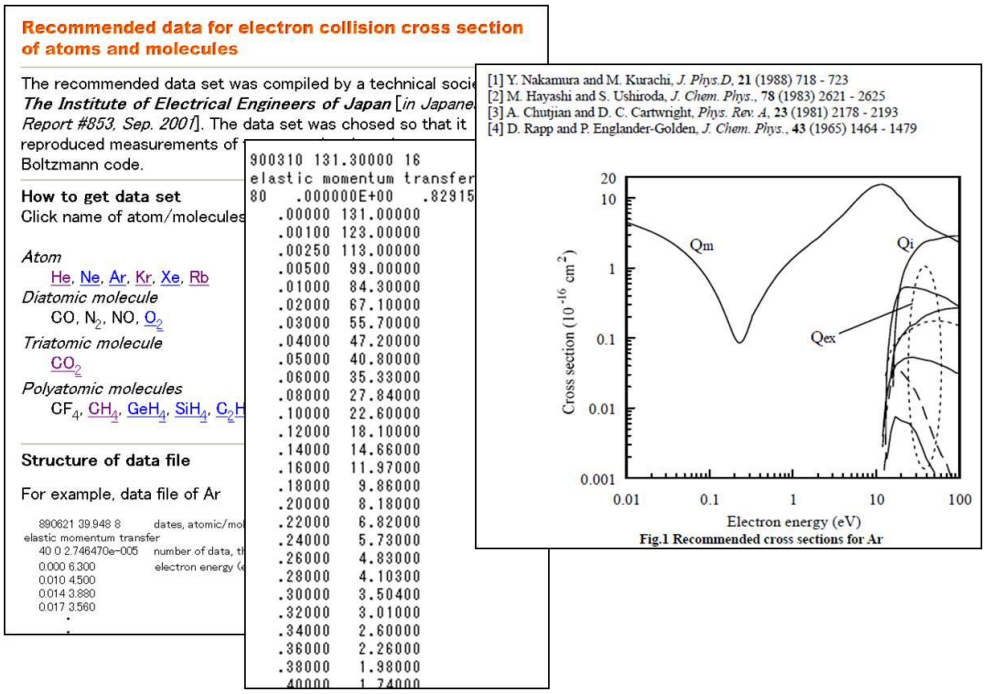

Figure 4: Web page for recommended data set of electron collision cross sections. http://dpsalvia.nifs.ac.jp/DB/IEEJ/.

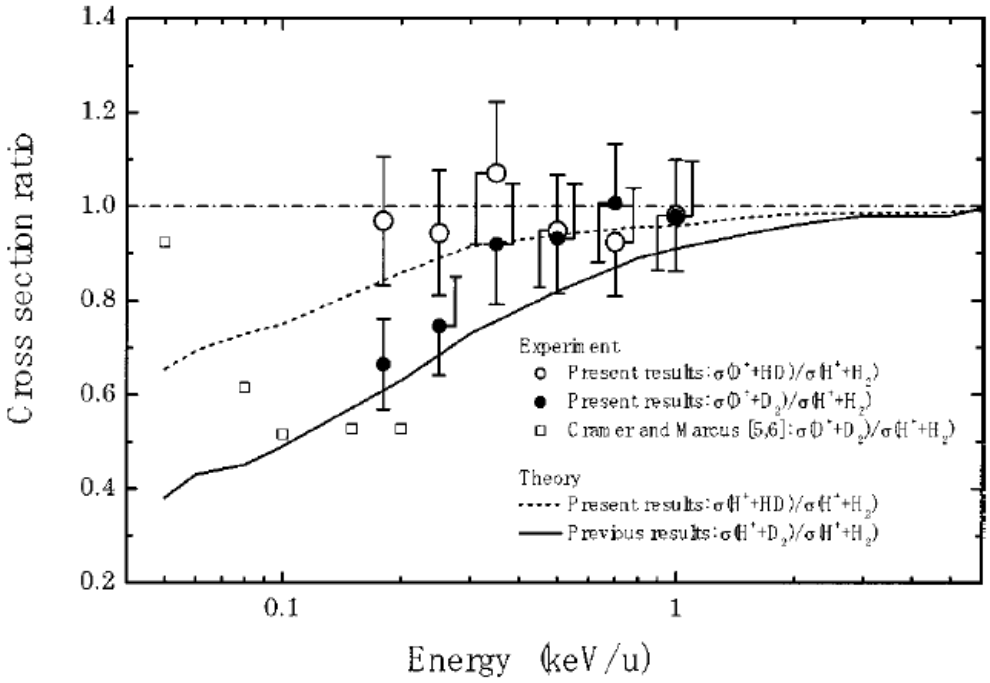

Figure 5: Hydrogen isotopic effects in electron transfer. Figure shows cross section ratios of electron transfer in collision of hydrogen nuclei and hydrogen molecules. Circles stand for experiments by Kusakabe *et al.* [7], and curves molecular-orbital close-coupling calculations.

Linear polarization of photon emission from reflected neutrals of atomic hydrogen at metal PFCs

D. Kato[1*], T. Kenmotsu[2] , K. Ohya[3] , and T. Tanabe[4]

1 National Institute for Fusion Science, 322-6 Oroshi-cho, Toki, Gifu 509-5292, Japan

2 Doshisha University, Kyoto 610-0321, Japan

3 The University of Tokushima, Tokushima 770-8506, Japan

4 Kyushu University, Fukuoka 812-8581, Japan

Abstract

This paper presents theoretical results for linear polarization of Lyman-α and Balmer-α emission following single electron capture by hydrogen nuclei to excited levels above Mo surfaces. The polarization degrees are evaluated for photons from the hydrogen atoms outgoing along surface normal with translation velocities of 0.05-1 au. In this geometry, the excited states are aligned with respect to the surface normal (quantization axis). Significant polarization degrees are obtained for electric-dipole photons emitted at right angle to the surface normal; the linear polarization preferentially along the surface plane at lower translation velocities turns to the surface normal at higher velocities.

Keywords: hydrogen recycling, reflection, ion-surface interaction, excitation, electron capture, alignment, linear polarization.

1. Introduction

High-Z refractory metals are adopted for plasma-facing-components (PFCs) in magnetic confinement devices. Tungsten is one of prime candidates for the PFCs of ITER. Twin-limiter (Carbon and Tungsten) experiments at TEXTOR clearly showed larger penetration depth of neutral hydrogen atoms in front of the tungsten limiter; intensities of Balmer-α emission from atomic hydrogen above the tungsten limiter distributed deeper into plasmas [1]. This indicates presence of high-energy (super-thermal) hydrogen atoms coming back into plasmas from the tungsten limiter. One can ascribe the

* Corresponding author's E-mail address: kato.daiji@nifs.ac.jp

high-energy recycling neutrals to reflected hydrogen atoms at the tungsten surfaces, since surfaces of high-Z target such as tungsten have large values of particle and energy reflection coefficients. Thus, it is inferred that the reflected hydrogen atoms are important contributors to photon emission above the high-Z targets.

Spectroscopic studies identified Doppler-shifted Balmer line emission from the high-energy hydrogen atoms created via the reflection [2]. The photon emission from the neutral hydrogen in front of PFC surfaces serves as a measure for degree of hydrogen recycling through the surfaces. In the measurements, one may often assume that photon emission from the neutrals is caused solely via collisional excitation in edge plasmas. Indeed, this naive assumption has been widely adopted, since excited state population created via interaction with the PFC surfaces was less understood. However, photon emission above the surfaces would be increased by presence of the excited states from the surfaces. Because, assuming lower electron densities in the edge plasmas, the excited states, except for meta-stable states, is depopulated preferentially by emitting photons rather than by non-radiative processes (e.g. electron-impact ionization and de-excitation). The measurements of the hydrogen recycling, therefore, include inherent uncertainties unless effects of the excited states are taken into account correctly.

In this paper, excited state populations of atomic hydrogen created via the reflection at the high-Z targets are investigated theoretically. Theoretical methods are described in Sec. 2. The present method has been validated by explaining measured Doppler-shifts of Balmer-α emission from neutrals of a deuteron-beam reflected at Mo surfaces [3]. In Sec. 3, results for excited state populations and linear polarization of photon emission are given for Mo target. The linear polarization is evaluated in geometries that photons are detected at 90 degree to the surface normal. Sec. 4 is devoted for concluding this paper.

2. Theoretical methods

In the present work, it is assumed that the excited states are formed via single electron capture by a hydrogen nucleus from conduction bands. The electron transfer is described by using semi-classical theories (electronic degrees of freedom are treated quantum mechanically, while nucleus motion

is represented by classical trajectories). In the present calculations, for the sake of simplicity, hydrogen nuclei recede from metal surfaces along straight-line classical trajectories of constant velocities. Although, the gist of the theory has been presented in our previous paper [4], mathematical formulations are given in the following sections. Many conduction electrons are involved in this process. Population of excites states resulted from such inherently many-body processes is evaluated by using density matrix theory. As described in the following sections, polarization of emitted photons is given in terms of statistical tensors of the density matrices.

2.1 Semi-classical theory for electron transfer between hydrogen nucleus and metal surface

We adopt the adiabatic expansion to describe electron wavefunctions in the rest frame of a moving nucleus, assuming nucleus translation velocities along surface normal v_z are slower than the Fermi velocity of conduction electrons. The adiabatic basis, $\{\Phi_\mu(\vec{r};D)\}$, are solutions for eigen-value problem of the adiabatic Hamiltonian at each nucleus-surface normal distance $D(t) = D_0 + v_z t$, which are read in the cylindrical coordinates $\vec{r} = (\vec{\rho}, z)$,

$$\left[-\frac{1}{2}\frac{\partial^2}{\partial z^2} - \frac{1}{2}\frac{\partial^2}{\partial \rho^2} + \frac{m^2 - 1/4}{2\rho^2} + V(\vec{r};D) \right] \Phi_\mu^{(m)} = \varepsilon_\mu^{(m)}(D)\Phi_\mu^{(m)}, \qquad (1)$$

under boundary conditions of $\Phi_\mu(z = \pm L) = \Phi_\mu(\rho = 0, \infty) = 0$. Atomic units are used throughout otherwise stated. In the present calculation, the quantization axis is taken along z axis whose range is truncated at L=80 Bohr radius. m in Eq. (1) stands for angular momentum quantum number along the quantization axis. The two-dimensional eigen-value problem was solved variationaly with L2 basis functions: Legendre and Laguerre polynomials for z and ρ coordinates, respectively. In Eq. (1), V is an effective potential energy composed of three electro-static potentials depending on D: the Coulomb attractive potential of the nucleus, an attractive potential well of the target surface, and a repulsive potential induced at the surface by the nuclear charge (i.e. the image charge in a classical term). The surface potential well was approximated by means of a semi-empirical formula

proposed by Jennings *et al.* [5]. The induced repulsive potential was calculated from the static linear density response function of electrons in the surface potential well [6]. It is noted that, in this approximation, interactions with a specific target surface are characterized by its workfunction and the Fermi energy (width of the conduction band). Fig. 1 plots the eigen-values $\varepsilon_{\mu}^{(m=0)}(D)$ in front of a Mo slab (30 Bohr thick). Near the surface, the eigen-values show complicated variation along D indicating disturbance of conduction levels by embedded atomic resonance levels. The atomic levels and the conduction levels are separate at larger distances; the classical image-potential curves, i.e. $-1/4D$ merge into asymptote for the isolate atomic levels. It is noted that all eigen-value curves in the figure lie above the Fermi level of Mo (about -0.17 au).

Variation of the electron wavefunctions associated with nucleus displacement along z are then expressed in a small interval $D \in [D_i, D_{i+1}(= D_i + \Delta D)]$,

$$\Psi_k^{(m)}(\vec{r}, D) = \sum_{\mu} \langle \vec{r} | \mu, m; D \rangle \chi_{\mu k}^{(m)}(D) . \tag{2}$$

The wavefunctions in the sector is propagated by using a spectral representation of the adiabatic Hamiltonian matrix,

$$\begin{aligned} \Psi_k^{(m)}(D_{i+1}) &= \exp\left[-i \int_{t_i}^{t_{i+1}} H_{ad}(D(t)) dt \right] \Psi_k^{(m)}(D_i) \\ &\approx \sum_{\mu} \langle \vec{r} | \mu, m; D_i \rangle \exp\left[-i \varepsilon_{\mu}^{(m)}(D_i) \Delta D / v_z \right] \chi_{\mu k}^{(m)}(D_i) \end{aligned} , \tag{3}$$

where ortho-normality of the adiabatic basis functions is used to obtain the second equation. This simple approximation is valid as long as ΔD is small enough so that results do not change significantly as the sector interval varies. From Eqs. (2) and (3), we obtain propagation equations for coefficients of the adiabatic expansion,

$$\chi_{\mu k}^{(m)}(D_{i+1}) = \sum_{\mu'} \langle \mu, m; D_{i+1} | \mu', m; D_i \rangle \exp\left[-i \varepsilon_{\mu'}^{(m)}(D_i) \Delta D / v_z \right] \chi_{\mu' k}^{(m)}(D_i) . \tag{4}$$

It is noted that, due to axial symmetry with respect to z, m is a constant of motion. Non-orthogonal overlap between the different set of the local adiabatic basis functions obtained at boundaries of the small sector $\langle \mu, m; D_{i+1} | \mu', m, D_i \rangle$ induces transitions between different μ states, which is

referred as non-adiabatic transition. For lower translation velocities, however, de-phased off-diagonal ($\mu \neq \mu'$) elements of the overlap are mutually canceled out, and therefore the non-adiabatic transition is suppressed.

In the present calculations, we assume that the hydrogen nucleus is initially situated in the vicinity of the surface (D_0=0 Bohr) then starts to move outward along z. An initial condition may be given by assuming that every adiabatic state at D_0 whose eigen-value below the Fermi level has a uniform population of 1, while higher states have no population. This naive assumption should be validated posteriorly. Accordingly, initial condition for the coefficients of the adiabatic expansion is given by,

$$\chi_{\mu k}^{(m)}(D_0) = \sum_{m'} \left\langle \mu, m; D_0 \left| \exp\left[i\vec{v}\cdot\vec{r}\right] \right| k, m'; D_0 \right\rangle \qquad \varepsilon_k^{(m')} \le \varepsilon_{\text{Fermi}}, \tag{5}$$

here k specifies adiabatic levels of the initial state, and truncated at the Fermi level according to the initial condition. The electron translation phase factor $\exp\left[i\vec{v}\cdot\vec{r}\right]$ represents Doppler shift of the target Fermi sphere along nuclear translation trajectories in the rest frame of the nucleus. The Doppler shift makes apparent electron population in conduction levels beyond the Fermi level, and that facilitates the so-called kinematic resonance electron transfer between excited atomic levels and the higher conduction levels.

2.2 Density matrix theory for excited state population and polarization of photon emission

Transition amplitudes for hydrogenic states $|nlm\rangle$ are projection of the coefficients for the adiabatic expansion at large distances (in the present calculations D is truncated at 50 Bohr),

$$a_{nlm}^{(k)} = \sum_{\mu} \left\langle nlm \left| \mu, m; D \right\rangle \chi_{\mu k}^{(m)}(D) \right. . \tag{6}$$

Density matrix is obtained by averaging the amplitudes over k,

$$\rho_{m,m'}^{(nl)} = \sum_{k} a_{nlm}^{(k)*} a_{nlm'}^{(k)} . \tag{7}$$

This is equivalent to neglecting coherence among the transition amplitudes for different adiabatic levels of the initial state. The incoherent summation is deduced formally by randomizing phases of the transition amplitudes for the different adiabatic levels. Diagonal elements of the density matrix give populations for the hydrogenic levels in the final state. Under assumption

that electronic interactions possess axial symmetry with respect to z, one obtains a diagonal density matrix, i.e. $\rho^{(nl)}_{m,m}\delta_{mm'}$, where $\delta_{mm'}$ is Kronecker delta, and $\rho^{(nl)}_{m,m} = \rho^{(nl)}_{-m,-m}$, which represents alignment of states. An equivalent description of the aligned system can be given in terms of statistical tensors,

$$\rho^{(nl)}_{k0} = \sum_{m}(-1)^{l-m}(lm, l-m \mid k0)\rho^{(nl)}_{m,m}, \tag{8}$$

where $(lm, l-m \mid k0)$ are the Clebsch-Gordan coefficients.

Figure 2 illustrates geometry for the linear polarization of photons emitted by an atom. In the dipole approximation, the linear polarization with respect to the z is expressed [7],

$$P = \frac{W_{//} - W_{\perp}}{W_{//} + W_{\perp}} = \frac{3\alpha^{\gamma}_{2} A^{(nl)}_{20}}{\alpha^{\gamma}_{2} A^{(nl)}_{20} - 2}. \tag{9}$$

$A^{(nl)}_{20} = \rho^{(nl)}_{20} / \rho^{(nl)}_{00}$ are alignment tensors, and

$$\alpha^{\gamma}_{2} = (-1)^{l+l_f+3}\sqrt{3(2l+1)/2}\begin{Bmatrix} l & l & 2 \\ 1 & 1 & l_f \end{Bmatrix}, \tag{10}$$

are anisotropy parameters for $l \to l_f$ radiative decay, where {...} are the 6-j symbols.

3. Results and Discussion

Figure 3 (a, b) shows results for populations of 2pm and 3dm hydrogenic levels and the linear polarization degrees for 2p-1s (Lyman-α) and 3d-2p (Balmer-α) transitions, respectively. The each population has a maximum at a certain nucleus velocity, and decreases at higher velocities. The peak velocities for 3dm levels are larger than those for 2pm levels. This trend is consistent with Massey's criterion: collision energy of the maximum electronic transition scales in proportion to the transition energy. In the present case, the transition energies are measured from the Fermi level.

Alignment in the population distribution is seen for the both levels depending on the nucleus translation velocity. Accordingly, finite linear polarization degrees are obtained as show in Fig. 3. The present results for Lyman-α seems contrast to results for grazing collision geometries; almost

zero linear polarization degrees have been found for measured Lyman-α emission from excited hydrogen atoms specularly reflected at grazing angles on a Ni(111) surface [8]. A theoretical prediction by Brako [9] using time-dependent Anderson Hamiltonian gave results consistent with the measurement, however, another theoretical study by Burgdörfer [10] based on the kinematic resonance electron transfer obtained finite linear polarization degrees for similar collision geometries on a Au surface. It should be emphasized here that almost zero translation velocities along the surface normal would be obtained for reflected particles after the grazing collisions, while the present studies are concerning with cases of larger normal velocities. Thus, the present cases cannot be compared to the grazing incidence cases, *i.e.* discrepancies between the present results and those should not be puzzling. In the present results, unknown oscillatory structures are seen in the lowest velocity region. The oscillatory structures might reflect oscillation of transition amplitudes between near degenerate levels which has been known for resonance electron transfer in slow ion-atom collisions [11].

For small velocities, the linear polarization degrees are negative indicating preferential alignment of the excited state population along surface plane. Similar results have been obtained theoretically by Burgdörfer [10] for Lyman-α emission following grazing collision on Au surfaces. This alignment may result from suppression of the resonance ionization (depopulation) of large m states, since its electronic clouds extend along the surface plane. The alignment turns to along the surface normal for higher velocities as indicated by positive polarization degrees. At higher velocities, net interaction between hydrogen nucleus and surfaces becomes weaker and described with perturbation theories. In the perturbation theories, electron capture probabilities are in proportion to overlap between wavefunctions of atomic and surface electrons. Since atomic states aligned along the surface normal have larger overlap, they possess lager probabilities for the electron capture. It is noted that the resonance ionization is also enhanced as the overlap becomes larger, however that is of the second or higher order processes in the perturbation series which are negligible in the weak interaction.

Reflection by normal incidence would produce outgoing particles with velocities distributed in a wide range. Apparent linear polarization degrees

of photons from the reflected particles are evaluated by averaging with the velocity distribution for the photon emitting particles $f(v)$,

$$\overline{P} = \int P(v) f(v) dv . \tag{11}$$

For normal incidence of a 5 keV deuteron beam, the mean energy, *i.e.* the first moments of the reflected energy distribution, of reflected neutrals is evaluated using particle and energy reflection coefficients provided by Eckstein [12] with his Monte-Carlo code (TRIM.SP [13,14]). The mean energy is obtained about 2.2 keV corresponding to $v \approx 0.2$. On may assume that the mean energy for the reflected particles is a reasonable approximation of that for the photon emitting particles, since the population distributions (Fig. 3) also peak near $v \approx 0.2$. We, therefore, approximate the apparent linear polarization degree by the value at the mean energy, which results in about -0.17 and -0.26 for Lyman-α and Balmer-α, respectively. It is noted that velocity variations of receding particles due to electrostatic interaction with metal surfaces are neglected in the present calculations, since the interaction energies (order of eV) are much smaller than kinetic energies of the photon emitting particles.

4. Conclusion

In this paper, mathematical formulations are given for semi-classical treatment of electron transfer between hydrogen nucleus and metal surfaces. Two mechanisms facilitate electron transfer to higher atomic levels beyond the Fermi level of target metals: firstly, the kinematical resonance electron transfer induced by the Doppler-shift of the Fermi sphere in the rest frame of a translating nucleus, secondly, the non-adiabatic transition induced by variation of electron wavefunctions associated with nucleus displacement along the surface normal. The present results show significant alignment of excited states formed via electron capture from metals surfaces, predicting finite linear polarization degrees of photon emission. In principle, photon emission from excited states created via collision with thermal plasma particles is not polarized. Therefore, the finite polarization may serve as experimental detection of the excited states created via the surface electron capture in reflected neutrals of edge plasmas.

Axial symmetry with respect to surface normal is assumed throughout the present work, which makes mathematical formulation simple. However,

it is straightforward to extend the present method for arbitrary collision angles to simulate complicated reflection dynamics. Direct coupling of the present semi-classical theories with classical Monte-Carlo codes is also an intriguing subject for future studies.

Acknowledgments

Present work are supported by JSPS-CAS Core-University Program on “Atomic and Molecular Processes in Plasma” and Grand in Aid for Scientific Research for Priority Areas “Tritium for Fusion” of MEXT, Japan.

References

[1] A. Huber, V. Philipps, A. Kirschner *et al., Proc. 25th European Physical Soc. Conf. Controlled Fusion and Plasma Physics,* June 14-18 1999, Maastricht, Netherlands.

[2] D.Reiter, P. Bogen and U Samm, J. Nucl. Mater. 196-198, 1059-1064 (1992).

[3] T. Tanabe, K. Ohya and N. Otsuki, J. Nucl. Mater. 220-222, 841-845 (1995).

[4] D. Kato *et al.*, J. Nucl. Mater. 390-391, 498-501 (2009).

[5] P.J. Jennings, R.O. Jones and M. Weinert, Phys. Rev. B 37, 6113-6120 (1988).

[6] A.G. Eguiluz, Phys. Rev. B 31, 3303-3314 (1985).

[7] V. V. Balashov, A. N. Grum–Grzhimailo and N. M. Kabachnik, Polarization and Correlation Phenomena in Atomic Collisions (Kluwer Academic Plenum Publishers, New York, 2000).

[8] H. Winter and H. Hagedorn, Nucl. Instr. and Meth. B 33, 350-353 (1988).

[9] R. Brako, Phys. Rev. B 30, 5629-5636 (1984).

[10] J. Burgdörfer, E. Kupfer and H. Gabriel, Phys. Rev. A 35, 4963-4976 (1987).

[11] *e.g.* R.K. Janev, P.S. Krstić and M.J. Raković, Phys. Rev. B 35, 7704-7707 (1987).

[12] W. Eckstein, IPP-Report 9/132 (2002).

[13] J. P. Biersack and W. Eckstein, Appl. Phys. A 34, 73-94 (1984).

[14] W. Eckstein, Computer Simulation of Ion-Solid Interactions (Springer-Verlag, Berlin, Heidelberg, 1991).

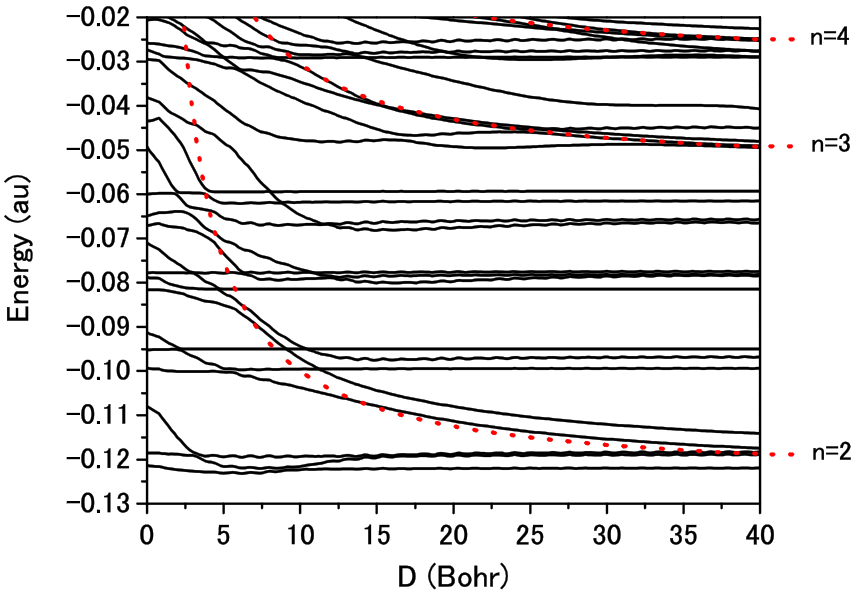

Figure 1: Eigen-value curves of single electron above Mo surface. Figure plots results for m=0 state only. Dotted curves are classical image potentials, 1/4D, merging into asymptote for isolated hydrogenic levels. 1 au energy = 27.21 eV.

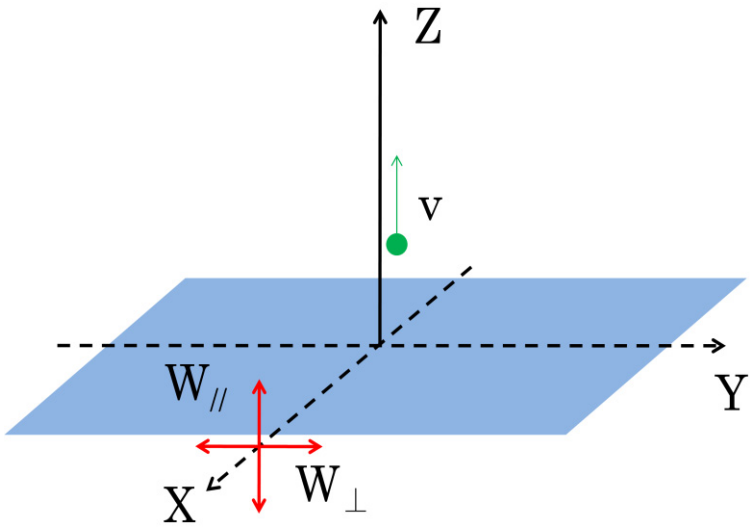

Figure 2: Geometry for photon emission. Photons are detected at right angle to surface normal (X-axis). $W_{//}$ is intensity of photons polarized along surface normal (Z-axis), $W_{\perp}$ along surface plane (Y-axis). Hydrogen atom is moving along Z-axis with constant translation velocities (v).

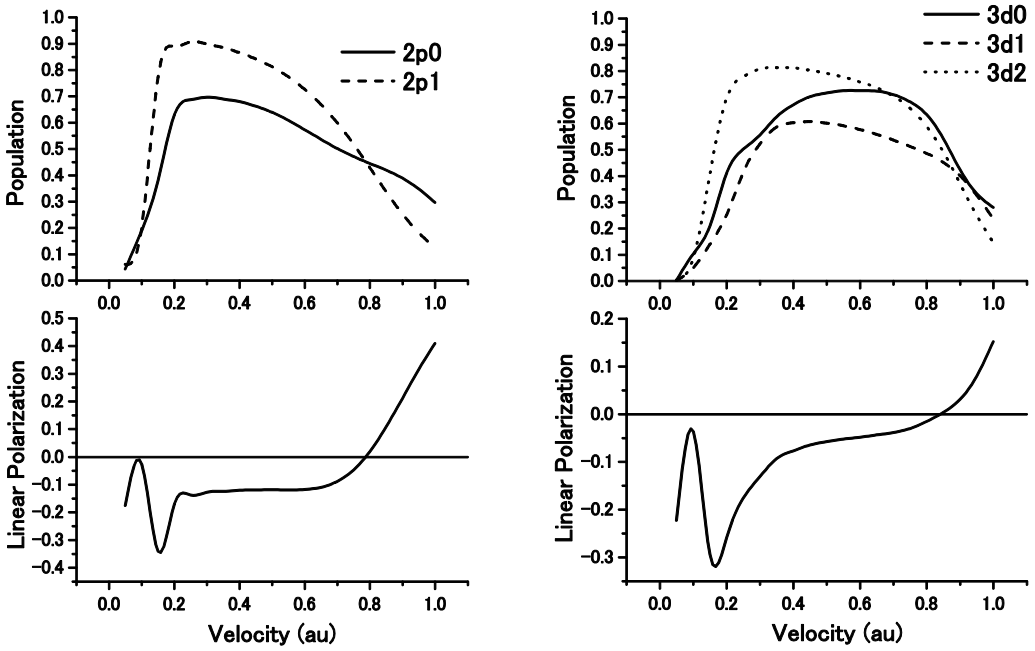

Figure 3: (a) Left: population of 2p*m* hydrogenic levels and linear polarization degrees for 2p→1s transition (Lyman-α) following single electron capture from Mo surface. (b) Right: population of 3d*m* hydrogenic levels and 3d → 2p transition (Balmer-α). 1 au velocity corresponds to kinetic energy of about 24.8 keV/u.

Calculations of polarization degrees for 3p $^2P_{3/2}$-3s $^2S_{1/2}$ transition of N^{4+}(3p $^2P_{3/2}$) produced in the N^{5+}-He and N^{5+}-H_2 collisions

L. Liu[1], Y. Q. Zhao[2], J. G. Wang[1], R. K. Janev[3] and H. Tanuma[4]

[1] The Key Laboratory of Computational Physics, Institute of applied physics and computational mathematics, P. O. Box 8009, P. R. China
[2]Department of Physics and Key Laboratory for Atomic and Molecular Nanosciences, Tsinghua University, Beijing 100084, P. R. China
[3]Macedonian Academy of Sciences and Arts, P. O. Box 428, 1000 Skopje, Macedonia
[4]Department of physics, Tokyo Metropolitan University, Tokyo 192-0397, Japan

Abstract

The magnetic substate-selective single electron capture cross sections in collisions of N^{5+} with He and H_2 are calculated using the two-center atomic orbital close-coupling method, and the polarization of emitted radiation from the excited state of N^{4+} is investigated for the projectile energies between 1.21 and 10keV/u. The polarization degrees for the 3p $^2P_{3/2}$ - 3s $^2S_{1/2}$ transition of N^{4+}(3p $^2P_{3/2}$) in both the N^{5+}+He and N^{5+}+H_2 collision systems are in general agreement with the experimental measurements. It is found both experimentally and theoretically that there exists a large difference in the polarization degrees between the N^{5+}+He and N^{5+}+H_2 collision processes, namely ~0.25 and ~0, respectively. By studying the time-evolution of electron capture dynamics in the two systems we have found that this difference is produced mainly by the interactions at the relatively small internuclear distances, consistent with the molecular picture of the collision dynamics.

In electron capture processes of highly charged ions with atoms and molecules, the captured electron usually populates the projectile excited states that decay by line radiation. Due to the fixed projectile velocity direction, the emitted lines can be polarized, and the polarization degree can give information about the magnetic sublevel population. This allows one to probe the collision dynamics on a more fundamental level. Numerous experiments have been devoted in the past [1-8] to the determination of photon polarization degree in collisions of multicharged ions with atomic and molecular targets. In the keV energy region, most of the experiments have measured the polarization of emitted radiation following the single-electron capture in collisions of highly charged ions with alkali atoms [4-6], and polarization degrees of 15~40% have been observed. However, in the experimental studies involving the charge transfer processes of He-like C^{4+}, N^{5+} and O^{6+} ions with He and H_2 targets [5, 7, 8], it was found that the polarization degree for the 3p $^2P_{3/2}$ - 3s $^2S_{1/2}$ transition lies in two regions: 0~7% for the O^{6+}+He and N^{5+}+H_2 collisions, and 17-21% and 16-24% for the N^{5+}+He and C^{4+}+H_2 collision systems, respectively. Particularly intriguing is the large difference in the polarization degrees for the N^{5+}+He and N^{5+}+H_2 systems in which the

projectile is the same ion and the targets are both two-electron systems.

On the theoretical side, the classical trajectory Monte Carlo (CTMC) method has been widely used to calculate the polarization degree of emitted radiation from excited states created in charge transfer processes of fully and partially stripped ions with alkali atoms [2, 9]. Although the agreement between experimental measurements and theoretical calculations is in most cases good, obtaining the magnetic state-selective cross sections from the fully classical distributions is an artcraft work. Two decades ago, Salin [10] calculated the magnetic (*m*-) state-selective capture cross sections in hydrogen atom-fully stripped multicharged ion systems by using the semiclassical molecular orbital close-coupling (MOCC) method, and discussed the role of the Stark effect in the angular momentum *l*-distribution of captured electrons in the field of residual target ion (see also [11]). While the *m*-state distribution of captured states is determined mainly by the interactions at small internuclear distances (rotational coupling of molecular states), the radial couplings (at avoided molecular energy curve crossings) at the intermediate and the Stark state mixing at large internuclear distances determine the distribution of angular momentum states of captured electron.

The *l*-state selective electron capture cross sections for the N^{5+}+He and N^{5+}+H_2 collision processes have been calculated by the MOCC method [12, 13], and measured by the photon emission spectroscopy method [7]. But to the best of our knowledge, no polarization degree calculations have been reported for these collision processes and the question of the observed large difference in their polarization degree remains open.

In the present work, the polarization degrees for the 3p $^2P_{3/2}$ - 3s $^2S_{1/2}$ transition of N^{4+}(3p $^2P_{3/2}$) produced in N^{5+}+He and N^{5+}+H_2 single-electron capture processes have been calculated and the dynamical mechanism of their differences in two processes have been established. The collision dynamics was described within the two-center atomic orbital close-coupling (TC-AOCC) method with plane-wave translational factors [14]. In the energy range 1.21-10keV/u considered in our study, the TC-AOCC method should provide an adequate description of collision dynamics of the above processes provided the TC-AO basis is adequately large. Atomic units will be used throughout unless explicitly indicated otherwise.

The atomic orbitals on the ion cores N^{5+}, He^+ and H_2^+ have been obtained by solving the Schrödinger equation with the model potentials

$$V_{N^{4+}}(r) = -\frac{5}{r} - \frac{2}{r}(1+5.605r)e^{-9.164r} \quad (1)$$

$$V_{He}(r) = -\frac{1}{r} - \frac{1}{r}(1+0.6535)e^{-2.697r} \quad (2)$$

$$V_{H_2}(r) = -\frac{1}{r}(1+e^{-6.4714r}) \quad (3)$$

taken from [12], [15] and [16], respectively.
The eigenvalue problem with the above model potentials has been solved variationally by taking the trial functions in the form [17]

$$\chi_{k,lm}(\vec{r}) = N_l(\xi_k) r^l e^{-\xi_k r} Y_{lm}(\vec{r}),$$

$$\xi_k = \gamma\beta^k, k = 1, 2, ..., N \quad (4)$$

where $N_l(\xi_k)$ is a normalization constant, $Y_{lm}(\vec{r})$ are the spherical harmonics, and γ and β are variational parameters, determined by minimization of the energy. The atomic states $\phi_{nlm}(\vec{r})$ are then obtained as superposition of $\chi_{k,lm}(\vec{r})$ basis functions

$$\phi_{nlm}(\vec{r}) = \sum_k c_{nk}\chi_{klm}(\vec{r}) \qquad (5)$$

where the expansion coefficients c_{nk} are determined by diagonalization of single-center Hamiltonian. This diagonalization yields the energies of the atomic states. The calculated energy levels are in good agreement with the NIST data [18].

Within the semiclassical approximation, with straight-line trajectories for the nuclear motion, the TC-AOCC equations are obtained [14] by expanding the total electron wave function Ψ in terms of bound atomic orbitals (5) multiplied by plane-wave ETFs (giving traveling AOs $\phi(\vec{r},t)$)

$$\Psi(\vec{r},t) = \sum_i a_i(t)\phi_i^A(\vec{r},t) + \sum_j b_j(t)\phi_j^B(\vec{r},t) \qquad (6)$$

and inserting it in the time dependent Schrödinger equation $(H - i\frac{\partial}{\partial t})\Psi = 0$, where the superscripts A and B indicate the projectile (N^{5+}) and the target (He or H_2), and H is the electronic Hamiltonian. The resulting coupled equations for the amplitudes $a_i(t)$ and $b_j(t)$ are then solved for specified initial conditions.

In the present calculations the expansion (6) included: all the states ϕ_i^A centered on N^{5+} with n ≤ 6, all the states ϕ_j^B centered on He^+ with n ≤ 3, and the 1s-6s ϕ_j^B states centered on H_2^+. They include all magnetic m-states within a given nl-subshell. The magnetic substate-selective cross sections is obtained as

$$\sigma_{lm}^{cx} = 2\pi\int_0^\infty |\, b_{lm}(+\infty)\,|^2\, bdb \qquad (7)$$

where b is the impact parameter. If the m-distribution of (l, m) states is not statistical, then the emitted photon spectrum is polarized. Taking the ion beam direction as the quantization axis, the degree of polarization is defined as

$$P = \frac{I_{//} - I_\perp}{I_{//} + I_\perp}, \qquad (8)$$

where $I_{//}$ and $I_\perp$ are the photon intensities with the electric vector parallel and perpendicular to the ion beam direction, respectively. P can be expressed as a function of the alignment parameter A_0 by [19]

$$P = \frac{I_{//} - I_\perp}{I_{//} + I_\perp} = \frac{3h(j_i, j_f)A_0(j_i)}{4 + h(j_i, j_f)A_0(j_i)}, \qquad (9)$$

where

$$h(j_i, j_f) = (-1)^{j_i - j_f} \begin{Bmatrix} j_i & j_i & 2 \\ 1 & 1 & j_f \end{Bmatrix} \begin{Bmatrix} j_i & j_i & 2 \\ 1 & 1 & j_i \end{Bmatrix}^{-1}, \qquad (10)$$

j_i and j_f are the total angular momenta of the initial and final state in the radiative transition, respectively. In the collision frame, the alignment parameter A_0 has the form [19]

$$A_0(j) = \frac{\sum_{mj}\{3m_j^2 - j(j+1)\}\sigma_{jm_j}}{j(j+1)\sum_{mj}\sigma_{jm_j}} = \frac{3 < m_j^2 >}{j(j+1)} - 1. \qquad (11)$$

Here σ_{jm_j} is the population of the (j, m_j) substate, which can be expressed in terms of the population cross section of (l, m) substate, σ_{lm},

$$\sigma_{jm_j} = \frac{1}{2}\sum_{m_l + m_s = m_j} |< lsm_l m_s \mid jm_j >|^2\, \sigma_{lm} \qquad (12)$$

where $< lsm_l m_s \mid jm_j >$ are the Clebsch-Gordan coefficients.

Due to the cylindrical symmetry around the beam axis, $\sigma_{lm} = \sigma_{l-m}$. In this work, we consider only the polarization degree for the $3p\ ^2P_{3/2}$ - $3s\ ^2S_{1/2}$ transition of $N^{4+}(3p\ ^2P_{3/2})$ and, consequently, only the population of $3p_0$ and $3p_1$ electron capture states is required. Inserting

Eqs. (10)-(12) into Eq. (9), the resulting polarization degree for the 3p $^2P_{3/2}$ - 3s $^2S_{1/2}$ transition has the form

$$P = \frac{3\tilde{\sigma}_{3/2,1/2} - 3\tilde{\sigma}_{3/2,3/2}}{5\tilde{\sigma}_{3/2,1/2} + 3\tilde{\sigma}_{3/2,3/2}} = \frac{6\sigma(3p_0) - 3\sigma(3p_1)}{10\sigma(3p_0) + 7\sigma(3p_1)}, \quad (13)$$

where, $\tilde{\sigma}_{3/2,1/2} = \sigma_{3/2,+1/2} + \sigma_{3/2,-1/2}$,

$\tilde{\sigma}_{3/2,3/2} = \sigma_{3/2,+3/2} + \sigma_{3/2,-3/2}$ and $\sigma(3p_1) = \sigma(3p_{+1}) + \sigma(3p_{-1})$. The populations of excited states are, thus, directly proportional to the electron capture cross sections.

In Fig. 1(a) and (b) we present the state-selective cross sections for capture to *3l* states of the N^{4+} ion for N^{5+}-He [panel(a)] and N^{5+}-H_2 [panel(b)] collision systems, respectively, which the predominantly populated capture states in the considered energy range. The corresponding experimental data [20, 21] and the MOCC results [22] are also given in this figure for comparison. All the results are mutually consistent regarding the energy behavior of the cross section but there exist discrepancies regarding its magnitude. The disagreement of our results with experimental data may be ascribed to the inadequate account of the electron correlations by the adopted one-particle model potentials. We note that the MOCC results of Ref. [22] are also outside the experimental error bars for most of the energies, which demonstrates the difficulties in the calculations of state-selective electron cross sections in many-electron systems. It is noteworthy that in the N^{5+}-He collision system, the dominant channel in the low energy region is the capture to 3s state, while for the N^{5+}-H_2 reaction, it is the capture to 3p and 3d states. This difference is mainly due to the different target structures of He atom and H_2 molecule.

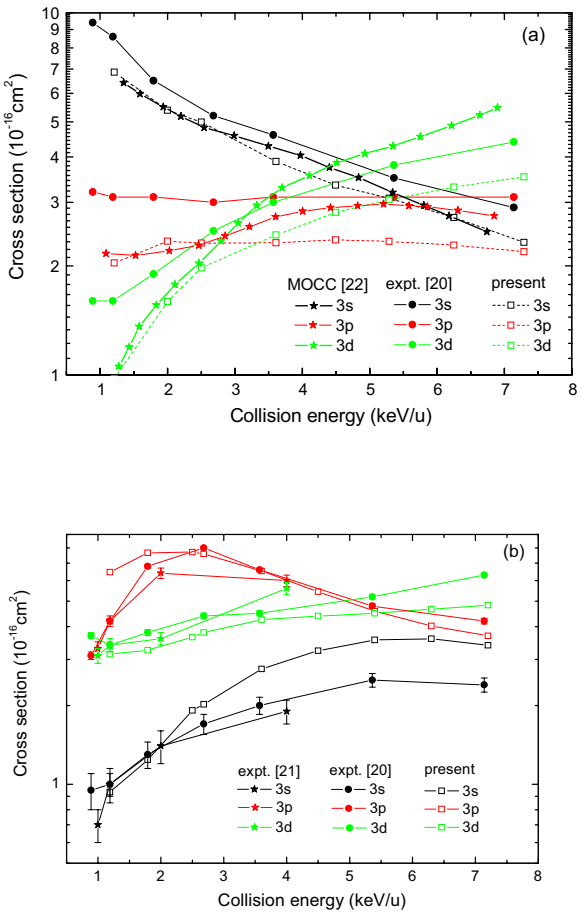

FIG. 1. Cross sections for electron capture to *3l* states of N^{4+} ion for N^{5+}-He (a) and N^{5+}-H_2 (b) collision systems. The filled symbols are the experimental data of Refs. [20, 21] and MOCC calculation of Ref. [22] and the open symbols are present AOCC results.

Figure 2 shows the calculated polarization degree, *P*, of the line corresponding to the 3p $^2P_{3/2}$ - 3s $^2S_{1/2}$ transition of N^{4+} ion as function of the projectile energy for N^{5+}-He (panel (a)) and N^{5+}-H_2 collisions (panel (b)), respectively. As in both collision systems the *3l* capture states are the predominantly populated in the considered energy range the contribution to the *3l* populations from the radiative cascades from higher *nl* states can be safely neglected. The polarization degree shown in Fig. 2 has, therefore, been calculated directly by Eq. (13). The calculated polarization degrees are compared

with the experimental values measured in Ref. [7]. For the N^{5+}-He system, the calculated polarization degree is around 0.25 for collision energies of 3-8keV/u. This corresponds to the ratios of *m*- partial cross sections: $\sigma(3p_0):\sigma(3p_{-1}):\sigma(3p_{+1})$ = 2.71:1:1, indicating a strong departure from the statistical distribution of magnetic sublevel population in $N^{4+}(3p)$. The polarization varies smoothly in the considered energy region, and this behavior, including the minimum around 5.3keV/u, is similar to that observed experimentally [7]. It is, however, about 15-25% higher than the measured value of about 0.20. In view of the use of a model potential to represent the interaction of captured electron with the many-electron ion core, this level of agreement can be considered as quite satisfactory.

For the N^{5+}-H_2 collision process, the calculated polarization degree is less than 0.06 in the energy range 3-8keV/u. This corresponds to a near-statistical distribution of the magnetic sublevel populations, with calculated *m*-partial cross section ratios $\sigma(3p_0):\sigma(3p_{-1}):\sigma(3p_{+1}) = 1.27:1:1$ for *P*=0.06 and 1.08:1:1 for *P*=0.02. In the experiment [7] a polarization degree of less than 0.06 has also been observed in this energy range, but the error bar is too large, so the present result can be considered to be consistent with the experiment.

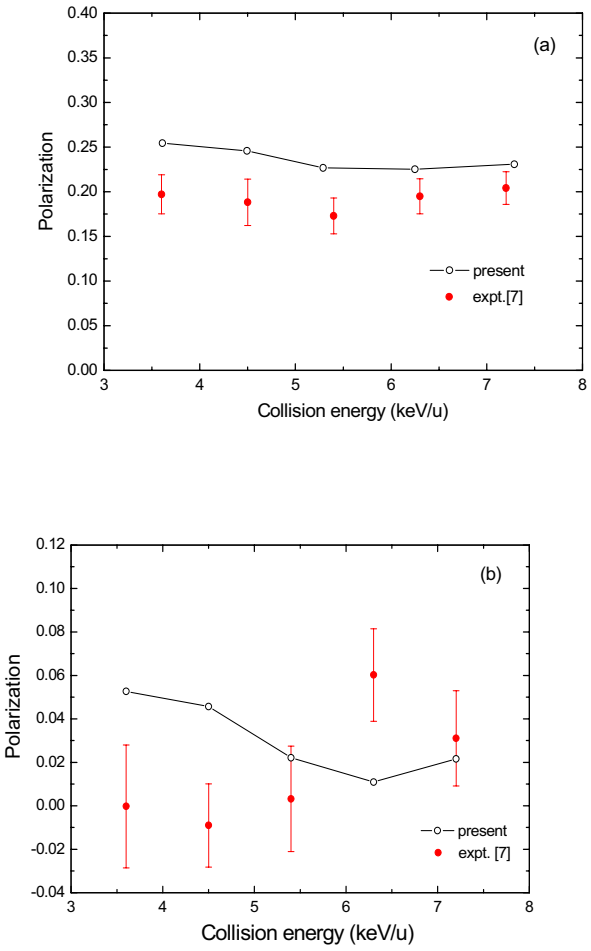

Fig. 2. The degree of polarization for the line corresponding to the 3p $^2P_{3/2}$-3s $^2S_{1/2}$ transition as a function of the projectile energy for N^{5+}-He (panel (a)) and N^{5+}-H_2 (panel (b)) collisions. Open circles: present result; filled circles: experimental data of Ref. [7].

Figures 2a and 2b show a striking difference in the polarization degree *P* of the 3p $^2P_{3/2}$ – 3s $^2S_{1/2}$ radiation in N^{5+}-He (*P*~0.25) and N^{5+}-H_2 (*P*~0) collision systems, despite the fact that the projectile is the same and both targets are two-electron systems.

In order to reveal the origin of this difference, we plot in Fig. 3 the time-evolution of weighted *m*-selective electron capture probabilities as function of the impact parameter for N^{5+}-He (panel (a)) and N^{5+}-H_2 (panel (b)) collision

systems at the energy of 3.61keV/u, and distances z along the direction of projectile velocity vector: z =vt = -4, 0, 4, 20, where z = 0 is the distance of closest approach. The interpretation of these figures can most easily be done if we invoke the molecular picture of the collision dynamics, in particular the fact that the initial molecular s_σ -state in both systems has diabatic potential energy crossings with the $N^{4+}(3l)$ +He^+, H_2^+ states at about R_{3s}=6.4, R_{3p}=7.7, and R_{3d}=8.2 for the N^{5+} +He system, and at about R_{3s}=4.2, R_{3p}=4.7 and R_{3d}=4.5 for the N^{5+} + H_2 system. When passing these energy crossing regions in the incoming stage of the collision, the molecular states correlating to the asymptotic 3s and m=0 substates of 3p and 3d states of N^{4+}+ He^+, H_2^+ are populated by radial coupling. At very small internuclear distances (the region of united atom), the rotational coupling populates also the m=1 substates of molecular states that correlate to $3p_1$ and $3d_1$ asymptotic states. In the outgoing stage of the collision, both the $3p_0$ and $3p_1$ substates enter the radial coupling region around R_{3p} but the interaction with the initial molecular s_σ -state affects (reduces) only the m=0 substate population. On the other hand, in the outgoing stage of the collision the returning flux along the s_σ -state also enters the R_{3p} strong coupling region and populates the $3p_0$ channel by radial coupling. At large internuclear distances (well outside the "molecular region") the 3s, $3p_0$ and $3d_0$ substates, as well as the $3p_1$ and $3d_1$, are mixed by the electric field of the residual ion (Stark mixing).

It is worth-noting in Fig.3, that the weighted probabilities for z = -4 in panel (a) and panel (b) of the figure are drastically (two orders of magnitude) different. This indicates that in the N^{5+} +He case the R_{3p} has been passed, while in the N^{5+} + H_2 not. In the time interval between z = -4 and z = 0, both collision systems have reached the internuclear distance region where rotational coupling is strong, and in the panels for z =0 we see a sizeable population of $3p_1$ state. At z =4, both the $3p_0$ and $3p_1$ populations are reduced with respect to the z =0 case due to radial coupling effects in the R_{3p} region. The significant reduction of the $3p_0$ and $3p_1$ populations observed at z =20 in the N^{5+} +He system can be attributed to the large extension of the radial coupling region around $R_{3p}^{He}(=7.7)$, to the strong non-adiabatic coupling, and the Stark mixing with the $3d_0$ and $3d_1$ states, respectively. In the N^{5+} + H_2 case ($R_{3p}^{H_2}=4.7$), it appears that all these effects are much weaker and the population of $3p_0$ and $3p_1$ states does not change considerably with respect to that at z =4.

The above molecular dynamics interpretation of the difference between the polarization degrees of 3p $^2P_{3/2}$ – 3s $^2S_{1/2}$ radiation in N^{5+}-He (P~0.25) and N^{5+}-H_2 (P~0) collision systems indicates that this difference is caused dominantly by the difference in the radial couplings between the states in the R_{3p} curve-crossing region which in the two systems lies at different internuclear distances. In the AOCC description of collision dynamics, employed in the present work, the molecular state radial couplings are represented by the electron exchange (non-diagonal) matrix elements of the Hamiltonian between the atomic states, the maxima of which are also distributed in the internuclear regions around the crossing of diabatic potential energies (diagonal matrix elements of the Hamiltonian). Therefore, the

conclusion regarding the difference in the polarization degrees of 3p $^2P_{3/2}$ – 3s $^2S_{1/2}$ radiation in the two considered systems, derived on the basis of molecular picture, remains valid in the AOCC dynamics picture as well.

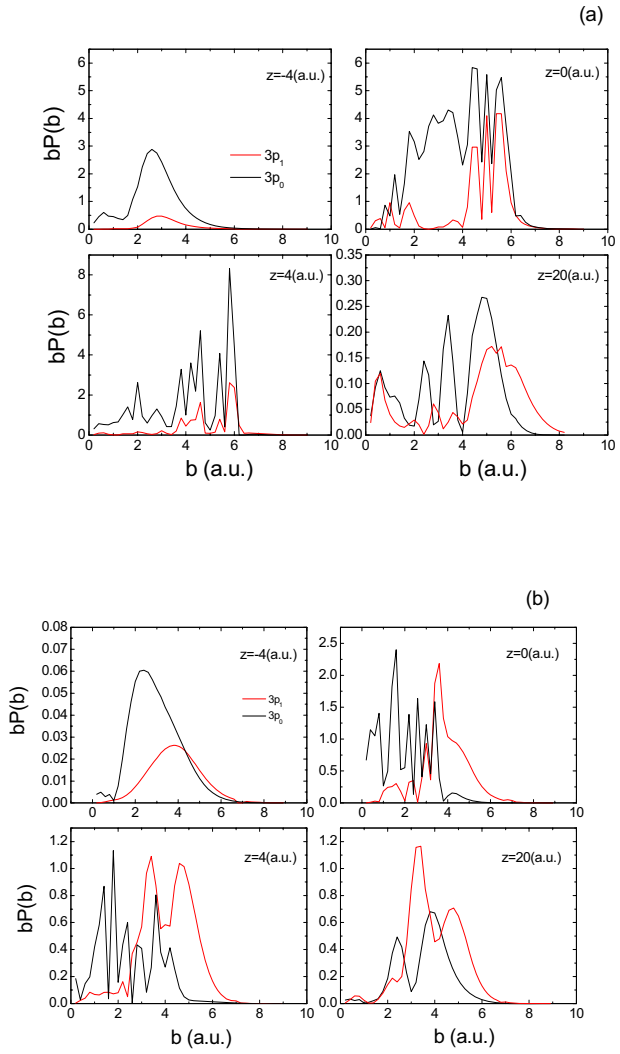

Fig. 3 Weighted probabilities *bP*(b) as a function of impact parameter for different collision times for N^{5+}-He (a) and N^{5+}-H_2 (b) collisions at the collision energy of 3.61keV/u.

Acknowledgements

One of the authors (L. L.) would like to acknowledge the warm hospitality of the Tokyo Metropolitan University during the period when this work was initiated. This work was supported by National Natural Science Foundation of China (Grants Nos. 10875017, 10734140 and 10604011) and the National Key Laboratory of Computational Physics Foundation (Grant No. 9140C6904030808).

References

[1] S. Schippers, P. Boduch, J van Buchem, F. W. Bliek, R. Hoekstra, R. Morgenstern and R. E. Olson, J. Phys. B: At. Mol. Opt. Phys. **28**, 3271 (1995)

[2] C. Laulhé, E. Jacquet, G. Cremer, J. Pascale, P. Boduch, G. Rieger, D. Lecler, M. chantepie and J. L. Cojan, Phys. Rev. A **52**, 3803 (1995)

[3] David M. Gauntt and Karsten Danzmann, Phys. Rev. A **46**, 5580 (1992)

[4] E. Jacquet, H. Kucal, V. Bazin, P. Boduch, M. Chantepie, G. Cremer, C. Laulhé and D. Lecler, Phys. Rev. A **62**, 022712 (2000)

[5] C. Laulhé, E. Jacquet, P. Boduch, M. Chantepie, G. Cremer, N. Ghérardi, X. Husson, D. Lecler, and J. Pascale, J. Phys. B **30**, 1517 (1997)

[6] C. Laulhé, E. Jacquet, G. Cremer, J. Pascale, P. Boduch, G. Rieger, M. Chantepie, and D. Lecler, Phys. Rev. A **55**, 1088 (1997)

[7] T. Hayakawa, R. A. Lomsadze, C. Verzani, H. Watanabe, H. Tanuma, B. D. DePaola and N. Kobayashi, Physica Scripta. T**92**, 322 (2001)

[8] H. Tanuma, T. Hayakawa, C. Verzani, H. Kano, H. Watanabe, B. D. DePaola and N. Kobayashi, J. Phys. B: At. Mol. Opt. Phys. **33**, 5091 (2000)

[9] S. Schippers, P. Boduch, J van Buchem, F. W. Bliek, R. Hoekstra, R. Morgenstern and R. E. Olson, J. Phys. B: At. Mol. Opt. Phys. **28**, 3271 (1995)

[10] A. Salin, J. Physique **45**, 671 (1984)

[11] V. A. Abramov, F. F. Baryshnikov and V. S. Lisitsa, Zh.Eksp.Teor.Fiz. **74**, 897 (1978) [Engl.transl.: Sov.Phys.-JETP **47**, 469(1979)]

[12] M. Gargaud and R. McCarroll, J. Phys. B: At. Mol. Phys. **18**, 463 (1985)

[13] M.-C. Bacchus-Montabonel, Phys. Rev. A **40**, 6088 (1989)
[14] W. Fritsch and C. D. Lin, Phys. Rep. **202**, 1 (1991)
[15] A. Kumar and B. C. Saha, Phys. Rev. A **59**, 1273 (1999)
[16] J. Kuang, Z. Chen and C. D. Lin, J. Phys. B: At. Mol. Opt. Phys. **28**, 2173 (1995)
[17] C. M. Reeves, J. Chem. Phys. **39**, 1 (1963)
[18] www.physics.nist.gov/physRefData/ASD/levels_form.html
[19] U. Fano and J. H. Macek, Rev. Mod. Phys. **45**, 553 (1973)
[20] D. Dijkkamp, D. Ćirić, E. Vlieg, A de Boer and F J de Heer, J. Phys. B: At. Mol. Phys. **18**, 4763 (1985)
[21] G. Lubinski, Z. Juhász, R. Morgenstern and R. Hoekstra, J. Phys. B: At. Mol. Opt. Phys. **33**, 5275 (2000)
[22] M. C. Bacchus-Montabonel and K. Amezian, Int. J. Quantum Chem. **38**, 615 (1990)

Radiative and collisional processes of highly charged heavy ions studied with electron beam ion traps

NAKAMURA Nobuyuki, Fred J. CURRELL[1], HU Zhimin, KATO Daiji[2], LI Yueming[3], OHTANI Shunsuke, SAKAUE A. Hiroyuki[2], TONG Xiao-Ming[4], WATANABE Hirofumi[5], WATANABE Tsutomu, YAMADA Chikashi

The University of Electro-Communications, Chofu, Tokyo 182-8585, JAPAN

1) Queen's University Belfast, Belfast BT7 1NN, United Kingdom

2) National Institute for Fusion Science, Toki, Gifu 509-5292, JAPAN

3) Institute of Applied Physics and Computational Mathematics, Beijing 100088

4) Doctoral Program in Materials Science, Graduate School of Pure and Applied Sciences, University of Tsukuba, Tsukuba, Ibaraki 305-8573, Japan

5) Chubu University, Kasugai-shi, Aichi, 487-8501, JAPAN

e-mail: n_nakamu@ils.uec.ac.jp

Abstract

We have been studying radiative and collisional processes of highly charged heavy ions using two electron beam ion traps (EBITs) at the University of Electro-Communications (UEC/Tokyo); one is the Tokyo-EBIT constructed in 1995 for the operation with a high energy (up to 200 keV) electron beam, and another is "CoBIT" constructed recently for the operation with a low energy (< 1 keV) electron beam. Recent activities using the two EBITs are presented.

Keywords: highly charged ion, electron beam ion trap, dielectronic recombination, atomic data, two-photon emission

1.Introduction

Atomic processes of highly charged ions are important for the understandings of high temperature plasmas, such as the solar corona and laboratory fusion plasmas. An electron beam ion trap (EBIT) [1] is a versatile device for studying both radiative and collisional processes of highly charged ions. It consists of a Penning-like ion trap and an electron beam going through the trap. Highly charged ions are produced through the successive ionization by the beam electrons. The EBIT plasma is thus a non-neutral plasma composed of trapped ions and a (quasi-)monoenergetic electron beam whose energy and current (density) can be easily controlled. Consequently, unlike other plasma devices and sources, an EBIT is useful for obtaining benchmark spectra under well-defined conditions and for observing resonant processes.

We have been using the Tokyo-EBIT [2, 3] to obtain such atomic data for highly charged ions. It was designed for the operation with a high-energy (up to 200 keV) electron beam for studying very highly charged ions. Recently we have constructed a compact EBIT [4] with a relatively low energy (below 1 keV) electron beam to study moderate charge state ions. The complementary use of these two EBITs enables us to study spectra of a wide range of charge states and also to study electron-collision processes over a wide range of interaction energy. In this paper, some recent activities using the two EBITs are presented.

2. Dielectronic recombination

Dielectronic recombination (DR) of highly charged ions is one of the most important processes in plasmas. An EBIT is a useful device for studying DR processes of highly charged heavy ions since it has a (quasi-)monoenergetic electron beam whose energy can be easily and rapidly controlled. By using the Tokyo-EBIT, we have been studying DR processes through both X-ray observations [5] and ion abundance measurements [6, 7]. The former has the advantage that absolute cross sections can be obtained by normalizing the X-ray intensity of DR to that of radiative recombination (RR), for which reliable theoretical cross sections can be obtained. On the other hand, it has the disadvantage that it is difficult to resolve the charge states mixed in the EBIT due to the intrinsic energy resolution of a solid state Ge detector. In contrast, the latter has the advantage that charge-state resolved measurements are available although it is difficult to obtain absolute cross sections. The ion abundance measurement is thus suitable for open shell systems for which it is difficult to concentrate the abundance on a single charge state.

Figure 1 (a) shows an example of the ion abundance measurements, in which the abundance ratio of B-like to Be-like Bi was measured as a function of the electron beam energy. This ratio can be expressed in terms of cross sections of relevant processes [7]:

$$\frac{n_B}{n_{Be}} = \frac{\sigma_{Be}^{RR} + \sigma_{Be}^{DR} + \langle \sigma_{Be}^{CX} \rangle}{\sigma_B^{ion}}, \tag{1}$$

where σ_{Be}^{RR} and σ_{Be}^{DR} are the radiative and dielectronic recombination cross sections for Be-like Bi, σ_B^{ion} the electron impact ionization cross section for B-like Bi, and $\langle \sigma_{Be}^{CX} \rangle$ the effective charge exchange cross section [8] for collisions with the residual gas. Since only σ_{Be}^{DR} has a sharp electron-energy dependence, structures on the smooth background in Fig.1 (a) correspond to σ_{Be}^{DR} (normalized by σ_B^{ion}) whereas the smooth background corresponds to the non-resonant terms $\sigma_{Be}^{RR} + \langle \sigma_{Be}^{CX} \rangle$ (normalized by σ_B^{ion}). As seen in the figure, the DR structures show asymmetric profiles arising from the interference between

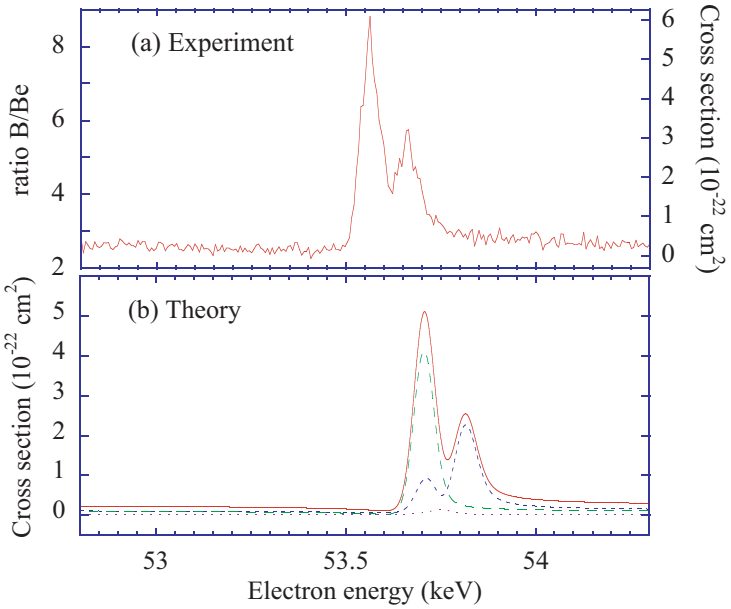

Figure 1: (a) Abundance ratio between B-like and Be-like Bi ions at the equilibrium for the $KL_{12}L_3$ DR region. (b) Theoretical result for the recombination cross section involving the resonant states. The data are convoluted with the experimental width (60 eV).

non-resonant (RR) and resonant (DR) processes. We have recently developed a theoretical method to calculate the full Green's function of multielectron systems and applied it to the recombination cross section involving resonant recombinations [9]. Figure 1 (b) represents the theoretical result, showing good agreement with the present experiment especially with respect to the peak profile.

3. Spectroscopy of tungsten ions

Tungsten is a major candidate for the divertor material of ITER, so that its spectroscopic data are strongly needed to diagnose and control the high temperature plasma in ITER. By using the two EBITs, we are systematically measuring spectra of highly charged tungsten ions with a wide range of charge states over a wide range of wavelength. In particular, we are currently interested in the visible region because a lot of effort has already been paid for the shorter wavelength range such as VUV and X-rays at the Berlin EBIT [10, 11]. Figure 2 shows the typical setup for visible spectroscopy [12], which is used both for the Tokyo-EBIT and for CoBIT although the focal length and the size of the lens are changed depending on the ion source used. Tungsten is injected into the EBIT as the vapor of $W(CO)_6$ through a gas injection system. To distinguish the lines

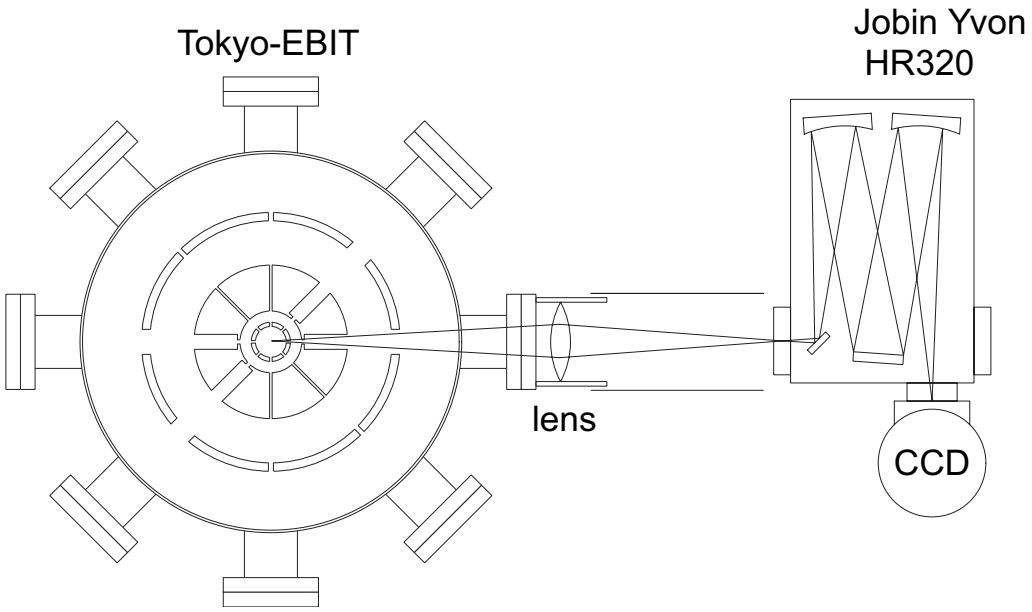

Figure 2: Experimental setup for visible spectroscopy. The cross-sectional view of the EBIT at the center of the drift tube is shown.

of tungsten from those of carbon and oxygen, spectra are also observed while injecting CO and O_2 and compared with the spectra obtained with $W(CO)_6$ injection. The charge state of the tungsten ion responsible for any line can be identified from the appearance energy by observing electron energy dependence although the comparisons with theoretical calculations are needed for the detailed identification. Resent results will soon be published elsewhere [13]

4. Observations of two-photon emission processes

Some processes can emit two photons at the same time or successively. For example, the KLM-DR process can emit K and L X-rays successively. Another example is the deexcitation of the 2s state in He-like or H-like ions. We are trying to observe these processes by surrounding the EBIT with two (or more) Ge detectors. Figure 3 shows the typical setup for the two-photon observation. Signals from two Ge detectors are recorded with a multi-parameter data acquisition system (IWATSU A3100). Both the pulse height (X-ray energy) and the arrival time of each signal are stored in the list mode. At present, the system is being tested and optimized especially for the time resolution through the coincidence measurement of K and L X-rays emitted in the KLM-DR process of Ba ions. Although the number of the detectors being used is only two, we are planning to increase it up to four.

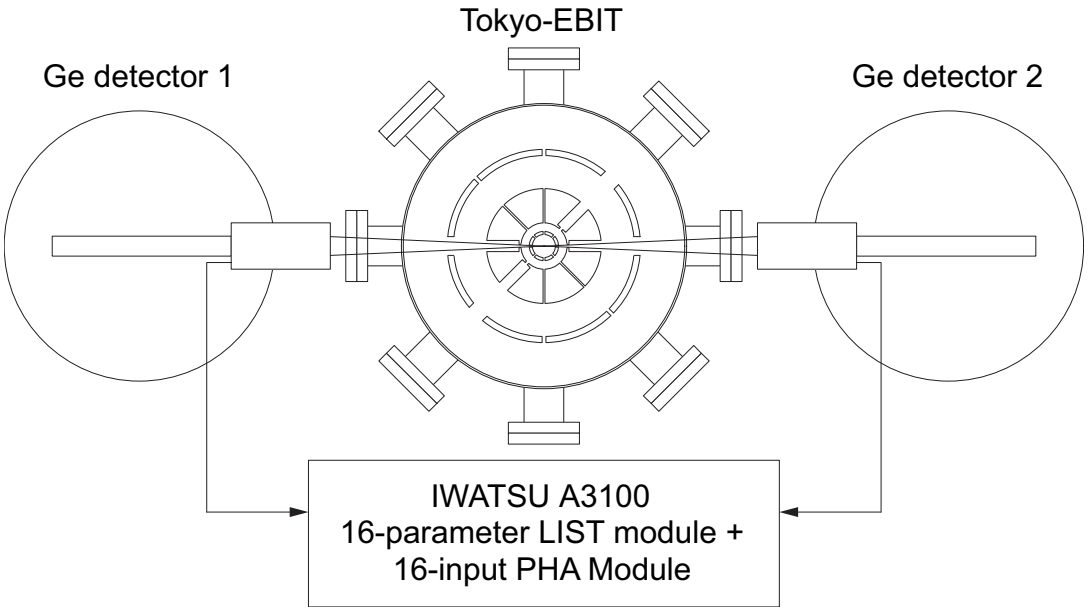

Figure 3: Experimental setup for the two-photon observation.

Acknowledgement This work was supported by KAKENHI (21340111) and the NIFS Collaboration Research Program (NIFS09KOAJ003).

References

[1] R. E. Marrs, M. A. Levine, D. A. Knapp, and J. R. Henderson, Phys. Rev. Lett. **60**, 1715 (1988).

[2] F. J. Currell, J. Asada, K. Ishii, A. Minoh, K. Motohashi, N. Nakamura, K. Nishizawa, S. Ohtani, K. Okazaki, M. Sakurai, H. Shiraishi, S. Tsurubuchi, and H. Watanabe, J. Phys. Soc. Jpn. **65**, 3186 (1996).

[3] N. Nakamura, J. Asada, F. J. Currell, T. Fukami, K. Motohashi, T. Nagata, E. Nojikawa, S. Ohtani, K. Okazaki, M. Sakurai, H. Shiraishi, S. Tsurubuchi, and H. Watanabe, Phys. Scr. **T73**, 362 (1997).

[4] N. Nakamura, A. Endo, Y. Nakai, Y. Kanai, K. Komaki, and Y. Yamazaki, Rev. Sci. Instrum. **75**, 3034 (2004).

[5] H. Watanabe, F. J. Currell, H. Kuramoto, Y. M. Li, S. Ohtani, B. O'Rourke, and X. M. Tong, J. Phys. B **34**, 5095 (2001).

[6] H. Watanabe, H. Tobiyama, A. P. Kavanagh, Y. M. Li, N. Nakamura, H. A. Sakaue, F. J. Currell, and S. Ohtani, Phys. Rev. A **75**, 012702 (2007).

[7] N. Nakamura, A. P. Kavanagh, H. Watanabe, H. A. Sakaue, Y. Li, D. Kato, F. J. Currell, and S. Ohtani, Phys. Rev. Lett. **100**, 073203 (2008).

[8] R. E. Marrs, S. R. Elliott, and D. A. Knapp, Phys. Rev. Lett. **72**, 4082 (1994).

[9] X. M. Tong, N. Nakamura, S. Ohtani, T. Watanabe, and N. Toshima, Phys. Rev. A **80**, 042502 (2009).

[10] R. Radtke, C. Biedermann, J. L. Schwob, P. Mandelbaum, and R. Doron, Phys. Rev. A **64**, 012720 (2001).

[11] C. Biedermann and R. Radtke, in *Proceedings of the 16th International Conference on Atomic Processes in Plasmas*, No. 1161 in *AIP Conference Proceedings*, edited by B. K. B (American Institute of Physics, New York, 2009), p. 95.

[12] H. Watanabe, D. Crosby, F. J. Currell, T. Fukami, D. Kato, S. Ohtani, J. D. Silver, and C. Yamada, Phys. Rev. A **63**, 042513 (2001).

[13] H. Watanabe, will be submitted. (2009).

X-ray polarization spectroscopy to study energy transport in ultra-high intensity laser produced plasmas

H Nishimura[a], Y Inubushi[a], Y Okano[a], S Fujioka[a], T Kai[a], T Kawamura[b], D Batani[c], A Morace[c], R Redaelli[c],C Fourment[d], J Santos[d], G Malka[e], A Boscheron[f], A Casner[g], M Koenig[h], T Nakamura[a], T Johzaki[a], H Nagatomo[a], and K Mima[a]

[a] *Institute of Laser Engineering, Osaka University, Suita, Osaka, Japan*
[b] *Tokyo Institute of Technology, Yokohama, Kanagawa, Japan*
[c] *University of Milan, Bicocca, Italy*
[d] *CELIA, Université de Bordeaux 1/ CNRS/CEA, Talence, France*
[e] *CENBG, Université de Bordeaux 1 /CNRS - IN2P3, Gradignan, France*
[f] *CEA/CESTA Le BARP, France*
[g] *CEA-DAM Ile de France, Bruyres-le-Chtel, France*
[h] *LULI, Ecole Polytechnique, Palaiseau Cedex, France*

Abstract. X-ray polarization spectroscopy was studied to derive directly the velocity distribution function (VDF) of hot electrons propagating in plasma created with a high intensity laser pulse. Polarization measurement was made at around 10^{18} W/cm^2 using a laser pulse (~10 J in ~1 ps) from Alisé facility at CEA/CESTA. Chlorinated triple-layer targets were irradiated, and Cl Heα line was observed with an x-ray polarization spectrometer. Polarization degrees were measured as a function of the target overcoat thickness, corresponding to the depth along pre-formed plasma. It is found that the polarization is weakly negative for thin coating, but becomes positive, and finally zero for thick coating. This result is consistent with predictions made with a time-dependent atomic kinetics code developed to gain an insight into the generation of polarized Cl Heα radiation. The de-polarization on the surface is attributed to excessive bulk electron temperature and that in the deep region to elastic-scattering processes by the isotropic bulk electrons in dense region.

Keywords: x-ray spectroscopy, polarization spectroscopy, hot electrons
PACS: 32.10.Dk, 32.30.Rj, 52.38.Kd 52.38.Ph, 52.57.Kk 52.70.La

INTRODUCTION

In the fast-ignitor plasma, there are two major components of electrons. The first component is hot electrons generated predominantly by collective processes in the laser–plasma interaction region [1], leading to initial distributions of hot electrons that are highly anisotropic. The second one is composed of cold bulk electrons. These form a return current for the hot electrons and will be heated mostly via ohmic and/or collisional processes [2]. Thus, the velocity distribution of cold electrons is isotropic. In terms of atomic processes, the fast electrons are mainly responsible for the inner-shell ionization, while the cold bulk electrons are responsible for the outer-shell

ionization. This categorization is thus useful to derive the bulk electron temperature using x-ray spectroscopy [3, 4]

Hot electron spectra are usually measured with electron spectrometers, but resultant spectra are substantially affected by self-generated target potential so that the spectra observed do not adequately quantify the hot electron transport [5]. Transition radiation is proposed as another method to derive the hot electron velocity distribution function (VDF) [6, 7], but should be performed at the rear side of the target where the plasma has a very sharp boundary. However, since hot electrons distributions derived by this method are subject to transport through the target, the original information at the interaction region might be lost. As it is of great importance to clarify the energy deposition processes by directly observing the VDF of electrons, development of other methods is urgently required. To address the VDF of the electrons, x-ray-line polarization spectroscopy as a diagnostic method has been studied for laser produced plasmas [8-11] and Z-pinch plasma [12]. In the early study, a single-layered, monolithic target was irradiated with an intense laser pulse at around 10^{16} W/cm^2 and polarization degree was observed as an integration over the depth of plasma so that detailed information of VDF in local plasma was lost [8]. In a series of study on x-ray polarization measurement polarization degree was measured at 10^{17} W/cm^2 using a triple-layered target and change of the polarization degrees from negative to positive signs was obtained, which is attributed to the change of VDF shape [9, 10]. Hakel *et al* proposed to use polarized satellite lines for the VDF measurement [9]. In practice, however, polarization degrees of these lines are weaker than that from He-like resonance line, thus, the observation becomes technically hard. Furthermore, the satellite lines usually merge with the inter-combination line and it is also hard to distinguish each other.

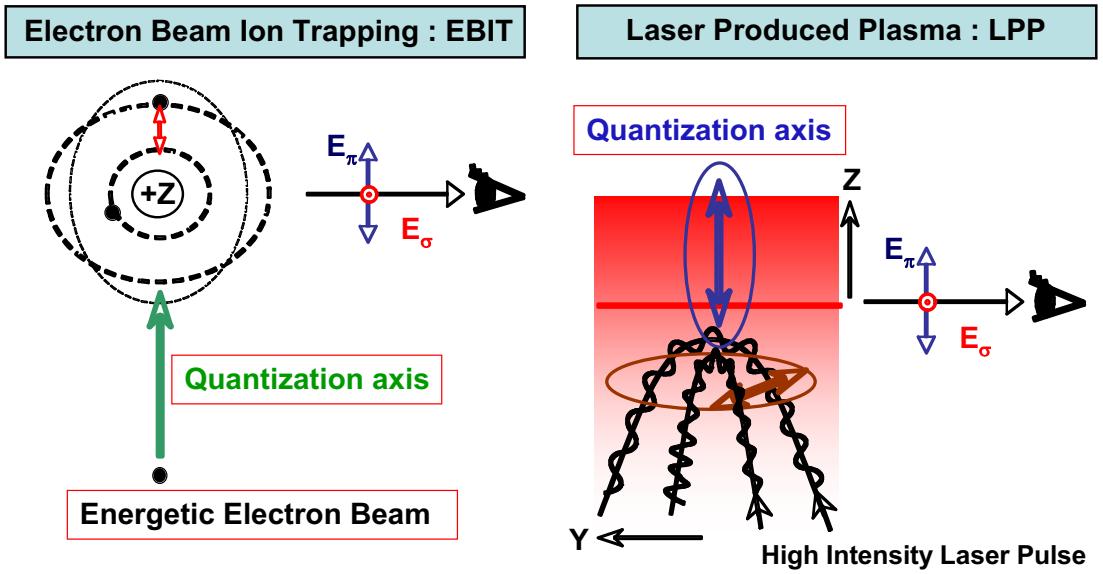

FIGURE 1. Electron impact on an ion causes selective excitation, leading to polarized x-ray emission. A good example is seen spectroscopic observation with electron beam ion trapping machine (EBIT).

Polarized x-rays are generated due to the anisotropy of fast electron VDF and the alignment creation associated with magnetic atomic sublevels is essential [13-15]. Thus, polarization spectroscopy in a low density region is practically useful due to the small effect of alignment breaking by elastic electron impacts. By utilizing this principle, the anisotropy of hot electron VDFs can be determined by observing the polarization degree P [8-11, 16]. In the case of a planar target irradiated by a high intensity laser pulse, hot electrons are so generated that they initially propagate nearly parallel to the density gradient, i.e., perpendicular to the target surface. Figure 1 shows similarity of polarized x-ray emission from an electron-beam ion trapping (EBIT) [17] to that in laser produced plasmas. This direction is referred to as the quantization axis hereinafter. The observed polarization degree P is defined as,

$$P = \frac{I_{II} - I_{\perp}}{I_{II} + I_{\perp}} \quad , \tag{1}$$

where I_{II} and $I_{\perp}$ are respectively the intensities of the x-ray radiation whose electric fields are parallel and perpendicular to the quantization axis for an observer. This definition has been employed in the EBIT polarization spectroscopy.

THEORETICAL STUDY ON POLARIZATION OF CL Heα LINE

A time dependent atomic kinetic code was developed for the polarization spectroscopy of Heα transition ($1s^2\ ^1S_0$ - $1s2p\ ^1P_1$) of chlorine [18]. Atomic cross-sections with magnetic sublevels for helium-like atoms were obtained using the Breit-Pauli R-matrix method [19]. The details are described in the study by Kai *et al.* [20]. Jacobs have formulated a polarization-density matrix for the investigation of the radiative emission from bound excited and auto-ionizing atomic states in an arbitrary arrangement of static (or quasi-static) electric and magnetic field. Its expression, however, has not been applied a plasma analysis yet [21]

Figure 2 shows dependence of polarization degree P on electron kinetic energy for Cl Heα line obtained simply with the ratio of the cross-sections. The electron energy is normalized with the transition energy for $1s2p\ ^1P_1$ -> $1s^2\ ^1S_0$. With increase in the electron energy, the polarization degree becomes smaller. This is an important feature of the polarization spectroscopy.

Radiative decay rates associated with LSJ states were obtained using the GRASP code [22], and the optical allowed transitions between JM-states were estimated using the Wigner-Eckert theorem [23]. For the polarized x-ray calculation, pre-process with a time-dependent atomic population kinetics code [24] must be separately carried out in advance. The basic calculation scheme to solve the population kinetics associated with the magnetic sublevels is given in Hakel *et al.* [9].

Figure 3 shows an example of calculation result. The polarization of above10% can be expected at the ion density $N_i = 4.5\text{x}10^{21}$ cm^{-3} (corresponding to ~ $0.05\rho_s$ where ρ_s is the solid density), the fast electron temperature along the quantization axis $T_{\text{Fast-z}}$ =10~50 keV and that perpendicular to the quantization axis $T_{\text{Fast-r}}$= 1 keV. The ratios

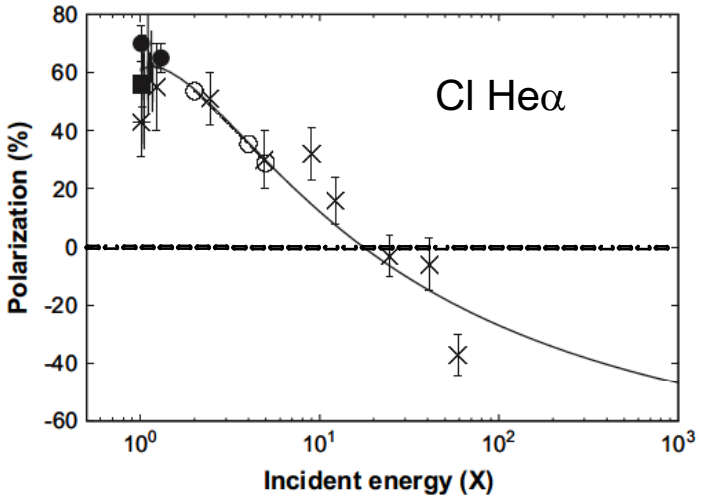

FIGURE 2. Dependence of polarization degree P on electron kinetic energy for Cl Heα line. The incident energy in the horizontal axis is normalized with the photon energy for Cl Heα line, i.e., 2.79 keV [20].

f_2/f_0 (here f_n denotes the Legendre polynomial of order n) of the fast electrons with near the threshold of $1s2p\ ^1P_1$-> $1s^2\ ^1S_0$ (about 2.79 keV) are 1.8~2.0, and those with the energies of 10~100 keV are 4.1~4.9. The anisotropy is high and the fast electrons with the energies of below 50 keV have a contribution to positive polarization [18].

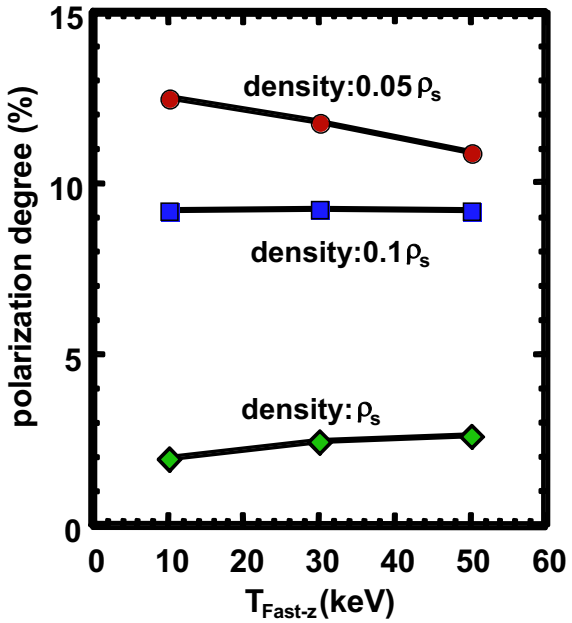

FIGURE 3. Dependence of polarization on the $T_{Fast\text{-}Z}$ and plasma density [18].

With increase in $T_{\text{Fast-z}}$ the polarization degree is reduced due to the increase in the number of the fast electrons with the energies of above 50 keV at about $0.05\rho_s$. However, at the high density of greater than about $0.1\rho_s$, the other atomic processes associated with $1s2p\ ^1P_1$ may also affect the dependence.

EXPERIMENT

X-ray polarization was measured using a laser pulse (~10 J in ~1 ps) from Alisé facility at CEA/CESTA. Pedestal component arriving in prior to the main pulse grows linearly from the noise level to 10^{-6} of the laser peak in 6 ns duration. Target used was a chlorinated triple-layer consisting of a 2x2x2 mm polyethylene substrate, a 0.5-μm-thick $C_2H_2Cl_2$ tracer layer, and a 0~6-μm-thick C_8H_8 parylene overcoat. It was irradiated with a laser spot of 58-μm-diam containing 50% of laser energy, yielding $4x10^{18}$ W/cm^2 average intensity. Laser was incident at 7 degrees from the target normal and Cl Heα line from the tracer layer was observed at 83 degrees from the target normal with an x-ray spectrometer having two orthogonal polarization channels. Assuming the quantization axis is along the laser axis, one channel detected the component in nearly parallel to the axis and the other channel the component perpendicular to it. Cross-calibration of mutual channels were made by rotating the whole body of the spectrometer around the line-of-sight by 45 degrees so that both channels detect the polarization components of the same amounts. In the calibration, a polyvinyl chloride (PVC: C_2H_3Cl) sheet was irradiated for various laser intensities. Calibration factor of 4.16±0.14 was obtained, showing experimental uncertainties of 3.4% of averaged value. Figure 4 shows the experimental set up and Fig. 5 shows typical spectra for various depths to the tracer.

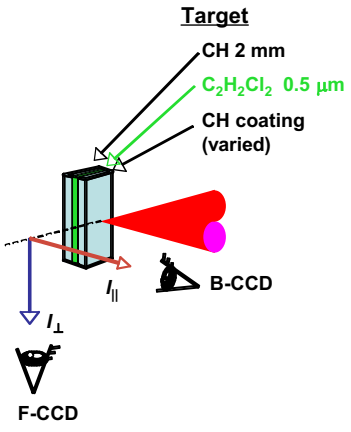

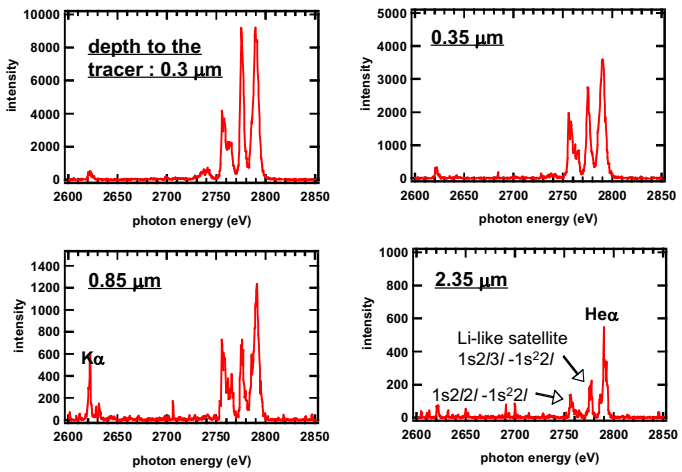

FIGURE 4. Experimental set up. **FIGURE 5.** Typical spectra for various depths to the tracer.

Polarization degrees were measured as a function of the overcoat thicknesses. This corresponds to the depth along the pre-formed plasma generated with a leakage pulse from Alisé system. Figure 6 shows dependence of polarization degree on the depth to the racer layer. Note here that the depth to the tracer layer is defined as the distance

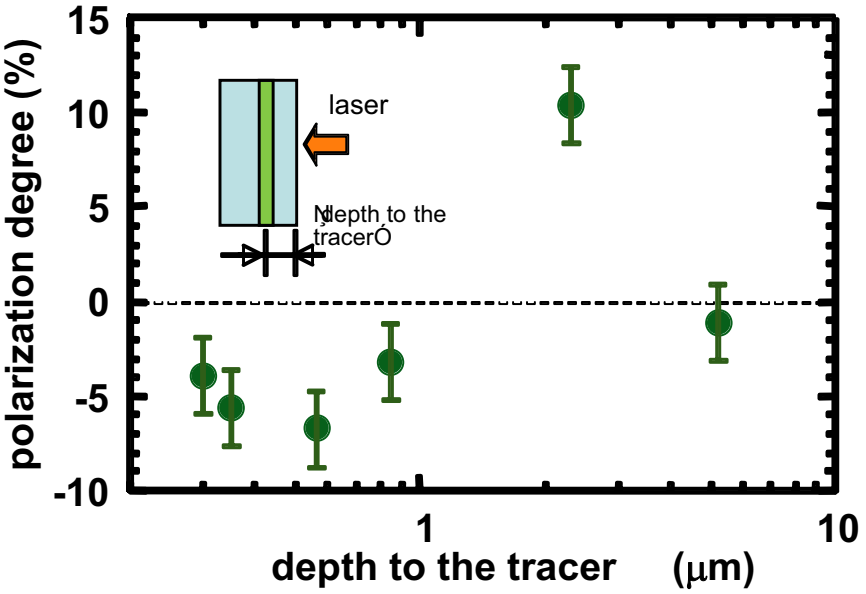

FIGURE 6. Dependence of polarization degree on the depth to the racer layer.

from the target surface to the tracer center. The polarization degree is weakly negative at the surface, becomes positive, and finally becomes zero with increase in the depth to the tracer. The result for thinner depth is consistent with the polarization measurement done at 10^{17} W/cm^2 [10, 11] where the polarization changes from -7% to +33% with increase in the overcoat thickness. Furthermore the polarization tends to be from negative to positive with increase in the depth. This trend is identical to the predictions made with the time-dependent atomic kinetics code. The de-polarization on the surface might be attributed to excessive bulk electron temperature and that in the deep region to the elastic-scattering processes by isotropic bulk electrons in dense region.

To the summary, x-ray polarization spectroscopy has been studied as a useful diagnostic tool to derive directly VDF of hot electrons propagating in the plasma created with a high intensity laser pulse. A new kinetic code dedicated for Cl Heα line polarization spectroscopy was developed to investigate the properties of hot electron VDF. X-ray polarization of Cl Heα was measured for the first time at above 10^{18} W/cm^2. The experimental results are consistent with the previous measurement at 10^{17} W/cm^2 and with the model predictions.

ACKNOWLEDGMENTS

The authors would like to appreciate Y.Kimura and T. Norimats for their contribution to target fabrication. This work was in part performed by auspice of MEXT (Japanese Ministry of Education, Culture, Sports, Science and Technology) projects on “Research on hot electron transport in ultra-high intensity laser produced plasma with x-ray polarization spectroscopy”, and “Mono-energetic quantum beam science with PW lasers”.

REFERENCES

1. Wilks S C and Kruer W L 1997 *IEEE J. Quantum Electron.* **33** 1954.
2. Sentoku Y, Mima K, Kaw P and Nishikawa K, 2003 *Phys Rev. Lett.* **90** 155001.
3. Nishimura H, *et al*., 2003, J. Quant. Spectrosc. Radiat. Transfer **81**, 327, *ibid.* 87, 211.
4. Kawamura T *et al*., 2002, Phys. Rev. **E 66**, 016402.
5. Norreys P A *et al.,* 2004 *Phys. Plasmas* **11** 2746.
6. Santos J J *et al.,* 2002 *Phys. Rev. Lett.* **89** 025001.
7. Zheng J *et al*., 2004 Phys. Rev. Lett. **92** 165001.
8. Kieffer J C *et al.,* 1992 *Phys. Rev. Lett.* **68** 480; Kieffer J C *et al* 1993 *Phys. Rev.* E **48** 4648.
9. Hakel, P., *et al*., 2004, *Phys. Rev.* E. **69**, 056405.
10. Nishimura, H *et al*., 2005, Plasma Phys. Control. Fusion **47**, B823.
11. Inubushi Y *et al*., 2006, JQSRT **99**, 305; 2007, *ibid* Phys. Rev. **E 75**, 026401.
12. Clothiaux, E.J., et al., 1997, JQSRT, **58**, 531.
13. Lombardi M and Pebay-peyroula J. C.1965, Acad. Sci., Paris, C. R.**261**, 1485.
14. Kallas Kh and Chaika M, 1969, Opt. Spectra **27**, 376.
15. Carrington C. G. and Corney A. 1969, Opt. Commun. **1**, 115.
16. Haug E, 1981, Sol. Phys. **71**, 77.
17. Beiersdorfer P and Slater M, 2001, Phys. Rev. **E 64**, 066408.
18. Kawamura T, *et al*., 2007, Phys. Rev. Lett. **99,** 115003.
19. Berrington K. A., Eissner W. B., and Norrington P. H, 1995, Comput. Phys. Commum. **92**, 290.
20. Kai T, Nakazaki S, Kawamura T, Nishimura H, and Mima K, 2007, Phys. Rev. **A 75**, 012703.
21. Jacobs, V.L., JQSRT **99**, 314-326 (2006)
22. Dyall K G, *et al*., 1989, Comput. Phys. Commun. **55**, 425.
23. Cowan R D, 1981, *The Theory of Atomic Structure and Spectra* (University of California Press).
24. Kawamura T, *et al*., in *Proceedings of the 3rd Int. Conf. of Inertial Fusion Sciences and Applications*, Monterey, 2003, 1022 (American Nuclear Society, Illinois, 2004).

Study of inner-shell excitation and relaxation processes in atomic and ionic Ne by means of soft x-ray spectroscopy

M. Oura
RIKEN SPring-8 Center, 1-1-1 Kouto, Sayo-cho, Sayo-gun, Hyogo 679-5148, Japan
e-mail: oura@spring8.or.jp

Abstract

By using soft x-ray spectroscopy, we investigate the inner-shell excitation and relaxation processes in atomic and ionic Ne targets. Resonant x-ray emission spectroscopy was applied to neutral Ne atom in the regions of the $[1s]np$ $(n = 3, 4, \cdots, \epsilon)$ excited states and $[1s2p]3pmp$ $(m = 3, 4)$ doubly excited states to obtain the spectroscopic information on the $[2p]np$ and $[2p^2]3pmp$ final electronic states, where square brackets indicate hole states. The energy levels of the $[2p^2]3pmp$ $(m = 3, 4)$ electronic states were spectroscopically measured for the first time. As for the ionic Ne target, on the other hand, the photoion yield spectroscopy was adopted to survey the $1s \rightarrow np$ $(n = 2, 3)$ resonant excitation and subsequent Auger decay processes for Ne^+ target-ions. The observed Ne^{2+} photoion yield spectrum is successfully explained by the theoretical calculations based on the multiconfiguration Dirac-Fock method.

Keywords: Ne, photoexcitation, soft x-ray emission spectroscopy, merged-beam method, MCDF calculation

1.Introduction

X-ray or soft x-ray spectroscopy is one of the powerful tools to diagnose the high temperature plasmas such as fusion and astrophysical plasmas [1-3]. For the precise plasma diagnostics, full understanding on the interaction between x-ray or soft x-ray photons and gaseous materials, including singly and multiply charged ions, is indispensable to determination of opacity as well as radiative power losses. Up to the present, with the advent of synchrotron radiation (SR) sources, in order to gain knowledge of photonic interaction with gaseous materials, the inner-shell photoexcitation / photoionization and subsequent decay processes have been extensively studied in the soft x-ray region and well understood for various atomic and molecular species [4].

As for the interaction between photons and ionic species, systematic studies of photoionization experiments on positive ions have been mostly restricted within the energy range of vacuum ultraviolet / extreme ultraviolet [5]. Very recently, K-shell photoionization experiments for multiply charged carbon ions have been successfully performed at

the Advanced Light Source (ALS) [6]. In the higher excitation energy, however, such experimental studies have been hampered due to the lack of the suitable facilities, although the experiments in the soft x-ray as well as x-ray regions are very important for many astrophysical applications. K-shell photoionization experiments on Ne^+ to Ne^{3+} ions have been rare cases, though they are not the absolute cross-section measurements [7,8] where the photoion yield spectra only for the $1s \rightarrow 2p$ resonant excitation region of Ne ions are available. In the present study, we have tried to investigate the photoionization processes of Ne^+ target-ions in the $1s \rightarrow 3p$ resonant excitation region. We also made the theoretical calculations based on the multiconfiguration Dirac-Fock (MCDF) method to interpret the resultant Ne^{2+} photoion yield spectrum observed.

Another important issue, on the other hand, for understanding on the interaction between photons and gaseous materials is the multiple excitation processes accompanying the inner-shell excitation / ionization. In particular, single-photon multielectron processes associated with the atomic inner-shell excitation / ionization had been attracting continuous interest for several decades because of its fundamental importance for understanding the intra-atomic *e-e* correlations. As for the Ne case for example, such phenomena had been studied by photoabsorption [9-16], photoemission [17-19] and Auger electron [20-22] spectroscopic methods. In the present study, we have applied the resonant soft x-ray emission (SXE) spectroscopy to atomic Ne in the regions of the $[1s]np$ $(n = 3, 4, \cdots, \epsilon)$ excited states and the $[1s2p]3pmp$ $(m = 3, 4)$ doubly excited states to obtain the spectroscopic information on the $[2p]np$ and $[2p^2]3pmp$ final electronic states.

Strictly speaking, all of these processes should be considered for the determination of opacity and radiative power losses for the precise plasma diagnostics. In this article, recent experimental results of resonant x-ray emission spectroscopy on neutral Ne atom and photoion yield spectroscopy on singly charged Ne ions are reported.

2. Experimental

The measurements were carried out on the a-branch of the soft x-ray undulator beamline BL17SU at SPring-8, an 8 GeV SR facility in Japan. This beamline is equipped with the high-resolution varied-line-spacing-plane-grating monochromator [23,24], which can provide highly-stabilized monochromatic soft x rays with resolving power $E/\Delta E$ of over 10,000. Energy calibration of the incident photon beam was performed by recording the photoion yield spectra of Ne atom in the regions of the $[1s]np$ $(n = 3, 4, \cdots, \epsilon)$ excited states and the $[1s2p]3pmp$ $(m = 3, 4)$ doubly excited states. The accuracy of energy scale for the incident photon beam was estimated to be about ± 0.1 eV for the absolute scale. In the following subsections, the setup and the procedure for different type of experiments

are described.

2.1 Resonant x-ray emission spectroscopy on neutral Ne atom

The setup for the photon-in photon-out experiment was described in detail elsewhere [25,26] ; here only a brief description is given. The x-ray spectra emitted / scattered from the target Ne atom were recorded by using the high performance slit-less spectrometer equipped with the compact flange-mounted liquid flow-cell. Although this spectrometer is originally aimed at performing the spectroscopic studies on the liquid target [27,28], the target Ne gas was introduced into the flow-cell instead of the liquid in the present study. The flow-cell utilized a 150 nm thick Au-coated Si_3N_4 membrane window which separates the flowing gas at atmospheric pressure from the high vacuum. Calibration of the spectrometer was performed by measuring the normal fluorescence emitted from the core-ionized Ne and also the elastically scattered photons from the target. The estimated energy resolution of the spectrometer was about 675 meV at a photon energy of 870 eV.

2.2 Photon-ion merged-beam experiment on singly charged Ne ions

The experimental setup was almost the same as described previously [29,30] but with a few modifications, in which a compact parallel plate electrostatic analyzer (PPEA) was added to the cylindrical mirror analyzer (CMA) to form a tandem configuration. This modification has drastically reduced the huge background noise, which originates in the charge exchange reactions between the intense primary target-ion beam and the residual gas in the active volume of the CMA, and results in an improvement of the signal to noise ratio. This configuration, however, has forced us to detect only one product-ion species at a time.

The singly charged Ne ions were produced by the 10 GHz, 200 W electron cyclotron resonance ion source (ECRIS). The typical operating RF power for Ne^+ ion production was about 10 W. The ions produced in the ECRIS were then accelerated by the extraction voltage of 6 kV, and they were transported to the interaction region. Beam size of primary beam in the interaction region was measured using the beam scanning devices. The average beam diameter was measured to be 2 mm. Photon beam size in the interaction region, on the other hand, was about 0.6 mm in diameter. In the present study, however, we did not perform the measurements for degree of overlapping of the both beam densities (form factor) due to the instability of the ECRIS. The optimum voltage set for the interaction region, the CMA and the PPEA was applied so as to detect product-ion species.

Typical intensity of the Ne^+ target-ion beam was about 120 nA which corresponds to

the target density of about 1.5×10^6 ions/cm^3, and the photon flux was estimated to be of the order of 10^{12} s^{-1} with an energy resolution $E/\Delta E$ of 1,370. In the present study, we measured the Ne^{2+} ions as the product-ion species. The signal counting rate was about 20 s^{-1} at the $1s \rightarrow 2p$ resonant excitation while the counting rate of background was about 200 s^{-1}, *e.g.* in the previous setup it was 10,000 s^{-1} for 140 nA Ne^+ target-ion beam. Signals from the PPEA were collected for 10 sec at a given photon energy and then the incident photon energy was scanned. It took about 40 minutes to achieve each scan (12 eV energy range) and it was necessary to perform several scans in the same energy range in order to establish the partial photoion yield spectrum, since the counting rate for the signal of the product-ion species was too low. In the present study, four and twenty-two scans were made for the $1s \rightarrow 2p$ and $1s \rightarrow 3p$ resonant excitation regions, respectively. All the data were normalized by the ion intensity, the photon beam intensity, and the measurement time.

3. Results and discussion

In order to interpret the excitation / relaxation properties for the processes discussed in this paper, we have carried out atomic structure calculations for making an energy diagram of the excited and relaxed states of the neutral Ne as well as the Ne ions based on the MCDF method using GRASP^2 [31], a revised version of the MCDF code [32]. Figure 1 schematically shows the calculated energy diagram for the Ne-Ne^{3+} drawn together with the typical excitation / relaxation channels. In fact, there are numerous levels, we have drawn only the typical electronic configurations, and the representative excitation / relaxation channels.

As for the resonant x-ray emission spectroscopy, the excitation / relaxation channels are depicted as A-A′ and B-B′ channels. The channel A-A′ corresponds to the photon-in photon-out process via the singly-excited intermediate core-hole state, such as the $[1s]np$ ($n = 3, 4, \cdots$) Rydberg states. The channel B-B′, on the other hand, it is the process via the doubly-excited intermediate state, *e.g.* the $[1s2p]3p^2$ state. In both cases, the electronic states involved in the processes are strictly restricted due to the dipole selection rule. The final electronic states, such as the $[2p]np$ as well as the $[2p^2]3p^2$, can be selectively studied only through this method.

As for the photon-ion merged-beam experiment, the initial states have the electronic configuration of the $[2p]$ ($J_i^\pi = 1/2^-$ or $3/2^-$) states. In the present study, we have measured the excitation / relaxation channels of C-C′ and D-D′, respectively. The channel C mainly results in the Ne^{2+} ions, but in the case of the channel D the definite fraction

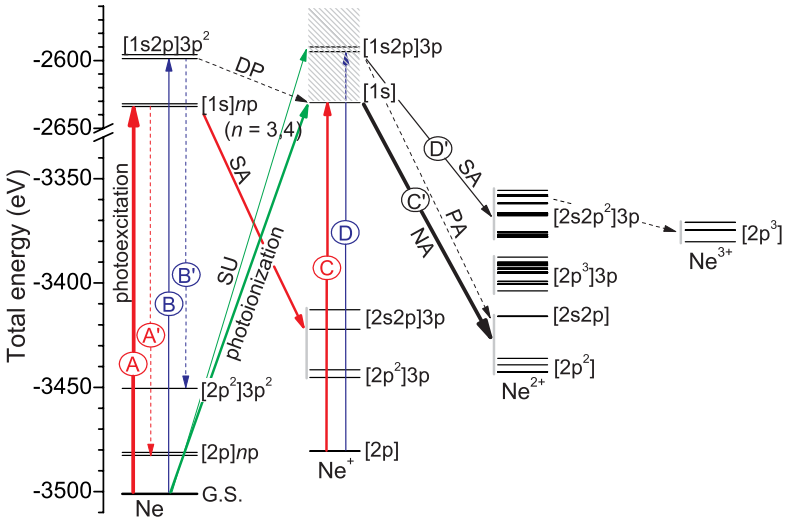

Figure 1: Calculated energy diagram of the excited and relaxed states of the neutral Ne as well as the Ne ions. The typical excitation / relaxation channels are shown as thick- or thin-solid arrows, whereas the minor channels are shown as dotted arrows. SU: shakeup, DP: double participator, NA: normal Auger, SA: spectator Auger, PA: participator Auger..

of the $[1s2p]3p$ excited states may lead to the Ne^{3+} ions through the cascade processes.

3.1 Resonant x-ray emission spectra

Figures 2∼4 show the resonant SXE spectra measured in the regions of the $[1s]np$ ($n = 3, 4, \cdots, \epsilon$) singly excited states and the $[1s2p]3pmp$ ($m = 3, 4$) doubly excited states. All the SXE spectra shown in Figs 2-4 are raw spectra, *i.e.* no correction is made for absorption by the Si_3N_4 membrane window and also for self-absorption.

In Fig.2, eight SXE spectra (lower panel) of the $[1s]np$ ($n = 3 - 5$) singly excited Ne atom measured at eight different excitation energies are shown together with the photoion yield spectrum (top panel) recorded in the same energy region. All of these SXE spectra are the spectator-type transitions, while the SXE peaks associated with the participator-type transition are out of the energy range. Lower-left panel represents the spectra measured at off-resonance (a) and on-resonance energies (b)-(d), respectively. Most of the spectra have shoulders at lower energy side, these are probably due to the strays. Red vertical lines in (a)-(c) show the energy positions of the resonant SXE peak having the $[1s]3p$ character of the intermediate state. The energy vari-

ation shown as the position shift of red vertical lines corresponds to the Raman shift. Lower-right panel, on the other hand, shows the spectra measured with the valley excitation (e)-(h), *i.e.* the excitation between two resonances. Blue vertical lines represent the energy positions of the resonant SXE peak related to the $[1s]3p$ character of the intermediate state, whereas red vertical lines are concerning with the $[1s]4p$ character. It can be clearly recognized that the intensities for both characters are comparable around 868.28 eV but the $[1s]3p/[1s]4p$ intensity ratio reverses as the excitation energy approaches the $[1s]4p$ resonance. As in the case of the resonance excitation, the energy variation shown as the position shifts of vertical lines corresponds to the Raman shift.

Figure 3(a) represents the linear dispersion for both of the resonant SXE peaks related to the $[1s]np$ ($n = 3, 4$) character of the intermediate state. Figure 3(b) shows the resonant enhancements of the intensity's variation of the SXE peaks as a function of the relative energy. Such linear dispersion as well as the resonant enhancement are the characteristic behaviour of the resonant Raman scattering, although the line-narrowing effect is not observed because the resolution of the SXE spectrometer, *e.g.* $E/\Delta E \sim 1,290$, was not good enough to extract the information for the line width. The widths of the intensity's variation curves show in Fig.3(b) are relating to the partial width of the $[1s]np$ ($n = 3, 4$) intermediate states.

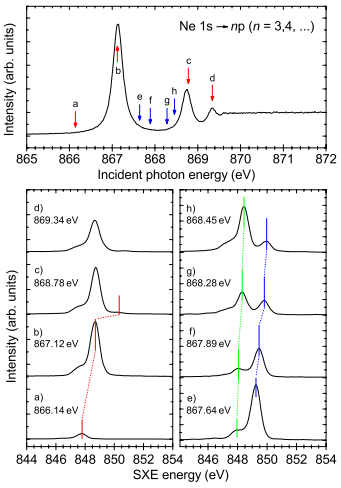

Figure 2: Soft x-ray emission (SXE) spectra (lower panels) recorded by tuning the excitation energies to the energy points indicated by arrows in the photoion yield spectrum (top panel).

Figure 4 represents the resonant SXE spectra leading to the final electronic configuration of $[2p^2]3pmp$ ($m = 3, 4$) states measured at the $[1s2p]3pmp$ double excitation resonances. The inset shows the photoion yield spectrum recorded in the energy region of the $[1s2p]3pmp$ ($m = 3, 4$) double excitation resonance. In the previous studies, Oura *et al.* have been asserting the resonance at 905.64 eV can be assigned to be $[1s2p](^1\mathrm{P})3p^2$ resonance [14,20,21], but Kato *et al.* have recently reassigned that resonance to be $[1s2p](^3\mathrm{P})3p4p$ [16]. In the present study, we can recognize three resonant peaks in the spectrum measured at 905.64 eV, thus a rigorous calculation for this spectrum might conclude a controversy for the assignment. Therefore such rigorous calculation is definitely called for.

3.2 Photon-ion merged-beam experiment

Figure 5(a) shows the experimental results of photoion yield measurements from Ne^+ target-ions to Ne^{2+} product-ions in the $843 \sim 895$ eV energy range, in which $855 \sim 881$ eV energy range is skipped because no structure is expected to be observed. The gray thin-solid-line indicates the normalized spectrum and the thick-solid-line shows the spectrum smoothed by five points smoothing method. As was mentioned previously, we did not perform the form-factor measurements in the present study due to the instability of the ECRIS. Therefore, the ordinate in Fig.5(a) is in the relative scale, but the intensity ratio between the $1s \rightarrow 2p$ and $1s \rightarrow 3p$ excitation regions reflects the ratio of the partial photoionization cross sections.

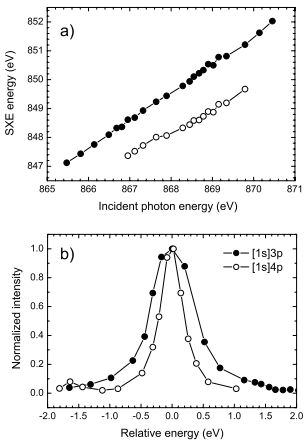

Figure 3: (a) Relationship between the incident photon energy and the peak energy of the resonant soft x-ray emission (SXE) via the $[1s]3p$ (closed circles) and $[1s]4p$ (open circles) intermediate states. Linear dispersions for the resonant SXE are clearly visible. (b) Relative intensity curves for the resonant SXE as a function of the energy relative to the resonance.

In the $1s \rightarrow 2p$ resonant excitation region, four scans were achieved to check the performance of the revised analyzer and compared the resultant photoion yield spectrum with that obtained in the previous study as shown in inset of Fig.5. With the aid of this measurement, we could confirm that the revised analyzer worked appropriately and the signal to noise ratio was improved significantly. The Ne^+ target-ions extracted from the ECRIS have initial states of the $[2p]$ ($^2P_{3/2}$ and $^2P_{1/2}$) electronic configurations. When we excite a $1s$ electron of the target-ions to the unoccupied $2p$ orbital, an intermediate state of the $[1s]$ ($^2S_{1/2}$) configuration will be produced, *e.g.* channel C in Fig.1. The electronic configuration of this intermediate state is just the same as that of the $1s$ photoionized Ne^+ ion. Therefore, we know that this state mainly relaxes through the normal K-LL Auger decays [33], *e.g.* channel C′ in Fig.1, giving rise to the Ne^{2+} product-ions [34]. Although small amount of the Ne^{3+} and Ne^{4+} ions will be also populated as the results of double and triple Auger decay processes, the Ne^{2+} ions are the dominant product-ions in the $1s \rightarrow 2p$ resonant excitation region. We notice here that such normal K-LL Auger transitions

will be observed as the resonant Auger emissions if we measure the electrons emitted from the intermediate $[1s]$ ($^2S_{1/2}$) state in the present study. Recently, Schlachter *et al.* have performed the similar photoionization study of the C^+ target-ions in the vicinity of the K-edge with much higher quality [35]. They have extracted energies, line widths and lifetimes of K-shell vacancy states for the $1s \rightarrow 2p$ inner-shell photoexcitation in C^+ ions. If we could achieve better statistics with finer resolution, we could similarly discuss such things for K-shell vacant Ne^+ ions. In the present study, however, it is unfortunate that the system resolution was not good enough for such discussions.

In the $1s \rightarrow 3p$ resonant excitation region, on the other hand, twenty-two scans were made. Although the resultant photoion yield spectrum is still in low statistics, we can recognize weak structures around 885.2 and 889.7 eV. In this case, from the analogy of the resonant Auger process for the $[1s]3p$ excited state of neutral Ne atom [36], it is expected that the spectator Auger transitions will be the leading decay processes for the $[1s2p]3p$ excited states of Ne^+ ions. If the spectator Auger decays occur, the $[2s^22p]3p$, $[2s2p^2]3p$, or $[2p^3]3p$ states will be populated as the resultant Ne^{2+} product-ions. Among them, however, the $[2s^22p]3p$ and $[2s2p^2]3p$ states are expected to decay further through the second step Auger processes which give rise to the Ne^{3+} ions as the product-ions. If the participator Auger decays take place, on the other hand, the $[2s2p]$ or $[2p^2]$ state will be the final ionic state, and in this case the Ne^{2+} ions are the plausible product-ions. But we should notice that the transition rate for the participator Auger process is much smaller than that of the spectator Auger process. Thus we may neglect the contribution of the participator Auger process here. Therefore, the observed photoion yield spectrum in the $1s \rightarrow 3p$ resonant excitation region shown in Fig.5(a) reflects the partial photoionization cross sections leading to the Ne^{2+} product-ions.

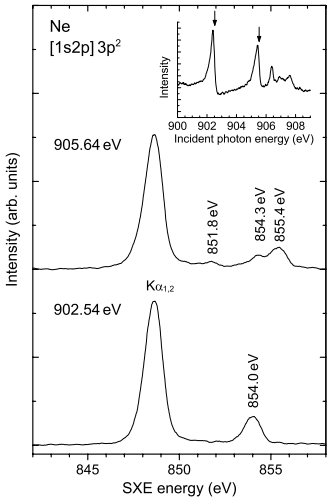

Figure 4: Soft x-ray emission (SXE) spectra measured at the $[1s2p]3p^2$ double excitation resonance of Ne atom. The inset represents the photoion yield spectra recorded at corresponding energy. The arrows in the inset depict the energy points where the SXE spectra were measured.

In order to understand the observed spectra, energy levels and dipole oscillator strengths for the $1s \rightarrow np$ $(n = 2 - 7)$ transitions were calculated using a set of codes GRASP92

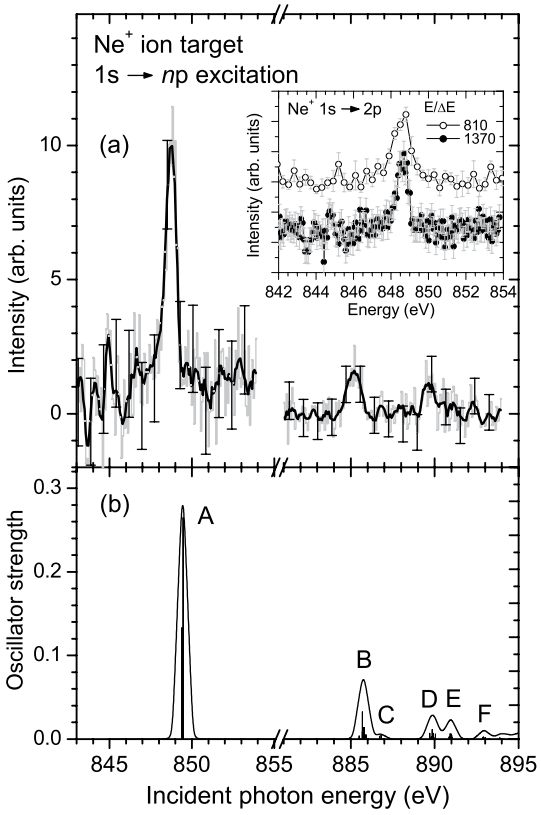

Figure 5: (a) Relative photoion yields of Ne^{2+} from Ne^{+} target-ions in the $1s \rightarrow np$ ($n = 2, 3$) resonant excitation region. (b) Calculated photoion yield spectrum for Ne^{+} target-ions in the $1s \rightarrow np$ ($n = 2-7$) resonant excitation region. Bar graph shows the oscillator strength calculated by the MCDF method. Solid curve indicates the convoluted spectrum with the overall resolution as in the present experiment. Inset shows the comparison of the Ne^{2+} photoion yield spectra recorded with different resolution of the incident photon beam in the region of the Ne^{+} $1s \rightarrow 2p$ resonance. Open circles represent the previously measured spectra with $E/\Delta E \sim 810$ [7]. Closed circles show the present results.

(General purpose Relativistic Atomic Structure Program 92) [37], which is an extension of the earlier version GRASP [32], CESD99 (a program for the Complete Expansion of jj-coupled symmetry functions into Slater Determinants) [38], and REOS99 (a program for RElaxed-orbital Oscillator Strength calculations) [39]. To obtain correctly the $1s \rightarrow np$ ($n = 2 - 7$) excitation energies and the dipole excitation functions, we need to evaluate properly (1) the contraction of the residual $1s$ electronic orbital as well as the contraction of the $2p$-subshell electronic orbitals after the $1s$ hole creation, (2) the difference in magnitudes of $2p$ intrashell correlations for initial ($[2p]$) and excited ($[1s]$, $[1s2p]np$) states of Ne^+ ions. The following procedure was applied to the present calculations. First, the Ne^+ $[2p]$ ($^2P_{3/2}$ and $^2P_{1/2}$) states were calculated to describe the initial states of the target-ions. We obtained a value $0.158a_0$ for the mean radius of $1s$ orbital, where a_0 is the Bohr radius, and $0.876a_0$ ($0.858a_0$) for the $2p$ ($2s$) orbital. For the calculation of the initial states, we considered the atomic orbitals up to $3d$ to effectively include the electron correlation effects which are encountered through the two electron excitation configurations. We peformed an additional MCDF calculation including up to all the possible two electron excitations from $2s$ and $2p$ subshells after making the MCDF calculation with a minimal orbital set. Table 1 shows the resultant ionic state functions, which are represented by the linear combination of configuration state functions, optimized for the initial states. Second, we calculated the Ne^+ $[1s]$ ($^2S_{1/2}$) excited state. Here, we have paid a special attention to the orthogonality of a correlation orbital $3s$ with the lower lying s orbitals to avoid the spurious couplings of a correlation configuration $[1s2p^2]3s^2$ with lower lying states such as the $[2p^2]3s$. We may either simply exclude the $3s$ orbital from the list of correlation orbitals or optimize the lower lying states simultaneously together with the $[2p^2]3s$. We have chosen the latter option to keep the correlation effects from $3s$ orbital still to be included in the actual numerical calculations. For the $[1s]$ excited state, we have the values $0.154a_0$, $0.816a_0$, and $0.799a_0$ for the $1s$, $2s$, and $2p$ orbital radii, respectively. We took the energy difference between these states, and we made this energy difference to be the excitation energy of the $1s \rightarrow 2p$ transition for the Ne^+ target-ions. Third, we calculated the Ne^{2+} $[1s2p]$ electronic configuration as initial vectors for the $1s$, $2s$, and $2p$ orbitals to obtain the minimal basis for the $[1s2p]np$ ($n = 2 - 7$) states. The orbitals were optimized in the framework of the MCDF method. Then the single electron orbitals were added and optimized from the lower to higher lying orbitals in stepwise. When we optimized the np ($n \geq 4$) orbitals, we fixed all the orbitals with the principal quantum numbers less than n. Finally, we calculated the energies and the oscillator strengths for the $[1s2p]np$ up to $n = 7$.

Although the GRASP provides a method of calculating the oscillator strengths between

Table 1: Optimized ionic state functions for the initial states

J_i^π	Initial state configuration
$1/2^-$	0.980 of $[2p]\ ^2\mathrm{P}_{1/2}$ + 0.002 of $[2p^3]3d^2\ ^2\mathrm{P}_{1/2}$ + 0.002 of $[2p^3]3p^2\ ^2\mathrm{P}_{1/2} + \cdots$
$3/2^-$	0.980 of $[2p]\ ^2\mathrm{P}_{3/2}$ + 0.004 of $[2p^3]3p^2\ ^2\mathrm{P}_{3/2}$ + 0.002 of $[2s2p]3d\ ^2\mathrm{P}_{3/2} + \cdots$

the electronic states, this can be achieved when we adopt a unique orthnormal set of single orbital bases. In the present calculation, we have used an alternative way to fit to the case of core-level excitation for the Ne^+ target-ions. In order to fully take account of the orbital relaxation due to the electron escape from inner-shell, the single electron orbitals for the excited states were optimized separately from the ones for the initial states. We obtained a pair of different orthonormal basis sets for excited and initial states, and they are not necessarily orthogonal. To calculate the oscillator strengths for the $1s \rightarrow np$ $(n = 2 - 7)$ excited states, the program CESD99 [38] and REOS99 [39], which apply relativistic wave functions optimized by the GRASP92 package, were adopted to properly take account of the non-orthgonality of the bases between the initial and excited states. Finally, all the transition energies were corrected using the results of the $1s \rightarrow 2p$ transition energies calculated in the second phase of the present procedure.

In Fig.5(b), we present the results of theoretical calculations. The bar graph indicates the oscillator strengths of 116 transitions for the $[1s2p]np$ $(n = 2-7)$ resonant excitations calculated based on the velocity form transition dipole matrix elements. The solid curve in the figure represents the convoluted spectrum. The calculated energy levels having oscillator strengths larger than 3×10^{-3} are summarized together with their characteristics in Table 2. According to the summary shown in Table 2, it is noticed instantly that the pronounced peak labeled 'A' in Fig.5(b) originates from the $1s \rightarrow 2p$ resonant excitations. These excitations are the inverse processes of the normal $K\alpha_{1,2}$ x-ray emission from the $1s$ vacancy state produced by photoionization of atomic Ne. The calculated transition energy of 849.44 eV reproduces well both of the present experimental result of 848.66 eV and the $K\alpha_{1,2}$ x-ray energy of 848.6 eV reported by Bearden [40]. The structure labeled 'B' consists of more than ten transitions (transitions #7 $\sim$ #21) leading to the $[1s2p](^3\mathrm{P})3p$ electronic configuration. Here we should note that the unpaired $1s$ and $2p$ electrons can couple to either a singlet or a triplet parent state, and then the outermost subshell electron couples to this parent state to yield the final state symmetry [41]. Among these transitions #7 $\sim$ #21, the transition leading to the final state of $^2\mathrm{D}_{5/2}$ has the largest contribution. The very weak structure labeled 'C', which appeared as a shoulder of the peak 'B', is assigned to be originated from the transitions leading to the $[1s2p](^3\mathrm{P})3p\ ^2\mathrm{S}_{1/2}$

Table 2: Calculated energy levels and oscillator strengths for the $[1s2p]np$ ($n = 2-6$) resonant excitations from the $[2p]$ ($^2\mathrm{P}_{3/2}$ and $^2\mathrm{P}_{1/2}$) initial states. The calculated energy levels having oscillator strengths larger than 3×10^{-3} are listed in this table. The transition numbers # correspond to the transitions in energy order. $(^3\mathrm{P})$: $[1s2p](^3\mathrm{P})$, $(^1\mathrm{P})$: $[1s2p](^1\mathrm{P})$

#	Energy (eV)	J_i^π	J_f^π	Oscillator strength	Upper state configuration
1	849.38	$1/2^-$	$1/2^+$	0.1330	0.968 of $[1s]\ ^2\mathrm{S}_{1/2}$ + 0.016 of $(^3P)3p\ ^2\mathrm{S}_{1/2}$
2	849.47	$3/2^-$	$1/2^+$	0.2648	0.968 of $[1s]\ ^2\mathrm{S}_{1/2}$ + 0.016 of $(^3P)3p\ ^2\mathrm{S}_{1/2}$
7	885.50	$3/2^-$	$5/2^+$	0.0038	0.878 of $(^3\mathrm{P})3p\ ^4\mathrm{D}_{5/2}$ + 0.076 of $(^3\mathrm{P})3p\ ^2\mathrm{D}_{5/2}$ + $\cdots$
10	885.69	$1/2^-$	$3/2^+$	0.0089	0.720 of $(^3\mathrm{P})3p\ ^2\mathrm{D}_{3/2}$ + 0.186 of $(^3\mathrm{P})3p\ ^2\mathrm{P}_{3/2}$ + $\cdots$
11	885.69	$3/2^-$	$5/2^+$	0.0325	0.823 of $(^3\mathrm{P})3p\ ^2\mathrm{D}_{5/2}$ + 0.143 of $(^3\mathrm{P})3p\ ^4\mathrm{P}_{5/2}$ + $\cdots$
14	885.77	$3/2^-$	$5/2^+$	0.0045	0.813 of $(^3\mathrm{P})3p\ ^4\mathrm{P}_{5/2}$ + 0.100 of $(^3\mathrm{P})3p\ ^2\mathrm{D}_{5/2}$ + $\cdots$
15	885.78	$3/2^-$	$3/2^+$	0.0139	0.720 of $(^3\mathrm{P})3p\ ^2\mathrm{D}_{3/2}$ + 0.186 of $(^3\mathrm{P})3p\ ^2\mathrm{P}_{3/2}$ + $\cdots$
16	885.80	$3/2^-$	$3/2^+$	0.0061	0.640 of $(^3\mathrm{P})3p\ ^4\mathrm{P}_{3/2}$ + 0.297 of $(^3\mathrm{P})3p\ ^2\mathrm{P}_{3/2}$ + $\cdots$
17	885.80	$1/2^-$	$3/2^+$	0.0139	0.510 of $(^3\mathrm{P})3p\ ^2\mathrm{P}_{3/2}$ + 0.232 of $(^3\mathrm{P})3p\ ^2\mathrm{D}_{3/2}$ + $\cdots$
19	885.81	$1/2^-$	$1/2^+$	0.0074	0.966 of $(^3\mathrm{P})3p\ ^2\mathrm{P}_{1/2}$ + 0.024 of $(^3\mathrm{P})3p\ ^4\mathrm{P}_{1/2}$
20	885.89	$3/2^-$	$3/2^+$	0.0052	0.510 of $(^3\mathrm{P})3p\ ^2\mathrm{P}_{3/2}$ + 0.232 of $(^3\mathrm{P})3p\ ^2\mathrm{D}_{3/2}$ + $\cdots$
21	885.91	$3/2^-$	$1/2^+$	0.0047	0.966 of $(^3\mathrm{P})3p\ ^2\mathrm{P}_{1/2}$ + 0.024 of $(^3\mathrm{P})3p\ ^4\mathrm{P}_{1/2}$
22	886.71	$1/2^-$	$1/2^+$	0.0034	0.889 of $(^3\mathrm{P})3p\ ^2\mathrm{S}_{1/2}$ + 0.068 of $(^1\mathrm{P})3p\ ^2\mathrm{S}_{1/2}$ + $\cdots$
23	886.80	$3/2^-$	$1/2^+$	0.0049	0.889 of $(^3\mathrm{P})3p\ ^2\mathrm{S}_{1/2}$ + 0.068 of $(^1\mathrm{P})3p\ ^2\mathrm{S}_{1/2}$ + $\cdots$
24	889.71	$1/2^-$	$3/2^+$	0.0072	0.993 of $(^1\mathrm{P})3p\ ^2\mathrm{D}_{3/2}$
27	889.85	$3/2^-$	$5/2^+$	0.0115	0.997 of $(^1\mathrm{P})3p\ ^2\mathrm{D}_{5/2}$
28	889.90	$3/2^-$	$1/2^+$	0.0071	0.794 of $(^1\mathrm{P})3p\ ^2\mathrm{S}_{1/2}$ + 0.153 of $(^3\mathrm{P})4p\ ^2\mathrm{S}_{1/2}$ + $\cdots$
29	889.93	$1/2^-$	$1/2^+$	0.0032	0.995 of $(^1\mathrm{P})3p\ ^2\mathrm{P}_{1/2}$
32	890.05	$3/2^-$	$3/2^+$	0.0062	0.992 of $(^1\mathrm{P})3p\ ^2\mathrm{P}_{3/2}$
40	890.91	$3/2^-$	$5/2^+$	0.0066	0.569 of $(^3\mathrm{P})4p\ ^2\mathrm{D}_{5/2}$ + 0.425 of $(^3\mathrm{P})4p\ ^4\mathrm{P}_{5/2}$
41	890.92	$1/2^-$	$3/2^+$	0.0032	0.488 of $(^3\mathrm{P})4p\ ^4\mathrm{P}_{3/2}$ + 0.369 of $(^3\mathrm{P})3p\ ^2\mathrm{D}_{3/2}$ + $\cdots$
45	890.99	$3/2^-$	$3/2^+$	0.0060	0.605 of $(^3\mathrm{P})4p\ ^2\mathrm{P}_{3/2}$ + 0.285 of $(^3\mathrm{P})4p\ ^4\mathrm{D}_{3/2}$ + $\cdots$
46	891.00	$3/2^-$	$5/2^+$	0.0032	0.421 of $(^3\mathrm{P})4p\ ^4\mathrm{P}_{5/2}$ + 0.317 of $(^3\mathrm{P})4p\ ^4\mathrm{D}_{5/2}$ + $\cdots$
48	891.01	$1/2^-$	$3/2^+$	0.0045	0.436 of $(^3\mathrm{P})3p\ ^2\mathrm{D}_{3/2}$ + 0.260 of $(^3\mathrm{P})4p\ ^4\mathrm{P}_{3/2}$ + $\cdots$

state (transitions #22 and #23). This state is identical to that of the shakeup satellite $3p_L$ observed in the core-level photoemission spectrum of Ne atom [18]. Thus we may expect a population of weak transitions leading to the corresponding shakeup satellite $3p_U$, which has the electronic configuration of the $[1s2p](^1\mathrm{P})3p\ ^2\mathrm{S}_{1/2}$. We can find such transition in Table 2, *i.e.* transition #28, and this transition is a member of the constituents of the structure 'D'. Averaged energy difference between these transitions leading to $3p_L$ and $3p_U$ states is found to be 3.15 eV, which is comparable to the energy difference of the shakeup satellites of 3.41 eV [18]. As we see in Table 2, the structure 'D' can be assigned to be originated from the transitions leading to the $[1s2p](^1\mathrm{P})3p$ electronic configuration. Similarly, the weak structures labeled 'E' and 'F' can be attributed to the transitions leading to the $[1s2p](^3\mathrm{P})4p$ and $[1s2p](^3\mathrm{P})5p$ electronic configurations, respectively. As can be seen in the figure, the absolute energy position for the $1s \rightarrow 2p$ resonant excitation is well reproduced by the present calculations. The calculations have also shown weak structures in the $1s \rightarrow np$ $(n = 3 - 7)$ resonant excitation region. These weak structures may be related to the observed weak structures, which are located at 885.2 and 889.7 eV in Fig.5(a), and those structures can be assigned to be the $1s \rightarrow 3p$ resonant excitations with the aid of the summary shown in Table 2.

4. Summary

With the aid of soft x-ray spectroscopy, we studied the inner-shell excitation and relaxation processes in atomic and ionic Ne targets. Resonant x-ray emission spectroscopy on neutral Ne atom was successfully applied to gain the spectroscopic information on the $[2p]np$ $(n = 3, 4, \cdots, \epsilon)$ and $[2p^2]3pmp$ $(m = 3, 4)$ final electronic states in the regions of the $[1s]np$ excited states and the $[1s2p]3p^2$ doubly excited states. The energy levels of the $[2p^2]3p^2$ electronic states was spectroscopically measured for the first time.

As for the ionic Ne target, we could record the relative photoion yields of Ne^{2+} product-ions from Ne^+ target-ions in the $1s \rightarrow np$ $(n = 2, 3)$ resonant excitation region using the photon-ion merged-beam apparatus. The observed spectrum was interpreted by the MCDF calculations successfully. The pronounced peak observed at 848.66 eV is obviously assigned to be due to the $1s \rightarrow 2p$ resonant excitation process. The weak structures observed at 885.2 and 889.7 eV are plausibly attributed to the $1s \rightarrow 3p$ resonant excitations leading to the electronic configurations of the $[1s2p](^3\mathrm{P})3p$ and $[1s2p](^1\mathrm{P})3p$, respectively.

Acknowledgement

The author is grateful to Professor F.Koike of Kitasato University for providing us the results of MCDF calculations using GRASP92 and for giving us the opportunity to carry

out the GRASP^2 calculations on his workstation. The author would like to thank to Drs. T.Tokushima, Y.Harada and H.Yamaoka of RIKEN for invaluable contributions to the experiments. The author also thanks to Drs. Y.Senba, H.Ohashi, T.Takeuchi, Mr. H.Kishimoto and Mr. T.Miura of JASRI for their technical assistance. The author is also grateful to Drs. S.Shin and T.Ishikawa of RIKEN SPring-8 Center for their understanding during the accomplishment of this experiment at BL17SU.

References

[1] Donne A J H, Barnsley R and von Hellermann M G 2008 *AIP Conf. Proc.* **1058** 195
[2] Cohen D H 2009 *AIP Conf. Proc.* **1161** 132
[3] Dasgupta A *et al* 2009 *AIP Conf. Proc.* **1161** 207
[4] See, for example, Ueda K 2006 *J. Phys. Soc. Jpn.* **75** 032001 and references cited therein
[5] Hassan N El *et al* 2009 *Phys. Rev. A* **79** 033415 and references cited therein
[6] Muller A *et al* 2009 *J. Phys. B* **42** 235602 and references cited therein
[7] Yamaoka H *et al* 2002 *Phys. Rev. A* **65** 012709
[8] Oura M *et al* 2001 *Phys. Rev. A* **63** 014704
[9] Wuilleumier F 1971 *J. Phys.* **32** C4-88
[10] Esteva J M *et al* 1983 *J. Phys. B* **16** L263
[11] Sukhorukov V L *et al* 1987 *J. Phys.* **48** 1677
[12] Hudson E *et al* 1994 *Phys. Rev. B* **49** 3701
[13] Avaldi L *et al* 1996 *J. Phys. B* **29** L737
[14] Oura M *et al* 2004 *Phys. Rev. A* **70** 022710
[15] Oura M *et al* 2004 *Phys. Rev. A* **70** 062502
[16] Kato M *et al* 2006 *J. Phys. B* **39** 2059
[17] Gelius U 1974 *J. Electron Spectrosc. Relat. Phenom.* **5** 985
[18] Svensson S *et al* 1988 *J. Electron Spectrosc. Relat. Phenom.* **47** 327
[19] Oura M *et al* 2006 *J. Phys. B* **39** 4637
[20] Oura M *et al* 2005 *J. Phys. Soc. Jpn.* **74** 1154
[21] Oura M *et al* 2007 *Radiat. Phys. Chem.* **76** 469
[22] Oura M, Senba Y and Ohashi H 2008 *Phys. Rev. A* **77** 054702
[23] Ohashi H *et al* 2007 *AIP Conf. Proc.* **879** 523
[24] Senba Y *et al* 2007 *AIP Conf. Proc.* **879** 718
[25] Tokushima T *et al* 2006 *Rev. Sci. Instrum.* **77** 063107
[26] Tokushima T *et al* 2009 *Phys. Chem. Chem. Phys.* **11** 1679
[27] Tokushima T *et al* 2008 *Chem. Phys. Lett.* **460** 387

[28] Horikawa Y *et al* 2009 *Phys. Chem. Chem. Phys.* **11** 8676
[29] Oura M *et al* 1998 *J. Synchrotron Radiat.* **5** 1058
[30] Oura M *et al* 2000 *Rev. Sci. Instrum.* **71** 1206
[31] Parpia F A, Grant I P, and Fisher C F 1992 *private communications*
[32] Dyall K G *et al* 1989 *Comput. Phys. Commun.* **55** 425
[33] Albiez A *et al* 1990 *Z. Phys. D* **16** 97
[34] Morgan D V, Sagurton M and Bartlett R J 1997 *Phys. Rev. A* **55** 1113
[35] Schlachter A S *et al* 2004 *J. Phys. B* **37** L103
[36] Aksela H *et al* 1989 *Phys. Rev. A* **39** 3401
[37] Parpia F A, Fischer C F and Grant I P 1996 *Comput. Phys. Commun.* **94** 249
[38] Fritzsche S and Anton J 2000 *Comput. Phys. Commun.* **124** 353
[39] Fritzsche S, Fischer C F and Dong C Z 2000 *Comput. Phys. Commun.* **124** 340
[40] Bearden J A 1967 *Rev. Mod. Phys.* **39** 78
[41] The triplet parent state falls at a lower binding energy and is referred to as the lower shakeup state, *e.g.* $3p_L$. Similarly, the singlet parent state locating at a higher binding energy is referred to be the upper shakeup state, *e.g.* $3p_U$.

Analyses of EUV Spectra from Xenon, Tin and Tungsten Ions Observed in LHD Plasmas

SUZUKI Chihiro, KATO Takako, SAKAUE A. Hiroyuki, KATO Daiji, MURAKAMI Izumi, SATO Kuninori, TAMURA Naoki, SUDO Shigeru, YAMAMOTO Norimasa[1], TANUMA Hajime[2], OHASHI Hayato[2], D'ARCY Rebekah[3], and O'SULLIVAN Gerard[3]

National Institute for Fusion Science, 322-6 Oroshi-cho, Toki 509-5292, Japan

1) Institute of Laser Engineering, Osaka University, 2-6 Yamadaoka, Suita 565-0871, Japan

2) Tokyo Metropolitan University, 1-1 Minami-Osawa, Hachioji 192-0397, Japan

3) University College Dublin, Belfield, Dublin 4, Ireland

e-mail: csuzuki@nifs.ac.jp

Abstract

We have measured extreme ultra-violet (EUV) spectra from highly charged xenon, tin and tungsten ions in the Large Helical Device (LHD) by a grazing incidence spectrometer. We have commonly observed broad spectral features arising from unresolved transition array (UTA) of open $4d$ subshell ions around 13.5 nm, 10.8 nm and 5.0 nm for tin, xenon and tungsten, respectively. As for tin and xenon, the broad features due to the UTA appear when the discharges are approaching radiation collapse. In stably sustained discharges, on the other hand, different spectral features with sharp discrete lines are observed. According to the comparisons with other experimental data or theoretical calculations, most of the strong discrete lines from xenon and tin have been assigned to the transitions of higher charge states with open $4s$ or $4p$ subshell ions. As for tungsten, such a feature with discrete lines has not been observed yet even if core plasma temperature is high, in contrast to the spectra observed in other tokamaks. The comparisons with theoretical calculations suggest the contribution of open $4f$ subshell tungsten ions to the smaller broad peak observed around 6 nm.

Keywords: EUV spectra, LHD, xenon, tin, tungsten, UTA, Cowan code

1. Introduction

High temperature (>1 keV) and low density ($\simeq 10^{19}$ m^{-3}) plasmas produced in the Large Helical Device (LHD) at the National Institute for Fusion Science can be considered as a characteristic light source including substantial extreme ultra-violet (EUV) emissions from highly charged ions of high-Z impurities. In the LHD plasmas, the effects of line broadening and self absorption tend to be relatively weak under optically thin conditions

in contrast to laser and/or discharge produced high density ($>10^{23}$ m^{-3}) and low temperature ($\simeq$50 eV) plasmas. Therefore the LHD plasmas have an advantage as sources of experimental databases of EUV spectra from various materials for benchmarking with theoretical calculations of spectral lines.

In this context, we have measured EUV spectra from highly charged xenon, tin and tungsten ions in the LHD by a grazing incidence spectrometer so far [1,2,3]. Recently EUV emission spectra of these materials have drawn considerable attention in the field of fusion or other industrial applications. Xenon and tin have been investigated as candidate materials in the development of EUV light source for the next generation semiconductor lithography [4], and tungsten as a plasma facing component in the forthcoming International Thermonuclear Experimental Reactor (ITER) project [5].

A number of charge states of these ions with open $4d$ subshell electrons tend to generate strong quasi-continuum emission overlaid by many lines due to $4p^6 4d^m$–$4p^5 4d^{m+1}$ + $4p^6 4d^{m-1} 4f$ transitions in the EUV wavelength regions [6]. This quasi-continuum feature is often referred to as unresolved transition array (UTA). In the LHD, the UTA features are observed especially under the conditions that the dominant ion charge states are relatively low. In addition, we observe a very different spectrum consisting of several strong discrete lines for tin and xenon when the dominant charge states are higher.

The experimental and theoretical analyses of the quasi-continuum and discrete spectral features measured in the LHD are reviewed in this study. The assignments of the spectral lines and features have been carried out by comparisons with previous articles, results from the charge exchange (CX) collisions experiments [7] or theoretical calculations with the Hartree-Fock Configuration Interaction (HFCI) code of Cowan [8].

2. Observed Spectra

The LHD is one of the largest devices for magnetically confined fusion research equipped with several superconducting helical and poloidal coils. The major and minor radii of the torus plasma are typically 3.75 m and 0.6 m, respectively, which results in a huge plasma volume ($\simeq$30 m^3). The magnetic field strength used in this study is 2.75 T at the plasma center. A small amount ($\simeq$0.1 % of bulk ion) of solid tin or tungsten was introduced into the hydrogen plasma by injecting a tracer encapsulated solid pellet (TESPEL) [9], while xenon was introduced by a gas puffing. Spatial profiles of electron density and temperature were measured by a laser Thomson scattering diagnostic system. The EUV spectra were recorded by a grazing incidence spectrometer SOXMOS [10] whose groove density and focal length are 600 mm^{-1} and 1 m, respectively. The overall spectral resolution was about 0.01 nm. The wavelength of the spectrometer was calibrated by

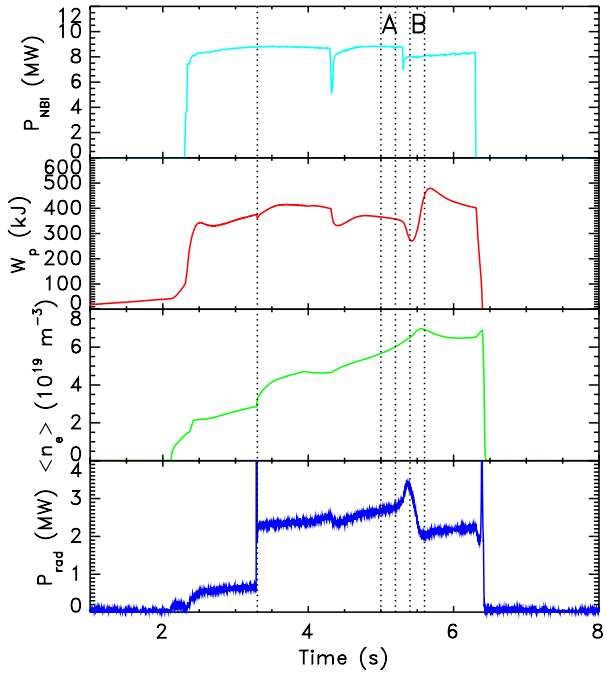

Figure 1: Time sequences of neutral beam injection (NBI) heating power (P_{NBI}), stored energy (W_p), line averaged electron density ($\langle n_e \rangle$) and total radiated power (P_{rad}) in a typical LHD discharge with a tin pellet injection at 3.3 s. The plasma was stably maintained after the pellet injection. However, the plasma was getting close to radiation collapse at around 5.4 s as indicated by a dip of the stored energy.

observing lines of the known iron and argon ions from plasmas with iron or argon injection. Consequently, we could determine the absolute wavelength with an accuracy of ± 0.01 nm.

An example of the time evolution of a discharge with a tin pellet injection is shown in Fig. 1, where neutral beam injection (NBI) heating power (P_{NBI}), stored energy (W_p), line averaged electron density ($\langle n_e \rangle$) and total radiated power (P_{rad}) are drawn. Though the total radiated power rapidly increased at the time of the pellet injection at 3.3 s, the plasma was sustained afterward because of sufficient heating power. However, it is notable that the plasma was getting close to radiation collapse at around 5.4 s as indicated in a dip of the stored energy. Temporal variations of the electron temperature measured by the Thomson scattering diagnostic indicate that a region of very cold plasma would be formed near the edge due to slight shrinking of the temperature profile during this period. This results in a drastic change in the average charge state distribution and

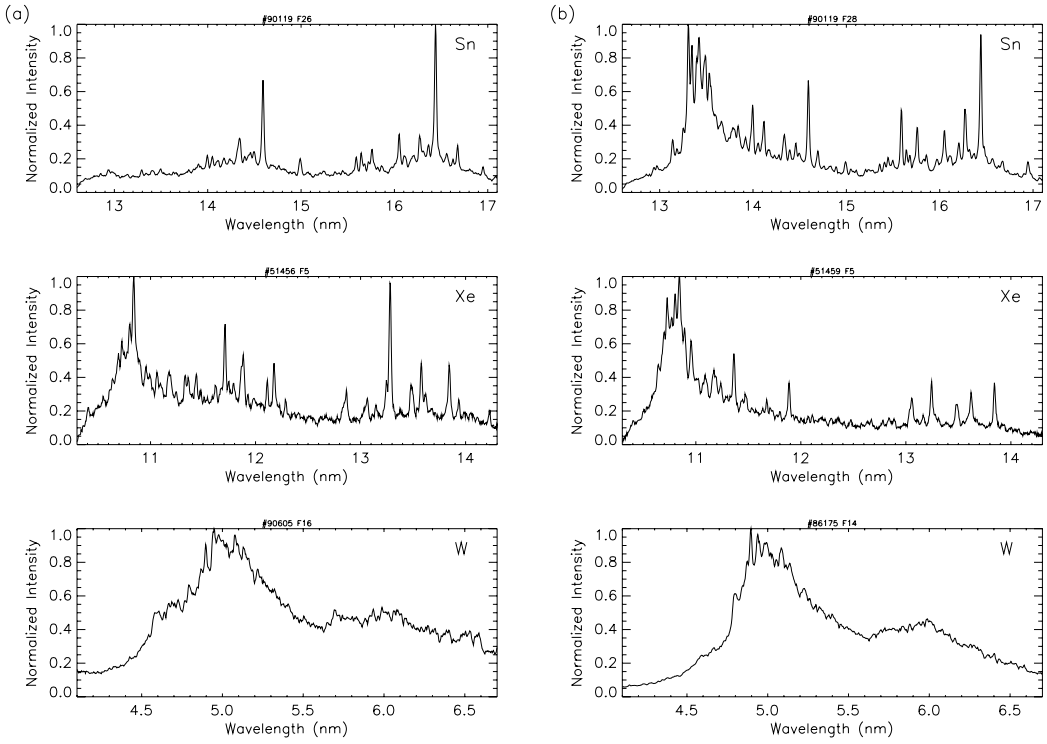

Figure 2: Typical examples of the EUV spectra of tin, xenon and tungsten ions measured (a) in high temperature stable plasmas, and (b) in low temperature plasmas approaching radiation collapse.

spectral appearance between the periods A and B indicated in Fig. 1. The EUV spectra measured during these periods are included in the top panel of Fig. 2 (a) and (b).

Figure 2 displays the typical EUV spectra of tin, xenon, and tungsten measured (a) in high temperature stable plasmas, and (b) in low temperature plasmas approaching radiation collapse. As shown in Fig. 2 (b), broad spectral features arising from the UTA of $4p^6 4d^m$–$4p^5 4d^{m+1}$ + $4p^6 4d^{m-1} 4f$ transitions of open $4d$ subshell ions are commonly observed around 13.5 nm, 10.8 nm and 5.0 nm for tin, xenon and tungsten, respectively, in low temperature plasmas close to radiation collapse. If the plasma is stably sustained, the UTA feature of tin is essentially absent and a sparse spectrum with many discrete lines is observed as shown in Fig. 2 (a). As for xenon, the discrete lines become more intense in the longer wavelength side though a trace of the quasi-continuum feature still remains around 10.8 nm. These discrete lines of tin and xenon are found to be arising from open $4p$ or $4s$ subshell ions, as described in the next section. On the other hand, the discrete feature was absent in the case of tungsten even under the higher temperature condition.

This dependence of the spectral feature on atomic number can be qualitatively explained by the difference in ionization potentials of the charge states relevant to each spectral feature of the EUV emission. In general, open $4s$ or $4p$ subshell ions contribute to the discrete line spectral feature because of smaller number of electrons and energy levels in subshells relevant to EUV emission, while open $4d$ subshell ions are related to the UTA feature because of very large number of energy levels in the subshell. The ionization potentials of open $4s$ or $4p$ subshell ions are approximately 380–620 eV and 550–830 eV for tin and xenon, respectively, and 1800–2400 eV for tungsten. Therefore it is difficult to observe the discrete spectral lines of tungsten even in higher electron temperature plasmas in LHD. However, discrete lines due to open $4s$ or $4p$ subshell tungsten ions were clearly observed in other tokamak devices [5,11]. This is primarily because electron temperature is generally higher than that in LHD.

3. Analyses

The analyses of the UTA structure for tin and xenon are not discussed here because they have already been done in detail [12,13]. In this study, most of the strong discrete lines from tin and xenon are assigned to be transitions of higher charge states with open $4s$ or $4p$ subshell ions according to comparisons with other experimental data or theoretical calculations. The most intense lines are assigned to the $4p$-$4d$ or $4d$-$4f$ transitions between excited states of Cu-like or Zn-like ions. For example, the lines of Sn XXII (Cu-like) and Sn XXI (Zn-like) identified by comparison with data from previous articles [14,15] are listed in table 1, where the wavelength reported in the previous articles are also shown. The analyses for the discrete lines of xenon ions have been done in the same way, and the results can be found in ref. [2]. The two very intense lines for tin (14.596 and 16.441 nm) are due to transitions between excited states ($4p\ ^2\mathrm{P} - 4d\ ^2\mathrm{D}$) of Sn XXII. It is noteworthy that the corresponding lines of Cu-like ions also appear for xenon as an intense doublet observed at 11.902 and 13.839 nm [2].

Since the charge state distribution for Fig. 2 (b) is expected to be lower than that for Fig. 2 (a), it is reasonably expected that lines from $4p$-$4d$ transitions of Ga-like and Ge-like tin ions are also superposed in the tin case of Fig. 2 (b). However, there is no previous data available for these ions. Hence the theoretical calculations were performed for $4p$-$4d$ transitions of Sn XX and Sn XIX ions using the Cowan code. Consequently, we have succeeded to assign most of the remaining strong spectral lines as shown in Fig. 3 where the calculated wavelengths and gf values (statistically weighted oscillator strength) are presented. The spectrum obtained in the CX collisions between Sn^{20+} and helium [16] is also plotted in Fig. 3 (c) to check the line positions of Sn XX. The calculated wavelengths

Table 1: List of the identified lines of Sn XXII and Sn XXI. The wavelengths observed in LHD and in the previous articles [14,15] are denoted by λ_{LHD} and λ_{ref}, respectively.

Ions	λ_{LHD} (nm)	Transition	λ_{ref} (nm)
Sn XXII	14.596	$4p\ ^2\mathrm{P}_{1/2} - 4d\ ^2\mathrm{D}_{3/2}$	14.6021
	15.646	$4d\ ^2\mathrm{D}_{3/2} - 4f\ ^2\mathrm{F}_{5/2}$	15.6518
	16.055	$4d\ ^2\mathrm{D}_{5/2} - 4f\ ^2\mathrm{F}_{7/2}$	16.0563
	16.441	$4p\ ^2\mathrm{P}_{3/2} - 4d\ ^2\mathrm{D}_{5/2}$	16.4360
	16.946	$4p\ ^2\mathrm{P}_{3/2} - 4d\ ^2\mathrm{D}_{3/2}$	16.9379
Sn XXI	15.764	$4p\ ^3\mathrm{P}_2 - 4d\ ^3\mathrm{D}_3$	15.7638
	16.274	$4p\ ^1\mathrm{P}_1 - 4d\ ^1\mathrm{D}_2$	16.2737

for these lines are systematically shifted by longer wavelength in comparison with the measured ones except for a line at 14.698 nm. These discrepancies can be attributed to an overestimation in Slater Condon parameters and the lack of scaling of the spin-orbit integrals in the calculation.

In the case of tungsten, the strong line group between 4.9 and 5.1 nm as shown in Fig. 2 can be attributed to the previously identified $4d$-$4f$ resonance lines of Ag- to Rh-like tungsten ions [5]. The strong $4p$-$4d$ Cu-like transitions are absent here in contrast to those of tin and xenon. Moreover, smaller broad peak structure appearing around 6 nm region is quite noticeable.

To further investigate the contribution of various transitions to the structure, detailed calculations were performed with the Cowan code. As a result, the smaller broad peak observed around 6 nm cannot be explained only by the open $4d$ subshell ions (W XXX–W XXXVIII), and the contribution of lower charge states with open $4f$ subshell ions is suggested. Figure 4 shows the line strengths (gf values) for $4d$-$4f$ (blue) and $4f$-$5d$ (red) transitions in open $4f$ W XXII–W XXVII calculated by the Cowan code. From our calculations the main contribution from $4f$-$5d$ transitions in particular W XXII–W XXV are expected to give rise to structure in the 5.5–7 nm region. This result suggests the contribution of open $4f$ subshell tungsten ions to the smaller broad peak observed around 6 nm. However, the calculated gf values for $4f$-$5d$ transitions are considerably smaller than those of $4d$-$4f$ transitions, which is not in agreement with the observation. Hence the further investigation is necessary for the assignment of this spectral feature.

4. Summary

We have summarized the present studies on EUV spectra from highly charged tin,

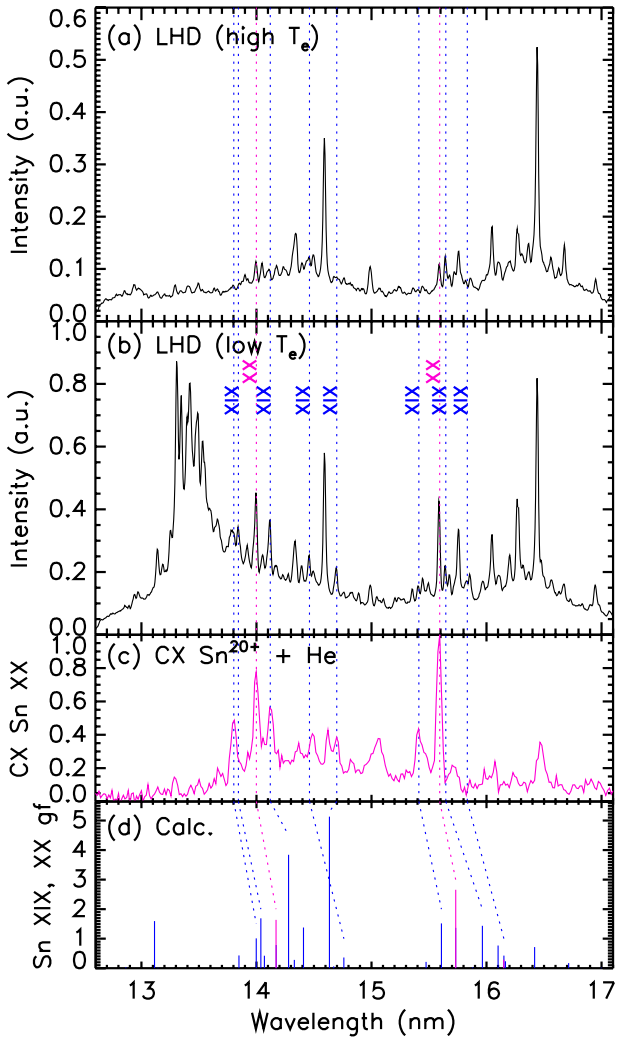

Figure 3: The measured EUV spectra (13–17 nm) during (a) 5.0–5.2 s and (b) 5.4–5.6 s in the discharge shown in Fig. 1, (c) spectrum obtained in the CX collisions between Sn^{20+} and helium gas [16], and (d) A bar graph of gf values of 4p-4d transitions of Sn XIX (blue) and Sn XX (pink) calculated by Cowan code. The assignments of the measured peaks performed by comparison with this calculation in this study are indicated by dotted lines.

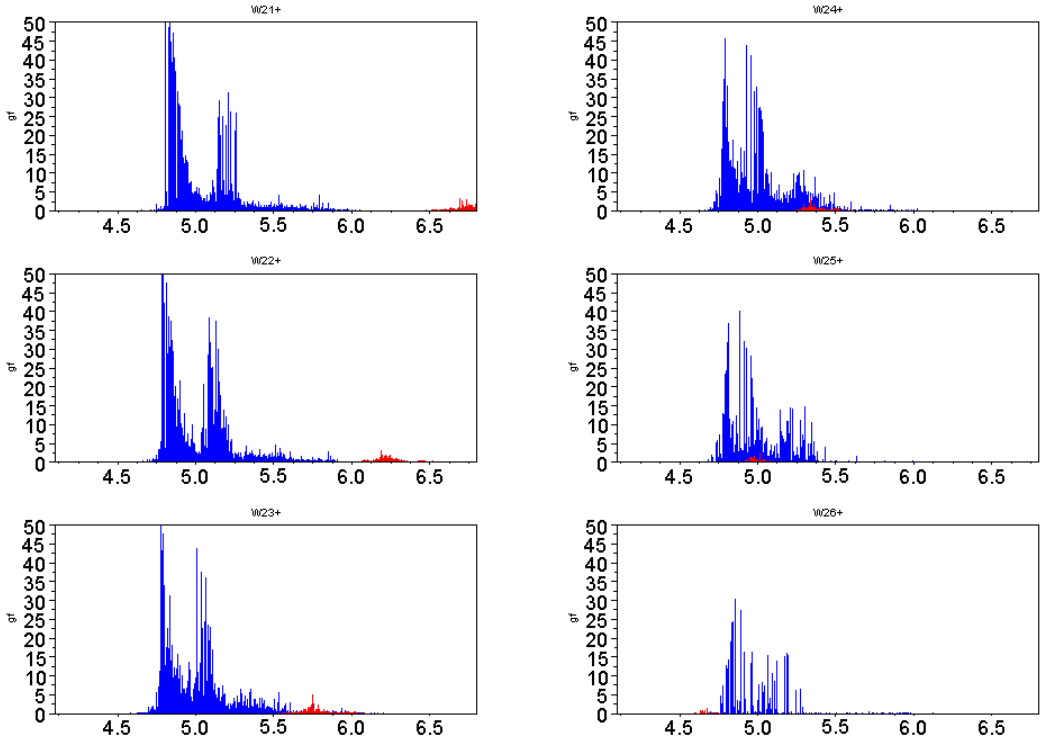

Figure 4: Calculated line strengths for $4d$-$4f$ (blue) and $4f$-$5d$ (red) transitions in W XXII–W XXVII.

xenon and tungsten ions in low density and high temperature plasmas produced in the LHD. For plasmas close to radiation collapse, quasi-continuum spectra from open $4d$ subshell ions dominate the EUV emission, while in stable discharges at higher temperature, open $4d$ subshell emission is hardly observed in the cases of tin. According to the comparisons with the other experimental data and theoretical calculations, most of the discrete intense lines were successfully assigned to the transitions between excited states from open $4s$ and $4p$ subshell ions. In the case of tungsten, emission from open $4d$ subshell ions is always present, and a feature with discrete lines has not been observed yet even if core plasma temperature is high, in contrast to the spectra observed in other tokamaks. The comparisons with theoretical calculations suggest the contribution of open $4f$ subshell ions to the smaller broad peak observed around 6 nm.

Acknowledgement

The authors acknowledge the LHD experiment group for their assistance. This work was partly supported by the MEXT under the leading project for EUV lithography source development.

References

[1] C. Suzuki et al, J. Phys.: Conf. Series, **163**, 012019 (2009).
[2] T. Kato et al, J. Phys. B, **41**, 035703 (2008).
[3] C. Suzuki et al, to be published in J. Phys. B, **43**, (2010).
[4] K. Nishihara et al, Phys. Plasmas, **15**, 056708 (2008).
[5] T. Pütterich et al., Plasma Phys. Contrl. Fusion, **50**, 085016 (2008).
[6] G. O'Sullivan and R. Faulkner, Opt. Eng., **33**, 3978 (1994).
[7] H. Tanuma et al, Nucl. Instr. and Meth. B, **235**, 331 (2005).
[8] R. D. Cowan *The Theory of Atomic Structure and Spectra* (Berkeley: University of California Press) (1991).
[9] S. Sudo, J. Plasma Fusion Res., **69**, 1349 (1993).
[10] J. L. Schwob, A. W. Wouters, and S. Suckewer, Rev. Sci. Instrum., **58**, 1601 (1987).
[11] T. Nakano et al, Nucl. Fusion, **49**, 115024 (2009).
[12] S. S. Churilov and A. N. Ryabtsev, Phys. Scr., **73**, 614 (2006).
[13] S. S. Churilov, Y. N. Joshi, J. Reader, and R. R. Kildiyarova, Phys. Scr., **70**, 126 (2004).
[14] J. Reader, N. Acquista, and D. Cooper, J. Opt. Soc. Am., **73**, 1765 (1983).
[15] C. M. Brown et al, At. Data Nucl. Data Tables, **58**, 203 (1994).
[16] H. Ohashi et al, J. Phys.: Conf. Series., **163**, 012071 (2009).

Research of the density-dependent dielectronic recombination rate coefficient of Ne-like Ni^{+18} in hot dense plasma according to the autoionization state

Wei Wang and Gang Jiang

Institute of Atomic and Molecular Physics, Sichuan University, Chengdu, Sichuan 610065, China

E-mail: arthurpandm@yahoo.com and gjiang@scu.edu.cn

Abstract

In hot dense plasma, the dielectronic recombination (DR) which greatly influences the ionization balance strongly depends on electron density. To research the precise density-dependent DR rate and provide a foundation for further study in hot dense plasmas, a method to calculate the density-dependent DR rate coefficient for highly ionized atoms is provided according to the most important atomic processes changing the population of doubly excited autoionization states. We calculate the density-dependent DR rate coefficient of Ne-like Ni^{18+} ion as one portion of our ongoing work to predict the change of DR rate with increasing electron density and to analyze the effect of those atomic processes on DR rate, which we mostly concern. The coefficient is displayed as a function of temperature at different density so that it is clearer to see the change of the resonant peak. Results show that the DR rate coefficient changes distinctly at density greater than $10^{-21}cm^{-3}$. At different temperatures, the ways by which the rate coefficients and the peaks of resonance vary with increasing density differ obviously among different channels.

Keywords: Dielectronic recombination, electron density, atomic process and autoionization state.

PACS: 34.80.Lx

1. Introduction

With the development of the fusion plasma and the improvement of the plasma generator and the measuring equipment of plasmas, people pay more and more attention to the hot dense plasma such as the plasma in Inertial Confinement Fusion and some astrophysical plasma in outer space. Advanced and sophisticated apparatuses facilitate the research of specific features in hot dense plasma such as the fluid, optical and spectroscopic properties. However, so many important physical quantities cannot be directly probed by the equipment due to the extreme physical condition, and all of those researches need large numbers of large-scale plasma simulations containing plentiful atomic data which is quite different from the data of usual plasma; thereby theoretical researches of those physical quantities based on atomic physics must be carried on. Hence the problem which physicists are facing is to discover new theories and new methods for calculations of the atomic structure and process in the plasma with high density and high temperature. However atomic physics in the dense plasma is more difficult and it is different from atomic physics of plasmas on which people have done a lot of work. That is because for any ion in the dense plasma, its interactions among electrons and ions are much stronger and more complex so that stationary states of particles and state-to-state transitions of particles get more complicated and display special features. In the

dense plasma, the rate of dielectronic recombination (DR) will change apparently [1] as the density of free electron goes up. Moreover, as one of the most important recombination processes in the dense plasma, it strongly influences the ionization balance in plasmas; besides the dielectronic satellite line is very useful in the plasma diagnosis. Even the investigation of physical effects such as the radiative transport strongly relies on the DR process. This means that in the research of hot dense plasma, it is indispensable to study the DR process and the dielectronic satellite line in the dense plasma. Therefore it is essential to gain the precise knowledge of the DR rate coefficient containing the density factor. However, it is so difficult to provide a formula using which one can obtain very accurate data about the DR rate in dense plasmas, since the atomic structure and process themselves and the connection between them which we adequately studied in low-density plasmas become more complicated in the dense plasma. Consequently, we can only research the subject from different angles step by step. Therefore, even though the real change of atomic processes is influenced by the change of the structure of ions in the dense plasma, we can firstly ignore the change of the atomic structure and only focus on the feature of atomic dynamic processes. In this way, we can provide useful theories and data which could be adopted as a basis in further and more precise researches of the hot dense plasma. So far people have done a lot of work concerning the dielectronic recombination. However, in most plasmas of interest in astrophysics, the density of electron is relatively low and ions are mostly in their ground states. Therefore, people put forward the theory of dielectronic recombination which is based on low-density coronal model [2]. This neither shows the relationship between the rate coefficient of DR and the electron density, nor provides an appreciate method to calculate the DR rate in dense plasma.

Later, from [3] to [5], people began to doubt the valid range of the formula for calculating the DR rate and put forward some new simple computing methods. In addition, their results of calculation showed that at electron density of $3\times 10^{20}\mathrm{cm}^{-3}$ and temperature of 1.0keV, the rate coefficient of DR of Ne-like selenium ions equaled $1.8\times 10^{-11}\mathrm{cm}^{3}\mathrm{sec}^{-1}$, 0.5 times that at zero density, while the rate coefficient of DR of F-like selenium ions was $1.3\times 10^{-11}\mathrm{cm}^{3}\mathrm{sec}^{-1}$, 1/3 times that at zero density. Jacobs and Davis [6] originally employed the quantum mechanical method to compute the rate of atomic dynamic processes associated with doubly excited states and obtained the rate coefficient of DR process. Then, with the development of computer, on the basis of the collisional-radiative model, Jacobs and Blaha noted that when the electron density increased, the population of ions in particular doubly excited levels greatly differed from that of low electron density because of corresponding atomic processes, and such difference strongly influenced the intensity of dielectronic satellite lines. Such theoretical results were then demonstrated by Zigler et al. in experiments [7]. In 2000, E. Behar et al. [8] calculated the total coefficient of DR of Ne-like iron ions based on the collisional-radiative model. Their results presented that when electron temperature is 200eV, the rate coefficient of DR at density of $10^{24}\mathrm{cm}^{-3}$ was twice as great as that at zero density, when the temperature is 100eV, the rate coefficient at density of $10^{24}\mathrm{cm}^{-3}$ is ten times as great as that at zero density.

These results stimulate us to consider again how the electron density influences the DR rate. Moreover, they let us accept that as the electron density increases, atomic processes able to populating or depopulating the doubly excited autoionization states effectively impacts the

rate coefficient of DR. And according to those atomic processes, we could understand how the DR rate changes with increasing electron density. To the best of our knowledge, there are few people who research the density-dependent DR rate according to those atomic processes. But in the recent research of fusion plasmas, such knowledge is quite needed. Because physical processes influencing the autoionization state is so complex plus that related competitive atomic processes will change as the parameter of the plasma varies, the population of autoionization states is so sensitive to the electron density and displays special features. However those processes can be related by the rate equation. Here in this paper, our purpose is to provide a rate equation about the doubly excited autoionization state which involves the most important processes in plasma such as radiative decay, collisional excitation, deexcitation, autoionization, electron-impact ionization and electron capture. And then, based on such equation, the formula of density-dependent rate coefficient of DR which can reflect the effect of those atomic processes on the DR rate is derived. Moreover we aim to discuss the effect of the most important two-body processes on the DR rate rather than other processes in plasma such as three-body recombination. However it can be added to our formula easily and we are now carrying on this task. Our method follows the work of E. Behar et al. [8] to which we make some modification.

We are carrying on continuous work about the density-depandent DR rate, and in this paper, our data from the calculation as representative result is used to discuss the influence of those atomic processes associated with the autoionization states on the DR rate coefficient and to predict the change of the rate coefficient of DR as the electron density and temperature vary. In other words we give and discuss the feature of the changing DR rate by concise results with adequate information rather than to compare rate coefficients of different channels. The data is displayed in the form where the DR rate coefficient is as a function of the electron temperature corresponding to different electron density so that we can not only see the rate coefficient at different plasma temperatures and density, but also see the trends of varying rate coefficients and the change of resonant peaks which cannot be shown by calculating the data only for several discrete temperatures as in [8] and [9]. With our result of calculation, one can analyze the feature of DR rate that we report, and then develop more accurate density-dependent DR rate on the basis of this result and experiment results.

2. Theory

As one of inelastic scattering processes between electrons and ions, the dielectronic recombination often can be treated as a two-step process. The first step is a resonant dielectronic capture of a free electron by the ion. The recombining ion in state m and the free electron form a doubly excited autoionization state j. Then, in the second step, since the doubly excited state is instable, the DR process is not completed until the ion decays to a singly excited state k through radiative decay or collisioanl deexcitation. In the low-density plasma the deexcitation rate is often ignored. Even though in quantum mechanics, more generally, the doubly excited state is just the intermediate state in the expansion of the cross section, the two-step description can provide us a very visual model so that we could discuss the rate coefficient of DR using the collisional-radiative model by focusing on various atomic process associated with doubly excited state.

To gain the density-dependent rate coefficient of dielectronic recombination, we need to

establish the relation between the rate coefficient and the population of the doubly excited state. In dense plasma, dynamic processes associated to the population of the doubly excited state are various ionization, combination or capture processes between discrete level and continuum level, and various transition processes between discrete levels. For simplicity, we use the bold to denote the matrix representing the rate coefficient of atomic processes and the column representing the population of discrete energy level. Thus, in steady state, the rate equation of the doubly excited state is

$$\frac{d}{dt}\mathbf{N_l} = \boldsymbol{\beta}_\mathbf{l} + (\mathbf{D_{en}} - \mathbf{D_{re}} - \mathbf{I_l})\mathbf{N_l} = 0, \tag{1}$$

where the l th row of column $\mathbf{N_l}$ is the population N_l of the l th energy level; the l th row of column $\boldsymbol{\beta}_\mathbf{l}$ is the rate coefficient of capture or combination enhancing the population of the l th energy level; the element $[\mathbf{D_{en}}]_{ll'}$ of the matrix $\mathbf{D_{en}}$ is the total rate coefficient of atomic processes enhancing N_l from level l' to level l; the element $[\mathbf{D_{re}}]_{ll}$ of the diagonal matrix $\mathbf{D_{re}}$ is the total rate coefficient of atomic processes from the level l to all other discrete levels; the element $[\mathbf{I_l}]_{ll}$ of the diagonal matrix $\mathbf{I_l}$ is the total rate coefficient of ionization from the level l. Then according to (1), the population of the doubly excited level can be written as

$$\mathbf{N_l} = (\mathbf{D_{re}} + \mathbf{I_l} - \mathbf{D_{en}})^{-1}\boldsymbol{\beta}_\mathbf{l} = \mathbf{D}^{-1}\boldsymbol{\beta}_\mathbf{l}, \tag{2}$$

where the matrix D represents all transition processes and ionization processes corresponding to the doubly excited state. Now, we need to establish the relation between the DR rate coefficient and the population of the doubly excited state. In this paper, we are interested in the effect of all transition processes and ionization processes associated with the doubly excited state on the population of the doubly excited state. All the processes considered are shown below.

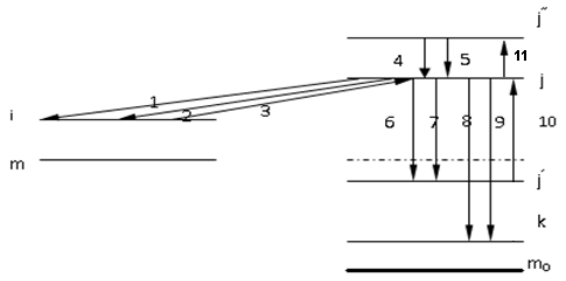

Fig 1. Effect of transition and ionization processes corresponding to doubly excited states on the doubly excited state j. 1 Autoionization, 2 electron-impact ionization, 3 dielectronic capture, 4 raidative transition from doubly excited states with higher energy to state j, 5 collisional deexcitation from doubly excited states with higher energy to state j, 6 radiative decay toward doubly excited states below the ionization limit, 7 collisional deexcitation toward doubly excited states below the ionization limit, 8 radiative decay toward stable singly excited states, 9 collisional deexcitation toward stable singly excited states, 10 collisional excitation from doubly excited states with lower energy, 11 collisional excitation from state j to doubly excited states with higher energy.

In this case, by assuming that N_j is exclusively determined by the initial capture and followed transition and ionization processes, the number of ions in unit volume which go through a dielectronic recombination process from the initial state m to the doubly excited j then to the singly excited state k is equal to N_j multiplied by the total rate coefficient of stabilizing decay. That means,

$$N_m N_e \boldsymbol{\alpha}_{\mathbf{mjk}} = \mathbf{S}\mathbf{N}_{\mathbf{j}} \tag{3}$$

where the element $[\boldsymbol{\alpha}_{\mathbf{mjk}}]_j$ of the matrix $\boldsymbol{\alpha}_{\mathbf{mjk}}$ is the DR rate coefficient from m to j then to k[9]. Additionally, because we only consider the doubly excited state, each element of the column matrix represents a doubly excited energy level. Hence the total DR rate coefficient from the initial state m is

$$\alpha_m = \sum_j \sum_k [\boldsymbol{\alpha}_{\mathbf{mjk}}]_j \quad . \tag{4}$$

Here in formula (3), the element $[\mathbf{S}]_{jj'}$ of the matrix $\mathbf{S}$ representing the total transition from the doubly excited state j to the singly excited state k is $\delta_{jj'}(A_{jk} + N_e Q_{jk})$, where A_{jk} is the rate coefficient of radiative transition from j to k, and Q_{jk} is the rate coefficient of deexcitation from j to k.

Formula (3) provides the relation between the DR rate coefficient and the population of the doubly excited state. As a result, we can obtain

$$\boldsymbol{\alpha}_{\mathbf{mjk}} = \frac{\mathbf{S}(\mathbf{D}^{-1}\boldsymbol{\beta}_{\mathbf{j}})}{N_m N_e} \quad , \tag{5}$$

where the element $[\boldsymbol{\beta}_{\mathbf{j}}]_j$ of the column matrix $\boldsymbol{\beta}_{\mathbf{j}}$ is $N_m N_e \beta_{mj}$, the rate coefficient of dielectronic capture from the state m to the state j, and the element of the matrix $\mathbf{D}$ representing the transition processes and the ionization processes of the doubly excited state is

$$[\mathbf{D}]_{jj'} = \delta_{jj'}(N_e \sum_{j'} Q_{jj'} + \sum_{j'<j} A_{jj'} + A_j^a + S_j + N_e \sum_k Q_{jk} + \sum_k A_{jk}) - N_e Q_{j'j} - A_{j'j} \quad , \tag{6}$$

where A represents the radiative transition, Q represents the collisional transition, A^a represents the autoionization and S represents the collisional ionization. Thus, formula (5) gives the method to calculate the DR rate coefficient considering the effect of all transition processes and ionization processes associated with the doubly excited state in dense plasmas. Furthermore, formula (6) shows that the DR rate coefficient is a function of the electron density.

It is noticeable that the matrix $\mathbf{D}$ is not diagonal. But while the doubly excited energy levels

are spaced so closely that the population of them are nearly the same in local thermal equilibrium,

$$[\mathbf{D}]_{jj'} = \delta_{jj'}(N_e\sum_{j'}Q_{jj'} + \sum_{j'<j}A_{jj'} + A_j^a + S_j + N_e\sum_k Q_{jk} + \sum_k A_{jk} - N_e\sum_{j'}Q_{j'j} - \sum_{j'}A_{j'j}) . \quad (7)$$

Now the matrix is diagonal. And we obtain the element of the column matrix on the left side of formula (5),

$$[\boldsymbol{\alpha}_{\mathbf{mjk}}]_j = \beta_{mj} \times \frac{A_{jk} + N_e Q_{jk}}{N_e\sum_{j'}Q_{jj'} + \sum_{j'<j}A_{jj'} + A_j^a + S_j + N_e\sum_k Q_{jk} + \sum_k A_{jk} - N_e\sum_{j'}Q_{j'j} - \sum_{j'}A_{j'j}} . \quad (8)$$

This is a new formula like the original formula of DR rate coefficient in plasmas with low electron density[10], but representing a very different meaning.

3. Calculation of Ne-like Ni ions

Our goal here is not to provide extremely accurate data about the rate coefficient of DR of Ne-like Ni ions. Instead, we emphasize the trend of how the coefficient changes with increasing electron density considering the effect of the transition processes among doubly excited states and the ionization processes corresponding to the doubly excited state. Our results of calculation are made by modified Cowan Code (RCN34/RCN21/RCG91) to which so many new codes has been added by the author. Because it is time consuming to combine different programs for carrying out our calculation or to explore totally new codes, we temporarily use formula in [11-12] to compute the rate coefficient of collisional deexcitation and ionization in the modified Cowan Code to calculate the rate coefficient of DR. It is notable that although such formula may not give extremely precise data, but it is demonstrated that such formula can considerably accurately depict the feature and shape of varying rate coefficients and the tendency of how those coefficients vary with changing parameters such as temperature.

Since the effect of those atomic processes on the DR rate will be quenched for ions with very high ion charge as [9] reported, we do not provide the data of ions with high ion charge for it cannot clearly show the feature reflecting the electron density. Our results of calculation are the representative rate coefficients of DR of Ne-like Ni ions through the recombination channel 2p-3d and 2p-4d, for reports of such ions are widespread, and we found the data of such ions could sufficiently display the trends of the changing DR rate with increasing density.

Indeed, it is difficult to figure out which channel of DR is important and representative, so summing results of different channels as many as possible is a good method to give precise data. And this way is also more convenient for comparing results of theoretical calculation with data from experiments. However, this method may be not suitable for providing the tendency of how the rate coefficient varies with changing parameters. That is because the summation of many coefficients of different channels will conceal some important features of the way by which DR rate changes with increasing electron density. On the other side of the coin, we cannot totally rely on the DR processes through state-to-state channels. The reason is that under the modern framework of calculating atomic structure, the computer cannot provide enough precise data about atomic quality of the vector in rigged Hilbert space

containing continuum states. It is impractical to analyze the effect of electron density on DR rate according to the case of individual state-to-state channel. Our aim here is not to discuss the difference of the DR rate among various channels but to give and discuss the feature of the DR rate influenced by those atomic processes with increasing electron density by concise results with adequate information. We hereby provide the data of 5 particular channels of 2p-3d (3p, 3d, 4p, 4d) and 2p-4d (4d) of Ne-like Ni ions and their total, since they can clearly represent the common features of other channels, and reveal some problems.

Table 1. Rate coefficient of DR of Ne-like Ni ions through the channel 2p-3d (total channel with spectator electron 3p, 3d, 4s, 4p and 4d)

	Rate coefficient of DR(cm^3sec^{-1})						
T_e (kev)	$N_e(cm^{-3})0\sim10^{18}$	$N_e(cm^{-3})10^{19}$	$N_e(cm^{-3})10^{20}$	$N_e(cm^{-3})10^{21}$	$N_e(cm^{-3})10^{22}$	$N_e(cm^{-3})10^{23}$	$N_e(cm^{-3})10^{24}$
0.2	1.93211E-11	1.92501E-11	1.91331E-11	1.90831E-11	1.89922E-11	1.89391E-11	1.98773E-11
0.3	1.96918E-11	1.96438E-11	1.95148E-11	1.94488E-11	1.93829E-11	1.92717E-11	1.95859E-11
0.4	1.75042E-11	1.74732E-11	1.73622E-11	1.72892E-11	1.72372E-11	1.7151E-11	1.78621E-11
0.5	1.51189E-11	1.50989E-11	1.50109E-11	1.49379E-11	1.48959E-11	1.48396E-11	1.54708E-11
0.6	1.30386E-11	1.30256E-11	1.29566E-11	1.28856E-11	1.28516E-11	1.32448E-11	1.30925E-11
0.7	1.13179E-11	1.13089E-11	1.12539E-11	1.11879E-11	1.11579E-11	1.1087E-11	1.16608E-11
0.8	9.9073E-12	9.9003E-12	9.8573E-12	9.7953E-12	9.7703E-12	9.7143E-12	1.10414E-11
0.9	8.74827E-12	8.74227E-12	8.70827E-12	8.65327E-12	8.62927E-12	8.58031E-12	8.53526E-12
1	7.78911E-12	7.78511E-12	7.75711E-12	7.70631E-12	7.68331E-12	7.64194E-12	7.65568E-12
1.1	6.98627E-12	6.98327E-12	6.96127E-12	6.91347E-12	6.89347E-12	6.85859E-12	6.81824E-12
1.2	6.30912E-12	6.30712E-12	6.28812E-12	6.24522E-12	6.22533E-12	6.19504E-12	6.15409E-12
1.3	5.73162E-12	5.72962E-12	5.71362E-12	5.67562E-12	5.65572E-12	5.63703E-12	5.60658E-12
1.4	5.23615E-12	5.23415E-12	5.22115E-12	5.18625E-12	5.16825E-12	5.14676E-12	5.11332E-12
1.5	4.80807E-12	4.80607E-12	4.79507E-12	4.76217E-12	4.74518E-12	4.72568E-12	4.68994E-12
1.6	4.43237E-12	4.43137E-12	4.42147E-12	4.39227E-12	4.37527E-12	4.35888E-12	4.33574E-12

Table 1 shows the rate coefficient of DR through the channel $e+1s^22s^22p^6 \Leftrightarrow 1s^22s^22p^53dnl \rightarrow 1s^22s^22p^6nl$. In general, the data clearly shows the enhancement of the coefficients as the electron density increases at temperatures lower 900eV, and reduction at temperatures greater than that value. For fixed density, the coefficients go up to some peaks and then decrease. Under the case, the peak shows the property of the nature of resonance of the DR process. However, the change of rate coefficient of DR in the table does not show some very sharp features which could be displayed in following figures of specific channels. It should be noted that only sharp features shown in specific channels can provide sufficient description of our work as the foundation for further research.

Figures 2 to 10 are respectively rate coefficients of channels of 2p-3d with spectator 3p, 3d, 4p and 4d, and channels of 2p-4d with spectator 4d.

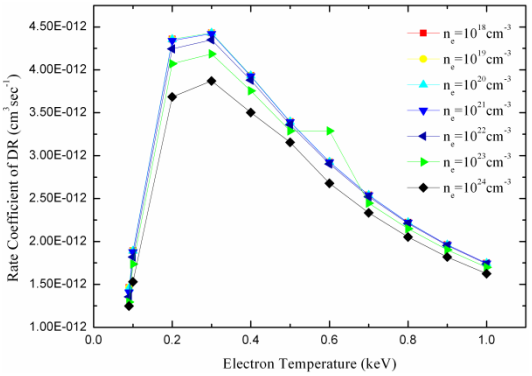

Fig 2. Rate coefficient of DR of Ne-like Ni ions through the channel 2p-3d with spectator electron 3p

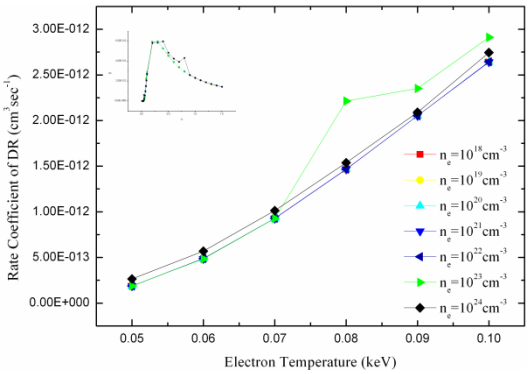

Fig 3. Rate coefficient of DR of Ne-like Ni ions through the channel 2p-3d with spectator electron 3d at temperatures lower than 0.1 keV

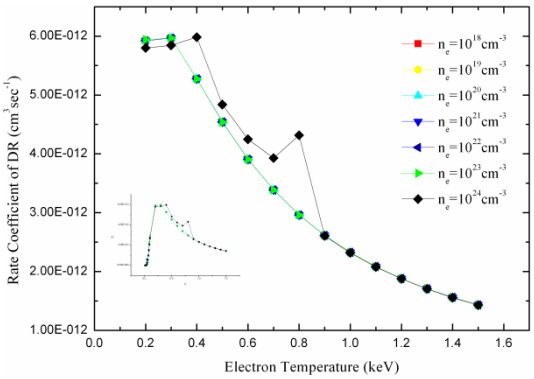

Fig 4. Rate coefficient of DR of Ne-like Ni ions through the channel 2p-3d with spectator electron 3d at temperatures greater than 0.1 keV

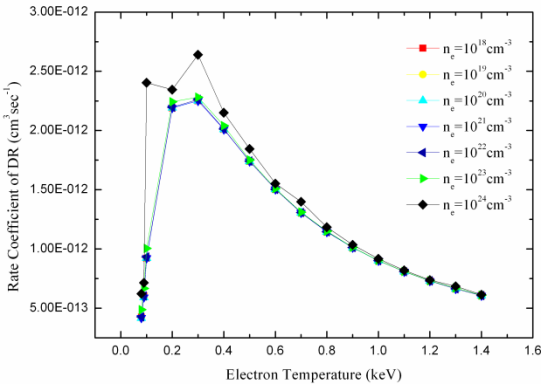

Fig 5. Rate coefficient of DR of Ne-like Ni ions through the channel 2p-3d with spectator electron 4p

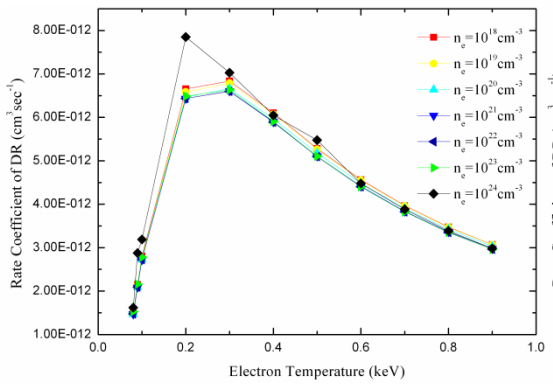

Fig 6. Rate coefficient of DR of Ne-like Ni ions through the channel 2p-3d with spectator electron 4d

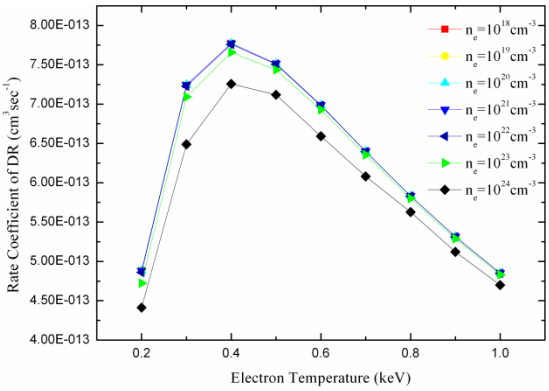

Fig 7. Rate coefficient of DR of Ne-like Ni ions through the channel 2p-4d with spectator electron 4d

In figure 2, we can see that the rate coefficient of DR generally decreases at all temperatures with increasing electron density except at a short range of temperature from 0.4

keV to 0.7 keV. Furthermore, the increase of the rate coefficient happens only for electron density of $10^{23}cm^{-3}$, i.e. it is not monotonically increasing. Not like figure 2, the increase of the coefficient in figure 3 corresponds to a different and larger range of temperature, from temperature lower than 0.05 keV to temperature equal to 0.9 keV. However, from both figure 2 and figure 3, we can see that the rate coefficient of DR decreases with increasing electron density at temperatures greater than some specific value, and as the temperature goes up, the coefficient change caused by the density gets quite small. If one turns to figure 4 and 5, he will find that except for the feature discussed above, there are changes of the resonant peak in the two figures. The change of the resonant peak contains the change of the position of the peak and the value of the peak. Then, figure 6 and 7 show that the ranges of the enhancement of the rate coefficient of DR by electron density are different among different channels and for specific channels the ways by which the coefficient changes with the increasing density are quite different, for instance the coefficient in figure 7 shows monotonically decrease at all temperatures as electron density goes up. To sum up, the feature of the trend of changing rate coefficient of DR with increasing density can be concluded as that for specific channels there are certain ranges of temperature (normally from 0.1 to 1.0 keV) at positions within which the coefficients change distinctly and the ways by which the coefficients change correspond to the channels, besides we observe increase of the coefficient at lower temperatures while we see decrease of that at temperatures greater than some value, accompanying with those features we see the change of the number, the position and the value of the resonant peak of the coefficient. Those features shown in the six figures reflect the density-dependent change of the rate of state-to-state DR process. The reason why there are some enhancements of DR rate coefficient by the density effect is that collisional processes transfer the ions from levels with strong autoionization rates to levels with lower autoionization rates but with not quite different radiative rates. The fact that at temperatures higher than some value, the rate coefficient will decreases as the density goes up can be attributed to that the ionization rate will increase apparently with increasing temperature while the stabilization rate will not. When the branching ratio of DR does not contain those atomic processes which will change as the temperature varies, the formula of the rate coefficient of DR has the factor of temperature $e^{-E_j/kt_e}/T_e^{3/2}$. This mathematically clarifies that the resonant peak of DR has the position of temperature dependent on the energy of specific level, and the value of the peak dependent on those atomic processes associated with the doubly excited state. However, under our framework to calculate the DR rate, we have considered the temperature-dependent collisional processes that will contribute to the population of the doubly excited state. Consequently, for each state-to-state DR channel with different energy, the position and value of the resonant peak will be affected not only by the energy but also by the branching ratio as a function of electron temperature. Furthermore, the density effect will enhance the influence of the branching ratio to the resonant peak. This provides a simple explanation of the special features in figure 4 and 5, but detailed and accurate analysis of this question needs more advanced calculations of the atomic structure in order to provide convincing reasons concerning the relationship between the coefficient of the state-to-state DR process and the increasing electron density.

4.**Conclusion**

In this paper, we aim to discuss the density-dependent DR rate coefficient according to the autoionization state by focusing on the effect of the transition and ionization processes corresponding to the doubly excited states on the DR rate with increasing electron density. On the basis of our method and results, one can carry on the essential further research on the subject. We use a formula to calculate the rate coefficient of DR containing the electron density factor based on the collisional-radiative model according to the autoionization state. Then by the calculation of Ne-like Ni ions, we predict some important features of the changing DR rate coefficient. We display rate coefficients of several channels as functions of the electron temperature corresponding to different electron density. These data display the common features of the changing rate and reveal some problems. Those problems need more advanced calculations of the atomic structure to more reasonably explain. Moreover we found that the for specific channels there are certain ranges of temperature at positions within which the coefficients change distinctly and the ways by which the coefficients change correspond to the channels. In addition, we find increase of the coefficient at lower temperatures while we see decrease of that at temperatures greater than some value, besides there is the change of the number, the position and the value of the resonant peak of the coefficient. We owe such features involving the change of the resonant peak to the effect of atomic processes associated with the autoionization states. The factor determining the position and the value of the resonant peak is impacted by those atomic processes. Thus our method and results can provide a basis for the further study of accurate atomic data in the research of hot dense plasma.

Reference

[1] Glenger SH et al 1999 *Phys. Rev. Lett.* **82** 97

[2] Seaton M J and Storey P J 1976 *Atomic Processes and Applications* ed P G Burke and B L Moiseiwitsch (North Holland, Amsterdam) p133

[3] Goldberg L and Dupree A K 1967 *Nature* **215** 41

[4] Burgess A and Summers H P 1969 *Astrophys. J.* **157** 1007

[5] Hagelstein P L and Rosen M D 1986 *Phys. Rev.* A **34** 1931

[6] Jacobs V L Blaha M 1980 *Phys. Rev.* A **21** 525

[7] Zigler A, Jacobs V L, Newman D A, Burkhalter P G, Nagel D J, Luk T S, McPhersom A, Boyer K and Rhodes C K 1992 *Phys. Rev.* A **45** 1569

[8] Behar E, Doron R, Mandelbaum P, Schwob J L and Jacobs V L 2000 *JQSRT* **65** 83

[9] Behar E, Doron R, Mandelbaum P and Schwob J L 2000 *Phys. Rev. A* **61** 062708

[10] Shore Bruce W 1969 *Astrophys. J.* **158** 1205

[11] Regemorter H V 1962 *Astrophys. J.* **136** 906

[12] Younger S M 1981 *Phys. Rev.* A **24** 1272

Influence of Debye plasma on the KLL dielectronic recombination of H-like helium ions

Zhang Denghong [1], Dong Chenzhong [1,2],Jiang Jun[1] and Li Bowen[1]

1) College of Physics and Electronic Engineering, Northwest Normal University, Lanzhou 730070, China

2) Joint Laboratory of Atomic and Molecular Physics, NWNU & IMP CAS, Lanzhou 730070, China

e-mail: dongcz@nwnu.edu.cn

Abstract

By using the Debye shielding model, the effects of plasmas screening on dielectronic recombination processes of the H-like helium ions are investigated. It is found that plasmas screening can change the Auger decay rate of the doubly excited $(2p_{3/2}^2)_2$ state remarkably. As a result, the dielectronic recombination cross sections from the $(2p_{3/2}^2)_2$ doubly excited state increases with decreasing of the Debye length.

Keywords: dielectronic recombination, plasma screening, electron correlation

1.Introduction

With the development of new application for x-ray radiation from hot plasmas, the field of atomic physics in hot and dense plasma environments has gained rapid progress in recent years[1,2,3].In contrast to free ions in vacuum, the atomic/ionic potential in hot plasma will be screened by the surrounding ions and fast electrons. Such screening will alter the electrons wavefunctions of ions embedded in a plasma, and therefore influence on its energy levels and decay properties[4].

Dielectronic recombination (DR) can play important role in the determination of the ionization balance of high temperature plasmas and in the formation of excited state population[5]. Knowledge of DR cross sections is, therefore, necessary for theoretical modeling of plasmas, whether in the laboratory or in astrophysical sources such as the solar corona. DR also leads to the satellite lines emission that are observed in many high temperature and density plasmas such as tokamaks and inertial-confinement fusion (ICF) plasmas, which are highly useful for plasma diagnostics. DR can be regarded as a resonance radiative recombination process, in which an electron undergoes radiationless capture into an autoionizing doubly excited state and subsequently the doubly excited state stabilizes by radiative decay. Recently, some investigations have shown that hot and dense plasma environments can effect on energy level structure and decay properties of the

doubly excited state[3,6,7,8,9]. Therefore, one can expect that plasma should influence the dielectronic recombination process.

In the present work, the influence of the plasmas screening is investigated for the KLL dielectronic recombination of H-like Helium ions in the framework of the multi-configuration Dirac-Fock (MCDF) theory. In order to model a weakly coupled hot plasma, a Debye-Hückel potential has been used.

2. Theoretical methods

In this work all the atomic calculations are determined within the relativistic formalism of the self-consistent multi-configuration Dirac-Fock (MCDF) equations. The MCDF approximation of atomic states and transitions among them has been described in detail in literature (see, e.g., [10], and reference therein). This model for the electronic structure of free atoms and ions has been implemented, for instance, in the GRASP92[11]. Only a brief outline of the theory is given bellow.

In the MCDF model, an atomic state wavefunction (ASF) is represented as a linear combination of configuration state functions (CSFs) with same parity P and angular momentum (J, M)

$$\psi_\alpha(PJM) = \sum_{r=1}^{n_c} c_r(\alpha)\,|\gamma_r PJM\rangle, \tag{1}$$

where n_c is the number of configuration state wavefunction (CSF) and $\{c_r(\alpha)\}$ are configuration mixing coefficents of the atomic state in this basis. The CSFs are antisymmetrized products of a common set of *orthonormal* orbitals which are optimized on the basis of the relativistic Dirac-Coulomb Hamiltonian.

In order to describe the plasma shielding effects on the electronic properties, the Dirac-Coulomb Hamiltonian will be modified the following form

$$H_{DC} = \sum_i (c\alpha \cdot \mathbf{p} + \beta c^2) + (\sum_i V(r_i) + \sum_{i>j} \frac{1}{r_{ij}}) e^{-\frac{r_i}{\lambda}}. \tag{2}$$

It include a Debye-Hückel potential,which can be considered to represent well the plasma effect between charged particles.Here λ is called Debye shielding length and it is a function of temperature and density of the plasma, given by

$$\lambda = [\frac{kT_e}{4\pi n_e}]^{1/2}. \tag{3}$$

where T_e and n_e are the plasma electron temperature and density, respectively, and k is the Boltzmann constant. Therefore, different plasma conditions can be simulated by changing suitably the screening parameters.

The DR strength S_{ijk} is given by[12]

$$S_{ijk}(\varepsilon_j) = \frac{\pi^2}{\varepsilon_j}\frac{g_j}{2g_i}\frac{A^a_{ji}A^r_{jk}}{\sum_{k'}A^r_{jk'} + \sum_{i'}A^a_{ji'}} \tag{4}$$

where ε_j is the free electron energy;Ar_{jk} is the Einstein coefficient for spontaneous radiative decay from the excited state j to the final state k while Aa_{ji} is the rate for autoionization from the resonant state j to the non-resonant electron-continuum state i.

The convoluted cross section is given by [13]

$$\sigma_t{}^{DR}(\varepsilon) = \sum_{j,k}\frac{S_{ijk}(\varepsilon_j)}{\sqrt{2\pi}\Gamma}\exp\left[-\frac{(\varepsilon-\varepsilon_j)^2}{2\Gamma^2}\right] \tag{5}$$

3. Results and discussion

In order to show our calculation reliability, as an example, we list the calculated values of eigenenergies and widths of the doubly excited $(2p_{1/2}2p_{3/2})_2$ and $(2p^2_{3/2})_2$ state in plasmas for different Debye shielding length λ in Table 1. For the purpose of comparison, other authors' results[8,9,14-16] are also presented. It is found that the agreement with other calculation is good in general,especially for eigenenergies.

Table 1: The eigenenergies and widths of doubly excited state $(2p_{1/2}2p_{3/2})_2$ and $(2p^2_{3/2})_2$ of helium atom in plasmas for different Debye shielding length λ in atomic units.

	$(2p_{1/2}2p_{3/2})_2$				$(2p^2_{3/2})_2$	
	-E		Γ		-E	
λ	This work	Ref.[8]	This work	Ref.[8]	This work	Ref.[9]
∞	0.700	0.702	2.60[-3]	2.35[-3]	0.70955	0.7105
				2.24±0.4[-3][a]		0.7105[b]
						0.70999[c]
100	0.667	0.672	2.57[-3]	2.35[-3]	0.67706	0.68081
50	0.635	0.643	2.53[-3]	2.34[-3]	0.64557	0.65173
30	0.594	0.605	2.47[-3]	2.32[-3]	0.60506	0.61390
20	0.546	0.560	2.38[-3]	2.29[-3]	0.55671	0.56810

[a]Ref.[14]
[b]Ref.[15]
[c]Ref.[16]

The DR cross sections of the H-like helium ions for KLL resonance in plasmas for different Debye shielding length λ are given in Fig.1. It can be seen that the DR spectroscopy is divided into three peaks, mainly from the $2s_{1/2}2p_{1/2}$, $2p_{1/2}2p_{3/2}$ and $2p^2_{1/2}$ doubly excited states. With the decreasing of the Debye shielding length, all of those peaks shift

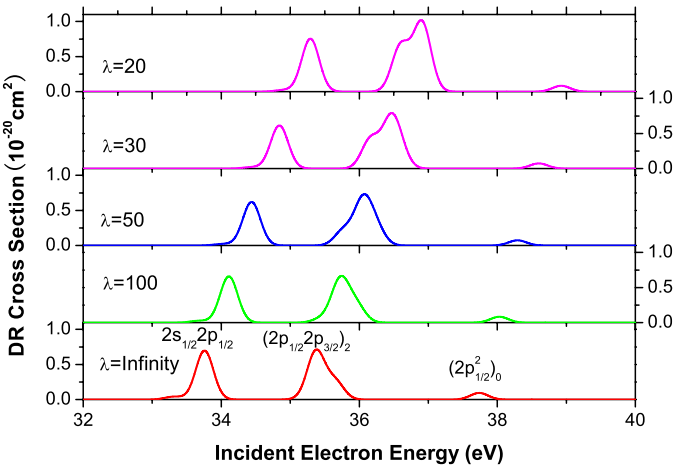

Figure 1: The KLL Dielectronic recombination cross of the H-like Helium ions as function of incident electron energy for the different Debye shielding length λ in atomic units.

to high energy. As far as the shape of peaks is concerned, the left and right peak are not almost changed but the left shoulder of the middle peak rises gradually when the Debye shielding length decreases. From the energy position, the left shoulder of the middle peak correspond to the doubly excited state $(2p^2_{3/2})_2$.

In Fig. 2, we plot eigenenergies of the doubly excited states $(2p^2_{3/2})_2$ and $(2p_{1/2}2p_{3/2})_2$ of helium atom versus the inverse of Debye shielding length λ. It can be seen that the energy levels of both states will shift to continuum with the decreasing of Debye shielding length λ. It will lead to more stronger correlation between the doubly excited $(2p^2_{3/2})_2$ and $(2p_{1/2}2p_{3/2})_2$ states. As seen in Fig.3, We plot configuration mixing coefficients of the $(2p^2_{3/2})_2$ state versus the inverse of the Debye shielding length λ for helium atom in Fig.3. It can be seen that the excited $(2p^2_{3/2})_2$ state mainly includes the contribution from the $(2p_{1/2}2p_{3/2})_2$ state. With the decreasing of the Debye shielding length λ, the mixing coefficient of the excited $(2p^2_{3/2})_2$ state decreases gradually, however, the mixing coefficient of the excited $(2p_{1/2}2p_{3/2})_2$ state increases. In Fig. 4 and Fig. 5,we plot Auger rates versus the inverse of the Debye shielding length λ for the doubly excited $(2p_{1/2}2p_{3/2})_2$ and $(2p^2_{3/2})_2$ states, respectively. It can be found the Auger rate of the excited $(2p_{1/2}2p_{3/2})_2$ state decreases while the Auger rate of the excited increases, with the decreasing of the Debye shielding length λ. It can be also found that the excited $(2p_{1/2}2p_{3/2})_2$ state have very large Auger decay rate, reaching to the order of magnitude 10^{14}, while the Auger

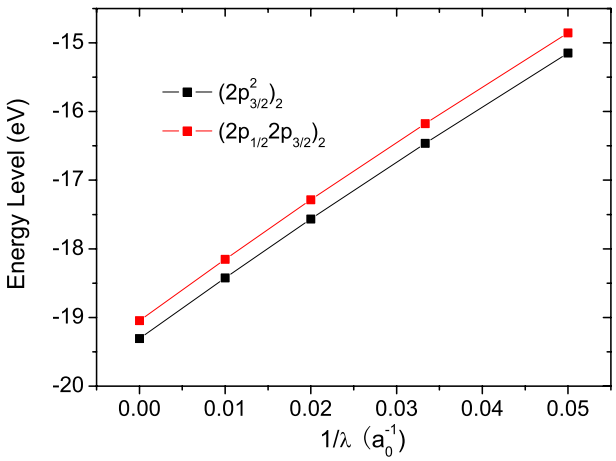

Figure 2: The energy level as function of the inverse of Debye shielding length λ for doubly excited states $(2p_{3/2}^2)_2$ and $(2p_{1/2}2p_{3/2})_2$ of helium atom.

rate of the excited $(2p_{3/2}^2)_2$ state is relatively small at the case of no plasma shielding, i.e., $\lambda = \infty$. With the reducing of the Debye shielding length λ, the component of the excited $(2p_{1/2}2p_{3/2})_2$ state in the excited $(2p_{3/2}^2)_2$ state increases gradually(see Fig.3). This is just the reason for the increasing of the Auger rate for the excited $(2p_{3/2}^2)_2$ state when the Debye shielding length λ reduce. Then it results in the raising of the left shoulder,as shown in figure 2.

Summary

In this work, We have investigated the KLL DR processes of the H-like helium ions in plasmas for different Debye lengths with in the framework of the MCDF approximation. In contrast to other doubly excited $2l2l'$, the influence of Debye plasma on the excited $(2p_{3/2}^2)_2$ state is very strong and can increase its Auger decay rate several order of magnitude, thus the shape of DR cross sections of the H-like helium ions change significantly.

Acknowledgement

This work has been supported by the National Natural Science Foundation of China (Grant No.10774122, 10876028), the Specialized Research Fund for the Doctoral Program

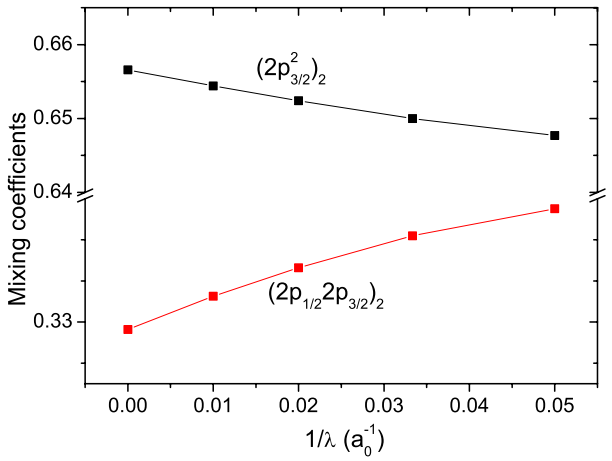

Figure 3: Configuration mixing coefficients of the $(2p^2_{3/2})_2$ state as function of the inverse of the Debye shielding length λ for helium atom.

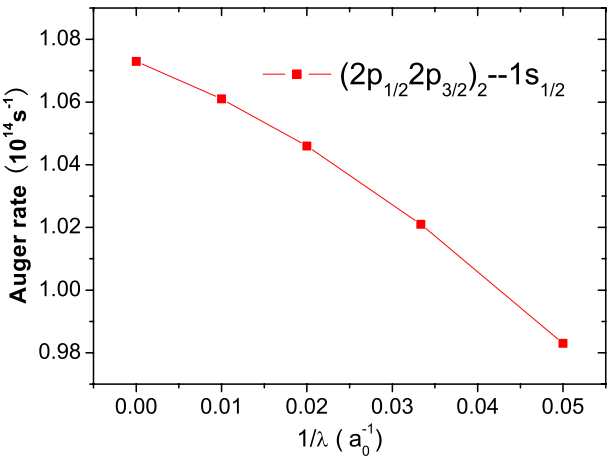

Figure 4: Auger rates as function of the inverse of the Debye shielding length λ for doubly excited state $(2p_{1/2}2p_{3/2})_2$ of helium atom.

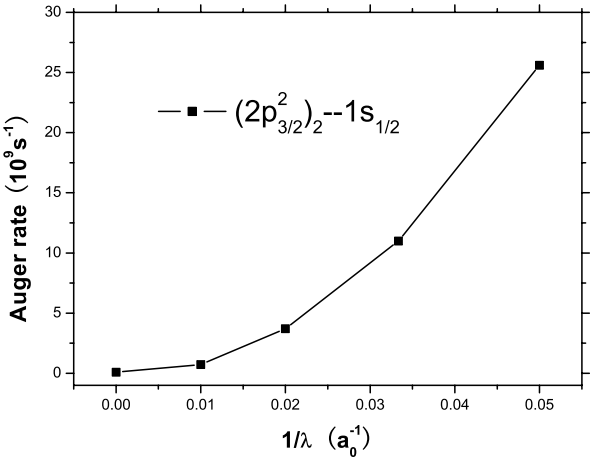

Figure 5: Auger rates as function of the inverse of the Debye shielding length λ for doubly excited state $(2p^2_{3/2})_2$ of helium atom.

of Higher Education of China (Grant No. 20070736001), the Foundation of Center of theoretical Nuclear Physics of National Laboratory of Heavy Ion Accelerrator of Lanzhou, and the Foundation of Northwest Normal University(NWNU-KJCXGC-03-21).

References

[1] D. Salzman, Atomic Physics in Hot Plasmas (Oxford University Press, Oxford, 1998).

[2] M. S. Murillo and J. C. Weisheit, Phys. Rep. **302**, 1 (1998).

[3] S. Kar and Y. K. Ho, Phys. Rev. A **72**,010703(R), (2005).

[4] B. Saha and S. Fritzsche,Phys. Rev. A **73**,036405, (2006).

[5] A. Burgess and M. J. Seaton, Mon. Not. R. Astron. Soc. **127**, 355 (1964).

[6] S. Kar and Y. K. Ho, JQSRT. **107**, 315(2007)

[7] S. Kar and Y. K. Ho, Chem. Phys. Lett. **402**, 544 2005.

[8] S. Kar and Y. K. Ho,Phys. Scr. **75**, 13 2007

[9] S. Kar and Y. K. Ho,J. Phys. B. **40**, 1403 2007

[10] I. P. Grant et al, Comput. Phys. Commun. **21**, 207 1980

[11] F. A. Parpia, C. F. Fischer and I. P. Grant, Comput. Phys.Commun. **94**, 249 1996

[12 D.H. Zhang, C.Z. Dong, L.Y. Xie, et al., Acta Phys. Sinica **55**, 0112 (2006)

[13] Y.L. Shi, C.Z. Dong, D.H. Zhang, Phys. Lett. A **372**,4913 (2008)

[14] H. G. Berry, R. L. Brooks, J. E. Hardis and W. J. Ray,Nucl. Instrum. Methods **202** 73 (1982)

[15]H. Doyle ,M. Oppenheimer and G. W. F.Drake, Phys. Rev. A **5**, 26 (1972)

[16]J. Callaway, Phys. Lett. A **66**, 201 (1978)

Measurements of electron number density and plasma temperature using LIBS

Wenfeng Luo, Jie Tang, Haojing Wang and Wei Zhao
State Key Laboratory of Transient Optics and Photonics, Xi'an Institute of Optics and Precision Mechanics, Chinese Academy of Sciences, Xi'an 710119, China
e-mail:luowf@opt.ac.cn

Abstract

Plasma produced by the radiation of a 1064 nm Nd:YAG laser focused onto a standard aluminum alloy E311 was studied spectroscopically. The electron density (N_e) inferred by measuring the Stark broadened line profile of Cu I 324.75 nm at a distance of 1.5 mm from the target surface with the laser irradiance of 3.27 GW/cm^2. The electron temperature (T_e) was determined using the Boltzmann plot method with eight neutral iron lines. At the same time, the validity of the assumption of local thermodynamic equilibrium (LTE) was discussed in light of the results obtained.

Keywords: Laser-induced breakdown spectroscopy, plasma, electron density, electron temperature, emission spectroscopy

1.Introduction

A luminous plasma can be produced using laser light energy to remove a portion of a sample by melting, fusion, ionization, erosion, and explosion. Qualitative and quantitative information about the sample's chemical composition can be obtained by measuring the emission spectrum from the laser-induced plasma. This measurement technology is known as laser-induced breakdown spectroscopy (LIBS) [1] [2]. LIBS offers several advantages over some of the conventional techniques such as little or no sample preparation, cost effectiveness, small sampling requirement, simplicity, quickness and its in-situ, real time characteristics [3]. Therefore, LIBS has been shown to be very useful in the analysis of the elemental composition of metal alloys [4], impurities on the surface of inorganic materials [5] and trace analysis of metal ions in aqueous solutions [6].

The main factors that influence the emitted line intensity by the plasma are its temperature and the electron number density [7]. The number density of the emitting species depends on the total mass ablated by the laser. The vaporized ablated matter, in turn, depends on the absorption of the laser radiation which is related to the electron density of the plasma [1]. Therefore, knowledge of the plasma temperature and electron density is vital to understand the laser-matter interaction processes [1][7].

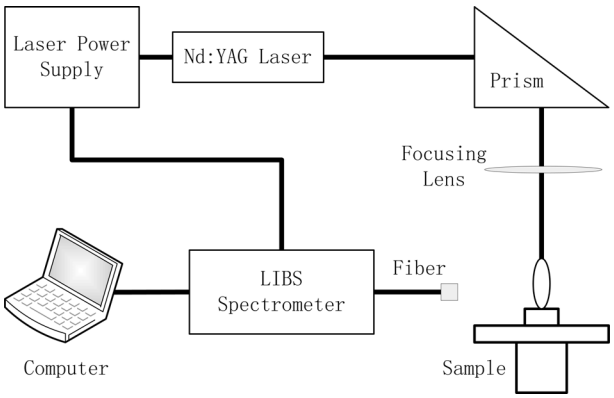

Figure 1: Experimental arrangement

The objective of the present work is to measure the electron density and plasma temperature in the aluminum alloy (E311) plasma using LIBS. The N_e at the distance of 1.5 mm from the target surface with a laser power density of 3.27 GW/cm^2 was inferred using the Stark broadened profile of neutral copper line at 324.75 nm while T_e is estimated using the Boltzmann plot method of eight neutral iron lines between 425 nm and 442 nm. At the same time, the LTE was also discussed in the light of the experimental results.

2. Experimental

Figure 1 shows a schematic diagram of the experimental setup in this work. The Q-switched Nd:YAG laser (SGR, Beamtech Optronics, 1064 nm, 1 Hz, 19.7 ns, 81 mJ/pulse) was focused by a lens (f = 150 mm) onto the surface of a standard aluminum alloy (E311, Shanghai Research Institute of Materials). The beam radius after focusing was 200 $\pm$ 10 μm measured with a microscope (OLYMPUS BX51) which resulted in a laser power density of 3.27 GW/cm^2. The emission from the plume was registered by AvaSpec-2048FT-5 detection system (Avantes, Holland) in conjunction with an optical fiber (200 μm in diameter), placed at right angle to the direction of the plasma expansion with the minimum integrated time of 2 ms and the delay time of 5 μs. Each channel of the AvaSpec-2048FT-5 detection system has a slit width of 10 μm with 2048 element linear CCD and an optical resolution of about 0.08 nm with 2400-grooves/mm. The AvaSpec-2048FT-5 detection system was triggered by the Q-switch of the Nd:YAG laser. The data acquired were stored in a personal computer through AvaSoft-LIBS for subsequent analysis. All the experiments were performed at room temperature in air at atmospheric pressure.

3. Emission spectra

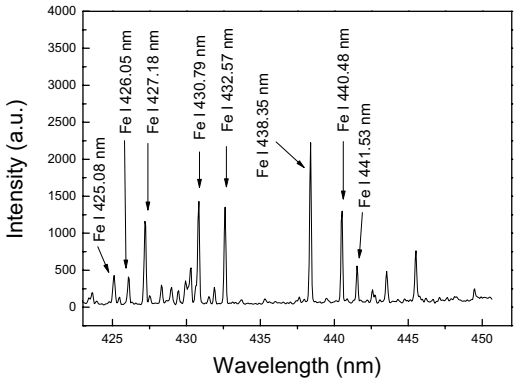

Figure 2: The emission spectrum of the aluminum plasma generated by the 1064 nm laser at a distance of 1.5 mm from the target surface with the laser irradiance of 3.27 GW/cm^2.

Figure 2 shows a typical part of the spectrum of the aluminum alloy plasma. The laser-induced plasma spectrum consists of an intense continuum and a number of neutral as well as ionic lines of the component species. At early plasma times, the signal is mostly dominated by the continuum emission which is attributed to the collisions of electrons with ions and atoms and the recombination of electrons with ions. As time progresses, continuum background diminished while ionic and atomic emission lines become dominant [1][2]. The assignment of these atomic lines shown by the arrows in figure 2 is done using NIST database [8].

4. Measurement of electron number density

Electron density is an important parameter that is used to describe a plasma environment and gives indications about the thermal equilibrium. A common method for spectroscopic determination of N_e is based on the Stark effect of the atomic or ionic lines whereas for typical LIBS, other broadening mechanisms including the contribution of ion broadening could be negligible [2]. Therefore, the Stark broadening $\Delta\lambda_{1/2}$ (nm) can be simplified to equation (1) [1]

$$\Delta\lambda_{1/2} = 2w(\frac{N_e}{10^{16}}) \tag{1}$$

where w (nm) is the electron impact width parameter [9]. For the estimation of N_e, the Stark broadened line profile of the 324.75 nm Cu I emission line was used. The experimental result at 1.5 mm above the target surface with the irradiance of 3.27 GW/cm^2 is shown in figure 3 and fits fairly well with a typical Lorentzian profile. The electron density is approximately 1.8×10^{17} cm^{-3}.

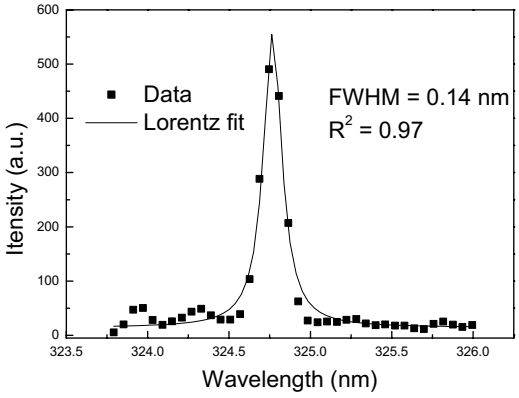

Figure 3: Typical Stark broadened profile of Cu I at 324.75 nm for the 1064 nm laser irradiation at a distance of 1.5 mm from the target surface with the laser power density of 3.27 GW/cm^2.

5. Measurement of plasma temperature

Plasma descriptions start by trying to characterize the properties of the assembly of atoms, molecules, electrons and ions rather than the individual species. If thermodynamic equilibrium exists, then plasma properties, such as the relative populations of energy level, the distribution of the speed of the particles, can be described through the concept of temperature [2]. Under the LTE condition, the kinetic temperature and the excitation temperature are identical and can be determined from the Boltzmann plot method. The population of the excited states follows the Boltzmann distribution and their relative spectral line intensity I_{mn} is given as [10]

$$\ln(\frac{\lambda_{mn} I_{mn}}{h c g_m A_{mn}}) = -\frac{E_m}{k T_e} + \ln(\frac{N(T)}{U(T)}) \tag{2}$$

where λ_{mn} is the wavelength, A_{mn} the transition probability, g_m the statistical weight of the upper level, h the Plank constant, c the speed of light in vacuum, respectively. E_m is the upper level energy, T_e the electron temperature, k the Boltzmann constant, $U(T)$ the partition function and $N(T)$ the total number density of species. Plotting the expression on the left-hand side of the equation versus E_m yields a slope of $-1/(kT_e)$. The plasma temperature can be obtained even without knowing $N(T)$ or $U(T)$.

Figure 4 is a typical Boltzmann plot for temperature determination using eight neutral iron lines (425.08 nm, 426.05 nm, 427.18 nm, 430.79 nm, 432.57 nm, 438.35 nm, 440.48

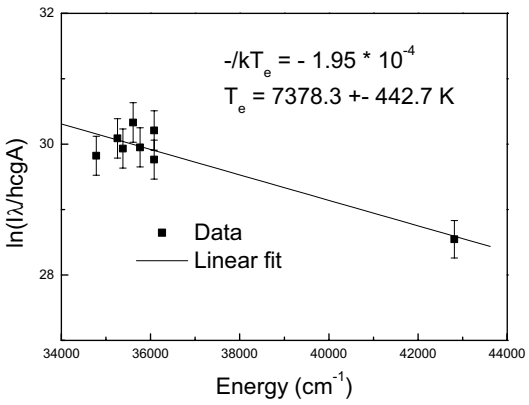

Figure 4: Boltzmann plot for temperature determination of a 1064 nm laser-induced plasma at the distance of 1.5 mm above the target surface with the laser power density of 3.27 GW/cm^2.

nm, 441.53 nm) of the laser-induced plasma obtained at the distance of 1.5 mm with the laser power density of 3.27 GW/cm^2, where the linear fit of the data is also represented. The parameters of these lines can be found in [8]. From the slope of -1.95 $\times$ 10^{-4}, the plasma temperature is T$_e$ = 7378.3 $\pm$ 442.7 K.

6. LTE

To determine the electron temperature, the plasma must satisfy the equilibrium conditions, i.e. the plasma must hold a state of LTE during the observation window. In a LTE plasma, the collisional excitation and de-excitation processes must dominate radiative processes and this requires a minimum electron density. The lower limit for the electron density for which the plasma will be in LTE is [11]

$$N_e(cm^{-3}) \geq 1.4 \times 10^{14} T^{1/2}(eV)[\Delta E(eV)]^3 \quad (3)$$

where ΔE (eV) is the energy difference between the upper and lower states. A minimum electron density of 6.1 $\times$ 10^{15} cm^{-3} for LTE to hold is needed with the Cu I 324.75 nm line transition (ΔE = 3.8 eV) [8]. As the requirement limit is much lower than the electron number density estimated, LTE is valid for the present condition.

3. Conclusion

In this paper, a transient and elongated plasma was produced by focusing the 1064 nm radiation from a Q-switched Nd:YAG onto the standard aluminum alloy (E311) in

air at atmospheric pressure. The electron number density and electron temperature were studied using spectroscopic technique at the height of 1.5 mm above the target surface with the laser power density of 3.27 GW/cm^2. The electron density inferred by measuring the Stark broadened line profile of Cu I nm was 1.8×10^{17} cm^{-3}. The electron temperature (7378.3 $\pm$ 442.7 K) was determined using the Boltzmann plot method with eight neutral iron lines between 425 nm and 442 nm. According to the experimental results, the assumption of local thermodynamic equilibrium was valid.

Acknowledgement

Research Supported by the CAS/SAFEA International Partnership Program for Creative Research Teams.

References

[1] J. P. Singh and S. N. Thakur, Laser-Induced Breakdown Spectroscopy, Amsterdam: Elsevier B. V. (2007).
[2] D. A. Cremers and L. J. Radziemski, Handbook of Laser-Induced Breakdown Spectroscopy, Chichester: John Wiley & Sons (2006).
[3] C. Barnett, E. Cahoon, J. R. Almirall, Spectrochim. Acta Part B, **63**, 1016 (2008).
[4] M. Sabsabi, P. Cielo, J. Anal. At. Spectrom., **10**, 643 (1995).
[5] D. Romero, J. M. F. Romero, J. J. Laserna, J. Anal. At. Spectrom., **14**, 199 (1999).
[6] L. M. Berman, P. J. Wolf, Appl. Spectrosc., **52**, 438 (1998).
[7] M. Sabsabi, P. Cielo, Appl. Spectrosc., **49**, 499 (1995).
[8] http://physics.nist.gov/PhysRefData/ASD/index.html
[9] M. A. Hafez, M. A. Khedr, F. F. Elaksher, Y. E. Gamal, Plasma Sources Sci. Technol., **12**, 185 (2003).
[10]N. M. Shaikh, S. Hafeez, B. Rashid, M. A. Baig, Eur. Phys. J. D, **44**, 371 (2007).
[11] G. Abdellatif, H. Imam, Spectrochim. Acta Part B, **57**, 1155 (2002).

Electron-impact excitation of Ti^{21+} in Debye plasmas

B.W.Li[1,2], C.Z.Dong[1,2], J. Jiang[1,2], and J.G.Wang[3]

1) College of Physics and Electronics Engineering, Northwest Normal University, Lanzhou 730070*, China*

2)Joint Laboratory of Atomic and Molecular Physics, NWNU & IMP CAS, Lanzhou 730000*, China*

3) Institute of Applied Physics and Computational Mathematic Beijing 100088*, China*

e-mail: koikef@kitasato-u.ac.jp

Abstract

The plasma screening effect on electron-impact excitation is studied by using the relativistic distorted-wave description and exemplified by the excitation of Ti^{21+} ion. The total and differential cross sections for the 1s-2s and 1s-2p excitations are calculated in the energy range from threshold to 5 times threshold energy, and the magnetic sublevel cross sections are also given. Comparison of present calculations with other results, when available, is made.

Keywords: Debye plasmas, electron-impact excitation, relativistic distorted-wave theory

1.Introduction

High dense plasma screening effects on atomic structure and collision dynamics have been subject to continuous studies during the last several decades [1-12]. Interest in the properties of such plasmas has been renewed in recent years with the development of inertial confinement fusion (ICF) and short-wavelength (X-ray and EUV) lasers. The energy loss of thermal electrons due to the collisions by atoms and ions is the main mechanism of the electron cooling in dense plasmas such as ICF and astrophysical plasmas of compact objects. Especially, the line emissions from these excited atoms and ions can provide the information on plasma parameters, such as the density and temperature. Therefore, the electron-impact and related photon processes have received considerable attention. Many authors have used the Debye-Hückel potentials to study the effect of the plasma environment upon atomic structure and collision dynamics in the weakly coupled plasmas, in which the electron-ion interaction is given by

$$V^{DH}(r) = -\frac{Z}{r}e^{-r/\lambda}, \tag{1}$$

here V(r) is the electron-nuclear interaction depending on the nuclear model, and

$$\lambda = \sqrt{\frac{kT_e}{4\pi n_e}}. \tag{2}$$

is the Debye screening length, T_e and n_e are the plasma electron temperature and density, respectively. k is the Boltzmann constant. The potential in Eq.(1) results from the linearization of the Poisson-Boltzmann equation, and is reliable to describe the electron-ion interaction in the weakly coupled plasmas, where the average Coulomb energy between charged particles is smaller than the average kinetic energy of the particles. Actually, this model is suitable for a wide class of laboratory and astrophysical plasmas, such as stellar atmospheres and inertial confinement fusion plasmas, *etc.*

The central interest of the present work is to analyze the electron-impact excitation process of ions in hot and dense plasma by using the Debye-Hückel model. The Debye-Hückel potential has been incorporated into the framework of relativistic Dirac-Fock (DF) equations. The GRASP92 code [13] has been modified to calculate the atomic energies and bound state wavefunctions. For electron-impact excitation (EIE), the recently developed relativistic distort-wave (RDW) program by our group [14-15] has been used. A brief outline of the theory is given in the following section and Section III shows the results and discussions. Finally, a brief conclusion will be given in Section IV.

2. THEORETICAL METHOD

In the present work all the atomic calculations are carried out within the relativistic formalism of the Dirac-Fock equations. The Dirac-Fock approximation of atomic states and transitions among them has been described in detail in literature (see, e.g., [16-17], and reference therein). This model for the electronic structure of free atoms and ions has been implemented, for instance, in the GRASP92 [13]. Only a brief outline of the theory is given bellow.

For *free* ions, the one-electron Dirac operator in the Dirac-Fock model is given by

$$h_D = c\alpha \cdot \mathbf{p} + \beta c^2 + V(r), \tag{3}$$

The first and second terms describe the kinetic energy of the electron, and the third term is the interaction with nucleus. To describe the plasma effect on the electronic properties, one-electron Dirac operator will be modified to include Debye-Hückel potential in Eq.(1):

$$h_D^{DH} = c\alpha \cdot \mathbf{p} + \beta c^2 + V^{DH}(r), \tag{4}$$

The eigenfunctions of the Dirac equation in spherical polar coordinates have the form

$$\phi(x) = \frac{1}{r} \begin{bmatrix} P_{n,\kappa} & \chi^s_\kappa(r, m_s) \\ iQ_{n,\kappa} & \chi^s_{-\kappa}(r, m_s) \end{bmatrix} \tag{5}$$

here the radial amplitudes satisfy the radial reduced equations [18]

$$\left(c^2 + V^{DH}(r) - E)\right) P(r) + c\left(\frac{dQ(r)}{dr} - \frac{\kappa}{r}Q(r)\right) = 0, \tag{6}$$

$$c\left(\frac{dP(r)}{dr} + \frac{\kappa}{r}P(r)\right) + \left(-c^2 + V^{DH}(r) - E)\right) Q(r) = 0, \tag{7}$$

The wave functions for both the initial and final states of the collion systems are the antisymmetric wave functions of the total (N+1)-electron system including the target ion plus a continuum electron, which can be written as [14-15]

$$\Psi = \frac{1}{(N+1)^{1/2}} \sum_{p=1}^{N+1} (-1)^{N+1-p} \sum_{M_t,\, m} C(J_t j M_t m; JM) \Phi_{\beta_t J_t}(x_p^{-1}) u_{\kappa m \varepsilon}(x_p), \tag{8}$$

where C is Clebsch-Gordon coefficient, J_t, j, and J are the angular momentum quantum numbers of the target ion, continuum electron and the collision system, respectively. $\Phi_{\beta_t J_t}$ is the target-ion wave function. β_t denotes all other quantum numbers in addition to J_t. x_p designates the space and spin coordinates for electron p and x_p^{-1} is the space and spin coordinates of all the N electrons other than p. $u_{\kappa m \varepsilon}$ is the relativistic distorted-wave Dirac spinor for a continuum electron, and κ is the relativistic quantum number. The continuum wave functions are generated by the component COWF of RATIP package [18] by solving the coupled Dirac equation

$$\left(\frac{d}{dr} + \frac{\kappa}{r}\right) P_\kappa(r) - \left(2c - \frac{\varepsilon}{c} + \frac{V(r)e^{-r/\lambda}}{cr}\right) Q_\kappa = -\frac{X^{(P)}(r)}{r}, \tag{9}$$

$$\left(\frac{d}{dr} - \frac{\kappa}{r}\right) Q_\kappa(r) + \left(-\frac{\varepsilon}{c} + \frac{V(r)e^{-r/\lambda}}{cr}\right) P_\kappa = \frac{X^{(Q)}(r)}{r}. \tag{10}$$

where, c is the speed of light, and ε is the kinetic energy of the continuum electron. Direct and exchange potentials, V and X are given by Grant *et al.* [16].

The electron impact excitation (EIE) scattering amplitude $B_{m_{sf}}^{m_{si}}$ can be written as [14-15]

$$\begin{aligned} B_{m_{sf}}^{m_{si}} &= \frac{2a_0\pi^{1/2}}{k_i} \sum_{\substack{l_i, j_i, m_i, l_f \\ m_{if}, j_f, m_f}} \sum_{J,M} (i)^{l_i - l_f} (2l_i + 1)^{1/2} exp[i(\delta_{k_i} + \delta_{k_f})] Y_{lf}^{m_{lf}} C(l_i \frac{1}{2} 0 m_{s_i}; j_i m_i) \\ &\times C(l_f \frac{1}{2} m_{lf} m_{sf}; j_f m_f) C(J_i j_i M_i m_i; JM) C(J_f j_f M_f m_f; JM) R(\gamma_i, \gamma_f) \end{aligned} \tag{11}$$

where a_0 is the Bohr radius, C are Clebsch-Gordan coefficients. γ_i, γ_f, J and M are the quantum numbers corresponding to the total angular momentum of the complect system, target ion plus free electron, and its z component, respectively. m_{si}, l_i, j_i, m_{l_i} and m_i are the spin, orbital angular momentum, total angular momentum, and corresponding z component quantum numbers, respectively, for the incident electron. δ_{k_i} is the phase factor for the continuum electron. κ is the relativistic quantum number, which is related to the orbital and total angular momentum l and j. $R(\gamma_i, \gamma_f)$ is the collision matrix element, which is given by [4]

$$R(\gamma_i, \gamma_f) = \langle \Psi_i | \sum_{p,q\, p<q}^{N+1} \frac{1}{r_{pq}} e^{-\frac{r_p}{\lambda}} | \Psi_f \rangle, \tag{12}$$

The differential cross sections can be written as

$$\frac{dQ}{d\hat{k}_f} = \frac{1}{g_i} \sum_{M_i, M_j} \frac{1}{2} \sum_{m_{si}, m_{sf}} |B^{m_{si}}_{m_{sf}}|^2, \tag{13}$$

where g_i is the statistical weight of the initial level of the N-electron target ion.

3. RESULTS AND DISCUSSIONS

3.1. Wave functions and Energy levels

In Fig. 1 we show the electronic density distribution of bound wavefunctions of the 1s (penal (a)), 2s (penal (b)), $2p_{1/2}$ and $2p_{3/2}$ (penal (c)) states of Ti^{21+} for a number of the screening lengths λ. As one can see from Fig. 1, with the decreases of λ, the electronic densities spread broader, and its peaks are shifted towards the larger radial distance and the peak magnitude decreases. For $2p_{1/2}$ and $2p_{3/2}$ states, two wavefunctions detached slightly for the small λ. In Table 1, we show the orbital energies of these four considered states. For isolated H-like ion, the $n = 2$ levels are degenerated in non-relativistic calculation, i.e., the so called "l degeneracy", and the $2s_{1/2}$ and $2p_{1/2}$ are degenerated in relativistic calculation, i.e., the so called " κ degeneracy". However, in plasma environment these types of degeneracy have been lifted. Moreover, the transition energies of the $n = 2$ levels to the ground state are also given in Table 2. As the λ decreases, the transition energies decreases, resulting in the red shift of the spectroscopy from these states.

We plot the continuum wavefunctions at energy $\varepsilon = 0.05$ a.u. for the unscreened and the screened cases with λ = 50, 10, 3, 1 (Panel (a)) and at plasma screening length λ = 3 for several energies (Panel (b)) as show in Fig. 2. One can see that the continuum wavefunctions change dramatically with the Debye lengths. When the λ is fixed, the continuum wavefunctions show strong dependence on energies, the smaller the electron

energy is, the more remarkably the change of the continuum wavefunctions, including the phase shifts and amplitudes. These features have significant influence on electron-ion collision process in dense plasma as we will be discussed below.

3.2. Electron-impact excitation

3.2.1. Total EIE cross section

Fig. 3 shows the total electron impact excitation cross sections for the 1s $\rightarrow$ $2p_{1/2}$ and $2p_{3/2}$ excitations of Ti^{21+} in the unscreened and the screening cases with $\lambda = 3$ and 1.5. As a comparison, the total EIE cross sections of 1s $\rightarrow$ $2p_{3/2}$ excitation of Reed et al. [19] for *free* ion are also plotted in the figure. Our cross section is in a good agreement with the results of Reed et al. [19]. The plasma screening effect reduced the electron impact excitation cross sections remarkably. The plasma screening effects reduce the cross sections by factors of about 9% (1.1X, here X=E/ΔE, E is the energy of incident electron, and ΔE is the excitation energy), 13% (3X) and 14% (5X) for $\lambda = 3$ and 18% (1.1X), 24% (2X), and 27% (5X) for $\lambda = 1.5$ for 1s $\rightarrow$ $2p_{1/2}$ and $2p_{3/2}$ transition.

We also show the (forbidden) 1s $\rightarrow$ 2s excitation cross sections in Fig. 4. It can be seen in the presence of a plasma, the cross section does not reduce appreciably as 1s $\rightarrow$ 2p transition.

3.2.2. Excitation to the magnetic sublevels

In Fig. 5 we show the plasma effect on the electron impact excitation cross sections for excitation to the magnetic sublevels of $2p_{1/2}$ of Ti^{21+}. Because of symmetry of system, the cross section for m_i = -1/2 to m_f = -1/2 and 1/2 equal to that for m_i = 1/2 to m_f = 1/2 and -1/2, so only the results for m_i = -1/2 to m_f = -1/2 and 1/2 are showed here. The cross section from m_i = -1/2 to m_f = -1/2 decreases monotonously with the increasing of incident electron energy, while the cross section from m_i = -1/2 to m_f = 1/2 sublevels is nearly invariable in the higher electron energy. When the plasma effect is considered, the cross sections decreased remarkable. For example, when $\lambda = 1.5$, the plasma screening effect reduces the cross sections by factors of 21% (1.1X), 26% (3X) and 30% (5X) for the cross section from m_i = -1/2 to m_f = 1/2 transition, and by factors of 14% (1.1X), 22% (3X) and 24% (5X) for the m_i = -1/2 to m_f = -1/2 transition.

The EIE cross sections to the magnetic sublevels in the 1s $\rightarrow$ $2p_{3/2}$ excitation of Ti^{21+} are plotted in Fig.6 for the unscreened and the screening cases with $\lambda = 3$ and 1.5. As a comparison, the results of Reed et al. [19] for *free* Ti^{21+} are also included. It is clear that the m_f = 1/2 sublevel is preferentially populated in electron-impact excitation than m_f = 3/2. However, when electron energies lower than 3X, there is a significant discrepancy between our calculations and the results of Reed et al. [19], which will result in the difference of polarization degree. As a check on our numerical methods, we calculate

the polarization degree for the $2p_{3/2} \rightarrow 1s_{1/2}$ transition of Ti^{21+}. For H-like ions the polarization degree for the $2p_{3/2} \rightarrow 1s_{1/2}$ transition is given by [19]

$$P = \frac{3(\sigma_{1/2} - \sigma_{3/2})}{3\sigma_{3/2} + 5\sigma_{1/2}} \tag{14}$$

where $\sigma_{1/2}$ and $\sigma_{3/2}$ denote the cross sections for electron impact excitation from the ground level to the $m = 1/2$ and $3/2$ magnetic sublevels for the $1s \rightarrow 2p_{3/2}$ transition. The polarizations are shown in Fig. 7. Nakamura et al. [20] and Robbins et al. [21] have measured this polarization in an electron-beam ion trap. It can be seen that there is a systematic discrepancy between the experimental values and the RDW predictions of Reed et al. [20], and our RDW calculations are in a better agreement with the experimental results [20-21]. Furthermore, plasma effect on the polarization is also given in this figure. The polarization degrees are nearly unchanged near the threshold, and decrease for the higher electron energies. The reason is that plasma screening has different effect on the magnetic sublevels as one can see from Fig. 6. For instance, when $\lambda = 1.5$ the plasma effect reduces the cross sections by factors of 18% (1.1X), 25% (3X) and 29% (5X) on m = 1/2 magnetic sublevels, while by factors of 19% (1.1X), 22% (3X) and 24% (5X) on m = 3/2 magnetic sublevels.

3.2.3. Differential cross sections

The plasma effect on the differential cross sections (DCSs) of $1s \rightarrow 2p_{1/2}$, $1s \rightarrow 2p_{3/2}$ and $1s \rightarrow 2s_{1/2}$ excitations is shown in the Fig. 8. The small angle scattering is dominated for the case of high energy, and the plasma effect has little influence on the DCSs. While for near threshold energy scattering, the plasma effect is more sensitive. An interesting phenomenon that should be noted is that DCSs decreases for small angle scattering while it increases at large angle scattering for low energy scattering in plasma environment. This can be qualitatively interpreted as, with the increasing of the plasma screening interaction, the electron-nuclear interaction become weaken, this means for small incident energy, the electron is easier close to the nuclear, so large angle scattering is more likely to be happen for the low incident energy for the screening cases.

3.2. Influence of target wavefunction

Finally, we show the influence of including plasma effect on the target wavefunction on the electron-impact excitation process in Table 3. We can see that the plasma effect on bound wave functions in electron-impact excitation can be ignored for large Debye length, for example, for $\lambda = 1.5$, this influence is about 0.7% for $1s \rightarrow 2p_{1/2}$ and $2p_{3/2}$ excitations and about 0.9% for $1s \rightarrow 2s$ transition at 1.5 - 4 times threshold energy. The reason is that the present collision system is a high charged ion, and the strong Coulumb interactions between the ion and the electrons in the ground and low excited states can

not be effected obviously by the screening interaction.

3. Summary

In conclusion, the plasma screening effect on electron-impact excitation has been studied by using relativistic distorted-wave method, including formally the Debye-Hückel potential. As an example, the plasma screening effect of cross sections for the 1s $\rightarrow$ 2s and 1s $\rightarrow$ 2p excitations of Ti^{21+} ion has been analyzed. For differential cross sections, we found that it decreases for small angle scattering while it increases at large angle scattering for low energy scattering in plasma environment. Furthermore, the present method will be extend to the multi-electron system.

Acknowledgement

This work has been supported by the National Natural Science Foundation of China (Grant No.10774122, 10876028, 10964010), the Specialized Research Fund for the Doctoral Program of Higher Education of China (Grant No. 20070736001), the Foundation of Center of theoretical Nuclear Physics of National Laboratory of Heavy Ion Accelerrator of Lanzhou, and the Foundation of Northwest Normal University(NWNU-KJCXGC-03-21).

References

[1] M. S. Murillo and J. C. Weisheit *Phys. Rep.* **302**, 1 (1998).

[2] D. Salzman, "Atomic Physics in Hot Plasma" (Oxford Univ. Press, Oxford, 1998).

[3] G. J. Hutton, N. F. Lane, and J. C. Weisheit *J. Phys. B* **14** 4879 (1981).

[4] B. L. Whitten, N. F. Lane and J. C. Weisheit *Phys. Rev. A* **29**, 945 (1984).

[5] Y. D. Jung *Phys. Fluids B* **5**, 3432(1993).

[6] W. Hong, and Y. D. Jung *Phys. Plasmas* **3**, 2457 (1996).

[7] S. Kar, and Y. K. Ho *Phys. Plasma* **15**, 013301 (2008).

[8] S. Paul, and Y. K. Ho *Phys. Rev. A* **79**, 032714 (2009).

[9] Y. Y. Qi, J. G. Wang, and R. K. Janev *Phys. Rev. A* **78**, 062511 (2008).

[10] Y. Y. Qi, Y. Wu, J. G. Wang, and Y. Z. Qu *Phys. Plasma***16**, 023502 (2009).

[11] Y. Q. Li, J. H. Wu, and J. M. Yuan *Acta Phys. Sin.* **57**, 4042 (2008).

[12] B. W. Li, J. Jiang, C. Z. Dong, J. G. Wang, and X. B. Ding *Acta Phys. Sin.* **58**, 5262 (2009).

[13] F. A. Parpia, C. Froese Fischer, and I. P. Grant *Comput. Phys. Commun.* **94**, 249 (1996).

[14] J. Jiang, C. Z. Dong, L. Y. Xie, J. G. Wang, J. Yan, and S. Fritzsche *Chin. Phys. Lett.* **24**, 691 (2007).
[15] J. Jiang, C. Z. Dong, L. Y. Xie, and J. G. Wang *Phys. Rev. A* **78**, 022709 (2008).
[16] I. P. Grant *Advan. Phys.* **19**, 747 (1970).
[17] I. P. Grant "Relativistic Quantum theory of Atoms and Molecules" (Springer, 2007).
[18] S. Fritzsche *et al.*, Nucl. Instr. and Meth. in Phys. Res. B **205**, 93 (2003).
[19] K. J. Reed and M. H. Chen *Phys. Rev. A* **48**, 3644 (1993).
[20] N. Nakamura, D. Kato, N. Miura, T. Nakahara and S. Ohtani *Phys. Rev. A* **63**, 024501 (2001).
[21] D. R. Robbins et al. Phys. Rev. A 74, 022713 (2006).

Table 1: Binding energy (a.u.) of Ti^{21+} for different Debye lengths

	free	50	10	6	2	1	0.7	0.3	0.2	0.1
1s	243.5789	243.1392	241.3863	239.9727	232.7620	222.3013	213.6076	177.8129	149.9894	83.3806
2s	60.9939	60.5551	58.8233	57.4084	50.7011	41.7012	34.9037	13.2078	3.3620	
$2p_{1/2}$	60.9939	60.5550	58.8185	57.3950	50.5867	41.2811	34.1070	10.1892		
$2p_{3/2}$	60.5978	60.1588	58.4225	56.9994	50.1956	40.9038	33.7475	9.9570		

Table 2: Transition energy (eV) of Ti21+ for different Debye lengths

λ	Transition	Transition energy
∞	$1s \rightarrow 2s$	4968.3924
	$1s \rightarrow 2p_{1/2}$	4968.3894
	$1s \rightarrow 2p_{3/2}$	4979.1710
3	$1s \rightarrow 2s$	4961.9298
	$1s \rightarrow 2p_{1/2}$	4963.3518
	$1s \rightarrow 2p_{3/2}$	4974.0706
1.5	$1s \rightarrow 2s$	4943.5139
	$1s \rightarrow 2p_{1/2}$	4948.8916
	$1s \rightarrow 2p_{3/2}$	4959.4335
0.3	$1s \rightarrow 2s$	4479.1363
	$1s \rightarrow 2p_{1/2}$	4561.2767
	$1s \rightarrow 2p_{3/2}$	4567.5957

Table 3: Total electron impact excitation cross sections of the $1s \rightarrow 2p_{3/2}$ for Ti^{21+} ion as function of incident electron energy in threshold units

	$1s \rightarrow 2p_{1/2}$					$1s \rightarrow 2p_{3/2}$					$1s \rightarrow 2s_{1/2}$				
	free	$\lambda = 3$		$\lambda = 1.5$		*free*	$\lambda = 3$		$\lambda = 1.5$		*free*	$\lambda = 3$		$\lambda = 1.5$	
ϵ_i	ion	$\sigma^{\dagger}_{2p,1s}$	$\sigma^{\S}_{2p,1s}$	$\sigma^{\dagger}_{2p,1s}$	$\sigma^{\S}_{2p,1s}$	ion	$\sigma^{\dagger}_{2p,1s}$	$\sigma^{\S}_{2p,1s}$	$\sigma^{\dagger}_{2p,1s}$	$\sigma^{\S}_{2p,1s}$	ion	$\sigma^{\dagger}_{2s,1s}$	$\sigma^{\S}_{2s,1s}$	$\sigma^{\dagger}_{2s,1s}$	$\sigma^{\S}_{2s,1s}$
1.1	2.313	2.096	2.094	1.903	1.897	4.540	4.112	4.105	3.734	3.714	1.728	1.641	1.638	1.556	1.547
1.2	2.210	1.995	1.992	1.805	1.795	4.346	3.918	3.912	3.542	3.522	1.604	1.521	1.518	1.444	1.433
1.5	2.015	1.799	1.796	1.611	1.600	3.976	3.548	3.542	3.175	3.152	1.314	1.248	1.245	1.184	1.174
2.0	1.842	1.629	1.626	1.442	1.432	3.647	3.223	3.217	2.852	2.831	1.017	0.966	0.963	0.916	0.907
2.5	1.729	1.518	1.515	1.334	1.324	3.427	3.009	3.003	2.643	2.623	0.834	0.793	0.791	0.751	0.744
3.0	1.635	1.429	1.423	1.248	1.239	3.245	2.830	2.829	2.476	2.458	0.712	0.676	0.674	0.640	0.634
3.5	1.555	1.353	1.350	1.176	1.168	3.088	2.686	2.681	2.335	2.318	0.623	0.591	0.590	0.560	0.555
4.0	1.486	1.287	1.283	1.114	1.106	2.951	2.556	2.551	2.212	2.196	0.556	0.528	0.526	0.500	0.495
4.5	1.425	1.229	1.227	1.059	1.052	2.832	2.442	2.437	2.105	2.090	0.503	0.478	0.476	0.452	0.448
5.0	1.370	1.178	1.176	1.012	1.005	2.721	2.341	2.336	2.010	1.996	0.461	0.438	0.436	0.414	0.411

† Neglecting the plasma-screening effects on the atomic wave functions.
§ Including the plasma-screening effects on the atomic wave functions.

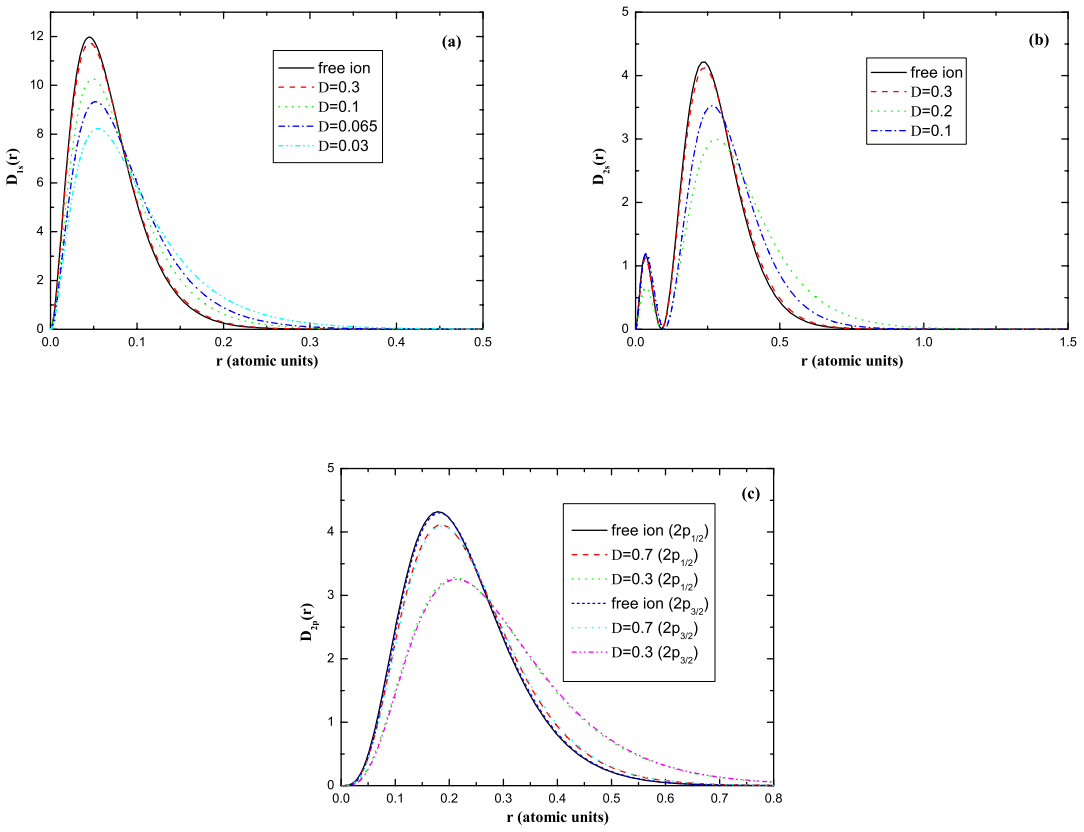

Figure 1: Electron density distribution of 1s (panel (a)), 2s (panel (b)), $2p_{1/2}$ and $2p_{3/2}$ (panel (c)) states for a number of screening lengths.

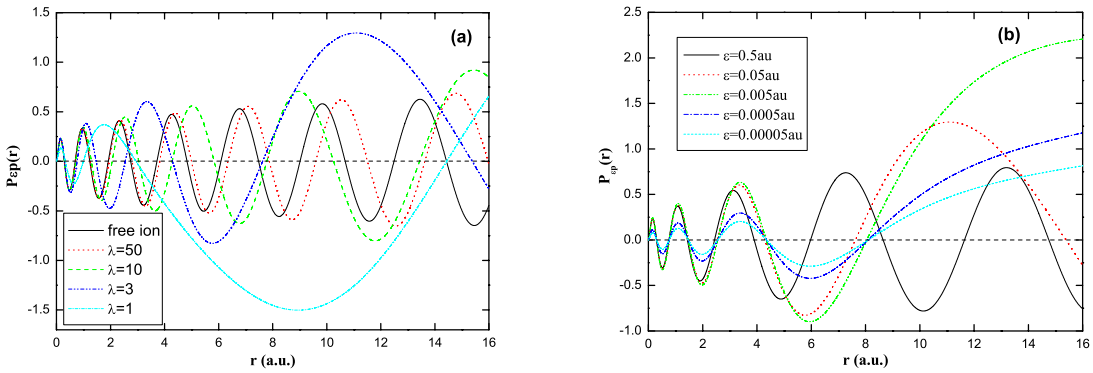

Figure 2: Continuum wave functions for a number of electron energies and screening lengths. Panel (a): fixed electron energy $\varepsilon = 0.05$ a.u.; Panel (b): fixed screening length $\lambda = 3$

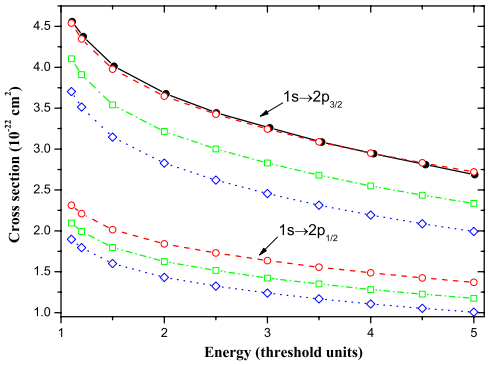

Figure 3: Total electron impact excitation cross sections of the 1s $2p_{1/2}$, $2p_{3/2}$for Ti^{21+} ion. Solid line: RDW calculations by Reed et al. [**?**] for free ion, open circles: the present RDW calculations for free ion, open square: the present RDW calculation at $\lambda = 3$, Open diamond: the present RDW calculation at $\lambda = 1.5$.

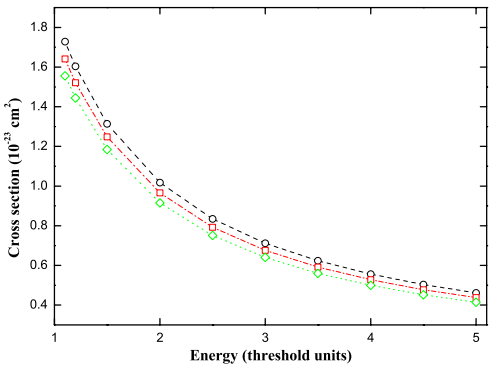

Figure 4: Total electron impact excitation cross sections of the 1s $\rightarrow$ 2s$_{1/2}$ for Ti^{21+} ion. Open circles: RDW calculations for free ion; open square: RDW calculation at $\lambda = 3$; Open diamond: RDW calculation at $\lambda = 1.5$.

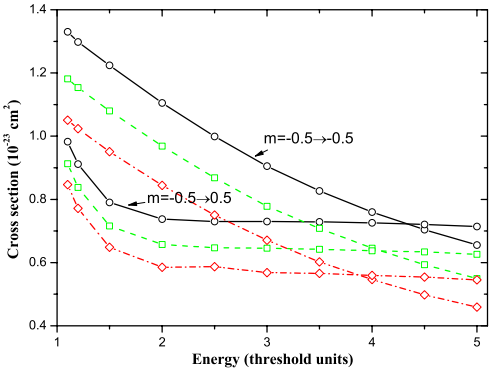

Figure 5: Cross sections for electron impact excitation of the 1s $\rightarrow$ 2p$_{3/2}$ to specific magnetic sublevels of Ti^{21+} as function of incident electron energy in threshold units as well as plasma screening length. The symbols are the same as in Fig. 3

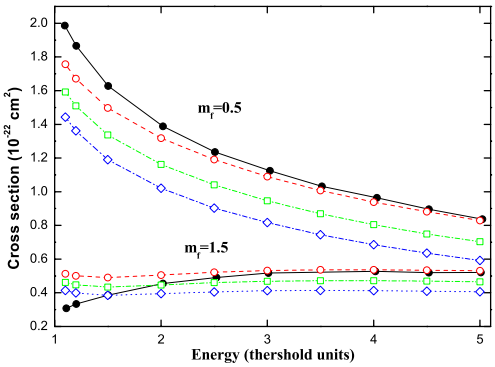

Figure 6: Cross sections for electron impact excitation of the 1s $\rightarrow$ $2p_{3/2}$ to specific magnetic sublevels of Ti^{21+} as function of incident electron energy in threshold units as well as plasma screening length. The symbols are the same as in Fig. 3

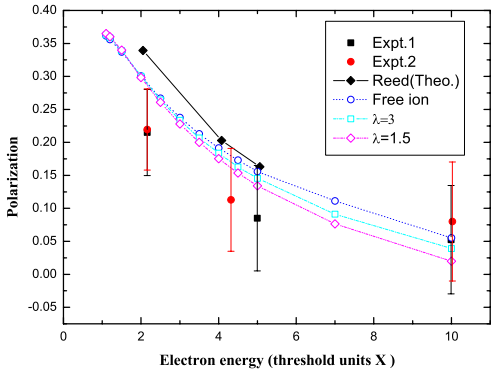

Figure 7: Comparison with measured[?] and theoretical values[?] polarization of the Lyman-α_1 emission line of Ti^{21+}. All electron-beam energies values are plotted in threshold units (X).

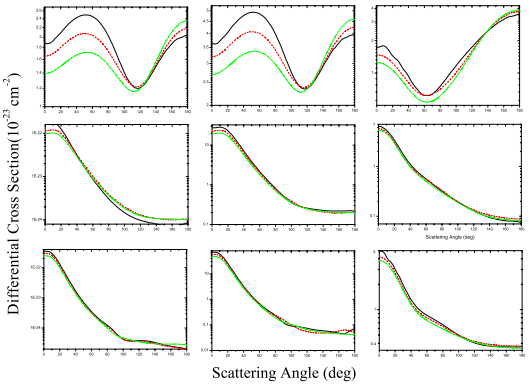

Figure 8: Differential cross sections for the excitation of the 1s→2p$_{3/2}$ and 1s→2s state of Ti^{21+} by electron impact as function of incident electron energy in threshold units. Solid line: RDW calculations for free ion; Dash line: RDW calculation at $\lambda = 3$; Dash dot dot line: RDW calculation at $\lambda = 1.5$

Interference effect involving doubly excited states $[1s2p](^{3,1}P)3p^2$ (J=1) in 1s photoionization of neon

WAN Jianjie[1] and DONG Chenzhong[1,2]

1) College of Physics and Electronic Engineering, Northwest Normal University, Lanzhou 730070, China

2) Joint Laboratory of Atomic and Molecular Physics, NWNU & IMP CAS, Lanzhou 730070, China

e-mail: dongcz@nwnu.edu.cn

Abstract

Within the framework of multiconfiguration Dirac-Fock (MCDF) method, the interference between photoionization and photoexcitation autoionization involving the doubly excited states $[1s2p](^{3,1}P)3p^2$ (J=1) of neon have been studied theoretically. The present results indicate the fine structure of the interference spectra in experiment and show the dominant contribution to the total profile resulting from some individual resonances. Reasonable agreement is found between the present calculations and other available theoretical and experimental results. In addition, some interesting trends of variation of Fano parameters q and ρ^2 have also been pointed out.

Keywords: doubly excited states, interference, photoionization, photoexcitation autoionization, MCDF, Fano parameter

1.Introduction

Multielectron effects and relaxation effects with the ionization and excitation of gaseous neon have been the subject of several experimental and theoretical studies in last decades. Especially, the multielectron effects connected with the 1s shell ionization of neon have been studied extensively [1-5]. For example, Esteva *et al* [1] have observed the high resolution spectrum of gaseous neon in the 1s region by using synchrotron radiation and confirmed their interpretation on the $[1s2p]3p^2$ final-state configuration. Avaldi *et al* have observed the Ne $[1s2p]3p^2$ doubly excited states both in a threshold photoelectron spectroscopy [2] and in photoabsorption experiments [3]. They attributed some features to inner-shell doubly excited and conjugate shakeup states in the [1s2p]nl satellite spectrum and elucidated information on the decay routes of the inner-shell doubly excited states through a comparison of the measured photoabsorption spectra and of the threshold photoelectron spectra. Recently, a series of experiments on doubly excited resonances of Ne have been carried out by Oura *et al* [4-6]. They measured the photoabsorption spectrum of Ne in the excitation energy region of the $[1s2s](^{3,1}S)nln'l'\ ^1P$ inner-shell

doubly excited states using high brilliant soft x-ray undulator radiation and analyzed the observed spectrum with the aid of multiconfiguration Dirac-Fock (MCDF) method [4]. Meanwhile, the angle-resolved resonant Auger emission from the doubly excited states $[1s2p](^{3,1}P)3p^2$ of Ne has been observed [5]. They also found the resonant enhancement of photoemission leading to the Ne^+ $[2p^2](^1D)3p\ ^2P$ state across the $[1s2p](^3P)3p^2\ ^1P$ doubly excited resonance of Ne [6]. In addition, Kato *et al* [7] have also implemented the systematical experiment to investigate high-resolution absolute photoabsorption cross section for Ne in the 1s2s and 1s2p double excitation.

However, the experimental and theoretical work above still lack of studies on fine interference structure even though such fine structure may be not important indeed in existing experiment up to today. In this Letter, the resonant excitation energy from the ground state $1s^22s^22p^6\ ^1S_0$ to the intermediate states $[1s2p](^{3,1}P)3p^2$ (J=1) and the corresponding bound-bound and continuum-bound transition matrix have been calculated by using two new components REOS99 [8] and AUGER [9] of RATIP package [10] and a newly developed relativistic photoionization program RERR06 [11-12] based on the MCDF method. The individual interference between photoionization and photoexcitation autoionization,

$$h\nu + 1s^22s^22p^6 \rightarrow [1s] + e^-, \tag{1}$$

$$h\nu + 1s^22s^22p^6 \rightarrow [1s2p](^{3,1}P)3p^2(J^P = 1^-) \rightarrow [1s] + e^-, \tag{2}$$

at the resonances above are focused on.

2. Theoretical methods

The interference effect has been studied with the aid of an isolated resonance scheme derived originally by Fano and coworkers [13-14]. The following expression for the total cross section $\sigma(\omega)$ for the case of a single discrete state interacting with one or more continuum states,

$$\sigma(\omega) = \sigma_{if}^{PI}(\omega)(\rho_{ijf}^2 \frac{(q_{ijf}+\tilde{\omega})^2}{1+\tilde{\omega}^2} + 1 - \rho_{ijf}^2), \tag{3}$$

where $\sigma(\omega)$ represents the (total) absorption cross section for the photon of energy ω, $\sigma_{if}^{PI}(\omega)$ is the photoionization cross section from initial ionic state i to final ionic state f,

$$\tilde{\omega} = \frac{\omega - E_r}{\frac{1}{2}\Gamma} = \frac{\omega - E_{ji} - \Delta_r}{\frac{1}{2}\Gamma} \tag{4}$$

describes the departure of the incident photon energy ω from an resonance center $E_r = E_{ji} + \Delta_r$, where $E_{ji} \equiv E_j - E_i$ is the resonance energy between states i and j. The quantity

Δ_r represents thus a shift with respect to E_{ji}. Γ is the linewidth of the resonance. The quantities $\sigma_{if}^{PI}(\omega)$, Γ, q and ρ^2 can be expressed in term of the radiative transition matrix elements for transitions from the initial state $|\Psi_i\rangle$ to the discrete state $|\Psi_j\rangle$, and to the continuum $|\Psi_f, \epsilon\kappa; \Psi_{f'}\rangle$, together with the Coulomb interaction matrix elements coupling the discrete state to the continuum. The Fano q parameter, which governs the shape of the total cross section, is given by

$$q_{ijf} = \frac{<\Phi_j\|O^{(L)}\|\Psi_i>}{\pi\sum_{\kappa}<\Psi_j\|\sum_{p<q}V_{pq}\|\Psi_f,\epsilon\kappa;\Psi_{f'}><\Psi_f,\epsilon\kappa;\Psi_{f'}\|O^{(L)}\|\Psi_i>}, \tag{5}$$

and the correlation coefficient ρ^2, which is a measure of the strength of the resonance, is defined as

$$\rho_{ijf}^2 = \frac{\left[\sum_{\kappa}<\Psi_j\|\sum_{p<q}V_{pq}\|\Psi_f,\epsilon\kappa;\Psi_{f'}><\Psi_f,\epsilon\kappa;\Psi_{f'}\|O^{(L)}\|\Psi_i>\right]^2}{\left[\sum_{\kappa}(<\Psi_j\|\sum_{p<q}V_{pq}\|\Psi_f,\epsilon\kappa;\Psi_{f'}>)^2\right]\left[\sum_{\kappa}(<\Psi_f,\epsilon\kappa;\Psi_{f'}\|O^{(L)}\|\Psi_i>)^2\right]}, \tag{6}$$

where and represent the radiative and Coulomb-Breit operators, respectively, and Φ_j is the discrete state modified by an admixture of the continuum states. The degree to which Φ_j is different from Ψ_j is dependent upon the energy variations of the continuum wave functions in the proximity of the resonance. In practice, it is easy to replace Φ_j with Ψ_j approximately. The Auger linewidth of the resonance is given by

$$\Gamma^{auger} = 2\pi\sum_{\kappa}\left|< \Psi_f, \epsilon\kappa; \Psi_{f'}\|\sum_{p<q}V_{pq}\|\Psi_j >\right|^2, \tag{7}$$

where Ψ_j is the ASF of the autoionization state j, while $\Psi_{f'}$ is the ASF of the system formed by an ionic state f and a continuum electron κ with energy ϵ. The two-electron operator V_{pq} in Eq. (7) is the sum of Coulomb and Breit operators, which has the form in atomic unit

$$V_{pq} = \frac{1}{r_{pq}} - \vec{\alpha_p}\cdot\vec{\alpha_q}\frac{cos(\omega_{pq}r_{pq})}{r_{pq}} + (\vec{\alpha_p}\cdot\nabla_p)(\vec{\alpha_q}\cdot\nabla_q)\frac{cos(\omega_{pq}r_{pq})-1}{\omega_{pq}^2 r_{pq}} \tag{8}$$

where $\vec{\alpha_p}$ and $\vec{\alpha_q}$ are the Dirac vector matrices, ω_{pq} is the wave number of the exchanged virtual photon, and the Auger rate is equal to the Auger linewidth in atomic units. The nonresonance background cross section is given by [12-13]

$$\sigma_{if}^{PI}(\omega) = 2\pi^2 a_0^2 \alpha \frac{df_{if}}{d\epsilon} \tag{9}$$

where a_0 is the Bohr radius, α is the fine structure constant, ω indicates the incident photon energy which yields according to the energy conservation law,

$$\epsilon = E_{if} + \omega, \tag{10}$$

$$E_{if} \equiv E_i - E_f, \tag{11}$$

and the so-called oscillator strength density is given as follows [11-12]

$$\frac{df_{if}}{d\epsilon} = \frac{\pi c}{(2L+1)\omega^2} \sum_{\kappa} \left| < \Psi_f, \epsilon\kappa; \Psi_{f'} \| O^{(L)} \| \Psi_i > \right|^2, \tag{12}$$

where Ψ_i is the ASF of the initial state i, while $\Psi_{f'}$ is the ASF of the system formed by an ionic state Ψ_f and a continuum electron κ with energy ϵ, is the energy of incident photon, c is the light velocity. While the matrix elements in Eqs. (5) and (6) are not strictly energy independent, they are slowly varying functions of energy, and the values of $\sigma_{if}^{PI}(\omega)$, Γ, q and ρ^2 are assumed to be constant in the vicinity of the resonance, moreover the linewidth Γ is assumed to be Γ^{auger} and the shift Δ_r is regarded as zero approximately in practical calculation so that the resonance center is only given by E_{ji} in this paper.

3. Results and discussion

In this work, we are not about to carry out highly accurate calculations and then the present calculations should be considered only model designed specifically to investigate the importance of the individual interference in 1s photoionization of Ne, because of the limited number of states included in these calculations. Table 1 lists the excitation energies, Auger widths, absorption oscillator strength, and Fano parameters q and ρ^2 for the intermediate [1s2p](^{3,1}P)3p^2 (J=1) states within the framework of isolated resonance. It is found that the average energy for the configuration [1s2p](^{3}P)3p^2 (J=1) is estimated, which is 900.46 eV, compared to the experimental and other theoretical values such as 902.40(10) eV [1], 902.42(5) eV [2], 902.68 eV [3], 902.45 eV [5], 902.44 eV [7] and 902.58 eV [7]. With the comparison, it is obviously that the present excitation energy is smaller than those other values by around 2 eV. This energy shift is attributed to underestimating electron correlation both in initial and intermediate states. Furthermore, we can also find that with the increase of the photon energy, the absorption oscillator strength vary in evidence for the excitation from the ground state to [1s2p](^{3}P)3p^2 (J=1) and the sixth absorption becomes the strongest one, the value of which is up to 1.27×10^{-3} (B) and 1.23×10^{-3} (C). This is easy to understand due to its spin-allowed transition. The result also indicates that the branch ratio from the ground state to this individual intermediate level [1s2p](^{3}P)3p^2(^{3}P$_2$) ^{1}P$_1$ is the largest. In addition, the average energy of the configuration [1s2p](^{1}P)3p^2 (J=1) is obtained as 904.85 eV. There are two larger resonances,

$[1s2p]({}^1P)3p^2({}^1D_2)\ {}^1P_1$ and $[1s2p]({}^1P)3p^2({}^1S_0)\ {}^1P_1$, due to spin-allowed transition. However, the absolute values of their q parameters are much greater than one so that their resonances are approximately symmetrical. Because of the undoubted identification of $[1s2p]({}^3P)3p^2$ (J=1) in experiment [5], only the comparison for $[1s2p]({}^3P)3p^2$ (J=1) is given. In Fig. 1, the calculated oscillator strength together with the experimental spectra is shown, and the oscillator strengths have been shifted by +2 eV for comparison.

Table 1: Excitation energies and absorption oscillator strength from the ground state to the intermediate states, Auger widths and Fano parameters within the framework of isolated resonance.

Label	State	Photon energy	Auger width	f_{ij}		q		ρ^2	
		E_{ij} (eV)	(meV)	B	C	B	C	B	C
1	$[1s2p]({}^3P)3p^2({}^3P_2)\ {}^5P_1$	899.701	0.03	3.04[-9]*	3.13[-9]	-1.61	-1.54	0.01	0.01
2	$[1s2p]({}^3P)3p^2({}^3P_2)\ {}^5D_1$	899.921	0.41	7.73[-7]	7.59[-7]	-2.72	-2.62	0.08	0.09
3	$[1s2p]({}^3P)3p^2({}^3P_2)\ {}^3P_1$	900.022	2.27	4.31[-6]	4.23[-6]	-2.65	-2.55	0.09	0.09
4	$[1s2p]({}^3P)3p^2({}^3P_2)\ {}^3D_1$	900.085	0.41	1.13[-5]	1.10[-5]	-3.12	-3.03	0.95	0.95
5	$[1s2p]({}^3P)3p^2({}^3P_2)\ {}^3S_1$	900.236	0.92	2.70[-5]	2.62[-5]	-3.12	-3.04	1.00	1.00
6	$[1s2p]({}^3P)3p^2({}^3P_2)\ {}^1P_1$	900.554	41.76	1.27[-3]	1.23[-3]	-3.19	-3.10	1.00	1.00
7	$[1s2p]({}^3P)3p^2({}^1D_2)\ {}^3D_1$	900.822	4.25	4.46[-6]	4.24[-6]	-4.99	-5.03	0.01	0.01
8	$[1s2p]({}^3P)3p^2({}^1D_2)\ {}^3P_1$	900.963	38.64	1.35[-6]	1.19[-6]	-22.00	279.17	0.00	0.00
9	$[1s2p]({}^3P)3p^2({}^1S_0)\ {}^3P_1$	901.804	4.68	2.78[-7]	2.51[-7]	9.37	6.52	0.00	0.00
10	$[1s2p]({}^1P)3p^2({}^3P_2)\ {}^3D_1$	904.249	0.01	1.34[-8]	1.29[-8]	-0.85	-0.82	0.68	0.68
11	$[1s2p]({}^1P)3p^2({}^3P_2)\ {}^3P_1$	904.345	0.35	4.50[-8]	6.17[-8]	-2.32	-2.54	0.01	0.01
12	$[1s2p]({}^1P)3p^2({}^3P_2)\ {}^3S_1$	904.492	0.01	1.01[-8]	9.55[-9]	-0.89	-0.87	0.30	0.29
13	$[1s2p]({}^1P)3p^2({}^1D_2)\ {}^1P_1$	905.123	0.56	1.30[-3]	1.24[-3]	-27.67	-26.80	0.98	0.98
14	$[1s2p]({}^1P)3p^2({}^1S_0)\ {}^1P_1$	906.054	0.04	1.53[-4]	1.46[-4]	-40.09	-38.69	0.87	0.87

*a[b] stands for $a \times 10^b$, for example 3.04[-9] is 3.04×10^{-9}.

Furthermore, as far as the whole trend is concerned it is clear to find that the Fano parameter q reduces from -2.65 at resonance $[1s2p]({}^3P)3p^2({}^3P_2)\ {}^3P_1$ to -4.99 at resonance $[1s2p]({}^3P)3p^2({}^1D_2)\ {}^3P_1$ as increasing the photon energy, and then suddenly becomes positive at resonance $[1s2p]({}^3P)3p^2({}^1S_0)\ {}^3P_1$. This variation trend maybe indicate that q reverse, which differs from the effect on Rydberg series discussed by Connerade *et al* [15], take place for the intra-configuration here and in principle it should be obvious to observe the gradually changed profile maybe only from the theoretical point of view. At the same time, the other Fano parameter ρ^2 approaches unity at the strongest resonance $[1s2p]({}^3P)3p^2({}^3P_2)\ {}^1P_1$, which shows the cross section corresponding to transition to states of the continuum that interact with the discrete autoionization state is determined by the direct photoionization cross section completely at this resonance, and then becomes close to zero at the resonances $[1s2p]({}^3P)3p^2({}^1D_2)\ {}^3D_1$, $[1s2p]({}^3P)3p^2({}^1D_2)\ {}^3P_1$ and $[1s2p]({}^3P)3p^2({}^1S_0)\ {}^3P_1$. Although the sign of q parameters of two gauges for $[1s2p]({}^3P)3p^2({}^1D_2)\ {}^3P_1$ are different, it is the fact that both the absolute values are rather

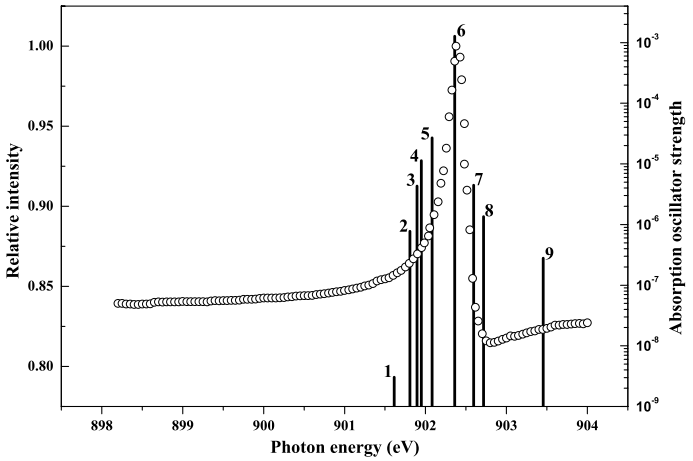

Figure 1: Relative intensity [5] for Ne in the region of the [1s2p](^{3}P)3p^2 (J=1) doubly excited states together with the calculated absorption oscillator strength in Babushkin gauge for the intermediate states above based on the multiconfiguration Dirac-Fock method.

larger. It is noted that there are two continuum channels, i.e. $p_{1/2}$ and $p_{3/2}$, within the relativistic calculation and the absolute values of the two partial q parameters are so close to each other for [1s2p](^{3}P)3p^2(^{1}D$_2$) ^{3}P$_1$ that the total q parameter is more sensitive to sign. In other words, the parameter q in Coulomb gauge is more sensitive to the transition matrix but this result shows the symmetrical profile on earth. In order to show the individual contributions from the different intermediate levels, figure 2 gives the individual interference spectra, which demonstrate indeed the contribution of [1s2p](^{3}P)3p^2(^{3}P$_2$) ^{1}P$_1$ is the most important and decisive to both the strength and profile.

4. Conclusion

In summary, we have preliminarily studied the excitation energies and absorption oscillator strengths from the ground state to the intermediate [1s2p](^{3,1}P)3p^2 (J=1) states, and have discussed the effects of the interference between the 1s photoionization and the relevant photoexcitation autoionization processes, and at the same time obtained the so-called Fano q and ρ^2 parameters for individual levels of the intermediate configuration. The present results have shown the absorption oscillator strength into the sixth intermediate level is the strongest and meanwhile the relevant profile is also dominant in the total photoabsorption spectra. It is worthwhile to note that maybe individual contribution plays a key role in the resulting spectra. And in the very case study, it is interesting to

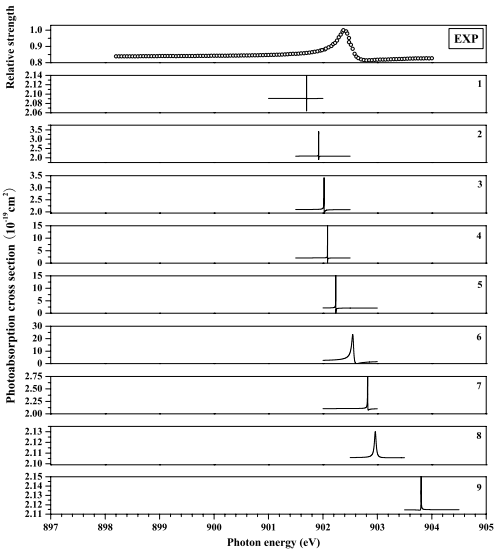

Figure 2: Comparison between the experimental spectra [5] and the individual interference profile in Babushkin gauge given by the virtue of the so-called isolated resonance approximation.

mention the fact that there is q reverse within the (same) single interference configuration with increasing the photon energy. It should be pointed out the experimental spectra may not be distinguished due to the low resolution and on the other hand the weak intensity and the narrow width. So only the sixth resonance shows itself dominant in the resulting spectra. Of course, the intermediate [1s2p](^{3,1}P)3p^2 (J=1) states lies in a narrow energy region and some levels may be considered degenerate state approximately, so it is necessary to implement a more complete calculation in order to obtain more reliable level structure and decay properties and a more complicated method for overlapping resonances needs to be take advantage of so as to investigate the interference scheme better in future work.

Acknowledgement

The authors would like to thank Dr. KOIKE Fumihiro for the valuable discussion. This work is partly supported by National Natural Science Foundation of China (Grant Nos. 10774122, 10847007, 10876028), the Core-University Program between Japanese Society of Promotion of Science and Chinese Academy of Sciences, the Specialized Research Fund for the Doctoral Program of Higher Education of China (Grant No. 20070736001), the Foundation of Center of Theoretical Nuclear Physics of National Laboratory of Heavy

Ion Accelerator of Lanzhou, and the Foundation of Northwest Normal University (Grant No. NWNU-KJCXGC-03-21).

References

[1] J. M. Esteva, B. Gauthé, P. Dhez and R. C. Karnatak, J. Phys. B **16**, L263 (1983).
[2] L. Avaldi, G. Dawber, R. Camilloni, G. C. King, M. Roper, M. R. F. Siggel, G. Stefani, M. Zitnik, A. Lisini and P. Decleva, Phys. Rev. A **51**, 5025 (1995).
[3] L. Avaldi, R. Camilloni, G. Stefani, C. Comicioli, M. Zacchigna, K. C. Prince, M. Zitnik, C. Quaresima, C. Ottaviani, C. Crotti and P. Perfetti, J. Phys. B **29**, L737 (1996).
[4] M. Oura, H. Yamaoka, Y. Senba, H. Ohashi and F. Koike, Phys. Rev. A **70**, 062502 (2004).
[5] M. Oura, Y. Tamenori, T. Hayaishi, Y. Kanai, H. Yoshii, K. Tsukamoto and F. Koike, Phys. Rev. A **70**, 022710 (2004).
[6] M. Oura, Y. Senba and H. Ohashi, Phys. Rev. A **77**, 054702 (2008).
[7] M. Kato, Y. Morishita, F. Koike, S. Fritzsche, H. Yamaoka, Y. Tamenori, K. Okada, T. Matsudo, T. Gejo, I. H. Suzuki and N. Saito, J. Phys. B **39**, 2059 (2006).
[8] S. Fritzsche, C. F. Fischer and C. Z. Dong, Comput. Phys. Commun. **124**, 340 (2000).
[9] S. Fritzsche, H. Aksela, C. Z. Dong, S. Heinäsmäki and J. E. Sienkiewicz , Nucl. Instr. Meth. Phys. Res. B **205**, 93 (2003).
[10] S. Fritzsche, J. Elec. Spec. Rel. Phenom., **114-116**, 1155 (2001).
[11] J. J. Wan, C. Z. Dong, C. C. Sang, X. B. Ding, L. Y. Xie and J. Jiang, J. Phys.: Conf. Ser. **58**, 367 (2007).
[12] C. C. Sang, J. J. Wan, C. Z. Dong, X. B. Ding and J. Jiang, Acta Phys. Sin. **57**, 2152 (2008) (in Chinese).
[13] U. Fano, Phys. Rev. **124**, 1866 (1961).
[14] U. Fano and J. W. Cooper, Phys. Rev. **137**, A1364 (1965).
[15] J. P. Connerade, Proc. R. Soc. Lond. A **362**, 361 (1978).

Hyperfine induced transitions for He-like, Be-like, and Mg-like ions

Jiguang Li [1], Huihui Kang [1], Chenzhong Dong [1,2], Per Jönsson [3], and Gediminas Gaigalas [4,5]

[1] *College of Physics and Electronic Engineering, Northwest Normal University, Lanzhou 730070, China*

[2] *Joint Laboratory of Atomic and Molecular Physics, NWNU & IMPCAS, Lanzhou 730070, China*

[3] *Nature, Environment, Society, Malmö University, S-20506, Malmö, Sweden*

[4] *Department of Physics, Vilnius Pedagogical University, Studentu 39, Vilnius LT-08106, Lithuania*

[5] *Institute of Theoretical Physics and Astronomy, A. Gostauto 12, Vilnius LT-01108, Lithuania*

e-mail: Dongcz@nwnu.edu.cn

Abstract

Hyperfine quenching rates for $1s2s\ ^1S_0 \rightarrow 1s^2\ ^1S_0$ M1 transition of He-like ions, $2s2p\ ^3P_0,\ ^3P_2 \rightarrow 2s^2\ ^1S_0$ E1 transition of Be-like ions and Mg-like ions have been calculated from relativistic configuration interaction wavefunctions including the frequency independent Breit interaction and QED effects. The present study not only supply accurate theoretical values for developing atomic clocks, diagnosing low-density plasma, probing nuclear properties, exploring weak interaction beyond standard model, but also to analyze some characteristics in hyperfine induced transitions.

Keywords: hyperfine induced transition; MCDF method; highly charged ion

1. Introduction

Hyperfine spectroscopy plays a key role in study of atomic and nuclear physics, especially which can be used to check fundamental interaction [1, 2, 3, 4, 5] such as electromagnetic and electroweak interaction with high accuracy, determine nuclear properties [6, 7, 8, 9, 10], develop atomic clock [11, 12, 13, 14, 15], and so on. Recently one kind of hyperfine transitions, which is known as hyperfine induced transition or hyperfine quenching, attracts more attention owing to analyzing spectra [16], determining isotopic ratios in stellar and diagnosing low-density plasma [17, 18] as well.

Relevant data are however still insufficient and in response to this we have performed systematic investigations on hyperfine induced transitions for He-like, Be-like and Mg-like

ions using GRASP2K [19] based on multi-configuration Dirac-Hartree-Fock method and HFST [20] package.

2. He-like ions

Gorshkov and Labzovskiĭ [21] and Labzowsky *et al.* [10] have proposed that the mixed hyperfine- and weak-quenching can be used to test parity-violation effects. The one photon transition $1s2s\ ^1S_0 \rightarrow 1s^2\ ^1S_0$ of He-like ions is considered a good candidate for these tests and experiments will be carried out at GSI [4]. Therefore, accurate hyperfine induced $1s2s\ ^1S_0 \rightarrow 1s^2\ ^1S_0$ M1 transition probabilities of He-like ions are important. We have performed systematic calculations along the He-like iso-electronic sequence.

The transition rate and corresponding wavelengths of He-like ions are given Table 1. Previous theoretical results of wavelength [22] are compared with present calculations in this table. The agreement between our value for ^{151}Eu and previous theoretical values by Labzowsky *et al.* [10] is very good. To predict the transition rate for any isotope in the iso-electronic sequence we follow Brage *et al.* [17] and factorize the hyperfine induced transition rate into nuclear and electronic parts

$$A_{HIT}(1s2s\ ^1S_0 \rightarrow 1s^2\ ^1S_0) = \mu_I^2(1 + 1/I)A^{el}(1s2s\ ^1S_0 \rightarrow 1s^2\ ^1S_0). \quad (1)$$

The electronic part A^{el} has a smooth behavior along the iso-electronic sequence making interpolation possible. From the data in Table 4 we obtain a fit of the form

$$A^{el} = 1.9708 \times 10^{-19}\, Z^{14.065} \quad (2)$$

where Z is the atomic number. The fit is shown in Figure 1. In order to show clearly the trend of A^{el} with Z, log(A) was plotted in this picture. Using the fitting formula we estimate the probability of ^{155}Gd with nuclear spin $I = 3/2$ and nuclear dipole moment $\mu_I = -0.2591\mu_N$ to 5.60 $\times 10^5$ s^{-1}. This value is in good agreement with the theoretical value 5.8 $\times 10^5$ s^{-1} given in [10].

2. Be-like ions

Many attentions have been paid on hyperfine induced $2s2p\ ^3P_0 \rightarrow 2s^2\ ^1S_0$ E1 transition of Be-like ions. Many years ago, Marques *et al.* first calculated the transition probabilities [23] through complex matrix method developed by them [24]. Due to neglecting an important contribution from the $2s2p\ ^1P_1$ level in the computational model, their results exist relatively large discrepancies. Later, Brage *et al.* further presented some results, which were calculated by perturbative method. The aim of their study is to determine the isotopic compositions and diagnose densities of low-density plasmas [17], therefore

Table 1: Hyperfine induced rates A_{HIT} in s^{-1} and corresponding wavelength λ in Å for the $1s2s^1S_0 \rightarrow 1s^2\ ^1S_0$ transition in He-like ions.

				λ(Å)		A_{HIT}	
Isotope	Z	I	μ_I	This work	Ref.[22]	This work	Ref.[10]
^{13}C	6	1/2	0.7024118(14)	40.7302	40.7304	2.6534[-8]	
^{19}F	9	1/2	2.628868(8)	16.9361	16.9404	1.0862[-4]	
^{29}Si	14	1/2	-0.55529(3)	6.6834	6.6848	2.4493[-3]	
^{47}Ti	22	5/2	-0.78848(1)	2.6214	2.6225	1.3010[0]	
^{57}Fe	26	1/2	0.9062300(9)	1.8584	1.8594	3.8221[-1]	
^{71}Ga	31	3/2	2.56227(2)	1.2941		1.9926[3]	
^{85}Rb	37	5/2	1.35298(10)	0.8987		5.5705[3]	
^{97}Mo	42	5/2	-0.9335(1)	0.6916	0.6923	1.5643[4]	
^{103}Rh	45	1/2	-0.8840(2)	0.5994		7.9312[4]	
^{117}Sn	50	1/2	-1.00104(7)	0.4814	0.4820	4.4904[5]	
^{131}Xe	54	3/2	0.691862(4)	0.4098	0.4104	3.5483[5]	
^{151}Eu	63	5/2	3.4717(6)	0.2958		6.7643[7]	6.8[7]
^{175}Lu	71	7/2	2.2323(11)	0.2289		1.4508[8]	
^{193}Ir	77	3/2	0.1637(6)	0.1917		3.3463[6]	

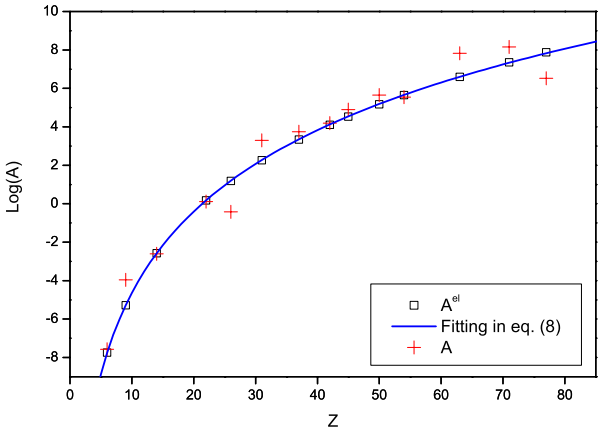

Figure 1: Logarithm of hyperfine induced rates A for the $1s2s^1S_0 \rightarrow 1s^2\ ^1S_0$ transition of He-like ions together with fit to the corresponding electronic quantity A^{el}.

the calculations were only restricted within those abundant elements in stellar. Recently, Cheng *et al.* also gave the probabilities by perturbative and radiative damping method [25] with high accuracy in order to explained the difference between the experimental value measured by Schippers *et al.* [26] and the previous theoretical result of Marques *et al.*[23]. The latest, Andersson *et al.* calculated the hyperfine induced $2s2p\ ^3P_2 \rightarrow 2s^2\ ^1S_0$ E1 transition probabilities for Be-like ions within $Z = 6 - 22$ [27]. In previous studies, the influence of interference effects on the HIT rates, caused by mixing from $^3P_1$ and $^1P_1$ perturbative states, has been emphasized already. However, in our present study it was found that the trend of interference effects with increasing atomic number Z is non-monotone [28]. Here the characteristics of the interference effects in the hyperfine induced $2s2p\ ^3P_2,\ ^3P_0 \rightarrow 2s^2\ ^1S_0$ E1 transition of Be-like ions were shown in detail.

In Table 2 we listed our calculated results for the HIT probabilities of $^3P_0$ level as well as other theoretical and experimental values [17, 23, 25, 26]. As can be seen from Table 1, the results of Marques *et al.* obviously deviate from others for two reasons. Firstly, they neglected the contribution from the perturbative state of $^1P_1$ to the HIT probabilities; Secondly, there are inherent problems with the transition energies used in their method [25]. The present calculational results, displayed in the forth column in Table 2, are in good agreement with others for ions with $Z \leq 30$, but not for ions with $Z > 30$. The reason for it is that we neglected high order Breit interactions and QED effects in electronic wavefunction calculations, which lead to relatively larger differences in transition energies for high-Z ions. Therefore, experimental [29] or other accurate theoretical transition energies [25] were used to correct the transition probabilities. These corrected results, labeled by corr., were presented in the fifth column of Table 2. It can be found that the consistency obviously becomes better comparing with the calculational values of Brage *et al.* and Cheng *et al.* for high-Z ions. While for Be-like ^{103}Rh ion the two orders of magnitude difference for the HIT probability results from the different magnetic dipole moment that was used.

In Table 3 we presented the HIT probabilities of $^3P_2$ level in connection with corresponding transition energies which were used to correct these probabilities as the same reason mentioned above. Additionally, theoretical results by Andersson *et al* were displayed in this table [27]. For $^3P_2$ level, it can split into several hyperfine sublevels in present of hyperfine interactions, which were labeled by total angular momentum F. For each hyperfine level satisfying selection rule of electric dipole can occur hyperfine induced E1 transition, and these probabilities are dependent on the total angular number F and the nuclear parameters. Comparing with those results by Andersson *et al.* [27], a good agreement for those overlapped ions can be found.

In order to show the characteristics of interference effects in these two transitions clearly, the reduced HIT amplitudes, which can be obtained as shown in Sec. 2, from perturbative $^3P_1$ and $^1P_1$ states were plotted in Fig. 2, respectively. As can be seen from this picture, the interference effects work within a wide range of atomic numbers. It is interesting that the trends of the HIT amplitudes with increasing atomic number Z are similar for these two transition. An obvious difference is that the HIT amplitude of $^1P_1$ is dominant in hyperfine induced $2s2p\ ^3P_2 \rightarrow 2s^2\ ^1S_0$ E1 transition while for hyperfine induced $2s2p\ ^3P_0 \rightarrow 2s^2\ ^1S_0$ E1 transition it is dominated by the HIT amplitude of $^3P_1$.

Furthermore, to reveal the characteristics of the interference effects in hyperfine induced $2s2p\ ^3P_0,\ ^3P_2 \rightarrow 2s^2\ ^1S_0$ transitions, we defined a function R^{el} as proportion to the ratio between the two reduced HIT amplitudes. For hyperfine induced $2s2p\ ^3P_0 \rightarrow 2s^2\ ^1S_0$ transition, R^{el} can be expressed as

$$R^{el}(^3P_0) = \frac{h_0^{el}\langle 2s^2\ ^1S_0||Q^{(1)}||2s2p\ ^1P_1\rangle}{h_1^{el}\langle 2s^2\ ^1S_0||Q^{(1)}||2s2p\ ^3P_1\rangle}, \quad (3)$$

and for hyperfine induced $2s2p\ ^3P_2 \rightarrow 2s^2\ ^1S_0$ transition, R^{el} can be expressed as

$$R^{el}(^3P_2) = \frac{h_1^{el}\langle 2s^2\ ^1S_0||Q^{(1)}||2s2p\ ^3P_1\rangle}{h_0^{el}\langle 2s^2\ ^1S_0||Q^{(1)}||2s2p\ ^1P_1\rangle}. \quad (4)$$

Under such definition, R^{el} is a real number between zero and one. According to this formula, the interference effect in the HIT becomes stronger if R^{el} approaches to one. The trend of R^{el} for the HITs of $^3P_0$ and $^3P_2$ level as function of atomic number Z was plotted in Fig. 3, respectively. It is worthy noting from this picture that the interference effects for these two HITs change non-monotonically with increasing atomic number Z. Also, there exists a minimum value for $R^{el}(^3P_0)$ near $Z = 9$ and for $R^{el}(^3P_2)$ near $Z = 7$, respectively. Therefore, the strongest interference effect occurs near $Z = 9$ for hyperfine induced $2s2p\ ^3P_0 \rightarrow 2s^2\ ^1S_0$ E1 transition and near $Z = 7$ for hyperfine induced $2s2p\ ^3P_2 \rightarrow 2s^2\ ^1S_0$ E1 transition.

2. Mg-like ions

Some works on hyperfine quenching of the $3s3p\ ^3P_0$ state of Mg-like ions were available in the literature. The most extensive study was carried out by Marques *et al.* [30] using the complex matrix method developed by Indelicato [24]. In this studies correlations were limited to the outer electrons, which may impair the accuracy for lower Z where core-valence effects are large. Later, rates were also calculated by Brage *et al.* using a perturbative approach [17] in order to determine isotopic abundance ratios and diagnose densities of low-density plasmas. Their calculations were restricted to those elements that

Table 2: Hyperfine induced $2s2p\ ^3P_0 \rightarrow 2s^2\ ^1S_0$ E1 transition probabilities in s^{-1} and corresponding transition energy in cm^{-1}. The calculational results were compared with other theoretical and experimental values. Here uncorr. means the present calculated transition energies were used to obtain hyperfine induced transition probabilities, while the corr. means transition energies taken from NIST database [29] were used to obtain this transition probabilities.

	Transition energy		This work					
ions	This work	NIST [29]	uncorr.	corr.	Ref.[17]	Ref.[25]	Ref.[23]	Expt.
^{13}C	52248	52367	8.28[-4]	8.33[-4]	9.04[-4]	8.223[-4]	2.00[-4]	
^{14}N	67251	67209	4.40[-4]	4.39[-4]	4.92[-4]	4.40[-4]	1.28[-4]	4[-4]±1.32[a]
^{19}F	96666	96590	1.17[-1]	1.17[-1]		1.208[-1]	3.60[-2]	
^{28}Si	169054	169802	5.89[-2]	5.97[-2]	6.08[-2]	6.011[-2]	2.16[-2]	
^{39}Ar	228716	228674	8.28[-1]	8.27[-1]				
^{47}Ti	289562	288190	6.80[-1]	6.71[-1]		6.727[-1]	3.56[-1]	5.6[-1][b]
^{57}Fe	352029	348180	4.98[-2]	4.82[-2]	5.45[-2]	4.783[-2]	3.27[-2]	
^{67}Zn	416600	409827[†]	5.00	4.76		4.732	4.13	
^{85}Rb	537174	523000	43.3	39.94		39.35	48.17	
^{103}Rh	693209	661772[†]	147.1	128.0		1.262	1.91	
^{131}Xe	903919	843105[†]	199.0	161.5		158.1	262.67	

[†] Cheng *et al.* [25]

[a] Brage *et al.* [18]

[b] Schippers *et al.* [26]

Table 3: Hyperfine induced $2s2p\ ^3P_2 \rightarrow 2s^2\ ^1S_0$ E1 transition probabilities (A_{HIT}) in s^{-1} associated with corresponding reduced hyperfine induced transition probabilities A^{el}_{HIT} in s^{-1} and transition energies ΔE from NIST database [29] in cm^{-1}.

ions	ΔE	A^{el}_{HIT}	F	A_{HIT}	Andersson [27]	ions	ΔE	A^{el}_{HIT}	F	A_{HIT}
^{13}C	52447	9.87[-4]	3/2	7.30[-4]	7.374[-4]	^{57}Fe	471780	1.24	3/2	1.52[-1]
			5/2	0					5/2	0
^{14}N	67412	2.52[-4]	1	2.08[-4]	2.185[-4]	^{67}Zn	640470	4.40	1/2	0
			2	3.69[-4]	3.887[-4]				3/2	8.81
			3	0					5/2	1.75[1]
^{19}F	97437	1.21[-3]	3/2	1.26[-1]	1.282[-1]				7/2	1.79[1]
			5/2	0					9/2	0
^{28}Si	177318	1.70[-2]	3/2	7.68[-2]		^{85}Rb	1094800	3.83[1]	1/2	0
			5/2	0					3/2	1.85[2]
^{39}Ar	252683	8.28[-2]	3/2	0					5/2	3.65[2]
			5/2	5.83[-1]					7/2	3.71[2]
			7/2	1.03					9/2	0
			9/2	9.76[-1]		^{103}Rh	2310547[†]	4.08[2]	3/2	4.79[2]
			11/2	0					5/2	0
^{47}Ti	347420	3.34[-1]	1/2	0		^{131}Xe	3785850	4.96[3]	1/2	3.95[3]
			3/2	4.82[-1]	4.952[-1]				3/2	1.30[4]
			5/2	1.03	1.057				5/2	1.30[4]
			7/2	1.17	1.192					
			9/2	0						

[†] Cheng *et al.* [25]

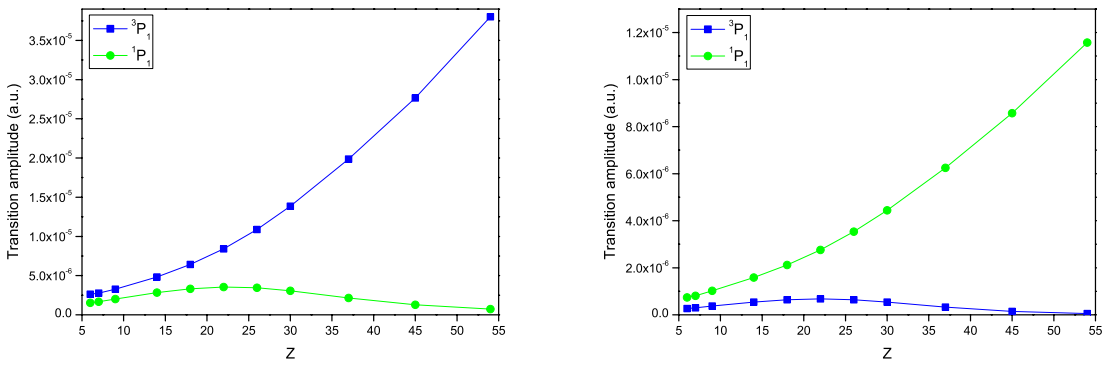

Figure 2: Transition amplitudes of the reduced hyperfine induced transitions in a.u.. Left: hyperfine induced $2s2p\ ^3P_0 \rightarrow 2s^2\ ^1S_0$ E1 transition; Right: hyperfine induced $2s2p\ ^3P_2 \rightarrow 2s^2\ ^1S_0$ E1 transition.

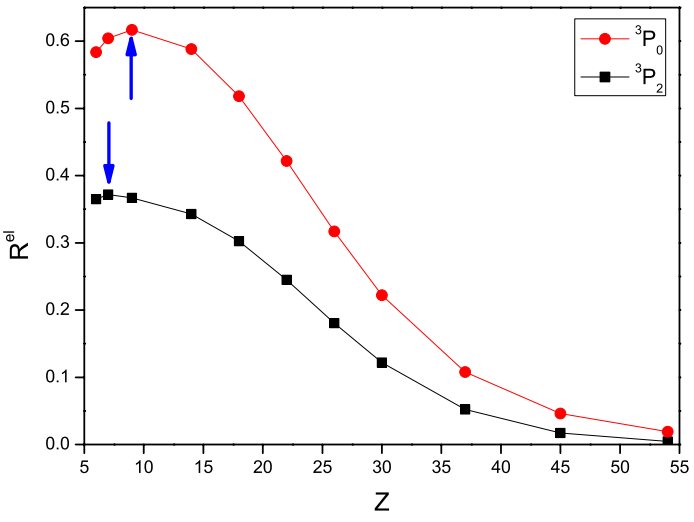

Figure 3: The trends of R^{el} for hyperfine induced $2s2p\ ^3P_0,\ ^3P_2 \rightarrow 2s^2\ ^1S_0$ E1 transitions with increasing atomic numbers Z. Two blue arrows label the positions where inference effects are the strongest for these two hyperfine induced transitions, respectively.

are abundant in stellar atmospheres. Therefore, accurate theoretical hyperfine induced $3s3p\ ^3P_0 \rightarrow 3s^2\ ^1S_0$ transition probabilities of Mg-like ions are still scarce. In particular, Rosenband *et al.* have recently measured the rates of $^{27}Al^+$ ions with high precise using quantum logic spectroscopy (QLS) technology [31]. In response to this we performed further investigations on the hyperfine induced transition rates of the $3s3p\ ^3P_0$ state for Mg-like ions [32].

Present calculational results were displayed in the table 4 together with corresponding wavelengths and other theoretical and experimental values. In this table, PT denotes perturbative results by Brage *et al.* [17], CM are complex matrix results obtained by Marques *et al.* [30]. As can be seen from this table, the agreement between our results and the values of Brage *et al.* is acceptable. Whereas the CM values differ from the present results and the ones of Brage *et al.* mainly for two reasons: limited correlation included in the Marques *et al.* calculation, and the inherent problems with the transition energies used in CM method [25]. We further compared present calculations with the latest experimental measurements [31], a good agreement for hyperfine induced rate of $^{27}Al^+$ was found.

In order to establish systematic trends for hyperfine quenching rates along the isoelectronic sequence we factorized the hyperfine induced transition rate into nuclear and electronic parts (see Brage *et al.* [17]),

$$A(^3P_0 \rightarrow\ ^1S_0) = [\mu_I^2(1 + I^{-1})]A_{el}(^3P_0 \rightarrow\ ^1S_0). \tag{5}$$

The reduced hyperfine induced transition rates A_{el} are relatively independent of nuclear effects. In Fig. 4. the reduced and total hyperfine induced transition rates were plotted along the isoelectronic sequence. The electronic part A_{el} has a smooth behavior along the isoelectronic sequence.

To estimate the transition rate for any isotope we fit a power function in Z

$$A_{el} = 1.087 \times 10^{-11} Z^{7.8004}. \tag{6}$$

The fitted function is shown in Fig. 4 and it gives a global description of the data. Higher accuracy can be obtained by spline interpolation based on the A_{el} values in table 4. In the figure the polynomial fit by Brage *et al.*, which is valid only for low Z, was also displayed.

Furthermore, we presented the hyperfine induced $3s3p\ ^3P_2 \rightarrow 3s^2\ ^1S_0$ E1 transition rates along Mg-like isoelectronic sequence [33]. In Fig 5 we presented graphically that the reduced HIT probabilities as well as the M1 and M2 transition probabilities as function of Z. Meanwhile the HIT probabilities were also plotted with scattered dot. From this

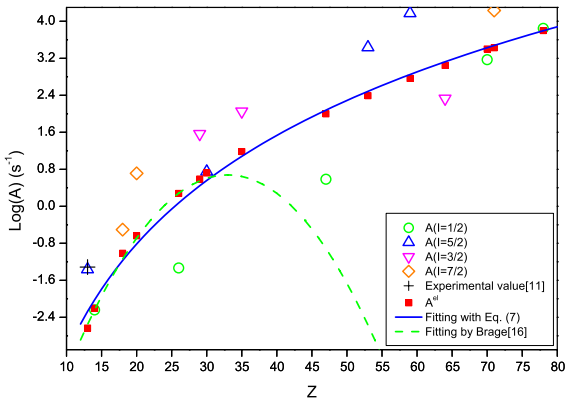

Figure 4: Logarithm of hyperfine induced rates A with different nuclear spin for $3s3p\ ^3P_0 \rightarrow 3s^2\ ^1S_0$ transition of Mg-like ions together with experimental value from Ref. [31]. Reduced hyperfine induced decay rates A_{el} and fitted curves are also displayed.

Table 4: Wavelengths (λ), probabilities (A) and reduced rates (A_{el}) for hyperfine induced transition $3s^2\ ^1S_0$ - $3s3p\ ^3P_0$ in Mg-like ions. Magnetic dipole moments (in μ_N) are taken from [**?**]. The results are compared with other theoretical and experimental values. PT and CM refer to perturbative and complex matrix results, respectively. Numbers in brackets represent powers of ten.

			$\lambda(\mathring{A})$			A (s^{-1})			
Z	I	μ_I	This work	Exp. [29]	A_{el}	This work	CM[30]	PT[17]	Exp. [31]
13	5/2	3.6415069	2669.080	2679.811	2.331[-3]	4.327[-2]			4.854[-2]
14	1/2	0.55529	1901.352	1900.529	6.227[-3]	5.760[-3]	3.545[-3]	5.23[-3]	
18	7/2	1.588	887.575	886.476	9.641[-2]	3.126[-1]			
20	7/2	1.3173	706.070	699.862	2.306[-1]	5.144[-1]	3.851[-1]	4.79[-1]	
26	1/2	0.09044	429.275	428.509	1.895	4.649[-2]	3.858[-2]	4.98[-2]	
29	3/2	2.3816	360.191	358.105	3.889	3.676[1]	2.930[1]		
30	5/2	0.8752049	339.548	339.390	5.249	5.629	4.275		
35	3/2	2.1064	267.978	268.230	1.525[1]	1.128[2]	9.320[1]		
47	1/2	0.11357	175.634		9.97[1]	3.858	4.735[1]		
53	5/2	2.81327	147.767		2.466[2]	2.732[3]	3.489[3]		
59	5/2	4.2754	126.523		5.833[2]	1.493[4]	1.898[4]		
64	3/2	0.3398	112.102		1.110[3]	2.136[2]	2.753[2]		
70	5/2	0.648	97.398		2.514[3]	1.478[3]	2.036[3]		
71	7/2	2.2323	95.429		2.678[3]	1.715[4]	2.296[4]		
78	1/2	0.60952	82.121		6.318[3]	7.042[3]	9.506[3]		

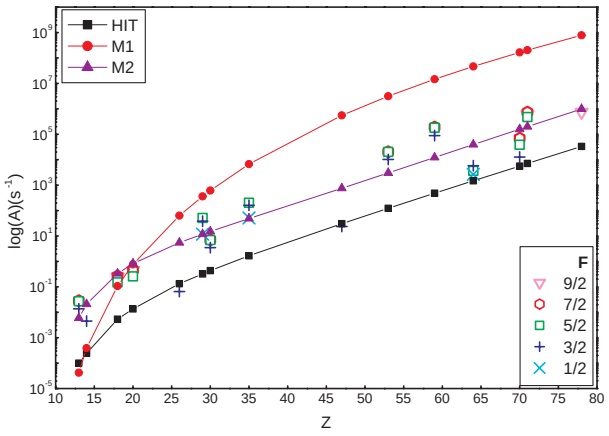

Figure 5: Logarithm of hyperfine induced transition A_{HIT} in connecting with reduced probabilities A_{el} relative to the magnetic quadurpole (M2) and magnetic dipole (M1) in s^{-1} for Mg-like ions.

picture we could see that the hyperfine induced transition is the dominant decay channel at the beginning of Mg-like isoelectronic sequence.

The lifetime of hyperfine level in $^3P_2$ state can be obtained in terms of

$$\tau = \frac{1}{A_{M1} + A_{M2} + A_{HIT}}, \tag{7}$$

in which the interference effect between M2 and hyperfine induced E1 transition was neglected [34, 35]. Present calculated results were listed in Table 3. For comparison, the lifetime τ' of $^3P_2$ levels without hyperfine interaction were displayed in this table. As can be seen from this table, the hyperfine induced transition obviously shorten the lifetime of $^3P_2$ level, especially Mg-like Al, Si, Ar, Ca, Fe and Cu ions. Moreover, the lifetime is dependent on total angular quantum number F. With increasing atomic number Z, the importance of this effect is decreasing because the magnetic dipole (M1) transition become the dominant decay channel here.

Acknowledgement

This work was supported by the National Nature Science Foundation of China (Grant No. 10774122, 10876028), the Core-university program between Japanese Society of Promotion of Science and Chinese Academy of Sciences, the specialized Research Fund for the Doctoral Program of Higher Education of China (Grant No. 20070736001), the Foundation of Theoretical Nuclear Physics of National Laboratory of Heavy Ion Accelerator of

Table 5: Lifetime of the individual hyperfine level in $^3P_2$ state in s with and without including hyperfine induced E1 transition for Mg-like ions. τ'=1/(A_{M1} + A_{M2}). Numbers in brackets represent powers of ten.

Elements	F	τ'	τ	Elements	F	τ'	τ
$^{27}_{13}$Al	1/2	1.678[2]	1.678[2]	$^{107}_{47}$Ag	3/2	1.812[-6]	1.812[-6]
	3/2	1.678[2]	6.281[1]		5/2	1.812[-6]	1.812[-6]
	5/2	1.678[2]	3.817[1]	$^{127}_{53}$I	1/2	3.184[-7]	3.184[-7]
	7/2	1.678[2]	3.662[1]		3/2	3.184[-7]	3.174[-7]
	9/2	1.678[2]	1.678[2]		5/2	3.184[-7]	3.164[-7]
$^{29}_{14}$Si	3/2	4.725[1]	3.897[1]		7/2	3.184[-7]	3.163[-7]
	5/2	4.725[1]	4.725[1]		9/2	3.184[-7]	3.184[-7]
$^{39}_{18}$Ar	3/2	2.277	2.277	$^{141}_{59}$Pr	1/2	6.857[-8]	6.857[-8]
	5/2	2.277	1.702		3/2	6.857[-8]	6.816[-8]
	7/2	2.277	1.423		5/2	6.857[-8]	6.774[-8]
	9/2	2.277	1.443		7/2	6.857[-8]	6.769[-8]
	11/2	2.277	2.277		9/2	6.857[-8]	6.857[-8]
$^{43}_{20}$Ca	3/2	6.334[-1]	6.334[-1]	$^{157}_{64}$Gd	1/2	2.155[-8]	2.155[-8]
	5/2	6.334[-1]	5.446[-1]		3/2	2.155[-8]	2.155[-8]
	7/2	6.334[-1]	4.911[-1]		5/2	2.155[-8]	2.155[-8]
	9/2	6.334[-1]	4.952[-1]		7/2	2.155[-8]	2.155[-8]
	11/2	6.334[-1]	6.334[-1]	$^{173}_{70}$Yb	1/2	6.032[-9]	6.032[-9]
$^{57}_{26}$Fe	3/2	1.463[-2]	1.461[-2]		3/2	6.032[-9]	6.031[-9]
	5/2	1.463[-2]	1.463[-2]		5/2	6.032[-9]	6.030[-9]
$^{29}_{66}$Cu	1/2	2.695[-3]	2.609[-3]		7/2	6.032[-9]	6.030[-9]
	3/2	2.695[-3]	2.439[-3]		9/2	6.032[-9]	6.032[-9]
	5/2	2.695[-3]	2.369[-3]	$^{175}_{71}$Lu	3/2	4.922[-9]	4.922[-9]
	7/2	2.695[-3]	2.695[-3]		5/2	4.922[-9]	4.913[-9]
$^{67}_{30}$Zn	1/2	1.594[-3]	1.594[-3]		7/2	4.922[-9]	4.905[-9]
	3/2	1.594[-3]	1.585[-3]		9/2	4.922[-9]	4.906[-9]
	5/2	1.594[-3]	1.576[-3]		11/2	4.922[-9]	4.922[-9]
	7/2	1.594[-3]	1.575[-3]	$^{195}_{78}$Pt	3/2	1.280[-9]	1.280[-9]
	9/2	1.594[-3]	1.594[-3]		5/2	1.280[-9]	1.280[-9]
$^{79}_{35}$Br	1/2	1.485[-4]	1.474[-4]				
	3/2	1.485[-4]	1.451[-4]				
	5/2	1.485[-4]	1.440[-4]				
	7/2	1.485[-4]	1.485[-4]				

Lanzhou. Financial support by the Swedish Research Council is gratefully acknowledged.

References

[1] S. C. Bennett and C. E. Wieman, Phys. Rev. Lett. **82** (1999) 2484.

[2] M. -A. Bouchiat, Phys. Rev. Lett. **100** (2008) 123003.

[3] L. N. Labzowsky, A. V. Nefiodov, G. Plunien, *et al.*, Phys. Rev. A **63** (2001) 054105.

[4] A. Bondarevskaya, A. Prozorov, L. N. Labzowsky, *et al.*, Phys. Lett. A **372** (2008) 6642.

[5] J. G. Li, P. Jönsson, G. Gaigalas and C. Z. Dong, Euro. Phys. J. D **55** (2009) 313.

[6] Jacek Bieroń and Pekka Pyykkö, Phys. Rev. Lett. **87** (2001) 133003.

[7] K. Beloy, A. Derevianko and W. R. Johnson, Phys. Rev. A **77** (2008) 012512.

[8] K. Okada, M. Wada, T. Nakamura, *et al.*, Phys. Rev. Lett. **101** (2008) 212502.

[9] H. Backe, A. Dretzke, S. Fritzsche, *et al.*, Hyperfine Interactions, **162** (2005) 3.

[10] L. N. Labzowsky, A. V. Nefiodov, G. Plunien, *et al.*, Phys. Rev. Lett. **84** (2000) 851.

[11] Th. Becker, *et al.*, Phys. Rev. A **63** (2001) 051802(R).

[12] M. Takamoto and H. Katori, Phys. Rev. Lett. **91** (2003) 223001.

[13] M. Petersen, R. Chicireanu, S. T. Dawkins, *et al.*, Phys. Rev. Lett. **101** (2008) 183004.

[14] S. G. Porsev and A. Derevianko, Phys. Rev. A **69** (2004) 042506.

[15] P. Jönsson and M. Andersson, J. Phys. B **40** (2007) 2417.

[16] M. Andersson, P. Jönsson and H. Sabel, J. Phys. B **39** (2006) 4239.

[17] T. Brage, P. G. Judge, A. Aboussaïd, M. R. Godefroid, P. Jönsson, A. Ynnerman, C. Froese Fischer and D. S. Leckrone, ApJ **500** (1998) 507.

[18] T. Brage, P. G. Judge, and C. R. Proffitt, Phys. Rev. Lett. **89** (2002) 281101.

[19] P. Jönsson, X. He, C. Froese Fischer and I.P. Grant, Comput. Phys. Commun. **177** (2007) 597.

[20] J. G. Li, G. Gaigalas and C. Z. Dong, (unpublished).

[21] V. G. Gorshkov and L. I. Labzovskiĭ, JETP Lett. **19** (1974) 394.

[22] D. R. Plante, W. R. Johnson and J. Sapirstein, Phys. Rev. A **49** (1994) 3519.

[23] J. P. Marques, F. Parente and P. Indelicato, Phys. Rev. A **47** (1993) 929.

[24] P. Indelicato, F. Parente and R. Marrus, Phys. Rev. A **40** (1989) 3505.

[25] K. T. Cheng, M. H. Chen and W. R. Johnson, Phys. Rev. A **77** (2008) 052504.

[26] S. Schippers *et al.*, Phys. Rev. Lett **98** (2007) 033001.

[27] M. Andersson, K. Yao, R. Hutton, *et al*, Phys. Rev. A **77** (2008) 042509.

[28] Jiguang Li and Chenzhong Dong, *Chin. Phys. Lett.* (Sumitted).

[29] Y. Ralchenko, A.E. Kramida, J. Reader and NIST ASD Team (2008). NIST Atomic Spectra Database (v 3.1.5) [online]. Available : `http://physics.nist.gov/asd3` [2008, June 26] National Institute of Standards and Technology, Gaithersburg, MD.

[30] Marques J P, Parente F, Indelicato P 1993 *At. Data Nucl. Data Tables* **55** 157.

[31] Rosenband T, et al. 2007 *Phys. Rev. Lett.* **98** 220801.

[32] Huihui Kang, Jiguang Li, Chenzhong Dong, and Gediminas Gaigalas, *J. Phys. B* **42** 195002.

[33] Huihui Kang, Jiguang Li, Chenzhong Dong, and Gediminas Gaigalas, *J. Phys. B* (submitted).

[34] Yao K, Andersson M, Brage T, Hutton R, Jönsson P, Zou Y M 2006 *Phys. Rev. Lett* **97** 183001.

[35] Yao K, Andersson M, Brage T, Jönsson P, Zou Y M 2007 *Phys. Rev. Lett* **98** 269903.

Theoretical simulation of extreme ultraviolet spectra of tin in laser-produced plasmas

M. G. Su, C. Z. Dong, Y. E. Luo, L. Y. Xie and Y. B. Fu
College of Physics and Electronics Engineering, Northwest Normal University, Lanzhou 730070*, China*
Joint Laboratory of Atomic and Molecular Physics, NWNU & IMP CAS, Lanzhou, 730000, China
P. Hayden, L. Gaynor, G. O'Sullivan and J. White
School of Physics, University College Dublin, Belfield, Dublin 4, Ireland
e-mail: Dongcz@nwnu.edu.cn

Abstract

Extreme ultraviolet (EUV) emission spectra from laser-produced Sn plasmas have been experimentally investigated at different power densities in the 9.5-18 nm wavelength range because of their application as extreme ultraviolet lithography (EUVL) sources. Experimental results indicate the presence of a broad reabsorption band and some pronounced dips because of opacity effects in the spectra. With increasing power densities, the reabsorption band shifts to the shorter wavelength side and the absorption dips become deeper. Theoretical calculations using the Cowan code show that the dips arise from the $4d-4f$ and $4p-4d$ transitions. Using detailed configuration accounting (DCA) with the term structures treated by the unresolved transition array (UTA) model, we analyze the opacity effects and simulate the spectra. By comparing the results of the simulations with experiments, it can be concluded that the plasma from a 5% Sn target gives essentially pure emission, while the spectra from a pure Sn target contains both emission and absorption, with electron temperatures ranging from 28 to 15 eV, and electron densities from 5.0×10^{20} to 3.7×10^{19} cm^{-3}, in going from the core to the outer plasma region.

Keywords: EUV, atomic structure, atomic transition, optical emission, relativistic theory, MCDF, configuration interaction, electron correlation

1. Introduction

The emission of extreme ultraviolet (EUV) radiation from laser-produced high-Z plasmas is being studied extensively for its application in next generation semiconductor manufacturing technology [1-8]. The wavelength of choice for a prospective light source has been selected as 13.5 nm, based on the availability of Mo/Si multilayer mirrors with reflectivity approaching 72% within a bandwidth of approximately 0.3 nm at this wavelength. Laser-produced Sn plasmas provide an attractive 13.5 nm light source due to their

compactness and high emissivity.

However, for pure Sn plasmas, the opacity is so high that 13.5 nm radiation emitted from deep within the plasma core is absorbed strongly during propagation through the surrounding plasma as it expands. That is to say, they are optically thick to 13.5 nm EUV light because the properties of Sn plasmas depend strongly on the parameters of the laser pulse (and target concentration), such as wavelength, pulse width, and focal spot size. Moreover, when the focal spot is larger, the EUV emission must pass through a longer plasma with higher density, and the reabsorption is even stronger [9]. In addition, the spectrum of tin in the EUV range does not consist of sharp and well separated features, but a bright quasi-continuum band or unresolved transition array (UTA) [10]. So it is difficult to fully analyze the measured experimental spectrum, though most of the strongest lines have recently been identified [11].

To date, considerable international efforts have been channelled into the experimental realization and optimization of EUV emission. In view of the application, only intense emission from the 2% BW around 13.5 nm is desired. Therefore, it is necessary to obtain detailed information on the positions and intensities of lines in the EUV spectra of tin and analyze the mechanisms that determine the relative intensity of the in-band spectra.

Tao *et al.* [9] reported the effect of focal spot size on in-band 13.5 nm extreme ultraviolet emission from a laser-produced Sn plasma and confirmed experimentally the strong reabsorption of EUV 13.5 nm light in the spectrum. Fujioka *et al.* [12] measured an absorption spectrum of a uniform Sn plasma generated by thermal x-rays in the 9-19 nm wavelength range for the first time and experimentally investigated opacity effects on extreme ultraviolet (EUV) emission from a laser-produced Sn plasma. Ohashi *et al.* [13] measured charge exchange spectra in $Sn^{q+}(q = 6 - 15)$-He collisions and confirmed the positions of $4p - 4d$ and $4d - nl$ ($nl = 4f, 5p$ and $5f$) transitions. Kieft *et al.* [14] studied the EUV tin spectra from discharge plasmas. Sasaki *et al.* [15] analyzed the effect of the satellite lines and opacity using the HULLAC code and the Whiam collisional-radiative model. In addition, John *et al.* [16] modeled the emission in an optically thick laser produced tin plasma using the 2D radiative MHD code Z*. All of the above works are very helpful for analyzing the spectra of hot dense Sn plasmas, and provide not only experimental results but also theoretical insights.

In this paper, we present some measured experimental spectra from laser produced Sn plasmas and provide a theoretical analysis of them. Firstly, we make systematic computations for atomic structure of a range of Sn ions, from Sn^{6+} to Sn^{13+}, using the Cowan code. In these calculations, the effect of configuration interaction (CI) is also considered, since CI considerably changes the position and strength of lines. Secondly, we

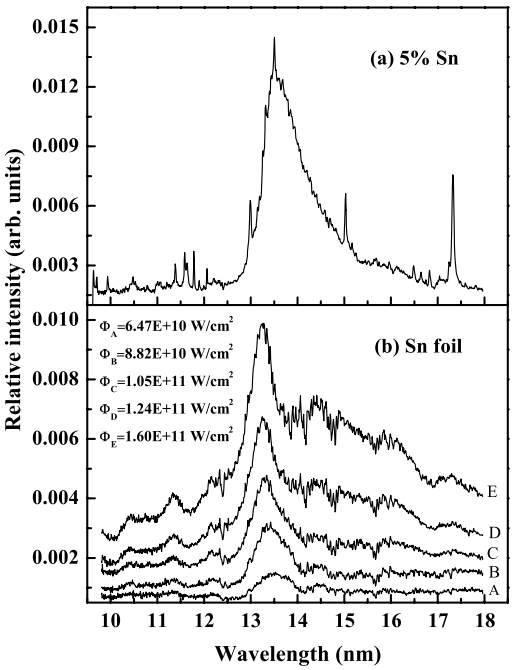

Figure 1: EUV spectra emitted by a laser-produced plasma formed on (a) 5% Sn and (b) pure tin target.

calculate the ion abundance and opacity of the plasma using the DCA/UTA code, which is very useful for the quantitative understanding of emission from laser-produced plasmas. Finally we present the simulated results and make a comparison with experimental data.

2. Experiment

The experimental setup in UCD [17,18] consists of a target chamber of diameter 400 mm, with the target holder containing the material of interest located at the centre of the chamber. The target holder was motorised, allowing a fresh surface to be exposed for each laser pulse. The laser used for the formation of the plasmas was a Nd:YAG laser, delivering up to 800 mJ in 15 ns. The fundamental wavelength, 1064 nm, was focused via a plano-convex lens to a spotsize of about 180 μm. The range of power densities used were obtained by varying the energy of the incident laser pulse, while maintaining the same focusing conditions.

The spectra were recorded on a Jenoptik 0.25 m grazing incidence, flat field spectro-

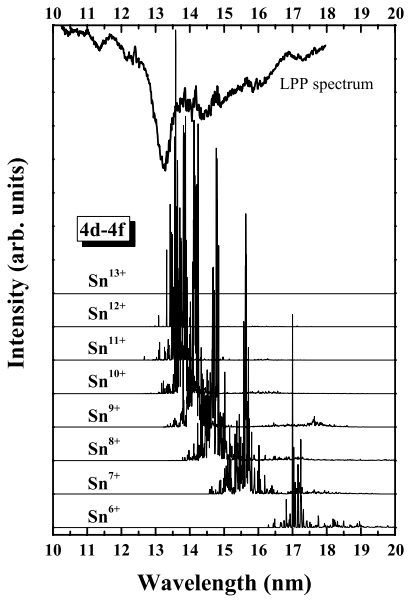

Figure 2: Theoretical calculated absorption peaks from 4d - 4f transition for Sn^{6+} to Sn^{13+}.

graph. This spectrograph was fitted with an absolutely calibrated backside illuminated x-ray CCD, covering the spectral range 9.5-18 nm. The spectrograph viewed the plasma at an angle of 45° to the incident laser pulse, and the plasma expanded parallel to the horizontal entrance slit of the spectrograph.

Fig. 1(a) shows the spectra from a target containing Sn at a concentration of 5% by number at a power density of 2.24×10^{11} W/cm^2. Fig. 1(b) shows the spectra of pure tin for power densities from 0.6-1.6 $\times 10^{11}$ W/cm^2. The following characteristics are observed in the experimental spectra: (1) the primary spectral feature is a broad quasicontinuum band; (2) absorption dips are present near 13.61 nm, 13.85 nm, 14.17 nm, 14.76 nm, 15.65 nm and 16.90 nm, in pure tin plasmas and (3) with increasing power density, the peak of the broad quasi-continuum band around 13.50 nm shifts to 13.25 nm and its width become narrower. In addition, the background continuum spectra of its left side becomes more intense. The information provided by these experimental spectra should be helpful for the identification of the spectral structure in the EUV spectral regime and for theoretical simulation.

3. Identification of the dips

Hartree-Fock (HF) approximation calculations with the Cowan code were used to generate theoretical spectra of transition oscillator strengths versus wavelength for a range of tin ions, from Sn^{6+} to Sn^{13+}. The theoretical spectral lines were convolved with a Gaussian function of full width at half maximum appropriate to the flat field spectrometer resolution at that wavelength to produce a theoretical spectrum for each ion stage. The resulting theoretical spectra were compared to the spectra obtained at different power densities and were used to aid the identification of spectral features in the experimental spectra.

In the present study, the configurations of tin ions from Sn^{6+} to Sn^{13+} included in the calculations are $4d^n$ for the ground state, $4d^{n-1}ml$ and $4p^5 4d^n(4d, ml)$ ($n = 1 - 8, ml = 4f, 5s, 5p, 5d, 5f, 6p$) for the one-electron excited states. These configurations contain open $4p$ and open $4d$ shells, so there exits a large number of near-degenerate energy levels when they couple with the electrons of other shells, especially, since the excitation energy from the ground state to $4d^{n-1}(4f, 5p)$ and $4p^5 4d^{n+1}$ are close to each other, the resulting configuration mixing considerably modifies the energy levels [15]. As a result, the spectra arising from transitions between these levels are extremely complex and significantly overlap with each other to form a UTA, that consists of a large number of resonance and satellite lines.

In order to optimize the output of the Cowan code, the Slater-Condon integrals (F^k, G^k and R^k) and spin-orbit integral (ζ) were adjusted to match the Cowan wavelength to the previously reported wavelength and the experimental results presented in this paper. Reduction of the values of F^k,G^k,R^k to 78% and ζ to 99% were found to best match the $4d - 4f$ transitions array reported by Ohashi *et al.* [13], as is indicated in Fig. 2. In this figure, the calculated $4d - 4f$ transition spectra from Sn^{6+} to Sn^{13+} are shown. For clarity, the experimental spectrum was reversed and placed at the top of this figure. By comparing the calculated transition spectra of different ions with the peak positions of the dips of the experimental spectrum, it can be clearly seen that there is good agreement. In addition, it is also seen that the bands corresponding to $4p - 4d$ and $4d - 4f$ transitions from Sn^{10+} to Sn^{13+} ions overlap each other, to form a broad feature near 13.5 nm. The other transition arrays at longer wavelengths are well separated, so these dips can make identification of the contribution of different Sn ions possible. Based on the scaling used, we also calculated other atomic data required for the same simulation.

4. Simulation and comparison of plasma spectra

As indicated in Fig. 1, there are very great differences between the experimental spectra of plasmas from the 5% and pure Sn targets. Fig. 1 (a) is essentially a pure

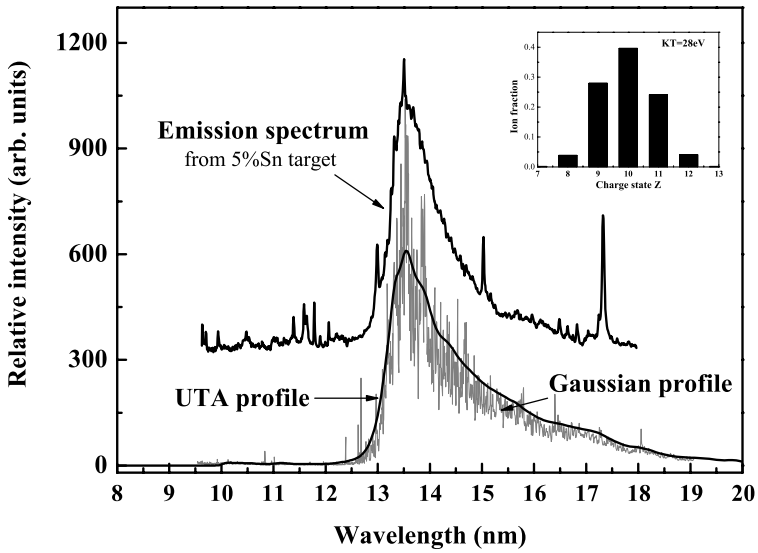

Figure 3: Comparison between theoretical and experimental spectra from 5% tin target.

emission spectrum which is optically thin and in which reabsorption effects and induced emission can be neglected. To estimate the plasma parameters, firstly, we assume that there is a local thermodynamic equilibrium population in the hot dense plasma, and the population of Sn ions is then calculated using detailed configuration accounting (DCA) with the term structures treated by the UTA model [19]. Next the theoretical spectral line intensities are multiplied by the corresponding ion fraction and then convolved with two different profiles to make a better comparison with experimental spectra, as indicated in Fig. 3. In this figure, the gray line shows the result using a Gaussian function of full width at half maximum appropriate to the flat field spectrometer resolution at this spectral range, which is 0.05 eV, and the black line shows the result using the UTA method [20]. In the UTA method, the averaged transition energy and width defined from the statistical weight of the upper level g_i and oscillator strength f_{ij} is given as:

$$\bar{E}_{UTA} = \frac{\sum[(g_i f_{ij})E_{ij}]}{\sum(g_i f_{ij})} \tag{1}$$

$$\Delta E_{UTA} = \sqrt{\frac{\sum[(g_i f_{ij})(E_{ij} - \bar{E}_{UTA})^2]}{\sum(g_i f_{ij})}} \tag{2}$$

Both results are obtained at $kT = 28$ eV and $N_e = 5 \times 10^{20}$ cm^{-3}. It can be seen

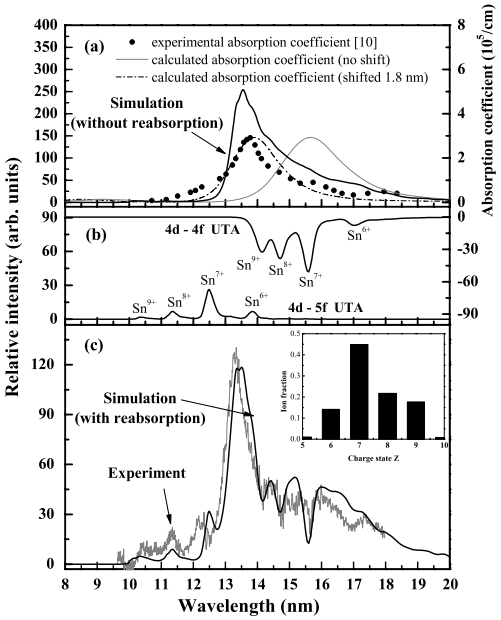

Figure 4: Theoretical simulation and comparison of laser produced Sn spectrum.

that there is very good agreement between them, and to some extent, the UTA method smoothes the contribution of different ions. Compared with the experimental spectrum, the UTA profile is seen to better match the experimental results.

However, compared with the emission spectrum in Fig. 1(a), the experimental spectra in Fig. 1(b) are more complex because of opacity effects. In the experimental set-up the signal reaching the collecting optics is the sum of signals from plasma volumes with different temperatures and densities, thus a single plasma parameter cannot successfully describe ion populations, especially the emission and re-absorption in less dense plasma volumes, i.e., the plasma spectra strongly depends on the experimental conditions. To analyze the formation of the plasma, we make the following assumptions: (1) it has a high temperature and density which gives rise to strong reabsorption effects in the main core region of the plasma; (2) there is weaker resonance line absorption and strong resonance line emission from the outer region of the plasma.

Under the assumptions made above, first, we estimated the absorption coefficients using the DTA/UTA method for $kT = 28$ eV and $N_e = 5 \times 10^{20}$ cm^{-3}. However, because in this calculations atomic structure calculations were obtained using the average atom model, a shift between the calculated and the measured energy of the absorption coefficients [12] of 1.8 nm was observed. However, the profiles were similar in both cases. In order to allow

for the error due to the different model, the calculated absorption coefficient was shifted by 1.8 nm to a shorter wavelength, and the result is indicated in Fig. 4(a). It is seen that, in the 12-17 nm spectral region, the absorption coefficients is approximately symmetric about 13.9 nm. Second, we estimated the ion populations in the plasma outer region which is at lower temperature and lower density. When $kT = 15$ eV and $N_e = 3.7 \times 10^{19}$ cm^{-3}, we find that there is good agreement between the $4p - 4d$, $4d - 4f$ and $4d - 5f$ UTA spectra from Sn^{6+} to Sn^{9+} and the experimental features, and their ion fractions are 14%, 45%, 22% and 17% respectively at this temperature. Both the $4 - 4$ and $4d - 5f$ UTAs are indicated in Fig. 4(b). Finally, the final simulated spectrum was obtained by subtracting the contribution from reabsorption effect and adding the contribution from induced emission. Fig. 4(c) shows the comparison between an experimental spectrum and a simulated one, and the inserted column chart presents the populations of lower ion stages from the outer region. From this figure, it can be clearly seen that there is good agreement between simulation and experiment. So we can conclude that, in the plasma produced by the pure Sn target, the electron temperature is reduced from 28 to 15 eV, and the electron density is reduced from 5.0×10^{20} to 3.7×10^{19} cm^{-3}, in moving from the plasma core to its periphery.

However, there are two obvious discrepancies between the simulated and experimental spectra: (1) there is a reversal in the spectral structure at around 12.5 nm. In fact, the dip at 12.5 nm arises from the $4d - 5f$ transition array of Sn^{7+}. At this wavelength there are relatively lower absorption and stronger emission effects at the same time because of the opacity effects; (2) the intensity at wavelengths below 13 nm is lower than that of experiment, while above 14 nm the reverse is true. These discrepancies may indicate that there should be a different proportionality coefficient between absorption and emission in the outer plasma. They will be modified by making more detailed and accurate calculations, and this work is now in progress.

5. Conclusion

In conclusion, the EUV spectra from laser-produced Sn plasmas were recorded and analyzed using the Cowan code. The present study has led to the identification of reabsorbtion structure corresponding to $4p - 4d$ and $4d - 4f$ transitions within the ions of Sn^{6+} up to Sn^{9+}. We also analyzed the important influence of opacity effects by using the DCA/UTA model and obtained a simulated spectrum, which is in good agreement with experimental spectra and concluded that the plasma from a 5% Sn target is essentially pure emission, while the plasma from a pure Sn target contains both emission and absorption. Furthermore, the electron temperature decreased from 28 to 15 eV, and electron

density from 5.0×10^{20} to 3.7×10^{19} cm^{-3}, in going from the core to the periphery of the EUV emitting zone.

Acknowledgement

This work has been supported by the National Natural Science Foundation of China (Grant No. 10434100, 10774122), the China/Ireland Science and Technology Collaboration Research Fund (CI-2004-07), the Specialized Research Fund for the Doctoral Program of Higher Education of China (Grant No. 20070736001) and the Foundation of Northwest Normal University (Grant No. NWNU-KJCXGC-03-21). Authors would like to thank Prof. F. Koike and Prof. J. G. Wang for many fruitful discussions.

References

[1] G. Kubiak, L. Bernardez and K. Krenz, Proc. SPIE **3331**, 81 (1998).
[2] C. Gwyn, D. Attwood and D. Sweeney, J. Vac. Sci. Technol. B **16**, 3142 (1998).
[3] L. A. Shmaenok, F. Bijkerk et al, Proc. SPIE **2523**, 113 (1995).
[4] M. Richardson, C. S. Koay, C. Keyser et al, Proc. SPIE **5196**, 119 (2004).
[5] H. Shields, S. W. Fornaca et al, Proc. SPIE **4688**, 94 (2002).
[6] U. Stamm, I. Ahmad, I. Balogh et al, Proc. SPIE **5037**, 119 (2004).
[7] I. W. Choi, H. Daido, S. Yamagami et al, J. Opt. Soc. Am. B **17**, 1616 (2000).
[8] T. Aota and T. Tomie. Phys. Rev. Lett. **94**, 015004 (2005).
[9] Y. Tao , S. S. Harilal, M. S. Tillack et al, Optics Letters **31**, 2492 (2006).
[10] P. Mandelbaum, M. Finkenthal et al, Phys. Rev. A **35**, 5051 (1987).
[11] S.S. Churilov and A. N. Ryabtsev, Phys. Scr. **73**, 614 (2006).
[12] S. Fujioka, H. Nishimura, K. Nishihara et al, Phys. Rev.Lett. **95**, 235004 (2005).
[13] H. Ohashi et al, Journal of Physics: Conference Series **58**, 235 (2007).
[14] E. R. Kieft, K. Garloff et al, Phys. Rev. E **71**, 036402 (2005).
[15] A. Sasaki et al, IEEE joural of selected topics in quantum electronics **10**, 1037 (2004).
[16] J. White, G. O'sullivan et al, Appl. Phys. Lett. **92**, 151501 (2008).
[17] P. Hayden, A. Cummings et al, J. Appl. Phys. **99**, 093302 (2006).
[18] P. Hayden, J. White, et al, Microelectronic Engineering **83**, 699 (2006).
[19] J. Yan and J. M. Li. Chin. Phys. Lett. **17**, 194 (2000).
[20] A. Sasaki, K. Nishihara et al, Appl. Phys. Lett. **85**, 5857(2004).

A semi-quantitative analysis of essential micronutrients in folium lycii using laser-induced breakdown spectroscopy technique

Duixiong Sun[1], Maogen Su[1], Chenzhong Dong[1], Dacheng Zhang[2], and Xinwen Ma[2]

1) College of Physics and Electronic Engineering, Northwest Normal University, Lanzhou, 730070, China

2) Institute of Modern Physics, the Chinese Academy of sciences, Lanzhou, 730000, China

e-mail: dongcz@nwnu.edu.cn

Abstract

In this paper, the capabilities of laser-induced breakdown spectroscopy (LIBS) for rapid analysis to multi-component plant are illustrated using a 1064 nm laser focused onto the surface of folium lycii. Based on homogeneous plasma assumption, nine of essential micronutrients in folium lycii are identified. Using Saha equation and Boltzmann plot method electron density and plasma temperature are obtained, and their relative concentration (Ca, Mg, Al, Si, Ti, Na, K, Li, and Sr) are obtained employing a semi-quantitative method.

Keywords: Plasma, LIBS, Folium lycii, Semi-quantitative analysis

1.Introduction

A sensitive and highly reliable technique that enables the detection and analysis of trace elements in food play a decisive role in food nutrition and can affect production of food industry. This is especially true for further processing of vegetables that are in direct contact with pollutants present in the soil and in the air [1]. Such analytical techniques provided useful assessments for safe and healthy consumption of foods and in particular of fruits and vegetables. They may also provide control and in-situ monitoring of the pollutants in the surrounding environment (soil, water, air) to which food, or more generally food products, are in direct contact [2, 3]. Among available elemental analysis techniques, the laser-induced breakdown spectroscopy technique has show in recent years its great potential for rapid qualitative and quantitative analysis of materials [4, 5, 6, 7]. Because of the lack of pre-treatment of the material, speed of analysis, capacity for multi-element detection, possibility of in situ or online analysis, and high sensitivity, this technique offers an attractive solution for a wide range of industrial and agricultural applications [8]. Qualitative or quantitative measurement can be achieved with LIBS either with calibration curve or calibration-free procedure [9, 10]. Traditionally, these

method used for inorganic sample analysis such as alloys, minerals and so on. However, it is still a relative new task to apply this technique for plant or more generally for organic sample analysis [11]. Some articles have used this technique to analyze trace element in plants and in particularly in leaves and fresh vegetables [12, 13, 14, 15, 16, 17].

Folium lycii are boiled and to be drink as tea, especially in China. It has been demonstrated that some of elements are benefit for body health in it. So it's necessary to detect what elements species exist in this kind of plants. In this work, some fresh folium leaves were pressed to wafer with diameter 2 cm and thick 0.5 cm after making them insolation for a long time, nine essential micronutrients in folium lycii are detected and the relative concentration of them also obtained by using semi-quantitative analysis method.

2.Experimental set-up

The similar instrument has been described in detail elsewhere [18] and is only described briefly here. The schematic setup of the typical LIBS system is shown in Fig. 2. An Nd: YAG nanosecond laser is employed, the ns laser generates a pulse with a width of 8 nanosecond and maximum pulsed energy of 540 mJ at 1064 nm, and 170 mJ at 532 nm. Its repetition rate is 10 Hz. The laser beam focused by a plano-convex lens with 300 mm focus length and the diameter of focus spot measured by moving knife-edge method is about $150\mu m$. The plasma spectra was recorded by fast trigger Fiber Optical spectrometer with four channels (AvaSpec-2048FT-4-DT, AVANTES B. V., Holland) which has two optical fibers to cover two wavelength range 230∼435 nm and 435∼1080 nm, with an resolution of 0.08nm. A 5 cm UV fused silica lens placed in front of the sample surface to collect the emitting signal. The spectrometer is connected to the flash lamp of the laser. A sample was cleaned by distilled water before experiments, and was moved using a step motor during the spectrum accumulation in order to have a fresh surface for each laser shot. Each spectral calibration is an average of 100 spectrums each of which recorded after a laser shot. The least integral time of detected device CCD is 2 ms, 800ns delay is set for improving signal-to-background ratio. The experiments have been performed under normal atmosphere pressure and at room temperature.

3. Results and discussion

3.1 Selection of the spectral lines

The plasma temperature and electron density have a stronger dependence to the integral intensity of spectral lines, it will induce much deviation if some lines with strong interference or stronger self-absorption are included [19]. Therefore, the spectral lines selected from spectra must be isolated and with a good profile. Additionally, Stronger

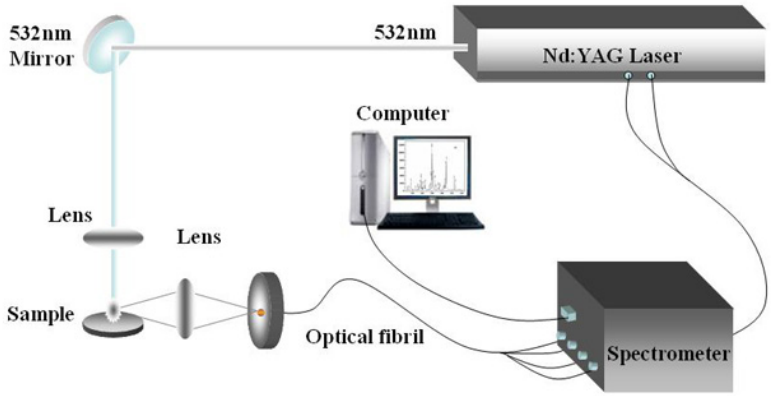

Figure 1: Schematic representation of the experimental set-up.

self-absorption lines may decrease concentration in calculating, especially resonance lines, so non-resonance lines are selected in avoiding stronger self-absorption effects[19].

Spectral lines emitted by the laser-induced plasma are broadened by a variety of mechanisms such as nature, resonance, Stark, Vander Waals and Doppler broadening. Additionally, the apparatus broadening of spectrometer increases the widths of all spectral lines as well [18]. As a results, the real spectral lines detected by spectrometer are the Vogit profile which is the convolution of Gauss and Lorentz profiles. In this work, the spectral lines used to the calculation are fitted by Vogit profiles as Fig.2 shown. During data analysis spectroscopic data for the line emissions are taken from NIST spectra database [20]. The identified elemental species mainly arise from neutral and single ionization ions. Therefore, the double and higher ionization ions are ignored in the calculation of element concentration.

3.2 Plasma temperatures

For plasma characterization, the excitation energy of a given species (given energy and given ionization degree) is in general retrieved using well known Boltzmann plot method. Assuming the LTE is established within plasma, the population in different energy levels is governed by Boltzmann distribution. The line integral intensity corresponding to the transition between two levels E_k and E_i of atomic or ion species can be expressed [18]

$$I_{ki}^{\lambda} = N_s A_{ki} \frac{g_k \exp(-\frac{E_k}{kT})}{U_s(T)} \tag{1}$$

Where λ is the wavelength of the transition, N_s is the number density (particle/cm_{-3})

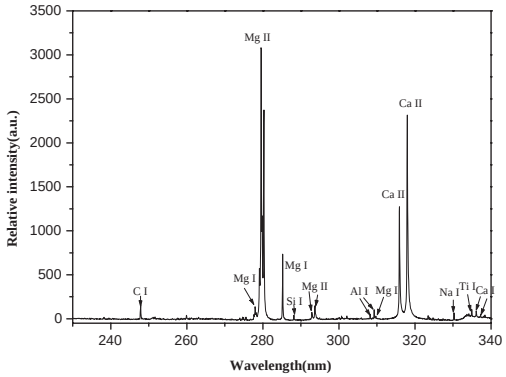

Figure 2: Typical time-integrated LIBS spectra of folium lycii.

of the emitting atoms or ions for each species, A_{ki} is the transition probability for the given line, g_k is the k level degeneracy, k is the Boltzmann constant, T is the plasma temperature, and $U_s(T)$ is the partition function for the emitting species at the plasma temperature. Therefore, the plasma temperature can be deduced from equation (1) for a given element species. Namely,

$$\ln \frac{I_1}{I_2} = -\frac{E_k^1 - E_k^2}{kT} + const \tag{2}$$

where 1 and 2 refer to the individual lines in the pair. The advantage of equation (2) for determining excitation temperature is avoidance to using transition probability and level degeneracy, because there is a much inaccuracy on atomic structure calculation about transition probability. The accuracy in the temperature determination increases with an increase in energy difference $E_k^1 - E_k^2$ in the above equation. Therefore, plotting the left hand side of equation (2) versus the excited level energy difference, the plasma temperature can be obtained from the slop of obtained straight line. In this work, the mainly spectral lines identified from spectrums comes from emission of calcium, additionally, some of these lines emitted from the same ionization stage have large energy difference. Therefore, the plasma temperature accuracy can be improved by using these lines in Boltzmann plot. According to Fig. 3, the plasma temperature is obtained from Boltzmann plot method, which is about 12697±357 K. This value will be used to calculate electron density and elements relative concentration from Saha equation as described in detail in following.

3.3 Electron density

As one of the most of important parameters in plasma the electron density could reveal

Table 1: Spectral lines for calculating plasma temperature.

Species	$\lambda(nm)$	A_{ki} $(10^8 s^{-1})$	E_k(eV)	g_k
Ca I	335.02	0.178	5.59	5.0
Ca I	336.19	0.223	5.59	7.0
Ca I	422.67	0.218	2.93	3.0
Ca I	428.30	0.434	4.78	5.0
Ca I	428.94	0.600	4.77	3.0
Ca I	429.90	0.466	4.77	3.0
Ca I	430.77	1.990	4.76	1.0
Ca I	431.87	0.740	4.77	3.0

Table 2: Electron density calculated from calcium emission lines.

Species	$\lambda(nm)$	A_{ki} $(10^8 s^{-1})$	Int.(a.u)	$N_e(10^{18} cm^{-3})$
Ca I	428.30	0.434	592.30	
Ca II	373.69	1.700	1052.60	5.592
Ca I	431.87	0.740	629.05	
Ca II	370.60	0.880	523.77	6.079
Ca I	422.67	2.180	3879.30	
Ca II	393.37	1.470	14533.00	5.467

the state of the plasma take in (weakly coupled plasma, strongly coupled plasma and degenerate plasma), and it can be obtained by using one of spectral line's half width $\Delta\lambda_{FWHM}$ for the width of stark-broadened spectral lines in plasma depends mainly on electron density N_e [19]. If conditions of LTE and optical thin fulfilled in the plasma, the Saha-Boltzmann equation can be used to calculate electron density N_e (cm^{-3}) [18],

$$N_e = 6.04 \times 10^{21} (\frac{I\lambda}{A_{ki} g_k})_{atom} (\frac{A_{ki} g_k}{I\lambda})_{ion} \exp(\frac{V - E_{atom} - E_{ion}}{kT}) \tag{3}$$

In this expression, I is a parameter from experiment, V is the ionization potential of atomic species. Table.2 shows the electron density calculated from equation (3) according to the emission lines of calcium element.

3.4 Element concentration

If only the concentration of one species of given element is obtained from equation (1), it is possible to deduct the concentration of the other ionization stages by making use of the Saha equation, which relates the concentration of consecutive ionization stages[18]:

$$\frac{N_e N_I^M}{N_A^M} = 2 \frac{(2\pi m_e kT)^{3/2}}{h^3} \frac{U_I(T)}{U_A(T)} \exp(-\frac{E_{ion}}{kT}) \tag{4}$$

where N_e is the electronic density (e/cm^3); N_A and N_I are the population of the ground state of the neutral atomic species and that of the single ionized species, respectively,

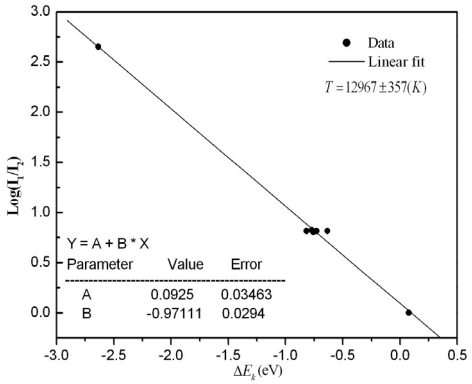

Figure 3: Boltzmann plot for several atomic lines emitted by calcium.

m_e is the mass of electron, $U_A(T)$ and $U_I(T)$ are partition function correspond to atomic and ionic species, respectively, and E_{ion} is the ionization potential of atomic species in its ground state.

Once line integral intensity I was obtained by experiment, the atomic or ion species concentration can be get from equation (1), in especially case, only one species spectral lines of neutral atomic species or ion species recorded from same element, the another species concentration can be obtained by using equation (4), so the total concentration for a given element is given by [1]

$$C_M^{tot} = C_A^M + C_I^M. \tag{5}$$

Because the intensity of spectral lines is relative so the element concentration getting from equation (1) are also relative concentration. This simple semi-quantitative analysis can be performed with carbon element as reference which is compared with other elements detected in this experiment. Fig.4 shows the relative concentration without Sr of detected elements in this experiment, because absence of atomic lines and transition parameters in NIST database. The absolutely error are as large 20% to 50%. The more precise results may be obtained by using ps laser and very short integral time.

4. Conclusions

In this article we have investigated the laser-induced breakdown spectroscopy on folium lycii, nine of essential micronutrients were identified and their relative concentrations are also obtained in this experiment condition. Based on plasma homogeneous assumption the plasma temperature and electron density have been obtained, and the elements concentrations have been calculated by using these plasma parameters from Saha-Boltzman

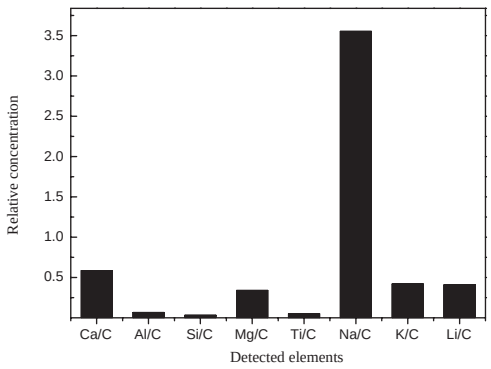

Figure 4: Relative concentration of detected elements.

equation. It is found that the results are very sensitive for selections of spectral lines.The protocol of this paper was different between calibration-free methods, the absolutely concentration may caused large deviation because the normalized factor. Some of deviation caused by effects of self-absorption will be investigated in future work. From this work, it approved that the LIBS technical used in detecting element in plant are fulfilled.

References

[1] W. Q. Lei, V. Motto-Ros, M. Boueri, Q. L. Ma, D. C. Zhang, L.J. Zhang, H. P Zeng, J. Yu, 2009 **64** 891

[2] D. Vousta, A. Grimanis, C. Samara, 1996 *Environ.Pollut.* **94** 325

[3] S. Delibacak, O. L. Elmaci, M. Secer, A. Bodur, 2002 *Int. J. Water.* **2** 196

[4] I. B. Gornushkin, J. M. Anzano, L. A. King, B. W. Smith, N. Omenetto, 1999 *Spectrochimica Acta Part B.* **54** 491

[5] D. Bulajic, M. Corsi, G. Cristoforetti, S. Legnaioli, V. Palleschi, A. Salvetti, E. Tognoni, 2002 *Spectrochimica Acta Part B.* **57** 339

[6] P. Yaroshchyk, D. Body, R.J.S. Morrison, B. L. Chadwick, 2006 *Spectrochimica Acta Part B.* **61** 200

[7] J. O. Caceres, J. Tornero Lopez, H. H. Telle, A. Gonzalez Urena, 2001 *Spectrochimica Acta Part B.* **56** 831

[8] R. Noll, V. Sturm, U. Aydin, D. Eilers, C. Gehlen, M. Hhne, A. Lamott, J. Makowe, J. Vrenegor, 2008 *Spectrochimica Acta Part B.* **63** 1159

[9] A. Ciucci, M. Corsi, V. Palleschi, S. Rastelli, A. Salvetti, E. Tognoni, 1999 *Appl. Spectrosc.* **53** 960

[10] R. Fantoni, L. Caneve, F. Colao, L. Fornarini, V. Lazic, V. Spizzichino, 2008 *Spectrochimica Acta Part B.* **63** 1097

[11] J. Yu, M. Baudelet, 2006 *French patent, number of deposit:* FR **06 51720**

[12] Q. Sun,M. Tran, B. W. Smith, J. D. Winefordner, 1999 *Can. J. Anal. Sci. Spectrosc.* **44** 164

[13] A. Assion, M. Wollenhaupt, L. Haag, F. Maiorov, C. Sarpe-Tudoran, M. Winter, U. Kutschera, T. Baumert, 2003 *Appl. Phys.* **77** 391

[14] L. C. Trevizan, D. Santos Jr., R. E. Samad, N. D. Vieira, L. C. Nunes, I. A. Runi, F. J. Krug, 2009 *Spectrochim. Acta Part B.* on line publicating

[15] O. Samek, J. Lambert, R. Hergenrder, M. Liska, J. Kaiser, K. Novotny, and Kukhlevsky, 2006 *Laser Phys. Lett.* **3** 21

[16] B. Myriam, H. Q. Zuo, M. Baudelet , J. Yu, Z. Zhang, J. Zhang, 2007 *Chin. Phys. Lett.* **24** 3406

[17] P. Miloslav, C. Tom, P. Mria, P. Petra, A. Krejcov, 2009 *J. Anal. At.Spectrom.* **24** 953

[18] W. A. Miziolek, V. Palleschi, *et.al* 2006 *Laser-induced Breakdown Spectroscopy (LIBS) Fundamentals and Applications*,Cambridge Univesity Press

[19] D. A. Cremers and L. J. Radziemski 2006 *Handbook of Laser-induced Breakdown Spectroscopy* (Chichester: John Wiley &Sons.Ltd)

[20] National Institute of standards and technology, Atomic spectra database,*http://www.nist.gov/srd/index.htm*

Transport Coefficients of Lightning Discharge Plasma on Plateau Area in China

CHANG Zhengshi, YUAN Ping, and QU Haiyan
College of Physics and Electronic Engineering, Northwest Normal University, Lanzhou, 730070,China
e-mail: yuanp@nwnu.edu.cn

Abstract

According to the 4 spectra of cloud-to-ground(CG) lightning discharge channel captured by a Slit-less spectrograph in Qinghai and Tibet plateaus, the electrical conductivities are calculated and, for the first time, the thermal conductivities of electrons and thermal diffusivities of electrons are calculated by applying the transport theory of air plasma to the lightning channels. The results are compared with literature values, in general, a satisfactory agreement. These transport characteristic parameters have more important value for further research on the current and energy of lightning discharge channel.

Keywords: electrical conductivity, lightning discharge plasma, thermal conductivity of electrons, thermal diffusivity of electrons

1.Introduction

As we know, the large current and the strong electro-magnetic radiation effect of lightning are the main roots of injury, forest-fire and the paralysis of power and communication system. Lightning, certainly, can also improve environment and climate. So, study on the physical process and characteristic parameters of lightning discharge channel is indispensable. Some of the characteristic parameters, such as the temperatures, electron densities, the particle densities of every ionized-state and pressures, have been obtained [1-7]. Besides, electrical conductivity, thermal conductivity of electrons and thermal diffusivity of electrons, which are essential parameters reflecting the transport properties of lightning channel, are also important to the research on distribution and transport characteristics of channel current and energy as well as physical mechanism of the lightning discharge process. Uman [8] obtained the electric conductivity of one flash at near peak temperature by solving the Boltzmann equation accurately. Meanwhile, Gorin et al [9] measured the conductivities of laboratory sparks. At the end of the 1990s, Rakov [10] gave the order of magnitude of lightning electrical conductivity, at more than 30000K, by modeling lightning channel as R-L-C transmission line and solving the Telegrapher equations derived from the Maxwell's equations. So far, there have been none reports

on the thermal conductivity of electrons and thermal diffusivity of electrons of lightning channel.

In this paper, according to the spectra of lightning flashes, combined with the temperatures, electron densities [5-7], pressures and the particle densities of every ionized-state [7] of lightning channels, the electrical conductivity, thermal conductivity of electrons and thermal diffusivity of electrons of lightning discharge plasma are calculated by applying the transport theory of air plasma [11-20] to the lightning channel. There is a good agreement between the electrical conductivities of lightning channels in this paper and the reported data [8-10], and the reliability for thermal conductivities of electrons and thermal diffusivities of electrons obtained is confirmed by comparing these values with the correlative data of high temperature air plasma [11] under the similar conditions. These parameters will offer reference data to the study on the distribution and transport property of the channel current and energy as well as the physical mechanism of the lightning discharge process.

2.Theoretical Method

2.1.Basic Assumptions

In order to study characteristic parameters of lightning channel, following assumptions must be made: (i) The lightning discharge channel is optically thin; (ii) the channel is in Local thermodynamic equilibrium (LTE); (iii) As far as the lightning channel is concerned, the thermodynamic properties of dry and moist air are approximately the same. The validity of these assumptions has been detailedly proved by Orville [1,21]. The study on temperature, electron density, particle densities of each ionized-state and pressure have been illuminated in references [5-7], so we won't explain any more here.

2.2.The Transport Characteristic Parameters of Lightning Plasma

Electrical conductivity represents the transport of electrons and ions duing to gradients in concentration, pressure and temperature in plasma; thermal conductivity describes the transport of thermal energy resulting from the presence of thermal gradients, chemical reactions in the plasma; thermal diffusion represents the transfer of mass from a region to another duing to a temperature gradient [11]. The calculations of these three transport characteristic parameters rely on not only temperature and particle densities of plasma but also the collision integrals of inter-particles. While choice of inter-particles potential is very important in the calculation of collision integral of inter-particles. So we select the shielded Coulomb potential [12] as inter-particles potential according to the shielding effect of other particles to colliding particles.

In addition, the study on particle density [7] of lighting plasma indicates that the

relative concentration of particles with thrice or higher ionization degree is so low that their contribution to characteristic parameters of lightning channel can be neglected. Therefore, the components of channel are mainly N, N^+, N^{2+}, O, O^+, O^{2+}, Ar, Ar^+, Ar^{2+} and electrons. The collisions between electron and electron as well as electron and singly or secondly ionized atoms are chiefly considered in the calculation. The collision integrals for interactions between particles i and j are defined as [13-15]

$$Q_{ij}^{(l,s)} = \frac{4(l+1)}{(s+1)![2l+1-(-1)^l]} \cdot \int_0^\infty exp(-\gamma^2)\gamma^{2s+3} Q_{ij}^{(l)}(g) d\gamma \tag{1}$$

$Q_{ij}^{(l)}(g)$the transport cross-section

$$Q_{ij}^{(l)} = 2\pi \int_0^\infty (1 - cos^l\theta) b db \tag{2}$$

where, $\gamma = \sqrt{\frac{\mu_{ij}}{2kT}} g$, g is the initial reduced relative speed of the colliding particles, μ_{ij} the reduced mass, b the impact parameter, θ the deflection angle, which is a function of b , g, and $V(r)$, here

$$\theta = \pi - 2b \int_0^\infty \frac{dr}{\sqrt{1 - \frac{2V(r)}{\mu_{ij} g^2} - (\frac{b}{r})^2}} \tag{3}$$

and $V(r)$ is the inter-particles potential (the shielding Coulomb potential)

$$V(r) = \frac{1}{4\pi\varepsilon_0} \frac{Z_i e^2}{r} \exp(-\frac{r}{\lambda_D}) \tag{4}$$

λ_D is Debye length

$$\lambda_D = [\frac{e^2}{\varepsilon_0 k} \frac{1}{T} (n_e + \sum_{i \neq e} Z_i^2 n_i)]^{-\frac{1}{2}} \tag{5}$$

where, n_e is the electron density, n_i the particle density, T the temperature of the lightning channel, k the Boltzmann's constant, ε_0 the dielectric constant in vacuum, Z_i the partition function.

From Eqs.(1) to (5), collision integral [13,17] could be acquired. And then, electrical conductivity, thermal conductivity of electrons and thermal diffusivity of electrons of lighting channel are expressed as follow:

Electrical Conductivity [15]

$$\sigma = 3n_e^2 e^2 \sqrt{\frac{\pi}{2m_e kT}} \begin{vmatrix} q^{11} & q^{12} \\ q^{21} & q^{22} \end{vmatrix} \left(\begin{vmatrix} q^{00} & q^{01} & q^{02} \\ q^{10} & q^{11} & q^{12} \\ q^{20} & q^{21} & q^{22} \end{vmatrix} \right)^{-1} \tag{6}$$

Thermal conductivity of electrons[15]

$$\lambda_e = \frac{75n_e^2k}{8}\left(\frac{2\pi kT}{m_e}\right)^{\frac{1}{2}} q^{22}\begin{vmatrix} q^{11} & q^{12} \\ q^{21} & q^{22} \end{vmatrix}^{-1} \tag{7}$$

Thermal diffusivity of electrons [15]

$$D_e^T = \frac{15n_e^2\sqrt{2\pi m_e kT}}{4}\begin{vmatrix} q^{01} & q^{02} \\ q^{21} & q^{22} \end{vmatrix}\left(\begin{vmatrix} q^{00} & q^{01} & q^{02} \\ q^{10} & q^{11} & q^{12} \\ q^{20} & q^{21} & q^{22} \end{vmatrix}\right)^{-1} \tag{8}$$

Where, q^{mp} elements [15] are determined from the electron density, particle density and collision integral in lightning channel.

3. Results and Analysis

During the interval 2002-2004, a number of spectrograms (original spectra) of CG lightning channel, which are time-integrated slit-less spectra of whole channel outer cloud, were recorded by a slit-less spectrograph in Qinghai and Tibet plateaus. In this work, four of these spectrograms have been chosen and listed in Fig. 1, and the relative intensity distribution of lines at a given position where the channel are straighter and good resolving of lines in each spectrograms are also given in Fig. 2. The time when the lightning took place has been given under each figure.

On the basis of temperature, electron density, pressure and the particle densities mentioned above, applying transport theory of air plasma to lightning channel, and considering the collisions between electrons as well as electron and N^+, N^{2+}, O^+, O^{2+}, Ar^+, Ar^{2+}, the electrical conductivities, thermal conductivities of electrons and thermal diffusivities of electrons of lightning discharge plasma are calculated from equation (6), (7), (8). And the results are listed in table 1. Where, the rows represent temperature T, electron density N_e, pressure P, electrical conductivity σ, thermal conductivity of electrons λ_e and thermal diffusivity of electrons D_e^T, respectively. It can be seen from table 1 that the mean value of electrical conductivity of lightning discharge plasma obtained in this work is about $2.34\times\ 10^4$ S m^{-1}. Previous study about electrical conductivity of lightning channel is quite few. Uman [8] got the electrical conductivity of 1.80×10^4 S m^{-1} in lightning channel at 24000K (near peak temperature). The electrical conductivity of lightning channel also obtained by Rakov [10], which is of the order of magnitude of 10^4 S m^{-1} at channel temperature not less than 30000K. It can be seen that except for a small difference caused by difference of temperature, air density and other regional factors among different lightning and regions, the present electrical conductivities and values of Uman and Rakov, in general, agree well. Moreover, the electric conductivity of

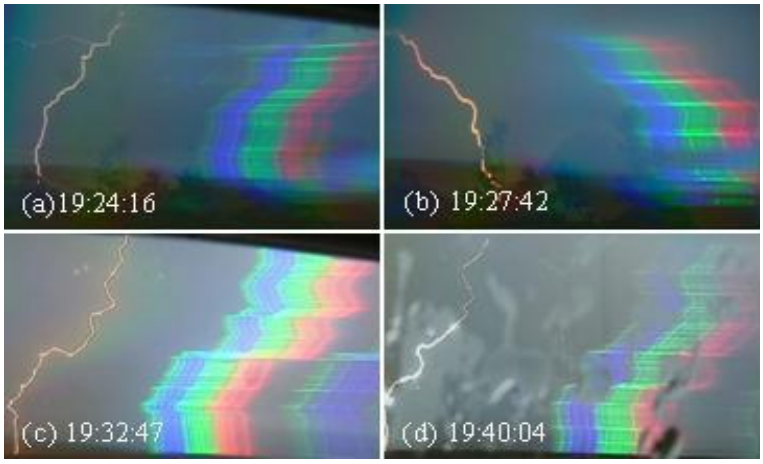

Figure 1: spectrogram of CG lightning discharge in Qinghai and Tibet.

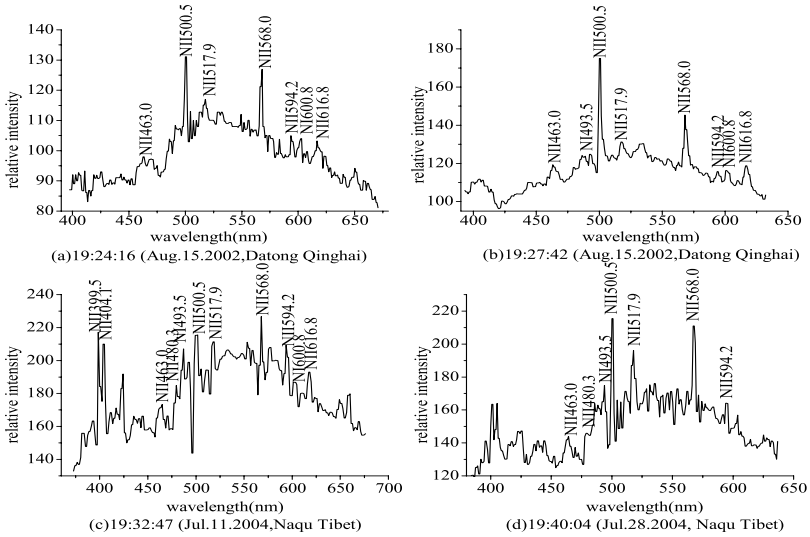

Figure 2: The relative intensity distributions of lines in the spectra at a given position.

spark discharge measured by Gorin et al. is 1.0×10^4-5.0×10^4 S m^{-1} [9] at 20000-40000K, while the electrical conductivities in this work are just in this range. And Capitelli [11] et al. found that electrical conductivities of high temperature air plasma were 1.402×10^4 S m^{-1} and 1.399×10^4 S m^{-1} when the pressure was 1atm and the temperature was approximate to lightning discharge plasma. According to D'Angola [18] et al. obtained that electrical conductivity was positive correlation with pressure at least between 15000K and 30000K, and all the pressures are higher than 10atm (certainly higher than 1atm) and temperatures are higher than 28000K in this work, so these are also reasonable that the present electric conductivities are bigger than air plasma under close temperature and 1atm. Analysis above shows the validity of the electrical conductivities we get and the

Table.1 Transport properties of different lightning discharge return in two regions.

Properties coefficients	This work				Other works				
	Datong(Qinhai)		Naqu(Tibet)		Lightning		lab.spark[9]	Air plasma[8]	
	19:24:16	19:27:42	19:32:47	19:40:04	Uman[8]	Rakov[10]			
$T(\times10^4)$ [K]	2.855	2.853	2.913	2.950	2.40	$\geq$3.00	2.00$\sim$4.00	2.80	3.00
$N_e(\times10^{18})$ [cm^{-3}]	1.866	1.774	1.780	1.466	4.30				
P [atm]	14.24	13.52	13.75	11.34				1.0	1.0
$\sigma(\times10^4)$ [S/m]	2.369	2.344	2.375	2.292	1.8	$\sim^\star$	1.0$\sim$5.0	1.402	1.399
λ_e [W/(m·K)]	8.524	8.429	8.767	8.642				5.300	5.926
$D_e^T(\times10^{-7})$ [kg/(m·s)]	1.968	1.952	2.029	2.016				1.414	1.560

Note: * means that the magnitude of electric conductivity is 10^4S/m when temperature is higher than 30000K.

reasonableness of the method used in this paper. And further infer the validity of thermal conductivity of electrons and thermal diffusivity of electrons as follow.

Up to now, there are no reports on thermal conductivity of electrons and thermal diffusivity of electrons of lightning discharge plasma. So in table 1 only air plasma's values under similar conditions are listed for reference. In the table, thermal conductivities of electrons of 4 lightning channels, whose pressures are higher than 10atm, are about 8.59 W m^{-1}K^{-1} . And Capitelli [11] et al. found that the values of high temperature air plasma, under 1 atm, are 5.300 W m^{-1}K^{-1} and 5.926 W m^{-1}K^{-1}. According to D'Angola's [18] research that (at least at 15000K-30000K) the thermal conductivity is positive correlation with pressure at the same temperature, it is reasonable that the result in this work is higher than that of Capitelli et al, because our pressure 10 atm is higher than Capitelli et al's.

The thermal diffusivities acquired here is are about 2.0×10^{-7} kg m^{-1} s^{-1}. And the data of air plasma [11]are 1.414×10^{-7} kg m^{-1}s^{-1} and 1.560×10^{-7} kg m^{-1} s^{-1}. As the study [17] on transport characteristics indicates thermal diffusivity of double temperatures N_2-O_2 plasma (at least at 15000K-45000K) is positive correlation with pressure, it is reasonable that our result is higher than air plasma's, because the pressure 10 atm in this work is higher than air plasma's 1 atm.

From discussion above, we can see that the thermal conductivity of electrons and ther-

mal diffusivity of electrons obtained for the 4 lightning channels are reasonable.

3. Conclusion

Applying transport theory of air plasma to study on physical characteristics of lightning channel, electrical conductivities, thermal conductivities of electrons and thermal diffusivities of electrons of 4 lightning channels have been obtained by spectral analysis. The electrical conductivity is about 2.34×10^4 S m^{-1}, which is in a good agreement with the reported values. Thermal conductivity of electrons is about 8.59 W m^{-1} K^{-1} and thermal diffusivity of electrons is about 2.0×10^{-7} kg m^{-1} s^{-1}. Compared with the values of air plasma under similar conditions, these two parameters, in general, are reasonable.

References

[1] R. E. Orville,J. Atmos. Sci., **25**,839(1968).
[2] M. A. Uman, J. Atmos and Terre. Phys.,**26**,123(1964).
[3] M. A. Uman, and R. E. Orville, J. Geophys. Res.,**69**,5151(1964).
[4] M. A. Uman, R. E. Orville, and L.E.Salanave, J. Atoms Sci., **21**, 306(1963).
[5] Y. H. Ouyang et al, Spectrosc. Spect. Anal.,**26**, 1988(2006).
[6] J. Wang et al,Science in China Series D: Earth Sciences, **39**,229(2009).
[7] J. Wang et al, Spectrosc. Spect. Anal.,**28**, 2003(2008).
[8] M. A. Uman, J. Atmos and Terre Phys., **26**, 1215(1964).
[9] B. N. Gorin, and A.Ya. Inkov, **7**,235(1962).
[10] V. A. Rakov, J. Geophys Res., **103**,1879(1998).
[11] M. Capitelli et al, Eur. Phys. J. D., **11**, 279(2000).
[12] R. L. Liboff, Phys. Fluid., **2**, 40(1959).
[13] M. Capitelli et al, Thermophys. Heat Transf., **14**,259(2000).
[14] M. Capitelli et al, Plasma Chem and Plasma Proc.(Supplement), **16**,267S(1996).
[15] R. S. Devoto, Phys. Fluid., **10** ,2105(1967).
[16] R. S. Devoto, Phys. Fluid., **19** ,22(1976).
[17] S. Ghorui et al, Plasma Chem and Plasma Proc., **28**,553(2008).
[18] A. D'Angola et al, Eur. Phys. J. D., **46**,129(2008).
[19] V. Colombo, E. Ghedini and P. Sanibondi, Progress in Nuclear Energy, **50**, 921(2008).
[20] D. Han et al, Chin. Phys. Lett., **24**, 2297(2007).
[21] R. E. Orville, J. Atmos. Sci., **25**, 852(1968).

Electron Scattering Experiments for studies of Atomic Processes

Y. Sakai*, K.Yamamoto*, N.Umeda†, L.F.Zhu‡§, Z.S.Yuan‡§, N.Miyauchi*, N.Nakamura †, C.Yamada†, K.Z.Xu‡§, S.Ohtani†, and T. Watanabe†¶

* Dept. of physics, Toho University, Chiba 274-8510, Japan
† Inst. for Laser Science, University of Electro-Communications, Tokyo 182-8585, Japan
‡ Hofei National Lab. for Physical Science at Microscale, Hofei 230026, China
§Dept. of Modernphyasics, University of Science and Technology of China, Hofei 230026, China
¶ Dept. of physics, Tokyo Metropolitan University, Tokyo 192-0364, Japan

Abstract

Electron scattering experiments have the capability for studies of atomic processes. In particular, the electron energy-loss spectroscopy is one of the powerful tools for these studies. We have measured electron energy-loss spectra of some simple molecules and rare gas atoms as the project of the JSPS-CAS Core-University Program since 2001. In this paper, we picked up three topics from among some experimental results. One is a measurement of generalized oscillator strength(GOS) of the nitric oxide. In this study, we had found that the GOS curves determined from the electron energy-loss spectra show a strange behavior in small momentum transfer region. The theoretical calculations cannot reproduce this strange behavior. The second is about the sub-shell excitation of rare gas atoms. When sub-shell excitation levels are coupled to the ionization continuum, the spectra have feature structures that are called Fano profile. We had found that the line profile depends on the incident electron energy and the scattering angle. Finally, the development of the scattered electron–ion coincidence (SEICO) experiments is described. In the SEICO experiments, because we can select an electric excitation state, the information similar to photo-dissociative ionization can be obtained in spite of the electron scattering experiments.

.

Keywords: electron energy-loss spectroscopy, generalized oscillator strength Fano profile, coincidence experiment

1.Introduction

In order to study atomic and molecular processes in plasma we have carried out the electron scattering experiments as the project of the JSPS-CAS Core-University Program since 2001. The electron energy-loss spectroscopy is one of the powerful tools in the electron scattering experiment for these studies. We have measured the electron energy-loss spectra of atoms and molecules, and have discussed the electron scattering processes.

Since the intensity of each spectrum corresponds to the differential cross section (DCS), we can determine the quantity called generalized oscillator strength (GOS). The concept of GOS was introduced by Bethe [1] in 1930 based on the first Born approximation (FBA). It is an important property of the atom which manifests the atomic wave-function directly, and relates to other important physical constants. Essentially the GOS is a function of only scattered electron momentum, K and does not depend on the electron impact energy E.

However, similar quantity named apparent GOS can be introduced even if the FBA is not valid. Then it depends on impact energy E, too. The apparent GOS $F(K,E)$ is given by

$$F(K,E) = \frac{W}{2}\frac{k_i}{k_f}K^2\frac{d\sigma}{d\Omega} \quad . \qquad (1)$$

Where $\frac{d\sigma}{d\Omega}$ is the DCS, W is the excitation energy, k_i and k_f are the incident and scattered electron momentum, respectively. All quantities in Eq.(1) are in atomic units. The apparent GOS is a quantity which converges to the GOS as the electron energy increases.

The GOS has another key feature. The limiting value of the GOS as K^2 approaches zero gives the optical oscillator strength (OOS) whether the Born approximation is valid or not. In our studies, this feature is often used to normalize the experimental value.

In this paper, we report three experimental results, which are the measurement of GOS of the nitric oxide, the sub-shell excitation of rare gas atoms, and the development of the scattered electron-ion coincidence (SEICO) experiments.

2. Experimental set-up

The electron energy-loss spectrometer used for our experiments except for SEICO experiments is shown in Fig.1. This was in the Institute for Laser Science, University of Electro-Communications. The detail information for this apparatus has been described in the previous papers.[2,3] Briefly, the electron energy loss spectrometer consists of an electron energy selector situated in front of the interaction region to get a monochromatic electron beam and an energy analyzer to analyze the scattered electrons. Both energy selector and analyzer are simulated hemi-spherical analyzers called "Jost type" [4], and each mean trajectory radius is 50 and 80 mm, respectively. The typical energy resolution is about 50 - 70 meV full width at half maximum (FWHM) at the incident electron current over 10 nA for all incident electron energies. The energy selector is rotatable around the collision center from -5◦ to +110◦. Calibration of the scattering angles was performed by use of the symmetrical nature and the value of the scattering intensity ratio of the peaks for 2^1S excitation to 2^1P excitation in electron energy-loss spectra of helium [5]. The 2^1P excitation peak was also used for the calibration of the excitation energy.

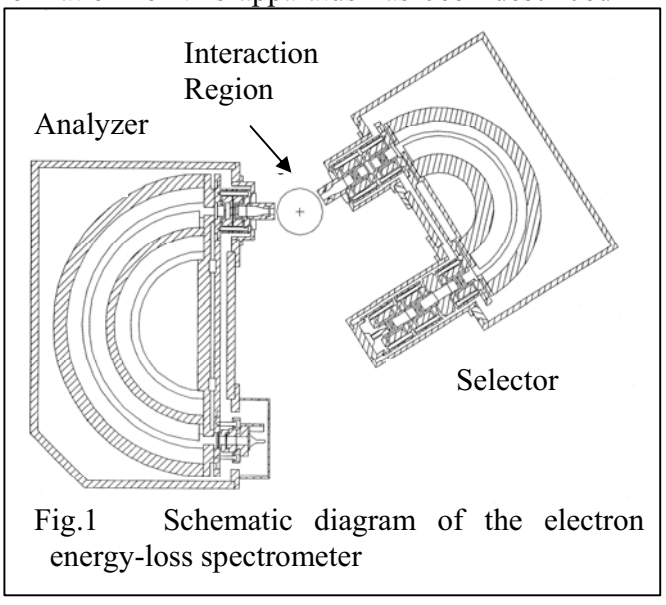

Fig.1 Schematic diagram of the electron energy-loss spectrometer

The new coincidence apparatus for SEICO experiments will be described in section 3.3. The SEICO apparatus is a kind of (e, e+ion) spectrometer, which has the capability to

measure time-of-flight (TOF) mass spectra in coincidence with energy selected inelastically scattered electrons.

3. Result and Discussion

3.1 Measurement of generalized oscillator strength of the nitric oxide

Nitric oxide(NO) is a simple diatomic molecule, which has the valence shell of $(2\pi)^1$ in the grand $X^2\Pi$state. It plays a important role in the physics and chemistry of the Earth's upper atmosphere. The reason for its importance in atmospheric chemistry is because the production and loss mechanisms for nitric oxide are strongly dependent on the interaction of the major constituents of the atmosphere (mainly N_2 and O_2) with solar radiation and energetic charged particles. However, since the generalized oscillator strengths (GOSs) of the lowest optically allowed transition($X^2\Pi^+ \rightarrow A^2\Sigma^+$) are extremely weak, there are few works reported about the differential cross sections (DCSs) and the GOSs of this transition.

In the present experiments, we have obtained the electron energy-loss spectra of NO for incident electron energies of 300 and 500 eV and the scattering angle range from 2.2 to 10 degree. Figure 2 shows the typical electron energy-loss spectrum of NO in the energy region of 5.0 – 7.8 eV. In this region, there are mainly 4 excitation states $(2\pi)^{-1}3s\sigma(A^2\Sigma^+)$, $(2\pi)^{-1}3p\pi(C^2\Pi)$, $(2\pi)^{-1}3p\sigma(D^2\Sigma^+)$, and $(1\pi)^{-1}2\pi^{-2}(B^2\Pi)$. Each state has $\gamma(X\rightarrow A^2\Sigma^+)$, $\delta(C^2\Pi)$, $\varepsilon(D^2\Sigma^+)$ and $\beta(B^2\Pi)$ bands, respectively.

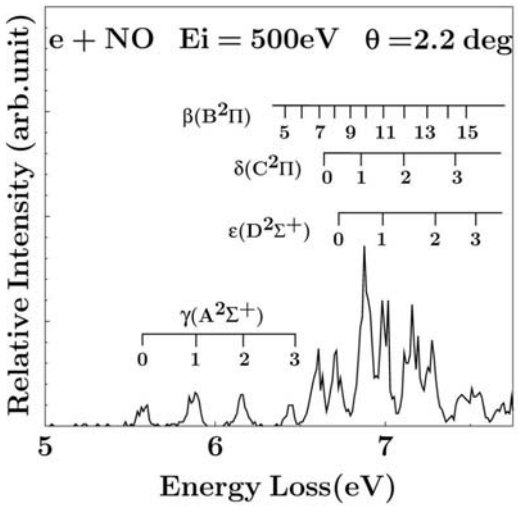

Fig.2 Electron energy-loss spectrum of NO in the energy region of 5.0 – 8.0 eV.

We used the peak of δ(v=1) for normalization. Since the peak intensity corresponds to the DCS, we can obtain the relative DCS from observed energy-loss spectra at each angle and incident energy. Using Eq.(1), we can obtain the relative GOS, too. The GOS is related with the optical oscillator strength(OOS) f_0 using the expansion formula proposed by Dillon and Lassettre[6], which is independent of the validity of the Born approximation,

$$F(K) = \frac{1}{1+x^2}\left[f_0 + \sum_{n=1}^{m} f_n \left\{ \frac{x}{(1+x^2)^{1/2}} \right\}^n \right] , \qquad x = \frac{K}{\sqrt{2I} + \sqrt{2(I-W)}} , \tag{2}$$

where f_n is a series of coefficients, and I is the ionization energy. In order to obtain the limit of the relative GOS at $K^2=0$, we have fitted the relative GOS value using the least-squares fitting method with polynominals of the form (2). Since the extrapolation of this experimental result to zero momentum transfer should be identical to the absolute OOS [7], we can determine each absolute GOS for the δ series (v=1) transition at each energy. After

each GOS is converted to the DCS, we use each DCS of the δ(v=1) transition as the normalization standard.

The determined GOS curves of γ and ε bands are shown in Fig.3. The characters at the magnitude of momentum transfer K^2=0 are the optical oscillator strength obtained by Zhu et.al.[7] Every GOS curve has a peak at K^2∼0.2. This feature is only in γ band. Although the γ band is optically allowed transition, this behavior looks like the optically forbidden ones. This behavior is similar to that of CO($X^1\Sigma^+ \rightarrow B^1\Sigma^+$) which is an optically allowed transition and N_2($X^1\Sigma_g^+ \rightarrow B^1\Sigma_g^+$) which is a forbidden transition for symmetry of parity. Therefore we think that this GOS behavior is an effect of pseudo-symmetry of parity. The theoretical calculations cannot reproduce this strange behavior.

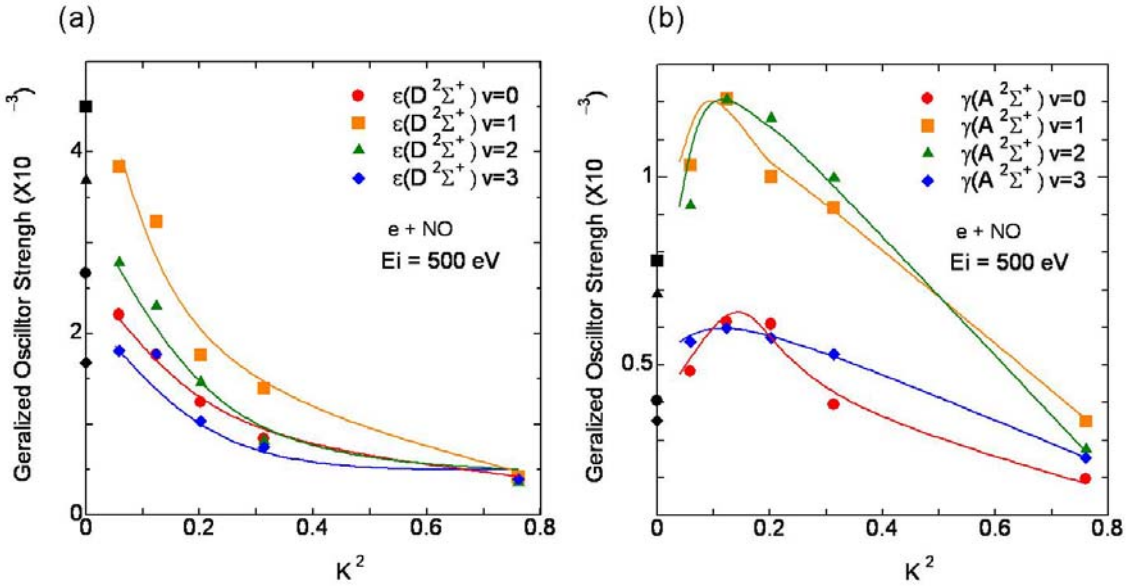

Fig.3 Generalizzed Oscillatous strengths of ε($X \rightarrow D^2\Sigma^+$) and γ($X \rightarrow A^2\Sigma^+$) transitions of NO.

3.2 Sub-shell excitation of rare gas atoms

We had also studied the sub-shell excitations like 2s excitation of neon, 3s of argon, 4s of krypton, and 5s of xenon, by electron impact. In the sub-shell excitation region the rare gas atoms are ionized either directly or via the other discrete states. Then feature shape appears to the cross section curve because discrete state is coupled to the ionization continuum. This is a window resonance, which are called Fano profile.[8] This resonance type was found first by Codling and co-workers in photo-absorption spectrum.[9,10] Brion and co-workers[11] had also found the window resonance in electron energy-loss spectra of rare atoms. They carried out the electron impact experiments at the condition of optical limit. In this case, the electron energy-loss spectra are obtained by using fast incident electrons and observing forward scattering electrons.

In the present studies, the q-parameters that characterize the Fano profiles have been obtained by using lower incident electron, about sub-shell excitations of rare gas atoms. We

had found the phenomena that the q-parameters have been changed with change of the incident energy and scattering angle. A part of result of these experiments has already been reported by our group.[12, 13]

3.3 Scattered electron – ion coincidence experiment

The third topic is about the development of the scattered electron-ion coincidence (SEICO) experiments. Figure 4 shows the schematic diagram of the SEICO spectrometer. This new spectrometer consists of a pulsed electron gun, an electron energy analyzer, and a time-of-flight (TOF) mass analyzer, which has capability to collect mass selected ions in coincidence with energy selected scattered electrons as a function of electron energy-loss[14]. The collision energies of incident electrons are 50-300 eV. The incident electrons from the pulsed electron gun collide at right angles with the target molecules effused from the nozzle (cross beam geometry). After colliding with the target molecules, electrons are analyzed with the electron energy analyzer. The typical energy resolution is about 0.5 eV (FWHM). The produced ions are extracted from the collision region by pulsed electric field, and are analyzed with the TOF mass analyzer. We use this spectrometer for non-dipole (e,e+ion) experiments.

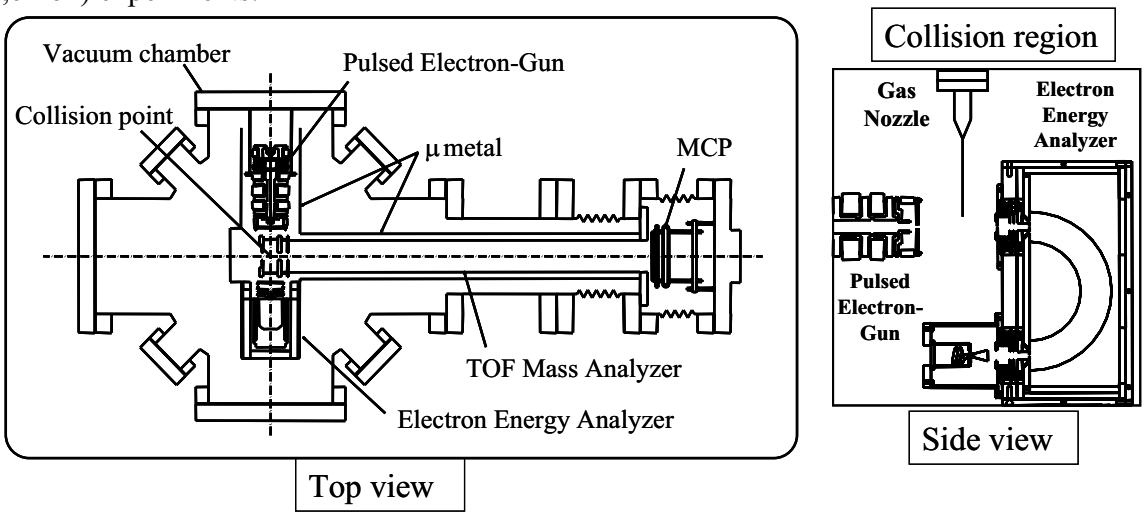

Fig.4 Schematic diagram of the SEICO spectrometer.

The ionization efficiency of molecular hydrogen by 200 eV electron impact and 7 degree scattering angle are shown in Fig.5 as a function of the energy-loss. In Fig.5, both of photo-ionization result[15] and dipole(e,e+ion) experiment one[16] are shown together for the comparison. It is a evidence of an optically-forbidden doubly excited state of molecular hydrogen that the little dip not seen in both photo-ionization and dipole(e,e+ion) spectra appeared around 28 eV energy-loss. Although it is not denied that fast H^+ ions were not detected completely, the lack of ioniza-tion efficiency above 30 eV energy-loss region indicates that a lot of optically-forbidden doubly excited states exist in this region.

4. Conclusion

In this paper, we have introduced our electron scattering experiments for the study of atomic and molecular processes as the project of the JSPS-CAS Core-University Program. The experiment on the electron scattering is very important for complete understanding of an atomic molecular process in plasma. Especially, we hope a new coincidence apparatus like SEICO spectrometer can contribute to studies on the atomic and molecular processes in plasma.

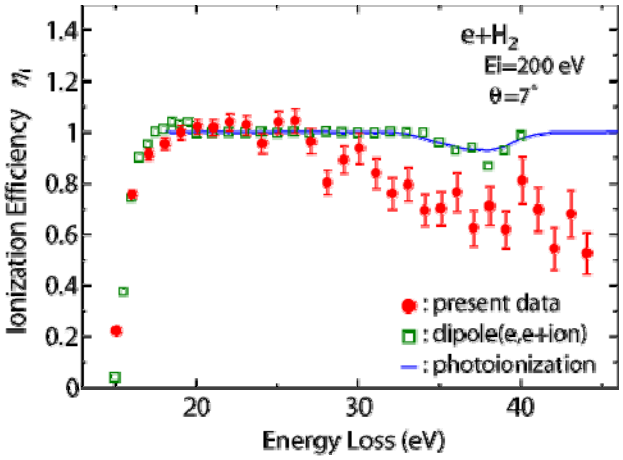

Fig.5 Ionization efficiency of H_2

Acknowledgement

This work was supported from the Core-University Program on Plasma and Nuclear Fusion.

References

[1] H. Bethe, Ann. Phys. (Leipzig) **5**, 325 (1930).
[2] G.P.Li, T.Takayanagi, K.Wakiya, H.Suzuki, T.Ajiro, S.Yagi, S.S.Kamo, and H.Takuma, Phys. Rev. A **38**,1240 (1988).
[3] T.Takayanagi, G.P.Li, K.Wakiya, H.Suzuki, T.Ajiro, T.Inaba, S.S.kano, and H.Takuma, Phys. Rev. A **41**, 5948 (1990).
[4] K.Jost, J. Phys. E **12**, 1006(1979).
[5] T. Y. Suzuki, H. Suzuki, F. J. Currell, S. Ohtani, Y. Sakai, T. Takayanagi, and K. Wakiya, Phys. Rev. A **57**, 1832 (1998).
[6] M.A.Dillon, and E.N.Lassettre, J.Chem. Phys. **62**, 2373(1975).
[7] L. F. Zhu, Z. P. Zhong, Z. S. Yuan, W. H. Zhang, X. J. Liu, X. M. Jiang, K. Z. Xu and J.-M. Li, Chin. Phys. **11**, 1149(2002).
[8] U.Fano, Phys. Rev. **124**, 1866 (1961).
[9] R.P.Madden and K.Codling, Phys. Rev. Lett. **10**, 516(1961).
[10] R.P.Madden D.L.Ederer, and K.Codling, Phys. Rev. **177**, 136(1969).
[11] W.F.Chan, G.Cooper, X.Guo, G.R.Burton, and C.E.Brion, Phys. Rev. A **46**,149(1992).
[12] Y. Sakai, 2006 *NIFS-PROC-73* 108.
[13] Z.S.Yuan, Y.Sakai, N.Umeda, Y.Fujita, T.Takayanagi, C.Yamada, N.Nakamura, S.Ohtani, L.F.Zhu, and K.Z.Xu, J.Phys. B **39**, 5097(2006).
[14] K. Yamamoto, N. Miyauchi, S. Yamada and Y.Sakai, 2008 *NIFS-PROC-73* 145.
[15] Y. M. Chung, E.-M. Lee, T. Masuoka, and James A. R. Samson., J. Chem. Phys., **99**, 885 (1993).
[16] C Backx, G R Wight and M J Van der Wiel., J. Phys. B, **9**, 315 (1976).

AMPP09

Oct 26-31,2009,Xian,China

The Second Announcement

The 3rd China-Japan Joint Seminar on Atomic and Molecular Processes in Plasma (AMPP09)

October 26 – 31, 2009, Xian, China

In this announcement we would like to give some more information about AMPP09.

➢ Pre-registration

It's recommended that you should pre-register in the conference pre-register system as soon as possible (before 15 Sept., 2009). If you don't prefer to register on-line, you also can fill in the txt form in the attachment named "information.txt" and email it to dingxb@nwnu.edu.cn. It is important for the arrangement of the hotel and scientific program. For the attendee, who had already registered, doesn't need to register again.

➢ Abstract

The abstract should be written in English and not more than 1 page. It should put the emphasis on new developments or at least reflect the progress on the related scope. The *Latex* and Microsoft Word® template and instruction for preparation of abstract are provided in the seminar website (http://www.nwnu.edu.cn/ampp/AMPP09/). You can just edit the template file without modifying other configuration of the page. It is recommended to submit the abstract and related files by email ~~it~~ to dingxb@nwnu.edu.cn . After you send your abstract, a short receipt will be sent to you in 1 or 2 days in order to make sure we have got your abstract.

Please keep in mind: The deadline for submission of abstract is 1st Oct., 2009.

➢ Talk and Proceeding

1. All the participants who give a contribution are arranged an oral presentation for about 40 minutes (30 minutes will be for talk, and 5-10 minutes for discussion).
2. We will supply the screen display system that is connected with a PC. A Windows-based PC with Acrobat Reader and PowerPoint 2003 is available. The users are requested to supply their presentation by flash disk.
3. The contributions to this seminar will be published as one issue of the NIFS science report series. It's better to take your full paper when you take part in the seminar. The template of full paper can be downloaded from the seminar website a little later.
4. The contributions to this seminar will also be submitted to Plasma Science and Technology (IOP). It's recommended to take the full paper when you attend the seminar. And every participant will possibly be arranged to cross review the paper.

➢ Poster

If you would like to show more works, you can bring a poster with you. The size of the poster should be smaller than 60cm×90cm. After you registered, you can give it to the local organizers, and the local organizers will arrange the poster session during the seminar.

➢ Arrival and Accommodation

The local organizers will be looking forward to your arrival in Xian Jiaoda Nanyang Hotel on Oct. 26, 2009. All the participants can take taxi or airport bus to go to the hotel. It will take 40 minutes from the Xianyang airport to the hotel.

Registration would be made in the reception desk when you arrive at the hotel. For convenience of the arrangement, all the participants are encouraged to inform their arrival and departure dates, times, and the flight numbers to dingxb@nwnu.edu.cn in advance.

Hotel rooms will be arranged for all the participants by the local organizers.

➢ Weather and Temperature

The weather is likely to be warm and dry in Xian but the temperature difference between the day and night is quite big (about 20℃ in day and 10℃ in night). We suggest you to bring a thin coat with you.

Contact

Prof. Dr. Dong Chenzhong
Email: dongcz@nwnu.edu.cn
Phone: +86-(0)931-7972416, 7971503
Fax: +86-(0)931-7971277
Mail: Northwest Normal University,
Anning East Road 967, Anning, Lanzhou
730070 China

Dr. Fumihiro Koike
Email: koikef@kitasato-u.ac.jp
Phone: +81-(0) 42-778-9225, 8029
Fax: +81-(0) 42-778-8441
Mail: Kitasato University, Kitasato
1-15-1 Sagamihara
228-8555 Japan

Seminar Secretary

Dr. Ding Xiaobin
Email: dingxb@nwnu.edu.cn
Alternative Email: ding.xiaobin2004@gmail.com
Phone: +86-(0)931-7971148

For more information, please visit: http://www.nwnu.edu.cn/ampp/AMPP09/

The 3rd China-Japan Joint Seminar on Atomic and Molecular Processes in Plasmas

Scientific Program

Monday, October 26: Welcome

08:30 – 18:00 Arrival and Registration

18:00 – 19:30 Welcome Reception

Tuesday, October 27: Sessions 1 - 4

07:00 – 08:10 Breakfast

08:30 – 09:10 Opening Remarks (Chair: Prof. Chenzhong Dong)

i. T. Kato, Opening Speech.

ii Wang Limin, President of Northwest Normal University, China

iii Wan Baonian, Institute of Plasma Physics, Chinese Academy of Sciences

iv F. Koike, delegate of AMPP 2009

v Taking a Photo for all participants

09:20 – 10:40 Session 1 (Chair: Prof. Li Jiamin)

1. Undecided
   Tu-nan Chang, University of Southern California, USA
2. Behavior of carbon ions during radiation collapse and non- radiation collapse
   Takako Kato, NIFS, Japan

10:40 – 11:00 Coffee break

11:00 – 12:20 Session 2 (Chair: Dr. F. Koike)

3. Collision processes related to heavy ion beam probe diagnostics
   Masaki Nishiura, NIFS, Japan
4. A scenario to provide atomic data for fusion research in the stage of precision physics
   Jiamin Li, Shanghai Jiao Tong University, China

12:20 – 14:10 Lunch Break

14:30 – 16:30 Session 3 (Chair: Prof. Tu-nan Chang)

5. Electron Correlation Effects of Heavy Atomic Ions in EUVL Plasmas
   F. Koike, Kitasato University, Japan
6. Undecided
   Yamin Zou, Fudan University, China
7. New Era of Solar Plasma Diagnostics by the EUV Imaging Spectrometer (EIS) on Board the Hinode Mission
   Tetsuya Watanabe, National Astronomical Observatory, Japan

16:30 – 16:50 Coffee break

16:50 – 18:10 Session 4 (Chair: Prof. Takako Kato)

8. Charge transfer cross section of multiply charged ions in collisions with He and H_2
   Kunikazu ISHII, Nara Women's University, Japan
9. Undecided
   Jun Jiang, Northwest Normal University, China

18:10 – 20:00 Conference Banquet

Wednesday, October 28: Session 5 - 7

07:00 – 8:10 Breakfast

08:30 – 10:30 Session 5 (Chair: Prof. H. Nishimura)

10. Charge exchange spectroscopy of multiply charged ions of astrophysical interest
    Hajime. Tanuma, Tokyo Metropolitan University, Japan
11. Photoionization of Hydrogen Atom with Screened Coulomb Interaction
    Yueying Qi, Jiaxing University, China
12. Observation of magnetic dipole forbidden transitions in LHD and its application to plasma diagnostics
    Shigeru MORITA, NIFS, Japan

10:30 – 10:50 Coffee break

10:50 – 12:10 Session 6 (Chair: Prof. Jiamin Yang)

13. Atomic and molecular processes in low temperature plasma by electron impact
    Masamitsu Hoshino, Sophia University, Japan
14. The Spectral Diagnosis and its radiative transportation
    Bin Duan, Institute of Applied Physics and Computation Mathematics, China

12:10 – 14:10 Lunch Break

14:30 – 16:30 Session 7 (Chair: Dr. A. Ichimura)

15. Electron stereodynamics in charge-asymmetric Coulomb explosion of N_2 molecules with slow highly charged ions
    Atsushi ICHIMURA, Institute of Space and Astronautical Science, Japan
16. Spectrum Simulation of Li-like Oxygen Plasma
    Banglin Deng, Sichuan University, China
17. Recoil momentum and fragmentation of molecular ions in slow collisions of $Ar^{6+} + N_2$
    Yoko INOUE, Nara Women's University, China

16:30 – 18:00 Visiting the Xi'an city

18:00 – 20:00 Dinner with local dishes

Thursday, October 29: Session 8 – 11

07:00 – 08:10 Breakfast

08:30 – 10:30 Session8 (Chair: Prof. Roger Hutton)

18. Hydrogen recycling diagnostics with excited hydrogen atoms formed above metal surfaces
    Daiji Kato, NIFS, Japan
19. Polarization degree for 3p $^2P_{3/2}$-3s $^2S_{1/2}$ transition of N^{4+} ion produced in the N^{5+}-He and N^{5+}-H_2 collisions
    Ling Liu, Institute of Applied Physics and Computation Mathematics, China
20. Recent activities at the Tokyo-EBIT (tentative)
    Nobuyuki NAKAMURA, The University of Electro-Communications, Japan

10:30 – 10:50 Coffee break

10:50 – 12:10 Session 9 (Chair: Dr. Daiji Kato)

21. Some Historic and Current Aspects of Plasma Diagnostics Using Atomic Spectroscopy
    Roger Hutton, Fudan University, China

22. X-ray polarization spectroscopy for hot electron transport in high intensity laser produced plasma
Hiroaki Nishimura, Institute of Laser Engineering, Osaka University, Japan

12:10 – 14:10 Lunch Break

14:30 – 16:30 Session 10 (Chair: Prof. Yamin Zou)

23. Study of excitation and relaxation processes of multiply excited Ne by means of soft x-ray spectroscopy
Masaki Oura, RIKEN SPring-8 Center, Japan

24. Investigations on X-ray Emission Spectra from Laser-produced Al Plasmas
Yang Jiamin, Research Center of Laser Fusion, Chinese Academy of Engineering Physics, China

25. Spectroscopy of Highly Charged Ions in Electron Beam Ion Trap (tentative)
Hiroyuki Sakaue, NIFS, Japan

16:30 – 16:50 Coffee break

16:50 – 18:50 Session 11 (Chair: Dr. H. Tanuma)

26. Electron Scattering Experiments for Studies of Atomic Processes
Yasuhiro Sakai, Toho University, Japan

27. The satellites of La1 X-Ray transitions spectra of 4d transition metals for lead as predicted by HFS calculations.
Surendra Poonia, Division of Natural Resources and Environment, Central Arid Zone Research Institute, India

28. Analyses of EUV Spectra from Xenon, Tin and Tungsten Ions Observed in LHD Plasmas
Chihiro Suzuki, NIFS, Japan

29. Ion beams with glass capillaries
Takao M. Kojima, RIKEN, Japan

18:50 – 20:00 Conference Banquet by the Organizer Committeee of the Seminar

Friday, October 30

9:00 – 16:30 Session 12

Individual discussions on the future prospect of collaborative activities

18:00 – 20:00 Dinner

Saturday, October 31:

07:00 – 08:10 Breakfast

08:30 –09:30 Overall Discussions

09:45 – 10:30 Summary talks

i. F. Koike, Kitasato University

ii. Dong Chenzhong, Northwest Normal University

Adjourn

List of Participants

Participant		Affiliation	E-mail address
Atsushi	Ichimura	Institute of Space and Astronautical Science	ichimura@isas.jaxa.jp
Banglin	Deng	Sichuan Univeristy	hanoi_1314@163.com
Bowen	Li	Northwest Normal University	libw2007@gmail.com
Cheng	Gao	Naitional Defense University	gaocheng@nudt.edu.cn
Chenzhong	Dong	Northwest Normal University	dongcz@nwnu.edu.cn
Chihiro	Suzuki	National Institute for Fusion Science	csuzuki@lhd.nifs.ac.jp
Daiji	Kato	National Institute for Fusion Science	kato.daiji@nifs.ac.jp
Denghong	Zhang	Northwest Normal University	zhangdh@nwnu.edu.cn
Duixiong	Song	Northwest Normal University	sdx_0102@126.com
Fumihiro	Koike	Kitasato University	koikef@kitasato-u.ac.jp
Guoli	Wang	Northwest Normal University	wanggl@nwnu.edu.cn
Hajime	Tanuma	Tokyo Metropolitan University	tanuma@phys.metro-u.ac.jp
Hiroaki	Nishimura	Osaka University	nishimu@ile.osaka-u.ac.jp
Hiroyuki	Sakaue	National Institute for Fusion Science	sakaue@nifs.ac.jp
Huihui	Kang	Northwest Normal University	lzkhh2009@163.com
Jiamin	Yang	Research Center of Laser Fusion, CAEP	yjm70018@my-public.sc.cninfo.net
Jia-Ming	Li	Shanghai Jiao Tong University	lijm@sjtu.edu.cn
Jianguo	Wang	Institute of Applied Physics and Computational Mathematics	wang_jianguo@iapcm.ac.cn
Jianjie	Wan	Northwest Normal University	jack_wan1982@163.com
Jianmin	Yuan	Naitional Defense University	jmyuan@nudt.edu.cn
Jiguang	Li	Northwest Normal University	phys_ljg@yahoo.com.cn
Jiyan	Zhang	Research Center of Laser Fusion, CAEP	zhangjiyanzjy@sina.com
Jun	Jiang	Northwest Normal University	phyjiang@yeah.net
Jun	Wang	Jiangsu University	qc001@ujs.edu.cn
Kunikazu	Ishii	Nara Women's University	ishii@cc.nara-wu.ac.jp
Ling	Liu	Institute of Applied Physics and Computational Mathematics	liu_ling@iapcm.ac.cn
Luyou	Xie	Northwest Normal University	xiely@nwnu.edu.cn
Maogen	Su	Northwest Normal University	sumg@nwnu.edu.cn
Masaki	Nishiura	National Institute for Fusion Science	nishiura@nifs.ac.jp
Masaki	Oura	RIKEN SPring-8 Center	oura@spring8.or.jp

Masamitsu	Hoshino	Sophia University	masami-h@sophia.ac.jp
Nobuyuki	Nakamura	The University of Electro-Communications	n_nakamu@ils.uec.ac.jp
Pengcheng	Li	Northwest Normal University	lipc@nwnu.edu.cn
Ping	Yuan	Northwest Normal University	yuanp@nwnu.edu.cn
Roger	Hutton	Fudan University	rhutton@fudan.edu.cn
Shigeru	Morita	National Institute for Fusion Science	morita@nifs.ac.jp
Shixian	Qu	Shanxi Normal University	sxqu@snnu.edu.cn
Takako	Kato	National Institute for Fusion Science	kato.takako@nifs.ac.jp
Takao	Kojima	RIKEN	kojima@riken.jp
Tetsuya	Watanabe	National Astronomical Observatory	watanabe@uvlab.mtk.nao.ac.jp
Tu-Nan	Chang	University of Southern California	tnchang@usc.edu
Wei	Wang	Sichuan University	arthurpandm@yahoo.com
Wenfeng	Luo	Xi'an Institute of Optics and Precision Mechanics, CAS	luowf@opt.ac.cn
Xiangli	Wang	Northwest Normal University	wxl2002wxl@163.com
Xiaobin	Ding	Northwest Normal University	dingxb@nwnu.edu.cn
Xiaobin	Liu	Northwest Normal University	liuxb_tsts@sohu.com
Xiaoxin	Zhou	Northwest Normal University	zhouxx@nwnu.edu.cn
Yaming	Zou	Fudan University	zouym@fudan.end.cn
Yanbiao	Fu	Northwest Normal University	fuyb@nwnu.edu.cn
Yang	Zhao	China Academy of Engineering Physics	edwardszy@yahoo.com
Yasuhiro	Sakai	Toho University	sakai@ph.sci.toho-u.ac.jp
Yizhi	Qu	Graduate University, CAS	yzqu@gucas.ac.cn
Yoko	Inoue	Nara Women's University	bay.inoue@cc.nara-wu.ac.jp
Yong	Wu	Institute of Applied Physics and Computational Mathematics	wu_yong@iapcm.ac.cn
Yueying	Qi	Jiaxing University	qi_yying@yahoo.com.cn